CRYSTAL STRUCTURES OF INTERMETALLIC COMPOUNDS

Edited by

J. H. Westbrook

Brookline Technologies, Ballston Spa, New York, USA

and

R. L. Fleischer

Union College, Schenectady, New York, USA

JOHN WILEY & SONS, LTD

Chichester · New York · Weinheim · Brisbane · Singapore · Toronto

Baffins Lane, Chichester,
West Sussex PO19 1UD, England

National 01243 779777
International (+44) 1243 779777
e-mail (for orders and customer service enquiries): cs-books@wiley.co.uk
Visit our Home Page on http://www.wiley.co.uk
or http://www.wiley.com

Other Wiley Editorial Offices

John Wiley & Sons, Inc., 605 Third Avenue,
New York, NY 10158-0012, USA

WILEY-VCH Verlag GmbH, Pappelallee 3,
D-69469 Weinheim, Germany

Jacaranda Wiley Ltd, 33 Park Road, Milton,
Queensland 4064, Australia

John Wiley & Sons (Asia) Pte Ltd, 2 Clementi Loop #02-01,
Jin Xing Distripark, Singapore 129809

John Wiley & Sons (Canada) Ltd, 22 Worcester Road,
Rexdale, Ontario M9W 1L1, Canada

Library of Congress Cataloging-in-Publication Data

Crystal structures in intermetallic compounds / edited by J. H. Westbrook and R. L. Fleischer.
p. cm.
'This volume is one of four now being published, each of which consists of reprints of chapters from the 1995 comprehensive two-volume set—Intermetallic compounds, principles and practice . . . selected sets of chapters are collected, each set being on a single theme . . . reprint volume 1'—Pref.
Includes bibliographical references and index.
ISBN 0-471-60880-7 (pbk. : alk. paper)—ISBN 0-471-60814-9 (set)
1. Intermetallic compounds—Structure. 2. Crystallography. 3. Alloys. 4. Physical metallurgy. I. Westbrook, J. H. (Jack Hall), 1924– II. Fleischer, R. L. (Robert Louis), 1930– III. Title: Intermetallic compounds.

TA483.C79 2000
620.1'699—dc21 99-052446

British Library Cataloguing in Publication Data

A catalogue record for this book is available from the British Library

ISBN 0 471 60880 7
ISBN 0 471 60814 9 (set)

Typeset by Dobbie Typesetting Ltd, Tavistock, Devon
Printed and bound in Great Britain by Antony Rowe, Chippenham, Wiltshire
This book is printed on acid-free paper responsibly manufactured from sustainable forestry, in which at least two trees are planted for each one used for paper production.

Dedication

To the memory of

John Herbert Hollomon
1919–1985

Wise, vigorous, effective advocate of the relevance and value of scientific research in industry.

His strong belief in the synergetic interaction of Principles and Practice in the field of metallurgy impelled him to assemble an innovative, diverse staff at General Electric, and to inspire independent exploration that benefited both science and engineering.

Contributors

Oksana Bodak
Department of Inorganic Chemistry,
L'viv State University,
Lomonosova str. 6, 290005,
L'viv 5, Ukraine

Jo L. C. Daams,
Philips Research Laboratories,
Prof. Holstlaan 4, 5656AA,
Eindhoven,
The Netherlands

Evgen Gladyshevskii
Department of Inorganic Chemistry,
L'viv State University,
Lomonosov Str. 6,
290005, L'viv 5, Ukraine

Jürgen Hauck
Institut für Festkörperforschung,
KFA Forschungszentrum,
Postfach 1913, D-52425 Jülich,
Germany

Erwin E. Hellner
Institute for Mineralogy,
Philipps University, Lahnberge,
D-35043 Marburg, Germany

Kenneth F. Kelton
Department of Physics,
Campus Box 1105
Washington University,
St Louis, MO 63310-4899, USA

Carl C. Koch
Department of Materials Science
and Engineering, North Carolina
State University, Raleigh,
NC 27695, USA

Klaus Mika
Institute für Festkörperforschung,
KFA Forschungszentrum,
Postfach 1913, D-52425 Julich,
Germany

Michael V. Nevitt
Department of Physics and
Astronomy, Clemson University,
231 Kinard Laboratory,
Clemson,
SC 29634, USA

Erwin Parthé
Department of Inorganic Chemistry,
Université de Genève,
Quai Erenest Ansermet 30,
CH-1211, Geneva 4, Switzerland and
Institute for Mineralogy and
Crystallography, Universität Wien,
Geozentrum, Althanstrasse 14 A-1090,
Vienna, Austria

David G. Pettifor
Department of Materials,
University of Oxford,
Parks Road, Oxford
OX1 3PH,UK

Roland Schwartz
Institute for Mineralogy,
Philipps University,
Lahnberge, D-35043 Marburg,
Germany

Walter L. Roth
1552 Baker Avenue,
Schenectady,
NY 12309, USA

Pierre Villars
Intermetallic Phases Data Bank
(IPDB) and Materials
Phases Data System (MPDS),
PO Box 1, CH-6354 Vitznau,
Switzerland

De hoc, multi noscunt multa,
omnes aliquid nemo satis,

(Concerning this, many know much,
each a little, none enough.)

—anonymous Latin epigram

Preface to the 1995 Edition

Intermetallic compounds were last comprehensively reviewed in 1967 in a volume that was edited by one of us (JHW). At that time the field was described as of special interest because it was undergoing 'exponential proliferation'. That trend continues to the present. The number of intermetallic entries in the Permuterm Subject Index shows a doubling period of less than nine years, having reached roughly 1800 entries per year in 1993. Apart from scholarly interest, intermetallics have now become of substantial commercial significance; for some, such as Ni_3Al, world-wide use is in the 1000s of tons; for others, for example III–V semiconducting compounds, although the quantities employed are not in tonnage numbers, their value as vital components of electronic circuits is in the billions of dollars.

From the 1967 book we remind the reader that 'The first published paper dealing with intermetallic compounds appeared in 1839, and more than sixty years elapsed before . . . the first review paper by Neville in 1900. However, new results were then appearing so rapidly that fifteen years later two books were printed, devoted exclusively to this subject, one by Desch in England and one by Giua and Giua in Italy'. More recently, conference volumes that deal exclusively with intermetallics but typically only within specific, limited sub-topical subject areas have become common. The scope of the present work is as broad as that of its 1967 predecessor. However, the increased volume of activity in intermetallics and the increased significance of their applications have necessitated an expansion from the 27 chapters of the earlier work to the 75 chapters of the present treatise.

First, what are intermetallic compounds? Generally, such a compound is a structure in which the two or more metal constituents are in relatively fixed abundance ratios and are usually ordered on two or more sublattices, each with its own distinct population of atoms. Often substantial or complete disorder may obtain, as a result of low ordering energy or the intervention of some external agency, for example extreme cooling rates, radiation, etc. Deviations from precise stoichiometry are frequently permitted on one or both sides of the nominal ideal atomic ratios, necessitating a partial disorder. Here we include as intermetallic compounds all metal–metal compounds, both ordered and disordered, binary and multicomponent. Even the metal–metal aspect of the definition is often relaxed by including some metal–metalloid compounds, such as silicides, tellurides, and semiconductors. We believe this inclusion is appropriate since the phenomenology of many such compounds is nearly identical to metal–metal ones, and they provide useful examples of principles, properties, and practices.

The burgeoning literature on intermetallics and the lack of a comprehensive single source of up-to-date descriptions of where we are, what we need to know, and what we can do with intermetallics created the incentive for the present pair of volumes. This work was planned to provide state-of-the-art assessments of theory, experiment, and practice that will form a solid base for workers who wish to know more than their own particular area. Each author was asked to set forth the principles of his or her subject in terms that are meaningful to scientists and engineers who are not specialists in the author's field, and then to progress to include knowledge that workers in their own areas would wish to have. Concluding sections of most chapters give the authors' critical assessment of the state of their subject and of where they believe further effort is merited.

This work is divided into two volumes in order that each be of manageable size. The first, on the theme Principles, is directed at the science of intermetallics—how do we understand their formation, structure and properties? The Practice volume considers commercial production and engineering applications of intermetallic compounds. The reader who browses carefully will recognize that the immediacy of the practice described ranges from hoped-for use, to beginnings of use, to actual commercial application—depending on the specific subject. Some of the hoped-for uses are fated never to be realized, but the authors have aimed to reveal what the obstacles are so that the reader may make his or her own assessment (and possibly provide a solution!).

We conferred carefully with many people in order to identify authorities for each subject; having recruited contributors for the project, we then strove to assist them in achieving clarity and thoroughness from outline to draft to final manuscript. The contributors cooperated superbly, and we thank them for their hard work and high achievement. We sought experts wherever they were to be found, and our international set of nearly 100 authors turned out to be almost equally divided between the United States and 14 other countries. Manuscripts have in fact come from all inhabited continents.

We planned this work as an aid to both scientists and engineers. It can serve as a base for those who wish to know about intermetallics as an area in which to begin research. Equally it is a resource to workers who are already active in the field and need, or wish, to expand their knowledge of related science or practical technology. We expect that many chapters are appropriate source matter for special topic or seminar courses at the advanced undergraduate and various graduate school levels. It is hoped that passage of the next 25 years will reveal some influence of this treatise on the further development of this field.

As an assist to readers we have provided in the following pages a consolidated acronym list and some crystallographic tables. Nomenclature for crystal structure types is often complex, and some of the authors have introduced their own. Generally we have asked authors to include both of two commonly used types of symbols as they introduce structures. The two-part table following this preface lists many of the common types—by Strukturbericht symbol, prototype name (termed a *structure type*), and Pearson symbol. Strukturbericht symbols are only partly significant and systematic: A's are not compound structures but consist of a single lattice of atoms (except for A15!); B's are equiatomic ordered structures; C's have 2-to-1 atomic abundance ratios, D0's 3-to-1. Structure type compounds are the specific ones used to designate a particular structure. Thus B2 compounds are also referred to as CsCl compounds. Many structures are better known to metallurgists and mineralogists by names other than the formula of the structure type chosen by crystallographers, e.g. Laves, fluorite, Heusler, etc. Such names have been added in selected cases. The Pearson symbols tell the crystal symmetry and the number of atoms per unit cell. Thus, B2, CsCl has a primitive (P) cubic (c) structure with 2 atoms per cell and hence the Pearson symbol (cP2). The Pearson designation is informative, but it is not necessarily unique. Although there is only one cP2 structure, Villars and Calvert list two cP4s, three cF12s and twenty-two hP9s. Thus to be definitive, both the structure type and the Pearson symbol need to be given, or the Pearson and the Strukturbericht symbol.

The index in each volume includes the subjects in *both* volumes of this work, in order that the reader may be able to locate any subject that is addressed. Although the purpose of such combined indices is not to induce the owner of a single volume to purchase the other, it possibly may help to reduce the barrier to such action.

We have benefited from outstanding secretarial help during the three years of this project, first by Phillis Liu, then Constance Remscheid at General Electric, finally Mary Carey at Rensselaer Polytechnic Institute. We appreciate the hospitality of the General Electric Research and Development Center during the inception and middle period of preparing these volumes. Assembling the final product has been eased for us by the continuing efforts and cheerful good counsel at John Wiley of Jonathan Agbenyega, Irene Cooper, Philip Hastings, Vanessa Lutman and Cliff Morgan.

J. H. WESTBROOK, *Ballston Spa, New York*
R. L. FLEISCHER, *Schenectady, New York*

> Upon these considerations, we have been induced to undertake the present extensive work, the purpose of which is to instruct rather than to amuse; in which nothing will be omitted that is elegant or great; but the principal regard will be shown to what is necessary and useful.
>
> —Isaac Ware, 1756

Preface to the Reprint Volumes from Intermetallic Compounds: Principles and Practice

This volume is one of four now being published, each of which consists of reprints of chapters from the 1995 comprehensive two-volume set *Intermetallic Compounds: Principles and Practice*. In the present volumes selected sets of chapters are collected, each set being on a single theme. In this format readers who are interested in a particular aspect of intermetallic compounds can have a less weighty volume specific to their subject; a volume that can be produced more economically than the full, original 1900-page set; and that includes a modest updating of the subject matter.

The subjects in most cases are taken from one or more chapter groupings of the original Volume 1 or 2: Hence reprint volume 1, *Crystal Structures of Intermetallic Compounds*, contains the ten chapters from the original work under the heading Crystal Structures; reprint volume 2, *Basic Mechanical Properties and Lattice Defects of Intermetallic Compounds*, contains three from Property Fundamentals, four chapters from Defect Structures, and two from Kinetics and Phase Transformations; reprint volume 3, *Structural Applications of Intermetallic Compounds* contains the thirteen chapters that were under that same topic; and finally reprint volume 4, *Magnetic, Electrical, and Optical Properties and Applications of Intermetallic Compounds*, contains two chapters from the section on Property Fundamentals, seven from Electromagnetic Applications and one from Miscellaneous. Although each chapter is reprinted nearly intact (only typographic and factual errors corrected), the author or authors were given the option of adding a brief addendum in order to add whatever new perspective has arisen over the intervening few years. Some have chosen to do so; some have not, either in the preferred case because they felt none was needed or because the four-month window of opportunity they were given to satisfy our and the publisher's desire for promptness did not fit their work schedule. Corrections to the original chapters that were so lengthy that they would upset the original pagination are to be found in the addenda at the end of each relevant chapter.

Where an addendum is particularly relevant to a portion of the original chapter being reproduced, a margin mark (*) alerts the reader to refer to the added pages at the end of the chapter. Cross-references to other chapters relate to the original 1995 two-volume work, the tables of contents of which appear at the end of this volume.

JHW
RLF

Acronyms

2D	two-dimensional
3D	three-dimensional
6D	six-dimensional
ACAR	angular correlation of annihilation radiation
ACPAR	angular correlation of positron annihilation radiation
AE	atomic environment
AES	Auger electron spectroscopy
AET	atomic environment type
AIM	argon induction melting
ALCHEMI	atom location by channeling enhanced microanalysis
ALE	atomic layer epitaxy
AM	air mass
AMT	Advanced Materials Technology, Inc.
AN	atomic number
AP	atom probe
AP	atomic property
APB	antiphase boundary
APD	antiphase domain
APD	avalanche photodetector
APE	atomic property expression
APW	augmented plane wave
AR	antireflection
ARIPES	angle-resolved inverse photoemission spectroscopy
ARPES	angle-resolved photoemission spectroscopy
ASA	atomic-sphere approximation
ASW	augmented spherical wave
BC	bond charge
b.c.c.	body-centered cubic
BCS	Bardeen–Cooper–Schrieffer (theory of superconductivity)
b.c.t.	body-centered tetragonal
BH	buried heterostructure
BIS	bremsstrahlung isochromat spektroskopie
BM	Bowles–Mackenzie (theory of martensitic transformation)
BSCCO	bismuth–strontium–calcium–copper oxide
BSE	back-scattered electrons
BT	Bhatia–Thornton (partial structure factor for liquid alloys)
BW	Bragg–Williams (theory of ordering)
BZ	Brillouin zone
CAM	c-axis modulated
CANDU	Canadian deuterium–uranium (power reactor)
CAP	consolidated under atmospheric pressure
CAT	computer-assisted tomography
CBLM	cluster Bethe lattice method
CC	cluster center
CCD	charge-coupled device
CCGSE	concentric-circle grating surface-emitting (laser)
CCIC	cabled conductor in conduit
CCMAI	crystal chemical model of atomic interactions
c.c.p.	cubic close-packed
CCT	continuous cooling transformation
CD	compact disc
CD	climb dislocation
CEBAF	continuous electron-beam accelerator facility
CEF	crystalline electric field
CERN	Centre Européenne Recherche Nucléaire
CFT	concentration-functional theory
CMC	ceramic–matrix composite
CN	coördination number

CO	cubo-octahedron
CP	coördination polyhedron
CPA	coherent-potential approximation
CRSS	critical resolved shear stress
CS	chemisorption
CSF	complex stacking fault
CSL	coincidence-site lattice
CSRO	chemical short-range order
CT	chisel toughness
CTE	coefficient of thermal expansion
CVD	chemical vapor deposition
CVM	cluster variation method
CW	cold worked
CW	concentration wave
CW	continuous wave
CWM	Connolly–Williams method (theory of phase transformations)
D–A	donor–acceptor
DB	diffusion bonding
DBTT	ductile–brittle transition temperature
DC	direct chill (casting)
DC	direct current
DCA	direct configurational averaging
DF	density functional
DFB	distributed feedback
DFT	density-functional theory
DH	double heterojunction
d.h.c.p.	double hexagonal close-packed
dHvA	de Haas–van Alphen (effect)
DLZR	directional levitation zone melting
DOS	density of states
DPA	displacement per atom
DPC	demonstration poloidal coil
DRP	dense random packing
DS	directional solidification
DSC	displacement shift complete
e/a	electron/atom (ratio)
EAM	embedded-atom method
EBPVD	electron beam physical vapor deposition
ECI	effective cluster interaction
ECM	embedded-cluster method
EDC	electro-optic directional coupler
EDM	electrodischarge machining
EDX	energy-dispersive X-ray (spectroscopy)
EELS	electron energy-loss spectroscopy
EMF	electromotive force
EPI	effective pair interaction
ESF	extrinsic stacking fault
ESR	electroslag refined
ETP	electrolytic tough pitch (copper)
EXAFS	extended X-ray absorption fine structure
f.c.c.	face-centered cubic
f.c.t.	face-centered tetragonal
FENIX	Fusion Engineering International Experimental Magnet Facility
FET	field effect transistor
FIM	field ion microscopy
FLAPW	full-potential linearized augmented plane wave
FLASTO	full-potential linearized augmented Slater-type orbital
FLMTO	full-potential linearized muffin-tin orbital
FOM	figure of merit
FP	Fabry–Perot (laser)
FT	phase transformation
FZ	floating zone
GB	gain × bandwidth (product)
GB	grain boundary
GFT	glass-forming tendency
GGA	generalized gradient approximation
GITT	galvanostatic intermittent titration technique
GPM	generalized perturbation method
GRPA	generalized random-phase approximation
GS	ground state
GT	Goody–Thomas (electronegativity)
HB	horizontal Bridgman
HBT	heterojunction bipolar transistor
HCF	high-cycle fatigue
h.c.p.	hexagonal close-packed
HEMT	high-electron-mobility transistor
HIP	hot isostatic pressing
HPT	heterojunction phototransmitter
HR	high resolution
HREM	high-resolution electron microscopy
HRTEM	high-resolution transmission electron microscopy
HSCT	high-speed civil transport
HTS	high-temperature superconductor
HVEM	high-voltage electron microscopy
HVTEM	high-voltage transmission electron microscopy
IAE	irregular atomic environment
IAET	irregular atomic environment type

IC	integrated circuit
IC	investment cast
IDOS	integrated density of states
IEM	interstitial-electron model
IGC	Intermagnetics General
IHPTET	integrated high-performance turbine engine technology
ILS	invariant line strain
IMC	intermetallic compound
IMC	intermetallic matrix composite
IMC	inverse Monte Carlo (method)
IPM	independent-particle method (approximation)
IPS	invariant plan strain
IQC	icosahedral quasicrystal
IR	infrared
ISF	intrinsic stacking fault
IT	(positive) inner tetrahedron
ITER	International Thermonuclear Experimental Reactor
IV	intermediate valence
JFET	junction field-effect transistor
KKR	Korringa–Kohn–Rostoker (bond-calculation method)
KSV	Khantha–Cserti–Vitek (deformation model)
KTP	potassium titanyl phosphate
KW	Kear–Wilsdorf (dislocation locking mechanism)
LA	longitudinal acoustic (wave)
LAPW	linearized augmented plane wave
LASTO	linearized augmented Slater-type orbital
LCAO	linear combination of atomic orbitals
LCF	low-cycle fatigue
LCT	large coil task
LCW	Lock–Crisp–West (radiation analysis)
LD	laser diode
LDA	local-density approximation
LEC	liquid-encapsulated Czochralski
LED	light-emitting diode
LEED	Low-energy electron diffraction
LEISS	low-energy ion scattering spectroscopy
LHC	Large Hadron Collider
LKKR	Layered KKR (structure calculation)
LME	liquid metal embrittlement
LMTO	linearized muffin-tin orbital
LNT	liquid nitrogen temperature
LO	longitudinal optical (wave)
LPCVD	low-pressure chemical vapor deposition
LPE	liquid-phase epitaxy
LPPS	low-pressure plasma spraying
LPS	long-period superstructure
LRO	long-range order
LSDA	local spin-density approximation
LSI	large-scale integration
μSR	muon spin relaxation
MA	mechanical alloying
MAPW	modified augmented plane wave
MB	Martinov–Basanov (electronegativity)
MBE	molecular beam epitaxy
MBT	metal–base transistor
MC	Monte Carlo
MCS	Monte Carlo simulation
MD	molecular dynamics
MEE	migration-enhanced epitaxy
MESFET	metal Schottky field-effect transistor
MFTF	Mirror Fusion Test Facility
MISFET	metal–insulator–semiconductor field effect transistor
MJR	McDonald jelly roll (superconducting cable construction)
MLR	multi-layer reflector
MMC	metal–matrix composite
MN	Mendeleev number
MO	magneto-optical
MOCVD	metal–organic chemical vapor deposition
MOS	metal–oxide–semiconductor
MOSFET	metal–oxide–semiconductor field effect transistor
MOVPE	metal–organic vapor phase epitaxy
MQW	multiple quantum well
MRI	magnetic resonance imaging
MRSS	maximum resolved shear stress
MRT	orthodontic NiTi alloy
MT	muffin tin
MTD	martensitic transformation diagram
MVA	million volt-amperes
NASP	National AeroSpace Plane
NET	Next European Torus (fusion device)
NHE	normal hydrogen electrode
NMI	National Maglev Initiative
NMR	nuclear magnetic resonance
NN	nearest neighbor
NNH	nearest-neighbor histogram

NNN	next nearest neighbor
NOR	negative OR (logic operator)
NSR	notch/strength ratio
OAZ	oxidation-affected zone
ODR	oxygen dissolution reaction
ODS	oxide dispersion-strengthened
OEIC	optoelectronic integrated circuit
OH	octahedron
ORNL	Oak Ridge National Laboratory
OT	(negative) outer tetrahedron
OTMC	orthorhomic Ti-matrix composites
PAS	positron annihilation spectrosxopy
PBC	periodic bond chain
PBT	permeable-base transistor
PCM	phase-change material
PCT	pressure–composition–temperature
PD	phase diagram
PDF	pair distribution function
PDOS	phonon density of states
PFC	planar flow casting
PH	*Pearson's Handbook*
PHACOMP	phase computation
PKA	primary knock-on atom
PL	photoluminescence
PM	powder metallurgy
PMTC	phenomenological martensite transformation concept
PN	periodic number
pnpn	type of photothyristor
PPDF	partial pair distribution function
PPM	path-probability method
PPV	Paidar–Pope–Vitek ($L1_2$ hardening model)
PS	Pearson symbol
PT	phase transformation
PTMC	phenomenological theory of martensite crystallography
PVD	physical vapor deposition
PZT	lead zirconate titanate (ceramic)
QC	quasicrystal(line)
QCSE	quantum confined Stark effect
QFD	quantum formation diagram
QN	quantum number
QSD	quantum structural diagram
QW	quantum well
RBS	Rutherford back scattering
RC	ribbon comminution
RCS	replacement-collision sequence
RDF	radial distribution function
RDS	rate-dermining step
RE	rare earth (metal)
RF	radiofrequency
RHE	reversible hydrogen electrode
RIM	rigid-ion model
RKKY	Ruderman–Kittel–Kasuya–Yoshida (electron interactions)
r.m.s.	root mean square
RRR	residual resistivity ratio
RS	rapidly solidified
RSP	rapid solidification processing
RSS	resolved shear stress
RT	room temperature
RUS	resonance ultrasound spectroscopy
SAD	selected-area diffraction
SAED	selected-area electron diffraction
SAGBO	stress-assisted grain-boundary oxidation
SAM-APD	separate absorption and multiplication avalanche photodetector
s.c.	simple cubic
SC	semiconductor
SCE	standard colomel electrode
SCH	separate confinement heterostructures
SDC	specific damping capacity
SDW	spin-density wave
SEM	scanning electron microscopy
SESF	superlattice extrinsic stacking fault
SF	stacking fault
SG	spin glass
SHS	self-propagating high-temperature synthesis
SI/VLSI	semi-insulating very large-scale integration
SIA	self-interstitial atom
SIC	self-interaction correlation
SIM	stress-induced martensite
SIMS	secondary-ion mass spectrometry
SIS	superconductor–insulator–superconductor
SISF	superlattice intrinsic stacking fault
SIT	static inductance transistor
SM	semimetal
SMA	second-moment approximation
SMA	shape-memory alloy
SME	shape-memory effect
SPF	superplastic forming
SQUID	superconducting quantum interference device
SRO	short-range order
SSAR	solid-state amorphizing reaction
SSD	structural stability diagram

SSF	superlattice stacking fault
STA	*Atlas of Crystal Structure Types*
STEM	scanning transmission electron microscopy
STM	scanning tunneling microscopy
SV	Sodani-Vitole change of Paidar *et al.* model
TA	transverse acoustic (wave)
TB	tight binding
TCP	topologically close-packed
TD	thoria dispersion
TDFS	temperature dependence of flow stress
TE	thermoelectric
TE	transverse electric (field)
TEC	thermoelectric cooler
TEG	thermoelectric generator
TEM	transmission electron microscopy
TEP	triethylphosphene
TGW	Teatum–Gschneidner–Waber (atomic radius)
TIP	thermally induced porosity
TK	Takeuchi–Kuramoto (dislocation locking mechanism)
TM	transition metal
TM	transverse magnetic (field)
TMA	titanium–molybdenum–aluminum (alloy)
TO	transverse optical (wave)
TPA	two-photon absorption
TSRO	topological short-range ordering
TT	truncated tetrahedron
TTS	tubular tin source
TTT	time–temperature–transformation
UHF	ultra-high frequency
UHV	ultra-high vacuum
ULSI	ultra large-scale integration
USW	ultrasonic wave
UTS	ultimate tensile strength
UV	ultraviolet
VAR	vacuum arc refined
VCSEL	vertical-cavity surface-emitting laser
VEC	valence-electron concentration
VGF	vertical gradient freezing
VHF	very high frequency
VIM	vacuum induction melting
VLS	vapor–liquid–solid
VLSI	very large-scale integration
VPE	vapor phase epitaxy
VPS	vacuum plasma spraying
VUV	vacuum ultraviolet
WB	weak beam
WGPD	waveguide photodetector
WLR	Wechsler–Lieberman–Read (theory of martensitic transformation)
WS	Wigner–Seitz (cell)
WSS	Winterbon–Sigmund–Sanders (model of irradiation damage)
wt.ppm	weight parts per million
XC	exchange–correlation
XD™	exothermic dispersion (synthesis process)
XIM	X-ray inspection module
XPS	X-ray photoelectron spectroscopy
XRD	X-ray diffraction
XUV	extreme ultraviolet
YAG	yttrium aluminum garnet
ZIF	zero insertion force

*Crystal Structure Nomenclature**

Arranged Alphabetically by Pearson-Symbol Designation

Pearson symbol	Prototype	Strukturbericht designation	Space group	Pearson symbol	Prototype	Strukturbericht designation	Space group
*cF*4	Cu	*A*1	$Fm\bar{3}m$	*cP*6	Ag_2O	*C*3	$Pn\bar{3}m$
*cF*8	C (diamond)	*A*4	$Fd\bar{3}m$	*cP*7	CaB_6	$D2_1$	$Pm\bar{3}m$
	NaCl (rock salt)	*B*1	$Fm\bar{3}m$	*cP*8	Cr_3Si (βW)	*A*15	$Pm\bar{3}n$
	ZnS (sphalerite)	*B*3	$F\bar{4}3m$		FeSi	*B*20	$P2_13$
*cF*12	CaF_2 (fluorite)	*C*1	$Fm\bar{3}m$		Cu_3VS_4 (sulvanite)	$H2_4$	$P\bar{4}3m$
	MgAgAs	$C1_b$	$F\bar{4}3m$	*cP*12	FeS_2 (pyrite)	*C*2	$Pa3$
*cF*16	$AlCu_2Mn$ (Heusler)	$L2_1$	$Fm\bar{3}m$		NiSbS (ullmanite)	$F0_1$	$P2_13$
	BiF_3 ($AlFe_3$)	$D0_3$	$Fm\bar{3}m$	*cP*20	βMn	*A*13	$P4_132$
	NaTl	*B*32	$Fd\bar{3}m$	*cP*36	$BaHg_{11}$	$D2_e$	$Pm\bar{3}m$
*cF*24	$AuBe_5$	$C15_b$	$F\bar{4}3m$	*cP*39	Mg_2Zn_{11}	$D8_c$	$Pm\bar{3}$
	SiO_2 (β cristobalite)	*C*9	$Fd\bar{3}m$	*cP*52	Cu_9Al_4 (γ brass)	$D8_3$	$P\bar{4}3m$
	Cu_2Mg (Laves)	*C*15	$Fd\bar{3}m$	*hP*1	$HgSn_{6\text{-}10}$	A_f	$P6/mmm$
*cF*32	$CuPt_3$	$L1_a$	$Fm\bar{3}c$	*hP*2	Mg	*A*3	$P6_3/mmc$
*cF*52	UB_{12}	$D2_f$	$Fm\bar{3}m$		WC	B_h	$P\bar{6}m2$
*cF*56	Al_2MgO_4 (spinel)	$H1_1$	$Fd\bar{3}m$	*hP*3	AlB_2	*C*32	$P6/mmm$
	Co_3S_4	$D7_2$	$Fd\bar{3}m$		CdI_2	*C*6	$P\bar{3}m1$
*cF*68	Co_9S_8	$D8_9$	$Fm\bar{3}m$		Fe_2N	*L*′3	$P6_3/mmc$
*cF*80	Sb_2O_3 (senarmontite)	$D5_4$	$Fd\bar{3}m$		$LiZn_2$	C_k	$P6_3/mmc$
*cF*112	Fe_3W_3C (η carbide)	$E9_3$	$Fd\bar{3}m$		γSe	*A*8	$P3_121$
	$NaZn_{13}$	$D2_3$	$Fm\bar{3}c$	*hP*4	αLa	*A*3′	$P6_3/mmc$
*cF*116	$Cr_{23}C_6$	$D8_4$	$Fm\bar{3}m$		BN	B_k	$P6_3/mmc$
	$Mn_{23}Th_6$, $Cu_{16}Mg_6Si_7$ (G-phase)	$D8_e$	$Fm\bar{3}m$		C (graphite)	*A*9	$P6_3/mmc$
*cI*2	W	*A*2	$Im\bar{3}m$		NiAs	$B8_1$	$P6_3/mmc$
*cI*16	CoU	B_d	$I2_13$		ZnS (wurtzite)	*B*4	$P6_3mc$
*cI*28	Th_3P_4	$D7_3$	$I\bar{4}3d$	*hP*5	La_2O_3	$D5_2$	$P\bar{3}m1$
*cI*32	$CoAs_3$ (skutterudite)	$D0_2$	$Im\bar{3}$		Ni_2Al_3	$D5_{13}$	$P\bar{3}m1$
*cI*40	Ge_7Ir_3	$D8_f$	$Im\bar{3}m$	*hP*6	$CaCu_5$	$D2_d$	$P6/mmm$
	Pu_2C_3	$D5_c$	$I\bar{4}3d$		CoSn	*B*35	$P6/mmm$
*cI*52	Cu_5Zn_8 (γ brass)	$D8_2$	$I\bar{4}3m$		Cu_2Te	C_h	$P6/mmm$
	Fe_3Zn_{10} (γ brass)	$D8_1$	$Im\bar{3}m$		HgS	*B*9	$P3_121$
*cI*54	Sb_2Tl_7	$L2_2$	$Im\bar{3}m$		MoS_2	*C*7	$P6_3/mmc$
*cI*58	αMn (χ-phase)	*A*12	$I\bar{4}3m$		Ni_2In	$B8_2$	$P6_3mc$
*cI*76	$Cu_{15}Si_4$	$D8_6$	$I\bar{4}3d$	*hP*8	Na_3As	$D0_{18}$	$P6_3/mmc$
*cI*80	Mn_2O_3	$D5_3$	$Ia\bar{3}$		Ni_3Sn	$D0_{19}$	$P6_3/mmc$
*cI*96	$AlLi_3N_2$	$E9_d$	$Ia\bar{3}$		TiAs	B_i	$P6_3/mmc$
*cI*162	$Mg_{32}(Al,Zn)_{49}$	$D8_e$	$Im\bar{3}$	*hP*9	$CrSi_2$	*C*40	$P6_222$
*cP*1	αPo	A_h	$Pm\bar{3}m$		Fe_2P	*C*22	$P\bar{6}2m$
*cP*2	CsCl	*B*2	$Pm\bar{3}m$		ζAgZn	B_b	$P\bar{3}$
*cP*4	$AuCu_3$	$L1_2$	$Pm\bar{3}m$		SiO_2 (high quartz)	*C*8	$P6_222$
	ReO_3	$D0_9$	$Pm\bar{3}m$	*hP*10	Pt_2Sn_3	$D5_b$	$P6_3/mmc$
*cP*5	$AlFe_3C$ (perovskite)	$L1'_2$	$Pm\bar{3}m$	*hP*12	CuS	*B*18	$P6_3/mmc$
	$CaTiO_3$ (perovskite)	$E2_1$	$Pm\bar{3}m$		$MgZn_2$ (Laves)	*C*14	$P6_3/mmc$
	Fe_4N	$L1'$	$P\bar{4}3m$		SiO_2 (β tridymite)	*C*10	$P6_3/mmc$

continued

*Adapted (with additions and corrections) from *ASM Handbook*, Vol. 3, 10th ed, ASM International, Materials Park, OH.

Arranged Alphabetically by Pearson-Symbol Designation (*continued*)

Pearson symbol	Prototype	Strukturbericht designation	Space group
*hP*14	W_2B_5	$D8_h$	$P6_3/mmc$
*hP*16	Mn_5Si_3	$D8_8$	$P6_3/mcm$
	Ni_3Ti	$D0_{24}$	$P6_3/mmc$
*hP*18	Al_4C_4Si	$E9_4$	$P6_3mc$
	$Al_8FeMg_3Si_6$	$E9_b$	$P\bar{6}2m$
	Mg_2Ni	C_e	$P6_222$
*hP*20	Fe_3Th_7	$D10_2$	$P6_3mc$
	Th_7S_{12}	$D8_k$	$P6_3/m$
*hP*24	Cu_3P	$D0_{21}$	$P6_3cm$
	$MgNi_2$ (Laves)	$C36$	$P6_3/mmc$
*hP*28	Co_2Al_5	$D8_{11}$	$P6_3/mmc$
*hR*1	αHg	$A10$	$R\bar{3}m$
	βPo	A_i	$R\bar{3}m$
*hR*2	αAs	$A7$	$R\bar{3}m$
*hR*3	αSm	$C19$	$R\bar{3}m$
*hR*4	$NaCrS_2$	$F5_1$	$R\bar{3}m$
*hR*5	Bi_2Te_3	$C33$	$R\bar{3}m$
	Ni_3S_2	$D5_g$	$R32$
*hR*6	$CaSi_2$	$C12$	$R\bar{3}m$
	NiS (millerite)	$B13$	$R\bar{3}m$
*hR*7	Al_4C_3	$D7_1$	$R\bar{3}m$
	Mo_2B_5	$D8_i$	$R\bar{3}m$
*hR*10	αAl_2O_3 (corundum)	$D5_1$	$R\bar{3}c$
*hR*12	$BaPb_3$		$R\bar{3}m$
*hR*13	Fe_7W_6 (μ-phase)	$D8_5$	$R\bar{3}m$
*hR*15	B_4C	$D1_g$	$R\bar{3}m$
*hR*20	$HoAl_3$		$R\bar{3}m$
*hR*26	Cr_5Al_8	$D8_{10}$	$R\bar{3}m$
*hR*32	CuPt	$L1_1$	$R\bar{3}m$
*mC*6	$AuTe_2$ (calaverite)	$C34$	$C2/m$
*mC*8	CuO (tenorite)	$B26$	$C2/c$
*mC*12	ThC_2	C_g	$C2/c$
*mC*14	δNi_3Sn_4	$D7_a$	$C2/m$
*mC*16	$FeKS_2$	$F5_a$	$C2/c$
*mP*12	$AgAuTe_4$ (sylvanite)	$E1_b$	$P2/c$
	ZrO_2	$C43$	$P2_1/c$
*mP*20	As_2S_3	$D5_f$	$P2_1/c$
*mP*22	Co_2Al_9	$D8_d$	$P2_1/c$
*mP*24	FeAsS	$E0_7$	$P2_1/c$
*mP*32	AsS (realgar)	B_f	$P2_1/c$
	βSe	A_f	$P2_1/c$
*mP*64	αSe	A_k	$P2_1/c$
*oC*4	αU	$A20$	$Cmcm$
*oC*8	CaSi	B_c	$Cmmc$
	αGa	$A11$	$Cmca$
	CrB	$B33$	$Cmcm$
	I_2	$A14$	$Cmca$
	P (black)	$A17$	$Cmca$
*oC*12	$ZrSi_2$	$C49$	$Cmcm$
*oC*16	BRe_3	$E1_a$	$Cmcm$
*oC*20	$PdSn_4$	$D1_c$	$Aba2$
*oC*24	$PdSn_2$	C_e	$Aba2$
*oC*28	Al_6Mn	$D2_h$	$Cmcm$
*oF*24	$TiSi_2$	$C54$	$Fddd$
*oF*40	Mn_4B	$D1_f$	$Fddd$
*oF*48	$CuMg_2$	C_b	$Fddd$
*oF*72	GeS_2	$C44$	$Fdd2$
*oF*128	αS	$A16$	$Fddd$
*oI*12	SiS_2	$C42$	$Ibam$
*oI*14	Ta_3B_4	$D7_b$	$Immm$
*oI*20	Al_4U	$D1_b$	$Imma$
*oI*28	Ga_2Mg_5	$D8_g$	$Ibam$
*oP*4	AuCd	$B19$	$Pmma$
*oP*6	FeS_2 (marcasite)	$C18$	$Pnnm$
	$CaCl_2$	$C35$	$Pnnm$
*oP*8	αNp	A_c	$Pnma$
	ηNiSi	B_d	$Pbnm$
*oP*8	βCu_3Ti	$D0_a$	$Pmmn$
	FeB	$B27$	$Pnma$
	GeS	$B16$	$Pnma$
	SnS	$B29$	$Pmcn$
	MnP	$B31$	$Pnma$
	TiB	B_m	$Pnma$
*oP*12	Co_2Si, NiSiTi (E-phase)	$C23$	$Pnma$
	Co_2Si	$C37$	$Pbnm$
	$HgCl_2$	$C28$	$Pmnb$
*oP*16	Al_3Ni	$D0_{20}$	$Pnma$
	$AsMn_3$	$D0_d$	$Pmmn$
	BaS_3	$D0_{17}$	$P42_1m$
	CdSb	B_g	$Pbca$
	CuS_2Sb (wolfsbergite)	$F5_6$	$Pnma$
	Fe_3C (cementite)	$D0_{11}$	$Pnma$
*oP*20	Cr_3C_2	$D5_{10}$	$Pnma$
	Sb_2S_3	$D5_8$	$Pnma$
	Sb_2O_3 (valentinite)	$D5_{11}$	$Pccn$
*oP*24	$AuTe_2$ (krennerite)	$C46$	$Pma2$
	$CuFe_2S_3$ (cubanite)	$E9_e$	$Pnma$
	TiO_2 (brookite)	$C21$	$Pbca$
*oP*40	Cr_7C_3	$D10_1$	$Pnma$
*tI*2	αPa	A_a	$I4/mmm$
	In	$A6$	$I4/mmm$
*tI*4	βSn	$A5$	$I4_1/amd$
*tI*6	CaC_2	$C11_a$	$I4/mmm$
	$MoSi_2$	$C11_b$	$I4/mmm$
	ThH_2	$L'2_b$	$I4/mmm$
*tI*8	Al_3Ti	$D0_{22}$	$I4/mmm$
*tI*10	Al_4Ba	$D1_3$	$I4/mmm$
	MoNi$_4$	$D1_e$	$I4/m$
*tI*12	Al_2Cu	$C16$	$I4/mcm$
	$ThSi_2$	C_c	$I4_1/amd$
*tI*14	Al_2CdS_4	$E3$	$I\bar{4}$
*tI*16	Al_3Zr	$D0_{23}$	$I4/mmm$
	$CuFeS_2$ (chalcopyrite)	$E1_1$	$I\bar{4}2d$
	Cu_2FeSnS_4 (stannite)	$H2_6$	$I\bar{4}2m$
	Ir_3Si	$D0_c$	$I4/mcm$
	MoB	B_g	$I4_1/amd$
	SiU_3	$D0_c$	$I4/mcm$
	TlSe	$B37$	$I4/mcm$
*tI*18	Fe_8N	$D2_g$	$I4/mmm$
*tI*26	$Mn_{12}Th$	$D2_b$	$I4/mmm$
*tI*28	MnU_6	$D2_c$	$I4/mcm$
*tI*32	Cr_5B_3	$D8_i$	$I4/mcm$
	Ni_3P	$D0_e$	$I\bar{4}$
	W_5Si_3	$D8_m$	$I4/mcm$
*tP*2	δCuTi	$L2_a$	$P4/mmm$
*tP*4	βNp	A_d	$P42_12$
	AuCu	$L1_0$	$P4/mmm$
	$CuTi_3$	$L6_0$	$P4/mmm$
	γCuTi	$B11$	$P4/nmm$
	PbO	$B10$	$P4/nmm$
	Pb_3Sr		$P4/mmm$
	PtS	$B17$	$P4_2/mmc$
*tP*6	Cu_2Sb	$C38$	$P4/nmm$
	PbFCl	$E0_1$	$P4/nmm$
	TiO_2 (rutile)	$C4$	$P4_2/mnm$
*tP*10	Pb_4Pt	$D1_d$	$P4/nbm$
	Si_2U_3	$D5_a$	$P4/mbm$
*tP*16	PdS	$B34$	$P4_2/m$
*tP*20	B_4Th	$D1_e$	$P4/mbm$
*tP*30	βU	A_b	$P4_2/mnm$
	σCrFe	$D8_b$	$P4_2/mnm$
*tP*40	Al_7Cu_2Fe	$E9_a$	$P4/mnc$
	Zn_3P_2	$D5_9$	$P4_2/nmc$
*tP*50	γB	A_g	$P4_2/nnm$

Arranged Alphabetically by Strukturbericht Designation

Strukturbericht designation	Prototype	Pearson symbol	Space group	Strukturbericht designation	Prototype	Pearson symbol	Space group
A_a	αPa	$tI2$	$I4/mmm$	$B20$	FeSi	$cP8$	$P2_13$
A_b	βU	$tP30$	$P4_2/mnm$	$B26$	CuO (tenorite)	$mC8$	$C2/c$
A_c	αNp	$oP8$	$Pnma$	$B27$	FeB	$oP8$	$Pnma$
A_d	βNp	$tP4$	$P42_12$	$B29$	SnS	$oP8$	$Pmcn$
A_f	$HgSn_{\sim 10}$	$hP1$	$P6/mmm$	$B31$	MnP	$oP8$	$Pnma$
A_g	γB	$tP50$	$P4_2/nnm$	$B32$	NaTl	$cF16$	$Fd\bar{3}m$
A_h	αPo	$cP1$	$Pm\bar{3}m$	$B33(=B_f)$	CrB	$oC8$	$Cmcm$
A_i	βPo	$hR1$	$R\bar{3}m$	$B34$	PdS	$tP16$	$P4_2/m$
A_k	αSe	$mP64$	$P2_1/c$	$B35$	CoSn	$hP6$	$P6/mmm$
A_l	βSe	$mP32$	$P2_1/c$	$B37$	TlSe	$tI16$	$I4/mcm$
$A1$	Cu	$cF4$	$Fm\bar{3}m$	C_a	Mg_2Ni	$hP18$	$P6_222$
$A2$	W	$cI2$	$Im\bar{3}m$	C_b	$CuMg_2$	$oF48$	$Fddd$
$A3$	Mg	$hP2$	$P6_3/mmc$	C_c	$ThSi_2$	$tI12$	$I4_1/amd$
$A3'$	αLa	$hP4$	$P6_3/mmc$	C_e	$PdSn_2$	$oC24$	$Aba2$
$A4$	C (diamond)	$cF8$	$Fd\bar{3}m$	C_g	ThC_2	$mC12$	$C2/c$
$A5$	βSn	$tI4$	$I4_1/amd$	C_h	Cu_2Te	$hP6$	$P6/mmm$
$A6$	In	$tI2$	$I4/mmm$	C_k	$LiZn_2$	$hP3$	$P6_3/mmc$
$A7$	αAs	$hR2$	$R\bar{3}m$	$C1$	CaF_2 (fluorite)	$cF12$	$Fm\bar{3}m$
$A8$	γSe	$hP3$	$P3_121$	$C1_b$	MgAgAs	$cF12$	$F\bar{4}3m$
$A9$	C (graphite)	$hP4$	$P6_3/mmc$	$C2$	FeS_2 (pyrite)	$cP12$	$Pa3$
$A10$	αHg	$hR1$	$R\bar{3}m$	$C3$	Ag_2O	$cP6$	$Pn\bar{3}m$
$A11$	αGa	$oC8$	$Cmca$	$C4$	TiO_2 (rutile)	$tP6$	$P4_2/mnm$
$A12$	αMn (χ-phase)	$cI58$	$I\bar{4}3m$	$C6$	CdI_2	$hP3$	$P\bar{3}m1$
$A13$	βMn	$cP20$	$P4_132$	$C7$	MoS_2	$hP6$	$P6_3/mmc$
$A14$	I_2	$oC8$	$Cmca$	$C8$	SiO_2 (high quartz)	$hP9$	$P6_222$
$A15$	Cr_3Si (β-W)	$cP8$	$Pm\bar{3}n$	$C9$	SiO_2 (β cristobalite)	$cF24$	$Fd\bar{3}m$
$A16$	αS	$oF128$	$Fddd$	$C10$	SiO_2 (β tridymite)	$hP12$	$P6_3/mmc$
$A17$	P (black)	$oC8$	$Cmca$	$C11_a$	CaC_2	$tI6$	$I4/mmm$
$A20$	αU	$oC4$	$Cmcm$	$C11_b$	$MoSi_2$	$tI6$	$I4/mmm$
B_a	CoU	$cI16$	$I2_13$	$C12$	$CaSi_2$	$hR6$	$R\bar{3}m$
B_b	ζAgZn	$hP9$	$P\bar{3}$	$C14$	$MgZn_2$ } Laves	$hP12$	$P6_3/mmc$
B_c	CaSi	$oC8$	$Cmmc$	$C15$	Cu_2Mg } Laves	$cF24$	$Fd\bar{3}m$
B_d	ηNiSi	$oP8$	$Pbnm$	$C15_b$	$AuBe_5$	$cF24$	$F\bar{4}3m$
B_e	CdSb	$oP16$	$Pbca$	$C16$	Al_2Cu	$tI12$	$I4/mcm$
$B_f(=B33)$	CrB	$oC8$	$Cmcm$	$C18$	FeS_2 (marcasite)	$oP6$	$Pnnm$
B_g	MoB	$tI16$	$I4_1/amd$	$C19$	αSm	$hR3$	$R\bar{3}m$
B_h	WC	$hP2$	$P\bar{6}m2$	$C21$	TiO_2 (brookite)	$oP24$	$Pbca$
B_i	TiAs	$hP8$	$P6_3/mmc$	$C22$	Fe_2P	$hP9$	$P\bar{6}2m$
B_k	BN	$hP4$	$P6_3/mmc$	$C23$	Co_2Si, NiSiTi (E-phase)	$oP12$	$Pnma$
B_l	AsS (realgar)	$mP32$	$P2_1/c$	$C28$	$HgCl_2$	$oP12$	$Pmnb$
B_m	TiB	$oP8$	$Pnma$	$C32$	AlB_2	$hP3$	$P6/mmm$
$B1$	NaCl (rock salt)	$cF8$	$Fm\bar{3}m$	$C33$	Bi_2Te_3	$hR5$	$R\bar{3}m$
$B2$	CsCl	$cP2$	$Pm\bar{3}m$	$C34$	$AuTe_2$ (calaverite)	$mC6$	$C2/m$
$B3$	ZnS (sphalerite)	$cF8$	$F\bar{4}3m$	$C35$	$CaCl_2$	$oP6$	$Pnnm$
$B4$	ZnS (wurtzite)	$hP4$	$P6_3mc$	$C36$	$MgNi_2$ (Laves)	$hP24$	$P6_3/mmc$
$B8_1$	NiAs	$hP4$	$P6_3mmc$	$C37$	Co_2Si	$oP12$	$Pbnm$
$B8_2$	Ni_2In	$hP6$	$P6_3mmc$	$C38$	Cu_2Sb	$tP6$	$P4/nmm$
$B9$	HgS (cinnabar)	$hP6$	$P3_121$	$C40$	$CrSi_2$	$hP9$	$P6_222$
$B10$	PbO	$tP4$	$P4/nmm$	$C42$	SiS_2	$oI12$	$Ibam$
$B11$	γCuTi	$tP4$	$P4/nmm$	$C43$	ZrO_2	$mP12$	$P2_1/c$
$B13$	NiS (millerite)	$hR6$	$R\bar{3}m$	$C44$	GeS_2	$oF72$	$Fdd2$
$B16$	GeS	$oP8$	$Pnma$	$C46$	$AuTe_2$ (krennerite)	$oP24$	$Pma2$
$B17$	PtS (cooperite)	$tP4$	$P4_2/mmc$	$C49$	$ZrSi_2$	$oC12$	$Cmcm$
$B18$	CuS (rovelite)	$hP12$	$P6_3/mmc$	$C54$	$TiSi_2$	$oF24$	$Fddd$
$B19$	AuCd	$oP4$	$Pmma$	$D0_a$	$βCu_3Ti$	$oP8$	$Pmmn$
				$D0_c$	SiU_3	$tI16$	$I4/mcm$

continued

Arranged Alphabetically by Strukturbericht Designation (*continued*)

Strukturbericht designation	Prototype	Pearson symbol	Space group
$D0_c'$	Ir_3Si	$tI16$	$I4/mcm$
$D0_d$	$AsMn_3$	$oP16$	$Pmmn$
$D0_e$	Ni_3P	$tI32$	$I\bar{4}$
$D0_z$	$CoAs_3$ (skutterudite)	$cI32$	$Im\bar{3}$
$D0_3$	BiF_3, $AlFe_3$	$cF16$	$Fm\bar{3}m$
$D0_9$	ReO_3	$cP4$	$Pm\bar{3}m$
$D0_{11}$	Fe_3C (cementite)	$oP16$	$Pnma$
$D0_{17}$	BaS_3	$oP16$	$P42_1m$
$D0_{18}$	Na_3As	$hP8$	$P6_3/mmc$
$D0_{19}$	Ni_3Sn	$hP8$	$P6_3/mmc$
$D0_{20}$	Al_3Ni	$oP16$	$Pnma$
$D0_{21}$	Cu_3P	$hP24$	$P6_3cm$
$D0_{22}$	Al_3Ti	$tI8$	$I4/mmm$
$D0_{23}$	Al_3Zr	$tI16$	$I4/mmm$
$D0_{24}$	Ni_3Ti	$hP16$	$P6_3/mmc$
$D1_a$	$MoNi_4$	$tI10$	$I4/m$
$D1_b$	Al_4U	$oI20$	$Imma$
$D1_c$	$PdSn_4$	$oC20$	$Aba2$
$D1_d$	Pb_4Pt	$tP10$	$P4/nbm$
$D1_e$	B_4Th	$tP20$	$P4/mbm$
$D1_f$	Mn_4B	$oF40$	$Fddd$
$D1_g$	B_4C	$hR15$	$R\bar{3}m$
$D1_3$	Al_4Ba	$tI10$	$I4/mmm$
$D2_b$	$Mn_{12}Th$	$tI26$	$I4/mmm$
$D2_c$	MnU_6	$tI28$	$I4/mcm$
$D2_d$	$CaCu_5$	$hP6$	$P6/mmm$
$D2_e$	$BaHg_{11}$	$cP36$	$Pm\bar{3}m$
$D2_f$	UB_{12}	$cF52$	$Fm\bar{3}m$
$D2_g$	Fe_8N	$tI18$	$I4/mmm$
$D2_h$	Al_6Mn	$oC28$	$Cmcm$
$D2_1$	CaB_6	$cP7$	$Pm\bar{3}m$
$D2_3$	$NaZn_{13}$	$cF112$	$Fm\bar{3}c$
$D5_a$	Si_2U_3	$tP10$	$P4/mbm$
$D5_b$	Pt_2Sn_3	$hP10$	$P6_3/mmc$
$D5_c$	Pu_2C_3	$cI40$	$I\bar{4}3d$
$D5_e$	Ni_3S_2	$hR5$	$R32$
$D5_f$	As_2S_3	$mP20$	$P2_1/c$
$D5_1$	αAl_2O_3 (corundum)	$hR10$	$R\bar{3}c$
$D5_2$	La_2O_3	$hP5$	$P\bar{3}m1$
$D5_3$	Mn_2O_3	$cI80$	$Ia\bar{3}$
$D5_4$	Sb_2O_3 (senarmontite)	$cF80$	$Fd\bar{3}m$
$D5_8$	Sb_2S_3	$oP20$	$Pnma$
$D5_9$	Zn_3P_2	$tP40$	$P4_2/nmc$
$D5_{10}$	Cr_3C_2	$oP20$	$Pnma$
$D5_{11}$	Sb_2O_3 (valentinite)	$oP20$	$Pccn$
$D5_{13}$	Ni_2Al_3	$hP5$	$P\bar{3}m1$
$D7_a$	δNi_3Sn_4	$mC14$	$C2/m$
$D7_b$	Ta_3B_4	$oI14$	$Immm$
$D7_1$	Al_4C_3	$hR7$	$R\bar{3}m$
$D7_2$	Co_3S_4	$cF56$	$Fd\bar{3}m$
$D7_3$	Th_7P_4	$cI28$	$I\bar{4}3d$
$D8_a$	$Mn_{23}Th_6$, $Cu_{16}Mg_6Si_7$ (G-phase)	$cF116$	$Fm\bar{3}m$
$D8_b$	σCrFe	$tP30$	$P4_2/mnm$
$D8_c$	Mg_2Zn_{11}	$cP39$	$Pm\bar{3}$
$D8_d$	Co_2Al_9	$mP22$	$P2_1/c$
$D8_e$	$Mg_{32}(Al,Zn)_{49}$	$cI162$	$Im\bar{3}$
$D8_f$	Ge_7Ir_3	$cI40$	$Im\bar{3}m$
$D8_g$	Ga_2Mg_5	$oI28$	$Ibam$
$D8_h$	W_2B_5	$hP14$	$P6_3/mmc$
$D8_i$	Mo_2B_5	$hR7$	$R\bar{3}m$
$D8_k$	Th_7S_{12}	$hP20$	$P6_3/m$
$D8_l$	Cr_5B_3	$tI32$	$I4/mcm$
$D8_m$	W_5Si_3	$tI32$	$I4/mcm$
$D8_1$	Fe_3Zn_{10}	$cI52$	$Im\bar{3}m$
$D8_2$	Cu_5Zn_8 γ brass	$cI52$	$I\bar{4}3m$
$D8_3$	Cu_9Al_4	$cP52$	$P\bar{4}3m$
$D8_4$	$Cr_{23}C_6$	$cF116$	$Fm\bar{3}m$
$D8_5$	Fe_7W_6 (μ-phase)	$hR13$	$R\bar{3}m$
$D8_6$	$Cu_{15}Si_4$	$cI76$	$I\bar{4}3d$
$D8_8$	Mn_5Si_3	$hP16$	$P6_3/mcm$
$D8_9$	Co_9S_8	$cF68$	$Fm\bar{3}m$
$D8_{10}$	Cr_5Al_8	$hR26$	$R\bar{3}m$
$D8_{11}$	Co_2Al_5	$hP28$	$P6_3/mmc$
$D10_1$	Cr_7C_3	$oP40$	$Pnma$
$D10_2$	Fe_3Th_7	$hP20$	$P6_3mc$
$E0_1$	PbFCl	$tP6$	$P4/nmm$
$E0_7$	FeAsS	$mP24$	$P2_1/c$
$E1_a$	$MgCuAl_2$	$oC16$	$Cmcm$
$E1_b$	$AgAuTe_4$ (sylvanite)	$mP12$	$P2/c$
$E1_1$	$CuFeS_2$ (chalcopyrite)	$tI16$	$I\bar{4}2d$
$E2_1$	$CaTiO_3$ (perovskite)	$cP5$	$Pm\bar{3}m$
$E3$	Al_2CdS_4	$tI14$	$I\bar{4}$
$E9_a$	Al_2Cu_2Fe	$tP40$	$P4/mnc$
$E9_b$	$Al_8FeMg_3Si_6$	$hP18$	$P\bar{6}2m$
$E9_c$	Mn_3Al_9Si	$hP26$	$P6_3/mmc$
$E9_d$	$AlLi_3N_2$	$cI96$	$Ia\bar{3}$
$E9_e$	$CuFe_2S_3$ (cubanite)	$oP24$	$Pnma$
$E9_3$	Fe_3W_3C (η carbide)	$cF112$	$Fd\bar{3}m$
$E9_4$	Al_4C_4Si	$hP18$	$P6_3mc$
$F0_1$	NiSbS (ullmanite)	$cP12$	$P2_13$
$F5_a$	$FeKS_2$	$mC16$	$C2/c$
$F5_1$	$NaCrS_2$	$hR4$	$R\bar{3}m$
$F5_6$	CuS_2Sb (wolfsbergite)	$oP16$	$Pnma$
$H1_1$	Al_2MgO_4 (spinel)	$cF56$	$Fd\bar{3}m$
$H2_4$	Cu_3VS_4 (sulvanite)	$cP8$	$P\bar{4}3m$
$H2_6$	Cu_2FeSnS_4	$tI16$	$I\bar{4}2m$
$L1'$	Fe_4N	$cP5$	$Pm\bar{3}m$
$L1_a$	$CuPt_3$	$cF32$	$Fm\bar{3}c$
$L1_0$	AuCu	$tP4$	$P4/mmm$
$L1_0$(M)	AuCuII	$oI40$	$Imma$
$L1_1$	CuPt	$hR32$	$R\bar{3}m$
$L1_2$	$AuCu_3$	$cP4$	$Pm\bar{3}m$
$L1_2'$	$AlFe_3C$ (perovskite)	$cP5$	$Pm\bar{3}m$
$L2_a'$	δCuTi	$tP2$	$P4/mmm$
$L2_b'$	ThH_2	$tI6$	$I4/mmm$
$L2_1$	$AlCu_2Mn$ (Heusler)	$cF16$	$Fm\bar{3}m$
$L2_2$	Sb_2Tl_7	$cI54$	$Im\bar{3}m$
$L3'$	Fe_2N	$hP3$	$P6_3/mmc$
$L6_0$	$CuTi_3$	$tP4$	$P4/mmm$

Contents

Chapter 1

Factors Governing Crystal Structures

Pierre Villars

Intermetallic Phases Data Bank (IPDB) and Materials Phases Data System (MPDS), Postal Box 1, CH-6354 Vitznau, Switzerland

1. Introduction

The fundamentals of the constitution of an alloying system are determined by the crystal structure of its intermetallic compounds and its phase diagram. Knowing these fundamentals enables scientists to solve many problems in materials science, and therefore it is important to have easy access to the experimentally determined data, especially as the experimental work to determine such information is very time- and cost-intensive.

Recently, scientists working in this field have had the advantage of access to comprehensive, up-to-date handbooks for crystal structures as well as for phase diagrams. *Pearson's Handbook of Crystallographic Data for Intermetallic Phases*, second edition (Villars and Calvert, 1991) contains critically evaluated crystallographic data for over 25 000 distinctly different intermetallic compounds (over 50 000 binary, ternary, etc., entries) covering the world literature from 1913 to 1989. The *Atlas of Crystal Structures for Intermetallic Phases* (Daams *et al.*, 1991), a companion of *Pearson's Handbook*, contains for most of the intermetallic compounds in *Pearson's Handbook* graphical representations of the crystal structures. The handbook *Binary Alloy Phase Diagrams*, second edition (Massalski *et al.*, 1991) contains about 4000 phase diagrams, most of them critically evaluated phase diagrams. In 1994 ASM International will publish the *Handbook of Ternary Alloy Phase Diagrams* (Villars *et al.*, 1993), which comprehensively covers the world literature from 1900 to 1989 and will contain information for over 8800 ternary systems including over 15 000 isothermal sections, liquidus and solidus projections, as well as vertical sections. For the literature up to the year 1977, there also exists the very comprehensive *Multicomponent Alloy, Constitution Bibliography* (Prince, 1956, 1978, 1981).

Looking at the research activities in the last 20 years with respect to the number of systems investigated, grouped according to binary, ternary, and quaternary systems, a shift in the ongoing research from binary to ternary and quaternary systems is clearly seen. The research field of multinary systems is a huge field for potential novel materials with optimized known physical properties (e.g. tP68 $BFe_{14}Nd_2$-type permanent magnets and, in the inorganic field, the new high-T_c superconductors) as well as 'new' physical properties, as the recent past has proven with the quasicrystals (see Chapter 20 by Kelton in this volume). All this was achieved by moving from the binary to the ternary and quaternary systems, but this trend confronts us with many additional 'difficult-to-handle' problems. We have to be aware that in the future most research will be done on multinary systems; therefore, in this chapter we will first discuss the binary intermetallic compounds (systems), also called binaries, and whenever possible extend the discussion to ternary intermetallic compounds (systems), called ternaries. We will try to show the main problems by extending to ternaries our knowledge gained by investigation of binaries and propose ideas which, according to the author, have a high probability of success in the quantitative extension to multinaries of regularities found in binaries. The experimental variables we have are the selection of the chemical elements, their possible combinations, their

Crystal Structures of Intermetallic Compounds. Edited by J. H. Westbrook and R. L. Fleischer

concentrations, the temperature, and the pressure. Of enormous consequence from the practical point of view is the variety of combination possibilities of the chemical elements and the increase in the possible number of combinations on going from binaries to multinaries accompanied by a much larger available concentration range. Unfortunately, the number of available experimentally determined data is in inverse proportion to these opportunities.

We have a relatively robust database for binaries, but a sparse database for ternaries, and almost no data for quaternaries. This is quantitatively demonstrated by looking at the relevant numbers of binary, ternary, and quaternary systems. In the binary systems, taking 100 chemical elements into account, there exist $(100 \times 99)/(1 \times 2) = 4950$ binary systems, a large number, but still, with united, coordinated international research efforts, all these systems could be experimentally investigated by the end of this century. Therefore, one would inevitably have found among these the most interesting and economically important binary materials. Massalski *et al.* (1991) and Villars and Calvert (1991) contain information on about 4000 systems, so already we have a very robust database with about 80% of the possible systems fully or partly investigated experimentally. With the ternary systems the situation looks completely different. There exist $(100 \times 99 \times 98)/(1 \times 2 \times 3) = 161\,700$ systems. Villars and Calvert (1991) and Villars *et al.* (1994) contain experimentally determined data for only about 8800 systems, most of which have only been partly investigated. So here we have a sparse database with only about 5% of the potentially available systems having been partly investigated. In addition, in order to establish structures and phase relationships, one has to prepare and investigate at least 10 times more samples per system in the ternary case compared to the binary case. In the quaternary case with $(100 \times 99 \times 98 \times 97)/(1 \times 2 \times 3 \times 4) = 3\,921\,225$ potential systems, less than 0.1% have been partly investigated. Without having very good guidelines, it is a hopeless situation to search systematically for novel materials with an adequate success rate in multinary systems. Therefore, the only practicable way to go is, with the help of the robust binary database, to find regularities, such as laws, rules, principles, factors, tendencies, and patterns valid within the binaries, and then to extend these to the ternaries and quaternaries in such a way that the binaries and multinaries can be treated together; otherwise the regularities would be based on too few data sets and therefore would not be trustworthy. In addition, the regularities should show an accuracy clearly above randomness to be of practical use (these can easily be checked with the available experimentally determined data).

To increase the efficiency in the successful search for 'new' intermetallic compounds, the main efforts should go toward creating an internationally accessible information-prediction system incorporating all databases (experimentally determined facts) as well as generally valid principles and the 'highest-quality' regularities. The problems involved in such a project have been reviewed by Westbrook (1993). The combination of the experience and intuition of the experimentalist together with easy access to the data already experimentally determined in the form of up-to-date handbooks as well as access to the envisioned information-prediction system would very much help to coordinate world research activities. Furthermore, it would reduce the number of unwanted duplications as well as increase the probability of investigating first the most promising systems and not, as in the past, provide us with the systems in a random statistical sequence. Otherwise we will have to wait until the year 5500 for the next 140 generations of scientists to investigate the ternary systems, assuming an activity rate similar to that in this century.

2. Strategy to Find the Factors Governing Crystal Structure

When we talk about factors governing crystal structures we intend to reduce these to atomic property expressions (APEs) of the constituent chemical elements, so that the existing experimental data can be systematized. For the purpose of this chapter, we consider that the only regularities of real practical value are those able to systematize a large group of data with an accuracy in the range of at least 95%. For the not yet experimentally investigated systems, one goes in exactly the reverse way, assuming the validity of the regularity found for a well-defined group of data. The more data considered, the more trustworthy is a prediction based on such regularities. To make predictions one starts from the chemical elements, their concentrations, and the tabulated atomic properties (APs) of the elements, and calculates the APEs for a system of interest. Therefore, APs are only of practical interest where they are known for most chemical elements with adequate accuracy. From the APEs, in the context of the considered regularity, one can predict how the systems of interest most probably (with an accuracy of at least 95%) will behave. Then scientists can decide which systems are promising to investigate experimentally.

In principle, it would be sufficient to use as input only the atomic numbers (ANs) and the compositions of the intermetallic compounds of the systems under consideration. Slater (1956) once made a comment as follows: 'I don't understand why you metallurgists are so busy in working out experimentally the constitution [crystal structure and phase diagram] of multinary systems. We know the structure of the atoms [needing only the AN], we have the laws of quantum mechanics, and we have electronic calculation machines, which can solve the pertinent equation rather quickly!' Some 35 years later Chelikowsky (1991) writes in an excellent review the following: 'Although the interactions in intermetallic compounds are well understood, it is not an easy task to evaluate the total energy of solids, even at absolute zero. As the energy of an isolated atom is in the order of about 10^6 eV, but the cohesive energy only in the order of about 1–10 eV/atom, one must have a method that is accurate to one part on 10^6, or better.' The other fact that greatly complicates evaluating the cohesive energy by theoretical methods is the number of particles involved. Given that a macroscopic solid may contain 10^{23} nuclei and electrons, it is impossible to determine the total energy of the crystal structure without some approximations. Within the last 15 years, two advances have made it possible to predict the cohesive energy of solids by numerical solutions of the quantum-mechanical equations of motion, e.g. the Schrödinger equation: the invention of high-speed computers and the device of one-electron potentials, which greatly simplifies many-body interactions.

The accuracy of these computations is usually not at the same level as experiment. Nonetheless, it is now possible, for chemical elements and simple intermetallic

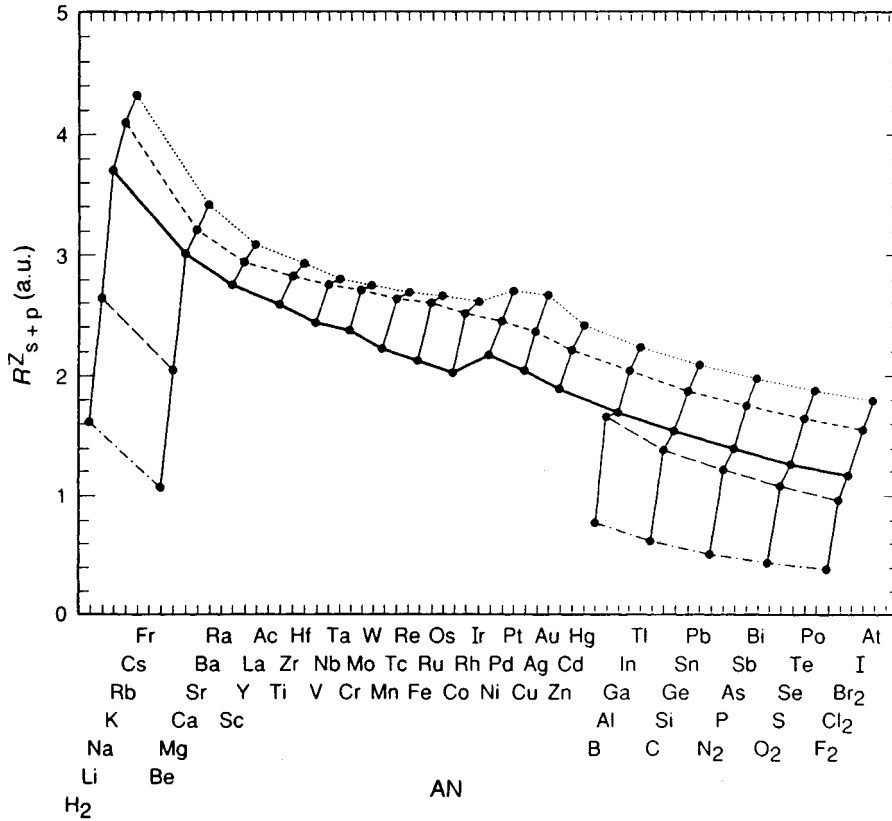

Figure 1. An atomic property, AP, versus a function of atomic number, AN, plot of the pseudopotential radii after Zunger, R^Z_{s+p}, representing an example of the size factor. In such diagrams the chemical elements are ordered by increasing group number and each group is ordered by increasing quantum number. This special atomic-number (AN) scale was used instead of a linearly increasing atomic-number scale because it gives units of comparable size for distance between the atoms within any group as well as along any period. The scale chosen for the comparison, of course, does not affect the number of factors (groups), only the appearance of the patterns changes

compounds, to predict whether a given crystal structure is the most stable one at 0 K and 1 atm. We have to stress that the crystal structures (and from *Pearson's Handbook* (Villars and Calvert, 1991) we know there are at least 2750 different ones) have to be given as input for first-principles calculations, and this for each potential intermetallic compound. Assuming the potential intermetallic compound crystallizes in one of the 2750 known crystal structures and knowing its nominal stoichiometry—AB, AB_2, etc.—it may still, in some cases, require a few hundred first-principles calculations for each potential intermetallic compound; even with high-speed computers, this is not yet workable. But the larger problem is that the differences of the cohesive energies of those few hundred calculations will be so small that the accuracy would have to be in the range of one part in 10^9 to determine the most stable crystal structure. The complexity of the above-mentioned problem shows that one cannot expect that within the next decade the constitution (crystal structure and phase diagram) of multinary systems will be calculated from first principles.

Meanwhile it is therefore sensible to adopt semi-empirical approaches based on the experimentally known data to search for the most reliable regularities. As at the moment it is impossible to start only from the atomic property AN, it is obvious to try to find out which other APs of the chemical elements are needed to describe the alloying behavior. Villars (1983) conducted a survey of 53 different APs as a function of the AN (182 variables in all when the different methods of determination are taken into account), and it was found that there were only five main groups, here called *factors*. The results are best seen in AP versus AN plots, as shown in Figure 1 for the pseudopotential radii R^Z_{s+p} after Zunger (1981) for s, p, and d elements. The f elements have been left out because in most cases only incomplete data are available. In all but a few cases (19 out of 182) very regular symmetric patterns were obtained in such plots; this means a regular behavior within a group with increasing quantum number (QN) as well as along a period with increasing AN.

In these diagrams the chemical elements are ordered by increasing group number and each group is ordered by increasing quantum number. This special 'AN' scale was used instead of a linearly increasing AN scale because it gives units of comparable size for distance between atoms within any group as well as along any period. The scale chosen for comparison does not affect the number of factors (groups), of course; only the appearance of the patterns changes. It should be stressed that the equivalence of APs belonging to the same group is of a qualitative, not a quantitative nature. Adherence to one or another of the five factors is very obvious. Table 1 summarizes the idealized characteristics

Table 1. Idealized characteristics of the 'patterns' in the atomic property (AP) versus atomic number (AN) plots of the five factor (groups)

	Long periods			Groups		
Factors (groups)	First	Second	Third	s elements	d elements	p elements
Size factor	Straight lines with negative slopes and a slight maximum around the Ni and Cu group elements			Straight lines with positive slopes		
Atomic-number factor	Straight lines with positive slopes			Straight lines with positive slopes		
Cohesive-energy factor	*s and d elements* Line with two maxima at the V group and the Co group	Line with a clear maximum at the V group	Line with a clear maximum at the Mn group	Straight lines with negative slopes	The first two and the last two are irregular; the rest are straight lines with positive slopes	Straight lines with negative slopes
	p elements Straight lines with negative slopes					
Electrochemical factor	*s and d elements* Lines with a maximum around V to Ni group			Straight lines with negative slopes	The first two and the last two are irregular; the rest are straight lines with positive slopes	Straight lines with negative slopes
	p elements Straight lines with positive slopes					
Valence-electron factor	Straight lines with positive slopes and a discontinuity at Cu			For every group, horizontal straight lines		

Table 2. Atomic properties (APs) of the chemical elements grouped according to the five factors (groups)

Factors (groups)	Element property determined experimentally or derived from a model	Number of data sets
Size factor	Classical crossing points of the self-consistently screened, non-local atomic pseudopotentials	
	Radius of maximum radial electron density for outer orbitals from Hermann–Skillman calculations[a]	
	Renormalized orbital radius	
	Radius calculated by Hartree–Fock–Slater method	
	Ionic radius	15
	Softness parameter	
	Atomic volume	6
	Metallic radius	6
	Covalent radius	3
	Reduced thermodynamic potential at 298 K	3
	Electrochemical weight equivalent	2
	Entropy of solid elements at 298 K	6
	Density	3
Atomic-number factor	Atomic number	
	Atomic weight	
	Principal quantum number	
	Atomic electron scattering factor	3
	Bond energy of deep-lying electrons	4
	Specific heat	2
Cohesive-energy factor	Wavelength of K and L series	2
	Maximum number of electrons in the solid element	2
	Melting point	7
	Boiling point	4
	Heat of fusion	6
	Heat of vaporization	5
	Heat of sublimation	4
	Energy for atomization of 1 mol of the solid element at 0 K	
	Bulk modulus	3
	Young's modulus	4
	Torsion modulus	4
	Compression modulus	3
	Crystal lattice energy	3
	Dimer dissociation energy	
	Surface tension	3
	Liquid–solid interfacial energy	2
	Enthalpy of formation of monovacancies	3
	Cohesive energy	
	Solubility parameter	4
	Compressibility modulus	2
	Linear coefficient of thermal expansion at 273 K	2
Electrochemical factor	Electronegativity	13
	Chemical potential (after Miedema)[b]	
	$n_{WS}^{1/3}$ (after Miedema)[b]	
	s electron binding energy	
	s–p parameter	
	Positron annihilation rate	2
	Electron affinity	3
	Hardness	5
	Normal electrode potential	3
	First ionization potential	3
	Term value (after Herman and Skillman)[a]	
Valence-electron factor	Number of valence electrons (corresponding to group number)	
	Number of vacancies or holes in the d bands above the Fermi level	

[a]Herman and Skillman (1963).
[b]de Boer *et al.* (1988).

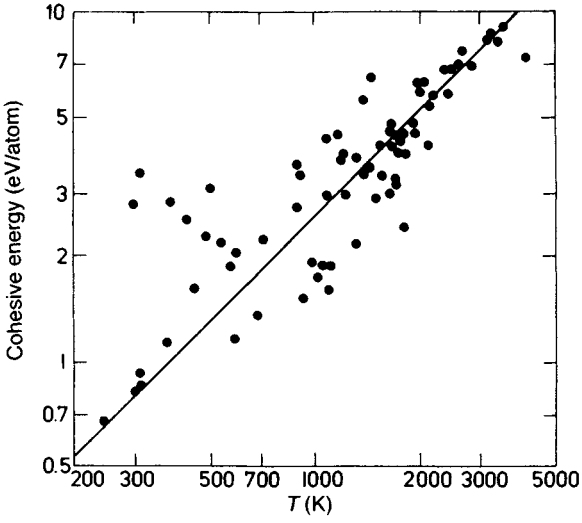

Figure 2. Plot for the chemical elements of the relationship of two atomic properties, APs, belonging to the cohesive-energy factor (group), namely cohesive energy and melting point T (Chelikowsky, 1979)

of those five factors in AP versus AN diagrams, and Table 2 lists the 53 APs grouped by those five factors. Figure 2 shows two APs belonging to the same factor plotted against each other, the cohesive energy versus melting point T of the chemical elements. As a first approximation a linear dependence may be seen to exist.

The five factors (groups) are:

- Size factor
- Atomic-number factor
- Cohesive-energy factor
- Electrochemical factor
- Valence-electron factor

In Table 3 we have given, in periodic table representation for the chemical elements, an AP for each factor for which accurate and complete data are available as well as (and this is very important for practical use) values that are independent of the constituent chemical elements of a compound. These are: pseudopotential radius after Zunger (1981), R^{Z}_{s+p}; atomic number, AN; melting point, T; electronegativity after Martynov and Batsanov (1980), $X^{M\&B}$; and group number = number of valence electrons, V. It is clearly shown in Table 3 that there exist no overall tendencies between those five factors, so they represent the most independent factors. In recent years some other APs have come to the attention of the author like, for example, average electron distances in the structures of the individual elements (Schubert, 1990), the energodynamic potential (Volchenkova, 1989), and vibrational frequencies and dissociation energies of homonuclear diatomic molecules (Suffczynski, 1987), etc.; however, all of them could be assigned to one of the five factors chosen.

In Section 4 we will always check to determine to which factor(s) the AP and respectively the APE belong that are successful in organizing large groups of experimentally determined data. At the end we will find out which of those five factors are governing crystal structures.

3. Compound-Formation Diagrams

A fundamental question that has to be answered first before discussing crystal structures is: 'Which systems form at least one "new" intermetallic compound?'

3.1 Binary System

The most outstanding model for binary systems is Miedema's model, which is excellently explained in the series *Cohesion and Structure*, volume 1 (de Boer *et al.*, 1988). Two APs of the constituent chemical elements enter the description of enthalpies of formation ΔH^{for}: the chemical potential for electronic charge (electronegativity) X^{M} and the electron density at the boundary of the Wigner–Seitz atomic cell, n_{WS}. Both APs belong to the electrochemical factor group. Table 2.4 of de Boer *et al.* (1988) gives the most recent recommended values for X^{M} and n_{WS} for most chemical elements. The key expression for the sign of the enthalpy of formation ΔH^{for} of binary alloys is

$$\Delta \overline{H}^{\text{interface}}_{\text{A in B}} \propto [-(\Delta X^{M})^2 + (Q/P)(\Delta n^{1/3}_{WS})^2] \qquad (1)$$

P and Q are constants for certain groups of systems, e.g. systems containing only transition elements. The concept that the energy effect upon alloying is generated solely at the contact surfaces between dissimilar Wigner–Seitz atomic cells results consequently in the fact that ΔH^{for} does not vary with the concentration as long as the basis atomic cell A remains fully surrounded by dissimilar atomic cells B. For intermetallic compounds the elastic mismatch effect will be of no practical importance, since only crystal structures that are favorable for the given constituent chemical element sizes will be realized. Therefore, relation (1) directly applies to intermetallic compounds AB_y if they are sufficiently rich in B such that A atoms are completely

Table 3. Five atomic properties (APs) of the chemical elements, each representing an accurate and complete example of our five factors (groups). The first to fifth bars from left to right within a chemical element box are:

(i) R^Z_{s+p}	pseudopotential radii after Zunger (1981)	for the size factor
(ii) AN	atomic number	for the atomic-number factor
(iii) T	melting point	for the cohesive-energy factor
(iv) $X^{M\&B}$	electronegativity after Martynov and Batsanov (1980)	for the electrochemical factor
(v) V	valence-electron number	for the valence-electron factor

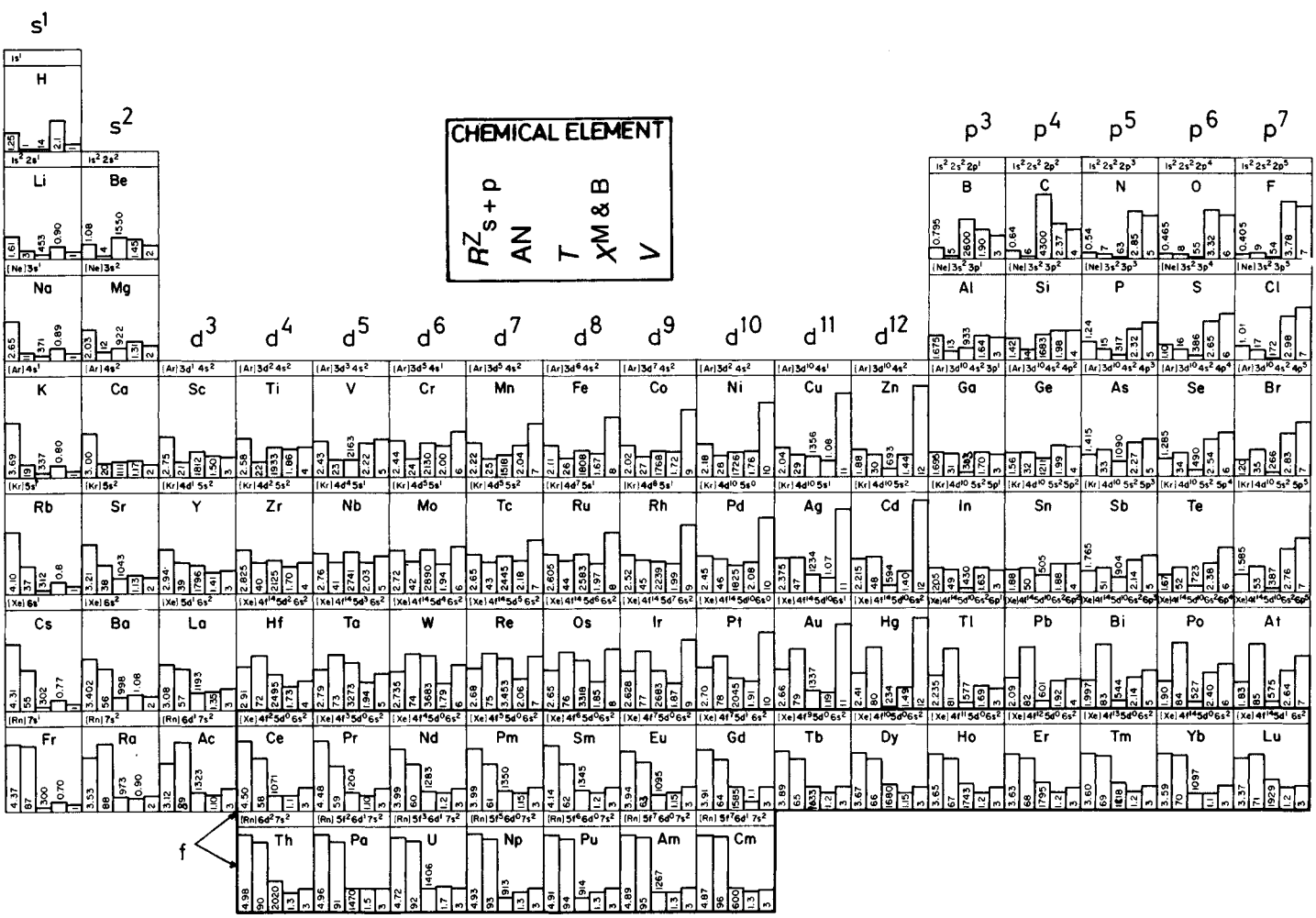

surrounded by B neighbors, and therefore the enthalpy of formation ΔH^{for} of the intermetallic compound AB_y per mole of A is equal to

$$\Delta H^{for}_{AB_y} = \Delta \bar{H}^{interface}_{A \text{ in } B} \quad (2)$$

Assuming that Q and P are truly constant for arbitrary choices of the constituent chemical elements, the sign of the enthalpy of formation is simply determined by the ratio

$$W = |\Delta X^M| / |\Delta n^{1/3}_{WS}| \quad (3)$$

For $W > Q/P$ the ΔH^{for} value is negative, while in the opposite case the ΔH^{for} value is positive. The analysis of the sign of the predicted and experimental $\Delta H^{for} < 0$ is demonstrated for binary systems including two transition metals (Figure 3). Each symbol in the X^M versus

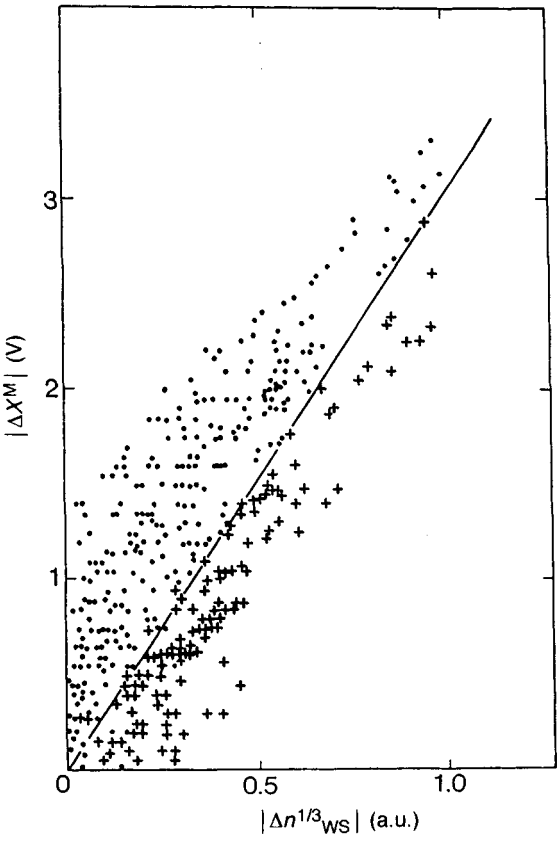

Figure 3. Miedema's two-dimensional compound-formation map for binary systems containing two transition metals. For the meaning of the '+' and '●' symbols, see text; each symbol represents one binary system

n_{WS} diagram corresponds to a particular binary system. Since information on phase diagrams is easier to retrieve than numerical values of ΔH^{for}, in assigning '+' or '●' to the points in this plot, the following criteria are used: '●' in the binary systems with one or more intermetallic compounds that are stable at low temperature, indicating $\Delta H^{for} < 0$; and '+' if there is no intermetallic compound in the binary system or if both terminal solid solubilities are smaller than 10 at .%, indicating $\Delta H^{for} > 0$. There are complications in binary systems combining non-transition metals with transition metals. If the analysis is performed in the same way as in Figure 3, the demarcation line deviates from a straight line, and there appears to be a systematic deviation, which can be resolved more favourably by recognizing a dependence on the number of conduction electrons of the non-transition metal.

Another semiempirical approach by Villars has also proven to be successful and is described in Villars (1985). The demarcation lines (surfaces) are much more complicated and consequently less trustworthy; therefore we recommend the use of Miedema's model. Nevertheless in Villars' model one gets, for the case where intermetallic compounds are absent in binary systems, additional information as to the following four phase diagram types: complete solid solubility, complete solid insolubility, simple eutectic, and simple peritectic systems. Figure 4 shows a part of a chemical element versus chemical element plot (Villars *et al.*, 1989). Each field represents a binary system. For the systems where experimentally determined phase diagrams show the absence of intermetallic compounds, '×' is given. Where no experimental data are available, predictions are given indicated by '\' (after Miedema) and '/' (after Villars, only given in the cases where Miedema gave no prediction). Figure 4 shows that, upon alloying, the s–s, d^{3-7}–d^{3-7}, f–f, s–d^{3-7}, s–f and d^{3-7}–f chemical element combinations almost always result in the absence of intermetallic compounds; see element designations in Table 3.

3.2 Ternary Systems

Attempts to extend Miedema's model to ternary systems failed. The extension of compound-formation maps to ternary systems is described in Villars (1986). In the ternary systems we face two additional major problems: only very few ternary systems are fully determined, and for many of them only a part of an isothermal section has been experimentally determined. During an extensive literature search (Villars and Calvert, 1985) we found in 1984 information on 5598

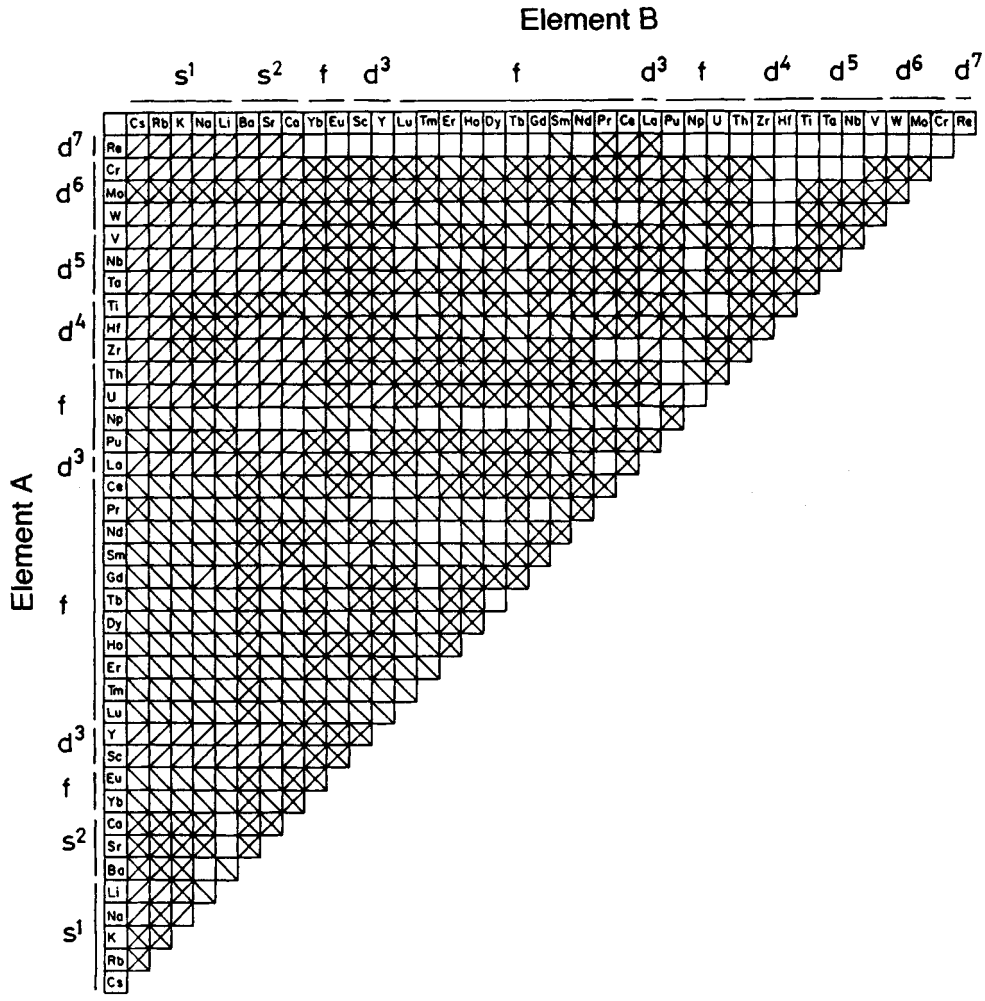

Figure 4. Part of a chemical element versus chemical element plot containing the experimental data and predictions for compound formation or respectively its absence in binary systems. For the meaning of the symbols, see text

ternary systems, which represents only 3.6% of the possible 161 700 systems. Furthermore, looking at the alloying situation from the constitutional point of view, the situation becomes definitely more problematic. Having in mind the two additional difficulties, which cannot be avoided, one can only have confidence in a prediction for ternary systems if it is possible to separate the two groups (compound formation and respectively its absence) in one diagram with relatively simple demarcation lines in a two-dimensional diagram or respectively demarcation surfaces in a three-dimensional diagram. The absence of compound formation is experimentally established for 550 ternary systems (0.3%). Based on the experimental fact that no ternary system with compound formation is known whose binary systems are all of the type that do not form intermetallic compounds, we included all combinations (ternary systems) that are surrounded by the 583 experimentally established binary phase diagrams showing no compound formation and ended up with 1602 additional ternary systems where the absence of intermetallic compounds is expected (assuming the correctness of the above-mentioned statement). All together we thus know 2152 ternary systems in which no 'new' ternary intermetallic compound is formed (1.3%). To assign a ternary system to the compound-forming group, we do not need to have a complete isothermal section, since knowledge of a single ternary compound with a fully determined or

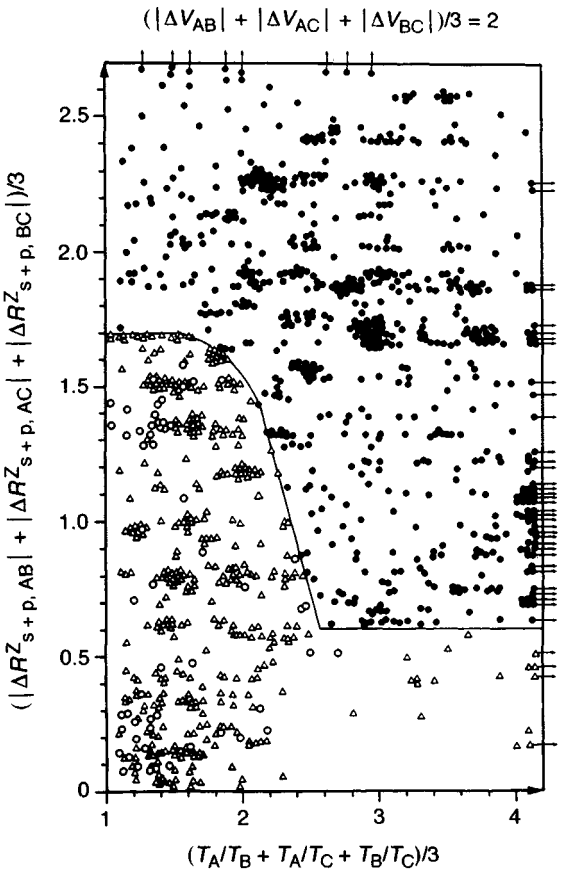

Figure 5. Villars' three-dimensional compound-formation plot of the section for VE = 2 for ternary systems. For the meaning of '△', '○' and '●' symbols, see text; each symbol represents one ternary system

assigned structure is sufficient. For all such ternary systems we checked where the nearby binary intermetallic compounds have the same crystal structure. Where we found this situation we assumed a solid solubility range between the binary and ternary intermetallic compounds and therefore excluded those systems from the new-compound-formation group. By adjusting our coordinates used for the binary systems (Villars, 1985) to the ternary systems, we came to the following coordinates:

- the magnitude of Zunger's pseudopotential radii sums,

$$(|\Delta R^Z_{s+p,AB}| + |\Delta R^Z_{s+p,AC}| + |\Delta R^Z_{s+p,BC}|)/3 \qquad (4)$$

- the magnitude of the difference in the number of valence electrons,

$$(|\Delta V_{AB}| + |\Delta V_{AC}| + |\Delta V_{BC}|)/3 \qquad (5)$$

- and the sum of the ratios of the melting temperatures in kelvin,

$$(T_A/T_B + T_A/T_C + T_B/T_C)/3 \qquad (6)$$

where $T_A > T_B > T_C$. The values for R^Z_{s+p}, V, and T are given in Table 3.

In one three-dimensional diagram we plotted the 2152 systems where the absence of intermetallic compounds is observed and 5048 systems where compound formation is observed. For the user's convenience we made our plots on 12 sections with various isovalence-electron difference $(|\Delta V_{AB}| + |\Delta V_{AC}| + |\Delta V_{BC}|)/3$ values. Figure 5 shows such a section for $(|\Delta V_{AB}| + |\Delta V_{AC}| + |\Delta V_{BC}|)/3 = 2$. The symbol '△' stands for no compound formation determined by experiment; '○' stands for no compound formation by extrapolation from experimentally established binary phase diagrams, all showing absence of intermetallic compounds; and '●' stands for compound-forming systems. With a relatively simple demarcation surface it was possible to separate these two groups satisfactorily. Figure 6 shows the schematic three-dimensional formation diagram. The separation surface is based on 2152 + 5048 ternary systems and is accurate to 94%, which might be in the range of experimental accuracy. It is nicely seen from Figure 6 that the absence of 'new' intermetallic compounds is found along the three coordinates; this means that the magnitude of any one of the factors, i.e. the pseudopotential radii difference expression, or the valence-electron difference expression, the melting-point ratio expression of the constituent chemical elements, has to be small. In the cases where the values of any two or all three expressions are small, we also have absence of intermetallic compounds.

4. Regularities in Intermetallic Compounds

We have tried to summarize the most outstanding publications about regularities and gave special preference to the ones which included in their investigation large groups of well-defined data sets, in the range of hundreds to thousands of data sets. Again, whenever possible, we discuss first the binaries followed by the ternaries (multinaries) in the subsequent approaches.

Chapter 2

Close-Packed Structures

Jürgen Hauck and Klaus Mika

Institut für Festkörperforschung, KFA Forschungszentrum, D-52425 Jülich, Germany

1. Introduction

The large variety of metals, ordered and disordered alloys, and interstitial alloys with close-packed structures has fascinated many theoreticians and experimentalists and inspired them to write articles and books about this subject. A mathematical treatment for rigid-sphere packing, for example, was given by Patterson and Kasper (1959, 1967), while Schubert (1964, 1967) and Ogawa (1974) investigated long-period ordered alloys. The large number of crystal structures was classified by Wyckoff (1964), Pearson (1967, 1972), and Villars and Calvert (1986). The close-packed structures with coordination number (CN) 12 of each metal atom were represented on structure maps with metal atomic radii, electronegativity, and number of electrons as parameters (Villars and Hulliger, 1987; Villars *et al.*, 1989; Chapter 18 by Pettifor in this volume). In our present and previous investigations (Hauck *et al.*, 1988a, 1989) we have extended the numerical analysis of the environment from the 12 nearest neighbors to metal atoms at larger distances using the mathematical formulas of Patterson and Kasper (1959, 1967). All structures from the different compilations, from the simplest to the long-period ordered structures, can be ordered by this procedure in structure maps. These can be compared with the structure maps obtained by theoreticians, as e.g. Ducastelle (1991), with a different approach to the analysis of attractive or repulsive interactions between metal atoms in close-packed structures.

2. Stacking Sequences

When pure metals crystallize, the bonding tendencies of the individual atoms should be identical. The same environment can be expected for each metal atom. Two limiting situations may be discerned: either the structure is based on a three-dimensional (3D) framework of directional covalent bonds as in gray α-Sn with the diamond structure or it is a packing of spherical metal atoms as in the close-packed structures. Metal atoms with weak bonding behave like tennis balls packed in a basket. The packing consists of coplanar hexagonal layers (Figure 1). Successive layers are stacked with centers of spheres falling directly over the centers of the triangular interstices of the two-dimensional (2D) layer below. Each layer has two sets of triangular interstices as outlined for the unit cell in Figure 1. Each of the two

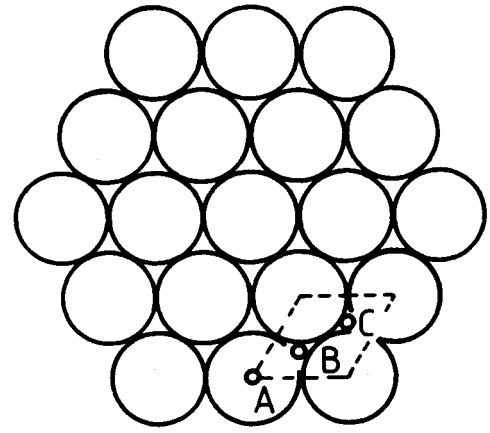

Figure 1. Close-packed hexagonal layers of spheres with position, e.g. A. The next hexagonal layer can be placed either on B or C positions. Hexagonal unit cells with $a = b = d$ (diameter of atoms), $c = n\sqrt{2/3}d$, n = number of layers

Crystal Structures of Intermetallic Compounds. Edited by J. H. Westbrook and R. L. Fleischer

sets forms the same lattice as the spheres themselves. The three different positions that can be occupied by metal atoms in successive layers are conventionally denoted as the A, B, and C positions (Figure 1). Different stacking sequences of hexagonal layers, which can be characterized by the sequence of positions, e.g. ABACB. . . , give rise to different crystal structures. The part of the volume of the basket that can be filled by the tennis balls reaches 74%, which is the highest possible density for packing of identical spherical atoms (Max, 1992). Therefore, these structures are called close-packed (for details see Patterson and Kasper, 1959, 1967).

Rigid spheres without long-range interactions form an infinite number of possible stacking sequences. Metallic cobalt can be obtained in this type of packing with a disordered sequence of A, B, and C positions after successive annealing above and below 450 °C (Wyckoff, 1964). At temperatures above 450 °C it prefers the ABCABC . . . packing; at lower temperatures and after long annealing it crystallizes in ABAB . . . packing. The periodic sequence ABAB . . . of two layers (AB) is called hexagonal close-packed (h.c.p. or h), and the periodic sequence ABCABC . . . of three layers (ABC) is cubic close-packed (c.c.p. or c), because of the hexagonal or cubic symmetry, respectively. The h.c.p. and c.c.p. metal structures are usually distinguished by the prototype elements Mg and Cu and the *Strukturbericht* or Pearson symbols (Table 1). Forty-eight of the 59 elements shown in Figure 2, the rare-earth and the actinide metals except Eu, U, Np (and the very unstable elements Pm, Es, Fm, etc.), can be obtained in a close-packed modification (Villars and Calvert, 1986). Some metals can even crystallize in the same structure type but with different lattice constants, as e.g. the low- and high-pressure forms of Ce with c.c.p. stacking (Villars and Calvert, 1986). The atomic radius of Ce decreases discontinuously with increasing pressure. Also the noble gases with very weak van der Waals forces crystallize in h.c.p. (He) or c.c.p. (He, Ne, Ar, Kr, Xe, Rn) structure (Wyckoff, 1964). The structure of solid He depends on the isotope. Other elements forming molecules, as e.g. O_2, F_2, I_2, B_{12} (Pauling, 1945, 1960; Wyckoff, 1964) or C_{60} fullerene (David *et al.*, 1991), crystallize in close-packed structures with rotational disorder of the molecules occurring at increased temperatures.

A few metals crystallize also in more complex close-packed structures with a maximum of nine layers

Table 1. Stacking sequences of $n \leqslant 9$ hexagonal layers with conventional or stacking symbols and number M^i of metal atoms with different coordination T_i, prototype with Pearson and *Strukturbericht* symbols, space group of undistorted structures, and population (maximum values from different compilations). The Hg and In structures at $n = 3$ are rhombohedral and tetragonal variants of the Cu structure

Layers n	Conventional symbols	Stacking symbols		M^i	Prototype (symbols)	Space group	Population
2	AB	hh	or $(h)_2$	1	Mg (hP2/A3)	$P6_3/mmc$	271
3	ABC	ccc	or $(c)_3$	1	Cu (cF4/A1)	$Fm\bar{3}m$	369
					Hg (hR1/A10)	$R\bar{3}m$	5
					In (tI2/A6)	I4/mmm	28
4	ABAC	chch	or $(ch)_2$	2	La (hP4)	$P6_3/mmc$	33
5	ABCAC	ccchh		2		$P\bar{3}m1$	
6a	ABCBAB	hchchh		3	M_xN_y	$P\bar{6}m2$	
6b	ABCACB	hcchcc	or $(hcc)_2$	2	M_xN_y	$P6_3/mmc$	
7a	ABCACAC	ccchhhh		3		$P\bar{3}m1$	
7b	ABCBCAC	cchhchh		3		$P\bar{3}m1$	
7c	ABCABAC	cccchch		3	M_xN_y	$P\bar{3}m1$	
8a	ABABACAC	chhhchhh	or $(chhh)_2$	2	M_xN_y	$P6_3/mmc$	
8b	ABCBABAB	hchchhhh		3		$P\bar{6}m2$	
8c	ABCBACAB	hchcchch		3		$P\bar{3}m1$	
8d	ABCACACB	hcchhhcc		4		$P\bar{6}m2$	
8e	ABCACABC	ccchhccc		3		$P\bar{3}m1$	
8f	ABCABACB	hccchccc	or $(hccc)_2$	3		$P6_3/mmc$	
9a	ABABCBCAC	chhchhchh	or $(chh)_3$	2	Sm (hR3)	$R\bar{3}m$	32
9b	ABCACACAC	ccchhhhhh		3		$P\bar{3}m1$	
9c	ABCBCACAC	cchhchhhh		3		P3m1	
9d	ABCABACAC	ccccchchh		4		P3m1	
9e	ABCACBCAC	ccchchchh		5		P3m1	
9f	ABCBCABAC	cchhcchch		4		$P\bar{3}m1$	
9g	ABCABCBAC	ccccchcch		4		$P\bar{3}m1$	

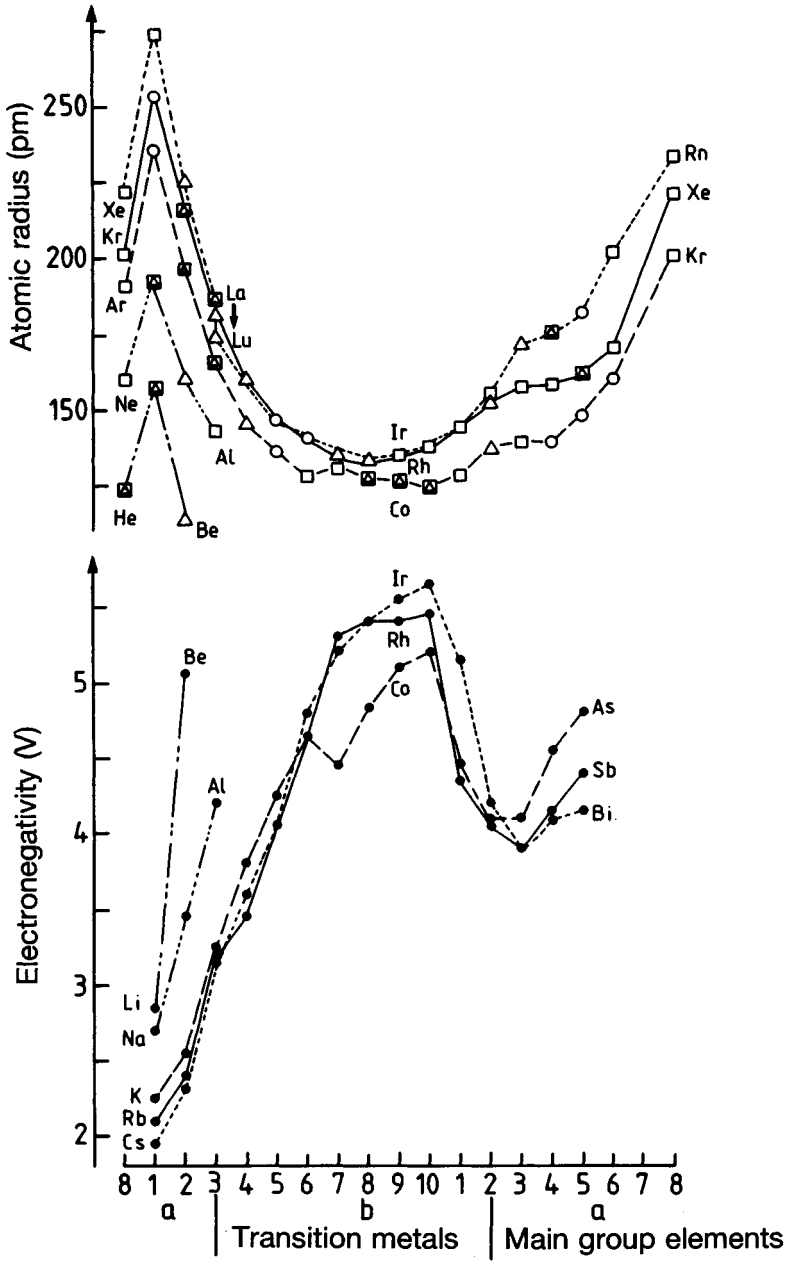

Figure 2. Electronegativity ϕ^* (de Boer *et al.*, 1988) and radii (Schubert, 1967) of 1a–8a main group and 1b–10b transition metals with cubic (□) or hexagonal (△) close-packed crystal structures. Some metals (○) are not observed in a close-packed modification

(Table 1). These structures can be described unambiguously by the stacking symbols h and c introduced by Pauling and Jagodzinski (Pearson, 1972; Mardix, 1990). This notation describes a layer as h or c type according to whether the layers on each side of it are the same type, such as B in ABA, or of different types, such as B in ABC. The two-layer h.c.p. sequence AB gets the symbol hh; the three-layer c.c.p. sequence ABC

has the symbol ccc. The lanthanides La to Sm, Gd, and the actinides Am to Cf crystallize in the ABAC or chch = $(ch)_2$ stacking (This stacking is identical to ABCB or hchc stacking by variation of the origin.) Sm, Gd, and the heavier lanthanides Tb to Ho, Tm, Lu can crystallize also in the ABABCBCAC or chhchhchh = $(chh)_3$ stacking. A comparison of the stacking symbols and population data in Table 1 shows the preference of the elemental metals for simple sequences hh, ccc, $(ch)_2$ or $(chh)_3$. Some more complex sequences are found in alloys M_xN_y (Table 1), which are discussed in Section 8.

The hh hexagonal close-packed and the ccc cubic close-packed structures are the only structure types with a single environment for close and distant neighbors of all atoms ($M^i = 1$). These structures have been observed in 673 binary and ternary systems (Villars and Hulliger, 1987). The five sequences of layers with two different environments of metal atoms ($M^i = 2$) (Pauling, 1945) have been found in 65 systems (Table 1). The metal atoms of the other sequences of layers contain three or more different environments. The tendency to small numbers M^i of metal atoms with different environment can be described by Pauling's rule of parsimony: the number of essentially different kinds of constituents in a crystal tends to be small (Pauling, 1929). The structures with one or two different environments of metal atoms also have the highest symmetry.

Atoms of close-packed structures with diameter $d = 1$ have $T_1 = 6$ nearest neighbors in the same layer and $T_1 = 6$ neighbors in the two adjacent layers (three in each) at distance d (Figure 3), for a total of 12. The number $T_2 = 6$ of second-nearest neighbors at distance $\sqrt{2}d$ is also identical for all close-packed structures. The atoms of the hh structure, however, have $T_3 = 2$ third-nearest neighbors at distance $\sqrt{8/3}d$ and 18 fourth-nearest neighbors at distance $\sqrt{3}d$; while atoms of ccc packing have 24 third-nearest neighbors at distance $\sqrt{3}d$ (Figure 3, Table 2). The coordination polyhedra of T_1, T_2, and T_3 neighbors of the h.c.p. structure

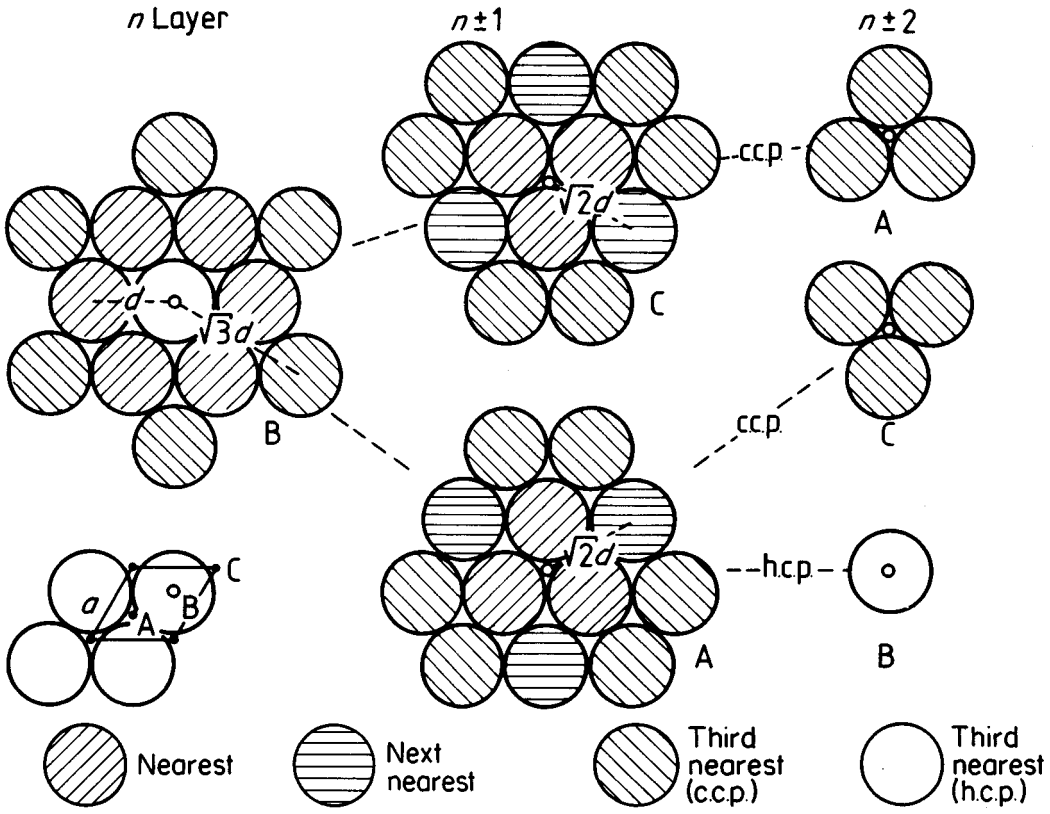

Figure 3. Metal atoms of five hexagonal layers n, $n \pm 1$, and $n \pm 2$. There are 12 nearest, six next-nearest, and 24 third-nearest metal atoms at distances d, $\sqrt{2}d$, and $\sqrt{3}d$ in ABC layers of c.c.p. structure; and 12 nearest, six next-nearest, and two third-nearest metal atoms at d, $\sqrt{2}d$, and $\sqrt{8/3}d$ in AB layers of h.c.p. structure

Table 2. Self-coordination numbers $T_i = T_i^{max}$ of pure metals in hexagonal and tetragonal plane, h.c.p., c.c.p., and interstitial atoms I° at octahedral sites of the h.c.p. metal lattice, and R_i^2/d^2 values in parentheses; R_i = radius of ith shell, d = diameter of spheres

	T_i^{max} (R_i^2/d^2)				
i	Hex. plane	Tetr. plane	h.c.p.	c.c.p.	I° (h.c.p.)
1	6 (1)	4 (1)	12 (1)	12 (1)	2 (2/3)
2	6 (3)	4 (2)	6 (2)	6 (2)	6 (1)
3	6 (4)	4 (4)	2 (8/3)	24 (3)	12 (5/3)
4	12 (7)	8 (5)	18 (3)	12 (4)	2 (8/3)
5	6 (9)	4 (8)	12 (11/3)	24 (5)	6 (3)
6	6 (12)	4 (9)	6 (4)	8 (6)	24 (11/3)
7	12 (13)	8 (10)	12 (5)	48 (7)	6 (4)
8	6 (16)	8 (13)	12 (17/3)	6 (8)	12 (14/3)
9	12 (19)	4 (16)	6 (6)	36 (9)	12 (17/3)
10	12 (21)	8 (17)	6 (19/3)	24 (10)	2 (6)

correspond to CN 12′, CN 6 (octahedron), and CN 2, and the coordination polyhedra of the c.c.p. lattice to CN 12 (cubooctahedron), CN 6, and CN 24″, as shown in Chapter 11 by Villars in this volume. The metal atoms of the experimentally observed sequences $(ch)_2$, ccchh, $(hcc)_2$, $(chhh)_2$, and $(chh)_3$ have two different values for T_3, T_4 and higher coordination shells. The more complex structures contain three or more metal atoms with different environments. The averaged T_3 and T_4 coordination values of these structures depend on the fraction, f, of h layers as given by $T_3 = 2f$ and $T_4 = 24 - 6f$.

The number M^i of metal atoms with different sets of T_i values is often identical to the number of Wyckoff positions, the number of symmetrically different atom positions. For example, the numbers of Wyckoff positions of the Mg, Cu, Sm, and La structures are identical to M^i, but for the $n = 8b$, 9b ($M^i = 3$) structures (Table 1) these numbers are larger than M^i (with values of 5 for example).

The different stacking sequences with n layers in A, B, or C positions can be described by hexagonal unit cells with the lattice parameters $a = b = d$ (diameter of atoms) and $c = n\sqrt{2/3}d$ (Figure 3). The smallest unit cell of ccc packing containing only one metal atom is rhombohedral with lattice constants $a = d$ and $\alpha = 60°$.

Usually, the ccc structure is described as the face-centered cubic (f.c.c.) lattice containing four metal atoms with lattice constants $a_c = \sqrt{2}d$. The f.c.c. lattice can also be considered as a stacking of tetragonal layers in the K and L positions (Figure 4). The c-axis of the hexagonal cell corresponds to one of the four space diagonals of the cubic cell. The only periodic 3D packing of spheres having close-packed hexagonal layers in four

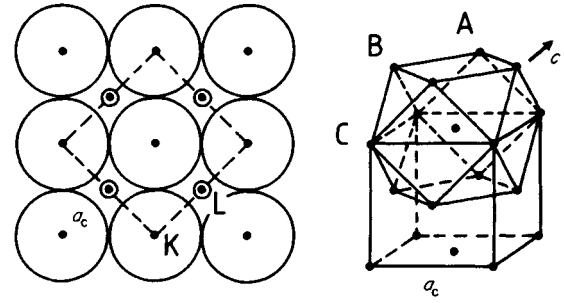

Figure 4. Packing of tetragonal layers at K and L positions in face-centered cubic metal structure and relation to c.c.p. stacking of hexagonal layers in ABC position

inclined directions is ccc. All other sequences are maintained in one direction only.

A comparison of the close-packed structures shows that the interactions between metal atoms, e.g. in the ccc Cu structure, must be strong enough to stabilize the atoms of the third layer at the proper position. The Sm atoms of chhchhchh structure must be stabilized in the ninth layer.

An interaction between metal atoms with directional bonding can also be deduced from the distortion of some crystal structures. The c/a ratios of the lattice constants of the hh hexagonal close-packed structures of Ca and Sr are almost ideal with $c/a = \sqrt{8/3} = 1.63$. The c/a ratio is slightly decreased to 1.56 for most h.c.p. metals and increased to $c/a = 1.86$ and 1.89 for Zn and Cd, respectively (Pauling, 1945, 1960; Wyckoff, 1964; Laves, 1967). The distance between layers is also increased in cubic close-packed Hg, Po, and Te with the rhombohedral angle $\alpha = 71$–$103°$ instead of $\alpha = 60°$ (Villars and Calvert, 1986).

The distance between two identical tetragonal layers of ccc packing, which is $a_c = \sqrt{2}d$ for cubic Cu, can be increased up to $1.66d$ in In, Ga, La or Ce or decreased to $1.33d$ in Pu or $1.0d$ in W. Tungsten has a body-centered cubic structure, which will be discussed by Hellner and Schwarz in Chapter 13 in this volume. The 74% density of the close-packed structures, however, is reduced by hexagonal or tetragonal distortions, e.g. to 68% for the body-centered cubic structure (Laves, 1967; Pearson, 1972). These strongly distorted structures are considered as different structure types in some compilations (Ho and Douglas, 1968). This is one reason that the population numbers of different structure types are only rough values for comparison. We have taken the maximum values from the compilations of Wyckoff (1964), Pearson (1972) or Villars and Calvert (1986) of experimentally determined crystal structures. The

undistorted structures are compared in the present chapter for the analysis of the self-coordination numbers T_i.

3. Alloy Formation

The atoms M and N, e.g. of a binary alloy M_xN_y, have different sizes and a different tendency to exchange electrons, which gives rise to different bonding. The electron density and the radii of the M and N atoms can be varied by charge transfer between the M and N atoms. The two parameters do not vary independently for most metals (Figure 2). The electronegativity values of the elements can be related to the electron work-function and indicate the tendency of a metal to exchange electrons (Pauling, 1945, 1960; de Boer *et al.*, 1988). The electronegativity increases with increasing number of electrons to a maximum for the 8b–10b transition elements. Those elements with an almost filled d shell try to accept electrons to complete the d shell with 10 electrons, while elements with few outer electrons like the 1a and 2a alkali and alkaline-earth or the 1b or 2b transition metals with lower electronegativity are ready to donate these electrons. The 1a and 2a metals are then stabilized in the spherical s^2p^6 shell of the noble gases, the 1b and 2b transition metals in the d^{10} shell with decreased radii. The electronegativity increases again for the 4a–7a elements because of the tendency to attain the stable s^2p^6 octet of the noble gases. The radii of metal atoms decrease with increasing number of electrons to a minimum for the stable d^{10} electron configuration (Schubert, 1967). Also the radii of the lanthanides La to Lu are decreased slightly as indicated by the arrow in Figure 2 as a result of the same effect of the filling of the inner 4f-electron shell. The relation between radii and electronegativity indicates the tendency to form spherical metal atoms in alloys. Some metals like Mo, which do not form close-packed structures because of directional bonding of the outer electrons, form close-packed structures in alloys, as e.g. cubic close-packed $MoNi_4$ or $MoPt_2$ (Sections 7 and 10). The directional interactions between metal atoms, however, can even be increased on the formation of an alloy. The CuPd or FeTi alloys, for example, crystallize in an ordered body-centered cubic structure in spite of the close-packed structures of the components. Other pairs of metals like Cu and Rh, with the c.c.p. structure, do not form compounds at all but segregate as two limited solid solutions.

The interactions between the M metal atoms in M_xN_y alloys can be attractive, as e.g. with segregation, or repulsive. Both interactions can be distinguished by an analysis of the self-coordination numbers T_i of M atoms with M atoms. Analysis of the different ways of sphere packing showed the same number $T_1 = 12$ and $T_2 = 6$ of nearest and next-nearest M atoms, respectively. These numbers are reduced on the formation of ordered M_xN_y alloys and can be used to obtain structure maps (Hauck *et al.*, 1988a, 1989; Mika and Hauck, 1990).

The derivation of structure maps will be outlined for the simple examples of the tetragonal and the hexagonal lattice nets of single metal-atom layers. The single tetragonal and hexagonal 2D layers of M atoms (Figures 1 and 4) are the basic units for describing the 3D close-packed metal structures (Beattie, 1967; Lima-de-Faria and Figueiredo, 1969; Beck, 1969).

4. M_xN_y Structure Map of a Single Tetragonal Layer

The metal atoms M and N of M_xN_y alloys can be ordered in a large number of different structures. The structures are characterized by the self-coordination numbers of the metal atoms (T_1, T_2, T_3) to obtain a subdivision of Pettifor's structure map (see Chapter 18 in this volume) for close-packed alloys with $T_1 = CN = 12$. The numerical procedure to obtain a structure map with a correlation between the different structures will be outlined for a single tetragonal layer occupied by M and N atoms (Figure 4). The procedure contains the following steps:

(1) A large variety of structures is obtained by a systematic variation of the unit cell (Figure 5(a)).
(2) The metal positions are occupied by M atoms to a maximum percentage of 50% at $y/x = 1$. The structures at higher M content are identical by exchange of the M and N atoms.
(3) The different crystal structures can be characterized by the coordination of the M atoms with other M atoms in the first, second, and third coordination shells (T_1, T_2, T_3) and the ratio (y/x) of N and M atoms, e.g. the notation 204;1 is used for the structure with $T_1 = 2$ metal atoms M at distance d, no M atoms in the second coordination shell, $T_3 = 4$ M atoms at distance $2d$ (Figure 5(b)) and $y/x = 1$. $T_1^{max} = T_2^{max} = T_3^{max} = 4$ are the maximum self-coordination numbers of the tetragonal layer. The coordination numbers of each shell are averaged for structures that have differently coordinated M atoms, e.g. the 323, 442, and 323 coordination numbers of the three types of M atoms in the first sketch in Figure 5(d) are averaged in the 3.3 2.7 2.7;1 structure.

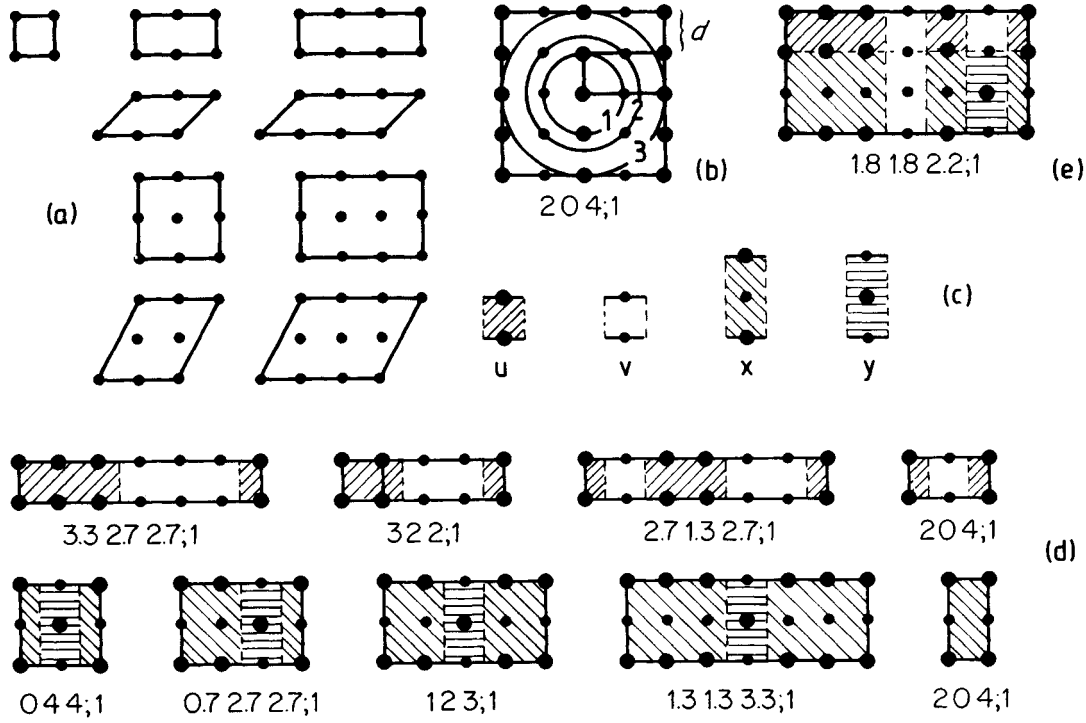

Figure 5. Tetragonal single layers for equal numbers of M and N atoms: (a) different unit cells; (b) occupation with M atoms (large circles) and characterization by T_1 T_2 T_3 self-coordination numbers and composition y/x; (c) different subunits for construction of different structures (d,e)

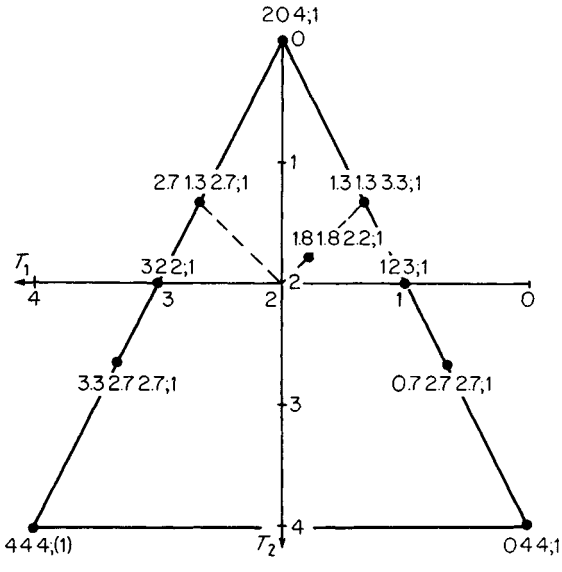

Figure 6. T_1, T_2 structural map of tetragonal single-layer structures T_1 T_2 T_3;1 of Figure 5

(4) The crystal structures characterized by the coordination numbers $T_1 T_2 T_3$ and a fixed composition y/x can be plotted as single points in a T_1–T_2–T_3 coordinate system or as projection in the T_1–T_2 plane as outlined for $T_1 T_2 T_3$;1 structures in Figure 6. All structures are found to fall within a triangle, with the three structures 444;(1), 204;1, and 044;1, which have a single environment of M atoms, at the corners. The structures 322;1 and 123;1 have one and three environments, respectively. The structure 444;(1), with the composition given by (1) in parentheses, is used to indicate that the structure can only be obtained in the limit of very large unit cells, because the N atoms must also have this environment.

(5) The structures shown on the structure map can be considered as combinations of the variously shaded structural units u, v, x, and y (Figures 5(c) and (d)). The structures on the left side of Figures 6 and 7 are obtained by the combination of u and v units, structures on the right side by a combination of x and y units. Points within the triangle are obtained by the combination of all the subunits (Figure 5(e)).

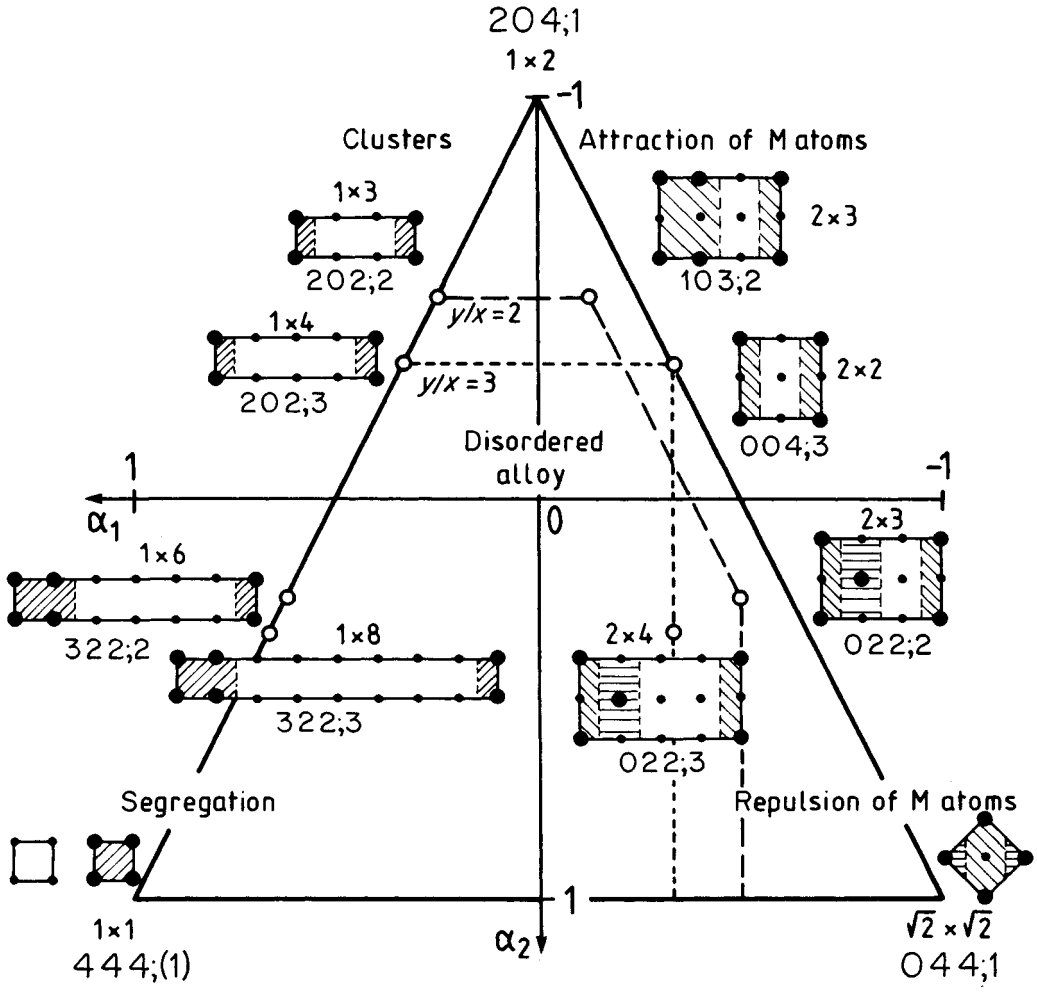

Figure 7. α_1, α_2 structural map of tetragonal single-layer structures $T_1T_2T_3;y/x$ and surface structures $l_1 \times l_2$

(6) Structures $T_1T_2T_3;\ y/x$ with different y/x values can be included in the same structure map (Figure 7) by using Cowley's short-range order parameter α_i (Ducastelle, 1991), which can vary within $-1 \leqslant \alpha_i \leqslant 1$. The α_i values can be obtained from the coordination numbers T_i^M and T_i^N of M and N atoms or from the T_i^M and y/x values (Hauck *et al.*, 1988a):

$$T_i^N = T_i^{max} - (T_i^{max} - T_i^M)x/y$$
$$\alpha_i T_i^{max} = T_i^M + T_i^N - T_i^{max}$$
$$\alpha_i T_i^{max} = T_i^M - (T_i^{max} - T_i^M)x/y$$

The coordination numbers T_i^M and T_i^N of M and N atoms are identical at the composition $y/x = 1$ but different at other compositions. Structures with different compositions can be obtained by using the same structural subunits. The area mapped out by the maximum range of α_1, α_2 values is different at different compositions, as outlined for $y/x = 2$ and $y/x = 3$ in Figure 7.

(7) The α_i values are zero for a random distribution of M and N atoms, because the mean value of $T_i^M + T_i^N$ equals T_i^{max}, which corresponds, for example to $T_1 = T_2 = T_3 = 2$ at composition $y/x = 1$ (Figure 7). Very small α_i values are expected for alloys with very weak interactions and in particular at high temperatures. Positive α_i values are obtained for attractive interactions of M atoms, i.e. for cluster formation or segregation. The 202;2 and 322;2 structures of Figure 7 consist of single and double

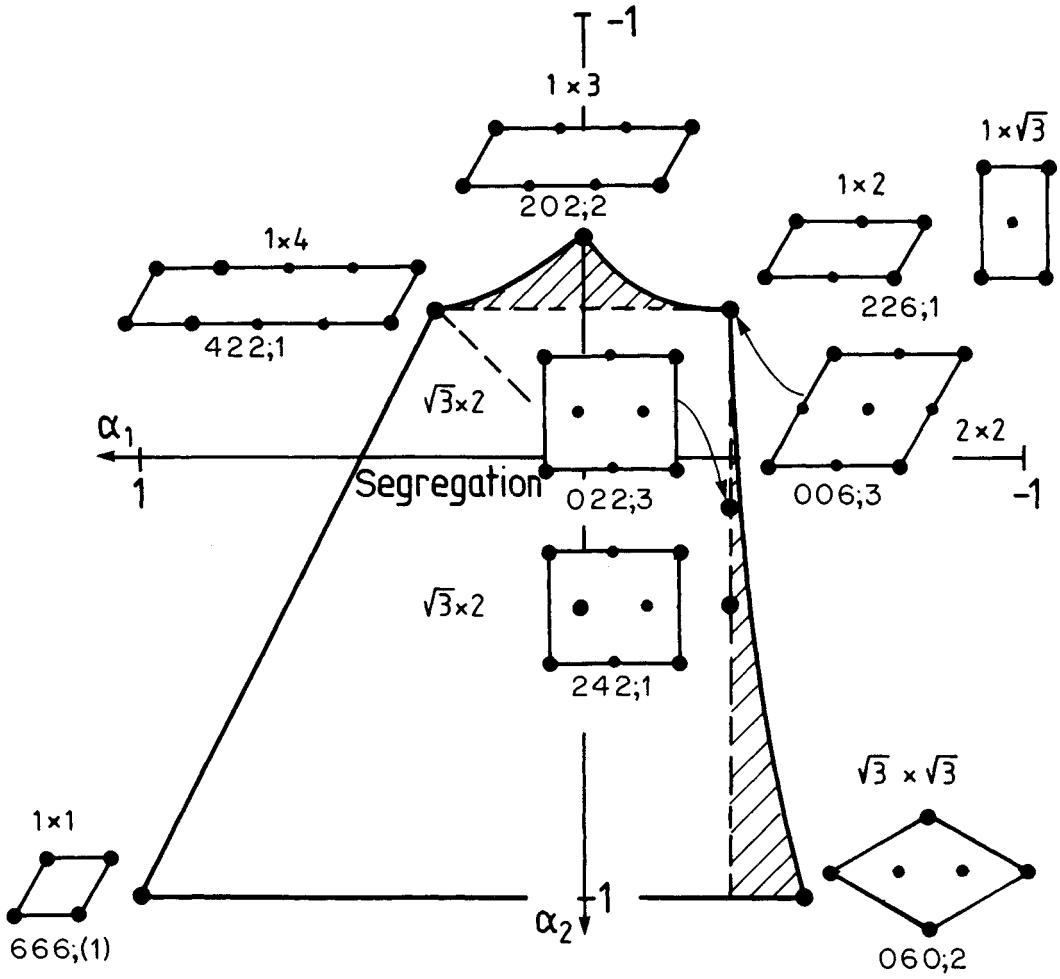

Figure 8. α_1, α_2 structural map of hexagonal single-layer structures $T_1T_2T_3;y/x$ and surface structures $l_1 \times l_2$

rows of M atoms, respectively. The size of the M and N clusters is increased to complete segregation of M and N atoms in the 444;(1) structure. Negative α_1 values indicate repulsive interactions between M atoms, e.g. Coulomb repulsion.

(8) Two-dimensional tetragonal structures are observed, for example, for gas molecules adsorbed on the (100) surfaces of c.c.p. metals (MacLaren *et al.*, 1987). The occupation of the surface of metal atoms with gas molecules depends on the size of the gas molecules, the equilibrium gas pressure, and the interaction between the molecules. The unit cell is usually described by the length of the two sides $l_1 \times l_2$ as outlined in Figure 7. There are different structures with identical unit cells for occupation of two or more positions, as can be seen by the two 2×3 structures 103;2 and 022;2.

5. Ordering of Atoms in Hexagonal Layers

Each metal atom within a hexagonal layer has $T_1^{max}=6$ nearest, $T_2^{max}=6$ next-nearest, and $T_3^{max}=6$ third-nearest neighbors at distances d, $\sqrt{3}d$, and $2d$, respectively (Figure 3). The structure map (Figure 8) contains six structures with a single environment at the corners of an irregular pentagon: 666;(1), 422;1, 202;2, 226;1, 006;3, and 060;2. The 226;1 and 006;3 structures have identical α_i values. The crystal structures existing along the different borderlines can be obtained by combinations of the structural elements in the same way as was done for the tetragonal plane structures. The cross-hatched area of the pentagon with the limiting structures 202;2 and 060;2 cannot be obtained at the composition $y/x=1$, because the borderlines depend on y/x (item (6) of Section 4).

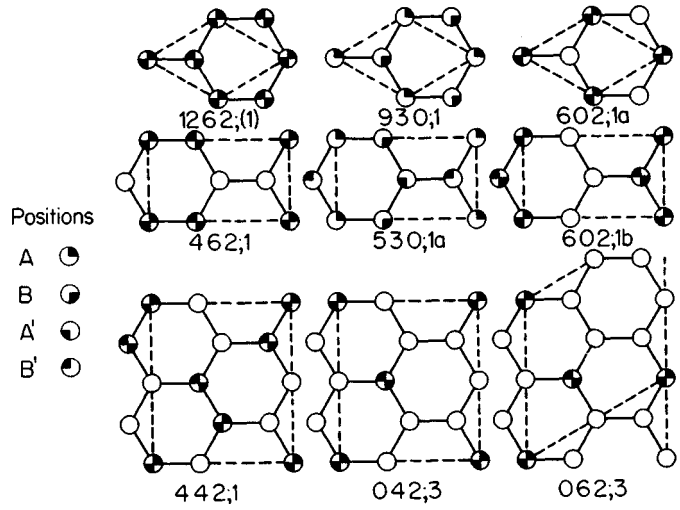

Figure 9. Five hexagonal close-packed structures M_xN_y: 1262;(1) Mg, 602;1a LiRh, 462;1 AuCd, 042;3 $TiCu_3$, and 062;3 $SnNi_3$; and four theoretical structures at the border of the structure map in Figure 10. Projection of four layers ABA'B' with M atoms at A, B, A' or B' positions. Nearest-neighbor A and B positions are connected by full lines; unit cells are indicated by broken lines

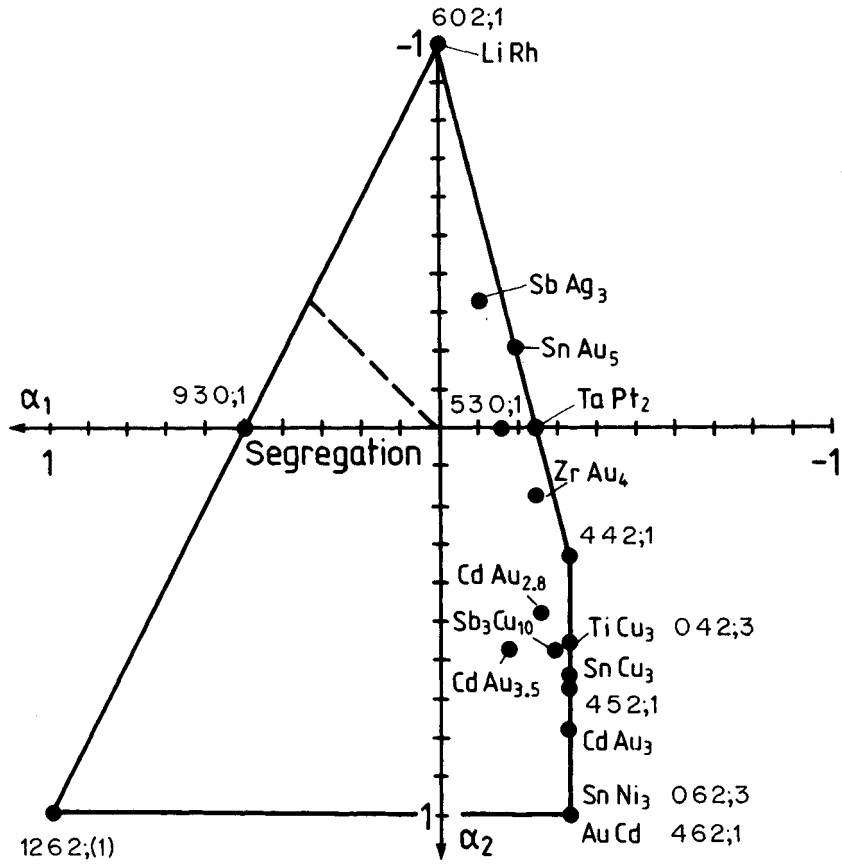

Figure 10. α_1, α_2 structure map of ordered h.c.p. structures

The two-dimensional structures of adsorbed gas molecules with the unit cells 1×1, 1×3, and $\sqrt{3}\times\sqrt{3}$ can be compared to the analogous structures 1×1, 1×2, and $\sqrt{2}\times\sqrt{2}$ of the tetragonal plane. The cells 1×2 and $1\times\sqrt{3}$ are different unit cells of the 226;1 structure.

6. Hexagonal Close-Packed Structures

The hexagonal close-packed alloys consist of two hexagonal layers in A and B positions with identical environment of 12 nearest, six next-nearest and two third-nearest neighbors at distances d, $\sqrt{2}d$, and $\sqrt{8/3}d$, respectively (Figure 3). The maximum α_1–α_2 range of ordered h.c.p. M_xN_y alloy structures is within a tetragon with the 1262;(1), 602;1, 442;1, 462;1, and 062;3 structures at the corners (Figures 9 and 10). The 530;1 and 930;1 structures are also at the corners in the three-dimensional α_1–α_2–α_3 space (Mika and Hauck, 1990). Several structures with a single environment of metal atoms are inside the structure map. The 930;1 structure with two layers of M atoms followed by two layers of N atoms can be considered as partially segregated sheets of M and N atoms. The M atoms of the 602;1a and 602;1b structures are clustered in layers and chains, respectively. The M atoms of the remaining structures of Figure 9 are as far apart as possible. The 462;1 and 062;3 structures with identical α_i values correspond to the AuCd and $SnNi_3$ structures. The other experimental structures are found at lower α_2 values.

The architecture of the different structures built up from structural subunits is more complicated than for those from single tetragonal or hexagonal layers. The construction of MN and MN_3 structures by the combination of u, v, x, and y units is shown in Figure 11. The $SnCu_3$ structure, for example, can be obtained by the combination of these units in the sequence u_4vu_4v. The theoretical structures at the left border of Figure 10 consist of alternating layers of M and N atoms. The other structures have layers with identical composition and environment of the M atoms in these layers (Table 3). Therefore, these structures can also be described by the type and the stacking sequence of hexagonal layers.

7. Cubic Close-Packed Structures

Each metal atom of the c.c.p. structure has $T_1^{max}=12$, $T_2^{max}=6$, and $T_3^{max}=24$ for the first-, second-, and third-nearest neighbors at distances d, $\sqrt{2}d$, and $\sqrt{3}d$ (Figure 3). The maximum $T_1T_2T_3$ values are reduced in M_xN_y alloys where $y/x\geqslant1$ (Table 4). The structure

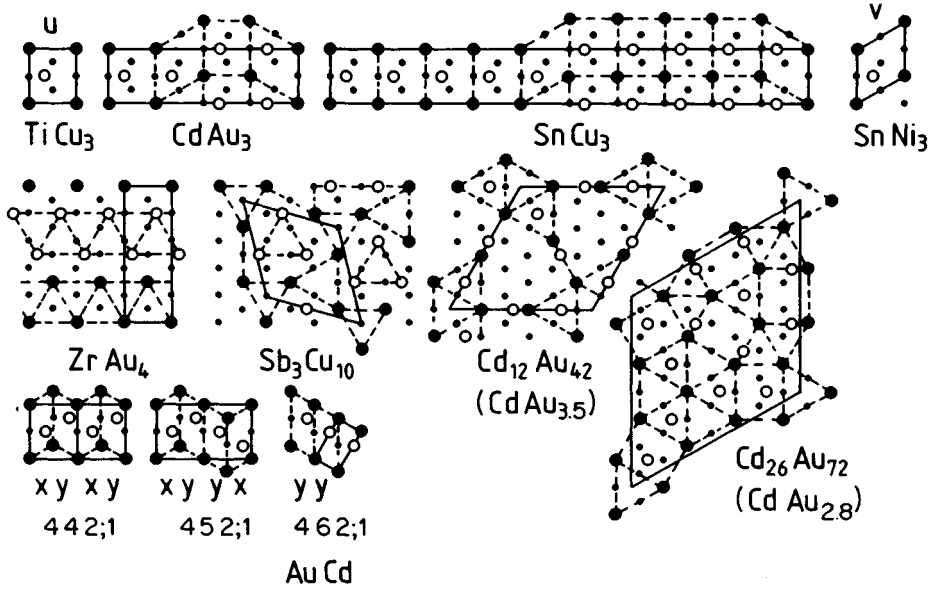

Figure 11. Architecture of h.c.p. MN and MN_3 structures at the right border of the structural map (Figure 10), and $ZrAu_4$, Sb_3Cu_{10}, $Cd_{12}Au_{42}$ ($CdAu_{3.5}$) and $Cd_{26}Au_{72}$ ($CdAu_{2.8}$) structures with two hexagonal layers. M atoms (●) and N atoms (·) of first layer, only M atoms (○) of second layer, u, v, x, y structural subunits for puzzle assembly of crystal structure architecture. Second- and third-nearest neighbors of single-layer M atoms are connected by broken lines for pattern recognition

Table 3. Hexagonal close-packed alloys M_xN_y characterized by the self-coordination numbers T_i of M atoms in the h.c.p. structure and in each hexagonal plane, number M^i of metal atoms with different sets of h.c.p. T_i values, and maximum population values from different compilations

$T_1T_2T_3;y/x$					
h.c.p.	hex. plane	M^i	Prototype (symbols)	Space group	Population
1262;(1)	666;(1)	1	Mg (hP2/A3)	$P6_3/mmc$	271
930;1	666;(1)	2		$P\bar{3}m1$	
602;1a	666;(1)	2	LiRh (hP2)	$P\bar{6}m2$	1
602;1b	226;1	2		Pmmn	
530;1a,b	226;1	2		C2/m; Fdd2	
462;1	226;1	2	AuCd (oP4/B19)	Pmma	14
442;1	242;1	2		Pnma	
622;1	242;1	2		Pbcm	
530;1d,e	242;1	2		$P2_1/c$; C2/c	
730;1a,b	422;1	2		P2/m; $P2_1/m$	
220;2a,b	060;2	2		C2/c; $P6_122$	
222;2	060;2	2	$TaPt_2$ (oC12)	Cmcm	1
0.9 3.7 2;2.8	0 2.3 2.8;2.8	12	$Cd_{26}Au_{72}$ (hP98)	$P6_3/mmc$	1
202;3	226;1	4	$SbAg_3$ (oP4)	Pmm2	1
042;3	022;3	3	$TiCu_3$ (oP8)	Pmmn	25
0 4.4 2;3	0 1.6 2.8;3	7	$SnCu_3$ (oC80)	Cmcm	1
052;3	014;3	5	$CdAu_3$ (oC32)	Cmcm	2
062;3	006;3	2	$SnNi_3$ (hP8/$D0_{19}$)	$P6_3/mmc$	86
042;3.3	022;3.3	5	Sb_3Cu_{10} (hP26)	$P6_3/m$	2
142;3.5	013;3.5	6	$Cd_{12}Au_{42}$ (hP54)	$P6_3/mcm$	1
022;4	040;4	5	$ZrAu_4$ (oP20)	Pnma	3
000;5	060;2	3	$SnAu_5$ (hR6)	R3	1

Table 4. Cubic close-packed alloys M_xN_y characterized by the self-coordination numbers T_i of M atoms in c.c.p. structure and in tetragonal planes (only occupied planes perpendicular to the direction with highest symmetry are included; in Ga_3Pt_5 two different planes exist), number M^i of metal atoms with different sets of T_i values, and maximum population values

$T_1T_2T_3;y/x$					
c.c.p.	tetr. plane	M^i	Prototype (symbols)	Space group	Population
12624;(1)	444;(1)	1	Cu (cF4/A1)	$Fm\bar{3}m$	369
6012;1a	204;1	2	CuPt (hR2/$L1_1$)	$R\bar{3}m$	1
6012;1b	204;1	2	CuPt (cF32/$L1_3$)	$Fd\bar{3}m$	1
6212;1a,b	204;1	2		Pmmn, $P4_2/mmc$	
4416;1	044;1	2	UPb (tI8)	$I4_1/amd$	2
4 5.6 9.6;1	044;1	6	CuAu II (oI40)	Imma	1
468;1	444;(1)	2	CuAu (tP4/$L1_0$)	P4/mmm	93
			NaHg (oC16)	Cmcm	8
546;1.25	121;1.25	3	V_4Zn_5 (tI18)	I4/mmm	1
356;1.5	333;0.25	4	Ti_2Ga_3 (tP10)	P4/m	1
2.7 4.7 5.3;1.7	004;3, 044;1	4	Ga_3Pt_5 (oC16)	Cmmm	5
22 12;2a	202;2	2	$MoPt_2$ (oI6)	Immm	8
248;2	044;1	3	$ZrSi_2$ (oC12/C49)	Cmcm	30
254;2a	044;1	4	$ZrGa_2$ (oC12)	Cmmm	2
254;2b	044;1	3	$HfGa_2$ (tI24)	$I4_1/amd$	8
1310;2.5	110;2.5	4	Mn_2Au_5 (mC14)	C2/m	1
0.8 48;2.6	044;1	10	Nb_5Ga_{13} (oC36)	Cmmm	1
0.7 3.3 9.3;2.7	0.7 1.3 0;2.7	6	Mo_3Al_8 (mC22)	C2/m	1
204;3	204;1	3	$CuPt_3$ (oC8)	Cmmm	1
048;3	044;1	3	$TiAl_3$ (tI8/$D0_{22}$)	I4/mmm	43
054;3	044;1	3	$ZrAl_3$ (tI16/$D0_{23}$)	I4/mmm	7
			$CdAu_3$ II (tI16)	I4mm	2
060;3	044;1	2	$AuCu_3$ (cP4/$L1_2$)	$Pm\bar{3}m$	386
			SiU_3 (tI16/$D0_c$)	I4/mcm	5
			$SrPb_3$ (tP4)	P4/mmm	15
028;4	000;4	2	$MoNi_4$ (tI10/$D1_a$)	I4/m	16
000;7	004;3	3	$GeCa_7$ (cF32)	$Fm\bar{3}m$	2
020;8	000;8	3	$TiPt_8$ (tI18)	I4/mmm	3

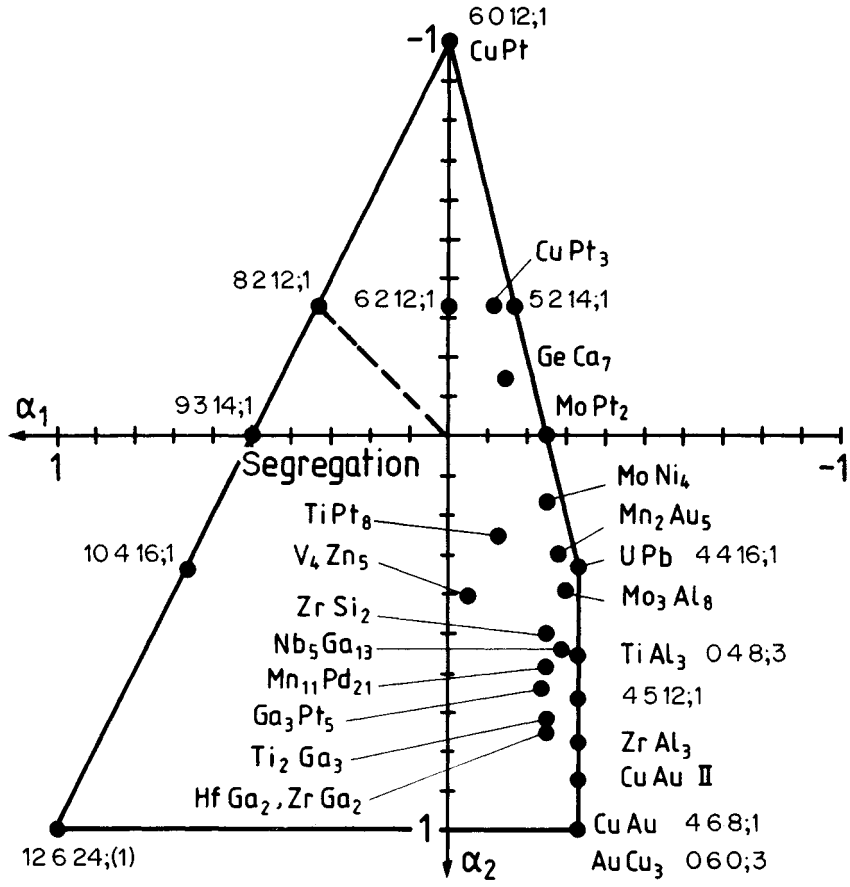

Figure 12. α_1, α_2 structure map of ordered c.c.p. structures

map contains 28 different structures with a single environment of M atoms (Hauck *et al.*, 1988a). The 12 6 24;(1), 6 0 12;1a,b, 44 16;1, and 468;1 structures are the limiting structures (Figures 12 and 13). The 60 12;1a and b structures are homometric structures—structures with identical T_i values, but different symmetry, as will be discussed in some detail in Section 9. The 060;3 $AuCu_3$ structure and the 468;1 CuAu structure have identical α_i values. These structures can be compared with the h.c.p. 062;3 $SnNi_3$ and 462;1 AuCd structures for the same T_1 and T_2 values (Figure 10). The 4416;1 UPb and the 048;3 $TiAl_3$ structures correspond to the h.c.p. 442;1 and 042;3 $TiCu_3$ structures. PtV crystallizes in the CuAu or AuCd structures (Villars and Hulliger, 1987). The 4416;1 UPb structure is identical to the NbP structure (Villars and Calvert, 1986). The architecture of structures along the 12 6 24;(1)–60 12;1a boundary is analogous to that for the h.c.p. structures. The M and N atoms are completely segregated in 12 6 24;(1) with decreasing thickness of hexagonal layers progressing along the boundary (first row in Figure 13). Close-packed planes of M and N atoms alternate in the 6012;1a CuPt structure as in the h.c.p. 602;1a LiRh structure. The c.c.p. structures at low α_1, including most experimental structures, can be assembled from tetragonal layers rather than from hexagonal layers alone as is the case of h.c.p. structures.

The limiting structures at the right border 060;3, 048;3, 468;1, and 4416;1 can be split into structural subunits u, v, x, and y, which can be combined like the parts of a puzzle to obtain the crystal structures found at the right border (Figure 14). The u′, v′, x′, and y′ subunits are obtained from the u, v, x, and y subunits by a variation of the origin. The $ZrAl_3$ structure is obtained from u and u′ units and the CuAu II structure from a combination of the x and y structural subunits. The MN_2 structures $ZrGa_2$, $HfGa_2$, and $ZrSi_2$, and the Nb_5Ga_{13} structure are obtained by combination of u,

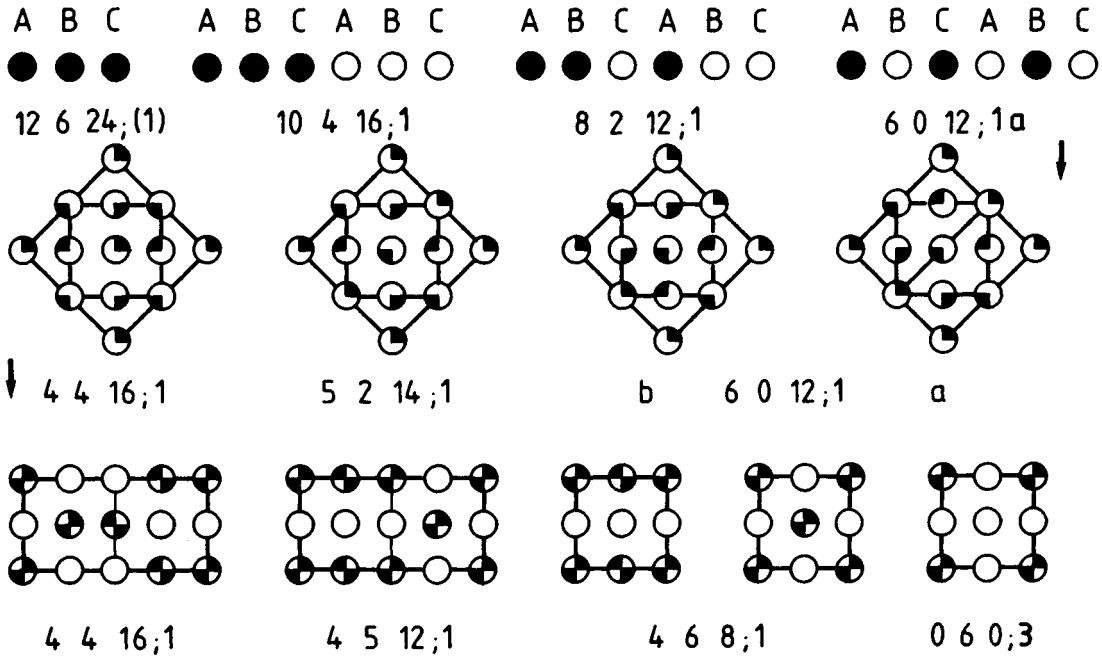

Figure 13. $T_1T_2T_3;y/x$ c.c.p. structures M_xN_y: 12 6 24;(1) Cu, 60 12;1 CuPt, 4416;1 UPb, 468;1 CuAu, and 060;3 $AuCu_3$; and theoretical structures at the border of the structure map (Figure 12). Occupation of hexagonal layers ABC. . . by M atoms in the first row and of four tetragonal layers KLK'L' in the other structures. Two unit cells of 6012;1a structure are shown in the second row

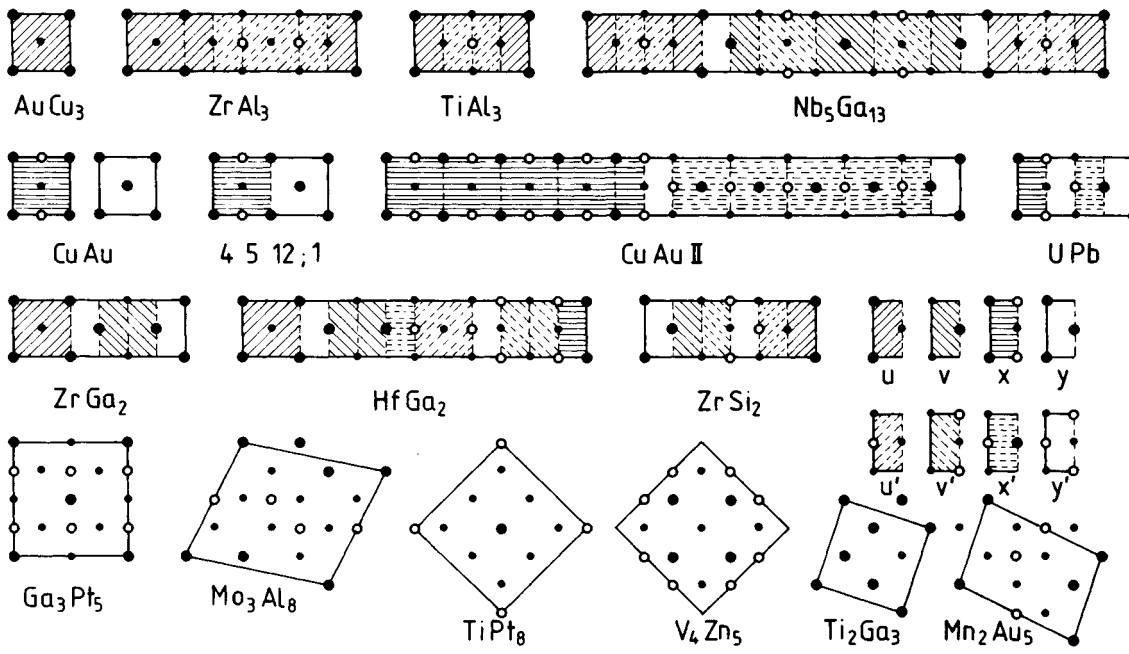

Figure 14. Architecture of c.c.p. MN_3, MN, and MN_2 structures from u, u', v, v', x, x', y, y' subunits and structures with two tetragonal layers with M atoms at $z=0$ (●) and $z=1/2$ (○). Positions of N atoms at $z=0$ (•) for pattern recognition

Table 5. Characterization of structures with a single environment of M atoms

	Tetr. layers	Hex. layers
CuAu	044;1, 444;(1)	226;1
UPb	044;1, 220;1	242;1
$AuCu_3$	044;1, 444;(1)	006;3
$TiAl_3$	044;1, 444;(1), 020;3	022;3

v, x, and y units (Figure 14). Other structures, like Ga_3Pt_5, Mo_3Al_8, $TiPt_8$, V_4Zn_5, Ti_2Ga_3, and Mn_2Au_5 (Figure 14) and the structures from homologous series (Section 10), $MoNi_4$ and $MoPt_2$, can be considered as a packing of two ordered tetragonal layers. The tetragonal M_xN_y layers perpendicular to the drawing plane are separated by layers of N atoms in Ga_3Pt_5 and Nb_5Ga_{13}, and in all MN_3 and MN_2 structures. Most of the experimental structures are at boundary lines for the given composition. The only exception in Table 4 is V_4Zn_5, which lies at the boundary line of the structure map belonging to the hexagonal layer (Figure 8).

The structures with a single environment of M atoms can be characterized by tetragonal or hexagonal layers with small unit cells, as shown in Table 5. The structures with $M^i > 2$ (Table 4), as e.g. the CuAu II or $ZrAl_3$ structure at the right boundary of the structure map (Figure 12), consist of u,v,x,y structure subunits, which are connected by 044;1 tetragonal planes. The other layers of the CuAu–UPb and $AuCu_3$–$TiAl_3$ parent structures do not fit together. The structural subunits of many structures on the right side of the structure map (Figure 12) are connected by 204;1 or 044;1 tetragonal planes (Table 4). Most (theoretical) structures on the left side of the structure map are connected by 666;(1) hexagonal planes.

The α_1, α_2 values of the different layers of a structure are sometimes similar to the α_1, α_2 values of the structure itself (Figures 7, 8, and 12) and are located in the same area of the structure map. An example is the 204;1 tetragonal and 226;1 hexagonal layer of the 60 12;1a CuPt structure. In other structures, as e.g. 22 12;2a $MoPt_2$, the 020;2 and 202;2 tetragonal layers or the 202;2 and 060;2 hexagonal layers are at different locations of the structure maps (Figures 7 and 8), probably because of the directional bonding of Mo atoms.

Table 6. Complex close-packed ordered alloys M_xN_y with the same hexagonal planes as h.c.p. or c.c.p. structures, and maximum population values

Layers	Stacking symbol	Hex. Plane $T_1T_2T_3;y/x$	Prototype (symbols)	Space group	Population
2	hh	226;1	AuCd (oP4/B19)	Pmma	14
3	ccc	226;1	CuAu (tP4/$L1_0$)	P4/mmm	93
6b	$(hcc)_2$	226;1	IrTa (oP12)	Pmma	4
9a	$(chh)_3$	226;1	$LiSn(Nb_2Rh_3)$ (mP6)	P2/m	2
2	hh	060;2	$SnAu_5$ (hR6)	R3	1
3	ccc	060;2	008;5	$P3_112$	
4	$(ch)_2$	060;2	WAl_5 (hP12)	$P6_322$	3
2	hh	006;3	$SnNi_3$ (hP8/$D0_{19}$)	$P6_3/mmc$	86
3	ccc	006;3	$AuCu_3$ (cP4/$L1_2$)	$Pm\bar{3}m$	386
4	$(ch)_2$	006;3	$TiNi_3$ (hP16/$D0_{24}$)	$P6_3/mmc$	12
6b	$(hcc)_2$	006;3	$PuAl_3$, VCo_3 (hP24)	$P\bar{6}_3/mmc$	7
7c	ccchch	006;3	$Ti(Pt_{0.89}Ni_{0.11})_3$ (hP28)	$P\bar{3}m1$	1
9a	$(chh)_3$	006;3	$BaPb_3$ (hR12)	$R\bar{3}m$	26
10	$(hhchc)_2$	006;3	γ-$Ta(Pd_{0.67}Rh_{0.33})_3$ (hP40)	$P\bar{6}_3/mmc$	1
12	$(hhcc)_3$	006;3	$PuGa_3$ (hR16)	$R\bar{3}m$	4
14	$(hhhchhc)_2$	006;3	$Ba(Pb_{0.8}Tl_{0.2})_3$ (hP56)	$P6_3/mmc$	1
15	$(hchcc)_3$	006;3	$HoAl_3$ (hR20)	$R\bar{3}m$	15
2	hh	022;3	$TiCu_3$ (oP8)	Pmmn	25
3	ccc	022;3	$TiAl_3$ (tI8/$D0_{22}$)	I4/mmm	40
6b	$(hcc)_2$	022;3	β-$NbPd_3$ (oP24)	Pmmn	2
12	$(hhcc)_3$	022;3	β-$NbPt_3$ (mP48)	$P2_1/m$	4
2	hh	014;3	$CdAu_3$ (oC32)	Cmcm	1
3	ccc	014;3	$ZrAl_3$ (tI16/$D0_{23}$)	I4/mmm	7
4	$(ch)_2$	014;3	$MgAu_3$ (oC64)	Cmcm	1
6a	hchchh	014;3	$CdAu_{2.8}$ (oC96)[a]	Amm2	1
9a	$(chh)_3$	014;3	$CdAu_{2.7}$ (mC576)	C2/m	1
10	$(hhchc)_2$	014;3	$MgAu_3$ (oC160)	Cmcm	1

[a] An alternative structure to this (h P98) is given in Table 3.

8. Ordered Structures of Complex Close-Packed Alloys

The complex close-packed metals (Table 1) are similar to h.c.p. stacking with only one direction of packing of the hexagonal layers. All structures of Table 1 contain a threefold axis in the *c* direction of the stacked layers. The metal atoms of the complex structures of Table 1 already have two or more different environments. The values of T_1 and T_2, however, are identical for all complex close-packed metals. The α_1–α_2 structure maps are the same as for h.c.p. and c.c.p. alloys. The architecture of the borderline structures resembles those of h.c.p. alloys containing hexagonal layers of M atoms. These structures can be divided into five groups corresponding to different α_1, α_2 values and different hexagonal layers (Table 6) (Beck 1969; Zhao *et al.*, 1991). The h.c.p. $CdAu_3$ structure, for example, with $\alpha_1 = -0.33$, $\alpha_2 = 0.78$, is gradually altered to the c.c.p. $ZrAl_3$ structure with different stacking of 0 1 4;3 hexagonal layers by variation of the Au content or partial substitution of Cd by In (Schubert, 1964) (Table 6). The c.c.p. 0 0 8;5 structure corresponding to h.c.p. $SnAu_5$ and $(ch)_2$ WAl_5 is only observed in the interstitial alloy V_6C_5 (see Section 14).

9. Structures with Identical Powder Patterns

Some c.c.p. and h.c.p. structures are homometric with identical coordination T_i of all atoms for all *i* (Figure 15) and some other structures differ only in higher coordination spheres (Hauck *et al.*, 1988a). The homometric structures cannot be distinguished by powder diffraction methods, if the lattice is undistorted (Patterson, 1944). Other structures are enantiomorphous, i.e. the crystal

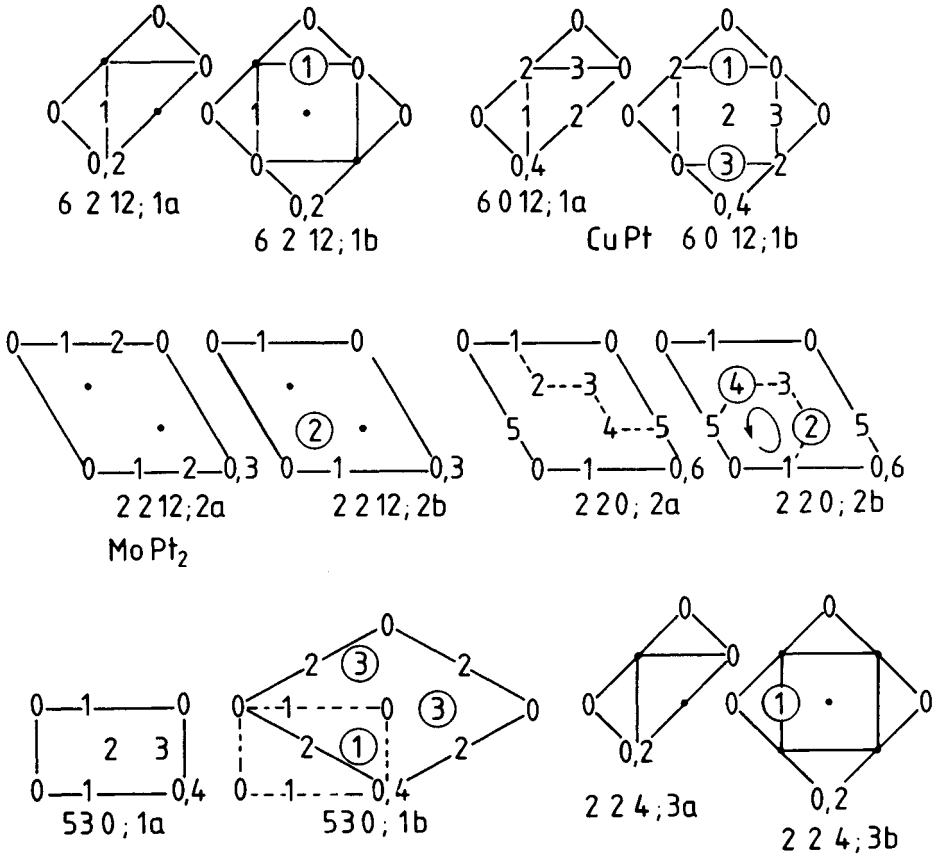

Figure 15. Examples of homometric pairs of structures with identical self-coordination numbers T_i: 6 2 12;1a,b, 6 0 12;1a,b, 2 2 12;2a,b, and 2 2 4;3a,b are c.c.p.; 2 2 0;2a,b, and 5 3 0;1a,b are h.c.p. The positions of M atoms are given by the projection height. The different M positions of homometric pairs are encircled. N atoms at $z = 0$ (•)

structures contain right- or left-hand screw axes that cannot be distinguished by powder diffraction. The homometric, but non-enantiomorphous, structures are characterized by adding a suffix a, b, c, . . . to their coordination descriptions. The h.c.p. 530;1a,b structures (Figure 15) are homometric, but differ from the homometric 530;1d,e structures in the fourth and higher coordination shells. The h.c.p. 602;1a,b structures (Figure 9) differ from the fourth coordination onward. The c.c.p. 2212;2c structure is different from the homometric 2212;2a,b structures (Figure 15) in the sixth and higher coordination shells. The crystal structures a, b, c, . . . with identical positions on the structure maps (Figures 10 and 12) are stabilized by about the same amount of lattice energy and are sometimes coexisting, as e.g. the 008;5b,e,f V_6C_5 stacking variants (Section 14).

There are also homometric structures of close-packed metal atoms with a different stacking sequence but identical T_i values (Mardix, 1990), e.g.

h c c h c h c c h h c h c h h
and h c c h c h c h h c c h h h c

which are two different structures containing the same unit cell with 15 layers and the same percentage (53.3%) of h layers in the same space group P3m1. Other structures of Table 1, e.g. 9a and 9c, or 9d and 9e, have identical T_i for $i = 1$–8 but differ in T_9 and higher coordination shells.

Table 7. Self-coordination numbers of some homologous series with different r and k values (see text)

		$T_1 T_2 T_3; y/x$	
r	k	c.c.p.	h.c.p.
2	2	2212;2a $MoPt_2$,b	220;2a,b
2	1	7418;0.5a Pt_2Mo,b	741;0.5a,b
2	0	12 6 24;0 Cu	12 6 2;0 Mg
3	3	060;3 $AuCu_3$	062;3 $SnNi_3$
3	2	468;1 CuAu	462;1 AuCd
3	1	8616;0.33 Cu_3Au	862;0.33 Ni_3Sn
3	0	12 6 24;0 Cu	12 6 2;0 Mg
4	4	028;4 $MoNi_4$	
4	3	3312;1.5	
4	2	6416;0.67	
4	1	9520;0.25 Ni_4Mo	
4	0	12 6 24;0 Cu	

10. Homologous Series of Structures

A second type of special structures exhibits identical α_i values but at different composition y/x. These structures have identical or closely related unit cells and form homologous series of structures that are filled up successively by M atoms until T_i^{max} is reached (Table 7). Each M and each N atom of these structures must have the same set of numbers $T_1 T_2 T_3$, respectively. The structure with the lowest M content $y/x = r = k$

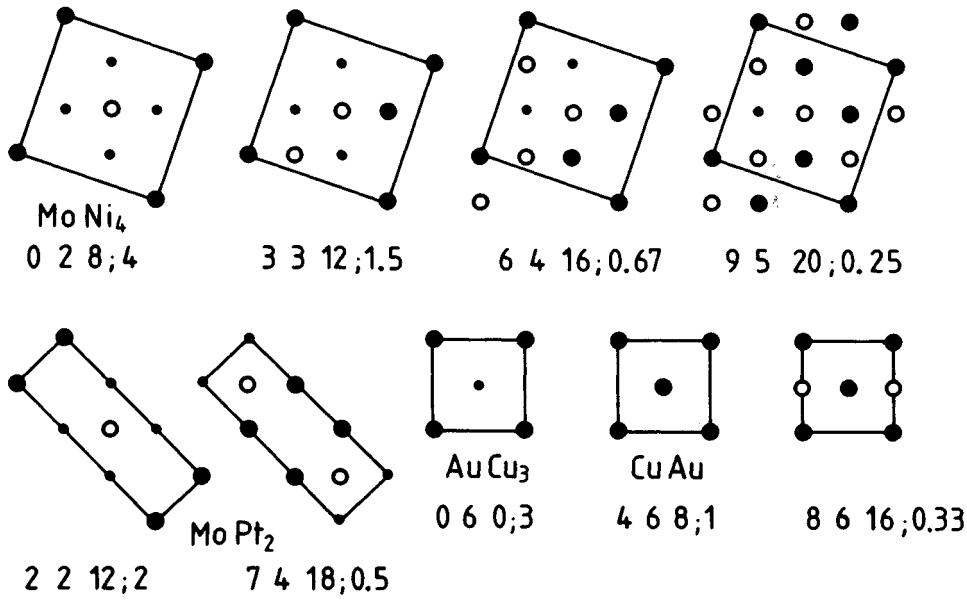

Figure 16. Examples of homologous crystal structures with identical α_i values at different concentrations y/x: M atoms at $z = 0$ (●) and $z = 0.5$ (○). Positions of N atoms (•) at $z = 0$ for pattern recognition

$(T_1^* T_2^* T_3^* r)$ is filled up with M atoms in steps of $k = 0, 1, \ldots, r$ (Hauck *et al.*, 1988a):

$$T_i(k) = T_i^{max} - (T_i^{max} - T_i^*)k/r$$

$$y/x = k/(r + 1 - k)$$

The homologous series of structures also contain structures with M and N atoms interchanged, as e.g. $AuCu_3$ and Cu_3Au (Table 7). There are three homologous series for c.c.p. and two series for h.c.p. with $r = 2$, 3, and 4, respectively (Table 7). The $r = 3$ series for the c.c.p. 060;3 $AuCu_3$ and 468;1 CuAu structures corresponds to the h.c.p. 062;3 $SnNi_3$ and 462;1 AuCd structures at identical α_1, α_2 values (Figures 10 and 12). The c.c.p. 2212;2 structures (Figure 16) can be compared with the h.c.p. 220;2 (Figure 15) or 222;2 $TaPt_2$ (Hauck *et al.*, 1988a) structures. The pairs of closely related c.c.p. structures 048;3 $TiAl_3$ and 4416;1 UPb (Figure 14) and the corresponding h.c.p. 042;3 $TiCu_3$ and 442;1 structures (Figure 11) are not homologous because of different α_2 values (Figures 10 and 12). The $TiPt_8$ and V_4Zn_5 structures with different α_i values even crystallize in the same space group at different y/x and can be considered as one structure type (Villars and Calvert, 1986), if the V_4Zn_5 structure is written as $Zn(V_4Zn_4)$.

11. Symmetry of Ordered Phases

The metal atoms of the h.c.p. and c.c.p. lattices have a single environment with a high point symmetry for the metal atoms (Hahn, 1983; Villars and Calvert, 1986):

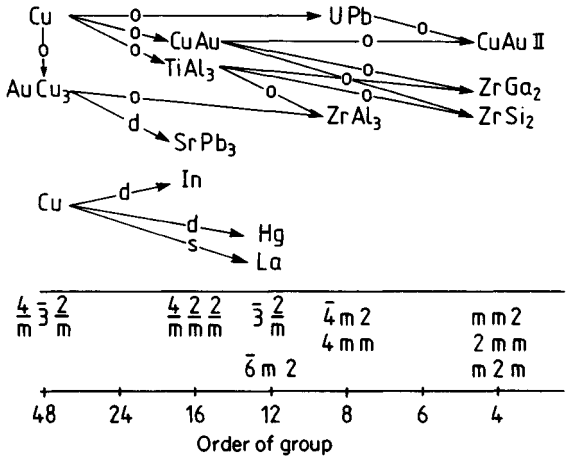

Figure 17. Crystallographic point-group symmetry of M atoms in different ordered alloys M_xN_y. The order of the point symmetry of M atoms is reduced by ordering (o), by stacking (s), e.g. of La atoms in chch layer sequence, or by distortion (d)

$\frac{4}{m}\bar{3}\frac{2}{m}$ for the Cu atoms with c.c.p. structure

$\bar{6}m2$ for the Mg atoms with h.c.p. structure

The site symmetry is reduced by distortion (d), e.g. of the Cu lattice, or by different stacking (s), as e.g. the $(ch)_2$ La structure, or by formation of ordered structures (o) (Figure 17). Structures with a single environment of all M and N atoms, as e.g. $AuCu_3$ or CuAu, are usually highly symmetric. Structures containing M atoms with different environments are built from different structural subunits, as e.g. $ZrAl_3$, CuAu II or $ZrGa_2$ (Figure 14). The symmetry of these structures is usually lower because of the different symmetry elements of the structural subunits. The populations of the different structure types obey Pauling's rule of parsimony: the number of essentially different kinds of constituents in a crystal tends to be small (Pauling, 1929). Structure types with a single environment of metal atoms M and N ($M^i = 2$ in Table 3) with high symmetry, as in the case of the h.c.p. alloys with AuCd or $SnNi_3$ structure or the c.c.p. alloys with CuAu, $AuCu_3$, $MoNi_4$ or $MoPt_2$ structure (Table 4), are observed frequently, whereas structures containing metal atoms with different environments, as e.g. CuAu II, $ZrGa_2$ or Mo_3Al_8, are rare. The fact that highly symmetric structures can only be constructed from M and N atoms with a single environment shows that the frequent observation of high symmetry (Laves, 1967) is a consequence of Pauling's rule for small numbers of constituents.

In most cases, the experimentally observed symmetry is identical with the symmetry determined for the undistorted lattice. This can be used to find a structural model of the ordered structure from electron diffraction patterns. Alloys with small single-crystal domains of ordered structures can be investigated by electron diffraction to determine the unit cell and the symmetry from the diffraction pattern. These values can be compared with the list of theoretical structures to calculate the powder pattern for X-ray or neutron diffraction.

The symmetry of a few ordered alloys, as e.g. NaHg, $CdAu_3$ II, SiU_3 or $SrPb_3$ (Table 4), is further decreased owing to distortion similar to that in tetragonal In or rhombohedral Hg compared to cubic Cu (Table 1).

12. Ising Model

Crystal structures of ordered alloys M_xN_y have been calculated for central pairwise interactions V_i ($i = 1, 2, 3, \ldots$) between nearest-, next-nearest-, third-nearest-neighbor, etc., metal atoms within the Ising model (see

Chapter 2 by Turchi in this volume). The results obtained for the single tetragonal layer (Kaburagi, 1978), the single hexagonal layer (Kudo and Katsura, 1976; Hiraga and Hirabayashi, 1977), h.c.p. (Kudo and Katsura, 1976) and c.c.p. (Kanamori and Kakehashi, 1977) alloys can be compared with the structures in the structure maps. The present notation $T_1T_2T_3;y/x$ for the self-coordination numbers T_i and concentration y/x is similar to the notation of the structures used by Kanamori and Kakehashi (1977). The interaction parameters V_1 and V_2 between nearest and next-nearest neighbors were varied in the Ising model calculations and the structures obtained by different procedures plotted in a V_1–V_2 coordinate system (de Novion and Landesman, 1985). These plots can be compared with the α_1–α_2 structural maps of Figures 7, 8, 10, and 12. The parameters α_i seem to be almost proportional to V_i. Only simple structures are obtained by variation of the V_1 and V_2 interaction parameters. The complex structures with different environments of M atoms are only found by the additional variation of V_3, V_4, etc. (Ducastelle, 1991). Structures at different positions on the borderline of the structure map, e.g. CuAu II compared to CuAu, are stabilized by different V_3, V_4, etc., which cause a slightly different V_2 and α_2 (Figure 12).

The interaction parameters $V_i=0$ for a statistical (random) distribution of M and N atoms correspond with $\alpha_i=0$. The α_i values are positive for attractive interactions between M atoms and negative for repulsive interactions. The structures can be classified within four fields by consideration of V_1, V_2 only: (I) V_1, $V_2<0$; (II) $V_1<0$, $V_2>0$; (III) $V_1>0$, $V_2<0$; and (IV) V_1, $V_2>0$. These areas are subdivided by the diagonals into Ia, Ib, etc. (Figure 18). Most experimental structures are in (I) or (II), with a repulsive interaction V_1 between nearest-neighbor M atoms. Structures in IIIa and IV, with attractive interactions V_1 between nearest-neighbor M atoms, already contain multiple layers of M and N atoms as a first step toward segregation. Structures with covalent bonding between M atoms are in Ia and IIIb. The structures of IIIb contain clusters, e.g. sheets or rows of M atoms.

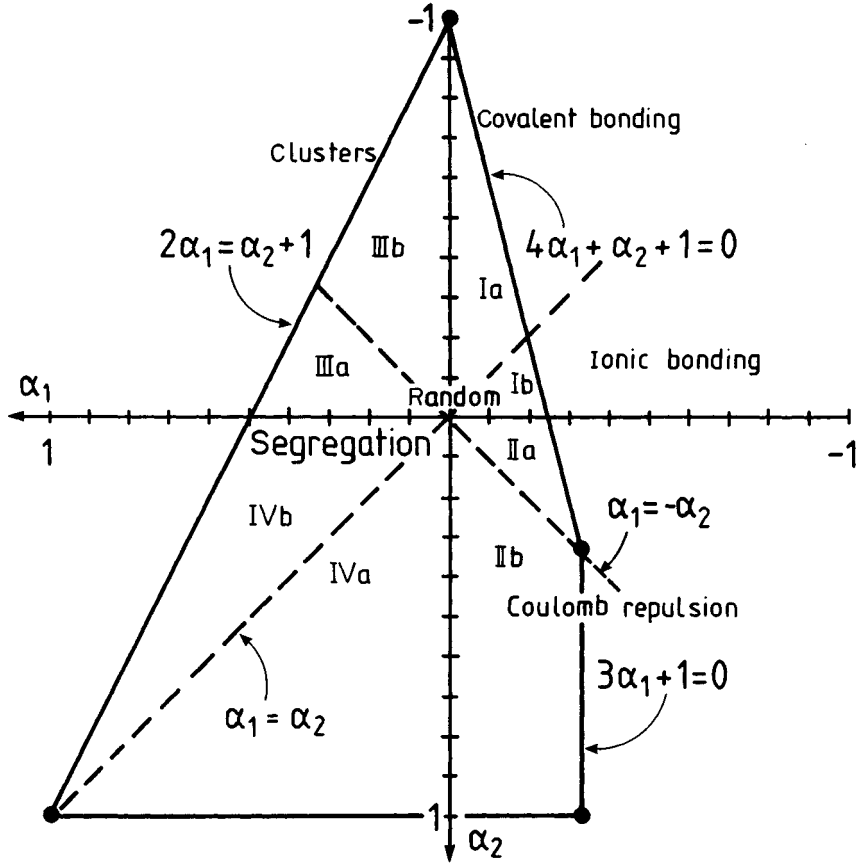

Figure 18. The different areas of the α_1, α_2 structure map of close-packed alloys as derived from the Ising model

The M atoms of structures in IIb are as far apart as possible, which can be correlated with repulsive interactions V_1 between nearest M atoms, e.g. Coulomb repulsion. These structures have the highest Madelung factors (Hauck *et al.*, 1988a). The crystal structures with covalent and ionic bonding are separated by the line $\alpha_1 = \alpha_2$. The M atoms of ionic compounds with low M content are expected at $T_1 = T_2 = 0$ because of the repulsive interactions. The relation $\alpha_1 = \alpha_2$, however, is also valid for covalent compounds with the relation $T_1/T_2 = T_1^{max}/T_2^{max}$, with preferential occupation of the inner coordination shells T_1 and T_2. The $\alpha_1 = \alpha_2$ line of dilute alloys intersects the borderline $4\alpha_1 + \alpha_2 + 1 = 0$ of the h.c.p. and c.c.p. structure maps at the concentration $y/x = 5$. Therefore, ionic and covalent compounds with $y/x \geqslant 5$ and $T_1 = T_2 = 0$ should be on the line $\alpha_1 = \alpha_2$. Ordered ionic compounds with $y/x < 5$ are expected with increased T_2, ordered covalent compounds with increased T_1.

The structures with a maximum interaction are at the outer borderlines. Structures with composition $y/x = 1$, 2, and 5 are on the borderline $4\alpha_1 + \alpha_2 + 1 = 0$ in (I, IIa); structures with $y/x = 1$ and 3 are on $3\alpha_1 + 1 = 0$ in (IIb); and structures with all compositions are on $2\alpha_1 = \alpha_2 + 1$ in (III, IVb). Structures with different compositions are in the field, e.g. structures with $y/x = 2$ are on $4\alpha_1 + 1 = 0$ in (II) (Figure 12) because of geometric restrictions of the close-packed metals. Structures with $y/x = 2$ are less frequent than structures with $y/x = 1$ or 3 (Table 4). They can be considered as a combination of structural subunits of composition $y/x = 1$ and 3, as was outlined before. Other structures inside the α_1–α_2 field like c.c.p. 6212;1a,b have the same composition as structures at the borderline, e.g. 60 12;1a,b, 52 14;1 or 8212;1 (Figure 12). These structures are supposed to be less favorable than structures at the borderline with maximum interactions between M atoms.

13. Occupation of Octahedral or Tetrahedral Interstices

Interstitial atoms I = H, C, N, O, . . . can occupy tetrahedral or octahedral interstices of the close-packed metal structures. There are one octahedral I^o and two tetrahedral I^t atoms per metal atom M for the composition $MI^oI_2^t$ at a complete occupation (Figure 19). Small spheres with radii less than 22.5% or 41.4% of the metal atom radii can be inserted in the voids between four or six metal atoms, respectively. The 74% density of the metal atom sphere packing is increased at complete occupation of all the tetrahedral and octahedral interstices by 1.7% and 5.3%, respectively, to a

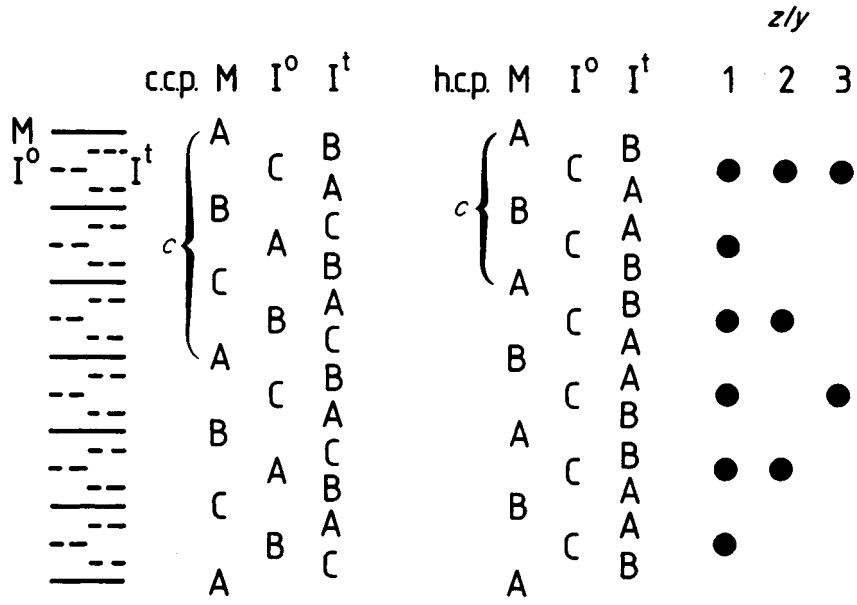

Figure 19. Position of interstitial atoms I^o and I^t in octahedral and tetrahedral sites of the ABC c.c.p. or AB h.c.p. M lattice. Only 1/2 or 1/3 (for ϵ-Ni_3C) of the octahedral sites I^o at identical positions in *c* direction of h.c.p. M lattice are occupied at $z/y = 2$ or 3, respectively

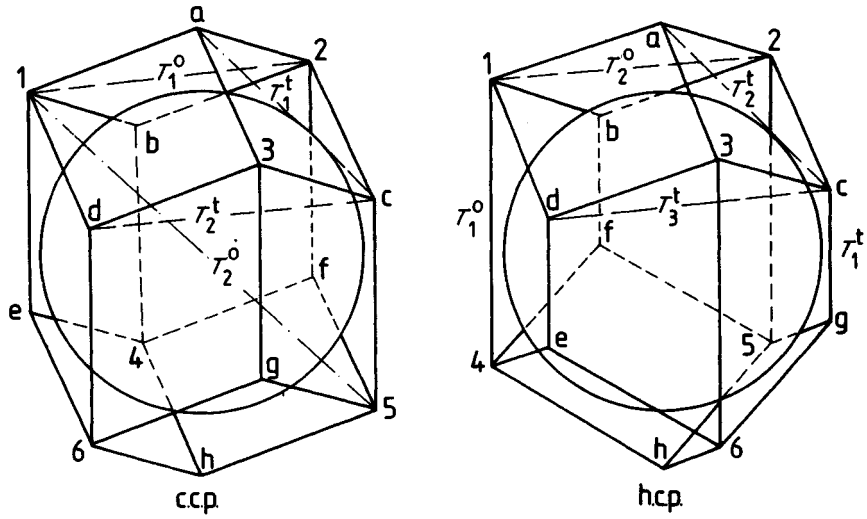

Figure 20. Positions 1–6 of octahedral and a–h of tetrahedral sites in the neighborhood of a c.c.p. or h.c.p. M atom. Some neighbors of the self-coordination numbers T_i^o and T_i^t of octahedral and tetrahedral interstices are shown

total density of 81%. A maximum radius of 59% of the metal atom radii is considered for I° atoms by Hägg's rule for interstitial alloys with increased metal atom distances (Toth, 1971).

The octahedral interstitial atoms I° of the c.c.p. metal structure are at successive positions ABC, similar to the metal atoms, but shifted by $c/2$ (Figure 19). The tetrahedral interstitial atoms I^t, with the twofold concentration of the I° atoms, form a repeated ABCABC sequence with distance $c/6$ between layers of interstitial atoms.

The octahedral atoms I° of the h.c.p. metal structure with an AB sequence of metal layers are all on C layers with distance $c/2$ between two layers (Figure 19). The tetrahedral sites are at A and B positions with the sequence BAAB and distance $c/4$ between layers of interstitial atoms I^t. The tetrahedral atoms I^t close to a metal atom are in positions analogous to those for octahedral sites. The h.c.p. metal atom at a B position, for example, contains two adjacent layers of I^t at A positions and two layers I° at C positions, whereas the I^t and I° atoms close to a B atom of the c.c.p. M lattice are at the different A and C positions in each case.

The spatial distributions of the six octahedral sites 1–6 and the eight tetrahedral sites a–h close to a c.c.p. and h.c.p. metal atom are shown in Figure 20. The nearest-neighbor I^t atoms of the h.c.p. structure, e.g. at c and g positions, are only $\sqrt{1/6}\,d$ apart compared

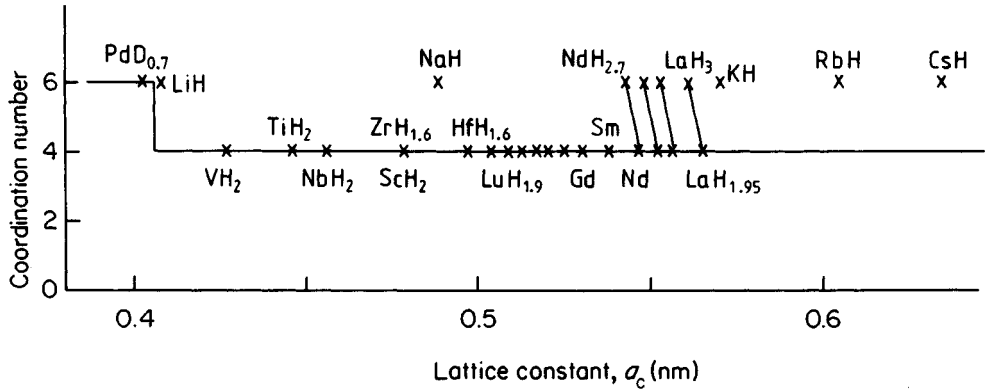

Figure 21. Coordination of hydrogen atoms in c.c.p. M structures with cubic lattice constants a_c

with $\sqrt{1/2}\,d$ in c.c.p. (Figure 20) (d = diameter of M atoms). The shortest distance between the I° atoms of the h.c.p. structure, e.g. at positions 1 and 4, is $\sqrt{2/3}d$ compared to d in the c.c.p. case. The second h.c.p. coordination shells T_2^t and T_2^o are at the same distance as the first c.c.p. coordination shells T_1^t and T_1^o.

The small hydrogen atoms can occupy both tetrahedral and octahedral interstices (Figure 21). The tetrahedral sites are occupied completely, e.g. in VH_2, and partially, e.g. in $ZrH_{1.6}$. The metal lattice of these hydrides is c.c.p. instead of h.c.p. (M = Ti, Zr, Hf, rare earths) or b.c.c. (M = V, Nb) for the pure metals. The preference for a c.c.p. instead of a h.c.p. metal lattice can be explained by the short distance between nearest tetrahedral sites in the h.c.p. structure (Hauck, 1983). The occupation of octahedral sites in MH with c.c.p. of the metal lattice (where M = Li, Na) instead of a h.c.p. structure is also preferred because of the larger distance between H atoms. Both sites are occupied in $MI^oI_2^t = MH_3$ with c.c.p. of the big rare-earth metals M = La to Nd, Yb and with h.c.p. of the small rare-earth metals M = Y, Nd, Sm, and Gd to Tm, Lu. NdH_3 is c.c.p. at $T > 350$ °C and h.c.p. at lower temperatures. The short distances between the nearest interstitial sites of the h.c.p. lattice are increased by a hexagonal distortion from $c/a = 1.63$ to ~ 1.80 (Villars and Calvert, 1986) (see also Chapter 21 by Schlapbach *et al.* in Volume 2).

The preference of H atoms for tetrahedral or octahedral interstices has been explained by the different size of the interstitial sites (Westlake, 1983) or the different mechanisms of MH bonding (Hauck, 1983). The first type of model considers a minimum hole size of 40 pm (or a critical metal atom radius of 139 pm) and a minimum distance of 210 pm between H atoms to be necessary. The larger octahedral site should be occupied in metals with small atomic radii, the smaller tetrahedral site in metals with large atomic radii.

The second type of model is based on a charge transfer between H and metal atoms with different electronegativities ϕ^*:

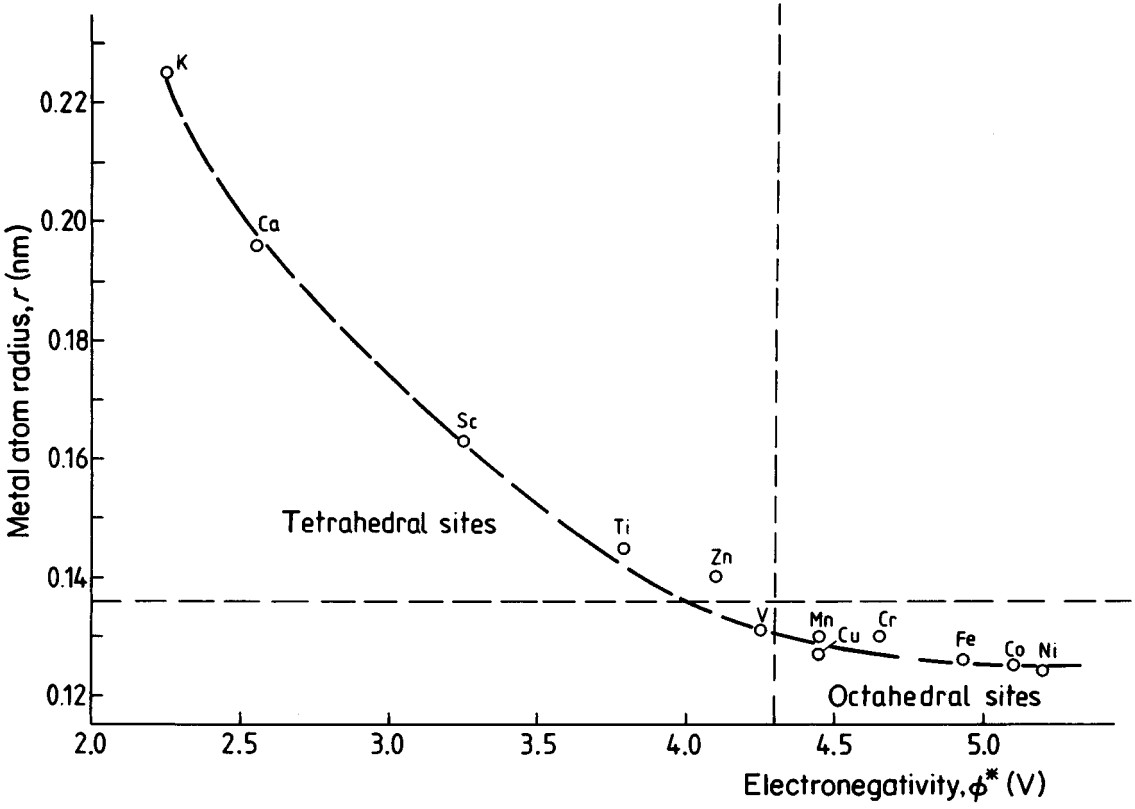

Figure 22. Hydrogen occupancy of octahedral sites in metals with small radii and high electronegativity, otherwise tetrahedral sites

$M^{\delta-}H^{\delta+}$ for metals with high ϕ^*,
e.g. M = Cr, Mn, Fe, Co, Ni, Pd
$M^{\delta+}H^{\delta-}$ for metals with low ϕ^*,
e.g. M = Li, Na, Ca, Sc, Y, Ti

The $H^{\delta+}$ atoms prefer the octahedral site with a bonding to the transition-metal d electrons. The $H^{\delta-}$ occupies octahedral interstices of metals with no d electrons, otherwise tetrahedral interstices. Both sites can be occupied in vanadium depending on temperature, hydrogen concentration, and isotope (Hauck, 1983).

The two models give the same prediction for most metals because of the correlation between small metal atom radii and high electronegativity (Figure 22). The critical radius of metal atoms, 139 pm, corresponds with the cubic lattice constant of 393 pm and can explain the variation from octahedral coordination in $PdD_{0.7}$ and LiH to the tetrahedral coordination in VH_2, etc. (Figure 21). Octahedral sites, however, are also occupied in NaH, KH, RbH or CsH, which have larger lattice constants. In rare-earth hydrides the smaller tetrahedral sites are occupied first, while octahedral sites are occupied at $H/M \gtrsim 1.95$. This behavior can be explained by the second type of model with H atoms as a sensitive probe for d electrons. The d electrons of the rare-earth metals are depleted with increasing H content because of the charge transfer to $H^{\delta-}$. The loss of d electrons gives rise to a metal–semiconductor transition, different magnetic properties, and smaller lattice constants.

The other interstitial atoms I = C, N, O, . . . are too big for the occupation of tetrahedral sites. They occupy octahedral sites in the close-packed M structures (see Tables 8 to 10) with composition M_zI_y, $0.5 \leqslant y/z \leqslant 1$. Most compounds are non-stoichiometric. Ordered phases with $y/z = 0.5$, 0.63, 0.75, 0.83, and 0.88 occur at low temperatures (Toth, 1971).

14. Ordered Cubic Close-Packed Interstitial Alloys

The interstitial atoms I = H, C, N, . . . can occupy the octahedral sites of the c.c.p. M structure at the composition M_zI_y with $0.5 \leqslant y/z \leqslant 1$. The remaining $(z-y)$ octahedral sites are empty. The larger number of metal atoms and interstitial atoms can be neglected in a description of the ordered structures, if the positions of the smaller number of vacant sites □ are considered in the formula $M_z\square_xI_y$, $x+y=z$. The positions of the M and I atoms must only be considered for the effect of lattice distortion caused by vacancy ordering and for

Table 8. Cubic close-packed interstitial alloys $M_z\square_xI_y$ with I = H, C, N and vacancies □ at octahedral sites. Some antitype structures $\square_xM_yI_z$, I = O, S, Se, F, Cl, I, with M atoms at octahedral interstices of close-packed I atoms are also included. Number M^i of M, I, and □ with different sets of T_i values (all minority components have only one set of T_i values), and maximum population values are also shown. For tetragonal planes the same holds as in Table 4

$T_1T_2T_3;y/x$					
c.c.p.	tetr. plane	M^i	Prototype (symbols)	Space group	Population
12 6 24;(1)	444;(1)	2	NaCl (cF8/B1)	$Fm\bar{3}m$	677
			NiO (hR2)	$R\bar{3}m$	4
			CoO, GeSb (tI4)	I4/mmm	4
6012;1a	204;1	3	Gd_2C, α-$NaFeO_2$ (hR3,4)	$R\bar{3}m$	5
6012;1b	204;1	3	Ti_2C (cF48)	$Fd\bar{3}m$	4
4416;1	044;1	3	Pd_2D, Ti_2N (tI12)	$I4_1/amd$	2
408;1.67		4	Ti_8C_5 (hR13)	$R\bar{3}m$	1
606;2	202;2	3	In_2S_3 (hP5)	$P\bar{3}m1$	1
3010;2a	102;2	5	$TiCl_3$, Li_2SnO_3 (mC32,48)	C2/c	6
3010;2b	103;2	5	$AlCl_3$ (mC16)	C2/m	10
3010;2c	102;2	4	$Sc_{0.67}S$ (oF80)	Fddd	1
2212;2a	202;2	4	$\square Ti_2\square O_2$ (oI8)	Immm	1
204;3	204;1	4	$Tm_{0.75}Se$, $OsCl_4$ (oC14,10)	Cmmm	2
208;3	004;3	4	HfI_4 (mC40)	C2/c	1
048;3	044;1	4	Nb_4N_3, SnF_4 (tI14,10)	I4/mmm	2
060;3	044;1	4,3	$\square Nb_3\square O_3$, Nb_4C_3 (cP6,7)	$Pm\bar{3}m$	2
107;4	000;4	4	UCl_5 (mP24)	$P2_1/c$	1
028;4	000;4	3	UF_5, $PdD_{0.8}$, $Ti_{0.8}O$ (tI12,18)	I4/m	2
008;5a	002;5	5	$Lu_{0.83}S$ (oF88)	Fddd	1
008;5b	000;5	5	V_6C_5 III (mC44)	C2/c	1
008;5e	002;5	5	V_6C_5 I, $Sc_{0.83}S$ (mC22)	C2/m	2
008;5f		5	V_6C_5 II, Li_5ReO_6 (hP33,36)	$P3_112$	2
006;7	000;7	5	V_8C_7 (cP60)	$P4_332$	1

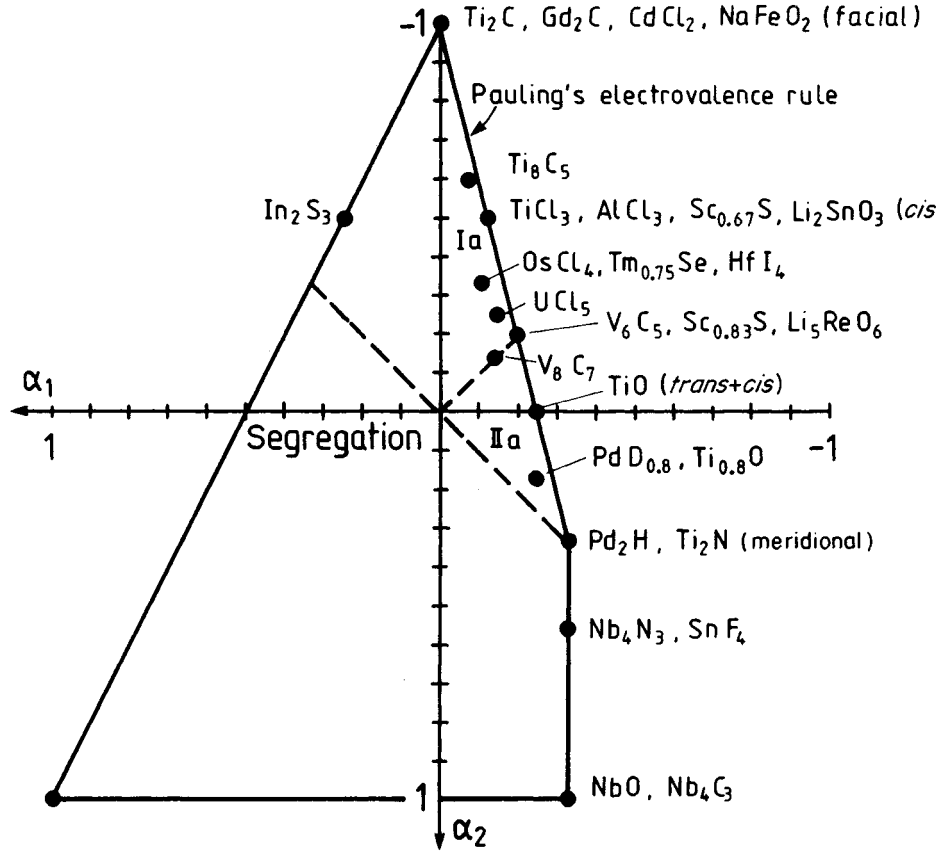

Figure 23. α_1, α_2 structure map of c.c.p. interstitial alloys $M_z\square_xI_y$. Some halides $\square_xM_yI_z$ with metal atoms at octahedral interstices of c.c.p. I lattice (antitype structure) are also included

the determination of the space group. The sublattice of vacancies plus interstitial atoms $\square_xI_y$ can be compared with the lattice of ordered M_xN_y alloys (Hauck *et al.*, 1988b). The vacancies and I atoms exhibit the same ABC layer sequence as the metal atoms of c.c.p. M (Figure 19). Therefore, the distribution of vacancies of the $\square_xI_y$ sublattice can be described by the same coordination numbers T_1, T_2, T_3 and concentration y/x as for ordered c.c.p. alloys M_xN_y (Table 8). The carbides Ti_2C, Gd_2C, Ti_8C_5, V_6C_5, and V_8C_7 are located in area Ia of the structural map, indicating covalent-type bonding, while the nitrides Ti_2N, Nb_4N_3 and the hydrides Pd_2H, $PdD_{0.8}$ are located at low α_1, indicating Coulomb-type interactions (Figure 23).

Two other types of interstitial alloys can be compared if the composition is formulated in a similar way to that used for the $M_z\square_xI_y$ compounds with the convention that $z \geqslant y \geqslant x$: $\square_xM_yI_z$ with I = O, S, Se, F, Cl, I as in $Ti_{0.8}O$, $Lu_{0.83}S$, $Tm_{0.75}Se$, SnF_4, $AlCl_3$ or HfI_4 (Table 8); and $\square_xM_y\square_xO_y$ as in $\square Ti_2\square O_2$ or $\square Nb_3\square O_3$ with vacancies in both sublattices.

The I = O, S, Se, F, Cl or I atoms are bigger than the M atoms. Therefore, the M atoms fill part of the octahedral interstices of the close-packed I lattice. The structures are the antitype of $M_z\square_xI_y$ (Lima-de-Faria *et al.*, 1990). The sublattices of M and I = O atoms of NbO and TiO are only partly filled. The vacancies of the M and the I sublattices form the same structure: 2212;2 for TiO and 060;3 for NbO.

Most interstitial alloys are metallic; some are superconducting, like PdD, TiC, NbN, TiO, NbO or $Sc_{0.83}S$ (Toth, 1971; Moodenbaugh *et al.*, 1978). The halides are non-metallic. Other non-metallic compounds that can be compared with the antitype structure $\square_xM_yI_z$ are the ternary oxides $M_xN_yI_z$, e.g. Li_5ReO_6, Li_2SnO_3 or α-$NaFeO_2$ (Table 8), with Re, Sn or Fe atoms at the vacancy positions.

The compositional parameters x, y, and $z = x + y$ of the non-metallic compounds cannot vary independently. The electroneutrality rule requires compensation of the negative charge of the oxygen or halide atoms. The charge $q(\mathrm{I}) = -2$ or -1, respectively, of these anions should be compensated by the electrovalence q_i/n_i of the p_i neighboring metal atoms with coordination number n_i and charge q_i as defined by Pauling (1929, 1945):

$$\sum \frac{p_i q_i}{n_i} = -q(\mathrm{I})$$

The I = O atoms of the $N_yM_xI_z$ compounds, e.g. Li_5ReO_6, Li_2SnO_3, and α-$NaFeO_2$, are coordinated by $p_M = 6x/z = 1$, 2 or 3, respectively, M atoms ($M = Re^{7+}$, Sn^{4+}, and Fe^{3+}) and $p_N = 6y/z = 5$, 4 or 3, respectively, N atoms ($N = Li^+$ or Na^+ atoms), which compensate the -2 charge of the oxygen atoms according to Pauling's electrovalence rule. The structures of these compounds correspond with the V_6C_5, $TiCl_3$, and Gd_2C structures (Table 8) and are at the borderline of the (I, IIa) field of the structure map (Figure 23) with the correlations $4\alpha_1 + \alpha_2 + 1 = 0$ and $\alpha_1 + \alpha_3 = 0$ between α_1, α_2, and α_3 values (Hauck *et al.*, 1989).

The metal atoms of the interstitial alloys M_zI_y, I = H, C, N, are surrounded by $p = 6y/z$ I atoms: $p = 3$ at $y/z = 0.5$, e.g. in $TiC_{0.5}$ or $TiN_{0.5}$; $p = 4$ at $y/z = 0.67$; and $p = 5$ at $y/z = 0.83$, e.g. in V_6C_5. The three I atoms of $MI_{0.5}$ are in the neighboring positions 1, 2, 3 (Figure 20) of facial configuration, as in $TiC_{0.5}$ or $GdC_{0.5}$, or further apart at 1, 2, 5 in meridional configuration, as in $PdH_{0.5}$ or $TiN_{0.5}$ (Table 9) (Hauck, 1981). The self-coordination number T_1 of the 6012;1b $TiC_{0.5}$ structure is increased compared with the 4416;1 $TiN_{0.5}$ structure, because of the close distance between I atoms in facial configuration. The M atoms of the facial configuration can be shifted to the C atoms to

Table 9. Interstitial alloys $M_z \square_x I_y$ with single configuration of tetrahedral or octahedral sites (Figure 20)

	y/z	M_zI_y	Configuration
c.c.p.	0.5	Ti_2C, Gd_2C	1-3 (facial)
	0.5	Ti_2N, Pd_2H	1, 2, 5 (meridional)
	0.67	Li_2SnO_3, $AlCl_3$	1-4 (*cis*)
	0.67	$\square Ti_2 \square O_2$, Li_2ZrO_3, Na_2PtO_3	1, 2, 5, 6 (*trans*)[a]
	0.75	Fe_3O_4	1-3, h
	0.83	V_6C_5, Li_5ReO_6	1-5
	1	TiC	1-6
	2	LaH_2	a-h
	2.5	$LaH_{2.5}$	1, 2, 5, a-h
	3	LaH_3, CeD_3	1-6, a-h
h.c.p.	0.5	Ta_2C	1-3
	0.5	Co_2C, ξ-Nb_2C, ζ,ϵ-Fe_2N	2-4
	0.67	Cr_2S_3	1-4
	0.67	α-Al_2O_3	2-5
	0.83	Cr_5S_6	1-5
	1	δ'-NbN	1-6
	3	HoD_3	1-6, a-h

[a]Some atoms of $\square Ti_2 \square O_2$, etc., have a *cis* configuration.

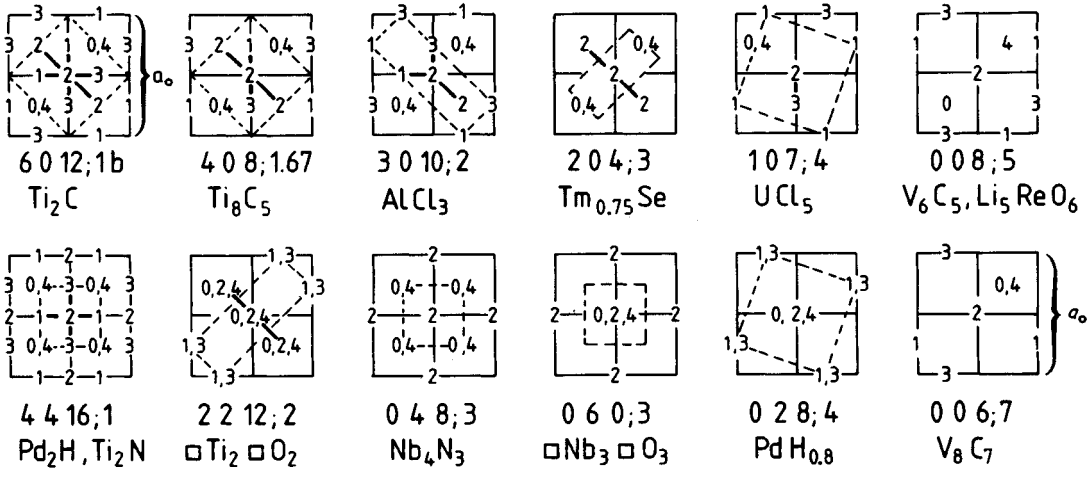

Figure 24. Self-coordination numbers $T_1\,T_2\,T_3$ of interstitial atoms in covalent (upper row) or ionic (lower row) compounds. An interstitial atom is placed in the middle of eight face-centered cubic cells with lattice constant a_c. The numbers z give the position of neighboring interstitial atoms at height $za_c/2$. Nearest neighbors are connected by bold lines. The broken lines indicate the unit cells. Ti_2C and V_8C_7 are cubic with lattice constant $a_0 = 2a_c$

decrease the M–C bonds by covalent bonding. A reduction of all Ti–N bonds with nitrogen atoms on meridional configuration 1, 2, 5 is not possible. The N atoms of the 4416;1 $TiN_{0.5}$ structure, however, are further apart and are stabilized by a 1.9% increased Madelung factor for the Coulomb interactions.

The other compounds with $y/z \neq 0.5$, 0.67 or 0.83, as e.g. Ti_8C_5, V_8C_7 or $PdD_{0.8}$, contain two different configurations of M atoms (Hauck *et al.*, 1988b). In Ti_8C_5, for example, with $p = 6y/z = 3.75$, two Ti atoms have three C atoms, and six Ti atoms four C atoms in the same configuration as the compounds Ti_2C and $AlCl_3$ (Table 9). Ti_8C_5 is located in the vicinity of Ti_2C and $AlCl_3$ of the structure map (Figure 23). The structures close to the borderline with only two different configurations obey Pauling's rule of parsimony (Pauling, 1929). The structures at or close to the borderline $3\alpha_1 + 1 = 0$, e.g. 060;3 and 468;1, which are observed as ordered alloys, are unfavorable for interstitial compounds because of two or more configurations. The Nb atoms, for example, of 060;3 Nb_4C_3 are surrounded either by four or six C atoms. The number of configurations, however, is reduced to a single configuration in NbO ($\square Nb_3 \square O_3$) and in ternary interstitial alloys $AlFe_3C$ and FeNiN (Section 18).

The T_1 and T_2 values in the $T_1 T_2 T_3; y/x$ notation of interstitial compounds describe the connection of octahedra by corners and edges, respectively. The 107;4 UCl_5 structure contains UCl_6 octahedra connected by a corner to $(UCl_5)_2$, while the UF_6 octahedra of the 028;4 UF_5 structure are connected by two edges in a one-dimensional row. The CTi_6 octahedra of the 6012;1b Ti_2C structure are linked by all corners, the NTi_6 octahedra of 4416;1 $TiN_{0.5}$ structure by four corners and four edges. The vacancies of 008;5 $V_6C_5\square$ or the Re atoms of 008;5 Li_5ReO_6 form isolated octahedra.

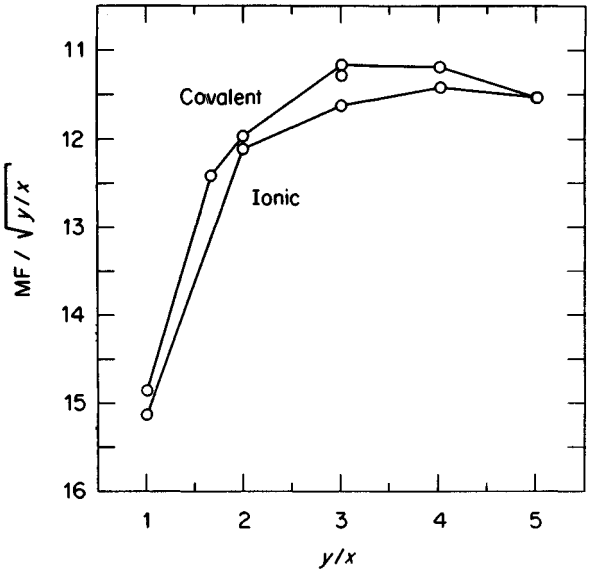

Figure 25. Madelung factors $MF/\sqrt{y/x}$ versus concentration y/x for the undistorted covalent and ionic compounds of Figure 24

The covalent and ionic compounds can be compared by two series of interstitial compounds $M_z\square_xI_y$, the Ti_2C series with covalent bonding and the Ti_2N series with ionic bonding (Figure 24).

The vacancies of the 4416;1 Ti_2N structure are filled up with interstitial atoms in such a way that they are as far apart as possible. These structures with 50, 33, 25, 20, and 12.5% vacancies, shown in the lower row of Figure 24, have a minimum of T_1 coordination. The vacancies of the 6012;1b Ti_2C structure in the upper structural series are successively occupied at increased T_1 and $T_2 = 0$. The increased T_1 coordination numbers of this series allow covalent bonding to interstitial atoms in neighboring facial or *cis* configuration. The Madelung factors of these structures are decreased by 1–3% (Figure 25). This difference of the lattice energy must be compensated by covalent bonding to stabilize the structure. The $\square V_6$ octahedra of $V_6C_5\square$ or ReO_6 octahedra of Li_5ReO_6 are isolated at the composition $y/x \geqslant 5$. The vacancies or Re^{7+} atoms are as far apart as possible for a maximum Coulomb energy. Covalent bonding is also favorable at this composition, because of the possibility of decreasing all Re–O bonds of ReO_6 or increasing all $\square$–V distances of the $\square V_6$ octahedra for covalent V–C bonding. Therefore, the 008;5 structure is favorable for both systems. This structure lies at the intersection of the $4\alpha_1 + \alpha_2 + 1 = 0$ boundary line of the structure map (Figure 23) and the $\alpha_1 = \alpha_2$ line for diluted alloys, as e.g. V_8C_7 with $T_1 = T_2 = 0$. The 008;5a–i structures are different stacking variants, which can occur in the same sample, like V_6C_5 I, II, and III, or as disordered structures. Some structures like 008;5e,f are homometric, analogous to 6012;1a,b Ti_2C and Gd_2C (see Section 9 and Figure 15) (Parthé and Yvon, 1970; Hauck *et al.*, 1988b).

15. Ordered Hexagonal Close-Packed Interstitial Alloys

The octahedral interstitial sites of the h.c.p. metals are all on C positions between each layer of metal atoms (Figure 19). The interstitial sites form a simple hexagonal lattice with a distance $c/2 = \sqrt{2/3}d$ between neighboring

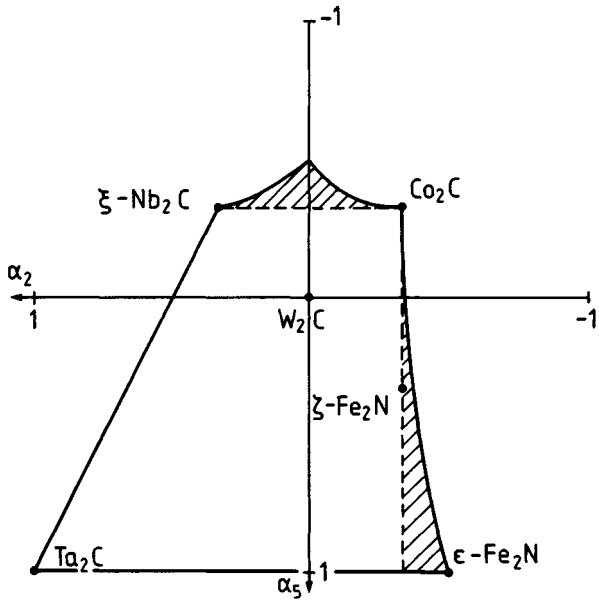

Figure 26. α_2, α_5 structure map of h.c.p. $M_z\square_xI_y$ interstitial alloys, corresponding to α_1, α_2 of hexagonal plane (Figure 8)

layers. The distance between two layers is only 82% of the shortest M–M distance (Table 2) in undistorted structures. This can explain why interstitial atom positions at identical projection sites are not occupied in adjacent layers because of the size of interstitial atoms or the Coulomb repulsion between these atoms. Therefore, the ordered distribution of I atoms in h.c.p. metals can be treated as single hexagonal layers (Hiraga and Hirabayashi, 1977). The coordinates of the structure map (Figure 26) are identical with the α_2–α_5 coordinates of the three-dimensional case (Table 2).

The formulas of these interstitial compounds are identical to those for c.c.p. interstitial alloys:

$M_z\square_xI_y$, $x+y=z$, for the small interstitial atoms I = N,C

$\square_xM_yI_z$, $x+y=z$, the antitype for bigger atoms I = O,I

Most ordered compounds have a composition $z/y=2$ because of the alternating empty and occupied sites in the *c* direction (Figure 19). The individual hexagonal layers are of different composition as outlined in Table 10. Frequently, a phase transition to the W_2C structure is observed at high temperatures with a disordered distribution of C atoms (Toth, 1971). The ϵ-Ni_3C and ϵ-Fe_3N structures contain 060;2 hexagonal layers (Table 10) with N or C atoms in different positions. These structures were observed in ZrO_x at $x=0.30$ and 0.34,

Table 10. Hexagonal close-packed interstitial alloys with different occupation of hexagonal planes of interstitial atoms, and maximum population values

Hex. plane $T_1T_2T_3;y/x$	Prototype (symbols)	Space group	Population
666;(1)	δ'-NbN (hP4/ $B8_1$)	$P6_3/mmc$	1
666;(1)	NiAs (hP4/$B8_1$)	$P6_3/mmc$	154
666;(1)	α-Ta_2C (hP3)	$P\bar{3}m1$	4
666;(1)	CdI_2 (hP3/C6)	$P\bar{3}m1$	52
422;1	ξ-Nb_2C (oP12)	Pnma	1
242;1	ζ-Fe_2N (oP12)	Pbcn	4
226;1	Co_2C (oP6)	Pnnm	2
226;1	$CaCl_2$ (oP6)	Pnnm	1
060;2	ϵ-Fe_2N (hP9)	$P\bar{3}1m$	9
060;2	ϵ-Fe_3N (hP8)	$P6_322$	4
060;2	ϵ-Ni_3C (hR8)	$R\bar{3}c$	2
disordered	W_2C (hP4/L'3)	$P6_3/mmc$	9

respectively, and more complex stacking variants at intermediate compositions (Hirabayashi *et al.*, 1974). Complete occupation of all octahedral sites is obtained in δ'-NbN and the NiAs antitype structure (Table 10) at the distortion of $c/a \sim 1.9$ (Villars and Calvert, 1986).

Recently new compounds $Na_{96}In_{97}Z_2$, Z = Ni, Pd or Pt with fullerene-like cages were obtained in the NiAs structure (Sevov and Corbett, 1993). In_{74} fullerenes, which are connected by pentagonal faces, form a h.c.p. structure. Distinct $M_{60}(=In_{48}Na_{12})$ polyhedra occupy the octahedral interstices. The In_{74} and M_{60} cages are centered by $In_{10}Z$ clusters.

16. Complex Close-Packed Interstitial Alloys

The octahedral positions in h.c.p. alloys with stacking symbol hh are identical, e.g. at CC (Figure 19), and different for c.c.p. alloys with stacking symbol ccc, e.g. at ABC. The octahedral positions in complex close-packed alloys are identical in the h layers and different in each c layer. The sequence CCBB, for example, is obtained for the four-layer structure chch and CABBB for the five-layer structure ccchh. Octahedral sites of neighboring layers are vacant ($\square$) at identical projection sites, e.g.

C [C] B [B] and C A B [B] B

because of the short distance between these octahedral sites. Therefore, the concentration of interstitial atoms is reduced (Parthé and Yvon, 1970).

The neighborhoods of M atoms in c and h layers correspond to c.c.p. and h.c.p. in Figure 20. They can

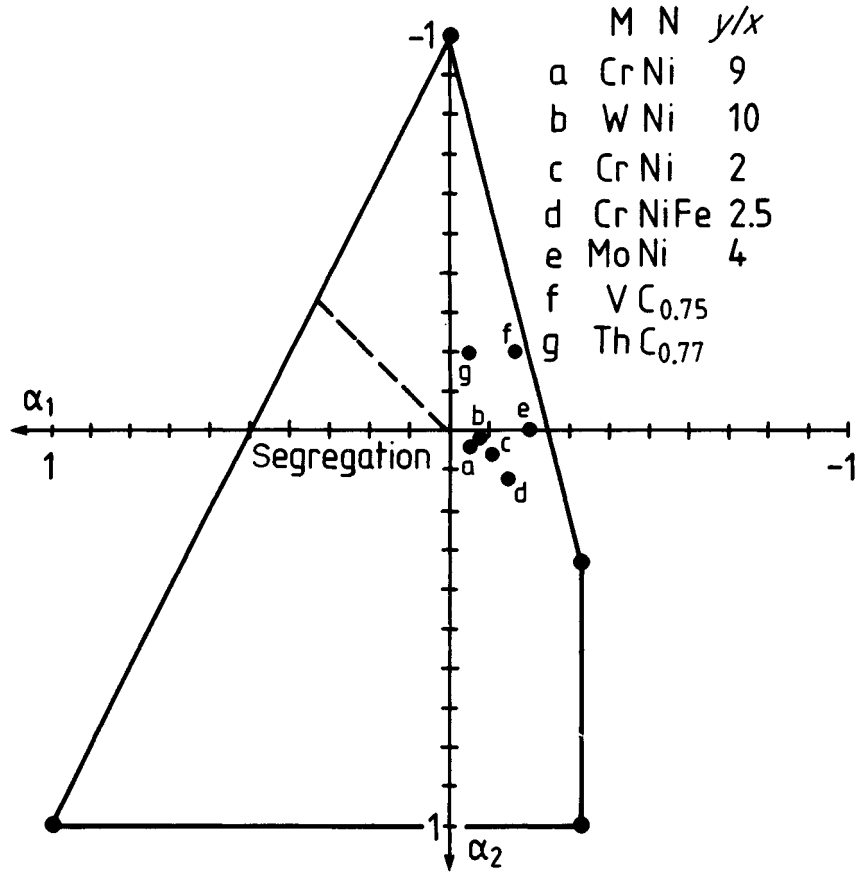

Figure 27. Experimental short-range order parameters α_1, α_2 of disordered alloys M_xN_y or $M_z\square_xC_y$ carbides within the c.c.p. α_1, α_2 structure map (Figures 12 and 23)

be converted to each other by rotation of the lower half by 60°. The complex close packing can be influenced by small variations of concentration or temperature in some compounds (Pearson, 1967, 1972). Some interstitial alloys occur in both ordered and disordered forms in complex close-packed M structures, as e.g. MoC and Mo_3C_2 in $(hcc)_2$. The structures of Sn_4P_3 and Ta_3MnN_4 are observed in $(ch)_2$, Ta_2VC_2 and Tb_2C in $(chh)_3$, Ti_3SiC_2 in $(chhh)_2$, and ζ-V_4C_3 in $(hhcc)_3$ (Pearson, 1967, 1972; Parthé and Yvon, 1970).

17. Disordered Alloys

Many alloys form extensive substitutional solid solutions, in particular alloys of metals with similar radii and electronegativity (Figure 2). Some alloys, as e.g. AuCu and $AuCu_3$, are disordered at high temperatures and become ordered at lower temperatures. The same applies to interstitial alloys, as e.g. V_6C_5 or Ti_2C, which have a disordered distribution of C atoms at high temperatures but an ordering of the C atoms (and vacancies) at lower temperatures (see Chapter 23 by de Novion in this volume). The X-ray or neutron diffraction patterns exhibit diffuse intensity, which is concentrated on lines or surfaces in reciprocal space. The diffuse intensity can be analyzed for the short-range order parameters α_i. The experimental values (Schweika, 1985; de Novion and Landesman, 1985) are usually between $\alpha_i = 0$ for a random distribution of metal or C atoms with no diffuse intensity and the values of the ordered alloys (Figure 27), and should shift to the values of the ordered alloys as the order-disorder transition temperature is approached. The relations $4\alpha_1 + \alpha_2 + 1 = 0$ and $\alpha_1 + \alpha_3 = 0$ were obtained for the α_1, α_2, α_3 short-range order parameters of oxides like $LiFeO_2$ and carbides from the shape of

the diffuse intensity patterns in reciprocal space (Sauvage *et al.*, 1974; Ducastelle, 1991). These relations can be explained by a disordered arrangement of carbon atoms in configurations allowed by Pauling's electrovalence rule (Table 9) or by the disordered T_i configurations 6012;1, 3010;2, 2212;2, 008;5 or 4416;1 (Figure 24) (Hauck, 1985). There are many stacking variants of these configurations (Hauck *et al.*, 1988b).

18. Ordered Ternary and Quaternary Compounds

Few ternary and quaternary ordered alloys with close-packed metal structures are known (Figure 28). Alloys with the composition $M^i_{x_i}N_y$, $x_i \leqslant y$, can be described by the self-coordination numbers T_i of the minority components $M^i_{x_i}$. There are three sets of T_i values for ternary and six sets for quaternary alloys. The α_1, α_2 values are identical for the 468;1 or 060;3 derivative structures or in the same area of the structure map, as e.g. for $\square_4Co_5Ge_7$. The T_i values of all $M^i_{x_i}$ can be averaged according to the frequency of their occurrence. These values can be compared with the self-coordination numbers of alloys with different sets of T_i values, which was discussed in Section 2 for close-packed metals with different stacking sequences. All metal atoms for $n=2$ and 3 (h.c.p. and c.c.p. structures) have the same environment ($M^i=1$) (Table 1). The $n=4$, 5, 6b, 8a, and 9a layer stackings of Table 1 contain $M^i=2$ metal atoms with different T_i values, the other structures three, four or five different sets of T_i values (Table 1). Therefore, the structures with two different T_i at the ratio y/x can be formulated as pseudobinary alloys MN ($n=4$, 8a), MN_2 ($n=6$b, 9a), and MN_4 ($n=5$). Other stacking sequences are pseudoternary, e.g. $M^1M^2_2N_3$ ($n=6$a), $M^1M^2_2N_4$ ($n=7$), $M^1M^2_2N_5$ ($n=8$b), $M^1M^2N_2$ ($n=8$c,e,f), $M^1M^2_4N_4$ ($n=9$b), and $M^1_2M^2_3N_4$ ($n=9$c). The population of the different structure types decreases with increasing M^i. Ordered binary and ternary alloys, however, have not been observed with these structures. The MN, MN_2, and MN_4 binary alloys, for example, favor other structures in the h.c.p. or c.c.p. structures (Tables 3 and 4). Most of the observed binary h.c.p. and c.c.p. M_xN_y compounds have two sets of T_i values, which are identical at concentration $y/x=1$. The ordered c.c.p. interstitial alloys $M_z\square_xI_y$ are ternary compounds similar to the isomorphous ternary oxides $NaFeO_2$, Li_2SnO_3, etc., with consideration of the vacancy positions $\square$ and with three sets of T_i values for M, I, and $\square$ in most compounds (Table 8). The vacancies of some compounds can be filled, as e.g. in Ti_2CH. The binary oxides TiO ($\square Ti_2\square O_2$) and NbO ($\square Nb_3\square O_3$) are pseudoquaternary with two identical sets of T_i (Table 8). These compounds can be compared with FeNiN$\square$ with identical T_i values for the metal atoms, the nitrogen atom, and the vacancy (Figure 28). The different metal atoms of these structures have a single configuration of interstitial atoms according to Pauling's rule of parsimony (Pauling, 1929).

Other alloys forming solid solutions, like the binary $CrNi_2$ or the ternary $CrNiFe_{2.5}$, are listed in the Cu structure type (Villars and Calvert, 1986) with a single environment of metal atoms, though the short-range order parameters are different from $\alpha_i=0$ (Figure 27). Metals with similar radii and electronegativities can also substitute for one component of an ordered binary alloy. Such ternary alloys have been investigated frequently to vary the structure of metals of binary alloys in small steps:

(i) The stacking sequences 7c and 14 were obtained by variation of the Ti–Pt–Ni and Ba–Pb–Tl compositions (Tables 1 and 6).

(ii) Structures with a different sequence of structural subunits were obtained, e.g. in $(Zr_3Al)(Al_3Si_5)$ (Schubert, 1964) with yvv'xuu'y'v'vx'u'u compared to $ZrSi_2$ (Figure 14) with yvv'y'u'u.

(iii) Homologous structures with identical environment of all atoms at different compositions (Table 7) can be filled up with different atoms. The Pd and Au atoms, e.g. of $PdAuCu_2$ (Figure 28), have the 060;3 coordination of the $AuCu_3$ structure. Both Pd and Au atoms together and the two Cu atoms together exhibit the 468;1 configuration of the CuAu structure.

(iv) Some alloys, as e.g. $RhZr_3$ ($AuCu_3$ structure), become unstable on hydrogen loading and segregate or become amorphous (Bowman, 1988).

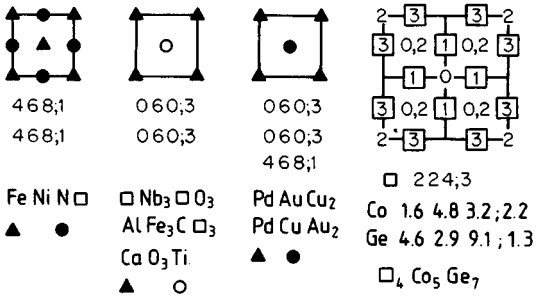

Figure 28. Ternary and quaternary compounds with $T_1T_2T_3$;y/x of different components with composition y/x. Only positions of minority elements are plotted, full and open symbols for elements at projection height $z=0$ and 0.5, respectively, or as multiples of $a_0/4$ in cubic Co_5Ge_7

(v) Other structures, which are unstable as pure alloys, can be stabilized by interstitial atoms, e.g. $AlFe_3$ with the $AuCu_3$ structure in $AlFe_3C$ (Figure 28). Among the 139 known compounds with this structure (Villars and Calvert, 1986) there are many alloys that are not stable without the presence of interstitial atoms. The atoms of the $AlFe_3C$ structure have the same positions as the atoms of the CaO_3Ti perovskite structure with oxygen atoms at the Fe positions. The sublattice of the metal atoms Ca and Ti in $CaTiO_3$, however, is body-centered with oxygen atoms at the octahedral interstices.

(vi) The crystal structures of some alloys can be varied by insertion of interstitial atoms. The c.c.p. $ZrAl_3$ structure, e.g. of $MnPd_3$ (Flanagan and Craft, 1992), changes to the $AuCu_3$ structure in $MnPd_3H\square_3$, which is isomorphous with $AlFe_3C\square_3$ (Figure 28).

If, however, the properties of the three or more components are too different or the concentration of the substituting component is too high, then the alloys become unstable and favor structures without close packing. As we pointed out at the beginning of this chapter, close packing can be expected for identical atoms or at least similar atoms with weak directional bonding and is not likely to be found in a child's drawer containing a collection of differently sized balls.

19. Notation

A, B, C	positions of metal atoms in hexagonal layers
K, L	positions of metal atoms in tetragonal layers
n	number of hexagonal layers
$n=2$	layers in A,B positions of h.c.p. or h hexagonal close-packed structure
$n=3$	layers in A,B,C positions of c.c.p. or c cubic close-packed structure
d	diameter of atoms = distance between the nearest M atoms
$a=d$, $c=n\sqrt{2/3}\,d$	hexagonal lattice constants of structures with n layers
f	fraction of h layers in complex close-packed structures
M_xN_y, $r=y/x\geqslant 1$	alloy composition with minority component M
T_i	self-coordination numbers for $i=1$, 2, . . . coordination shell
CN	coordination number
T_i^{max}	maximum self-coordination number in pure metals
$T_1T_2T_3;y/x$	characterization of crystal structures by the M atom environment, where T_i is the number of ith nearest neighbors and y/x the ratio of the components
α_i, $-1\leqslant\alpha_i\leqslant 1$	Cowley's short-range order parameter, $\alpha_i T_i^{max}=T_i-(T_i^{max}-T_i)/r$; the α_1, α_2 parameters are used for structural maps
$\pm V_i$	repulsive (−) or attractive (+) interactions between M atoms, e.g. Coulomb repulsion or covalent bonding
M^i	number of M and N atoms with different environments (= different T_i values)

20. References

Beattie, H. J. Jr (1967). In *Intermetallic Compounds* (ed. J. H. Westbrook). Wiley, New York, p. 144.

Beck, P. A. (1969). In *Advances in X-ray Analysis*, Vol. 12 (eds C. S. Barrett, J. B. Newkirk, and G. R. Mallett). Plenum, New York, p. 1.

Bowman, R. C. Jr (1988). In *Hydrogen Storage Materials* (ed. R. G. Barnes). *Mater. Sci. Forum*, **31**, 197.

David, W. I. F., Ibberson, R. M., Matthewman, J. C., Prassidec, K., Dennis, T. J. S., Hare, J. P., Kroto, H. W., Taylor, R., and Walton, D. R. M. (1991). *Nature*, **353**, 147.

de Boer, F. R., Boom, R., Mattens, W. C. M., Miedema, A. R., and Niessen, A. K. (1988). *Cohesion in Metals: Transition Metal Alloys* (*Cohesion and Structure*, Vol. 1) (eds F. R. de Boer and D. G. Pettifor). North-Holland, Amsterdam.

de Novion, C. H., and Landesman, J. P. (1985). *Pure Appl. Chem.*, **57**, 1391.

Ducastelle, F. (1991). *Order and Phase Stability in Alloys* (*Cohesion and Structure*, Vol 3) (eds F. R. de Boer and D. G. Pettifor). North-Holland, Amsterdam.

Flanagan, T. B., Craft, A. P., Niki, Y., Baba, K., and Sakamoto, Y. (1992). *J. Alloys and Compounds*, **184**, 69.

Hahn, Th. (ed.) (1983). *International Tables for Crystallography*, Vol. A. Reidel, Dordrecht.

Hauck, J. (1981). *J. Less-Common Met.*, **77**, 99.

Hauck, J. (1983). *J. Less-Common Met.*, **94**, 123.

Hauck, J. (1985). *J. Less-Common Met.*, **105**, 283.

Hauck, J., Henkel, D., and Mika, K. (1988a). *Z. Phys.*, **B71**, 187.

Hauck, J., Henkel, D., and Mika, K. (1988b). *Z. Kristallogr.*, **182**, 297.

Hauck, J., Henkel, D., and Mika, K. (1989). *Int. J. Modern Phys.*, **B3**, 1425.

Hirabayashi, M., Yamaguchi, S., Asano, H., and Hiraga, K. (1974). In *Order–Disorder Transformations in Alloys* (ed. H. Warlimont). Springer, Berlin, p. 266.

Hiraga, K., and Hirabayashi, M. (1977). *J. Physique*, **38**, C7, 224.

Ho, S.-M., and Douglas, B. E. (1968). *J. Chem. Educ.*, **45**, 474.

Kaburagi, M. (1978). *J. Phys. Soc. Japan*, **44**, 54.

Kanamori, J., and Kakehashi, Y. (1977). *J. Physique*, **38**, C7, 274.

Kudo, T., and Katsura, S. (1976). *Prog. Theor. Phys.*, **56**, 435.

Laves, F. (1967). In *Intermetallic Compounds* (ed. J. H. Westbrook). Wiley, New York, p. 129.

Lima-de-Faria, J., and Figueiredo, M. O. (1969). *Z. Kristallogr.*, **130**, 41, 54.

Lima-de-Faria, J., Hellner, E., Liebau, F., Makovicky, E., and Parthé, E. (1990). *Acta Crystallogr.*, **A46**, 1.

MacLaren, J. M., Pendry, J. B., Rous, P. J., Saldin, P. V., Samorjai, G. A., van Hove, M. A., and Vredensky, D. D. (1987). *Surface Crystallographic Information Service: A Handbook of Surface Structures*. Reidel, Dordrecht.

Mardix, S. (1990). *Acta Crystallogr.*, **A46**, 133.

Max,N. (1992). *Nature*, **355**, 115.

Mika, K., and Hauck, J. (1990). *Acta Crystallogr.*, **A46** (Suppl.), C-269.

Moodenbaugh, A. R., Johnston, D. C., Viswanathan, R., Shelton, R. N., DeLong, L. E., and Fertig, W. A. (1978). *J. Low Temp. Phys.*, **33**, 175.

Ogawa, S. (1974). In *Order–Disorder Transformations in Alloys* (ed. H. Warlimont). Springer, Berlin, p. 240.

Parthé, E., and Yvon, K. (1970). *Acta Crystallogr.*, **B26**, 153.

Patterson, A. L. (1944). *Phys. Rev.*, **65**, 195.

Patterson, A. L. and Kasper, J. S. (1959, 1967). In *International Tables for X-Ray Crystallography*, Vol. II (eds J. S. Kasper and K. Lonsdale). Kynoch Press, Birmingham, p. 342.

Pauling, L. (1929). *J. Am. Chem. Soc.*, **51**, 1010.

Pauling, L. (1945, 1960). *The Nature of the Chemical Bond*. Cornell University Press, Ithaca, NY.

Pearson, W. B. (1967). *A Handbook of Lattice Spacings and Structures of Metals and Alloys*, Vol. 2. Pergamon, London.

Pearson, W. B. (1972). *The Crystal Chemistry and Physics of Metals and Alloys*. Wiley, New York.

Sauvage, M., Parthé, E., and Yelon, W. B. (1974). *Acta Crystallogr.*, **A30**, 597.

Schubert, K. (1964). *Kristallstrukturen zweikomponentiger Phasen* (*Crystal Structures of Binary Phases*). Springer, Berlin.

Schubert, K. (1967). In *Intermetallic Compounds* (ed. J. H. Westbrook). Wiley, New York, p. 100.

Schweika, W. (1985). *Nahordnung und Wechselwirkungen in der Legierung* $Ni_{0.89}$ $Cr_{0.11}$. Jül Report 2004, Forschungszentrum Jülich.

Sevov, S. C., and Corbett, J. D. (1993). *Science*, **262**, 880.

Toth, L. E. (1971). *Transition Metal Carbides and Nitrides*. Academic Press, New York.

Villars, P., and Calvert, L. D. (1986). *Pearson's Handbook of Crystallographic Data for Intermetallic Phases*, Vols 1–3. American Society for Metals, Metals Park, OH.

Villars, P., and Hulliger, F. (1987). *J. Less-Common Met.*, **132**, 289.

Villars, P., Mathis, K., and Hulliger, F. (1989). In *The Structures of Binary Compounds* (*Cohesion and Structure*, Vol. 2) (eds F. R. de Boer and D. G. Pettifor). North-Holland, Amsterdam, p. 1.

Westlake, D. G. (1983). *J. Less-Common Met.*, **91**, 1.

Wyckoff, R. W. G. (1964). *Crystal Structures*, Vols 1–3. Interscience, New York. (Reprinted 1982 by Krieger, Malabar.)

Zhao, J.-T., Gelato, L., and Parthé, E. (1991). *Acta Crystallogr.*, **C47**, 479.

This chapter was originally published in 1995 as Chapter 12 in *Intermetallic Compounds*, Vol. 1: *Principles*, edited by J. H. Westbrook and R. L. Fleischer.

Chapter 3

Body-Centered Cubic Derivative Structures

Erwin E. Hellner and Roland Schwarz

Institute for Mineralogy, Philipps University, Marburg, Germany

1. Introduction to the Definition of Symbols

There is a great variety of body-centered structures (I family) among intermetallic compounds, which allows one to classify them into main types and subtypes, and which includes as well compounds where single points of the complex are replaced by coordination polyhedra. It was Hermann (1960) who developed a nomenclature for lattice complexes, which is useful in deriving all lattice complexes in space groups by subgroup relations, saying: 'This terminology has proved satisfactory for brief descriptions of space groups and crystal structures and may be used for the systematic treatment of a number of crystal-geometric problems which have been raised by Niggli, Weissenberg, Laves and the author. The practical application to such problems is to be the subject of further publications.' And Hermann, as the author of *Strukturbericht* volumes 1 and 2, knew what he was talking about; but sadly his life was too short to realize his ideas. Twelve years later we could publish the NBS Monograph 134 *Space Groups and Lattice Complexes* (Fischer *et al.*, 1973).

An important step had already been taken by publishing the first *Internationale Tabellen zur Bestimmung von Kristallstrukturen* (1935) edited by Hermann in cooperation with Astbury, Bradley, Jones, Lonsdale, Mauguin, Wyckoff, and others. In the first tables comparisons of different notations of crystal class (point groups) and space groups have been given by Schoenflies, Rinne *et al.* and Hermann–Mauguin (complete orthohexagonal), including the names of the general face forms by Schoenflies, Miers and Groth.

The category crystal class (point group*) was stated with a scheme showing all subgroup relationships and the names for the crystal forms and their special forms including limiting forms (Figure 1). The diagram gives a survey of the subgroup relations between various crystal classes. In this figure every connection line means that the crystal class at its lower end is a subgroup of that at the top. Double lines mean that the upper class contains the lower as subgroups in two non-equivalent positions. In the complete Hermann–Mauguin nomenclature, the subgroup relations are more clearly recognized than in the abbreviated forms. In the actual descriptions, every crystal class is given its proper Miller indices (*h k l*) for special and general forms, and a letter as a short reference. The face symmetry belonging to each form is also given and the representation in a stereographic projection; representations of the crystallographic point groups $222 = D_2$, $\bar{4}m2 = D_{2d}$, $\bar{3}12/m = D_{3d}$, and $\bar{4}3m = T_d$ in the orthorhombic, tetragonal, rhombohedral, and cubic systems are given in Table 1. The general face forms are rhombic disphenoid or tetrahedron, tetragonal scalenohedron, ditrigonal trapezohedron, and a hexakistetrahedron. In both cases D_{2d} and T_d the special form is a tetrahedron, in the first case a tetragonal tetrahedron. The duals of the face forms are the coordination polyhedra, for which a symbolism was developed by Donnay *et al.* (1964) (Table 2). In the chosen examples 4d 1, 8d 1, 12d 1, and

*A crystallographic point group is a group that maps a point lattice onto itself. Consequently, rotations and rotoinversions are restricted to the well-known 32 crystal cases formed by 1, 2, 3, 4, 6, and $\bar{1}$, $\bar{2}(=m)$, $\bar{3}$, $\bar{4}$, $\bar{6}$.

Crystal Structures of Intermetallic Compounds. Edited by J. H. Westbrook and R. L. Fleischer

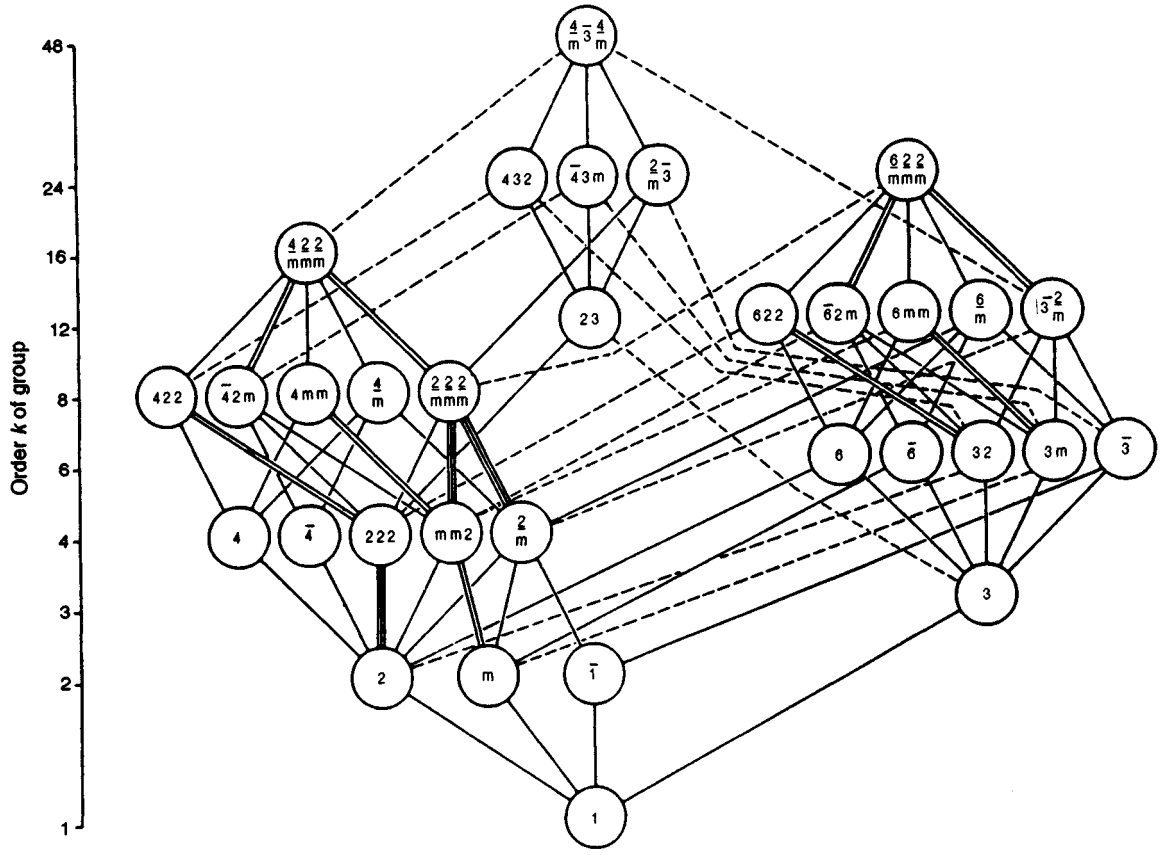

Figure 1 Maximal subgroups and minimal supergroups of the three-dimensional crystallographic point groups. Full lines indicate maximal subgroups; double or triple full lines mean that there are two or three maximal normal subgroups with the same symbol. Broken lines refer to sets of maximal conjugate subgroups. The group orders are given on the left. Full Hermann–Mauguin symbols are used

24d 1 are the general face forms, which characterize the crystal classes; the names of the faces are used by Groth as the names of the crystal classes. The other parts with point symmetry . . 2, . . m, etc., are reduced, special forms.

The term 'lattice complex' in three-dimensional space was introduced by Niggli (1919) in his book *Geometrische Kristallographie des Diskontinuums*: 'As already mentioned, the complex of equivalent points in a space system is comparable in every way with the complex of equivalent faces in a crystal class. In the normal crystallography each face form has a special symbol. Names, as cube, trapezohedron, scalenohedron, pedium, pinacoid etc., are given to simplify the description. We will call an equivalent point complex just a (simple) lattice complex and try to find simplifying symbolisms, which are useful for special reasons . . . .'

Several attempts have been made by Niggli. In the first *Internationale Tabellen* (1935) Hermann has a chapter on lattice complexes, either with no degree of freedom or with one degree (according to Niggli), invariant or univariant lattice complexes, tabulated and all the space groups in which they can be realized ('occur'). In the present table two point positions are allocated to the same lattice complex if they can be transformed into one another by any rotations or changes of scale, provided the corresponding crystal system and the directions of its axes are not altered thereby.

Just as all crystal forms of a particular type may be found in different point groups, the same lattice complex may occur in different space groups. For example, the complex P 'cubic primitive lattice' may be generated, for instance, in $Pm\bar{3}m$ 1a,b, $Fm\bar{3}m$ 8c,

and Ia$\bar{3}$ 8a,b with site symmetry m$\bar{3}$m, $\bar{4}$3m, and .$\bar{3}$. realized by Cl in CsCl, and F in CaF_2.

The body-centered cube (I) may be generated by space-group operators Im$\bar{3}$m a, Fd$\bar{3}$c a, and Ia$\bar{3}$d a, as realized in W metal and by Al in grossularite $Ca_3Al_2(SiO_4)_3$. By this criterion (space-group generators) the Wyckoff positions of all space groups (1731 entries in the space-group tables, 1128 types of Wyckoff sets) are uniquely assigned to 402 lattice complexes. If a lattice complex can be generated in different space-group types, one of them has the highest site symmetry, and is called the characteristic space group or standard representation of this lattice complex. All the other space groups are called subgroups of the space groups of the characteristic type.

The number of degrees of freedom of a lattice complex is the same as that of its Wyckoff position, i.e. the number of coordinate parameters that can vary

Table 1 The three-dimensional crystallographic point groups D_2, D_{2d}, D_{3d}, and T_d (see *International Tables for Crystallography*, 1983, table 10.2.2)

Orthorhombic system

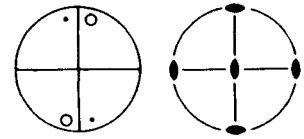

222	D_2			
4	d	1	Rhombic disphenoid or rhombic tetrahedron *Rhombic tetrahedron (u)*	$(h\,k\,l)$ $(\bar{h}\,\bar{k}\,l)$ $(\bar{h}\,k\,\bar{l})$ $(h\,\bar{k}\,\bar{l})$
			Rhombic prism *Rectangle through origin*	$(h\,k\,0)$ $(\bar{h}\,\bar{k}\,0)$ $(\bar{h}\,k\,0)$ $(h\,\bar{k}\,0)$
			Rhombic prism *Rectangle through origin*	$(h\,0\,l)$ $(\bar{h}\,0\,l)$ $(\bar{h}\,0\,\bar{l})$ $(h\,0\,\bar{l})$
			Rhombic prism *Rectangle through origin*	$(0\,k\,l)$ $(0\,\bar{k}\,l)$ $(0\,k\,\bar{l})$ $(0\,\bar{k}\,\bar{l})$
2	c	. . 2	Pinacoid or parallelohedron *Line segment through origin (q)*	$(0\,0\,1)$ $(0\,0\,\bar{1})$
2	b	. 2 .	Pinacoid or parallelohedron *Line segment through origin (m)*	$(0\,1\,0)$ $(0\,\bar{1}\,0)$
2	a	2 . .	Pinacoid or parallelohedron *Line segment through origin (i)*	$(1\,0\,0)$ $(\bar{1}\,0\,0)$
Symmetry of special projections			Along [1 0 0]: 2mm Along [0 1 0]: 2mm Along [0 0 1]: 2mm	

Tetragonal system

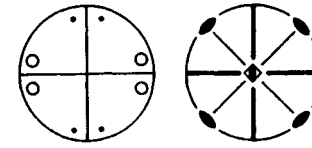

$\bar{4}$m2	D_{2d}			
8	d	1	Tetragonal scalenohedron	$(h\,k\,l)$ $(\bar{h}\,\bar{k}\,l)$ $(k\,\bar{h}\,\bar{l})$ $(\bar{k}\,h\,\bar{l})$
			Tetragonal tetrahedron cut off by pinacoid (l)	$(h\,\bar{k}\,l)$ $(\bar{h}\,k\,l)$ $(k\,h\,\bar{l})$ $(\bar{k}\,\bar{h}\,\bar{l})$
			Ditetragonal prism	$(h\,k\,0)$ $(\bar{h}\,\bar{k}\,0)$ $(k\,\bar{h}\,0)$ $(\bar{k}\,h\,0)$
			Truncated square through origin	$(h\,\bar{k}\,0)$ $(\bar{h}\,k\,0)$ $(k\,h\,0)$ $(\bar{k}\,\bar{h}\,0)$
			Tetragonal dipyramid	$(h\,h\,l)$ $(\bar{h}\,\bar{h}\,l)$ $(\bar{h}\,\bar{h}\,\bar{l})$ $(h\,\bar{h}\,\bar{l})$
			Tetragonal prism	$(h\,\bar{h}\,l)$ $(\bar{h}\,h\,l)$ $(h\,h\,\bar{l})$ $(\bar{h}\,\bar{h}\,\bar{l})$
4	c	. m .	Tetragonal disphenoid or tetragonal tetrahedron *Tetragonal tetrahedron (j)*	$(h\,0\,l)$ $(\bar{h}\,0\,l)$ $(0\,\bar{h}\,\bar{l})$ $(0\,h\,\bar{l})$
			Tetragonal prism *Square through origin*	$(1\,0\,0)$ $(\bar{1}\,0\,0)$ $(0\,\bar{1}\,0)$ $(0\,1\,0)$
4	b	. . 2	Tetragonal prism *Square through origin (h)*	$(1\,1\,0)$ $(\bar{1}\,\bar{1}\,0)$ $(1\,\bar{1}\,0)$ $(\bar{1}\,1\,0)$
1	a	2mm.	Pinacoid or parallelohedron *Line segment through origin (e)*	$(0\,0\,1)$ $(0\,0\,\bar{1})$
Symmetry of special projections			Along [0 0 1]: 4mm Along [1 0 0]: m Along [1 1 0]: 2mm	

(*continued*)

Table 1 (*continued*)

Trigonal system

$\bar{3}\,1\,m$ D_{3d}

$\bar{3}\,1\,\frac{2}{m}$

Hexagonal axes

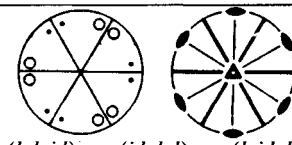

12	d	1	Ditrigonal scalenohedron or hexagonal scalenohedron	$(h\,k\,i\,l)$ $(\bar{k}\,\bar{h}\,\bar{i}\,\bar{l})$	$(i\,h\,k\,l)$ $(\bar{h}\,\bar{i}\,\bar{k}\,\bar{l})$	$(k\,i\,h\,\bar{l})$ $(\bar{i}\,\bar{k}\,\bar{h}\,\bar{l})$
			Trigonal antiprism sliced off by pinacoid (l)	$(h\,\bar{k}\,\bar{i}\,\bar{l})$ $(k\,h\,i\,l)$	$(\bar{i}\,\bar{h}\,k\,\bar{l})$ $(h\,i\,k\,l)$	$(\bar{k}\,\bar{i}\,\bar{h}\,\bar{l})$ $(i\,k\,h\,l)$
			Dihexagonal prism	$(h\,k\,i\,0)$	$(i\,h\,k\,0)$	$(k\,i\,h\,0)$
			Truncated hexagon through origin	$(\bar{k}\,\bar{h}\,\bar{i}\,0)$ $(h\,\bar{k}\,\bar{i}\,0)$ $(k\,h\,i\,0)$	$(\bar{h}\,\bar{i}\,k\,0)$ $(i\,\bar{h}\,k\,0)$ $(h\,i\,k\,0)$	$(\bar{i}\,\bar{k}\,h\,0)$ $(\bar{k}\,i\,\bar{h}\,0)$ $(i\,k\,h\,0)$
			Hexagonal dipyramid	$(h\,0\,\bar{h}\,l)$	$(\bar{h}\,h\,0\,l)$	$(0\,\bar{h}\,h\,l)$
			Hexagonal prism	$(\bar{h}\,0\,h\,\bar{l})$ $(0\,h\,\bar{h}\,l)$ $(h\,\bar{h}\,0\,l)$	$(h\,\bar{h}\,0\,\bar{l})$ $(h\,0\,\bar{h}\,l)$ $(\bar{h}\,h\,0\,l)$	$(0\,h\,\bar{h}\,\bar{l})$ $(\bar{h}\,0\,h\,l)$ $(0\,\bar{h}\,h\,l)$
6	c	. . m	Rhombohedron	$(h\,\bar{h}\,\bar{2}\,\bar{h}\,l)$	$(\bar{2}\,\bar{h}\,h\,h\,l)$	$(h\,\bar{2}\,\bar{h}\,h\,l)$
			Trigonal antiprism (k)	$(\bar{h}\,\bar{h}\,2\,h\,\bar{l})$	$(\bar{h}\,2\,h\,\bar{h}\,\bar{l})$	$(2\,h\,\bar{h}\,\bar{h}\,\bar{l})$
			Hexagonal prism	$(1\,\bar{1}\,\bar{2}\,0)$	$(\bar{2}\,1\,\bar{1}\,0)$	$(\bar{1}\,\bar{2}\,1\,0)$
			Hexagon through origin	$(\bar{1}\,\bar{1}\,2\,0)$	$(0\,2\,\bar{1}\,0)$	$(2\,\bar{1}\,\bar{1}\,0)$
6	b	. . 2	Hexagonal prism	$(1\,0\,\bar{1}\,0)$	$(\bar{1}\,1\,0\,0)$	$(0\,\bar{1}\,1\,0)$
			Hexagon through origin (i)	$(\bar{1}\,0\,1\,0)$	$(1\,\bar{1}\,0\,0)$	$(0\,1\,\bar{1}\,0)$
6	a	3 . m	Pinacoid or parallelohedron	$(0\,0\,0\,1)$	$(0\,0\,0\,\bar{1})$	
			Line segment through origin (e)			

Symmetry of special projections	Along [0 0 1]	Along [1 0 0]	Along [2 1 0]
	6mm	2mm	2

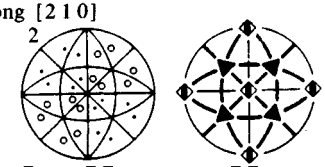

Cubic system

$\bar{4}\,3\,m$ T_d

24	d	1	Hexatetrahedron or hexakistetrahedron	$(h\,k\,l)$	$(\bar{h}\,\bar{k}\,l)$	$(\bar{h}\,k\,\bar{l})$	$(h\,\bar{k}\,\bar{l})$	$(k\,h\,l)$	$(\bar{k}\,\bar{h}\,l)$	$(k\,\bar{h}\,\bar{l})$	$(\bar{k}\,h\,\bar{l})$
			Cube truncated by two tetrahedra (j)	$(l\,h\,k)$ $(k\,l\,h)$	$(l\,\bar{h}\,\bar{k})$ $(\bar{k}\,l\,\bar{h})$	$(\bar{l}\,\bar{h}\,k)$ $(\bar{k}\,\bar{l}\,h)$	$(\bar{l}\,h\,\bar{k})$ $(h\,\bar{k}\,\bar{l})$	(l k h) $(h\,k\,l)$	$(l\,\bar{k}\,\bar{h})$ $(\bar{h}\,l\,\bar{k})$	$(\bar{l}\,k\,\bar{h})$ $(\bar{h}\,\bar{l}\,k)$	$(\bar{l}\,\bar{k}\,h)$ $(h\,\bar{l}\,\bar{k})$
12	c	. . m	Tetrahexahedron or tetrakishexahedron	$(0\,k\,l)$	$(0\,\bar{k}\,l)$	$(0\,k\,\bar{l})$	$(0\,\bar{k}\,\bar{l})$	$(k\,0\,l)$	$(\bar{k}\,0\,l)$	$(k\,0\,\bar{l})$	$(\bar{k}\,0\,\bar{l})$
			Octahedron truncated by cube	$(l\,0\,k)$ $(k\,l\,0)$	$(l\,0\,\bar{k})$ $(\bar{k}\,l\,0)$	$(\bar{l}\,0\,k)$ $(k\,\bar{l}\,0)$	$(\bar{l}\,0\,\bar{k})$ $(\bar{k}\,\bar{l}\,0)$	$(l\,k\,0)$ $(0\,l\,k)$	$(l\,\bar{k}\,0)$ $(0\,l\,\bar{k})$	$(\bar{l}\,k\,0)$ $(0\,\bar{l}\,k)$	$(\bar{l}\,\bar{k}\,0)$ $(0\,\bar{l}\,\bar{k})$
			Trigonotritetrahedron or tristetrahedron (for $\|h\|<\|l\|$)								
			Tetrahedron truncated by tetrahedron (i) (for $\|x\|<\|z\|$)	$(h\,h\,l)$ $(l\,h\,h)$ $(h\,l\,h)$	$(\bar{h}\,\bar{h}\,l)$ $(l\,\bar{h}\,\bar{h})$ $(\bar{h}\,l\,\bar{h})$	$(\bar{h}\,h\,\bar{l})$ $(\bar{l}\,\bar{h}\,h)$ $(h\,\bar{l}\,\bar{h})$	$(h\,\bar{h}\,\bar{l})$ $(\bar{l}\,h\,\bar{h})$ $(\bar{h}\,\bar{l}\,h)$				
			Tetragonotritetrahedron or deltohedron or deltoid-dodecahedron (for $\|h\|>\|l\|$)								
			Cube and two tetrahedra (i) (for $\|x\|>\|z\|$)								
			Rhombododecahedron	$(1\,1\,0)$	$(\bar{1}\,\bar{1}\,0)$	$(\bar{1}\,1\,0)$	$(1\,\bar{1}\,0)$				
			Cubooctahedron	$(0\,1\,1)$ $(1\,0\,1)$	$(0\,\bar{1}\,\bar{1})$ $(\bar{1}\,0\,\bar{1})$	$(0\,\bar{1}\,1)$ $(1\,0\,\bar{1})$	$(0\,1\,\bar{1})$ $(\bar{1}\,0\,1)$				
6	b	2 . mm	Cube or hexahedron	$(1\,0\,0)$	$(\bar{1}\,0\,0)$						
			Octahedron (f)	$(0\,1\,0)$ $(0\,0\,1)$	$(0\,\bar{1}\,0)$ $(0\,0\,\bar{1})$						
4	a	. 3 m	Tetrahedron	$(1\,1\,1)$	$(\bar{1}\,\bar{1}\,1)$	$(\bar{1}\,1\,\bar{1})$	$(1\,\bar{1}\,\bar{1})$				
			Tetrahedron (e)	or $(\bar{1}\,\bar{1}\,\bar{1})$	$(1\,1\,\bar{1})$	$(1\,\bar{1}\,1)$	$(\bar{1}\,1\,1)$				

Symmetry of special projections	Along [0 0 1]	Along [1 1 1]	Along [1 1 0]
	4mm	3m	m

Table 2 Symbols for coordination polyhedra and polygons (developed by Donnay *et al.* (1964) and expanded by publications in *Physics Data*, changed by Lima-de-Faria *et al.* (1990)) sorted alphabetically. Differing symbols are set **bold**

Donnay *et al.* (1964), expanded by publications in *Physics Data*	Lima-de-Faria *et al.* (1990)	
(1c) or (1l)	[1l]	Single point
(2c)	**[2n]**	Two atoms not collinear with the central point
(2l)	[2l]	Two atoms collinear with the central point
(3c)	**[3n]**	Triangle not coplanar with the central point
(3l)	[3l]	Triangle planar with the central point
(4c)	**[4n]**	Quadrangle not coplanar with the central point
(4l) or (4s)	[4l] or [4s]	Quadrangle coplanar with the central point
(4py)	**[4y]**	Trigonal pyramid
(4t)	[4t]	Tetrahedron
(4u)		Approximate quadrangle, four atoms nearly coplanar
(5by)	[5by]	Trigonal bipyramid
	[5l]	Pentagon coplanar with the central point
(6a)	**[6ap]**	Trigonal antiprism
(6l)		Hexagon coplanar with the central point
(6o)	[6o]	Octahedron
(6r)	**[6p]**	Trigonal prism
	[7by]	Pentagonal bipyramid
(7py)		Hexagonal pyramid
	[6p1c]	Monocapped trigonal prism
	[6p2c]	Bicapped trigonal prism
(8a)	**[8ap]**	Tetragonal antiprism
	[8acb]	Anticube
(8by)	[8by]	Hexagonal bipyramid
(8c)		Octagon not coplanar with the central point
(8cu)	**[8cb]**	Cube
(8d)	**[8do]**	Dodecahedron with triangular faces
(8r)	**[8p]**	Tetragonal prism
	[6p3c]	Tricapped trigonal prism
(9hco)		Halved cubooctahedron
(10r)		Pentagonal prism not coplanar with the central point
(12a)		Hexagonal antiprism not coplanar with the central point
(12aco)	[12aco]	Anticubooctahedron, twinned cubooctahedron
(12co)	[12co]	Cubooctahedron with triangular and quadrangular faces
(12d)		Cubooctahedron with square faces
(12i)	[12i]	Icosahedron
(12p)	[12p]	Hexagonal prism
(12tt)	[12tt]	Truncated tetrahedron with triangular and hexagonal faces
(12a2z)	**[14FK]**	Frank–Kasper polyhedron with 14 vertices
(15ttp)	**[15FK]**	Truncated trigonal prism, Frank–Kasper polyhedron with 15 vertices
(12tt4t)	**[16FK]**	Frank–Kasper polyhedron with 16 vertices
(16thr)		Tetragonal hexagon prism
(18cohc)		Cubooctahedron, hexacapped
(24co)		Cubooctahedron with triangular and octagonal faces
(24oc)		Cubooctahedron with quadrangular and hexagonal faces
(24scu)		Snub-cube

independently within the Wyckoff position. According to the number of degrees of freedom, a lattice complex is called invariant, univariant, bivariant, or trivariant. For invariant lattice complexes Hermann (1960) proposed capital letters to symbolize the geometrical arrangements:

P,I,F,C,A	letters are chosen in connection with the Bravais notation
J	from the American toy 'Jackstones' or 'Jacks' (three orthogonal arms with a common central intersection)
D	for 'diamond' arrangement
T	shortest connections of 'tetrahedra'
W	in connection with the 'β-W-A15' type
S	with the point symmetry $\bar{4}$ (Schoenflies S)
V	with the point symmetry 222 (Schoenflies V)
$^{+}$Y	planar trigonal surrounding (self-coordination)

The symbols of invariant lattice complexes are listed in Table 3. Note that, if invariant complexes allow pairs of enantiomorphic point configurations, these are distinguished by the sign + or − in front of the symbols.

Table 3 Symbols of invariant lattice complexes in their characteristic Wyckoff position

Lattice-complex symbol	Multiplicity	Coordinates	Crystal family	Characteristic Wyckoff position
C	2	$000, \frac{1}{2}\frac{1}{2}0$	o	Cmmm a
			m	C2/m a
D	8	$000, \frac{1}{4}\frac{1}{4}\frac{1}{4}, \frac{1}{2}\frac{1}{2}0Q, \frac{3}{4}\frac{3}{4}\frac{1}{4}Q$	c	$Fd\bar{3}m$ a
			o	Fddd a
v_D	4	$000, 0\frac{1}{2}\frac{1}{4}, \frac{1}{2}\frac{1}{2}\frac{1}{2}, \frac{1}{2}0\frac{3}{4}$	t	$I4_1/amd$ a
E	2	$\frac{1}{3}\frac{2}{3}\frac{1}{4}, \frac{2}{3}\frac{1}{3}\frac{3}{4}$	h	$P6_3/mmc$ c
F	4	$000, \frac{1}{2}\frac{1}{2}0Q$	c	$Fm\bar{3}m$ a
			o	Fmmm a
G	2	$\frac{1}{3}\frac{2}{3}0, \frac{2}{3}\frac{1}{3}0$	h	P6/mmm c
I	2	$000, \frac{1}{2}\frac{1}{2}\frac{1}{2}$	c	$Im\bar{3}m$ a
			t	I4/mmm a
			o	Immm a
J	3	$\frac{1}{2}\frac{1}{2}0Q$	c	$Pm\bar{3}m$ c
J*	6	$\frac{1}{2}\frac{1}{2}0Q, \frac{1}{2}00Q$	c	$Im\bar{3}m$ b
M	9	$\frac{1}{2}00, 0\frac{1}{2}0, \frac{1}{2}\frac{1}{2}0, \frac{5}{6}\frac{2}{3}\frac{2}{3}, \frac{1}{3}\frac{1}{6}\frac{2}{3}, \frac{5}{6}\frac{1}{6}\frac{2}{3}, \frac{1}{6}\frac{1}{3}\frac{1}{3}, \frac{2}{3}\frac{5}{6}\frac{1}{3}, \frac{1}{6}\frac{5}{6}\frac{1}{3}$	h	$R\bar{3}m$ e
N	3	$\frac{1}{2}00, 0\frac{1}{2}0, \frac{1}{2}\frac{1}{2}0$	h	P6/mmm f
P	1	000	c	$Pm\bar{3}m$ a
			t	P4/mmm a
			h	P6/mmm a
			o	Pmmm a
			m	$P2/m$ a
			a	$P\bar{1}$ a
+Q	3	$\frac{1}{2}00, 0\frac{1}{2}\frac{2}{3}, \frac{1}{2}\frac{1}{2}\frac{1}{3}$	h	$P6_222$ c
R	3	$000, \frac{1}{3}\frac{2}{3}\frac{2}{3}, \frac{2}{3}\frac{1}{3}\frac{1}{3}$	h	$R\bar{3}m$ a
S	12	$0\frac{1}{4}\frac{3}{8}Q, 0\frac{3}{4}\frac{1}{8}Q, \frac{1}{2}\frac{3}{4}Q, \frac{7}{8}, \frac{1}{2}\frac{1}{4}\frac{5}{8}Q$	c	$I\bar{4}3d$ a
S*	24	$0\frac{1}{4}\frac{3}{8}Q, 0\frac{3}{4}\frac{1}{8}Q, \frac{1}{2}\frac{3}{4}\frac{7}{8}Q, \frac{1}{2}\frac{1}{4}\frac{5}{8}Q, 0\frac{3}{4}\frac{5}{8}Q, 0\frac{1}{4}\frac{7}{8}Q,$ $\frac{1}{2}\frac{1}{4}\frac{1}{8}Q, \frac{1}{2}\frac{3}{4}\frac{3}{8}Q$	c	$Ia\bar{3}d$ d
T	16	$\frac{1}{8}\frac{1}{8}\frac{1}{8}, \frac{3}{8}\frac{1}{8}\frac{3}{8}Q, \frac{5}{8}\frac{5}{8}\frac{1}{8}Q, \frac{7}{8}\frac{5}{8}\frac{3}{8}Q, \frac{7}{8}\frac{1}{8}\frac{7}{8}Q, \frac{3}{8}\frac{5}{8}\frac{7}{8}Q$	c	$Fd\bar{3}m$ c
			o	Fddd c
^vT	8	$0\frac{1}{4}\frac{1}{8}, 0\frac{3}{4}\frac{1}{8}, \frac{1}{4}0\frac{7}{8}, \frac{3}{4}0\frac{7}{8}, \frac{1}{2}\frac{3}{4}\frac{5}{8}, \frac{1}{2}\frac{1}{4}\frac{5}{8}, \frac{3}{4}\frac{1}{2}\frac{3}{8}, \frac{1}{4}\frac{1}{2}\frac{3}{8}$	t	$I4_1/amd$ c
^+V	12	$0\frac{1}{4}\frac{1}{8}Q, 0\frac{3}{4}\frac{3}{8}Q, \frac{1}{2}\frac{3}{4}\frac{5}{8}Q, \frac{1}{2}\frac{1}{4}\frac{7}{8}Q$	c	$I4_132$ c
V*	24	$0\frac{1}{4}\frac{1}{8}Q, 0\frac{3}{4}\frac{3}{8}Q, \frac{1}{2}\frac{3}{4}\frac{5}{8}Q, \frac{1}{2}\frac{1}{4}\frac{7}{8}Q, 0\frac{3}{4}\frac{7}{8}Q, 0\frac{1}{4}\frac{5}{8}Q,$ $\frac{1}{2}\frac{1}{4}\frac{3}{8}Q, \frac{1}{2}\frac{3}{4}\frac{1}{8}Q$	c	$Ia\bar{3}d$ c
W	6	$0\frac{1}{2}\frac{1}{4}Q, 0\frac{1}{2}\frac{3}{4}Q$	c	$Pm\bar{3}n$ c
W*	12	$0\frac{1}{2}\frac{1}{4}Q, 0\frac{1}{2}\frac{3}{4}Q, \frac{1}{2}0\frac{3}{4}Q, \frac{1}{2}0\frac{1}{4}Q$	c	$Im\bar{3}m$ d
^+Y	4	$\frac{1}{8}\frac{1}{8}\frac{1}{8}, \frac{7}{8}\frac{5}{8}\frac{3}{8}Q$	c	$P4_332$ a
$^+Y^*$	8	$\frac{1}{8}\frac{1}{8}\frac{1}{8}, \frac{7}{8}\frac{5}{8}\frac{3}{8}Q, \frac{5}{8}\frac{5}{8}\frac{5}{8}, \frac{3}{8}\frac{1}{8}\frac{7}{8}Q$	c	$I4_132$ a
Y**	16	$\frac{1}{8}\frac{1}{8}\frac{1}{8}, \frac{7}{8}\frac{5}{8}\frac{3}{8}Q, \frac{5}{8}\frac{5}{8}\frac{5}{8}, \frac{3}{8}\frac{1}{8}\frac{7}{8}Q, \frac{7}{8}\frac{7}{8}\frac{7}{8}, \frac{1}{8}\frac{3}{8}\frac{5}{8}Q,$ $\frac{3}{8}\frac{3}{8}\frac{3}{8}, \frac{5}{8}\frac{7}{8}\frac{1}{8}Q$	c	$Ia\bar{3}d$ b

If the point configuration is shifted by the vector $(\frac{1}{2}\frac{1}{2}\frac{1}{2})$, $(\frac{1}{4}\frac{1}{4}\frac{1}{4})$ or $(\frac{3}{4}\frac{3}{4}\frac{3}{4})$ from the standard setting, the lattice complex symbol is followed by one, two or three primes on the capital letters, e.g. F′, F″ or F‴. The star * stands for a combination of two complexes, which can be mapped onto each other by $\bar{1}$ or $(\frac{1}{2}\frac{1}{2}\frac{1}{2})$. The invariant cubic lattice complexes are drawn in Figure 2. Symbols of the site sets and coordinates of the corresponding points are listed in Table 4. A site set is symbolized by a string of numbers and small letters. The product of the numbers gives the number of equipoints in the site set, whereas the letters

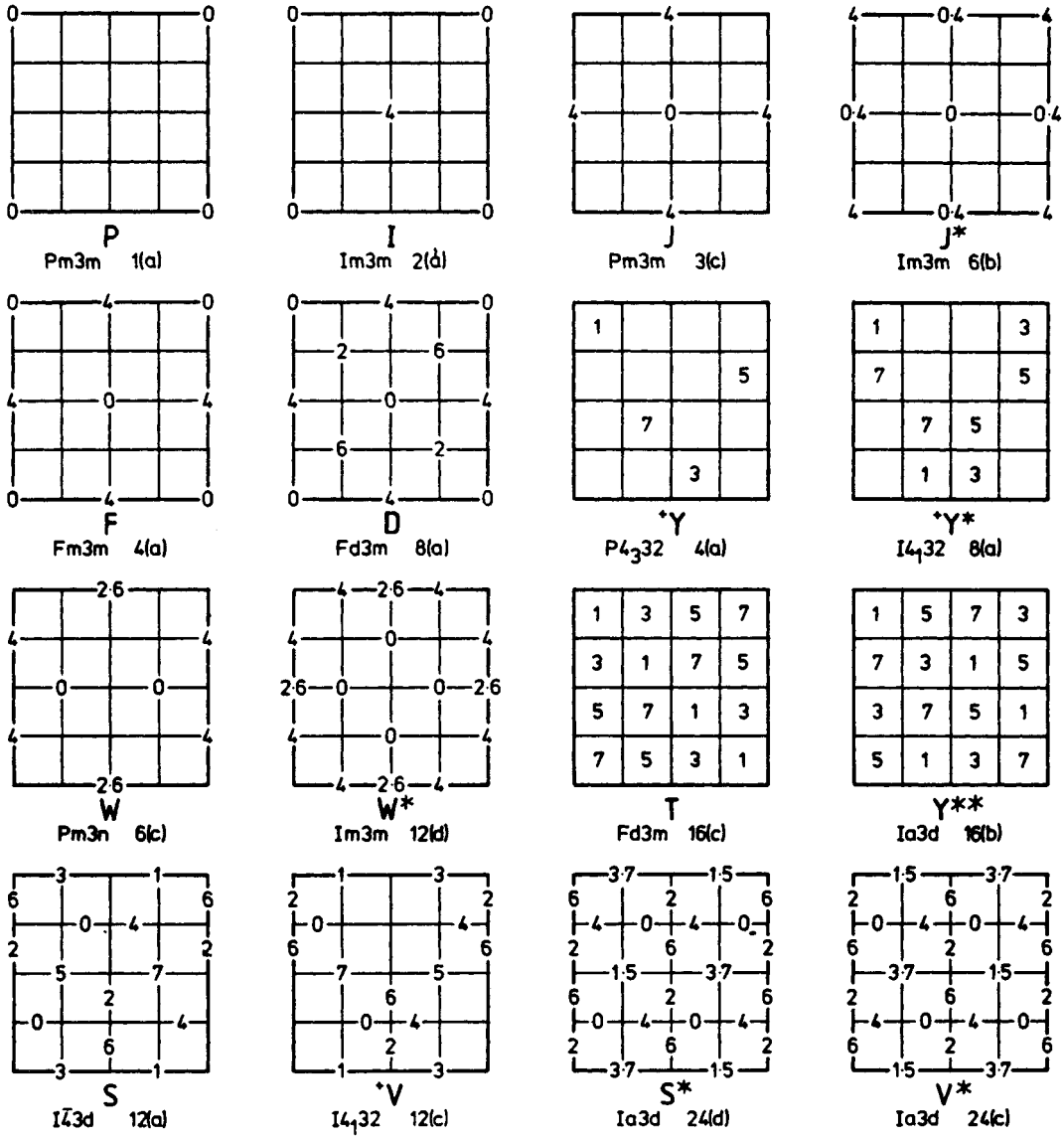

Figure 2 The 16 invariant lattice complexes in their standard settings. Numbers are given in eighths of projection axes. 0.4 means 0 *and* $4 = 4/8 = 1/2$

supply information about the degrees and directions of freedom. For characteristic Wyckoff positions, the descriptive symbols of lattice complexes with degrees of freedom consist, in general, of four consecutive parts: shift vector, distribution symmetry, central part, and site-set symbol. Either of the first two parts may be absent. The central part contains one, or more than one, symbol of an invariant lattice complex (see Fischer *et al.*, 1973).

Two examples now follow: (1) I4xxx I$\bar{4}$3m c xxx) designates site sets composed of tetrahedra in parallel orientations replacing the points of a cubic body-centered lattice; the vertices of these tetrahedra are located on body diagonals. (2) . . 2I4xxx (Pn$\bar{3}$m e xxx) represents the lattice complex for which, in contrast to example (1), the tetrahedra around 0 0 0 and $\frac{1}{2}\frac{1}{2}\frac{1}{2}$ differ in orientation; they are related by a twofold axis (. . 2) (= orientation symmetry) parallel to a face diagonal.

Table 4 Symbols of site sets and coordinates of corresponding points

Site-set symbol	Coordinate system	Coordinates of site-set points
1*x*	othc	*x* 0 0
1*x*2*y z*	ot	*x y z*; *x* $\bar{y}$ $\bar{z}$
	h	*x y z*; *x*−*y*, $\bar{y}$, $\bar{z}$
1*xx*	t	*x x* 0
1*xx*2 *y z*	t	*x y z*; *y x* $\bar{z}$
1*x*$\bar{x}$	h	*x* $\bar{x}$ 0
1*x*$\bar{x}$2*yz*	h	*x y z*; $\bar{y}$ $\bar{x}$ $\bar{z}$
1*xxx*	c	*x x x*
1*xxx*3*yz*	c	*x y z* Q
1*y*	mo	0 *y* 0
1*y*2*x*	o	*x y* 0; $\bar{x}$ *y* 0
1*z*	mothc	0 0 *z*
1*z*2 *x*	o	*x* 0 *z*; $\bar{x}$ 0 *z*
1*z*2*x*2*y*	o	*x y z*; $\bar{x}$ *y z*; *x* $\bar{y}$ *z*; $\bar{x}$ $\bar{y}$ *z*
1*z*2*xx*	t	*x x z*; $\bar{x}$ $\bar{x}$ *z*
1*z*2*y*	o	0 *y z*; 0 $\bar{y}$ *z*
1*z*4*xx*	t	*x x z*; $\bar{x}$ *x z*; *x* $\bar{x}$ *z*; $\bar{x}$ $\bar{x}$ *z*
1*z*2*xy*	o	*x y z*; $\bar{x}$ $\bar{y}$ *z*
1*xy*	moth	*x y* 0
1*xz*	mo	*x* 0 *z*
1*xyz*	o	*x y z*
2*x*	othc	±(*x* 0 0)
2*x*2*y*	ot	±(*x y* 0; $\bar{x}$ *y* 0)
2*x*2*y*2*z*	o	±(*x y z*; $\bar{x}$ *y z*; *x* $\bar{y}$ *z*; $\bar{x}$ $\bar{y}$ *z*)
2*x*2*z*	o	± (*x* 0 *z*; $\bar{x}$ 0 *z*)
2*x*2*yz*	ot	*x y z*; $\bar{x}$ $\bar{y}$ *z*; $\bar{x}$ *y* $\bar{z}$; *x* $\bar{y}$ $\bar{z}$
	h	*x y z*; $\bar{x}$ $\bar{y}$ *z*; *x*−*y*, $\bar{y}$, $\bar{z}$; *y*−*x*, *y*, $\bar{z}$
2*xx*	t	±(*x x* 0)
2*xx*2*y*	t	±(*x y* 0; *y x* 0)
2*xx*2*y*2*z*	t	±(*x y z*; *x y* $\bar{z}$; *y x z*; *y x* $\bar{z}$)
2*xx*2*z*	t	±(*x x z*; *x x* $\bar{z}$)
2*xx*2*yz*	t	*x y z*; $\bar{x}$ $\bar{y}$ *z*; *y x* $\bar{z}$; $\bar{y}$ $\bar{x}$ $\bar{z}$
2*x*$\bar{x}$	th	±(*x* $\bar{x}$ 0)
2*xxx*	rc	±(*x x x*)
2*y*	mo	±(0 *y* 0)
2*y*2*z*	o	±(0 *y z*; 0 $\bar{y}$ *z*)
2*z*	mothc	±(0 0 *z*)
2*xy*	moth	±(*x y* 0)
2*xy*2*z*	mo	±(*x y z*; $\bar{x}$ $\bar{y}$ *z*)
2*xy*	mo	±(*x* 0 *z*)
2*xz*2*y*	mo	±(*x y z*; $\bar{x}$ *y* $\bar{z}$)
2*xxz*	t	±(*x x z*)
2*yz*	o	±(0 *y z*)
2*yz*2 *x*	o	±(*x y z*; *x* $\bar{y}$ $\bar{z}$)
2*xyz*	amo	±(*x y z*)
3*x*	h	*x* 0 0; 0 *x* 0; $\bar{x}$ $\bar{x}$ 0
3*x*2*y*	h	*x y* 0; *y x* 0; $\bar{y}$, *x*−*y*, 0; *x*−*y*, $\bar{y}$, 0; $\bar{x}$, *y*−*x*, 0; *y*−*x*, $\bar{x}$, 0
3*x*2*y*2*z*	h	*x y z*; *x y* $\bar{z}$; *y x z*; *y x* $\bar{z}$; $\bar{y}$, *x*−*y*, *z*; $\bar{y}$, *x*−*y*, $\bar{z}$; *x*−*y*, $\bar{y}$, *z*; *x*−*y*, $\bar{y}$, $\bar{z}$; *y*−*x*, $\bar{x}$, *z*; *y*−*x*, $\bar{x}$, $\bar{z}$; $\bar{x}$, *y*−*x*, *z*; $\bar{x}$, *y*−*x*, $\bar{z}$
3*x*2*z*	h	*x* 0 *z*; *x* 0 $\bar{z}$; 0 *x z*;0 *x* $\bar{z}$; $\bar{x}$ $\bar{x}$ *z*; $\bar{x}$ $\bar{x}$ $\bar{z}$
3*x*2*yz*	h	*x y z*; *y x* $\bar{z}$; $\bar{y}$, *x*−*y*, *z*; *x*−*y*, $\bar{y}$, $\bar{z}$; $\bar{x}$, *y*−*x*, $\bar{z}$; *y*−*x*, $\bar{x}$, *z*
3*x*$\bar{x}$	rc	*x* $\bar{x}$ 0 Q
	h	*x* $\bar{x}$ 0; *x*, 2 *x*, 0; 2 $\bar{x}$, $\bar{x}$, 0
3*x*$\bar{x}$2*y*	h	*x y* 0; $\bar{y}$ $\bar{x}$ 0; $\bar{y}$, *x*−*y*, 0; *y*−*x*, *y*, 0; *x*, *x*−*y*, 0; *y*−*x*, $\bar{x}$, 0
3*x*$\bar{x}$2*y*2*z*	h	*x y z*; *x y* $\bar{z}$; $\bar{y}$ $\bar{x}$ *z*; $\bar{y}$ $\bar{x}$ $\bar{z}$; $\bar{y}$, *x*−*y*, *z*; $\bar{y}$, *x*−*y*, $\bar{z}$; *y*−*x*, *y*, *z*; *y*−*x*, *y*, $\bar{z}$; *x*, *x*−*y*, *z*; *x*, *x*−*y*, $\bar{z}$; *y*−*x*, $\bar{x}$, *z*; *y*−*x*, $\bar{x}$, $\bar{z}$
3*x*$\bar{x}$2*z*	h	*x* $\bar{x}$ *z*; *x* $\bar{x}$ $\bar{z}$; *x*, 2 *x*, *z*; *x*, 2 *x*, $\bar{z}$; 2 $\bar{x}$, $\bar{x}$, *z*; 2 $\bar{x}$, $\bar{x}$, $\bar{z}$
3*x*$\bar{x}$2*yz*	rc	*x y z* Q; $\bar{y}$ $\bar{x}$ $\bar{z}$ Q
	h	*x y z*; $\bar{y}$ $\bar{x}$ $\bar{z}$; $\bar{y}$, *x*−*y*, *z*; *y*−*x*, *y*, $\bar{z}$; *y*−*x*, $\bar{x}$, *z*; *x*, *x*−*y*, $\bar{z}$
3*z*	r	0 0 *z* Q
3*z*2*y*	r	0 *y z* Q; *y* 0 *z* Q
3*xy*	h	*x y* 0; $\bar{y}$, *x*−*y*, 0; *y*−*x*, $\bar{x}$, 0
3*xy*2*z*	h	*x y z*; *x y* $\bar{z}$; $\bar{y}$, *x*−*y*, *z*; $\bar{y}$, *x*−*y*, $\bar{z}$; *y*−*x*, $\bar{x}$, *z*; *y*−*x*, $\bar{x}$, $\bar{z}$
3*yz*	r	0 *y z* Q
4*x*	tc	±(*x* 0 0; 0 *x* 0)
4*x*2 *y*	t	±(*x y* 0; *x* $\bar{y}$ 0; *y x* 0; *y* $\bar{x}$ 0)
4*x*2*y*2*z*	t	±(*x y z*; *x y* $\bar{z}$; *x* $\bar{y}$ *z*; *x* $\bar{y}$ $\bar{z}$; *y x z*; *y x* $\bar{z}$; *y*$\bar{x}$ *z*; *y* $\bar{x}$ $\bar{z}$)
4*x*2*z*	t	±(*x* 0 *z*; *x* 0 $\bar{z}$; 0 *x z*; 0 *x* $\bar{z}$)
4*x*2*yz*	t	*x y z*; *y x* $\bar{z}$; *x* $\bar{y}$ *z*; $\bar{y}$ $\bar{x}$ $\bar{z}$; *y* $\bar{x}$ *z*; $\bar{x}$ *y* $\bar{z}$; $\bar{y}$ *x z*; *x* $\bar{y}$ $\bar{z}$
4*xx*	tc	±(*x x* 0; *x* $\bar{x}$ 0)
4*xx*2*z*	t	±(*x x z*; *x x* $\bar{z}$; *x* $\bar{x}$ *z*; *x* $\bar{x}$ $\bar{z}$)
4*xxx*	c	*x x x*; $\bar{x}$ $\bar{x}$ *x* Q
4*xy*	t	±(*x y* 0; *y* $\bar{x}$ 0)
4*xy*2*z*	t	±(*x y z*; *x y* $\bar{z}$; *y* $\bar{x}$ *z*; *y* $\bar{x}$ $\bar{z}$)
4*xz*	t	*x* 0 *z*; $\bar{x}$ 0 *z*; 0 *x z*; 0 $\bar{x}$ $\bar{z}$
4*xz*2*y*	t	*x y z*; *x* $\bar{y}$ *z*; $\bar{x}$ *y z*; $\bar{x}$ $\bar{y}$ *z*; *y x* $\bar{z}$; $\bar{y}$ *x* $\bar{z}$; *y* $\bar{x}$ $\bar{z}$; $\bar{y}$ $\bar{x}$ $\bar{z}$
4*xxz*	t	*x x z*; $\bar{x}$ $\bar{x}$ *z*; *x* $\bar{x}$ $\bar{z}$; $\bar{x}$ *x* $\bar{z}$
4*xxz*2*y*	t	*x y z*; *y x z*; $\bar{x}$ $\bar{y}$ *z*; $\bar{y}$ $\bar{x}$ *z*; *x* $\bar{y}$ $\bar{z}$; $\bar{y}$ *x* $\bar{z}$; $\bar{x}$ *y* $\bar{z}$; *y* $\bar{x}$ $\bar{z}$
4*xyz*	tc	*x y z*; $\bar{x}$ $\bar{y}$ *z*; *y* $\bar{x}$ $\bar{z}$; $\bar{y}$ *x* $\bar{z}$
6*x*	h	±(*x* 0 0; *x x* 0; 0 *x* 0)
6*x*2*y*	h	±(*x y* 0; *y x* 0; *x*, *x*−*y*, 0; *x*−*y*, *x*, 0; *y*, *y*−*x*, 0; *y*−*x*, *y*, 0)
6*x*2*y*2*z*	h	±(*x y z*; *x y* $\bar{z}$; *y x z*; *y x* $\bar{z}$; *x*, *x*−*y*, *z*; *x*, *x*−*y*, $\bar{z}$; *x*−*y*, *x*, *z*; *x*−*y*, *x*, $\bar{z}$; *y*, *y*−*x*, *z*; *y*, *y*−*x*, $\bar{z}$; *y*−*x*, *y*, *z*; *y*−*x*, *y*, $\bar{z}$)
6*x*2*z*	h	±(*x* 0 *z*; *x* 0 $\bar{z}$; *x x z*; *x x* $\bar{z}$; 0 *x z*; 0 *x* $\bar{z}$)
6*x*2*yz*	h	*x y z*; $\bar{x}$ $\bar{y}$ *z*; *y x* $\bar{z}$; $\bar{y}$ $\bar{x}$ $\bar{z}$; *x*, *x*−*y*, $\bar{z}$; $\bar{x}$, *y*−*x*, $\bar{z}$; *x*−*y*, *x*, *z*; *y*−*x*, $\bar{x}$, *z*; *y*, *y*−*x*, *z*; $\bar{y}$, *x*−*y*, *z*; *y*−*x*, *y*, $\bar{z}$; *x*−*y*, $\bar{y}$, $\bar{z}$

(*continued*)

Table 4 (*continued*)

Site-set symbol	Coordinate system	Coordinates of site-set points
$6x\bar{x}$	rc	$\pm(x\,\bar{x}\,0\,Q)$
	h	$\pm(x\,\bar{x}\,0;\ x,\ 2x,\ 0;\ 2\bar{x},\ 0)$
$6x\bar{x}2z$	h	$\pm(x\,\bar{x}\,z;\ x\,\bar{x}\,\bar{z};\ x,\ 2x,\ z;\ x,\ 2x,\ \bar{z};\ 2x,\ x,\ z;\ 2x,\ x,\ \bar{z})$
$6z$	c	$\pm(0\,0\,z\,Q)$
$6z2x$	c	$\pm(x\,0\,z\,Q;\ \bar{x}\,0\,z\,Q)$
$6z2x2y$	c	$\pm(x\,y\,z\,Q;\ x\,\bar{y}\,z\,Q;\ \bar{x}\,y\,z\,Q;\ \bar{x}\,\bar{y}\,z\,Q)$
$6z2xx$	c	$x\,x\,z\,Q;\ \bar{x}\,\bar{x}\,z\,Q;\ \bar{x}\,x\,\bar{z}\,Q;\ x\,\bar{x}\,\bar{z}\,Q$
$6z2xx2y$	c	$x\,y\,z\,Q;\ y\,x\,z\,Q;\ \bar{x}\,\bar{y}\,z\,Q;\ \bar{y}\,\bar{x}\,z\,Q;\ \bar{x}\,y\,\bar{z}\,Q;\ y\,\bar{x}\,\bar{z}\,Q;\ x\,\bar{y}\,\bar{z}\,Q;\ \bar{y}\,x\,\bar{z}\,Q$
$6z4x$	c	$\pm(x\,0\,z\,Q;\ \bar{x}\,0\,z\,Q;\ 0\,x\,z\,Q;\ 0\,\bar{x}\,z\,Q)$
$6z4x2y$	c	$\pm(x\,y\,z\,Q;\ x\,\bar{y}\,z\,Q;\ \bar{x}\,y\,z\,Q;\ \bar{x}\,\bar{y}\,z\,Q;\ y\,x\,z\,Q;\ \bar{y}\,x\,z\,Q;\ y\,\bar{x}\,z\,Q;\ \bar{y}\,\bar{x}\,z\,Q)$
$6z4xx$	c	$\pm(x\,x\,z\,Q;\ \bar{x}\,\bar{x}\,z\,Q;\ x\,\bar{x}\,z\,Q;\ \bar{x}\,x\,z\,Q)$
$6z2xy$	c	$x\,y\,z\,Q;\ \bar{x}\,\bar{y}\,z\,Q;\ x\,\bar{y}\,\bar{z}\,Q;\ \bar{x}\,y\,\bar{z}\,Q$
$6z4xy$	c	$x\,y\,z\,Q;\ \bar{x}\,\bar{y}\,z\,Q;\ y\,\bar{x}\,z\,Q;\ \bar{y}\,x\,z\,Q;\ x\,\bar{y}\,\bar{z}\,Q;\ \bar{x}\,y\,\bar{z}\,Q;\ \bar{y}\,\bar{x}\,\bar{z}\,Q;\ y\,x\,\bar{z}\,Q$
$6xy$	h	$\pm(x\,y\,0;\ y,\ y-x,\ 0;\ x-y,\ x,\ 0)$
$6xy2z$	h	$\pm(x\,y\,z;\ x\,y\,\bar{z};\ y,\ y-x,\ z;\ y,\ y-x,\ \bar{z};\ x-y,\ x,\ z;\ x-y,\ x,\ \bar{z})$
$6xz$	h	$\pm(x\,0\,z;\ 0\,x\,z;\ \bar{x}\,\bar{x}\,z)$
$6xz2y$	h	$\pm(x\,y\,z;\ y\,x\,z;\ x-y,\ \bar{y},\ z;\ \bar{y},\ x-y,\ z;\ \bar{x},\ y-x,\ z;\ y-x,\ \bar{x},\ z)$
$6xxz$	r	$\pm(x\,x\,z\,Q)$
$6xxz2y$	r	$\pm(x\,y\,z\,Q;\ y\,x\,z\,Q)$
$6x\bar{x}z$	h	$\pm(x\,\bar{x}\,z;\ x,\ 2x,\ z;\ 2\bar{x},\ \bar{x},\ z)$
$6x\bar{x}z2y$	h	$\pm(x\,y\,z;\ y\,x\,\bar{z};\ x,\ x-y,\ z;\ x-y,\ x,\ \bar{z};\ y-x,\ \bar{x},\ z;\ \bar{x},\ y-x,\ \bar{z})$
$6xyz$	rc	$\pm(x\,y\,z\,Q)$
	h	$\pm(x\,y\,z;\ \bar{y},\ x-y,\ z;\ y-x,\ \bar{x},\ z)$
$8xxx$	c	$\pm(x\,x\,x;\ x\,x\,\bar{x}\,Q)$
$12xx$	c	$\pm(x\,x\,0\,Q;\ x\,\bar{x}\,0\,Q)$

In consequence, the listing of space groups with their lattice complexes seems to be generally easy and goes automatically: see Table 5. Multiples of invariant lattice complexes are denoted by $n_a n_b n_c$, where the subscript numbers indicate that the cell is repeated n_a times along axis a, etc. So I_{113} gives an I complex tripled along c. The product $n_a n_b n_c$ gives the order of the new cell.

A framework is an arrangement of atoms or ions that are in contact with each other. The most essential attribute of a framework is the forming of proper voids suitable for occupation by the other atoms of the crystal structure. Most frameworks are defined using lattice complexes and polyhedra (Fischer and Koch, 1974).

A symbolism for coordination polyhedra was developed by Donnay *et al.* (1964) as the dual of the crystal forms. It begins with the multiplicity of the complex followed by a symbol for the coordination: l stands for planar surrounding, y for pyramidal, p for prismatic, a for antiprismatic, by for bipyramidal, t for tetrahedral, o for octahedral surrounding, etc. The International Union of Crystallography, Commission on Crystallographic Nomenclature, Subcommittee on the Nomenclature of Inorganic Structure Types (Lima-de-Faria *et al.*, 1990) proposed changes for some symbols. Table 2 shows symbols for coordination polyhedra as given by Donnay *et al.* (1964) and expanded by publications in *Physics Data* (see Hellner and Pearson, 1986) and as given by Lima-de-Faria *et al.* (1990).

For a crystal-chemical description of a crystal structure one needs to know the geometrical behavior of the homogeneous Wyckoff positions as they vary with the atomic parameters lattice axes relations and the angle between the axes and the sizes of the atoms or clusters. Discussions of sphere packing conditions for the tetragonal and cubic positions are given by Fischer (1971, 1973, 1974, 1991, 1993). But if more than two positions form the framework, one again needs some help by group–subgroup relations.

There is no unique way to describe crystal structures. We will use lattice complexes, frameworks, polyhedra, and nets (and combinations thereof) to describe b.c.c. derivative structures.

2. The I Framework

The I lattice complex consists of all body-centered cubic lattices. It corresponds to the sphere packing type 8/4/c1 (Fischer, 1973), i.e. 8 is the number of nearest neighbors, 4 the number of the smallest mesh to reach the nearest neighbor, and c1 is an enumeration of nets with the same coordination number (CN). Only one kind of void exists, i.e. flattened tetrahedra around a W* configuration. The maximal radius of the sphere, which fills up the voids, is very small (Hellner *et al.*, 1981).

Elemental representatives of the I structure (named the W A2 (cI2) type) are the alkali metals, the alkaline-earth metals, and some transition metals like Cr, β-Ti, V, and elements below them in the periodic table. The inclusion especially of the alkali atoms in this group,

Table 5 Assignments of Wyckoff positions to Wyckoff sets and lattice complexes in some space groups. Characteristic Wyckoff sets are marked by asterisks

229	**Im$\bar{3}$m**	
96 l	I6z4x2y	*Im$\bar{3}$m l
48 k	I6z4xx	*Im$\bar{3}$m k
48 j	I6z4x	*Im$\bar{3}$m j
48 i	$\frac{1}{4}\frac{1}{4}\frac{1}{4}$4..P26x$\bar{x}$	*Im$\bar{3}$m i
24 h	I12xx	*Im$\bar{3}$m h
24 g	.3.J*4x	*Im$\bar{3}$m g
16 f	I8xxx	*Im$\bar{3}$m f
12 e	I6z	*Im$\bar{3}$m e
12 d	W*	*Im$\bar{3}$m d
8 c	$\frac{1}{4}\frac{1}{4}\frac{1}{4}P_2$	Pm$\bar{3}$m a
6 b	J*	*Im$\bar{3}$m b
2 a	I	*Im$\bar{3}$m a

230	**Ia$\bar{3}$d**	
96 h	$\bar{4}$a..Y**3x$\bar{x}$2yz	*Ia$\bar{3}$d h
48 g	$\bar{4}$a..Y**3x$\bar{x}$	*Ia$\bar{3}$d g
48 f	.3.S*2z	*Ia$\bar{3}$d f
32 e	$\bar{4}$..Y**2xxx	*Ia$\bar{3}$d e
24 d	S*	*Ia$\bar{3}$d d
24 c	V*	*Ia$\bar{3}$d c
16 b	Y**	*Ia$\bar{3}$d b
16 a	I_2	Im$\bar{3}$m a

155	**R32 (hexagonal axes)**	
18 f	R3x2yz	*R32 f
9 e	00$\frac{1}{2}$R3x	*R32 d
9 d	R3x	
6 c	R2z	R$\bar{3}$m c
3 b	00$\frac{1}{2}$R	R$\bar{3}$m a
3 a	R	

155	**R32 (rhombohedral axes)**	
6 f	P3 2yz	*R32 f
3 e	$\frac{1}{2}\frac{1}{2}\frac{1}{2}$P3x$\bar{x}$	*R32 d
3 d	P3x$\bar{x}$	
2 c	P2xxx	R$\bar{3}$m c
1 b	$\frac{1}{2}\frac{1}{2}\frac{1}{2}$P	R$\bar{3}$m a
1 a	P	

217	**I$\bar{4}$3m**	
48 h	I6z2xx2y	*I$\bar{4}$3m h
24 g	I6z2xx	*I$\bar{4}$3m g
24 f	.3.J*4x	Im$\bar{3}$m g
12 e	I6z	Im$\bar{3}$m e
12 d	W*	Im$\bar{3}$m d
8 c	I4xxx	*I$\bar{4}$3m c
6 b	J*	Im$\bar{3}$m b
2 a	I	Im$\bar{3}$m a

220	**I$\bar{4}$3d**	
48 e	.3dS4xyz	*I$\bar{4}$3d e
24 d	.3.S2z	*I$\bar{4}$3d d
16 c	$\bar{4}$..I_2Y**1xxx	*I$\bar{4}$3d c
12 b	'S	*I$\bar{4}$3d a
12 a	S	

121	**I$\bar{4}$2m**	
16 j	I4xxx2y	*I$\bar{4}$2m j
8 i	I4xxz	*I$\bar{4}$2m i
8 h	0$\frac{1}{2}$0$(C2z)_c$	P4/mmm g
8 g	00$\frac{1}{2}$I4x	I4/mmm i
8 f	I4x	
4 e	I2x	I4/mmm e
4 d	0$\frac{1}{2}\frac{1}{4}C_c$	P4/mmm a
4 c	0$\frac{1}{2}$0C_c	P4/mmm a
2 b	00$\frac{1}{2}$I	I4/mmm a
2 a	I	

122	**I$\bar{4}$2d**	
16 e	.2.^{v}D4xyz	*I$\bar{4}$2d e
8 d	4..^{v}TF_c1x	*I$\bar{4}$2d d
8 c	^{v}D2z	$I4_1$/amd e
4 b	00$\frac{1}{2}$^{v}D	$I4_1$/amd a
4 a	^{v}D	

23	**I222**	
8 k	I2x2y2z	*I222 k
4 j	0$\frac{1}{2}$0I2z	Immm e
4 i	I2x	
4 h	$\frac{1}{2}$00I2y	
4 g	I2y	
4 f	00$\frac{1}{2}$I2x	
4 e	I2x	
2 d	0$\frac{1}{2}$0I	Immm a
2 c	00$\frac{1}{2}$I	
2 b	$\frac{1}{2}$00I	
2 a	I	

24	**$I2_12_12_1$**	
8 d	$\frac{1}{4}0\frac{1}{4}$..2C_cB_b1x2yz	*$I2_12_12_1$ d
4 c	0$\frac{1}{4}\frac{1}{4}$.2.B_bA_a1z	Imma e
4 b	$\frac{1}{4}\frac{1}{4}$02..A_aC_c1y	
4 a	$\frac{1}{4}0\frac{1}{4}$..2C_cB_b1x	

with only one s electron in the valence-band shell, has forced Pauling (1940) to propose the unsynchronized resonance of bonds between positive ions and covalently bonded clusters of two, three or four atoms, to explain the large electrical conductivity. The pseudopotential approach to band structure has been of interest to understand better the electronic properties in solids and its relation to the total energy of simple sp-bonded metals as given by Heine *et al.* (1970), including the fittings to experimental data (Cohen and Heine, 1970). Further, the orbital-dependent radii proposed by Simon and Bloch (1973) have been used by Zunger (1980) to demonstrate a structural separation plot for intermetallic compounds (see also Chapter 11 by Villars in this volume). In spite of these developments in theory and applications, there is no experimental information from photoelecton spectroscopy of metals with which to compare magnetic models for the alkali and noble metals from diatoms to the solid state (Malrieu *et al.*, 1984) including the valence-electron excitations in the alkali metals (vom Felde *et al.*, 1989) using electron energy-loss spectroscopy (EELS) (see also Chapter 6 by Singh in this volume).

Structures with a framework description can be categorized by splitting and order. Splittings for orders 1, 8, 27, and 216 are discussed in the following sections. Table 6 gives a comprehensive listing of b.c.c. derivative structures that can be described by I frameworks (Hellner and Sowa, 1985).

2.1 Splittings of the I lattice complex

A lattice complex is represented by its characteristic Wyckoff position in the space-group type that allows the highest site symmetry. In subgroups, the lattice complex is split in two or more Wyckoff positions. Some splittings of the I lattice complex are shown in Table 7.

The splitting of the I complex in $Pm\bar{3}m$ to P + P′ produces the CsCl B2 (cP2) type, the heteroplanar compound for the coordination number 8 with the ideal radius quotient $R_q = R_{cation}/R_{anion} = 0.91$ and a lower limit of $R_q = 0.73$; followed by NaCl B1 (cF8) type (F + F′) for CN 6 with $R_q = 0.414$; followed by the ZnS (zinc-blende) B3 (cF8) type (F + F″) for CN 4 with $R_q = 0.225$. A lattice-energy calculation has been proposed by Born (1923). Madelung (1918) has made a proposal for a simple summation of the energy terms. Some of the 300 intermetallic representatives of the B1 types statistically occupy both positions and have metallic band structures, but there exists an interesting heteropolarity in the intermetallic compounds Cs^+Au^- and Rb^+Au^- with $R_{Au^-} = 2.00$ Å (Knecht *et al.*, 1978); see Figure 3.

Hume-Rothery (1926) realized the importance of the ratio of the total number of valence electrons to the total number of atoms, the valence-electron concentration (VEC), in controlling the composition limits of metallic phases such as the disordered b.c.c. β-brass structures in CuZn, AgZn, AuZn, and AgCd with VEC = 1.5 but also Cu_3Al with VEC = 6/4 = 1.5 and in Cu_5Sn with VEC = 9/6 = 1.5; the β-manganese structure has the same VEC = 1.5 as Ag_3Al, Cu_5Si, and $CoZn_2$.

Jones (1934) has interpreted this in terms of the Bloch theory of metals, as inferred from experimental work on the Fermi surfaces.

2.1.1 The 8th Order of the I Complex

The 8th order of the I complex itself, named I_{222}, can be seen in the space group $Ia\bar{3}d$ in the Wyckoff position 16a, point symmetry $\bar{3}$ 000 and in $Fd\bar{3}c$ in 16a and 23 000: the first one is occupied in Ga_4Ni_3, the latter one by 16 Al in voltaite, a hydrous aluminum iron sulfate mineral.

As shown in Figure 4 from the $I_{222}m\bar{3}m$ (8th order) via $P_{222}n\bar{3}m$ to $Fd\bar{3}m$ one reaches the splitting product $D + D' = I_{222}$, which describes the NaTl structure. Zintl and Dullenkopf (1932) and Zintl (1939) described this type first and discussed the electron transfer from Na to Tl to get sp^3 hybridization, as in the elements of main group IV, C, Si, Ge, Sn. For the isotype I–II compounds, like LiZn or LiCd, a statistical occupation of the sp^3 hybridization was assumed to explain their paramagnetic behavior. Furthermore, the solubility of these compounds in liquid ammonia (NH_3) shows the presence of negative anions.

From $I_{222}m\bar{3}m$ via $P_{222}m\bar{3}m$ to $Fm\bar{3}m$ one reaches the splitting product $F + F' + P'_{222} = I_{222}$, which describes $AlMnCu_2$, the Heusler structure.

The subgroup $F\bar{4}3m$ of $Fm\bar{3}m$ permits all four Fs to exist; therefore $F + F' + F'' + F''' = I_{222}$ is occupied in $CuTiHg_2$. If one subtracts an F from I_{222} one gets a subclass ($I_{222} - F$) that has anti-CaF_2 or Mg_2Sn as a type compound.

The next splitting is found via $I_{222}m\bar{3}m$ to $P_{222}m\bar{3}m$ to $Im\bar{3}m$ to $Pm\bar{3}m$; $P + P' + J + J' + P'_{222} = I_{222}$ for the compound $Fe_{13}Ge_3$. In the space group $I2_13$ an 8 pointer on the body-diagonal is realized with one degree of freedom, namely 8a 3 xxx in the compound CoU with $x_{Co} = 0.294$, $x_U = 0.0347$ respectively. Therefore the description may be allowed to idealize the parameters to $x = 1/4$ and $x = 0$, and $P_2xxx + P'_2xxx \approx I_2xxx$, which is the type CoU.

Table 6 Frameworks of the I family and allocation of observed structure types thereto. Filled-up and defect frameworks are included herein. Numbers of known isotypic substances are those given in the compilation of Villars and Calvert (1985)

Substance	Symbol	Space group	Wyckoff	Framework	Number of substances
Order 1					
W	cI2	$Im\bar{3}m$	2a	[I]	241
β-Ag_2S	cI20	$Im\bar{3}m$	2a, 6b, 12d	$[I] + W^*_{si}, J^*_{si}$	1
Pa	tI2	I4/mmm	2a	[I]	3
β-CuZn (CsCl)	cP2	$Pm\bar{3}m$	1a, 1b	[I] = [P + P′]	401
HgMn	tP2	P4/mmm	1a, 1d	[I] = [P + P′]	7
NaCl	cF4	Fm3m	4a, 4b	F + F′	~700
ZnS (sphalerite)	cF8	F43m	4a, 4c	I = F + F″	120
Cu_2O (cuprite)	cP6	$Pn\bar{3}m$	2a, 4b	[I] + F″	3
FeS_2	oP6	Pnnm	2a, 4g	$[n..0\tfrac{1}{2}0I2xy] + I$	44
InS	oP8	Pnnm	$4g^2$	$n..0\tfrac{1}{2}0I2y + n..I2xy$	1
α-Po	cP1	$Pm\bar{3}m$	1a	[I − P′] = P	9
Order 2					
CuTi	tP4	P4/nmm	2c, 2c	$[I_{112}] = [0\tfrac{1}{2}0CI1z + 0\tfrac{1}{2}\tfrac{1}{2}CI1z]$	15
CaGaN	tP6	P4/nmm	$2c^2$	$[0\tfrac{1}{2}\tfrac{1}{8}I_{112}Iz] + 0\tfrac{1}{2}\tfrac{1}{2}CI1z$	4
Order 3					
$AlCu_2$($MoSi_2$ type) $c/a \approx 2.9$	tI6	I4/mmm	2a, 4e	$[I_{113}] = [I + 00\tfrac{1}{2}I2z]$	84
$MoPt_2$	oI6	Immm	2a, 4g	$[I_{131}Iy]$	8
C_2IrU_2, Mn_3N_2	tI10	I4/mmm	2a, $4e^2$	$[I_{113}] + I2z$	7
Al_4Ba	tI10	I4/mmm	2a, 4d, 4e	$[I_{113}] + 0\tfrac{1}{2}\tfrac{1}{4}C_{112}$	462
Order 4					
Pd_5Ti_3	tP8	P4/mmm	1a,b, 2g, $2h^2$	$[I_{114}] = [P_{114} + \tfrac{1}{2}\tfrac{1}{2}\tfrac{1}{2}P_{114}]$	1
Mo_3U_{22}	tP8	P4/nbm	2a, 2c, 4f	$[I_{114}] = [C + 0\tfrac{1}{2}0C + P'_{221}]$	1
β-Np	tC8	$C42_12$	4a, 4c	$I_{221}Iz$	3
Order 5					
Al_3Os_2	tI10	I4/mmm	2a, 4e, 4e	I_{115}	4
Order 6					
$AlAu_2$	oP12	Pnma	$4c^3$	$\bar{1}.2_1\tfrac{1}{8}\tfrac{1}{4}\tfrac{1}{5}I_{213}Ixz$	4
Order 7					
Cu_4Ti_3	tI14	I4/mmm	2a, $4e^3$	I_{117}	1
Order 8					
NaTl	cF16	$Fd\bar{3}m$	8a, 8b	$I_{222} = [D + D']$	34
$AlCu_2Mn$ (Heusler alloy), $BiLi_3$ (metallic)	cF16	$Fm\bar{3}m$	4a, 4b, 8c	$I_{222} = [F + F' + P'_{222}]$	204
HgNa	oC16	Cmcm	$4c^2$, 8g	$00\tfrac{1}{4}I1xy_{M(8)}$ $M(8) = \begin{pmatrix} 3 & \bar{1} & 0 \\ 1 & 3 & 0 \\ 0 & 0 & 1 \end{pmatrix}$	8
SiU_3	tI16	I4/mcm	4a, 4b, 8h	$00\tfrac{1}{4}I_{222}$	5
Li_2ZnSb	cF16	$F\bar{4}3m$	4a, 4b, 4c, 4d	$I_{222} = [F + F' + F'' + F''']$	34
$CuSi_2Zr$, AsCuSiZr	tC16	C4/amm	4a, 4b, $4c^2$	$I_{222} = [P_{222} + P'_{222}Iz]$	8
$GaPt_3$	tP16	P4/mbm	4e, 4f, 4g, 4h	$00\tfrac{1}{4}I_{222}Izx$	2
$Fe_{13}Ge_3$	cP16	$Pm\bar{3}m$	1a,b, 3c,d, 8g	$I_{222} = [P'_{222} + P_{222}]$ $= [P'_{222} + P + J + P' + J]$	—
BiF_3 (non-metallic)	cF16	$Fm\bar{3}m$	4b, 8c	$[I_{222} - F] + F = [P'_{222} + F'] + F$	—

Substance	Symbol	Space group	Wyckoff	Framework	Number of substances
C (diamond)	cF8	$Fd\bar{3}m$	8a	$[I_{222} - D'] = D$	9
NaCl (metallic)	cF8	$Fm\bar{3}m$	4a, 4b	$[I_{222} - P'_{222}] = [F + F']$	665
β-Hg_4Pt	cI10	$Im\bar{3}m$	2a, 8c	$[I_{222} - J^*] = [I + P'_{222}]$	4
Mg_2Sn	cF12	$Fm\bar{3}m$	4a, 8c	$[I_{222} - F'] = [F + P'_{222}]$	112
AsAgMg	cF12	$F\bar{4}3m$	4a, 4c, 4d	$[I_{222} - F'] = [F + F'' + F''']$	99
ThH_2	tF12	F4/mmm	4a, 8d	$[I_{222} - F']$ = metrically distorted cell	4
AsLiMn	tC12	C4/amm	4a,b,c	$[I_{222} - F''1z]$	2
$AsPd_5Tl$	tC14	C4/mmm	2a,c,d, 8i	$[I_{222} - 00\frac{1}{2}C]$	49
Order 9					
Te_4Ti_5	tI18	I4/m	2a, 8h, 8h	I_{331}	12
Order 27					
Tl_7Sb_2	cI54	$Im\bar{3}m$	2a, 12e, 16f, 24h	$I_{333} = [W^*(4t_c) + I(\bullet 8cu, 6o)]$	1
α-Mn	cI58	$I\bar{4}3m$	2a, 8c, $24g^2$	$W^*(4t_c) + I(\bullet 12tt, 4t^-)$	60
Cu_5Zn_8	cI52	$I\bar{4}3m$	$8c^2$, 12e, 24g	$W^*(4t_c) + I(4t^+, 4t^-, 6o)$ or $\approx [I_{333} - I] =$ $\approx I(io4t^+4t^-6o12co)$	17
γ-Al_4Cu_9	cP52	$P\bar{4}3m$	$4e^4$, 6f, 6g, $12i^2$	$\approx [I_{333} - I] = I(io4t^+4t^-6o12co)$	9
Ag_2Hg_3	cI52	I23	$8c^2$, 12d, 24f	$\approx [I_{333} - I] = [W^*(4t_c)] + I(io4t^+4t^-6o)$	1
Order 64					
In_3Li_{13}	cF128	$Fd\bar{3}m$	8a,b, 16c,d, 32e, 48f	$I_{444} = [D + D' + J^*_{222} + T + T' + F'''_{222}\underline{x}]$ $= [P_{444} + F''_{222}]$	1
$Pd_{4-x}Te$	cF120	$F\bar{4}3m$	4a,c, $16e^4$, 24f, 24g	$[I_{444} - D'] = [J_{222} + F + J'_{222} + F'' + T_{st} +$ $T' + T'' + T''']$	—
CoMnSb	cF120	$Fd\bar{3}m$	8a, 16c,d, 32e, 48f	$[I_{444} - D'] = [J_{222}x_{st} + F'''_{222}\underline{x} + T + T' + D]$	2
$Sc_{11}Ir_4$	cF120	$Fm\bar{3}m$	4a,b, 24d,e, $32f^2$	$[I_{444} - P'_{222}] = [F + F' + J_{222} + F(6o)$ $+ F'(8cu) + F(8cu)]$	4
$Mn_{23}Th_6$	cF116	$Fm\bar{3}m$	4b, 24d,e, $32f^2$	$[I_{444} - F, P'_{222}] = [F(8cu) + F'(8cu)$ $+ J'_{222}x + J_{222} + F']$	158
$Bi_4Cu_4Mn_3$	cF88	$Fm\bar{3}m$	8c, 24d, 24e, 32f	$[I_{444} - P_{222}, F'(8cu)] =$ $[P'_{222} + J_{222} + J'_{222} + F(8cu)]$	4
Ga_4Ni_3	cI112	$Ia\bar{3}d$	16a, 48f,g	$[I_{444} - Y^{**}] = [I_{222} + J^*_{222} + (P'_{444} - Y^{**})]$	3
Order 216					
$Li_{22}Pb_5$ $Li_{22}Si_5$	cF432	F23	4a–d, $16e^8$, $(24f,g)^2$, $48h^4$	$I_{666} = [W^*_{222}(4t_c) + I_{222}(\bullet io4t^+4t^-, 6o)]$	5
$Cu_{41}Sn_{11}$	cF416	$F\bar{4}3m$	$16e^8$, $24f^2$,g^2, $48h^4$	$\approx [I_{666} - I_{222}] = [W_2{}^*(4t_c)] + I_{222}(io4t^+4t^-6o)$ $= I_{222}[io4t^+4t^-6o12co]$	2
Mg_6Pd	cF396	$F\bar{4}3m$	4d, $16e^5$, $24f^2$,g, $48h^5$	$[I_{666} - ((I_{222} - F'''), F(4t^+), F'(4t^+), F'''(4t^+),$ $F'''(6o))] + F'''(12tt)$ or $[W^*_2(4t_c)] +$ $P_2(4t^-, 6o) + F''(4t^-, 4t^+, 6o) + F'''(\bullet 12tt, 4t^-)$	3
Na_6Tl	cF408	$F\bar{4}3m$	$16e^6$, $24f^2$,g, $48h^5$	$[I_{666} - (I_{222}, F(4t^+), F'''(4t^+), F'''(6o))] + F'''(12tt)$ or $[W^*_2(4t_c)] + D''(4t^-, 4t^+, 6o) + F(4t^-, 6o)$ $+ F'''(12tt, 4t^-)$	1
$Sm_{11}Cd_{45}$	cF448	$F\bar{4}3m$	4a,b,c,d, $16e^6$, 24f,g, $48h^6$	$[I_{666} - (F'(4t^+), F''(4t^+), F'(6o), F''(6o))]$ $+ F'(12tt), F''(12tt)$ or $W^*_2[4t_c] + D'''(\bullet 8c, 6o)$ $+ D''(\bullet 12tt, 4t^-)$	19

Table 7 Splittings of I Bravais lattices in different orders

Order	Space group	Splitting multiplicity	Framework symbol
1	$Im\bar{3}m$	2	I
	$Pm\bar{3}m$	1, 1	$I = P + P'$
8	$Ia\bar{3}d$ (r)	16	I_2
	$Fd\bar{3}c$ (a)	16	I_2
	$Im\bar{3}m$	2, 6, 8	$I_2 = [I + J^* + P_2']$
	$Fd\bar{3}m$	8, 8	$I_2 = [D + D']$
	$Fm\bar{3}m$	8, 4, 4	$I_2 = P_2' + F + F'$
	$F\bar{4}3m$	4, 4, 4, 4	$I_2 = [F + F' + F'' + F''']$
	$P\bar{4}3m$	1, 3, 1, 3, 4, 4	$I_2 = [P + J + P' + J' + F'' + F''']$
27	$Im\bar{3}m$	2, 12, 16, 24	$I_3 = [W^*(4t_c) + I + I(6o) + I(8cu)]$
64	$Fd\bar{3}m$	8, 8, 48, 16, 16, 32	$I_4 = [D + D' + J_2^* \underline{x} + T + T' + F_2''']$
	$Fm\bar{3}m$	4, 4, 24, 8, 24, 32, 32	$I_4 = [F + F' + J_2 + P_2' + J_2' \underline{x} + F_2'' + F_2''']$
216	$F\bar{4}3m$	4×4, 8×16, 4×24, 4×48	$I_6 = [W_2^*(4t_c) + I_2(\bullet 4t^+, 4t^-, 6o)]$

2.1.2 The 27th Order

The 27th order of the I complex is named I_{333} with the transformation matrix

$$\begin{pmatrix} 3 & 0 & 0 \\ 0 & 3 & 0 \\ 0 & 0 & 3 \end{pmatrix}$$

The number of points increases from 2 to 54: but this cannot be realized by a one-point configuration in a space group with only generators and translators. It must be a combination of lattice complexes with special parameters and interpenetration. But this configuration has already been recognized for Tl_7Sb_2 in *Strukturbericht* volume 1 (1931) by Ewald and Hermann as 'Substitutionsüberstruktur des A2-Typs'. Figure 5 shows the three main lattice complexes I(6o), I(8c), and W*(4t_c), plus two Tl atoms in I. The numbers indicate the heights in the projection direction a_3 in $n/6$. Besides the fact that only this one representative (Tl_7Sb_2) is known for I_{333} but with vacancies at the 2 pointer I (in 0 0 0 and $\frac{1}{2}\frac{1}{2}\frac{1}{2}$, the complex I(8c) splits into I(4t^+) and I(4t^-) with different distances to the origin and a z parameter for the W*(4t) complex. Subclasses of I_{333} include γ-brass, Cu_9Al_4, and Fe_3Zn_{10}. Representatives of the γ-brass structure (cI52) with the VEC = 21/13 ≈ 1.62 are the intermetallic compounds Cu_5Zn_8, Ag_5Zn_8, Au_5Zn_8, Cu_9Al_4, $Cu_{31}Sn_8$, $Cu_{31}Si_8$, Co_5Zn_{21}, Pt_5Zn_{21}, Rh_5Zn_{21}, and $Na_{31}Pb_8$. They can be regarded as a subclass of the I_{333} type. Another splitting is realized in the α-Mn structure (or χ phase) W*(4t) + I, I12tt, I4t, which has 58 atoms per cell. $Al_{12}Mg_{17}$ and $Re_{24}Ti_5$ are said to have the same α-Mn structure (cI58).

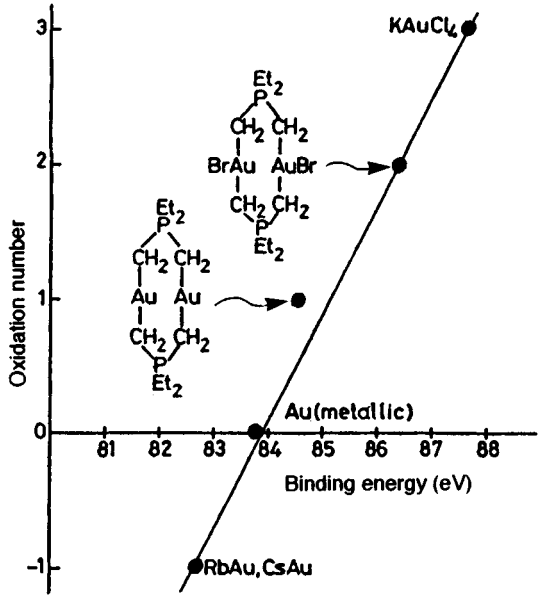

Figure 3 Binding energy of the Au($4f_{7/2}$) level in compounds with different oxidation states

2.1.3 The 64th Order

A structure type with more than 155 representatives, named $Mn_{23}Th_6$ cF116 $Fm\bar{3}m$, represents an I_{444} with vacancies of the CaF_2 type ($I_{444} - F, P_{222}'$).

The $Mg_6Cu_{16}Si_7$ type has been shown by Nagorson and Witte (1953) to be isotypic with $Mn_{23}Th_6$. But $Sc_{11}Ir_4$ cF120 $Fm\bar{3}m$ has an $I_{444} - P_2'$ type. (Structures in this group as well as those in Section 3.7 are also discussed in Chapter 17 by Nevitt and Koch in this volume).

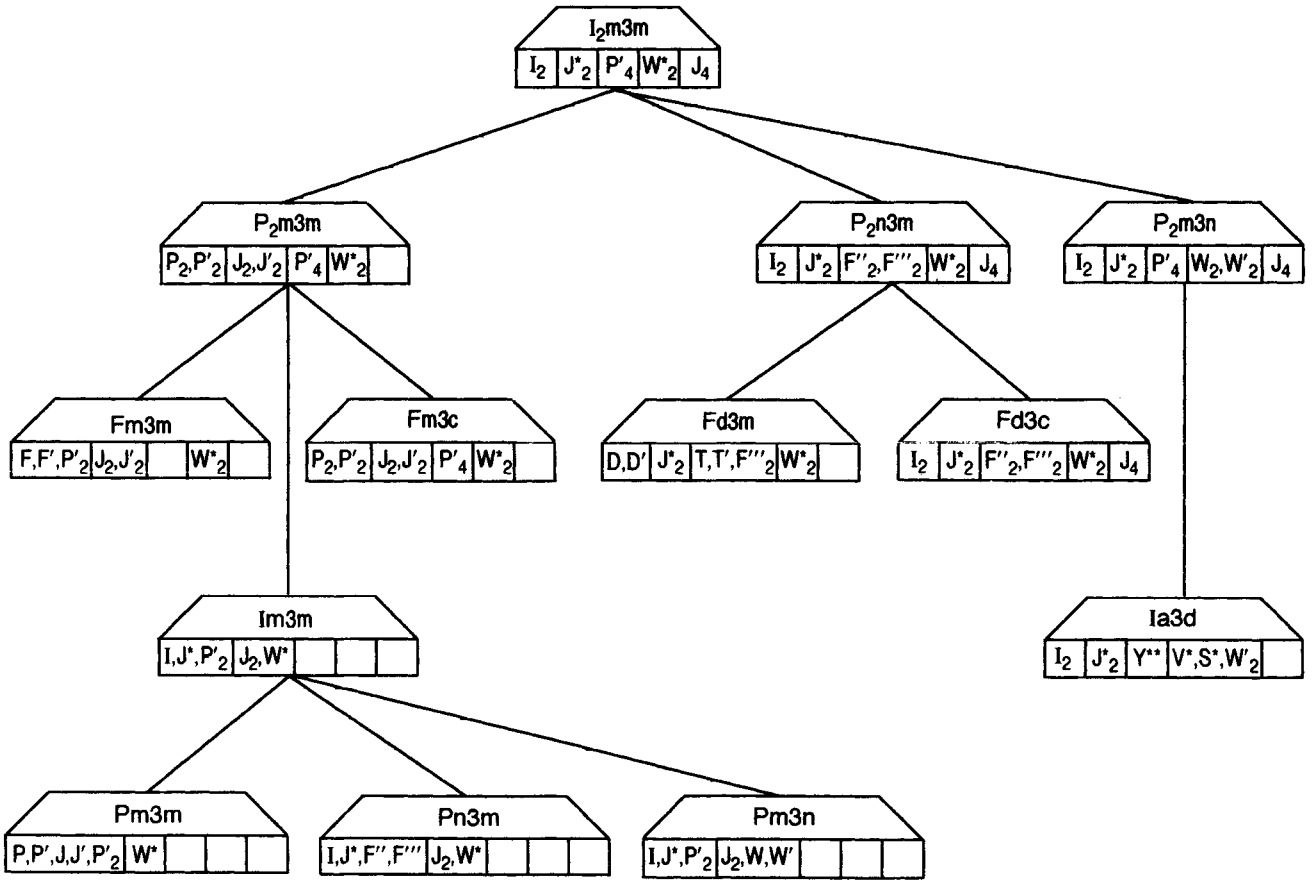

Figure 4 Splitting of point configurations belonging to invariant cubic lattice complexes or limiting forms in class-equivalent subgroups of Im3m

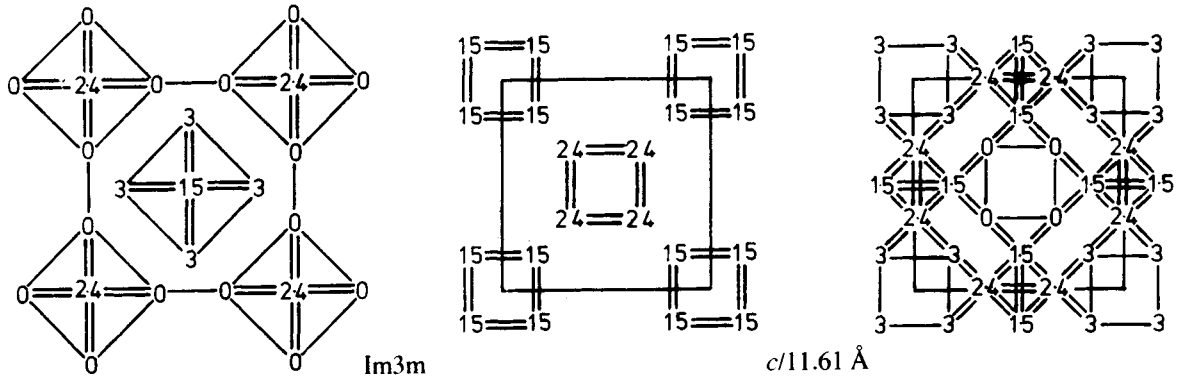

Ideal:	12e	x00	x=0.333 Å	16f	xxx	x=0.166 Å	24h	0xx	x=0.333 Å
Tl_7Sb_2:	12 Sb in		x=0.3138 Å	16 Tl in		x=0.1704 Å	24 Tl in		x=0.3497 Å
	and 2 Tl in I								

Figure 5 Lattice complexes I(6o), I(8c), and W*($4t_c$) (12e, 16f and 24h are atom positions in the Wyckoff notation)

2.1.4 The 216th Order

If one doubles the length of the axes in the cubic system for Tl_7Sb_2, Cu_5Zn_8, and the α-Mn type, one arrives at the $Li_{22}Si_5$, $Cu_{41}Sn_{11}$, and Na_6Tl types of 216th order, correlations that were found by our symbolism. Note that the VEC ≈ 1.635 for $Cu_{41}Sn_{11}$ is in the Hume-Rothery range, because the next higher VEC $= 7/4 = 1.75$ belongs to the hexagonal ϵ structure, i.e. $CuZn_3$ in the Cu–Zn binary system.

Table 8 is a slightly modified version of a table given by Fornasini *et al.* (1978). It is supplemented by the atomic parameters of Mg_6Pd (Samson, 1972) and Na_6Tl (Samson and Hansen, 1972). The three basic structures Tl_7Sb_2, α-Mn, and Cu_5Zn_8 contain only one type of nested polyhedra each. The two sets around 0 0 0 and $\frac{1}{2}\frac{1}{2}\frac{1}{2}$ within the corresponding unit cells are related by translations to each other. In the second column the corresponding cluster description is listed. All point configurations are either face-centered lattices or they form polyhedra around these lattices. The following symbols are used:

●	CC	cluster center
(12tt)	TT	truncated tetrahedron
($4t^+$)	IT	positive (inner) tetrahedron
($4t^-$)	OT	negative (outer) tetrahedron
(6o)	OH	octahedron
(12co)	CO	cubooctahedron

The structures of Tl_7Sb_2, α-Mn, and Cu_5Zn_8 are listed in the right part of Table 8, the corresponding descriptions with symbols of lattice complexes and coordination polyhedra are added in the last column. I(8c) symbolizes isolated cubes around an I configuration and W*($4t_c$) means corner-connected tetrahedra around a configuration of the cubic invariant lattice complex W*.

The different intermetallic phases included in Table 8 differ from each other by the occupation or non-occupation of some of the kinds of point configurations listed. Configurations W*($4t_c$) or, with respect to the crystal structures with enlarged unit cells, the corresponding configurations F(12co) + F′(12co) + F″(12co) + F‴(12co) = $W^*_{222}(4t_c)$, however, are occupied in every case. Therefore, a more careful discussion of these configurations seems appropriate.

In summary, within these eight crystal structures, the large voids around I or I_2 are filled in several different ways. With the aid of the symbols given above, the crystal structures are described in Table 6.

These symbols show very clearly the common feature of all these crystal structures, namely the three-dimensional connected frameworks W*($4t_c$) as illustrated in Figure 6. For a description of the geometrical and physical properties, this symbolism seems more adequate and useful than the cluster description (Hellner and Koch, 1981a,b).

In this context it may be mentioned that in Ir_3Ge_7 the W*($4t_c$) lattice complex collapses to a W* only, so that the description may more simply be I(8c), I(6o), W*; this description has been compared with the ideal Tl_7Sb_2 in I_{333} and Cu_5Zn_8 γ-brass by Hellner and Koch (1980).

3. Frameworks of the I Family with Polyhedra Allocated Around the i Points

The following frameworks do not correspond to a lattice complex. They are defined with the help of polyhedra located at the equipoints of the lattice complex, centered or not. Table 9 lists structures that can be described by such frameworks.

3.1 The I(4t) Framework

Such a framework may be described as a set of parallel-oriented tetrahedra, the centers of which form an I lattice. The tetrahedra do not share vertices but they are connected by additional shortest distances (cf. Figure 7). The parameter $x = 3/16$ is specialized with respect to sphere packings, but not with respect to Dirichlet domains.

3.2 The I(6o) Framework

An I(6o) framework as shown in Figure 8 consists of two configurations P(6o) and P′(6o) that are shifted relative to each other by $(\frac{1}{2}\frac{1}{2}\frac{1}{2})$. All distances between points of the P(6o) and P′(6o) configurations are longer than the shortest distances within the framework, i.e. the framework does not correspond to a sphere packing but to interpenetrating sphere packings of type 5/3/c3 (Fischer, 1973).

No crystal structure with a nearly ideal I(6o) framework has been found. In all cases the x parameter of the framework atoms is close to 1/4. In the structure of SF_6 cI14 $Im\bar{3}m$ the F–F distances within a fluorine octahedron are shorter than the distances between atoms from different polyhedra because of the S–F bondings.

3.3 The D(6o) Framework

A D(6o) framework consists of ideal octahedra, the centers of which form a D configuration, which is a

Table 8 The atomic parameters for five crystal structures of the 216th and three of the 27th orders. For $Li_{22}Si_5$ point position 48(h)*xyz*, the *x* and *y* coordinates are averaged to facilitate the comparison. For the basic structures the list of coordinates is extended to the array of eight unit cells corresponding to the enlarged unit cells of the further structures

Symbol of the point configuration	Cluster symbol			216th order					27th order			
				$Sm_{11}Cd_{45}$ $F\bar{4}3m$ $a_0=21.699$	Mg_6Pd $F\bar{4}3m$ $a=20.108$	Na_6Tl $F\bar{4}3m$ $a=24.154$	$Li_{22}Si_5$ $F23$ $a=18.75$	$Cu_{41}Sn_{11}$ $F\bar{4}3m$ $a=17.98$	α-Mn $I\bar{4}3m$ $a=8.911$	Tl_7Sb_2 $Im3m$ $a=11.618$	Cu_5Sn_8 $I\bar{4}3m$ $a=8.878$	
	Cluster A											
F	A CC	4(a) 000		Sm	—	—	Li	—	Mn	Tl	—	I
F(12tt)	A TT	48(h)*xxz*	*x*	—	—	—	—	—	Mn 0.0448×2	—	—	I(12tt)
			z						0.1410×2			
$F(4t^+)$	A IT	16(e)*xxx*	*x*	Cd 0.0834	—	—	Li 0.080	Cu 0.0573		Tl 0.0852×2	Zn 0.0545×2	$I(4t^+)$ I(8c)
$F(4t^-)$	A OT	16(e)*xxx*	*x*	Cd 0.9126	Pd 0.90038	Tl 0.90136	Si 0.911	Sn 0.9113	Mn 0.9089×2	Tl 0.9148×2	Cu 0.9140×2	$I(4t^-)$
F(6o)	A OH	24(f)*x*00	*x*	Cd 0.1573	Mg 0.10720	Na 0.10858	Li 0.167	Cu 0.1763		Sb 0.1569×2	Cu 0.1779×2	I(6o)J*(2l)
F(12co)	A CO	48(h)*xxz*	*x*	Sm 0.1735	Mg 0.14355	Na 0.14228	Li 0.164	Cu 0.1562	Mn 0.1785×2	Tl 0.1749×2	Zn 0.1564×2	$W^*(4t_c)$
			z	0.0142	0.03398	0.03346	0.005	0.0186	0.0173×2	0.0000	0.0183×2	
	Cluster B											
F″	B CC	4(c) $\frac{1}{4}\frac{1}{4}\frac{1}{4}$		Sm	—	—	Li	—	Mn	Tl	—	
F″(12tt)	B TT	48(h)*xxz*	*x*	Cd 0.2958	—	—	—	—	Mn 0.2948×2	—	—	
			z	0.3904					0.3910×2			
$F''(4t^+)$	B IT	16(e)*xxx*	*x*	—	Mg 0.30250	Na 0.30267	Li 0.330	Cu 0.3005		Tl 0.3352×2	Zn 0.3045×2	
$F''(4t^-)$	B OT	16(e)*xxx*	*x*	Cd 0.1636	Pd 0.16790	Tl 0.16755	Li 0.167	Cu 0.1657	Mn 0.1589×2	Ti 0.1648×2	Cu 0.1640×2	
F″(6o)	A OH	24(g)$x\frac{1}{4}\frac{1}{4}$	*x*	—	Mg 0.43518	Na 0.43185	Si 0.428	Cu 0.4241		Sb 0.4069×2	Cu 0.4279×2	
F″(12co)	A CO	48(h)*xxz*	*x*	Cd 0.4377	Mg 0.40605	Na 0.41016	Li 0.413	Sn 0.4084	Mn 0.4285×2	Ti 0.4249×2	Zn 0.4064×2	
			z	0.2627	0.27391	0.26791	0.250	0.2680	0.2673×2	0.0000	0.2683×2	
	Cluster C											
F′	C CC	4(b) $\frac{1}{2}\frac{1}{2}\frac{1}{2}$		Cd	—	—	Li	—	Mn	Tl	—	
F′(12tt)	C TT	48(h)*xxx*	*x*	Cd 0.5455	—	—	—	—	Mn 0.5448×2	—	—	
			z	0.6403					0.6410×2			
$F'(4t^+)$	C IT	16(e)*xxx*	*x*	—	—	Na 0.55549	Li 0.583	Cu 0.5504	—	Tl 0.5852×2	Zn 0.5545×2	
$F'(4t^-)$	C OT	16(e)*xxx*	*x*	Sm 0.4059	Pd 0.40653	Na 0.41542	Li 0.420	Cu 0.4166	Mn 0.4089×2	Tl 0.4148×2	Cu 0.4140×2	
F′(6o)	C OH	24(f)$x\frac{1}{2}\frac{1}{2}$	*x*	—	Mg 0.61866	Tl 0.66484	Si 0.678	Cu 0.6765	—	Sb 0.6569×2	Cu 0.6779×2	
F′(12co)	C CO	48(h)*xxz*	*x*	C 0.6728	Mg 0.65097	Na 0.65395	Li 0.662	Cu 0.6465	Mn 0.6785×2	Tl 0.6749×2	Zn 0.6564×2	
			z	0.5123	0.52812	0.52856	0.497	0.5278	0.5173×2	0.0000	0.5183×2	
	Cluster D											
F‴	D CC	4(d) $\frac{3}{4}\frac{3}{4}\frac{3}{4}$		Cd	Mg	—	Li	—	Mn	Tl	—	
F‴(12tt)	D TT	48(h)*xxz*	*x*	—	Mg 0.79984	Na 0.80191	—	—	Mn 0.7948×2	—	—	
			z		0.90720	0.90985			0.8910×2			
$F'''(4t^+)$	D IT	16(e)*xxz*	*x*	Cd 0.8297	—	—	Li 0.833	Cu 0.8062	—	Tl 0.8352×2	Zn 0.8045×2	
$F'''(4t^-)$	D OT	16(e)*xxx*	*x*	Sm 0.6618	Mg 0.66868	Na 0.67234	Si 0.665	Cu 0.6664	Mn 0.6589×2	Tl 0.6648×2	Cu 0.6640×2	
F‴(6o)	D OH	24(g)$x\frac{3}{4}\frac{3}{4}$	*x*	Cd 0.9105	—	—	Li 0.917	Sn 0.9309	—	Sb 0.9069×2	Cu 0.9279×2	
F‴(12co)	D CO	48(h)*xxx*	*x*	Cd 0.9161	Mg 0.94345	Na 0.94396	Li 0.917	Cu 0.9087	Mn 0.9285×2	Tl 0.9249×2	Zn 0.9064×2	
			z	0.7637	0.76760	0.76942	0.750	0.7631	0.7673×2	0.0000	0.7683×2	

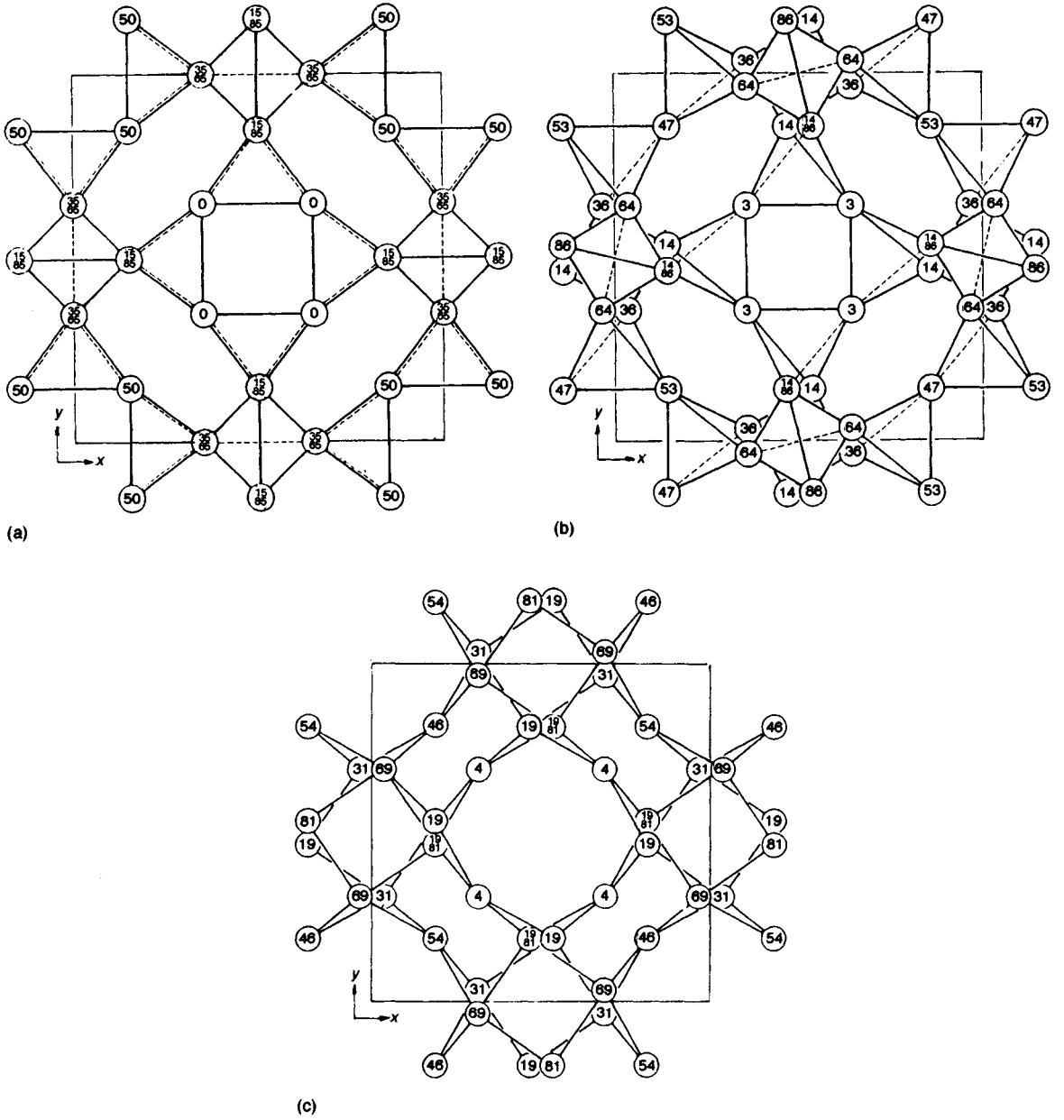

Figure 6 Frameworks of crystal structures of the 27th order. (a) Framework W*[4t_c] as part of the crystal structure of Tl_7Sb_2: symmetry Im3m 24(h) *xx*0, $x = 0.3497$, z coordinates in $n/100$. (b) Framework W*[4t_c] as part of the crystal structure of α-Mn: symmetry $I\bar{4}3m$ 24(g) *xxz*, $x = 0.3571$, $z = 0.0346$, z coordinates in $n/100$. (c) Framework W*[4t_c] as part of the crystal structure of Cu_5Zn_8: symmetry $I\bar{4}3m$ 24(g) *xxz*, $x = 0.3128$, $z = 0.0366$, z coordinates in $n/100$

subgroup of I_2. The axes of these octahedra are oriented parallel to the unit-cell edges and their vertices are connected by additonal shortest distances (cf. Figure 9). The corresponding sphere packing type is 8/3/c3 (Fischer, 1973).

In a D(6o) framework the ideal small octahedra around T are corner-connected. Each D octahedron shares faces with four T octahedra and four distorted D′(4t) octahedra; each T octahedron shares faces with two D octahedra and six D′(4t) octahedra. The edges of

Table 9 Frameworks of the I family with polyhedra allocated around the i points and observed structure types thereto. Numbers of known isotypic substances are those given in the compilation of Villars and Calvert (1985)

Substance	Symbol	Space group	Wyckoff	Framework	Number of substances
BFe	oP8	Pnma	$4c^2$	$\bar{1}.2_1 0\frac{1}{2}\frac{1}{2}$I (2l $\overset{1}{\underset{[010]}{\infty}}$) (●6r3l$_{var.con.}$)	106
$MoNi_4$	tI10	I4/m	2a, 8h	$[\frac{1}{2}\frac{1}{2}0I(4l)+I]$	16
$GeMg_2S_4$ (olivine)	oP28	Pnma	4a, $4c^4$, 8d	$\bar{1}.2_1$ $(00\frac{1}{2}$I2xy1z(●4t)+B_{121}, $\frac{1}{4}\frac{1}{4}\frac{1}{2}$F1xz)	14
PTi_3	tP32	$P4_2/n$	$8g^4$	$[I(4t)+00\frac{1}{2}I(4t)+\frac{3}{4}\frac{3}{4}\frac{1}{4}P_{221}(2l)+0\frac{1}{2}\frac{3}{4}C_{112}z(4t_{2e})]$	26
GeK	cP64	$P\bar{4}3n$	$8e^2$, $24i^2$	$[I(4t^+)+I(4t^-)+..n$ I(12tt)+W′$(4t^+)]$	6
SF_6	cI14	Im3m	2a, 12e	I(●6o)=I(6o)+I	—
$Re_7Si_6U_4$	cI34	$Im\bar{3}m$	a, c, d, e	$[P'_{222}+W^*+I(6o)]+I$	3
TiO_2 (rutile)	tP6	$P4_2/mnm$	2a, 4f	I(●6o$_c$)	18
$ErGa_4V_2$	tI14	I4/mmm	2a, 4d, 8h	$00\frac{1}{2}I(6o_{2c})+0\frac{1}{2}\frac{1}{4}C_{112}$	17
$MoNi_4$	tI10	I4/m	2a, 8h	$\frac{1}{2}\frac{1}{2}0I(6o_{2c})$	16
FeS_2 (marcasite)	oP6	Pnnm	2a, 4g	.n. I(●6o$_{var.con.}$)	44
$FeSb_2$	oP6	Pnn2	2a, 4c	n.. I(●6o)	4
CFe_2	oP6	Pnnm	2a, 4g	I(●6o$_{var.con.}$)	5
$RbNiCrF_6$	cF72	$Fd\bar{3}m$	b, c, f	D(6o)+D′,T	—
$NiTi_2$	cF96	$Fd\bar{3}m$	d, e, f	$[D(6o)+D'(4t^-)+T']$	60
Fe_6W_6C	cF104	$Fd\bar{3}m$	a, d, e, f	$[D(6o)+D'(4t^-)+T']+D$	3
Fe_3W_3C	cFI12	$Fd\bar{3}m$	c, d, e, f	$[D(6o)+D'(4t^-)+T']+T$	54
α-$RhBi_4$	cI120	$Ia\bar{3}d$	c, h	$..dI_{222}(6o)+V^*$	1
B_2CoW_2	oI10	Immm	2a, 4f, 4h	$0\frac{1}{2}\frac{1}{2}$I2y(●6r$_{4l,1e,4e}$)+I	15
B_4Ta_3	oI14	Immm	2c, $4g^2$, 4h	$\frac{1}{2}$00I2y(●6r$_{2\times 3l,4l,2e}$2l$_{2c}$ $\overset{2}{\underset{(010)}{\infty}}$)	17
BFe	oP8	Pnma	$4c^2$	$\bar{1}.2_1$ $0\frac{1}{2}\frac{1}{2}$I(2l $\overset{1}{\underset{[010]}{\infty}}$)(●6r3l$_{var.con.}$)	106
B_2IrMo_2	oP20	Pnnm	$4g^5$	n.. $0\frac{1}{2}$0I(2l(ll)(●6r3c$_{var.con.}$)	9
$Al_{11}La_3$	oI28	Immm	2a, 2c, 4g, 4j, $8l^2$	$(0\frac{1}{2}\frac{1}{2}I(6l_{2e})+0\frac{1}{4}\frac{1}{2}B_{121}1y(5l_{1e,1c})$ $\overset{1}{\underset{[010]}{\infty}}$)+$I_{13}$	15
B_2CoW_2	oI10	Immm	2a, 4f, 4h	I(●8l$_{4c}$)	15
Ir_3Sn_7	cI40	$Im\bar{3}m$	12d, 12e, 16f	$[I(8cu)+W^*+J^*(2l)]$	23
$46H_2O\cdot 8Cl$	cP54	$Pm\bar{3}n$	2a, 6c,d, 16i, 24k	$[I(8cu)+J^*(4l)+W]+I,W'$	
N_2	cP64	$Pm\bar{3}n$	16i, 48l	$[I(8cu)_{st}+W'(8a)_{st}]$	—
$Nd_5Mo_3O_{16}$	cP96	$Pn\bar{3}n$	8c, 12d,e, 16f, 48i	$[I(8cu)+J^*(8a)]+P'_{222}$,W*,I(6o)	—
Tl_7Sb_2	cI54	$Im\bar{3}m$	2a, 12e, 16f, 24h	$[I(8cu)+W^*(4t_c)+I(6o)+I]$	1
HfSiTe (Cu_2Sb type)	tP6	P4/nmm	2a, $2c^2$	$[0\frac{1}{2}\frac{1}{4}I(8a1z1z'_{var.con.})]$	193
W	cI2	$Im\bar{3}m$	2a	I(●12d$_{var.con.}$)	241
Te_4Ti_5	tI18	I4/m	2a, $8h^2$	I(●12co$_{2\times 4l}$)	12
$Cu_4Nb_5Si_4$ (filled-up Te_4Ti_5)	tI26	I4/m	2a, $8h^3$	I(●12co$_{2\times 4l}$)+etc.	3
Na_6Tl	cF408	$F\bar{4}3m$	$48h^4$	$[I_2(12co)]$+etc.=$W_2^*(4t_c)$+etc.	1

(*continued*)

Table 9 (*continued*)

Substance	Symbol	Space group	Wyckoff	Framework	Number of substances
Mg_6Pd	cF396	$F\bar{4}3m$	$48h^4$	$[I_2(12co)] + etc. = W_2{}^*(4t_c) + etc.$	2
$Sn_{11}Cu_{41}$ 8th order γ-brass	cF416	$F\bar{4}3m$	$48h^4$	$[I_2(12co)] + etc. = W_2{}^*(4t_c) + etc. = I_2(io(4t^+)(4t^-)(6o)(12co))$	2
$Sm_{11}Cd_{45}$	cF448	$F\bar{4}3m$	$48h^4$	$[I_2(12co)] + etc. = W_2{}^*(4t_c) + etc.$	19
$Na_6Al_{5.3}\cdot Si_{10.4}O_{32}$	cI60	$Im\bar{3}m$	8c, 12d, 16f, 24h	$[I(12co) + P'_{222}] + I(8cu)_{st}, W^*_{st}$	—
Pt_8Cd_{41}	cI392	$I\bar{4}3m$	$8c^4$, $12e^2$, 24f, $24g^9$, $48h^2$	$[[I(12co) + J^*(12co) + P'_{222}(12co)] + etc.]$	1
$H_3PW_{12}O_{40}\cdot 6H_2O$	cP160	$Pn\bar{3}m$	2a, 6d, 8e, 24h, k^4, 48l	$[I(\bullet 4t),(12co)(\bullet 6o)_{5c}] + J^*(4l,8r)_{st}, J^*$	—
$Al_{12}W$	cI26	$Im\bar{3}$	2a, 24g	$[I(12i) + I]$	6
$CoAs_3$	cI32	$Im\bar{3}$	8c, 24g	$[I(12i) + P'_{222}]$	19
Fe_4LaP_{12}	cI34	$Im\bar{3}$	2a, 8c, 24g	$[I(12i) + P'_{222}] + I$	40
H_3U	cP32	$Pm\bar{3}n$	2a, 6c, 24k	$..n\ I(12i) + I, W$	5
$Pr_3Rh_4Sn_{13}$	cP40	$Pm\bar{3}n$	2a, 6d, 8e, 24k	$[..n\ I(12i) + P'_{222}] + I, W'$	59
$NaZn_{13}$	cF112	$Fm\bar{3}c$	8a, 8b, 96i	$..c\ P_{222}(12i) + P_{222}, P'_{222}$	47
$Al_{11}La_3$	oI28	Immm	2a, 2c, 4g, 4j, $8l^2$	$I(\bullet 12r_{2\times 6l\ a}4l) + 00\frac{1}{2}I + 0\frac{1}{4}0B_{12l}1y$	15
Fe_4Si_2Zr	tP14	$P4_2/mnm$	2b, 4g, 8i	$n..\ 00\frac{1}{2}I(\bullet 12r_{2\times 6l,12c}6l)$	6
$Cu_4Si_4Zr_3$	oI22	Immm	2d, 4e, 4f, 4h, 8n	$0\frac{1}{2}0I(\bullet 12r_{2\times 6l\ a}6l_{2e}\overset{2}{\underset{(100)}{\infty}})$	26
Ni_5Si_3Y	oP36	Pnma	$4c^9$	$\bar{1}.2_1\frac{1}{7}\frac{1}{4}\frac{3}{4}I_{211}1xz(\bullet 12r6l)_{var.con.}$	7
α-Mn	cI58	$I\bar{4}3m$	2a, 8c, $24g^2$	$[I(\bullet 12tt, 4t^-) + W^*(4t_c)]$	60
$Ge_{38}P_8Br_8$	cP54	$P\bar{4}3n$	2a, 6c,d, $8e^2$, 24i	$[..n\ I(12tt) + I(4t^+) + I(4t^-) + W'] + I,W$	—
GeK	cP64	$P\bar{4}3n$	$8e^2$, $24i^2$	$[..n\ I(12tt) + I(4t^+) + I(4t^-) + W'(4t^+)]$	6
α-$SeCl_4$	cP160	$P\bar{4}3n$	$8e^2$, $24i^6$	$[I(12tt) + I(4t^-) + W(12tt) + W(4t^+)] + I(4t^+), W(4t^-)$	—
$ThMn_{12}$	tI26	I4/mmm	2a, 8f, 8i, 8j	$I(\bullet 16thr4l)$	132
$Mg_{32}(Al,Zn)_{49}$	cI162	$Im\bar{3}$	2a, $12e^2$, 16f, $24g^3$, 48h	$I(\bullet 20pd(\bullet 12tt)_{var.con.})$	10
$Ge_{38}P_8Br_8$	cP54	$P\bar{4}3n$	2a, 6c,d, $8e^2$, 24i	$..n\ I(\bullet 20pd) + W, W'$	—
$46H_2O\cdot 8Cl$	cP54	$Pm\bar{3}n$	2a, 6c,d, 16i, 24k	$[..n\ I(20pd) + W] + I,W$	—
$Pr_3Rh_4Sn_{13}$	cP40	$Pm\bar{3}n$	2a, 6d, 8e, 24k	$I(20pd_{8c}) + I, W'$	47
B_4CeCo_4	tP18	$P4_2/nmc$	2b, 8g, 8g	$I(\bullet 24scd)$	31
B_4Co_4Nd	tP18	$P4_2/n$	2b, 8g, 8g	$00\frac{1}{2}I(\bullet 24gon_{2\times 8l,8\times 4l})$	26
$BaCuO_2$	cI402	$Im\bar{3}m$	2a, 12d,e^3, 16f, $24h^2$, 48i, 48j, k^3	$[I(24cod) + [P'_{444} - I(8cu)] + W^* + J^*(8r)_{st} + J^*(2l) + P'_{222}(6o)] + etc.$	—
$Na_{30}Al_{30}Si_{66}O_{192}\cdot 98H_2O$ (zeolite ZK-5)	cI304	$Im\bar{3}m$	16f, 48i,j,k^2, 96l	$I(48cod(\bullet 4t_c)) + I(8cu)$	—

the D′ octahedra are 66% larger than the shortest distances within the framework. Each D′ octahedron is surrounded by four T′ antiprisms and four D′(4t) octahedra. A T′ antiprism has two common faces with D′ octahedra and six common faces with D′(4t) octahedra. As a consequence, each D′(4t) octahedron shares faces with one D octahedron, one D′ octahedron, three T octahedra, and three T′ antiprisms.

The 'centers' of the distorted D′(4t) octahedra lie in the interior of the large D′ octahedra. The shortest distances between these centers are much smaller than the sum of the radii for two D′(4t) voids calculated with the aid of the distances to the framework atoms. Therefore, it is not possible to locate atoms at the 'centers' of the D′(4t) voids, because such atoms would build up isolated tetrahedra without contact with any

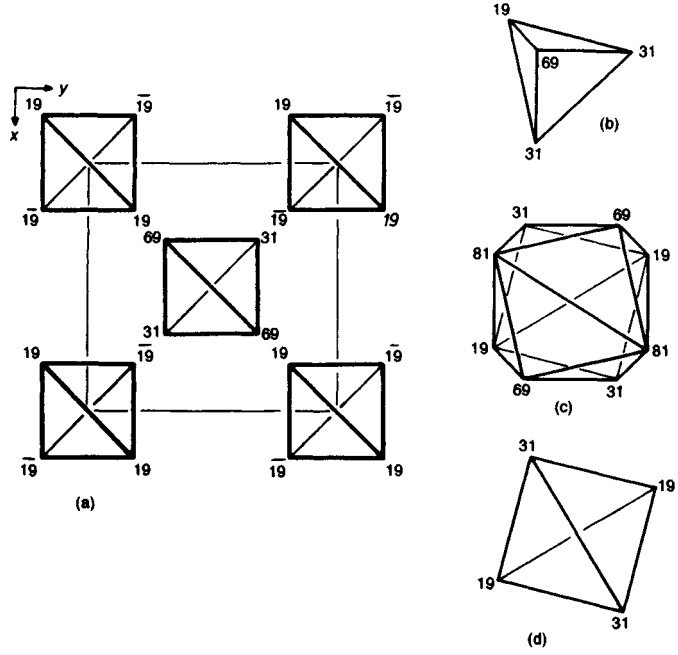

Figure 7 I(4t) framework: (a) point configuration with lines indicating the tetrahedra around I; (b) I(4t) tetrahedron around $\frac{3}{8}\frac{3}{8}\frac{3}{8}$; (c) J* dodecahedron (8d) with 8 vertices and 12 faces around $0\frac{1}{2}\frac{1}{2}$; (d) W* tetrahedron around $0\frac{1}{2}\frac{1}{4}$. z coordinates given in $a/100$

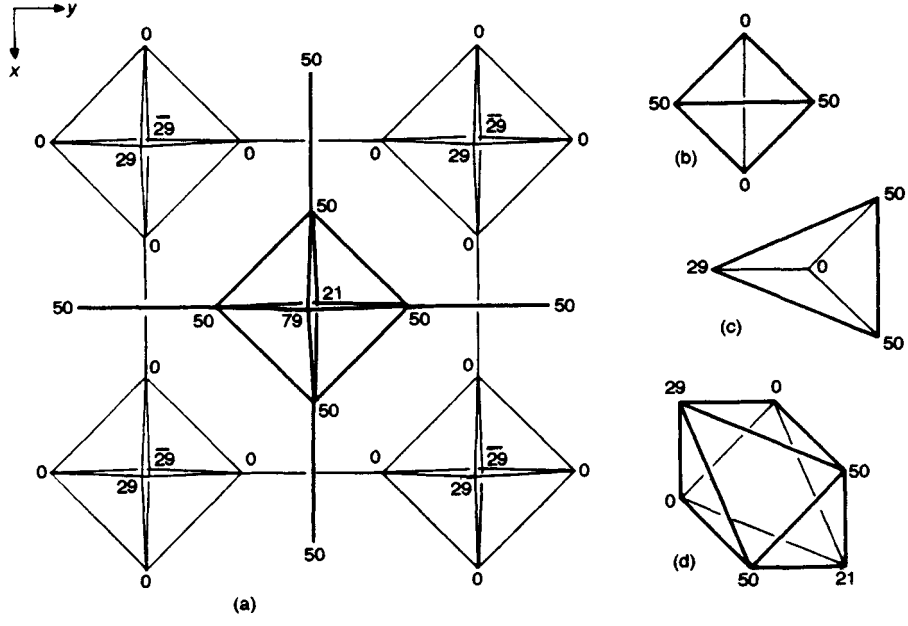

Figure 8 I(6o) framework: (a) point configuration with lines corresponding to sphere contacts, octahedra around I; (b) W* tetrahedron around $\frac{1}{2}0\frac{1}{4}$; (c) W*($4t_c$) tetrahedron around 00.3232 0.3232; (d) trigonal antiprism around $P\bar{3}_2'$, $\frac{1}{4}\frac{1}{4}\frac{1}{4}$. z coordinates given in $a/100$

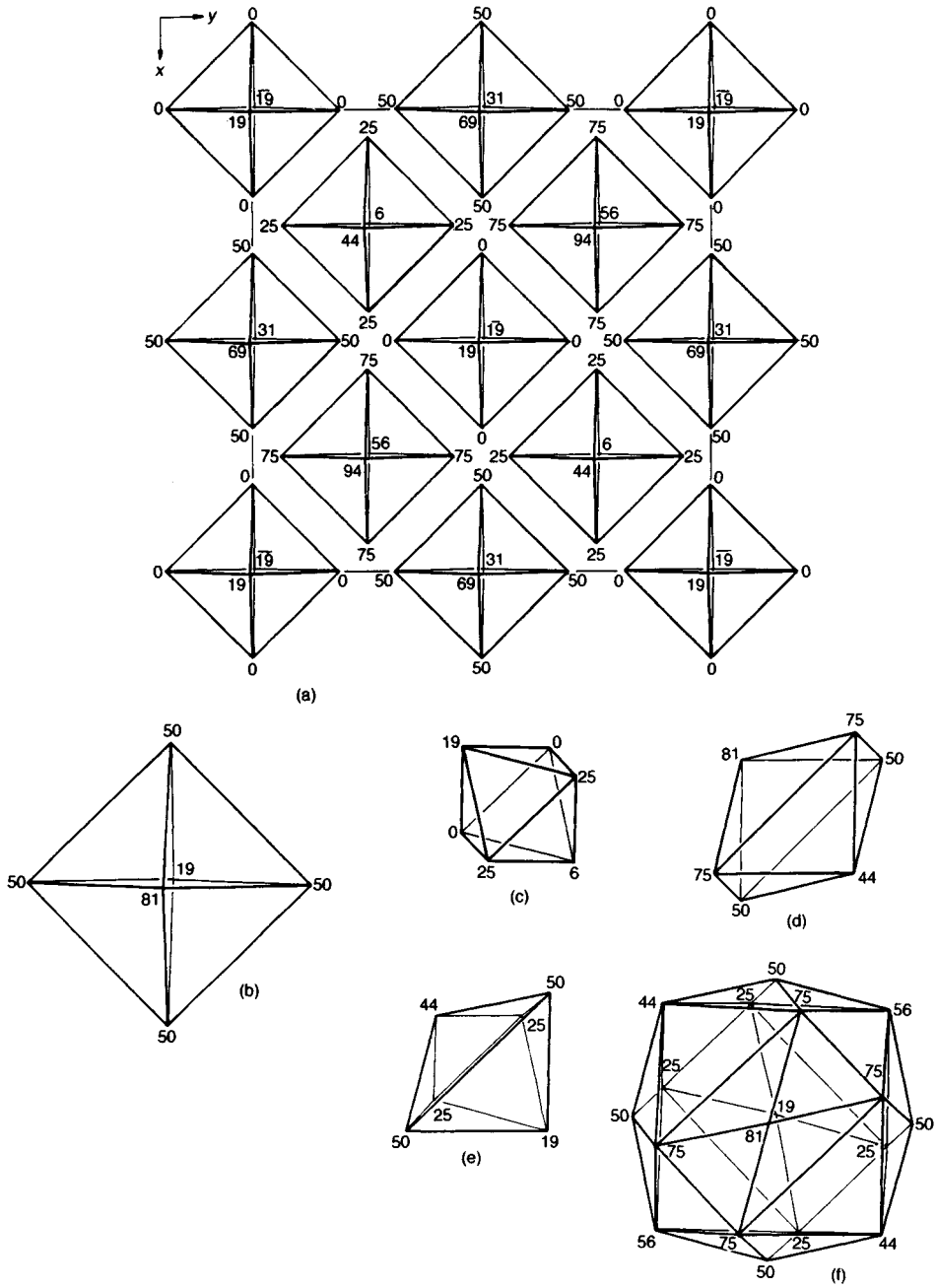

Figure 9 D(6o) framework: (a) point configuration with lines indicating the octahedra around D; (b) D′ octahedron around $\frac{1}{2}\frac{1}{2}\frac{1}{2}$; (c) T octahedron around $\frac{1}{8}\frac{1}{8}\frac{1}{8}$; (d) trigonal antiprism around T′, $\frac{5}{8}\frac{5}{8}\frac{5}{8}$; (e) D′(4t) octahedron 'around' 0.4375 0.4375 0.4375; (f) hexacapped cubooctahedron (18cohc) around D′, $\frac{1}{2}\frac{1}{2}\frac{1}{2}$, combined from a D′ octahedron, four T′ antiprisms, and four D′(4t) octahedra. z coordinates given in $a/100$

other atom of the crystal structure. For the description of some crystal structures it may be more adequate, therefore, to construct large coordination polyhedra around D′ made up from the first and from the second coordination shells. The difference of the distances is 15%. The resulting polyhedra with 18 vertices may be described as hexacapped cubooctahedra (18cohc). Each of them is a combination of the original D′ octahedron, four D′(4t) octahedra, and four T′ antiprisms. These large polyhedra overlap the T′ antiprisms.

Several crystal structures of different type show the D(6o) framework shown in Figure 9.

The crystal structures of Fe_3W_3C and Fe_6W_6C are very similar. They may be described by a basic framework D(6o) of tungsten atoms, the T′ and D′(4t) voids of which are occupied by iron atoms. The carbon atoms are located in the T and the D octahedra, respectively. The iron atoms by themselves, however, build up a second heterogeneous basic framework with smaller sphere radii. Taking this into account, the structures may be described as [D(6o)+(T′+D′(4t))]+T and [D(6o)+(T′+D′(4t))]+D, respectively.

In $NiTi_2$ three quarters of the Ti atoms form a basic framework D(6o). The other Ti atoms occupy the T′ voids, which allow radii almost equal to the radii of the framework atoms. The smaller Ni atoms form a D′(4t) arrangement (see also Chapter 17 by Nevitt and Koch in this volume).

3.4 The ..dI$_2$(6o) Framework

The ..dI$_2$(6o) framework of Figure 10 is related to the I(6o) framework in a similar way as the a..P$_2$(6o) framework to the P(6o) framework: an undistorted I(6o) framework with 96 points per unit cell and doubled translation periods can be built up in the general position of $Ia\bar{3}d$. Without losing shortest distances, the octahedra may be tilted in such a way that additional shortest distances are produced. Octahedra of different orientations can be mapped onto each other by glide reflections according to diagonal d glide planes. This is indicated by the orientation-symmetry part ..d of the framework symbol. The sphere packing type corresponding to such a framework is 6/3/c38. The respective Dirichlet domains are not especially simple, but they show some small faces that may be regarded as single points or lines for the derivation of the voids. From this view, six kinds of voids remain within a ..dI$_2$(6o) framework: ideal octahedra around I_2; slightly elongated tetrahedra around S*; trigonal prisms around Y** and tetragonal antiprisms around V*, both slightly deformed; highly distorted octahedra with twofold symmetry; and highly distorted tetrahedra in a general position.

With the high number of symmetrically different short distances within a ..dI$_2$(6o) framework, small changes of the coordinates permit adaptation to relatively different radii of atoms located in the voids. This explains the large variety of crystal structures with the garnet type, which contain ..dI$_2$(6o) frameworks. In addition some further structure types with such a framework exist. These other structure types differ with respect to the connections of the occupied voids (Hellner *et al.*, 1979).

The bismuth atoms of α-$RbBi_4$ may be regarded as a basic framework with the tetragonal antiprismatic voids occupied by rhodium atoms. In this structure the corners of the antiprisms have nearly equal distances from the centers.

3.5 The I(12i) Framework

An ideal I(12i) framework, as illustrated in Figure 11, consists of parallel-oriented icosahedra with centers forming an I lattice. The vertices of these icosahedra are connected by additional shortest distances. The corresponding sphere packing type is 9/3/c3. Each point of such an ideal framework has nine nearest neighbors and one additional neighbor with a slightly larger distance (6%). The coordination number of an I(12i) framework should therefore be regarded as 10. With very similar coordinates, sphere packings of another type (6/3/c10) may be obtained. Compared with 9/3/c3, four contacts per sphere are lost, but the additional tenth short distance of 9/3/c3 gives rise to the sixth sphere packing contact on 6/3/c10.

The aluminum atoms of WAl_{12} form a slightly distorted I(12i) basic framework with the icosahedral voids centered by the tungsten atoms.

In skutterudite, $CoAs_3$, the arsenic atoms form a highly distorted I(12i) configuration ($y=0.3431$, $z=0.1503$) with the octahedral voids occupied by cobalt atoms. The cobalt and arsenic atoms together form distorted pentagonal dodecahedra (20pd) around I. These dodecahedra share those eight vertices which refer to the cobalt atoms.

3.6 The ..nI(12i) Framework

A ..nI(12i) framework consists of ideal icosahedra with centers at I. The icosahedra around the points 0 0 0 and $\frac{1}{2}\,\frac{1}{2}\,\frac{1}{2}$ have opposite orientations but their axes are parallel to each other. These icosahedra can be mapped onto each other by a glide reflection along a diagonal

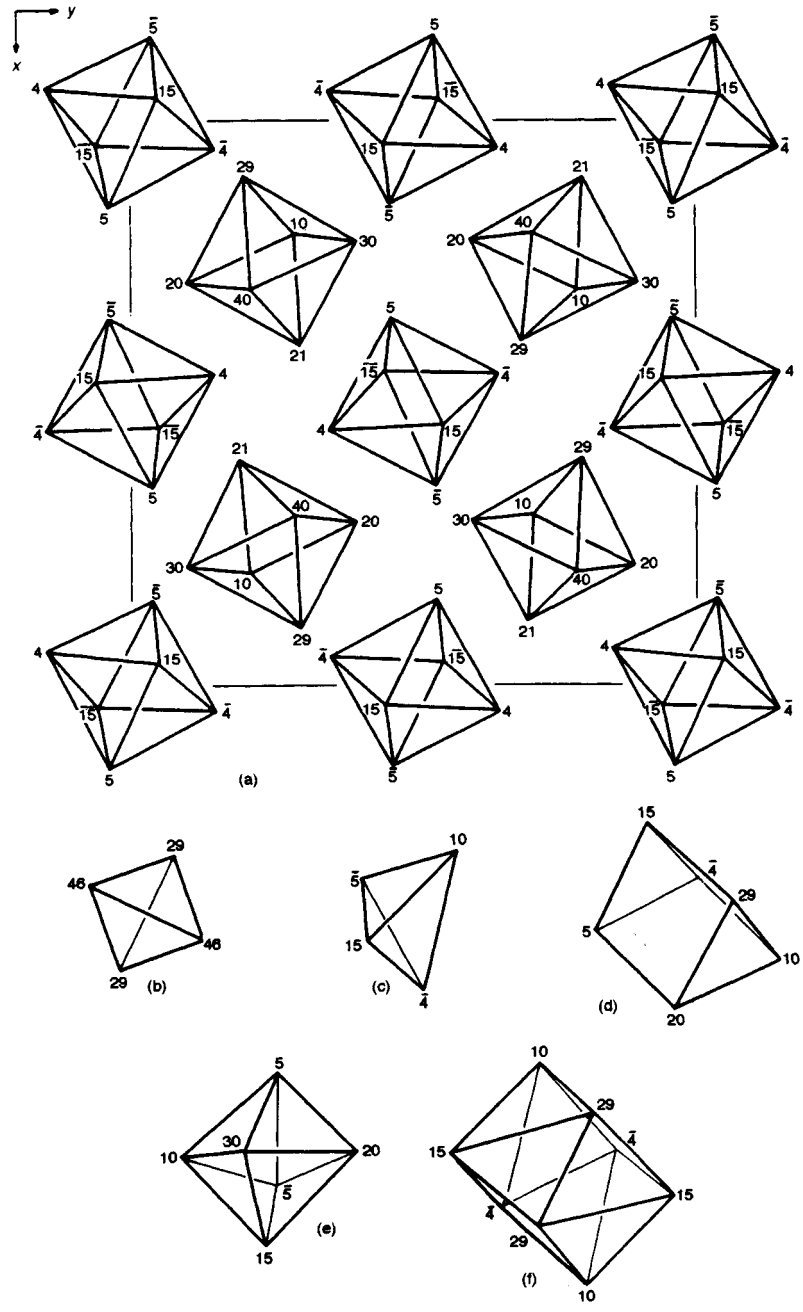

Figure 10 The ..dI$_2$(6o) framework: (a) point configuration with lines indicating the octahedra around I$_2$, only polyhedra in the lower half of the unit cell are shown; (b) S* tetrahedron around 0 $\frac{1}{4}$ $\frac{3}{8}$; (c) [P$_4'$-Y**]xx(2l) tetrahedron around 0.9197 0.1431 0.0339; (d) trigonal prism around Y**, $\frac{1}{8}$ $\frac{1}{8}$ $\frac{1}{8}$; (e) W$_2'$xx octahedron around 0.2971 0.9529 0.1250; (f) tetragonal antiprism around V*, 0 $\frac{1}{4}$ $\frac{1}{8}$. z coordinates given in $a/100$

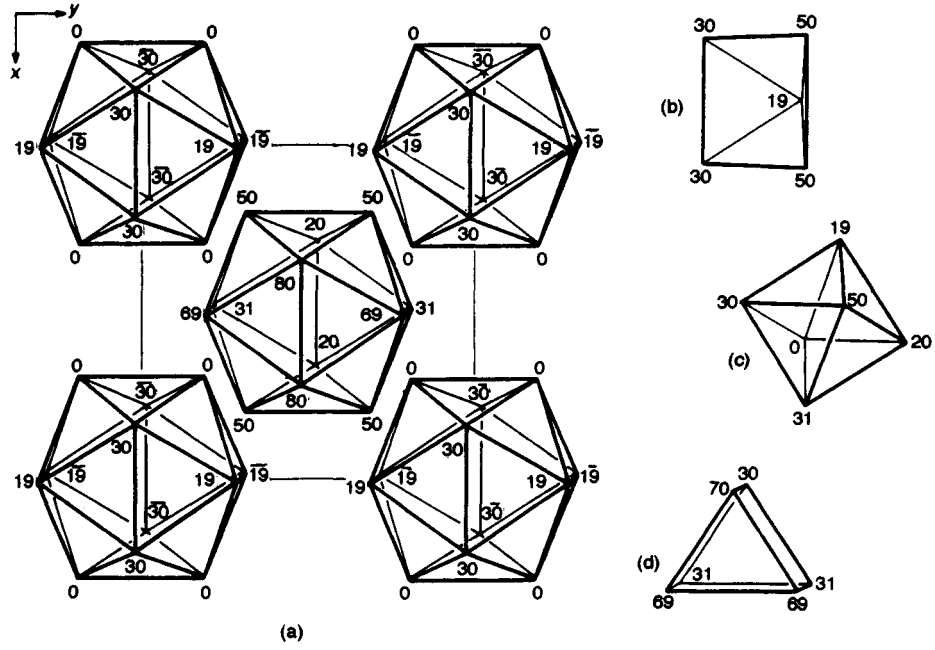

Figure 11 I(12i) framework: (a) point configuration with lines indicating the icosahedra around I; (b) four-sided pyramid around I(12i), 0 0.1575 0.4123; (c) P_2' octahedron around $\frac{1}{4}\ \frac{1}{4}\ \frac{1}{4}$; (d) trigonal prism around J* (2l), 0.3981 0 $\frac{1}{2}$. z coordinates given in $a/100$

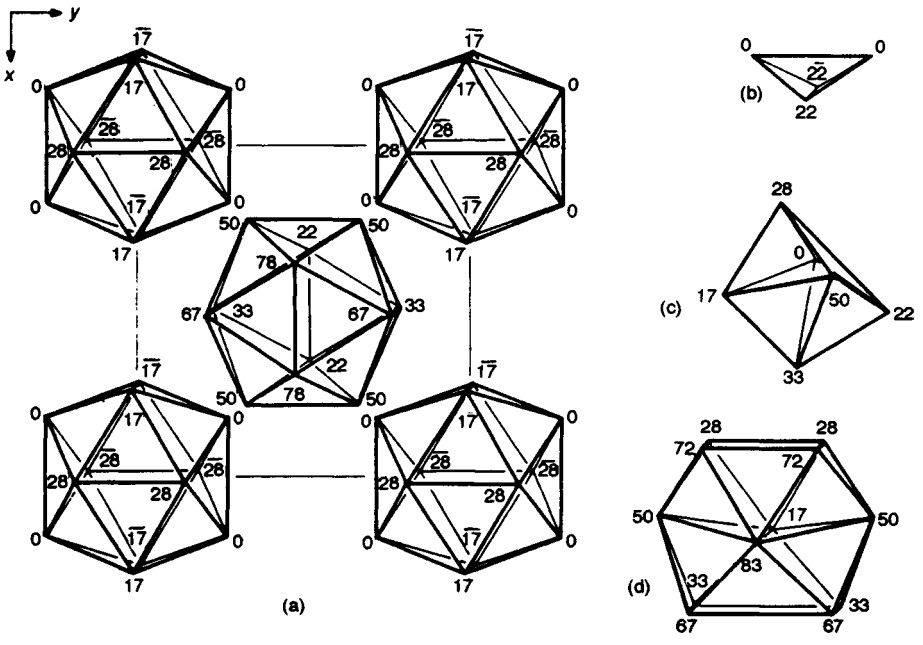

Figure 12 The ..nI(12i) framework: (a) point configuration with lines indicating the icosahedra around I; (b) W′ tetrahedron around $\frac{1}{4}\ \frac{1}{2}$ 0; (c) P_2' octahedron around $\frac{1}{4}\ \frac{1}{4}\ \frac{1}{4}$; (d) 12-coordinated polyhedron around W, $\frac{1}{4}$ 0 $\frac{1}{2}$. z coordinates given in $a/100$

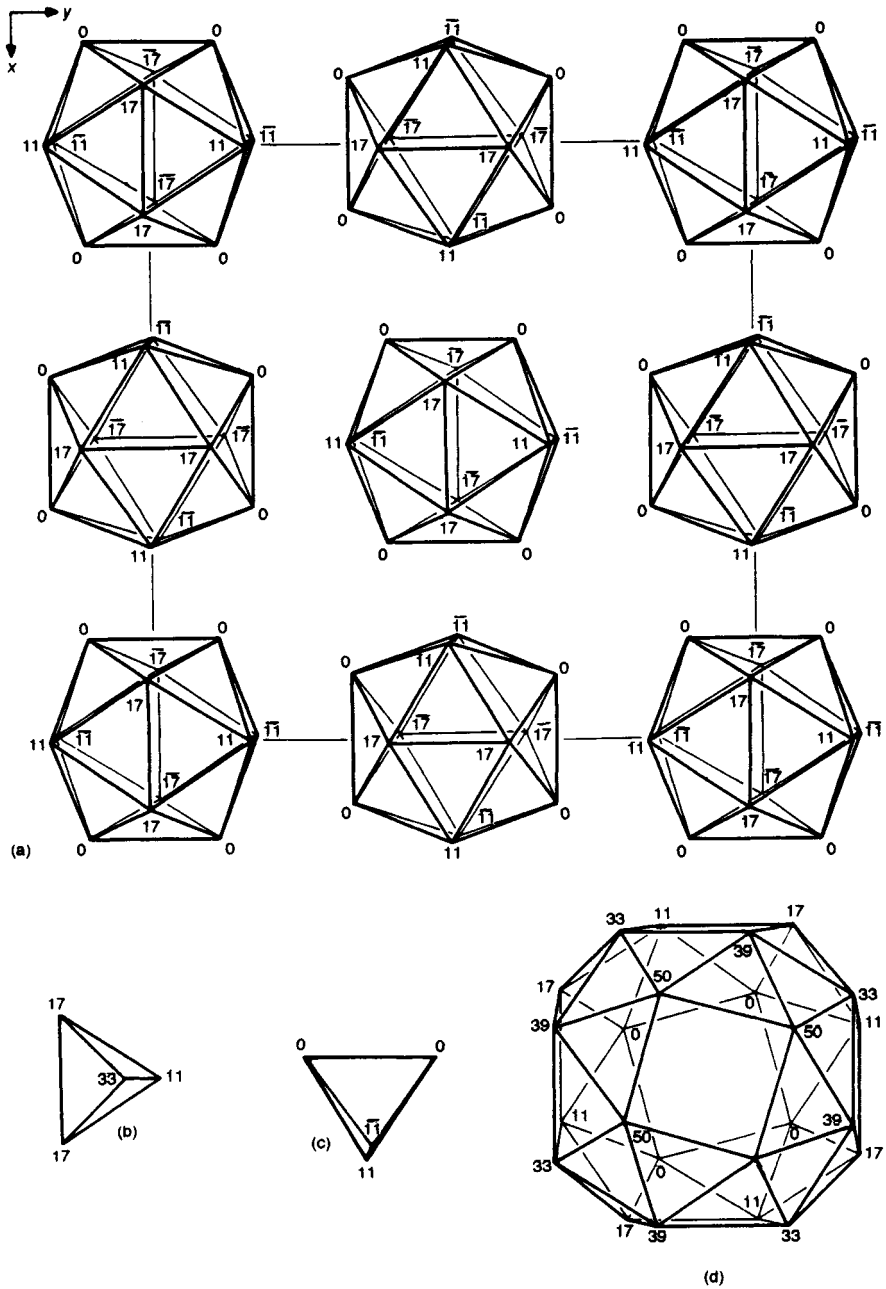

Figure 13 The ..cP$_2$(12i) framework: (a) point configuration with lines indicating the icosahedra around P$_2$, only polyhedra with centers at $z=0$ are shown; (b) tetrahedron around 96(i) 0 y z, 0 0.0752 0.1968; (c) J$_2'$ tetrahedron around $\frac{1}{4}$ 0 0; (d) P$_2'$ snub-cube (24scu) around $\frac{1}{4}$ $\frac{1}{4}$ $\frac{1}{4}$. z coordinates given in $a/100$

glide plane. The vertices of the icosahedra are connected by additional shortest distances (cf. Figure 12). The corresponding sphere packing type is 7/3/c1.

The crystal structure of UH_3 contains a distorted framework of this type built up by the hydrogen atoms ($y = 0.155$, $z = 0.31$). The uranium atoms fill up all 12 coordinated voids within the framework. In $AuZn_3$ the zinc atoms form a very similar configuration as a basic framework ($y = 0.16$, $z = 0.30$). The gold atoms occupy analogous positions as the uranium atoms in UH_3.

3.7 The ..cP$_2$(●12i) Framework

A member of the ..cP$_2$(●12i) family is the structure $NaZn_{13}$ in $Fm\bar{3}c$. A framework ..cP$_2$(12i) contains ideal icosahedra in two orientations (cf. Figure 13). The axes of all icosahedra are parallel to one another. Polyhedra of different orientations can be mapped onto each other by glide reflections along diagonal glide planes according to the orientation-symmetry symbol ..c given in front of the framework symbol; furthermore besides two small tetrahedra, one finds a large snub-cube, which is filled by large alkali, alkaline-earth, or rare-earth elements.

4. Nets in Orthohexagonal Arrangements

In {1 1 0}-type planes, the b.c.c. structure forms 3^6 nets of atoms consisting of isosceles triangles with angles of approximately 55°, 55°, and 70° (Figure 14). Each triangle thus has one unique corner and it is convenient to indicate this by chemical component in considering the ordered CsCl structure, since in {1 1 0} planes the triangles of the CsCl structure have two corners (55°) occupied by one component and one (70°) by the other. Indeed, it is seen that the 3^6 net is made up of two interpenetrating 4^4 rectangular nets. In the b.c.c. or CsCl structures, successive nets in [1 1 0] directions are stacked one above the other, so that the unique corners of the isosceles triangles of one net center the midpoint of the edge opposite the unique corner of the triangles in the nets above and below it, as shown in Figure 14, thus giving two stacking positions A° and B°.

In this way, b.c.c. structures and distorted b.c.c. structures can be described by nets. A more general approach is possible by orthohexagonal arrangements as defined in Hellner *et al.* (1992b) and Pearson (1993): A hexagonal unit cell can be described on orthorhombic axes in one of three possible orientations according to the matrices:

$$O_1 = \begin{pmatrix} 1 & 0 \\ 1 & 2 \end{pmatrix} O_2 = \begin{pmatrix} 1 & 1 \\ \bar{1} & 1 \end{pmatrix} \text{and } O_3 = \begin{pmatrix} 0 & 1 \\ \bar{2} & \bar{1} \end{pmatrix}$$

given in the *International Tables for X-Ray Crystallography* (1952, pp. 19, 21). Such an orthohexagonal cell (a, b, c) has dimensions, for example, $a = a_0$, $b = \sqrt{3}a_0$, $c = c_0$, where a_0 and c_0 are the dimensions of the primitive hexagonal cell. Atomic arrangements are primitive (P) in the hexagonal cell and centred (A, B, C or F) in the orthorhombic cell.

Previously Hellner (1986) had loosely used the symbol 'hC' to refer to the approximately orthohexagonal atomic arrangement in the few structures with tetragonal or orthorhombic symmetry in which it was observed. Our present study of orthorhombic structures reveals that the phenomenon is much more widespread than

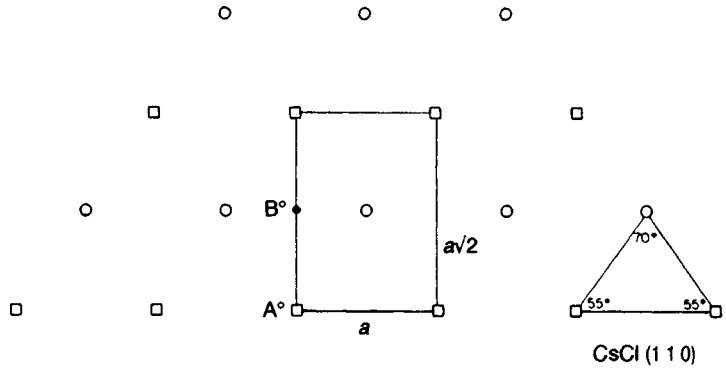

Figure 14 CsCl (or b.c.c. with one component atom) {1 1 0} plane of atoms, indicating triangle angles and two equivalent stacking sites A° and B°

previously imagined, so that it is necessary to adopt more precise symbols with which to describe it. Hence we now adopt a matrix notation ($|M|=2$) to describe the centered orthohexagonal arrangement indicating it by the superscript symobol 'o' (cf. ^{v}D, ^{v}T). This we follow by a, b, or c to indicate the unique axis of the tetragonal, orthorhombic, or monoclinic structure on the plane normal to which (i.e. 1 0 0), (0 1 0) or (0 0 1) respectively) the unit-cell edges (i.e. *b/c*, *a/c*, *a/b* respectively) have the approximate ratio $\sqrt{3}$ or $1/\sqrt{3}$ required for an orthohexagonal description. Thus we have the three matrices

$$oa=\begin{pmatrix}1&0&0\\0&1&1\\0&\bar{1}&1\end{pmatrix}\quad ob=\begin{pmatrix}1&0&\bar{1}\\0&1&0\\1&0&1\end{pmatrix}\quad \text{and}\quad oc=\begin{pmatrix}1&1&0\\\bar{1}&1&0\\0&0&1\end{pmatrix}$$

which can be applied to the primitive hexagonal lattice complexes or point configuration descriptors; e.g. ^{oa}H, ^{ob}H, ^{oc}H, ^{oa}G, ^{ob}G, ^{oc}G, ^{oa}N, ^{ob}N, ^{oc}N, ^{oa}hD, ^{oc}hT, $^{oc}\pm$Q, etc. It is only necessary to consider one orientation of each of these orthohexagonal arrangements, and we choose that corresponding to O_2 above. Although it should be obvious, perhaps it has to be stated that, in order to give a framework description in orthohexagonal terms, not only does the ratio of two unit-cell edges have to be approximately $1/\sqrt{3}$, but also the arrangement of the atoms on the plane defined by the ratio has to be appropriate; it does not suffice to have one condition alone satisfied. Thus, for example, in the SiTi oP8 structure, although the atomic arrangement on the (0 1 0) plane may correspond to a function of ^{ob}H, this description should not be used, as $c/a=1/1.375$ is far removed from the value $1/\sqrt{3}$

In Table 10 we give the primitive hexagonal lattice complexes H, G, and N in their standard settings and the corresponding point configurations ^{oc}H, ^{oc}G, and ^{oc}N in their standard settings in orthorhombic and monoclinic space groups when $a/b=\sqrt{3}$ (or $1/\sqrt{3}$), but it should be noted that here ^{oc}N is crystallographically heterogeneous.

We can now apply this notation to describe an approximately orthohexagonal arrangement of atoms when it is found on {1 0 0}-type planes of structures of any class, tetragonal, orthorhombic, monoclinic or anorthic, since the matrices *oa*, *ob*, and *oc* apply only to the transformation of primitive hexagonal to orthohexagonal, the hexagonal cell being taken with either *a*, *b*, or *c* unique for future comparisons. However, we also find approximately orthohexagonal arrangements to occur sometimes on {1 1 0}-type planes in crystals of these classes; indeed, it is the most frequent occurrence of orthohexagonal arrangements in the tetragonal class. Since we have no mechanism for structural description on {1 1 0}-type planes, such cells have to be reset so that the {1 1 0}-type planes become {1 0 0}-type planes.

In the tetragonal class this resetting can be indicated by specifying a space-group change, e.g. P→C, I→F, C→P_{22}, etc., but in the orthorhombic and lower classes the appropriate space-group changes have not been worked out. Hence the resetting has to be indicated by specifying the matrix change (generally $|M|=2$, subsequently referred to as $M(2)$ for ease in tabulating) that it involves. This matrix change must not be confused with that of primitive hexagonal to orthohexagonal, since it is quite independent thereof.

The reset tetragonal cells have axes *a*, *b*, *c* appropriate to the space group quoted, but in the lower classes the reset cells have new axes $a'=b'=(a^2+b^2)^{1/2}$, $a'=c'=(a^2+c^2)^{1/2}$ or $b'+c'=(b^2+c^2)^{1/2}$ and the ratios c/a', b/a' or a/b' equal $\sqrt{3}$ or its reciprocal, or an integral multiple of either in the case of a superstructure of the orthohexagonal cell.

Another reason for our change to matrix notation is that the previous use of the prefix h as in hC to refer to a centered orthohexagonal arrangement of atoms can be confused with its use in hD and hT where it signifies diamond, D, and tetrahedra, T, point configuration descriptions of these cubic lattice complexes when they occur in the *primitive* hexagonal cell. This confusion is now removed, and indeed we can, for example, describe ^{oc}hD without ambiguity.

Table 10 Standard settings of H, G, and N in the primitive hexagonal cell and of ^{oc}H, ^{oc}G, and ^{oc}N point configurations in orthorhombic and monoclinic cells with $b/a=\sqrt{3}$

	Primitive hexagonal setting in P6/mmm		Orthorhombic setting in Cmmm, $b/a=\sqrt{3}$		Monoclinic setting in C2/m (*b* unique), $b/a=\sqrt{3}$, $\beta=90°$	
3^6	H	1a	^{oc}H	2a	^{oc}H	2a
6^3	G	2c	^{oc}G	4i, $y=\frac{1}{3}$	^{oc}G	4g, $y=\frac{1}{3}$
6363	N	3f	^{oc}N	2b, 4e	^{oc}N	2b, 4e

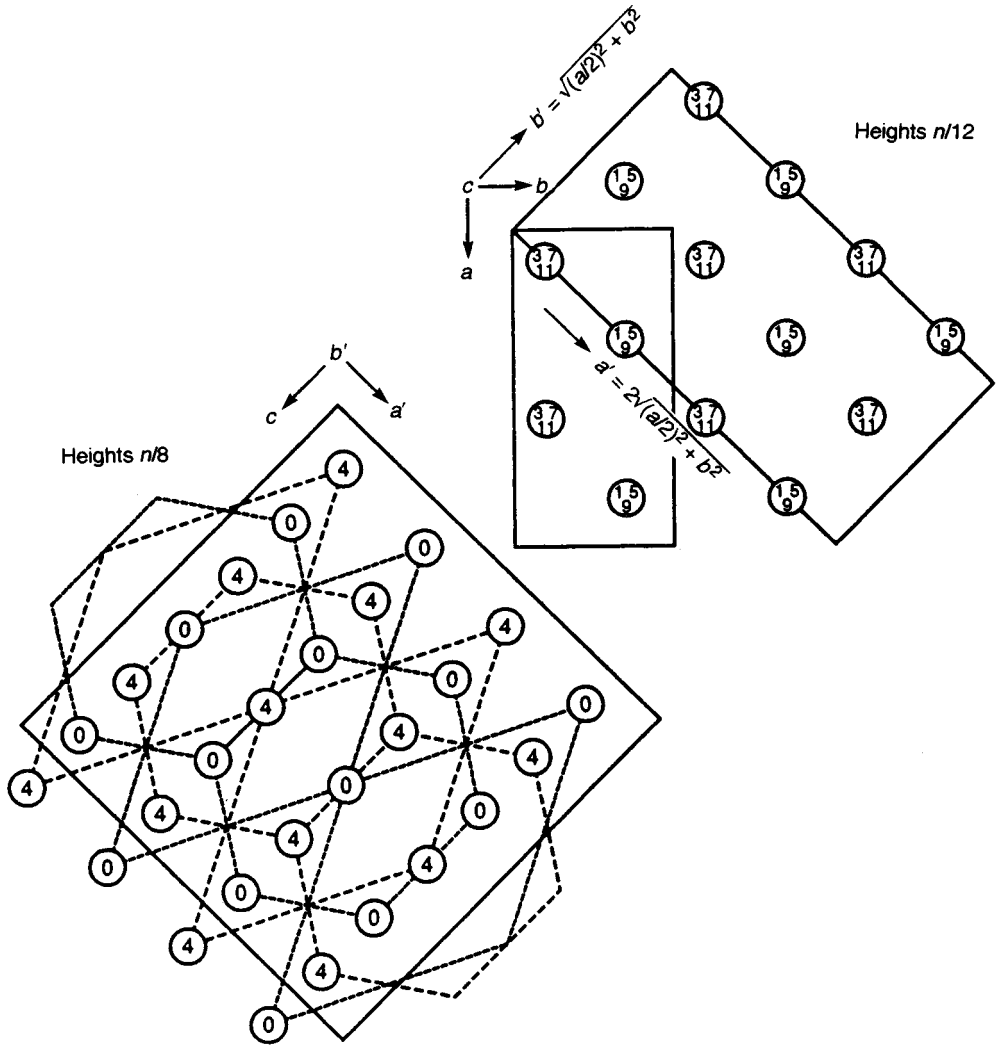

Figure 15 Diagram of the $AlAu_2$ oP12 structure with idealized metric $a/2 = b$ and idealized atom positions showing the $M(2) = \begin{pmatrix} 1 & 0 & \bar{1} \\ 0 & 1 & 0 \\ 1 & 0 & 1 \end{pmatrix}$ cell, the framework $(2f)\,\frac{1}{8}\,\frac{1}{2}\,\frac{1}{12}\,(^{ob}H_{211} + {}^{ob}G_{211})$ as a superstructure of the $MoSi_2$ tI6 structure

In the descriptions of tetragonal cells with orthohexagonal arrangements, complications do arise nevertheless, since projections down *A* and *B* are identical. When the orthohexagonal description occurs on (1 0 0) and (0 1 0) planes, we choose (0 1 0) so that the matrix symbol is ^{ob}H, etc. When it occurs on the (1 1 0) plane and a centered tetragonal setting is required, we choose (0 1 0) of the *centered* tetragonal cell so that again the matrix symbol in the centered cell is ^{ob}H, etc. However, because projections down *a* and *b* are identical, 'non-crystallographic' features may occur in the point configurations used to describe the structure. Although these may require splitting of Wyckoff sites so that half the atoms occur in one point

Table 11 Orthorhombic and tetragonal structures exhibiting centered pseudohexagonal atomic arrangements on {1 1 0}-type planes and requiring a centered orthorhombic or tetragonal cell for description. Note $1/\sqrt{3} = 0.577$

Substance	Symbol	Axial ratio	Space group	Wyckoff	Centered cell	Framework	Number of substances
Superstructures							
$CaCr_2Al_{10}$	tP52	$\frac{2c}{a\sqrt{2}} = 0.565$	P4/mmm	2a,c, 8g,h,i^2,j^2	tC104	${}^{ob}\frac{1}{4}\,\frac{1}{24}\,0H_{261}1y + \frac{1}{4}00G_{241}1x + \frac{1}{4}\,\frac{1}{8}\,0N_{241}1y)$	1
Edge-centered stacking							
Pa	tI2	$\frac{c}{a\sqrt{2}} = 0.582$	I4/mmm	2a	tF4	$(2f)^{ob}H$	3
Al_3Os_2	tI10	$\frac{c}{5a\sqrt{2}} = 0.646^a$	I4/mmm	2a, $4e^2$	tF20	$(10f)^{ob}H1z$	4
$MoSi_2$	tI6	$\frac{c}{a\sqrt{2}} = 1.734$	I4/mmm	2a, 4e	tF12	$(2f)^{ob}(H+G)$	84
$MoPt_2$	oI6	$\frac{b}{\sqrt{a^2+c^2}} = 1.722$	Immm	2a, 4g	$M(2)$	$(2f)^{oc'}(H+G)$, $M(2) = \begin{pmatrix} 1 & 0 & \bar{1} \\ 0 & 1 & 0 \\ 1 & 0 & 1 \end{pmatrix}$	8
$ReSi_2$	oI6	$\frac{c}{\sqrt{a^2+b^2}} = 1.731$	Immm	2a, 4i	$M(2)$	$(2f)^{ob'}(H+G)$, $M(2) = \begin{pmatrix} 1 & \bar{1} & 0 \\ 1 & 1 & 0 \\ 0 & 0 & 1 \end{pmatrix}$	1
$AlAu_2$	oP12	$\frac{c}{\sqrt{(a/2)^2+b^2}} = 1.895^b$	Pnma	$4c^3$	$M(2)$	$(2f)\frac{1}{8}\,\frac{1}{2}\,\frac{1}{12}\,{}^{ob'}(H+G)_{211}$, $a=c$, $M(2) = \begin{pmatrix} \frac{1}{2} & 2 & 0 \\ \frac{1}{2} & 1 & 0 \\ 1 & 0 & 1 \end{pmatrix}$	4
		$a \approx 2b^c$			$M(4)$	$(4f)0\,\frac{3}{8}\,\frac{1}{10}\,{}^{ob'}(H+G)_{211}$, $M(4) = \begin{pmatrix} 1 & \bar{2} & 0 \\ 1 & 2 & 0 \\ 1 & 0 & 1 \end{pmatrix}$	
Al_4Ba	tI10	$\frac{c}{a\sqrt{2}} = 1.739$	I4/mmm	2a, 4d,e	tF20	$(2f)(\frac{1}{4}\,\frac{1}{4}\,\frac{1}{4} + \frac{3}{4}\,\frac{1}{4}\,\frac{1}{4})^{ob}H(\bullet 4t_{re}\,\underset{(001)}{\overset{2}{\infty}}) + (2f)^{ob}H$ or $(4d)(000 + \frac{1}{2}00)^{ob}H - (2f)\frac{1}{2}00^{ob}H) + (2f)\frac{1}{2}00^{ob}H2z)$	462
$BaNiSn_3$	tI10	$\frac{c}{a\sqrt{2}} = 1.604$	I4/mmm	$2a^3$, 4b	tF20	$(4d)(000 + \frac{1}{2}00)^{ob}H1z + (2f)0\,\frac{1}{2}\,\frac{1}{6}\,{}^{ob}H1z$	6
Be_2CaGe_2	tP10	$\frac{c}{a\sqrt{2}} = 1.745$	P4/nmm	2a,b,c^3	tC20	$(2f)^{ob}(\frac{1}{4}\,\frac{1}{4}\,\frac{1}{4}H + (000 + \frac{1}{2}00)H(\bullet 4t_{4e}\,\underset{(001)}{\overset{2}{\infty}}))$ or $(4d)(000 + \frac{1}{2}00)^{ob}H - (2f)\frac{1}{4}\,\frac{3}{4}\,\frac{1}{4}\,{}^{ob}H) + (2f)\frac{1}{4}\,\frac{3}{4}\,\frac{1}{4}\,{}^{ob}H2z$	10

(continued)

Table 11 (*continued*)

Substance	Symbol	Axial ratio	Space group	Wyckoff	Centered cell	Framework	Number of substances
C_2IrU_2	tI10	$\frac{c}{a\sqrt{2}} = 2.537^d$	I4/mmm	2a, $4e^2$	tF20	$(2f)^{ob}(H + (000 + 00\frac{1}{2})G)$	6
$CoNb_4Si$	tP12	$\frac{c}{a\sqrt{2}} = 0.577$	P4/mcc	2a,c, 8m	tC24	$(2f)^{ob}((\frac{1}{4}00 + \frac{1}{4}0\frac{1}{2})H1y + (00\frac{1}{4} + 00\frac{3}{4})H + \frac{1}{4}\frac{3}{4}0G)$	19
Al_2Cu	tI12	$\frac{c}{a\sqrt{2}} = 0.568$	I4/mcm	4a, 8h	tF24	$(2f)^{ob}((00\frac{1}{4} + 00\frac{3}{4})H + (\frac{1}{4}00 + \frac{1}{4}0\frac{1}{2})H1y + \frac{1}{4}\frac{3}{4}0G)$ or $(2f)^{ob}((00\frac{1}{4} + 00\frac{3}{4})H(\bullet 4t^{2e}\ {}^{2}_{\infty}{}_{(100)} + (\frac{1}{4}00 + \frac{1}{4}0\frac{1}{2})H1y)$	101
$BaMg_2Sn_2$	tP20	$\frac{c}{a\sqrt{2}} = 1.750 \times 2$	P4/nmm	2a,b,c^6, 4f	tC40	$(2f)^{ob}(\frac{1}{4}\frac{1}{4}\frac{1}{8}H_{112} + (000 + \frac{1}{2}00)H_{112}(\bullet 4t_{4e}\ {}^{2}_{\infty}{}_{(001)}))$	3
Ga_5Mg_2	tI28	$\frac{c}{a\sqrt{2}} = 0.583$	I4/mmm	4e, 8h, I6n	tF56	$(2f)^{ob'}(G + (0\frac{1}{4}0 + 0\frac{1}{4}\frac{1}{2})H1y + (00\frac{1}{4} + 00\frac{3}{4})H1z + (\frac{1}{4}\frac{1}{4}\frac{1}{4} + \frac{1}{4}\frac{1}{4}\frac{3}{4})H2xyz)$	1
GaU	oC32	$\frac{\sqrt{a^2 + c^2}}{b} = 1.751$	Cmcm	4a,c, 8e,f,g	M(2)	$(2f)(00\frac{1}{2} + \frac{3}{4}0\frac{1}{4})^{oc'}N + (2f)(\frac{1}{8}0\frac{3}{8} + \frac{1}{8}\frac{1}{2}\frac{3}{8} + \frac{3}{8}0\frac{1}{8} + \frac{3}{8}\frac{1}{2}\frac{1}{8})^{oc'}H1xz + \frac{1}{8}\frac{1}{4}\frac{1}{8}I_{212}1y + \frac{1}{8}\frac{3}{4}\frac{1}{8}I_{212}2xz1y)$ $M(2) = \begin{pmatrix} 1 & 0 & \bar{1} \\ 0 & 1 & 0 \\ 1 & 0 & 1 \end{pmatrix}$	1
Ru_2Sn_3	tP20	$\frac{c}{a\sqrt{2}} = 0.568 \times 2$	$P\bar{4}c2$	2b,c, 4f,i, 8j	tC40	$(4d)[^{ob}H_{112} + (^{ob}G_{112} - \frac{1}{2}0\frac{1}{2}P(2l))]$	3

[a] Note, in centered cell, $5a/c = 1.548 < \sqrt{3}$.
[b] Idealized atom positions.
[c] Actual atom positions.
[d] Note this filled-up $MoSi_2$ structure is like a $MoSi_2$ structure phase such as $AuZr_2$ with $c/a \approx 3.5$ instead of 2.5.

configuration and half in another; this seems unavoidable!

$AlAu_2$ oP12 with $c/[(a/2)^2 + b^2]^{1/2} = 1.895$ is an interesting example of an orthorhombic structure that, with idealized $a/2 = b$ and idealized atom positions, can be set in a cell with $|M| = 2$ and can be described with an orthohexagonal framework: $(2f)\frac{1}{8}\frac{1}{2}\frac{1}{12}(^{ob}H_{211} + {}^{ob}G_{211})$; see Figure 15. This clearly shows it to be a superstructure of the $MoSi_2$ tI6 structure, which in the centred tF12 setting is described as $(2f)(^{ob}H + {}^{ob}G)$. It could be argued that the above ratio of 1.895 is considerably larger than the ideal ratio $1.732 = \sqrt{3}$; however, many substances with $MoSi_2$ structure also have axial ratios (c/a) considerably larger than the ideal value of $c/a = 2.45$ of $MoSi_2$ in I setting and required for an ideal orthohexagonal cell. Hence, slight

latitude in bending 'rules' may give benefits in showing structural relationships. $MoSi_2$ structures are also discussed in Chapter 17 by Nevitt and Koch in this volume.

Orthohexagonal atomic arrangements may exhibit one of the three possible cases of *edge-centered* stacking (f), (q), (d), which we have already had occasion to describe in conjunction with the earlier symbols hC and hG (e.g. Hellner *et al.*, 1990). With 3^6 nets there are only three possible variants of edge-centered stacking: (f) which involves two stacking sites A_o, B_o; (q) three sites B_o, C_o, D_o; and (d) four sites A_o, B_o, C_o, D_o (Hellner *et al.*, 1992b, ch. 2). We recognize this fact by henceforth referring to (2f), (3q), and (4d) in order to bring the nomenclature in parallel with that for median stacking, where we no longer refer to hexagonal and cubic close packing, respectively, as (h) and (c), but as (2h) and (3c). Thus we have achieved logical conformity with other stacking descriptions such as, for example, (4h), (6h), etc., which are observed in real structures.

Structures also occur in which the stacking is intermediate between the edge-centered and median positions. An example of this is found in the $TaPt_2$ structure (oC12, 4c and 8g of Cmcm). There is a superstructure of the centered pseudohexagonal cell along *a*, and since $b:a/3 = 1.708$, the angles of the triangles of the 3^6 nets formed by atoms on the (0 0 1) planes scarcely differ from 60° (see e.g. Hellner and Pearson, 1984). The cell contains two 3^6 layers stacked along [0 0 1], but the sites are certainly intermediate between edge-centered and median. In these circumstances, it appears that the best description that can be given is $(2\bar{1}h)0\,\frac{1}{4}\,\frac{1}{4}{}^{oc}H_{311}1y$.

Table 11 lists orthorhombic and tetragonal structures exhibiting centered pseudohexagonal descriptions.

5. Summary

The I structures are described with the 2 pointer I and its voids as a sphere packing type; the higher orders give the chance to describe them by splitting procedures, as in the 8th, 27th, 64th, and 216th orders. Especially the γ-brass structure is described as W*(4t) with large voids around I. The compound Tl_7Sb_2 is an ideal γ-brass with filled voids. The structures of 216th order are filled with clusters as in Tl_7Sb_2 and as in the α-Mn structure.

Other structures of the I family are frameworks with polyhedra around each i point, which can partly be handled as homogeneous sphere packings with self-coordination and different voids. Besides some heterogeneous cases, a net description follows at the end with orthopseudohexagonal settings and gives relations among a lot of hexagonal, rhombohedral, and lower-symmetry crystal classes.

If further information about the behavior in lower-symmetry space groups is wanted, see Hellner and Pearson (1986, 1987, 1988) and Hellner *et al.* (1992b, 1993) in *Physics Data* 16-5, 16-6, 16-7, 16-9, 16-10. In addition to the hexagonal and rhombohedral structures in *Physics Data* 16-8 (Hellner *et al.*, 1990), there is another survey in *Physics Data* 16-4 (Hellner *et al.*, 1992a).

6. References

Born, M. (1923). *Atomtheorie des festen Zustandes*. Leipzig, Berlin.

Cohen, M. L., and Heine, V. (1970). *Solid State Phys.*, **24**, 37.

Donnay, J. D. H., Hellner, E., and Niggli, A. (1964) *Z. Kristallogr.*, **120**, 369.

Fischer, W. (1971). *Z. Kristallogr.*, **133**, 18.

Fischer, W. (1973). *Z. Kristallogr.*, **138**, 129.

Fischer, W. (1974). *Z. Kristallogr.*, **140**, 50.

Fischer, W. (1991). *Z. Kristallogr.*, **194**, 67, 87.

Fischer, W. (1993). *Z. Kristallogr.*, **205**, 9.

Fischer, W., and Koch, E. (1974). *Z. Kristallogr.*, **139**, 266.

Fischer, W., Burzlaff, H., Hellner, E., and Donnay, J. D. H. (1973). *Space Groups and Lattice Complexes* (National Bureau of Standards, Monograph 134). US Department of Commerce.

Fornasini, M. L., Chabot, B., and Parthé, E. (1978) *Acta Crystallogr.*, **B34**, 2093.

Heine, C., Heine, V., and Weaire, D. (1970). *Solid State Phys.*, **24**, 1, 249.

Hellner, E. (1986). *Z. Kristallogr.*, **175**, 227.

Hellner, E., and Koch, E. (1980). *Can. J. Chem.*, **58**, 708.

Hellner, E., and Koch, E. (1981a). *Acta Crystallogr.*, **A37**, 1.

Hellner, E., and Koch, E., (1981b). *Acta Crystallogr.*, **B38**, 376.

Hellner, E., and Pearson, W. B. (1984). *Z. Kristallogr.*, **168**, 255.

Hellner, E., and Pearson, W. B. (1986). *Frameworks for 'Intermetallic Phases' with Structures in Space Groups of the 4-Stem of I4/mmm* (*Physics Data* 16-5). FIZ 4, Karlsruhe.

Hellner, E., and Pearson, W. B. (1987). *Structure Type Descriptions for Intermetallic Phases in the Space Groups I4/mmm and $I4_2/mcm$ and their Subgroups* (*Physics Data* 16-6). FIZ 4, Karlsruhe.

Hellner, E., and Pearson, W. B. (1988). *Structure Type Descriptions for Intermetallic Phases in the Space Groups $I4_1/amd$ and $I4_1/acd$ and their Subgroups* (*Physics Data* 16-7). FIZ 4, Karlsruhe.

Hellner, E., and Sowa, H. (1985) *The Cubic Structure Types Described in Their Space Group with the Aid of Frameworks* (*Physics Data* 16-3). FIZ 4, Karlsruhe.

Hellner, E., Gerlich, R., Koch, E., and Fischer, W. (1979). *The Oxygen Framework in Garnet and its Occurrence in the Structures of $Na_3Al_{12}Li_3F_{12}$, $Ca_3Al_{12}(OH)_{12}$, $RhBi_4$ and Hg_3TeO_6 (Physics Data* 16-1). FIZ 4, Karlsruhe.

Hellner, E., Koch, E., and Reinhardt, A. (1981). *The Homogeneous Frameworks of the Cubic Crystal Structures (Physics Data* 16-2). FIZ 4, Karlsruhe.

Hellner, E., Schwarz, R., and Pearson, W. B. (1990) *Structure Type Descriptions for Intermetallic Phases in the Hexagonal and Rhombohedral Systems (Physics Data* 16-8). FIZ 4, Karlsruhe.

Hellner, E., Schwarz, R., and Pearson, W. B. (1992a). *Introduction to an Inorganic Crystal Chemistry II (Physics Data* 16-4). FIZ 4, Karlsruhe.

Hellner, E., Schwarz, R., and Pearson, W. B. (1992b). *Structure Type Descriptions for Intermetallic Phases in the Orthorhombic System (Physics Data* 16-9). FIZ 4, Karlsruhe.

Hellner, E., Schwarz, R., and Pearson, W. B. (1993). *Structure Type Descriptions for Intermetallic Phases in the Monoclinic System (Physics Data* 16-10). FIZ 4, Karlsruhe.

Hermann, C. (1960). *Z. Kristallogr.*, **113**, 142.

Hume-Rothery, W. (1926). *The Structure of Metals and Alloys.* Institute of Metals, London.

International Tables for Crystallography (1983). Vol. A (ed T. Hahn). Reidel, Dordrecht.

International Tables for X-Ray Crystallography (1952). Vol. 1 (eds N. F. M. Henry and K. Lonsdale). Kynoch Press, Birmingham.

Internationale Tabellen zur Bestimmung von Kristallstrukturen (1935). Vol. 1 (ed. C. Hermann). Gebrüder Bornträger, Berlin.

Jones, H. (1934). *Proc. R. Soc.*, **A144**, 225.

Knecht, J., Fischer, R., Overhoff, H., and Hensel, F. (1978). *J. Chem. Soc., Chem. Commun.*, 905.

Lima-de-Faria, J., Hellner, E., Liebau, F., Makovicky, E., and Parthé, E. (1990). *Acta Crystallogr.*, **A46**, 1.

Madelung, O. (1918). *Phys. Z.*, **19**, 528.

Malrieu, J. P., Maynau, D., and Daudey, J. P. (1984). *Phys. Rev.*, **B30**, 1817.

Nagorson, G., and Witte, H. (1953). *Z. Anorg. Chem.*, **217**, 144.

Niggli, P. (1919). *Geometrische Kristallographie des Diskontinuums.* Leipzig.

Pauling, L. (1940). *The Nature of the Chemical Bond.* Cornell University Press, Ithaca, NY.

Pearson, W. B. (1993). *Z. Kristallogr.*, **204**, 239.

Samson, S., (1972). *Acta Crystallogr.*, **B28**, 936.

Samson, S., and Hansen, D. A. (1972). *Acta Crystallogr.*, **B28**, 930.

Simon, G., and Bloch, A. N. (1973). *Phys. Rev.*, **B7**, 2754.

Villars, P., and Calvert, L. D. (1985). *Pearson's Handbook of Crystallographic Data for Intermetallic Phases*, Vol. 1. American Society for Metals, Cleveland, OH.

vom Felde, A., Sprösser-Prou, J., and Fink, J. (1989). *Phys. Rev.*, **B40**, 10181.

Zintl, E. (1939). *Angew. Chem.*, **52**, 1.

Zintl, E., and Dullenkopf, W. (1932). *Z. Phys. Chem.*, **B16**, 183.

Zunger, A. (1980). *Phys. Rev.*, **B22**, 649.

This chapter was originally published in 1995 as Chapter 13 in *Intermetallic Compounds*, Vol. 1: *Principles*, edited by J. H. Westbrook and R. L. Fleischer.

Chapter 4
Wurtzite and Sphalerite Structures

Erwin Parthé

Laboratoire de Cristallographie aux Rayons X, Université de Genève, 24 Quai Ernest Ansermet, CH-1211, Geneva 4, Switzerland
and
Institute for Mineralogy and Crystallography, University of Vienna, Geozentrum, Althanstrasse 14, A-1090 Vienna, Austria

1. Introduction

Some 25 years ago when the same author wrote the chapter on 'Wurtzite and sphalerite type structures' for the first edition of *Intermetallic Compounds* (Parthé, 1967), these kinds of compounds, particularly III–V compounds such as InSb and GaAs, were the center of attention of solid-state physicists and chemists, who were excited by the new discoveries in semiconductor physics and the resulting new devices that revolutionized so many facets of our daily life. This was perhaps the reason why a chapter on wurtzite and sphalerite-related structures was included in the book, although these compounds are not intermetallics in the usual sense.

Today the center of action has shifted to other kinds of compounds such as the high-temperature oxide superconductors. These days, new wurtzite and sphalerite-related structures do not appear so often in the literature. However, the reader will be treated here to one of the few successful attempts to correlate structural features with composition. In particular, it will be shown that two parameters, to be calculated from the composition and the valence-electron contribution of the participating elements, can be used not only to pinpoint possible errors in the composition or structure of reported compounds, but also to predict probable structural features of unknown compounds.

2. Definition and Classification of Adamantane Structures

The topics of this chapter are the wurtzite and sphalerite structures and all the structures related to them as stacking and/or vacancy and/or substitutional variants. For these structures the summary term *adamantane* structures is often used.*

Adamantane structures, obtained only with normal-valence compounds, form a subdivision of the tetrahedral structures. The cations and anions occupy the Zn and S sites, respectively, of the wurtzite or sphalerite structure (or another stacking variant). Every atom on a cation (Zn) site is tetrahedrally coordinated by four anions. Conversely, every atom on an anion (S) site is tetrahedrally coordinated by four (or fewer in the case of a defect adamantane structure) cations.

The origin of the coining of the term 'adamantane structure' stems from the close geometrical relationship between the two diamond and the two ZnS modifications. As shown in Figure 1, the wurtzite and the sphalerite structures are ordered substitutional variants of the hexagonal diamond and the cubic diamond structure, respectively. The rare hexagonal diamond, also called *lonsdaleite* (Frondel and Marvin, 1967), is a stacking variant of the common cubic diamond.

The adamantane-structure compounds are conveniently classified according to three aspects:

*In the earlier literature can be found the term 'adamantine' structures (Spencer *et al.*, 1962); however, von Schnering (1989) pointed out that, since there are only single bonds present, it is more appropriate to denote these structures as 'adamantane' structures.

Crystal Structures of Intermetallic Compounds. Edited by J. H. Westbrook and R. L. Fleischer

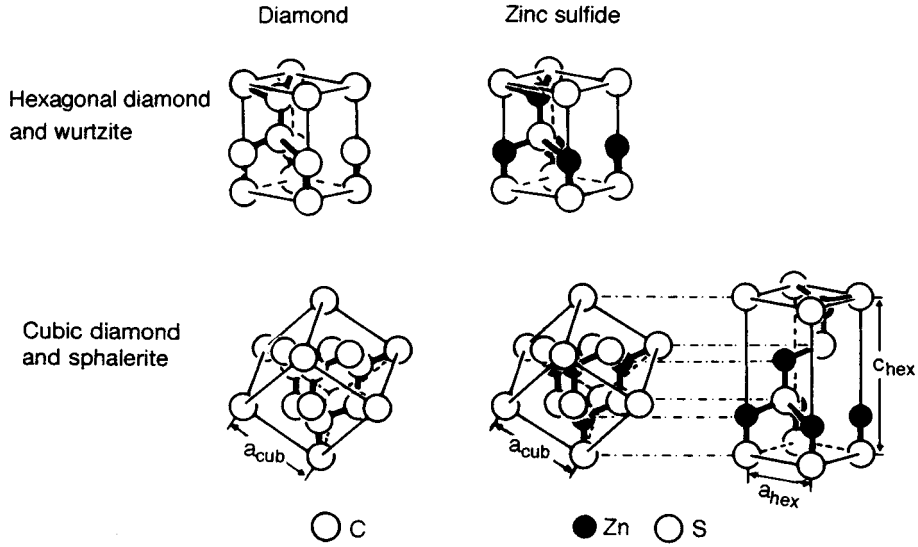

Figure 1. Structure of hexagonal diamond compared with that of wurtzite and of cubic diamond compared with sphalerite. For sphalerite the non-conventional triple-hexagonal cell is also shown, which is preferred when one wants to compare sphalerite with the other ZnS stacking variants. Small filled circles indicate Zn and large open circles C or S atoms

- The stacking of the ZnS base structure, as in wurtzite or as in sphalerite or as in a more complicated ZnS polytype.
- The percentage of vacant cation (Zn) sites, or, expressed differently, the overall cation-to-anion ratio. One distinguishes between *normal* adamantane-structure compounds with composition C_nA_n, where all Zn and S sites are fully occupied, and *defect* adamantane-structure compounds with composition $C_{n-p}\square_pA_n$, where some of the available Zn sites are not occupied ($\square$ stands for a vacancy). Examples of a normal and a corresponding defect adamantane-structure compound are ZnS (wurtzite) and α'-Ga_2S_3 (where one of three cation sites remains unoccupied).
- The substitutions on the cation (or anion) sites, leading to ternary or multinary adamantane structures. An example of a series of ordered substitutional derivatives of zinc blende is ZnS (sphalerite) → Cu_3SbS_4 (famatinite) → Cu_2FeSnS_4 (stannite).

We shall demonstrate below that the number of Zn site vacancies in a defect adamantane structure and the kind of atoms that may substitute on the Zn sites are not arbitrary, but depend on the valence-electron number of the participating atoms.

3. The ZnS Stacking Variants

Some 200 ZnS polytypes are known, all having hexagonal unit cells with base planes of the same size but with different cell heights. The S atom partial structures of all polytypes are close-packed with the Zn atoms occupying in regular fashion one of the two kinds of tetrahedral interstices. Five of these ZnS polytypes are presented in Figure 2. Instead of drawing the complete hexagonal or triple-hexagonal cells and all the atoms contained in them, as was done in Figure 1, only the $\{1\,1\,\bar{2}\,0\}$ planes of the cells and the arrangement of the atoms in these planes are shown in Figure 2.

The ZnS polytypes can be considered as an intergrowth of common identical slabs, which are stacked in a different way. Cutting the structures by slicing the S atoms along the horizontal planes, indicated by broken lines, one obtains the common identical $S_{1/2}$–Zn–$S_{1/2}$ slabs. As indicated on the upper left of Figure 2, there exist two possibilities of how two of these slabs can be intergrown. They differ by a rotation of the upper slab by 180° around the hexagonal axis. These two possibilities of slab stacking give rise to the formation of the different ZnS polytypes.

Assuming that a_h and c_h are the hexagonal unit-cell constants of a polytype, then the height of one slab is given by

$$d = a_h(2/3)^{1/2} = 0.8165a_h \qquad (1)$$

This value corresponds to the height of a tetrahedron with edge length a_h. For a polytype built up of N

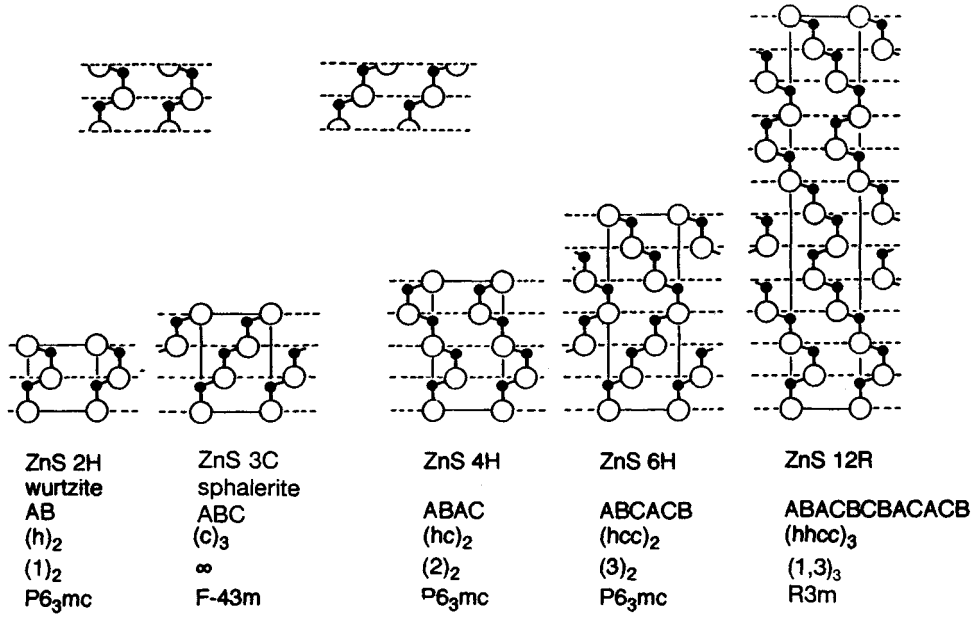

Figure 2. Atom arrangements in the $\{1\,1\bar{2}0\}$ planes of five ZnS polytypes, interpreted as an intergrowth of a common slab. For each polytype are given the Ramsdell, ABC, Jagodzinski–Wyckoff, and Zhdanov notations, and the space group. Small filled circles represent Zn atoms and large open circles S atoms

intergrown slabs, the c_h/a_h ratio of the hexagonal or triple-hexagonal unit cell is given by

$$c_h/a_h = N(2/3)^{1/2} = 0.8165N \qquad (2)$$

For the particular case of the ZnS polytypes, the numerical values are: $a_h \simeq 3.82_5$ Å, $d \simeq 3.12_3$ Å and $c_h \simeq 3.12_3 N$ Å.

Polytypes of great variety are found with binary normal adamantane-structure compounds, particularly with ZnS and SiC. In a table published by Mardix (1986) there are listed 196 properly identified ZnS polytypes. Mardix also advances an approach to explain the formation of the polytypes as a thermodynamic phenomenon taking place with the help of, but also regulated by restrictions imposed by, dislocations. These ideas have at present no direct relevance for ternary or multicomponent normal and defect adamantane-structure compounds, because as base structures only the common wurtzite (ZnS 2H) and sphalerite (ZnS 3C) structures occur here. One exception only has been reported. A modification of Cu_2ZnGeS_4 (Moodie and Whitfield, 1986) crystallizes with a structure that can be considered as a substitutional variant of ZnS 12R polytype (right-hand side of Figure 2).

Different notation schemes have been developed to characterize the stacking of the slabs. Four different polytype notations are listed below each drawing in Figure 2. Besides the well-known ABC notation, there are in common use the Jagodzinski–Wyckoff and the Zhdanov notations. From the last two one can also derive the proper space group for a polytype with a given kind of stacking. The details are discussed in the appendix (Section 10.1).

4. Valence-Electron Rules for Adamantane-Structure Compounds

The adamantane structures form a subdivision of the tetrahedral structures. The latter are formed by iono-covalent compounds for which two valence-electron rules can be formulated, one referring to the limiting ionic and the other to the limiting covalent bonding state. We shall first discuss the more general rules for tetrahedral structures and then the modified rules for adamantane structures.

4.1 Rules for Tetrahedral-Structure Compounds

The valence-electron rules for tetrahedral structures have been amply described in the literature (Parthé, 1972,

* 1990, 1992, 1996) and we can therefore restrict ourselves to a short repetition.

4.1.1 Ionic Bonding State

In the limiting ionic bonding state the valence electrons of the cations are transferred to the anions in order for them to obtain a stable octet configuration ns^2np^6. In the general case where the cations do not transfer all their valence electrons—they are used for bonds between themselves or for non-bonding orbitals on the cations—or where the anions, due to shared covalent bonds between themselves, do not need as many electrons to complete their octet shells, one can formulate the following valence-electron rule, known as the *generalized 8-N rule*:

$$\mathrm{VEC_A} = 8 + \mathrm{CC}/(n/m) - \mathrm{AA} \qquad \text{for } C_mA_n \qquad (3)$$

$\mathrm{VEC_A}$, the *partial valence-electron concentration* in respect to the anion, is defined as

$$\mathrm{VEC_A} = (me_C + ne_A)/n \qquad \text{for } C_mA_n \qquad (4)$$

and can be calculated alone from the composition of the compound and the valence-electron contribution of the participating elements (e_C, e_A). The right-hand part of (3) refers to structural features such as AA, the average number of anion–anion bonds per anion, and CC, the average number of cation–cation bonds per cation, and/or the electrons used for lone electron pairs.

Depending on the value of $\mathrm{VEC_A}$ one distinguishes between polyanionic-, and normal-, and polycationic-valence compounds.

- If $\mathrm{VEC_A} < 8$: polyanionic-valence compounds with $\mathrm{AA} > 0$.
- If $\mathrm{VEC_A} = 8$: normal-valence compounds with $\mathrm{AA} = \mathrm{CC} = 0$.
- If $\mathrm{VEC_A} > 8$: polycationic-valence compounds with $\mathrm{CC} > 0$.

4.1.2 Covalent Bonding State

In the limiting covalent bonding state all atoms form four tetrahedral sp^3 hybridized bonding orbitals, which overlap with the sp^3 orbitals of the neighboring atoms. To form an sp^3 hybrid each atom needs four valence electrons. Each orbit not used for bonding obtains a second electron and becomes a non-bonding orbital. One can formulate the following valence-electron rule, known as the *tetrahedral-structure equation*:

$$\mathrm{VEC} = 4 + N_{\mathrm{NBO}} \qquad \text{for } C_mA_n \qquad (5)$$

VEC, the *total valence-electron concentration*, is defined as

$$\mathrm{VEC} = (me_C + ne_A)/(m+n) \qquad \text{for } C_mA_n \qquad (6)$$

and can be calculated from the composition of the compound and the valence-electron contribution of the participating elements. The right-hand part of (5) contains the parameter N_{NBO}, the average number of non-bonding orbitals (≡ lone electron pairs) per atom. These lone electron pairs one can 'see' indirectly in a structure by the absence of an expected tetrahedral atom neighbor.

Depending on the value of VEC one distinguishes between normal and defect tetrahedral-structure compounds.

- If $\mathrm{VEC} < 4$: a tetrahedral structure cannot be formed.
- If $\mathrm{VEC} = 4$: normal tetrahedral-structure compound with $N_{\mathrm{NBO}} = 0$.
- If $\mathrm{VEC} > 4$: defect tetrahedral-structure compound with $N_{\mathrm{NBO}} > 0$.

4.2 The Adamantane-Structure Equation

As stated above, the adamantane structures form a subdivision of the tetrahedral structures. In the general case of a defect tetrahedral structure, only N_{NBO}, the average number of non-bonding orbitals per atom, is known, but not the relative positions of the non-bonding orbitals. In defect adamantane structures the non-bonding orbitals are grouped in quadruplets. Four non-bonding orbitals are positioned on the four anions surrounding a vacant Zn site. One can use in the chemical formula the symbol □, which indicates a vacant cation site and at the same time a quadruplet of non-bonding orbitals. Denoting the composition of a defect adamantane-structure compound (as a beginning) as $C_{m-p}\square_pA_n$ with p cation sites being unoccupied, the value of N_{NBO} can be expressed by

$$N_{\mathrm{NBO}} = 4p/[(m-p)+n] \qquad \text{for } C_{m-p}\square_pA_n \qquad (7)$$

Inserting (7) into (5), making use of (6), and multiplying by $[(m-p)+n]$, one obtains the following modified expression for the tetrahedral-structure equation:

$$(m-p)e_C + ne_A = 4[(m-p)+n] + 4p \qquad \text{for } C_{m-p}\square_pA_n \qquad (8)$$

Since adamantane-structure compounds are normal-valence compounds, one can also make use of (3)

in the special form where $CC = AA = 0$, which can be written as

$$(m-p)e_C + ne_A = 8n \qquad \text{for } C_{m-p}\square_pA_n \qquad (9)$$

Combining (8) with (9), one obtains as a result, that

$$m = n \qquad (10)$$

The total number of cation sites (occupied and non-occupied) is thus equal to the number of anion sites. The compositions of adamantane-structure compounds are thus C_nA_n or $C_{n-p}\square_pA_n$, for normal and defect compounds, respectively. Inserting (10) into (7) and (5) gives

$$N_{NBO} = 4p/[(n-p)+n] = VEC - 4 \qquad \text{for } C_{n-p}\square A_n \qquad (11)$$

and finally

$$p/n = 2 - 8/VEC \qquad \text{for } C_{n-p}\square_pA_n \qquad (12)$$

This is the *adamantane-structure equation* (Parthé, 1987).

Depending on the value of VEC one can distinguish between normal and defect adamantane-structure compounds.

- If VEC < 4: an adamantane structure cannot be formed
- If VEC = 4: normal adamantane-structure compound with composition C_nA_n.
- If VEC > 4: defect adamantane-structure compound with composition $C_{n-p}\square_pA_n$.

Occasionally the adamantane-structure equation is expressed in a different form. Rewriting (12) as

$$[(2n-p)VEC]/2n = 4 \qquad (13)$$

and substituting VEC by

$$VEC \equiv [(n-p)e_C + ne_A]/[(n-p)+n] \qquad \text{for } C_{n-p}\square_pA_n \qquad (14)$$

leads to another form of the adamantane-structure equation:

$$[(n-p)e_C + p0 + ne_A]/[(n-p)+p+n] = 4 \qquad \text{for } C_{n-p}\square_pA_n \qquad (15)$$

where $(n-p)$ is the number of occupied Zn sites, p the number of unoccupied Zn sites, and n the number of S sites.

The ratio of the number of valence electrons of all atoms divided by the number of all atoms and vacancies is always 4 (Pamplin, 1960), or, expressed differently, provided one counts the vacancies as 'zero-valent' atoms, the value of 'VEC' is always 4.

4.3 The Upper VEC Boundary

Adamantane structures cannot exist with compounds where VEC < 4 because there are not enough valence electrons available for each atom to form four sp^3 hybrid orbitals. However, there also exists an experimental upper VEC limit above which an adamantane structure does not form. With the VEC value increasing above 4, more and more cation sites remain unoccupied and consequently the average number of anion–cation bonds per anion, labelled $NB_{A\to C}$, decreases. The value of $NB_{A\to C}$ can be expressed by

$$NB_{A\to C} = 4 - 4(p/n) = 4[(8/VEC) - 1] \qquad (16)$$

Simple solutions of (12) and (16) together with known examples are given in Table 1.

The experimentally observed upper VEC limit occurs at 4.92_3 where three out of eight cation sites are unoccupied and each anion has, on average, only 2.5 tetrahedral bonds to surrounding cations. This VEC limit results from studies by Radaoutsan (1964) on the solubility of $GeSe_2$ (VEC = 5.33_3), a defect tetrahedral but not an adamantane structure) in $Ga_2\square Se_3$ (VEC = 4.80, a defect adamantane structure), which terminates at $Ga_4Ge\square_3Se_8$ (VEC = 4.92_3).

For compounds with larger VEC values, so many cation sites would be unoccupied that the average number of anion–cation bonds extending from an anion would be less than 2.5; or, expressed differently, an anion

Table 1. Simple solutions of the adamantane-structure equation for different values of VEC, p/n, and $NB_{A\to C}$ together with known examples of compounds with adamantane structures

Formula	VEC	p/n	$NB_{A\to C}$	Examples
C_nA_n	4	0	4	Cu_2ZnGeS_4 [1_2246_4], LiSiNO [1456]
$C_7\square A_8$	4.26_7	1/8	3.5	$Hg_5Ga_2Te_8$ [$2_53_2\square 6_8$]
$C_5\square A_6$	4.36_4	1/6	3.33_3	$Hg_3In_2Te_6$ [$2_33_2\square 6_6$]
$C_3\square A_4$	4.57_1	1/4	3	$CdGa_2Se_4$ [$23_2\square 6_4$], $Cd_3(AsI_3)$ [$2_3\square(57_3)$]
$C_2\square A_3$	4.8	1/3	2.66_7	Ga_2Se_3 [$3_2\square 6_3$], Si_2N_2O [$4_2\square 5_26$]
$C_5\square_3A_8$	4.92_3	3/8	2.5	$(Ga_4Ge)Se_8$ [$(3_4)\square_36_8$]
'C $\square$ A_2'	5.33_3	1/2	2	Impossible

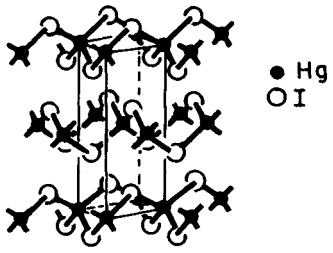

Figure 3. The layer structure of red HgI_2, which can be classified as a defect tetrahedral but not as defect adamantane structure (Parthé, 1990)

would have, on average more than 1.5 lone electron pairs attached to it. Owing to the mutual repulsion of the lone electron pairs, the few remaining anion–cation bonds often show a greater deviation from the ideal tetrahedral angle of 109.4°. Under these unfavorable circumstances, a wurtzite or sphalerite-related structure with a close-packed anion partial structure does not then form. Compounds with VEC > 4.92[3] may, however, crystallize with a defect tetrahedral structure.

One example is red HgI_2 with $VEC_A = 8$ and VEC = 5.333, shown in Figure 3. One recognizes slabs cut from the sphalerite structure; however, these slabs are not connected by covalent A–C–A bonds and are vertically and horizontally displaced with respect to each other. The layer structure of HgI_2 can thus not be considered as a sphalerite structure with cation vacancies. Nevertheless, it is a defect tetrahedral structure with $N_{NBO} = 4/3$ (two non-bonding orbitals on each iodine atom).

5. Compositions of Adamantane-Structure Compounds

The compositions of adamantane-structure compounds are controlled by the valence-electron rules given above and the valence-electron contribution of the elements.

Table 2. Elements found in adamantane-structure compounds and their valence-electron contribution

Number of valence electrons	B group elements	A and T group elements
1	Cu, Ag	Li
2	Zn, Cd	Be, Mg, Mn, Fe, Ni
3	B, Al, Ga, In	Fe
4	C, Si, Ge, Sn	
5	N, P, As, Sb	
6	O, S, Se, Te, Po	
7	Cl, Br, I	

The valence-electron numbers of the elements found in adamantane-structure compounds are listed in Table 2. They correspond (except for transition elements) to their group number in the periodic table of the elements. In the case of transition elements, where the valence-electron contribution can vary, magnetic measurements may permit the distinction between different valence states, such as between Fe^{2+} and Fe^{3+}.

To denote the compositions of adamantane-structure compounds, we shall not use the usual symbols of the chemical elements, but instead use numbers for them, which correspond to the number of valence electrons given in Table 2.

5.1 The Two Methods to Calculate Possible Compositions

There exist two methods to calculate the compositions of multicomponent adamantane-structure compounds: the cross-substitution method and the algebraic method.

5.1.1 The Cross-Substitution Method

The compositions of possible adamantane-structure compounds can be derived from the composition of an element with four valence electrons, such as diamond, by the repeated procedure called 'splitting.' This is the replacement of a pair of atoms of one kind by two different ones, one to the left and one to the right in the periodic table of elements, while keeping constant the ratio of number of valence electrons to number of atoms. The cross-substitution diagram or splitting diagram, shown in Table 3, is only one of the many possibilities. One can derive compositions not only of normal adamantane-structure but also of defect adamantane-structure compounds. In the latter case, one has to extend the list of valence-electron numbers by 0, an element with zero valence electrons being considered equivalent to a cation site vacancy □ in the structure.

5.1.2 The Algebraic Method

This method is best suited for a systematic search of all possible element combinations for a given general adamantane-structure composition. One looks for solutions of the adamantane-structure equation by systematically changing the valence-electron values of the atoms. In Table 5 a demonstration of the application of this method is given.

Table 3. Example of a cross-substitution or splitting diagram for the calculation of the compositions of adamantane-structure compounds together with known examples of normal and defect adamantane-structure compounds

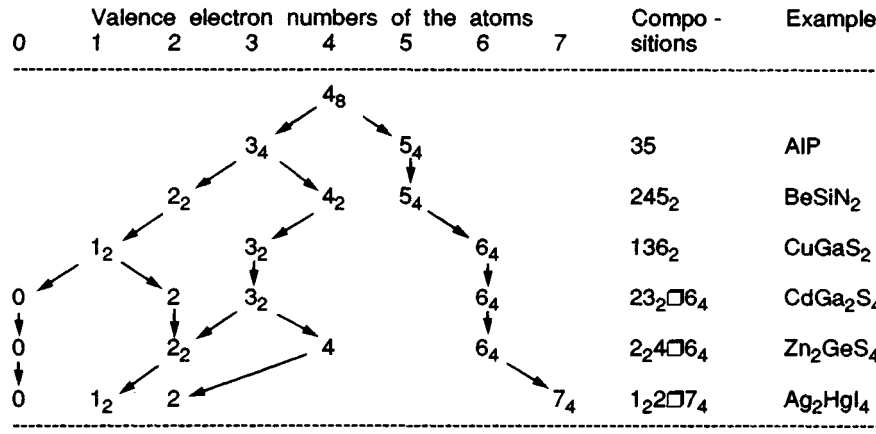

5.2 Binary Normal and Defect Adamantane-Structure Compounds

One first calculates the possible compositions of binary normal-valence compounds with $VEC_A = 8$ and then groups them according to their VEC value as shown in Table 4. Adamantane structures can occur only for $4 \leqslant VEC \leqslant 4.92_3$.

There exist four possible compositions for binary normal adamantane-structure compounds:

$$17, \quad 26, \quad 35, \quad 44 \tag{17}$$

and two for binary defect adamantane-structure compounds:

$$4_3 \square 5_4, \quad 3_2 \square 6_3 \tag{18}$$

5.3 Ternary Normal Adamantane-Structure Compounds

5.3.1 'Two-Cation' Compounds with Composition $C_{n-x}C'_xA_n$

The adamantane-structure equation (12) has for $p/n = 0$ the simple form

$$[(n-x)e_C + xe_{C'} + ne_A]/2n = 4 \quad \text{for } C_{n-x}C'_xA_n \tag{19}$$

which can be rewritten as

$$x/n = (8 - e_C - e_A)/(e_{C'} - e_C) \tag{20}$$

One calculates the values of x/n for all possible different values of $e_C < e_{C'} < e_A$. The results of the calculation are presented in Table 5. Of interest are the five solutions of x/n where $0 < x/n < 1$, which are printed in bold type. They correspond to the five possible compositions of 'two-cation' compounds:

$$14_25_3, \quad 245_2, \quad 136_2, \quad 1_246_3, \quad 1_356_4 \tag{21}$$

Table 4. Binary normal-valence compound compositions ordered according to their VEC value. Possible adamantane-structure compositions are printed in bold type

VEC	2.66_7	3.2	4	4.57_1	4.8	5.33_3
$e_A = 7$			**17**			27_2
$e_A = 6$	1_26		**26**		$3_2 \square 6_3$	46_2
$e_A = 5$		2_35_2	**35**	$4_3 \square 5_4$		
$e_A = 4$			**44**			

5.3.2 'Two-Anion' Compounds with Composition $C_nA_{n-y}A'_y$

The method described above can be modified to calculate y/n values. One finds thus the five possible compositions of 'two-anion' compounds:

$$3_34_27, \quad 3_246, \quad 2_257, \quad 2_347_2, \quad 2_437_3 \tag{22}$$

5.4 Multicomponent Adamantane-Structure Compounds

The compositions of possible quaternary (and more components) normal adamantane-structure compounds can be obtained by adding and subtracting the formulae listed in (17) and (21) or (22). The compositions of ternary (and more components) defect adamantane-structure compounds can be calculated by including also

Table 5. Values of x/n according to equation (20) for the calculation of the possible compositions of ternary normal adamantane-structure compounds of the 'two-cation' type

	$e_A=4$		$e_A=5$			$e_A=6$				$e_A=7$
	$e_{C'}=2$	$e_{C'}=3$	$e_{C'}=2$	$e_{C'}=3$	$e_{C'}=4$	$e_{C'}=2$	$e_{C'}=3$	$e_{C'}=4$	$e_{C'}=5$	
$e_C=1$	3/1	3/2	2/1	2/2	**2/3**	1/1	**1/2**	**1/3**	**1/4**	0
$e_C=2$		2/1		1/1	**1/2**		0	0	0	<0
$e_C=3$					0		<0	<0	<0	

the formulae of (18). The method is demonstrated by the following three examples, a quaternary normal and two defect ternary structures, respectively:

● LiSiNO [1456]

+2	6
$+1_4$	5_3
−24	5_2
14	56

● $Ag_2Hg\square I_4$ [$1_2 2\square 7_4$]

-1_4	7_4
$+3_2\square$	6_3
+2	6
$-1_2 3_2$	6_4
$1_2 2\square$	7_4

● $Ga_4Ge\square_3Se_8$ [$3_4 4\square_3 6_8$]

$+3_6\square_3$	6_9
$+1_2 4$	6_3
$-1_2 3_2$	6_4
$3_4 4\square_3$	6_8

The formulae (17), (18) and (21) or (22) can be added in any arbitrary proportion such as, for example:

$$(26)_{1-x}+(136_2)_x \equiv 1_x 2_{1-x} 3_x 6_{1+x}$$

or

$$(35)_{1-x}+(3_2\square 6_3)_x \equiv 3_{1+x}\square_x 5_{1-x} 6_{3x}$$

where $0 \leqslant x \leqslant 1$. As a result the compounds with quaternary normal and ternary defect adamantane structures are line compounds, their homogeneity range in the corresponding quaternary or ternary phase diagram consisting of a composition line.

Examples for quaternary line compounds of composition $1_x 2_{1-x} 3_x 6_{1+x}$ are the complete series of solid solutions ZnS–$CuGaS_2$ or $CdTe$–$CuInTe_2$ (Goryunova, 1965). Examples for ternary line compounds of composition $3_{1+x}\square x 5_{1-x} 6_{3x}$ are the complete series of solid solutions $GaAs$–Ga_2Se_3 or $InAs$–In_2Te_3 (Goryunova, 1965).

In Figure 4 are presented the composition lines for ternary adamantane structures in the 1–3–6, 2–3–6, and 3–4–6 ternary phase diagrams. One plots in a ternary diagram the line connecting points with $VEC_A=8$ and the lines corresponding to $VEC=4$ and $VEC=4.92_3$. Adamantane structures are found on the line for $VEC_A=8$ between the limits $4 \leqslant VEC \leqslant 4.92_3$. In most of these line compounds the cations and vacancies occupy the Zn sites in random fashion. With certain compositions, however, ordered structures may occur (as for example with $23_2\square 6_4$ $CdGa_2Se_4$ and $CdGa_2S_4$).

To obtain a quick idea if an adamantane structure would be possible and what its homogeneity range might be, one can make use of the master diagram (Parthé and

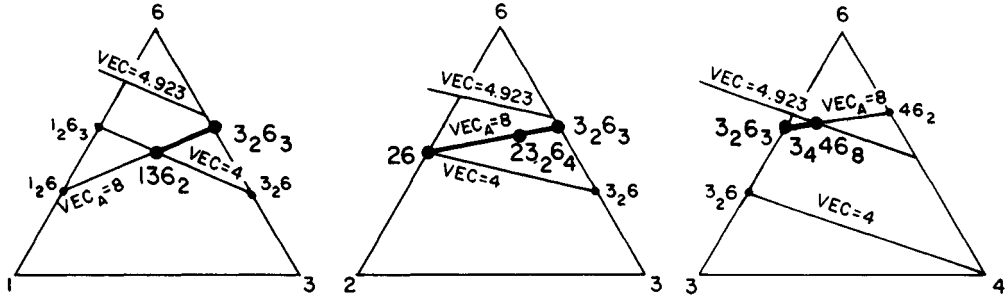

Figure 4. The homogeneity ranges of ternary defect adamantane-structure compounds in the 1-3-6, 2-3-6, and 3-4-6 phase diagrams. The linear composition ranges are indicated with thick lines. Compositions where ordered adamantane structures occur are written with bigger numbers

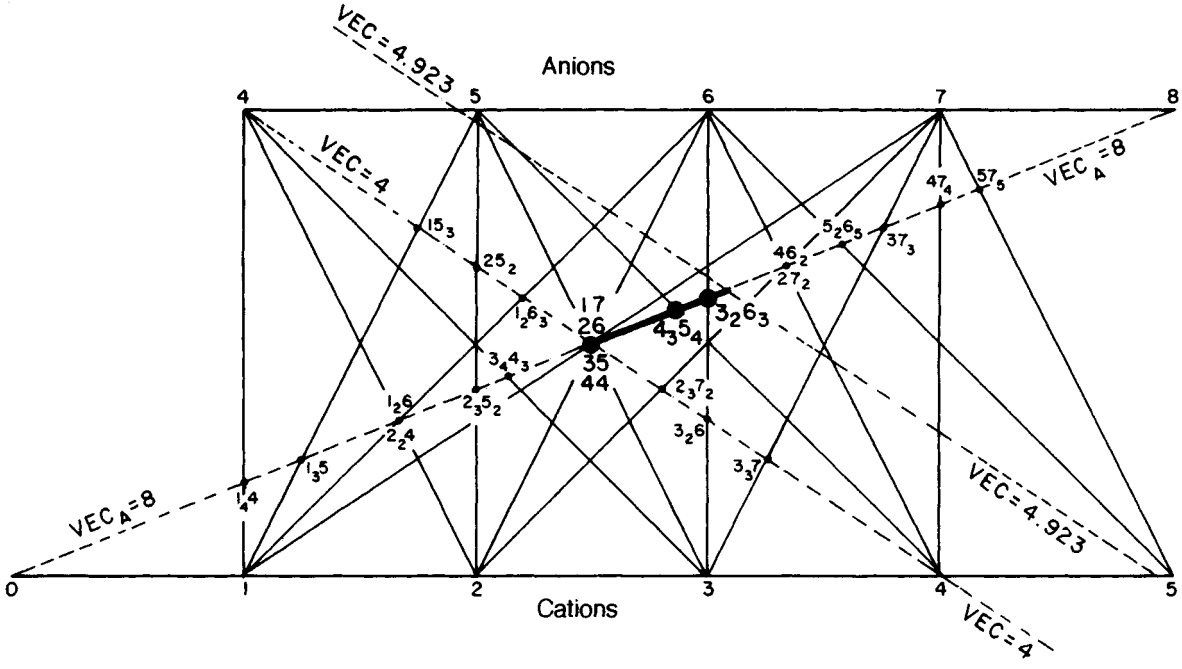

Figure 5. A master diagram to localize the possible homogeneity ranges of adamantane-structure compounds (modified after Parthé and Paufler, 1991)

Paufler, 1991) shown in Figure 5. The valence-electron numbers of the cations are given on the bottom line, those of the anions on the top line. By connecting appropriate points one obtains the triangle (in most cases, non equilateral) that corresponds to the ternary system of interest. Adamantane-structure compounds can be found only on the short thick line for which $VEC_A = 8$ and $4 \leqslant VEC \leqslant 4.92_3$. The following examples may demonstrate the use of the master diagram.

- System 2–3–7: An adamantane structure is not possible in this ternary system.
- System 1–3–5: An adamantane structure is possible only for a compound 35 that has no homogeneity range.
- System 2–4–6: A 'two-cation' adamantane structure is possible between 26 and $2_2 4_3 \square_3 6_8$ ($VEC = 4.92_3$, the upper limit of the short thick line where $p/n = 3/8$).
- System 3–4–5: A 'two-cation' adamantane structure might be possible on the tie line from 35 to $4_3 \square 5_4$.
- System 2–5–7: A 'two-anion' compound can occur on the composition line between $2_2 57$ ($VEC = 4$) and $2_5 \square_3 57_7$ ($VEC = 4.92_3$). The only known examples for compounds on this composition line are Cd_3PI_3 and Cd_3AsI_3 with disordered defect wurtzite structure (Rebbah *et al.*, 1981), and Zn_3PI_3 and Zn_3AsI_3 with disordered defect sphalerite structure (Suchow *et al.*, 1963).

Given that adamantane-structure compounds must lie along the short thick line of Figure 5, several classes of multicomponent solid solutions meet the requirements. The more elements with different valence electrons are involved, the more complicated becomes the shape of the possible homogeneity region (points → lines → planes→tetrahedra. . .). For an example, see the results of the system $InAs–ZnGeAs_2–CuInSe_2–Cu_2GeSe_3$, studied by Pamplin and Hasoon (1985). Only a few of the possible multicomponent solid solutions have been investigated in detail. However, tests have been made with selected single multicomponent compositions. For example, the seven-component compound $Cu_{11.5}Zn_{23}Ga_{7.5}Ge_8As_{16}Se_{30}Br_4$ where $VEC = 4$ and $VEC_A = 8$ crystallizes with a disordered zinc-blende structure (Parthé, 1972).

It should be emphasized that the valence-electron rules relate to the theoretically possible composition limits of adamantane-structure compounds. Depending on the system of interest, there may occur other competing, thermodynamically very stable compounds, as a

consequence of which the otherwise expected adamantane-structure compound either does not appear or its homogeneity range does not reach the lower and/or upper VEC limit. As discussed below, the tendency to form adamantane-structure compounds decreases if the elements are from high periods and the compounds become more metallic. It should also be remarked that the adamantane-structure compounds with their covalent bonds have, in the solid state, very small diffusion rates and the annealing time needed to obtain equilibrium may be extremely long (six months for certain compounds, after Woolley (1964)). There are known examples in the literature where the originally published solubility limits were later found to be too small because the time used for homogenizing the specimens had been too short.

5.5 Tolerated Deviations from the Expected VEC and VEC_A Values

Minimal deviations of the compositions from the expected theoretical VEC and VEC_A values in the range of $\Delta VEC/VEC \simeq \Delta VEC_A/VEC_A \simeq 10^{-4}$ can be tolerated without a destabilization of the crystal structure. The excess or deficiency of valence electrons provokes pronounced changes in the electrical and/or optical properties of the compounds. This has been confirmed, for example, for $CuInSe_2$ [$1_3 6_2$], where annealing either under maximum or under minimum Se pressure allows the conductivity to switch from p type to n type (Massé and Redjai, 1986).

The deviations from the ideal VEC value are very small indeed. The studies of the homogeneity range of GaP [35] by Jordan *et al.* (1974) serve as an example. At 1000°C the composition of the Ga-rich side of the homogeneity range is $Ga_{0.5001}P_{0.4999}$ (VEC = 3.9998) and, close to the melting point, $Gd_{0.5002}P_{0.4998}$ (VEC = 3.9996), while the composition of the P-rich side is $Ga_{0.5000}P_{0.5000}$ (VEC = 4) for both temperatures. This means that $\Delta VEC/VEC$ has values of 0.5×10^{-4} and 1.0×10^{-4}, respectively. In a more recent study of GaAs (Sajovec *et al.*, 1990), it was found that the maximum surplus of native interstitial defects over vacancy defects is about 5×10^{-5} defects per structure site.

For compounds where larger deviations in composition had been initially reported, it was shown later either that the composition stated was not correct or that the structure was not really an adamantane structure. An example is the compound 'Cu_2SnSe_4' with disordered sphalerite structure (Bok and deWit, 1963). Since $VEC = 4.28_6$ and $VEC_A = 7.5$, a compound with this composition should not crystallize with an adamantane structure. It appears very probable that 'Cu_2SnSe_4' is in reality identical with Cu_2SnSe_3 [$1_2 4 6_3$] where VEC = 4 and $VEC_A = 8$ (Rivet *et al.*, 1970). Assuming that the latter compound has a homogeneity range, expressed by $Cu_2Sn_{1+y}Se_{3+2y}$ [$1_2 4_{1+y} \square_y 6_{3+2y} \equiv (1_2 4 6_3)_{1+y} + (3_2 \square 6_3)_y - (136_2)_{2y}$; $0 \leqslant y \leqslant 4.5$], a possible adamantane-structure composition, closest to that reported by Bok and de Wit, would be $Cu_2Sn_{1.5}Se_4$ [$1_2 4_{1.5} \square_{0.5} 6_4$] with $VEC = 4.26_7$ and $VEC_A = 8$.

The only adamantane-structure compound that does not obey the rules in the normal way is the recently reported $NiSi_3P_4$ with famatinite Cu_3SbS_4 type, an ordered substitutional variant of the sphalerite type (Il'nitskaya *et al.*, 1991). The formation of an adamantane structure can be understood if one assumes that the Ni atoms do not contribute any valence electrons to the tetrahedral sp^3 hybrid bonds between the atoms. This $4_3 05_4$ compound should be a topic of further studies.

6. Ordered Adamantane-Structure Types

A list of completely determined adamantane-structure types, based on wurtzite and sphalerite, is given in the appendix (Section 10.2). Here we only discuss and present drawings of the most common ordered structure types.

6.1 Binary Adamantane-Structure Types

6.1.1 Binary Normal Adamantane-Structure Types

Binary normal adamantane-structure compounds with compositions as given by (17) adopt the wurtzite or the sphalerite-type structure (see Figure 1) or a stacking variant. The ideal c/a ratio of a wurtzite-type structure has according to (2) the value of $2(2/3)^{1/2} = 1.63_3$. The actual measured c/a values range from 1.60_0 (for AlN) to 1.65_6 (for BP). Fleet (1976) has shown that wurtzite-type compounds are stable relative to the sphalerite type when $c/a < 1.63_3$, but unstable when $c/a > 1.63_3$.

The question of the relative stability of the wurtzite and the sphalerite type is a recurring one, which is still waiting for an answer. O'Keeffe and Hyde (1978) pointed out that, in compounds which crystallize only with the wurtzite type (but not the sphalerite type), the cation–cation distance is close to the sum of the non-bonded radii and concluded that the existence of only a wurtzite-type structure was due to this fact.

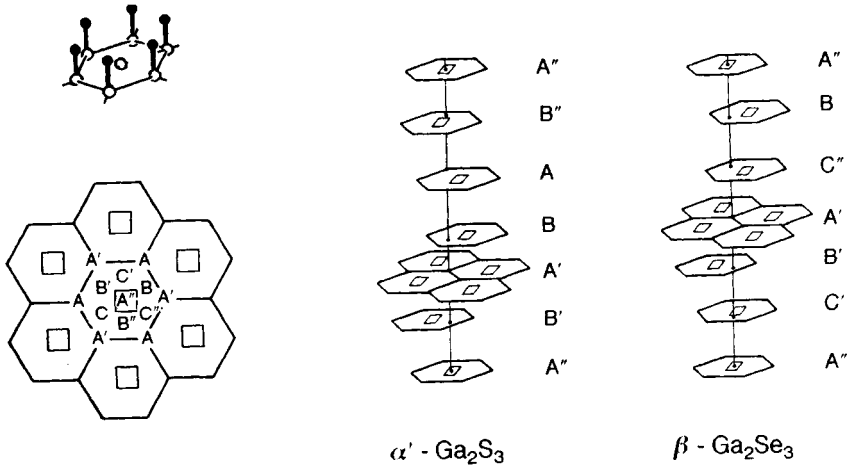

Figure 6. Two ordered binary defect adamantane-structure compounds with composition $3_2\square 6_3$. The defect ZnS slab, the stacking positions, and the slab stacking in α'-Ga_2S_3, and β-Ga_2Se_3, the first related to wurtzite and the second to sphalerite (Parthé, 1987; modified after Ollitrault-Fichet *et al.*, 1980; reproduced by permission of Academic Press, Orlando, FL)

6.1.2 Binary Defect Adamantane-Structure Types

As examples of types of binary defect adamantane-structure compounds, we show in Figure 6 schematic drawings of the structures of two $3_2\square 6_3$ compounds, α'-Ga_2Se_3 and β-Ga_2Se_3 (Ollitrault-Fichet *et al.*, 1980; Ghémard *et al.*, 1983). These structures can be described by a stacking of identical defect-ZnS-type slabs with ordered Zn site vacancies, that is, every third Zn site not being occupied. In the upper left corner of Figure 6 is shown a segment of such a defect slab where, for

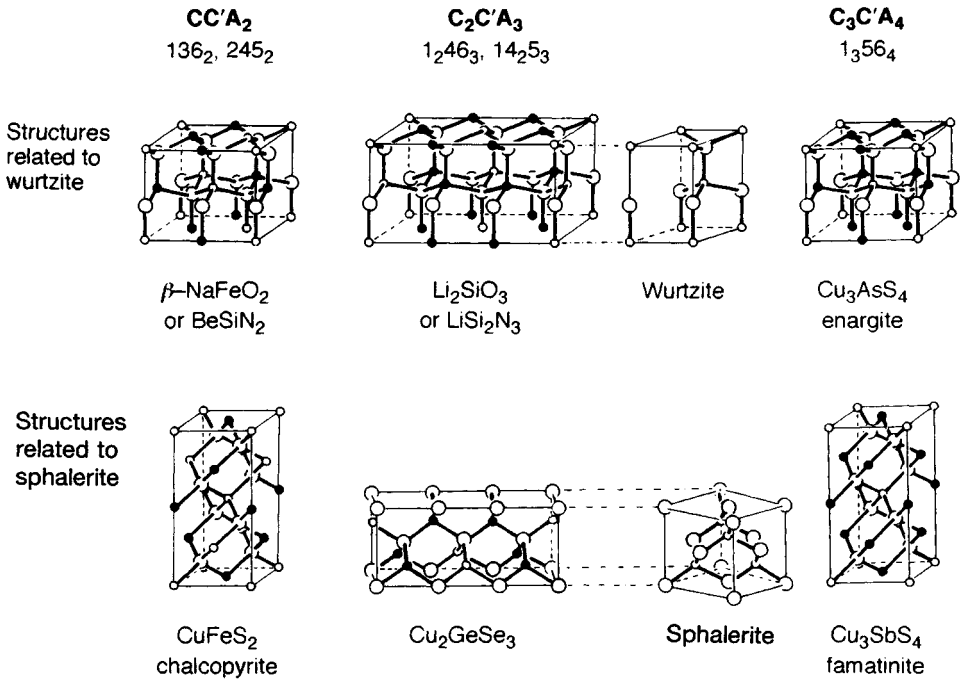

Figure 7. Six ternary normal adamantane-structure types. Cations are represented by small circles (modified after Parthé, 1987)

reasons of simplicity, the upper anion layer has been left out. The possible stacking positions of the defect-ZnS-type slabs are indicated in the diagram on the lower left of Figure 6. The corners of the hexagons correspond to the cation sites in the A″ slab, which are occupied, while the squares with A″ inscribed correspond to cation sites in the A″ slab, which are not occupied. The letters denoting the stacking positions, A, B, and C, are unprimed, primed or double-primed to characterize the six relative positions of the cation site vacancy. The drawings on the right indicate the stacking of these defect slabs in α'-Ga_2S_3 and β-Ga_2Se_3. The primes and double primes can be ignored if one simply wants to know the overall stacking, which is AB in α'-Ga_2S_3 and ABC in β-Ga_2Se_3. The ZnS base structures are thus wurtzite and zinc blende, respectively.

Adamantane-structure compounds of composition $3_2 \square 6_3$ that are more metallic (having elements from higher periods), such as In_2Te_3, have disordered structures, which means that vacancies and cations occupy the available cation sites at random.

6.2 Ternary 'Two-Cation' Normal Adamantane-Structure Types

The five possible compositions given by (21) can be separated into three groups according to the ratio C:C′ of the two kinds of cations:

$$CC'A_2, \quad C_2C'A_3, \quad C_3C'A_4$$

For each group, wurtzite- and sphalerite-related ordered ternary structure types are known (Parthé and Garin, 1971) and are shown in Figure 7. In principle, the same structure types could be adopted by ternary ordered 'two-anion' normal adamantane-structure compounds, for which the possible compositions are given by (22); however, no such compounds are known.

Pauling's electrostatic valence rule serves as a first guide in understanding the order of the atoms and vacancies on the structure sites of wurtzite and sphalerite. It postulates the preferred occurrence of an atom arrangement where the sum of the bond strengths (emanating from the surrounding cations) agrees with the formal charge of the anion.

As an example one may consider the β-$NaFeO_2$ structure, shown in the upper left part of Figure 7. Pauling's postulate is satisfied with the atom arrangement shown. It is possible to imagine an arrangement with a different atom order requiring a much smaller unit cell where all cations represented by small open circles are at $z = 0$ and all cations indicated with small filled circles at $z = 1/2$. This hypothetical structure will not be found in Nature because it violates Pauling's rule.

Pauling's postulate is, however, not infallible. For certain compositions Pauling's rule cannot be satisfied exactly, as for example the Li_2SiO_3 and Cu_2GeSe_3 types, shown in the middle part of Figure 7. In these cases a selective shortening or elongation of certain tetrahedral bonds may achieve a better effective valence balance. For more details, particularly with reference to wurtzite-derivative structures, see Baur and McLarnan (1982).

A modification of Pauling's rule by the bond-valence concept (O'Keeffe, 1989) allows the calculation of structural details. As an example, we consider the supposedly isotypic structures of Li_2SiO_3 and $LiSi_2N_3$. A detailed study of these two structures shows that the tetrahedra are deformed, but in Li_2SiO_2 and $LiSi_2N_3$ in different ways (for example, three short and one long Li–O, but one short and three long Si–N distances). These differences in the distances within a given

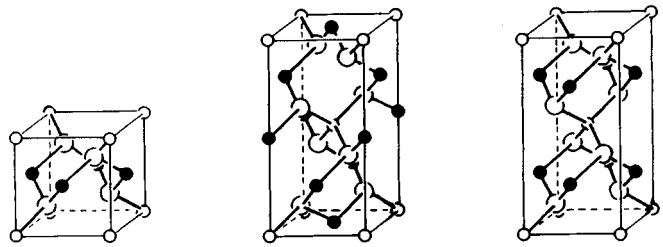

Figure 8. Three ternary ordered defect adamantane-structure types of composition $C_2C' \square A_4$, which are substitutional and vacancy derivatives of the sphalerite structure. Cations are represented by small circles, of which one-third are empty and two-thirds filled (Parthé, 1972)

tetrahedron are to be expected according to the bond-valence concept. The two structures are thus not isotypic in a rigorous sense, but constitute two branches of a common hypothetical structure type with undeformed tetrahedra.

6.3 Ternary Defect Adamantane-Structure Types

Ternary defect adamantane-structure compounds are, in general, line compounds. However, if the ratio of vacant to occupied cation sites has been specified, only discrete compositions are possible.

6.3.1 Structure Types of 'Two-Cation' Compounds with Composition $C_2C' \square A_4$

Since $p/n = 1/4$ these structure types can occur only with compounds for which VEC $= 4.57_1$. Using the algebraic method, one finds three possible compositions for $C_2C' \square A_4$ compounds:

$1_2 2 \square 7_4$, $2_2 4 \square 6_4$, $23_2 \square 6_4$

In Figure 8 three $C_2C' \square A_4$ structure types are shown that are vacancy and substitutional variants of the sphalerite type and where Pauling's electrostatic valence rule is satisfied. The most common structure type is the thiogallate $CdGa_2S_4$ (or β-Ag_2HgI_4) type, which is found not only with $1_2 2 \square 7_4$ and $23_2 \square 6_4$ but also with $2_2 4 \square 6_4$ compounds such as Hg_2GeSe_4 and Hg_2SnSe_4 (Motrya *et al.*, 1986). Also a wurtzite-related type exists, which has been found with β-$ZnAl_2S_4$ HT.

If the small circle in the center of the drawing of the β-Cu_2HgI_4 cell is filled, one has obtained a drawing of the structure of $AgIn_5Se_8$, an ordered $13_5 \square_2 6_8$ compound, which can thus be considered as an ordered cation substitution variant of β-Cu_2HgI_4.

6.3.2 Structure Type of 'Two-Anion' Compound with Composition $C_2 \square A_2A'$

For $p/n = 1/3$ and VEC $= 4.8$ three compositions are possible:

$2_2 \square 67_2$, $3_2 \square 47_2$, $4_2 \square 5_2 6$

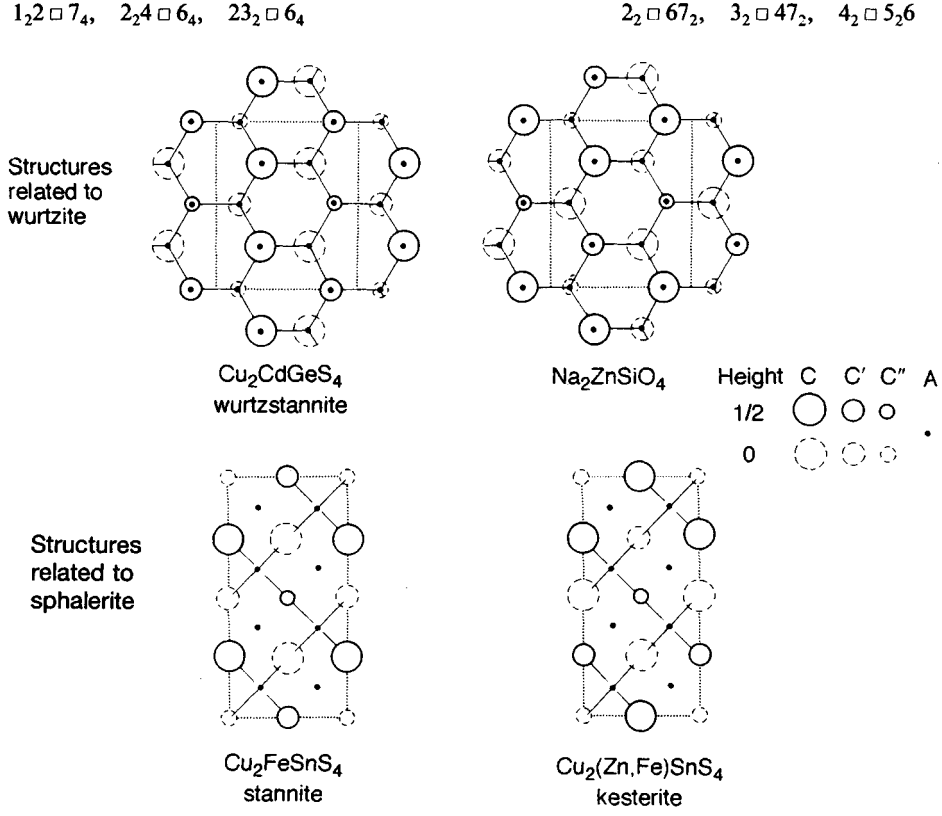

Figure 9. Cation ordering in two wurtzite- and two sphalerite-related quaternary normal adamantane-structure types of composition $C_2C'C''A_4$. Projection is along the shortest axis

An ordered ternary structure type based on wurtzite has been reported for Si_2N_2O.

6.4 Quaternary 'Three-Cation' Normal Adamantane-Structure Types of Composition $C_2C'C''A_4$

The 'three-cation' normal adamantane-structure compounds are in general also line compounds. However, if the composition has been specified as $C_2C'C''A_4$, there exist only four solutions of the adamantane-structure equation, which correspond to the compositions:

$$1_2246_4, \quad 12_236_4, \quad 23_245_4, \quad 134_25_4$$

The theoretically possible ordered structured types have been studied by Parthé *et al.* (1969), McLarnan and Baur (1982), and Baur and McLarnan (1982). Four structure types, which have been determined by X-ray diffraction studies, are presented in Figure 9 in a schematic way. Two are derived from wurtzite and two from sphalerite. Pauling's electrostatic valence rule is satisfied by all of them.

Most of the experimental studies were centered on the 1_2246_4 compounds (Schäfer and Nitsche, 1974, 1977; Guen *et al.*, 1979; Lamarche *et al.*, 1991). Some of the compounds of this family seem to be promising material for nonlinear optics. Only scarce information is available on the possible 134_25_4 compound $CuGaGe_2P_4$. 12_236_4 compounds, such as $AgCd_2InTe_4$ (Parthé *et al.*, 1969), and 23_245_4 compounds, such as $ZnIn_2GeAs_4$ (Pamplin and Hasoon, 1985), exist and are known to have sphalerite (or wurtzite) diffraction patterns. It appears that ordered quaternary structure types do not occur with these compounds. $ZnIn_2GeAs_4$ is just one point on the tie line between InAs and $ZnGeAs_2$, which form a complete series of solid solutions. However, since the formation of adamantane-structure compounds, as stated above, is not free of kinetic problems, it is doubtful that the reported results correspond in all cases to equilibrium conditions. Thus one cannot state with certainty that an ordered atom arrangement never forms. In addition, not powder but single-crystal diffraction experiments would be required for the study of the structure details.

6.5 Example for an Ordered 'Two-Cation' and 'Two-Anion' Normal Adamantane-Structure Type with Composition $CC'AA'$

For this composition there exist five possibilities:

$$1456, \quad (2356), \quad 2347, \quad (1357), \quad (1267)$$

Of particular interest are the two compositions without surrounding parentheses, which do not correspond to a mixture of binary normal adamantane structures. An ordered wurtzite-based quaternary structure type is known for α-LiSiNO. Compounds with sphalerite structure such as CuGePS are known, but they are not ordered (see Pamplin, 1987).

6.6 Quaternary 'Three-Cation' Defect Adamantane-Structure Compounds of Composition $CC'C''\square A_4$

For this general formula there exist only two particular compositions that agree with the adamantane-structure equation:

$$134\square 6_4, \quad 125\square 6_4$$

The composition $345\square 5_4$ is not included here since we restrict ourselves to solutions where the atoms that serve as cations have fewer valence electrons than the atoms we consider as anions. Adamantane-structure compounds are known only for the composition $134\square 6_4$, such as $AgInSnSe_4$ (Hughes *et al.*, 1980). These compounds are reported to have a partially disordered chalcopyrite structure. According to Pauling's electrostatic valence rule, one should expect an ordered crystal structure that is a cation ordering variant of the thiogallate $CdGa_2S_4$ type. An ordered wurtzite-related defect adamantane structure compound of composition $125\square 6_4$ is known for $AgZnPS_4$.

7. Additional Experimental Rules for Adamantane-Structure Compounds

It has been shown above how the possible compositions of adamantane-structure compounds can be calculated using the adamantane-structure equation. However, this valence-electron rule is a necessary but not a sufficient condition for the occurrence of an adamantane structure. Compounds are known for which the adamantane-structure equation is satisfied, but the observed structures are not adamantane structures. One simple example is NaCl (VEC = 4 and $VEC_A = 8$), which does not adopt a normal adamantane structure.

To predict whether a compound (with a permitted composition) will actually crystallize with an adamantane structure, one can make use of one of several structure separation plots. In each plot one finds an area where adamantane structures should occur and other regions

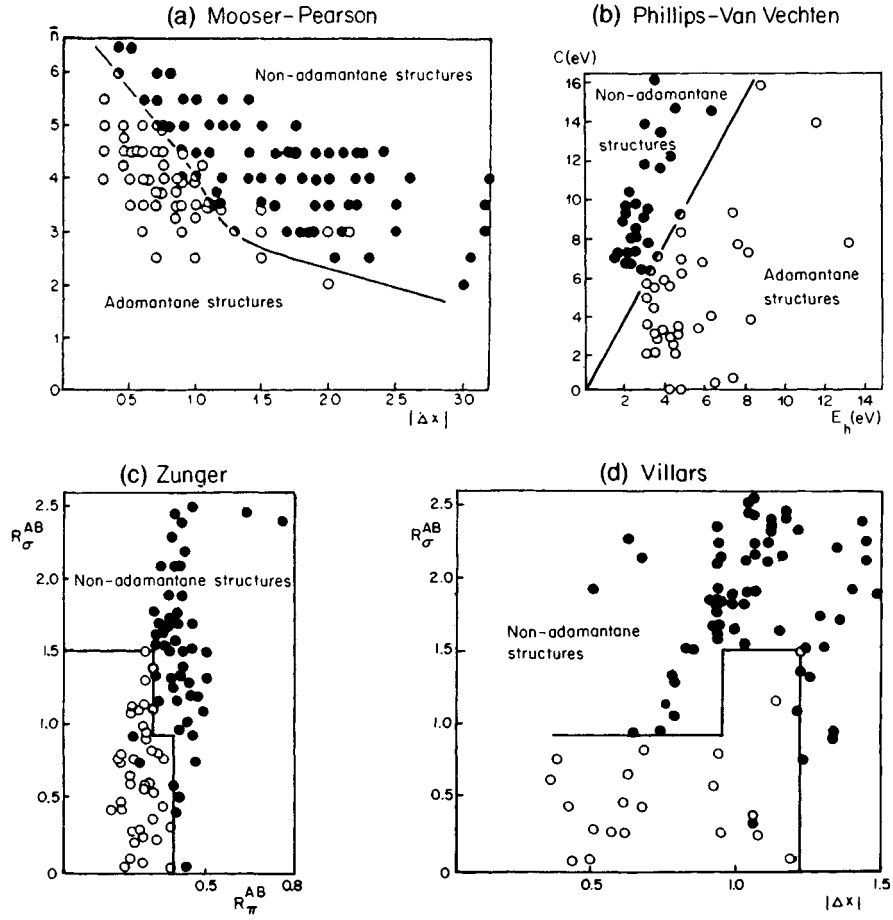

Figure 10. Structure separation plots for binary equiatomic normal-valence compounds according to (a) Mooser and Pearson, (b) Phillips and Van Vechten, (c) Zunger, and (d) Villars. Points corresponding to adamantane structures are indicated with open circles, those of non-adamantane structures with filled circles (modified after Parthé, 1987; reproduced by permission of the Materials Research Society, Pittsburgh)

where the formation of such a structure is unlikely. We shall restrict ourselves to a presentation of four structure separation plots (shown in Figure 10), which are all applicable to binary equiatomic normal-valence compounds.

Mooser and Pearson (1959) were the first to present such a plot. They use as ordinate $\bar{n}$, the average principal quantum number of the participating elements, and as abscissa $|\Delta x|$, the magnitude of the difference of Pauling's electronegativity values. A Mooser–Pearson $\bar{n}$ vs. $|\Delta x|$ plot for AB compounds with $VEC_A = 8$ is shown in Figure 10(a). This plot is based on the observation that the tendency to form directional bonds (as they occur in tetrahedral structures) decreases with the following:

- An increase of $\bar{n}$. With elements of higher periods a 'dehybridization' or 'metallization' occurs. The d and f orbitals now have an energy that is comparable with that of the s and p orbitals and the first two may form non-tetrahedral combinations with the s and p orbitals.
- An increase of $|\Delta x|$. The electrons now prefer to remain with the strongly electronegative element and do not participate any more in the formation of sp^3 orbitals.

Phillips and Van Vechten (see Phillips, 1981) base their plot on two parameters that can be obtained from the measurements of the optical absorption spectra of

the compounds and of the elements with a diamond structure. They use as ordinate C, the average ionic energy gap, and as abscissa E_h, the average homopolar energy gap. In the C vs. E_h structure separation plot after Phillips and Van Vechten, shown in Figure 10(b), the same compounds are considered as in Figure 10(a). There is a clear separation between adamantane- and non-adamantane-structure compounds; however, the energy gap of a compound has to be measured before a prediction of its crystal structure can be made.

Zunger (1980, 1981) calculates (density-functional) pseudopotential p- and s-orbital radii of the atoms. For his structure separation diagram of AB compounds, he uses as ordinate the difference between the total effective core radii of atoms A and B according to

$$R_\sigma^{AB} = |(r_p^A + r_s^A) - (r_p^B + r_s^B)| \qquad (23)$$

and as abscissa the sum of the 'orbital non-locality' of the s and p electrons on each site according to

$$R_\pi^{AB} = |r_p^A - r_s^A| + |r_p^B - r_s^B| \qquad (24)$$

A structure separation diagram R_σ^{AB} vs. R_π^{AB} for binary equiatomic normal-valence compounds is shown in Figure 10(c).

Villars (1983) uses for his structure stability diagrams three parameters: R_σ^{AB}, the difference of Zunger's pseudopotential radius sums as defined by (23); $|\Delta x|$, the magnitude of the difference of the Martynov–Batsanov electronegativity values of the participating atoms; and finally the sum of the number of valence electrons. Villars' R_σ^{AB} vs. $|\Delta x|$ diagram for compounds with eight valence electrons is presented in Figure 10(d). A more elaborate method has recently been described by Villars *et al.* (1989).

8. Concluding Remarks

It has been demonstrated how the adamantane-structure equation can be applied to predict possible adamantane-structure compositions. Using the structure separation plots, one can foresee whether the formation of an adamantane structure is likely or not. Many adamantane-structure compounds are already known. But there should exist many more; and, since systematic studies of those with more unusual compositions have been made only in part, it would be worth while to do this work. The adamantane-structure equation will certainly prove to be a valuable guide to searching and for what to expect when such experimental investigations are carried out. However, there also remain some theoretical questions which still have not been answered satisfactorily, such as the choice of the wurtzite or sphalerite base type. A new approach is needed here to find a solution to the problem.

9. Acknowledgements

The author thanks Ms Christine Boffi for her help with the typing of the manuscript and Ms Birgitta Künzler for help with the preparation of the drawings. This study was supported by the Swiss National Science Foundation under contract 20-28490.90 and the Alfred and Hilde Freissler Stiftung.

10. Appendix

10.1 Stacking Notations and Space Groups of ZnS and SiC Polytypes

10.1.1 Stacking Notations for Polytypes

Ramsdell notation The notation consists of a number corresponding to the number of slabs in the hexagonal or triple-hexagonal cell and a letter that indicates the crystal system (H = hexagonal, R = rhombohedral, that is trigonal with R Bravais lattice, T or L = trigonal with P Bravais lattice, C = cubic). The Ramsdell notation for the five polytypes presented in Figure 2 is listed there in the top row of text. This notation is not unambiguous since, for the case of polytypes with a higher number of slabs, differently stacked polytypes may have the same Ramsdell stacking symbol.

ABC notation Starting from the first slab in position A, one denotes the two other possible stacking positions by B and C. The slab stacking sequence in the structure is then expressed by a sequence of capital letters. In the ZnS and SiC polytypes, as in all close-packed structures, two successive layers cannot have the same stacking position letters. The notation is unambiguous (except for a permutation of the stacking letters); however, it is too cumbersome for the notation of very complicated stackings. Examples are shown in Figure 2.

Jagodzinski–Wyckoff notation The notation consists of a sequence of small letters, h and c, which are assigned to each slab depending on the sideways displacement of its two neighboring slabs, the one above and the one below. h is assigned to each slab where the

two neighboring slabs are displaced sideways in the same direction, and c to each slab where the two neighboring slabs are displaced sideways in different directions. The minimal h,c sequence (often by a factor of 2 or 3 shorter than the A,B,C sequence) is occasionally supplemented by an added subscript number, which, when multiplied by the number of h and c symbols within the parentheses, gives the number of slabs in one hexagonal or triple-hexagonal unit cell. Examples are given in the third row from the bottom in Figure 2.

Zhdanov notation In this notation one finds a sequence of numerals, each of which represents the number of repetitions or successions of slabs with a given sign for the sideways displacement of subsequent slabs, while the succeeding numeral represents the number of successions of opposite sign. Examples are found in the second row from the bottom in Figure 2. The Zhdanov stacking symbol can be obtained from the Jagodzinski-Wyckoff symbol as follows: The Jagodzinski-Wyckoff stacking symbol is divided into sections. Each section starts with the letter h. The numbers of letters in each section corresponds to the numerals of the Zhdanov stacking symbol.

10.1.2 Space Groups of ZnS and SiC Polytypes

The ZnS polytypes are non-centrosymmetric and have, except for cubic zinc blende, trigonal or hexagonal symmetry (space groups P3m1, R3m or $P6_3mc$). In order to find the proper trigonal or hexagonal space group of a ZnS or SiC polytype for which the minimal Zhdanov stacking formula $k_a l_b m_c \ldots$ is known, one needs to calculate three values:

- $N(=a+b+c+\ldots)$, the number of numerals in the minimal period,
- $s\ (=ak+bl+cm+\ \ldots\ )$, the normal sum of all numerals in the minimal period, and
- $\Sigma\pm$, the alternative sum of the numerals in the minimal period, i.e. the difference between the number of positive and negative displacements.

The space group and the Ramsdell symbol of the polytype can then be obtained from Table 6. Note that

Table 6. The space group and Ramsdell symbol of ZnS and SiC polytypes

N	$\Sigma\pm$	Space group	Ramsdell symbol
Odd	-	(186) $P6_3mc$	$2s$ H
Even	$3n\pm1$	(160) R3m	$3s$ R
Even	$3n$	(156) P3m1	s T

Table 7. Normal adamantane-structure types: $p/n=0$ and VEC = 4

Wurtzite-related types	Sphalerite-related types
CA	
ZnS, wurtzite hP4 (186) $P6_3mc$-b^2 SB1, 78 (see Figure 1)	ZnS, sphalerite cF8 (216) F-43m-*ca* SB1, 76 (see Figure 1)
CC'A$_2$	
β-$NaFe^{3+}O_2$ (or $BeSiN_2$) oP16 (33) $Pna2_1$-a^4 SR 18, 422; SR 32A, 28 (see Figure 7)	$CuFe^{3+}S_2$, chalcopyrite tI16 (122) I-42d-*dba* SB1, 279 see (Figure 7)
C$_2$C'A$_3$	
Li_2SiO_3 (or Cu_2SiS_3 HT or $LiSi_2N_3$) oS24 (36) $Cmc2_1$-b^2a^2 SR 37A, 74; SR 48A, 335; David (see Figure 7)	Cu_2GeSe_3 oI12 (44) Imm2-d^2ba SR37A, 73 (see Figure 7) *
C$_3$C'A$_4$	
Cu_3AsS_4, enargite (or Li_3PO_4 LT) oP16 (31) $Pmn2_1$-b^2a^4 SR 35A, 19; SR 32A, 355 (see Figure 7)	Cu_3SbS_4, famatinite tI16 (121) I-42m-*idba* SR 38A, 15 (see Figure 7)
C$_2$C'C''A$_4$	
Cu_2CdGeS_4, wurtzstannite (or Cu_2CdSiS_4) oP16 (31) $Pmn2_1$-b^2a^4 SR 34A, 47; SR 38A, 54 (see Figure 9)	$Cu_2Fe^{2+}SnS_4$, stannite tI16 (121) I-42m-*idba* SB3, 96 (see Figure 9)
Na_2ZnSiO_4 (or Li_2BeSiO_4, liberite) mP16 (7) Pc-a^8 SR 31A, 230; Joubert (see Figure 9)	$Cu_2(Zn,Fe^{2+})SnS_4$, kesterite tI16 (82) I-4-*gdcba* SR 44A, 56 (see Figure 9)
β-$Li_2Co^{2+}SiO_4$ oP32 (33) $Pna2_1$-a^8 SR 45A, 364	
Na_2MgSiO_4 mP32 (7) Pc-a^{16} SR 48A, 337	
C$_4$C'$_2$C''A$_7$	
$Cu_4Cu^{2+}Si_2S_7$ mS56 (6) Cc-a^{14} SR 49A, 26	$Cu_4Ni^{2+}Si_2S_7$ mS28 (5) C2-c^6ba SR 46A, 64
CC'AA'	
α-LiSiNO (or ZnAlNO) oP16 (29) $Pca2_1$-a^4 SR 46A, 137; Hyde	

References: *
David = David *et al.* (1973)
Joubert = Joubert-Bettan *et al.* (1969)
Hyde = Hyde *et al.* (1981)
SB = *Strukturbericht*
SR = *Structure Reports*

Table 8. Defect adamantane-structure types: $p/n > 0$ and VEC > 4

Wurtzite-related types	Sphalerite-related types
$C_{16.67}C'_{14}\square_{1.33}A_{32}$ ($p/n = 0.0417$, VEC = 4.085)	$Cu_{14}In_{16.67}Se_{32}$ cP63 – 0.64 (215) P-43m–i^4e^2dca SR 56A, 51
$C_{1.203}C'_{0.39}\square_{0.407}A_2$ ($p/n = 0.2035$, VEC = 4.453)	$Cu_{0.39}In_{1.203}Se_2$ tP16 – 3.02 (112) P-42c–*nfedb* SR 55A, 57
$C_2C'\square A_4$ ($p/n = 0.25$, VEC = 4.571)	
β-$ZnAl_2S_4$ HT oP32-4 (33) $Pna2_1$–a^8 SR 32A, 13	$CdIn_2Se_4$ tP7 (111) P-42m–*nfa* SR 19, 416 (see Figure 8)
	$CdGa_2S_4$, thiogallate (or β-Ag_2HgI_4) tI14 (82) I-4–*gcba* SR 19, 414; SR 40A, 157 (see Figure 8)
	β-Cu_2HgI_4 tI14 (121) I-42m–*ida* SB 2, 50,331 (see Figure 8)
$(C_2C')\square A_4$ ($p/n = 0.25$, VEC = 4.571)	$(MnIn_2)Te_4$ (or $(ZnIn_2)Se_4$) tI14 (121) I-42m–*ida* SR 41A, 79
$CC'C''\square A_4$ ($p/n = 0.25$, VEC = 4.571)	
$AgZnPS_4$ oP32 (33) $Pna2_1$–a^8 SR 52A, 77	
$C_5C'\square_2A_8$ ($p/n = 0.25$, VEC = 4.571)	$AgIn_5Se_8$ tP14(111)P-42–n^2ba SR 50A, 44
$C_2\square A_3$ ($p/n = 0.333$, VEC = 4.8)	
α'-Ga_2S_3 (or Al_2Se_3) mS20 (9) Cc–a^5 SR 19, 404; SR 31A, 17 (see Figure 6)	β-Ga_2Se_3 mS20 (9) Cc–a^5 SR 50A, 35 (see Figure 6)
α-Al_2S_3 hP30 (169) $P6_1$–a^6 Eisenmann	
B_2O_3 II HP oS20 (36) $Cmc2_1$–b^2a SR 33A, 259	
$C_2\square A_2A'$ ($p/n = 0.333$, VEC = 4.8)	
Si_2N_2O oS20 (36) $Cmc2_1$–b^2a SR29, 244; Sjöberg	

References: Eisenmann = Eisenmann (1992); Sjöberg = Sjöberg *et al.* (1991); SB = + *Strukturbericht*; SR = *Structure Reports*

s, 2*s* and 3*s* stand for numbers that can be obtained from the equation for *s* given above.

Example Besides rhombohedral ZnS 12R with stacking $(13)_3$, shown in Figure 2, there exist three more ZnS polytypes with 12 slabs in the unit cell. Their Zhdanov stacking symbols are $(6)_2$, 93, and 4422. The first polytype has space group $P6_3mc$, and the two others P3m1. The Ramsdell notations for these three structures are ZnS 12H and twice ZnS 12T.

10.2 List of Adamantane-Structure Types Based on Wurtzite or Sphalerite

Only completely determined crystal structure types are considered here. For each type is given the name, the Pearson classification symbol, the space-group number, the standardized Hermann–Mauguin space-group symbol, the Wyckoff sequence, and a reference. The Wyckoff sequence is the sequence of letters of occupied Wyckoff positions in the standardized structure description (Parthé *et al.*, 1993). Abbreviations used for references: SB, *Strukturberichte*; SR, *Structure Reports*. Structure details and lists of isotypic compounds published earlier * can be found in Parthé (1972). Normal and defect adamantane-structure types are listed in Tables 7 and 8, respectively.

11. References

Baur, W. H., and McLarnan, T. J. (1982). Observed Wurtzite Derivatives and Related Dipolar Tetrahedral Structures. *J. Solid State Chem.*, **42**, 300–321.

Bok, L. D. C., and de Wit, J. H. (1963). Zur Kenntnis einiger ternärer Sulfide und Selenide. *Z. Anorg. Allg. Chem.*, **324**, 162–167.

David, J., Laurent, Y., Charlot, J. P., and Lang, J. (1973). Etude Cristallographique d'un Nitrure 14_25_3. La Structure Tétraédrique Type Wurtzite de $LiSi_2N_3$. *Bull. Soc. Fr. Minér. Cristallogr.*, **96**, 21–24.

Eisenmann, B. (1992). Crystal Structure of α-Dialuminium Trisulfide, Al_2S_3. *Z. Kristallogr.*, **198**, 307–308.

Fleet, M. E. (1976). Axial Ratios of MX Compounds with the Wurtzite Structure. *Mater. Res. Bull.*, **11**, 1179–1184.

Frondel, C., and Marvin, U. B. (1967). Lonsdaleite, a Hexagonal Polymorph of Diamond. *Nature*, **214**, 587–589.

Ghémard, G., Jaulmes, S., Etienne, J., and Flahaut, J. (1983). Structure de la Phase Ordonnée du Sesquiséléniure de Gallium, Ga_2Se_3. *Acta Crystallogr.*, **C39**, 968–971.

Goryunova, N. A. (1965). The Chemistry of Diamond-like Semiconductors. Chapman and Hall, London.

Guen, L., Glaunsinger, W. S., and Wold. A. (1979). Physical Properties of the Quaternary Chalcogenides $Cu^{I}_2B^{II}C^{IV}X_4$. (B^{II} = Zn, Mn, Fe, Co; C^{IV} = Si, Ge, Sn; X = S, Se). *Mater. Res. Bull.*, **14**, 463–467.

Hughes, O. H., Woolley, J. C., Lopez-Rivera, S. A., and Pamplin, B. R. (1980). Quaternary Adamantine Selenides and Tellurides of the Form I III IV VI_4. *Solid State Commun.*, **35**, 573–575.

Hyde, B. G., O'Keeffe, M., and Shavers, C. L. (1981). Cation Packing and Molar Volume in Oxides and Nitrides with the Wurtzite Structure. *J. Solid State Chem.*, **39**, 265–267.

Il'nitskaya, O. N., Bruskov, V. A., Savalii, P. Yu., and Kuz'ma, Yu. B. (1991). The New Compound $NiSi_3P_4$ and its Structure. *Izv. Akad. Nauk SSSR, Neorg.Mater.*, **27**, 1311–1313.

Jordan, A. S., von Neida, A. R., Caruso, R., and Kim, C. K. (1974). Determination of the Solidus and Gallium and Phosphorus Vacancy Concentrations in GaP. *J. Electrochem. Soc.*, **121**, 153–158.

Joubert-Bettan, C. A., Lachenal, R., Bertaut, E. F., and Parthé, E. (1969). The Crystal Structures of Na_2ZnSiO_4, Na_2ZnGeO_4 and Na_2MgGeO_4. *J. Solid State Chem.*, **1**, 1–5.

Lamarche, A. M., Willsher, A., Chen, L., Lamarche, G., and Woolley, J. C. (1991). Crystal Structures of I_2-Mn-IV-VI_4 Compounds. *J. Solid State Chem.*, **94**, 313–318.

McLarnan, T. J., and Baur, W. H. (1982). Enumeration of Wurtzite Derivatives and Related Dipolar Tetrahedral Structures. *J. Solid State Chem.*, **42**, 283–299.

Mardix, S. (1986). Polytypism: A Controlled Thermodynamic Phenomenon. *Phys. Rev.*, **B33**, 8677–8684.

Massé, G., and Redjai, E. (1986). Lattice Defects in I–III–VI_2 Compounds. *J. Phys. Chem. Solids*, **47**, 99–104.

Moodie, A. F., and Whitfield, H. J. (1986). Determination of the Structure of Cu_2ZnGeS_4 Polymorphs by Lattice Imaging and Convergent-Beam Electron Diffraction, *Acta Crystallogr.*, **B42**, 236–247.

Mooser, E. and Pearson, W. B. (1959). On the Crystal Chemistry of Normal Valence Compounds. *Acta Crystallogr.*, **12**, 1015–1022.

Motrya, S. F., Voroshilov, Yu. V., Potori, M. V., and Semrad, E. E. (1986). Phase Equilibria in the $Ge(Sn)Se_2$–HgSe Systems. *Ukrainskii Khimicheskii Zh.*, **52**, 23–26 (*Soviet Progress in Chemistry*).

O'Keeffe, M. (1989). The Prediction and Interpretation of Bond Lengths in Crystals. *Struct. Bonding*, **71**, 161–190.

O'Keeffe, M., and Hyde, B. G. (1978). Non-Bonded Interactions and the Crystal Chemistry of Tetrahedral Structures Related to the Wurtzite Type (B4). *Acta Crystallogr.*, **B34**, 3519–3528.

Ollitrault-Fichet, R., Rivet, J., and Flahaut, J. (1980). Le Système Ga-Se et les Séléniures de Gallium. *J. Solid State Chem.*, **33**, 49–61.

Pamplin, B. R. (1960). Super-Cell Structures of Semiconductors. *Nature*, **188**, 136–137.

Pamplin, B. R. (1987). Ordering in the Adamantine Family of Compounds. In *Ternary and Multinary Compounds*, Proc. 7th Int. ICTMC Conf. Snowmass, CO, 1986 (eds S. K. Deb and A. Zunger). Materials Research Society, Pittsburgh, pp. 419–422.

Pamplin, B. R., and Hasoon, F. S. (1985). The System InAs–$ZnGeAs_2$–$CuInSe_2$–Cu_2GeSe_3. *Progr. Crystal Growth Charact. (Oxford)*, **10**, 213–215.

Parthé, E. (1967). Wurtzite and Zinc Blende Type Structures. In *Intermetallic Compounds* (ed. J. Westbrook). Wiley, New York, ch. 11, pp. 180–196.

Parthé, E. (1972). *Cristallochimie des Structures Tétraédriques*. Gordon and Breach, Paris.

Parthé, E. (1987). Structural Principles and Valence Electron Concentration Rules for Adamantine Structure Compounds. In *Ternary and Multinary Compounds, Proc. 7th Int. ICTMC Conf, Snowmass, CO,* 1986 (eds S. K. Deb and A. Zunger). Materials Research Society, Pittsburgh, pp. 3–17.

Parthé, E. (1990). *Elements of Inorganic Structural Chemistry, a Course on Selected Topics*. K. Sutter Parthé, Petit-Lancy, Switzerland.

Parthé, E. (1992). Valence Electron Rules for Compounds with Tetrahedral Structures and Anionic Tetrahedron Complexes. In *Modern Perspectives in Inorganic Crystal Chemistry* (*NATO ASI Ser. C*, Vol. 382) (ed. E. Parthé). Kluwer, Dordrecht, pp. 177–201.

Parthé, E. and Garin, J. (1971). Zinkblende- und Wurtzitüberstrukturen bei ternären Chalkogeniden der Zusammensetzung $I_2 4 6_3$. *Monatsh. Chem.*, **102**, 1197–1208.

Parthé, E., and Paufler, P. (1991). A Master Diagram for the Quick Localization of Possible Homogeneity Ranges of Adamantane Structure Compounds. *Acta Crystallogr.*, **B47**, 886–891.

Parthé, E., Cenzual, K., and Gladyshevskii, R. E. (1993). Standardization of Crystal Structure Data as an Aid to the Classification of Crystal Structure Types. *J. Alloys and Compounds*, **197**, 291–301.

Parthé, E., Yvon, K., and Deitch, R. H. (1969). The Crystal Structure of Cu_2CdGeS_4 and Other Quaternary Normal Tetrahedral Structure Compounds. *Acta Crystallogr.*, **B25**, 1164–1174.

Phillips, J. C. (1981). Quantum Theory and Crystal Chemistry. In *Structure and Bonding in Crystals* (eds M. O'Keeffe and A. Navrotsky). New York, Academic Press, Vol. 1, ch. 2, pp. 13–24.

Radaoutsan, S. I. (1964). Quelques Régularités dans les Propriétés des Semiconducteurs ayant la Structure Lacunaire de la Blende. In *Physique des Semiconducteurs. Comptes Rendus du 7e Congres International.* Dunod, Paris, pp. 1177–1184.

Rebbah, A., Yazbeck, J., and Deschanvres, A. (1981). Etude Structurale des Composés Cd_3YX_3 (Y = As, P; X = Cl, Br, I). *Rev. Chim. Min.*, **19**, 43–53.

Rivet, J., Laruelle, P., Flahaut, J., and Fichet, R. (1970). Diagrammes de Phases des Systèmes SnSe–Cu_2Se et $SnSe_2$–Cu_2Se. Phénomène Order–Désordre et

Conductivité Thermique du Composé Cu_2SnSe_3. *Bull. Soc. Chim. Fr.*, **1970**, 1667–1670.

Sajovec, F., Wolf, R., Fattah, A., Bickmann, K., Wenzl, H., Nagel, G., Rüfer, H., Tomzig, E., and de Bièvre, P. (1990). Defect Analysis on GaAs Crystals by Precision Measurements of Density and Lattice Parameters. *Phys. Status Solidi*, **A122**, 139–152.

Schäfer, W., and Nitsche, R. (1974). Tetrahedral Quaternary Chalcogenides of the Type Cu_2–II–IV–$S_4(Se_4)$. *Mater. Res. Bull.*, **9**, 645–654.

Schäfer, W. and Nitsche, R. (1977). Zur Systematik tetraedrischer Verbindungen vom Typ $Cu_2Me^{II}Me^{IV}Me^{VI}_4$ (Stannite und Wurtzstannite). *Z. Kristallogr.*, **145**, 356–370.

Sjöberg, J., Helgesson, G., and Idrestedt, I. (1991). Refinement of the Structure of Si_2N_2O. *Acta Crystallogr.*, **C47**, 2438–2441.

Spencer, R. M., Pamplin, B. R., and Wright, D. A. (1962). The Structures and Properties of Some Adamantine Compounds. In *The Physics of Semiconductors*. Institute of Physics and Physical Society, London, pp. 244–251.

Suchow, L., Witzen, M. B., and Stemple, N. R. (1963). Zinc Phosphide Iodide (Zn_3PI_3) and Zinc Arsenide Iodide (Zn_3AsI_3): New Compounds with Disordered Defect Zincblende Structure. *Inorg. Chem.*, **2**, 441–444.

Villars, P. (1983). A Three-Dimensional Structural Stability Diagram for 998 Binary AB Intermetallic Compounds. *J. Less-Common Met.*, **92**, 215–238.

Villars, P., Mathis, K., and Hulliger, F. (1989). Environment Classification and Structural Stability Maps. In *The Structures of Binary Compounds* (eds F. R. de Boer and D. G. Pettifor). North-Holland, Amsterdam, Vol. 2, pp. 1–103.

von Schnering, H. G. (1989). Personal communication.

Woolley, J. V. (1964). Alloy Semiconductors. In *Progress in Solid State Chemistry*. Pergamon, New York, Vol. 1, ch. 7, pp. 275–315.

Zunger, A. (1980). Structural Stability of 495 Binary Compounds. *Phys. Rev. Lett.*, **44**, 582–586.

Zunger, A. (1981). A Pseudopotential Viewpoint of the Electronic and Structural Properties of Crystals. In *Structure and Bonding in Crystals* (eds M. O'Keeffe and A. Navrotsky). Academic Press, New York, Vol. 1, ch. 5, pp. 73–135.

This chapter was originally published in 1995 as Chapter 14 under the title 'Wurtzite and Zinc-Blende Structures' in *Intermetallic Compounds*, Vol. 1: *Principles*, edited by J. H. Westbrook and R. L. Fleischer. The title change is to avoid any confusion for mineralogists, some of whom classify both hexagonal wurtzite and cubic sphalerite as 'zinc blende'.

Addendum

To replace the last two paragraphs on p. 128 and on the top of p. 129.

For ordered adamantane structures with composition $C_2C'A_3$ it is not possible to satisfy Pauling's electrostatic valence rule in an exact manner†. For certain anions the sum of the electrostatic bond strength values emanating from its neighbouring cations may be larger or smaller than its formal charge. To achieve a better effective valence balance this is compensated, in agreement with Coulomb's law, by elongating or shortening certain tetrahedral bonds between neighbours. The tetrahedra are thus distorted in a particular way. For a quick estimate of this distortion derived from bond-strength sums, see Parthé (1996) and for a more detailed calculation based on the bond-valence concept, see O'Keeffe (1989). An agreement between the observed and calculated elongations and shortenings of interatomic distances is a necessary (but not sufficient) condition for the choice of the correct super cell in adamantane structures and this can serve as a test.

In wurtzite-related orthorhombic Li_2SiO_3 (Figure 7) and supposedly isotypic $LiSi_2N_3$ one expects (and also finds experimentally) that the tetrahedra are distorted, but in a different way, i.e. LiO_4 tetrahedra have three short and one long Li–O bonds, but corresponding SiN_4 tetrahedra one short and three long Si–N bonds. The two structures are thus not isotypic in a rigorous

†It may be possible to satisfy Pauling's electrostatic valence rule even for composition $C_2C'A_3$ if the structure is partially ordered and has some sites where cations with different valence electrons are mixed. An example is found with tetragonal $(Cu(Cu_{\sim 5/9}Sn_{\sim 4/9})_3S_4$ ($\equiv Cu_2SnS_3$) crystallizing with stannite (or famatinite) type where some sites have mixed cation occupation.

sense, but constitute two branches of a common hypothetical structure type with undistorted tetrahedra. For other details on wurtzite-derivative structures, see Baur and McLarnan (1982).

In sphalerite-related orthorhombic Cu_2GeSe_3, determined nearly 30 years ago (Parthé and Garin, 1971), the expected tetrahedron distortions are not observed. The reason might be a wrong super cell choice with the resulting reported interatomic distance values corresponding to averages over longer and shorter distances. It appears worthwhile to reinvestigate the structure of Cu_2GeSe_3 using modern, up-to-date, single-crystal diffraction methods.

In the new sphalerite-related monoclinic structure of Cu_2GeS_3 (Chalbaud *et al.*, 1997) the agreement between expected and observed elongation and shortening of cation-anion distances has been verified.

Another $C_2C'A_3$ compound with a sphalerite-related structure is Cu_2SnS_3 for which there exist two seemingly conflicting sets of structure data. Chalbaud *et al.* (1999) report a fully ordered monoclinic structure which is isotypic to Cu_2GeS_3, discussed above. This structure was determined on a sample which had been annealed at 600 °C for fully 30 days. However, Chen *et al.* (1998) observed the tetragonal stannite type with some sites having mixed cation occupation. Their sample with composition $(Cu(Cu_{\sim 5/9}Sn_{\sim 4/9})_3S_4$ ($\equiv Cu_2SnS_3$) was annealed at 700 °C for 2 days. For the determination of a fully ordered structure it is obviously necessary to make really certain that the sample has been annealed for a sufficiently long time. In these adamantane structure compounds, characterized by an important percentage of covalent bonding, the reaction rate for atom ordering is low. To assure perfect ordering the annealing time should better be expressed in units of months instead of days.

Under the subheading $C_2C'A_3$ in Table 7, add two new blocks in the column on the right hand side, to be placed below the four-line block of Cu_2GeSe_3.

Cu_2GeS_3
mS24 (9) Cc–a^6
Chalbaud *et al.* (1997)

$(Cu(Cu_{\sim 5/9}Sn_{\sim 4/9})_3S_4 \equiv Cu_2SnS_3$
(partially ordered)
tI 16 (121) I–42m-*idba*
Stannite $Cu_2Fe^{2+}SnS_4$
or Famatinite Cu_3SbS_4
type Fe or Sb site occupied
by Cu only, others mixed
Chen *et al.* (1998)

References

Cenzual, K., Gladyshevskii, R., and Parthé, E. (1995). *TYPIX 1995 Database of Inorganic Structure Types.* Database on two floppy disks and User's Guide of 48 pages. Frankfurt: Gmelin-Institut für Anorganische Chemie.

Chalbaud de, L. M., Delgado de, G. D., Delgado, J. M., Mora, A. E., and Sagredo, V. (1997). *Mat. Res. Bull*, **32**, 1371–1376.

Chalbaud de, L. M., Delgado de, G. D., Delgado, J. M., Cenzual, K., and Sagredo, V. (1999). *J. Solid State Chem.*, submitted for publication.

Chen, X., Wada, H., Sato, A., and Mieno, M. (1998). *J. Solid State Chem.*, **139**, 144–151.

Parthé, E. (1996). *Elements of Inorganic Structural Chemistry. Selected Efforts to Predict Structural Features.* 2nd edition, 170 pages. K. Sutter Parthé Publisher, 49 Chemin du Gué, CH-1213 Petit-Lancy, Switzerland.

Wallinda, J. and Jeitschko, W. (1995). *J. Solid State Chem.*, **114**, 476–480.

Chapter 5

Atomic Environments in Some Related Intermetallic Structure Types

Jo L. C. Daams

Philips Research Laboratories, Prof. Holstlaan 4, 5656 AA Eindhoven, The Netherlands

1. Introduction

In Nature many simple and complicated intermetallic structures are realized and they are always legitimate. The mathematical models describing those structures are in general correct, but they do not always reveal the nature of the realized structure. This chapter illustrates the second statement in an analysis of some related structure types by examination of atomic environments.

Interpretation of chemical and/or physical properties of intermetallic compounds is mostly impossible without any knowledge of the crystal structure of those compounds. For example, information about the lattice symmetry is vital for the interpretation of magnetic anisotropy and piezo- and/or ferroelectricity; and band-structure calculations are not possible without knowledge of the complete crystal structure. It is therefore essential that we have some means for analyzing the published data for their validity and that we are able to check these data against the crystallographic rules as given e.g. in the *International Tables for Crystallography* (Hahn, 1983).

We have to keep in mind, however, that although some minor displacements of atoms can lead to changes in symmetry and thus in the strict mathematical description of the structure, they do not necessarily affect the crystal chemistry of the compound. This means that minor displacements of the atoms do not always have a large influence on the short-range atomic arrangement in the crystal structure.

With our atomic-environment approach, described in Section 2, it is possible to analyze crystal structures for their geometrical short-range atomic arrangements, and as a result we are able to define the observed atomic environments (AE) by their coordination number and their shape. While other chapters in this volume discuss crystal-structure families with obvious internal relationships, here we will analyse with the AE approach 10 very populous intermetallic structure types, as listed in Table 1, where their relationships are not so apparent from the usual descriptions. In Pearson's (1972) excellent book on *The Crystal Chemistry and Physics of Metals and Alloys* these 10 structure types (and others) are classified (ch. 9) as structure types dominated by triangular prismatic arrangements. In our approach we avoid this kind of classification, because it is in our opinion difficult to see this triangular prismatic motif; instead, we use, as we will explain later on, another classification based on the observed AEs in these structures.

The results of this analysis are given in Section 3, where we also compare the observed AEs and demonstrate how they can be used for the detection of relations between structure types. In most of the 10 analyzed structure types the AEs change as a function of the c/a ratio and/or are dependent on the values of the atomic coordinates (x, y, z) of one (or more) of the atoms in the asymmetrical unit. We show this dependence with the help of some examples.

The crystallographic data used in this analysis and given in Table 2 are collected from the second edition of *Pearson's Handbook of Crystallographic Data for Intermetallic Phases* (PH) as compiled by Villars and Calvert (1991). In the past many of the 10 structure types and the compounds crystallizing therein have been the subject of similar or partly identical studies, e.g.

Crystal Structures of Intermetallic Compounds. Edited by J. H. Westbrook and R. L. Fleischer

Table 1. List of the 10 analyzed structure types

Pearson symbol	Formula	Space-group symbol	Space-group number	No. of point sets	No. of compounds
hP2	CW	$P\bar{6}m2$	187	2	35
hP3	AlB_2	$P6/mmm$	191	2	330
hP6	$CaIn_2$	$P6_3/mmc$	194	2	149
hP6	$InNi_2$	$P6_3/mmc$	194	3	154
tP6	Cu_2Sb	$P4/nmm$	129	3	197
oC8	BCr	$Cmcm$	63	2	193
oP8	BFe	$Pnma$	62	2	121
tI10	Al_4Ba	$I4/mmm$	139	3	723
tI12	Si_2Th	$I4_1/amd$	141	2	82
oP12	Co_2Si	$Pnma$	62	3	495

the compounds crystallizing in the tI10 Al_4Ba structure have been studied by Pearson and Villars (1984) among others. Whenever necessary, we will give references to these studies, but it is impossible to give in this brief overview a complete bibliography.

2. The Atomic-Environment Approach

A crystal structure is completely determined by the following data:

- Chemical formula
- Space group and unit-cell dimensions
- Coordinates of the point sets (atomic positions) and their occupancy.

These characteristics lead to a fairly large number of different structure types; nearly 2800 types are listed in PH (Villars and Calvert, 1991), which makes it almost impossible to see connections or even to detect identities. Many of these structure types are depicted in the *Atlas of Crystal Structure Types for Intermetallic Phases* (Daams *et al.*, 1991). In this compilation, for each structure type, there is given a three-dimensional drawing and two projections, and for each point set a drawing of the atomic environment. A similar type of data representation has been made by Grin' and Gladyshevskii (1989), who give in their book *Gallides* the crystallographic data for all gallides. They also give for each structure type a complete description with one or two projections and some drawings of the AEs observed in the structure.

The aim of the concept, described more extensively in previous work (Daams *et al.*, 1992; Villars and Daams, 1993; Daams and Villars, 1993), and briefly recapitulated hereafter, is to define the AEs as clearly as possible, so that at the end of the analysis we will be able to group them into distinct atomic environment types (AETs).

We defined an AE using the method of Brunner and Schwarzenbach (1971), where all interatomic distances between an atom and its neighbors are plotted in a next-neighbor histogram (NNH) as is shown in Figure 1(a).

Table 2. Crystallographic data for the analyzed structure types

Pearson symbol	Formula	Atom	Wyckoff letter Multiplicity	Site Symmetry	x	y	z	Occupation
hP2	CW	W	1a	$\bar{6}m2$	0	0	0	1
		C	1d	$\bar{6}m2$	1/3	2/3	1/2	1
hP3	AlB_2	Al	1a	$6/mmm$	0	0	0	1
		B	2d	$\bar{6}m2$	1/3	2/3	1/2	1
hP6	$CaIn_2$	Ca	2b	$\bar{6}m2$	0	0	1/4	1
		In	4f	$3m.$	1/3	2/3	0.455	1
hP6	$InNi_2$	Ni1	2a	$\bar{3}m.$	0	0	0	1
		In	2c	$\bar{6}m2$	1/3	2/3	1/4	1
		Ni2	2d	$\bar{6}m2$	1/3	2/3	3/4	1
tP6	Cu_2Sb	Cu1	2a	$\bar{4}m2$	0	0	0	1
		Cu2	2c	$4mm$	0	1/2	0.270	1
		Sb	2c	$4mm$	0	1/2	0.700	1
oC8	BCr	B	4c	$m2m$	0	0.440	1/4	1
		Cr	4c	$m2m$	0	0.146	1/4	1
oP8	BFe	B	4c	$.m.$	0.036	1/4	0.610	1
		Fe	4c	$.m.$	0.180	1/4	0.125	1
tI10	Al_4Ba	Ba	2a	$4/mmm$	0	0	0	1
		Al1	4d	$\bar{4}m2$	0	1/2	1/4	1
		Al2	4e	$4mm$	0	0	0.380	1
tI12	Si_2Th	Th	4a	$\bar{4}m2$	0	0	0	1
		Si	8e	$2mm.$	0	0	0.4165	1
oP12	Co_2Si	Co1	4c	$.m.$	0.038	1/4	0.782	1
		Co2	4c	$.m.$	0.174	1/4	0.438	1
		Si	4c	$.m.$	0.702	1/4	0.389	1

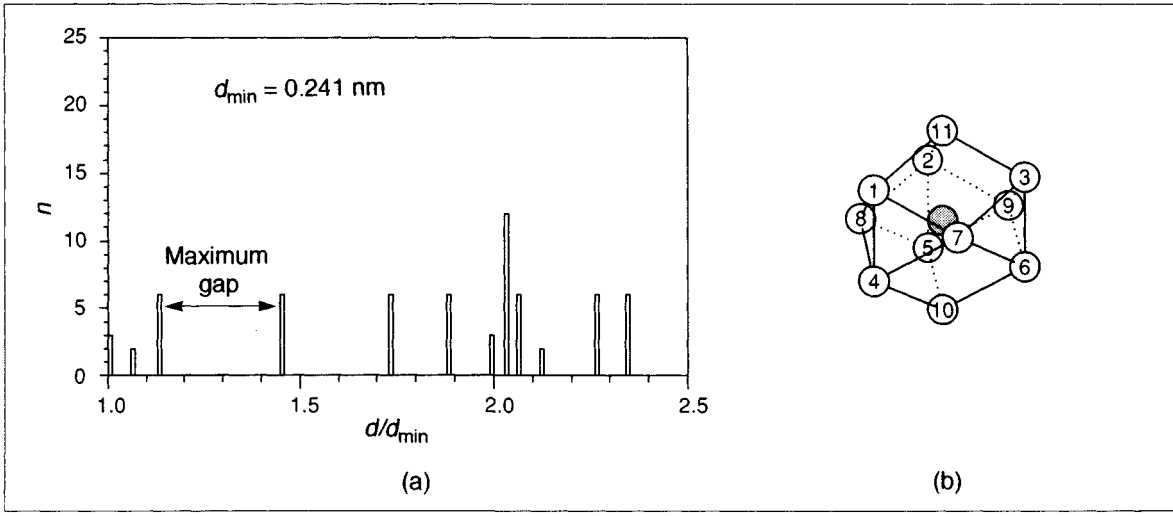

Figure 1. (a) A typical example of an NNH and (b) the AE (coordination polyhedron) belonging to this NNH

In most cases a clear maximum gap is revealed, as can be seen in Figure 1(a). All atoms to the left of this maximum gap belong to the AE of the central atom. This rule is called the maximum-gap rule, and the AE of Figure 1(b) is constructed according to this rule with the atoms to the left of the maximum gap. The AE environment shown in Figure 1(b) is the fully capped trigonal prism, which is a trigonal prism (atoms 1 to 6) with three atoms (atoms 7 to 9) capping the equatorial faces and two atoms (atoms 10 and 11) capping the polar faces of the prism.

In those cases where this rule leads to AEs with atoms beside the central atom enclosed or to AEs with atoms on one (or more) of the faces of the coordination polyhedron, we use the maximum-convex-volume rule. This rule is defined as the maximum volume around only one central atom enclosed by convex faces, with all the coordinating atoms lying at the intersections of at least three faces. This rule was also used in those cases where no clear maximum gap was detectable. In those cases where two (or more) equal, or practically equal, maximum gaps were observed, we kept the number of different AETs in a structure type as small as possible.

The AETs are characterized using codes and labels as explained in Daams and Villars (1993). The code of the idealized AE shown in Figure 1(b) is $9^{2.2}2^{0.3}$, which means that we have nine atoms (atoms 1 to 9) adjoining two triangles and two squares, and two atoms (atoms 10 and 11) adjoining no triangles and three squares. From the work mentioned earlier on the cubic structure types (Daams *et al.*, 1992), the rhombohedral structure types (Daams and Villars, 1993), and the elements (Villars and Daams, 1993), we think that after completion of the analysis of all symmetries we will have about 25 basic atomic environment types. Thus 90% of the intermetallic structures, with about 50 000 compounds, are composed of combinations of these AETs. It is important to mention that our AETs are not isolated 'building' units, as crystal structures may consist of interpenetrating AETs.

We would also like to stress that there are some other methods that can lead to the AETs as we have found them. However, we think that the method itself is not so important as long as the AETs found are unambiguously defined.

Another well-known local-environment construction is the so-called Voronoi polyhedron construction, also known as the Dirichlet construction or the Wigner–Seitz cell. This construction of the local environment in a structure generates AEs that look similar to but are not identical with our AETs. This Voronoi polyhedron is more often used by physicists, while our approach is more familiar to crystallographers. For example, Pearson used the Dirichlet construction in the analysis of the compounds crystallizing in tI10 Al_4Ba (Pearson, 1985a) and called the obtained local atomic environments the *Wirkungsbereich* of an atom (see also Pearson, 1985b).

For reasons we explain later, we think that methods which use (instead of crystal-structure-derived

interatomic distances) the metallic radii of the atoms are less reliable, e.g. Bruzzone *et al.* (1970), because the metallic radii of the atoms, as given by e.g. Pearson (1972) or the so-called Teatum radii (Teatum *et al.*, 1960), are strongly dependent on the alloying element(s). This view was also emphasized by Pearson (1972) and is confirmed by e.g. the work of Merlo (1988) and Miedema and Niessen (1982).

In his book *Structure of Substances* Aslanov (1989) uses comparable coordination polyhedra (AEs) in his so-called crystal chemical model of the atomic interactions (CCMAI). In this model it is assumed that all atomic interactions are a result of mutual attractions and repulsions of the atoms in the direct coordination spheres of the atoms. In Aslanov and Markov (1992), and references therein, they applied their model to intermetallic phase structures, and some of the structure types analyzed with our approach are also described in this study. The small differences that appear between our AEs and theirs are a result of the differences in defining which atoms belong to which coordination sphere. While in our approach this is a straightforward definition, based on the NNH, the definition is sometimes complicated in their model.

Although there are the above-mentioned differences between both approaches, it is quite obvious that there is a strong resemblance. It would be a challenging task to find and describe the agreement between both methods so that in the future we will have a number of 'standard building blocks' for intermetallics which can be used for explaining as well as for predicting new intermetallic structures and their physical properties.

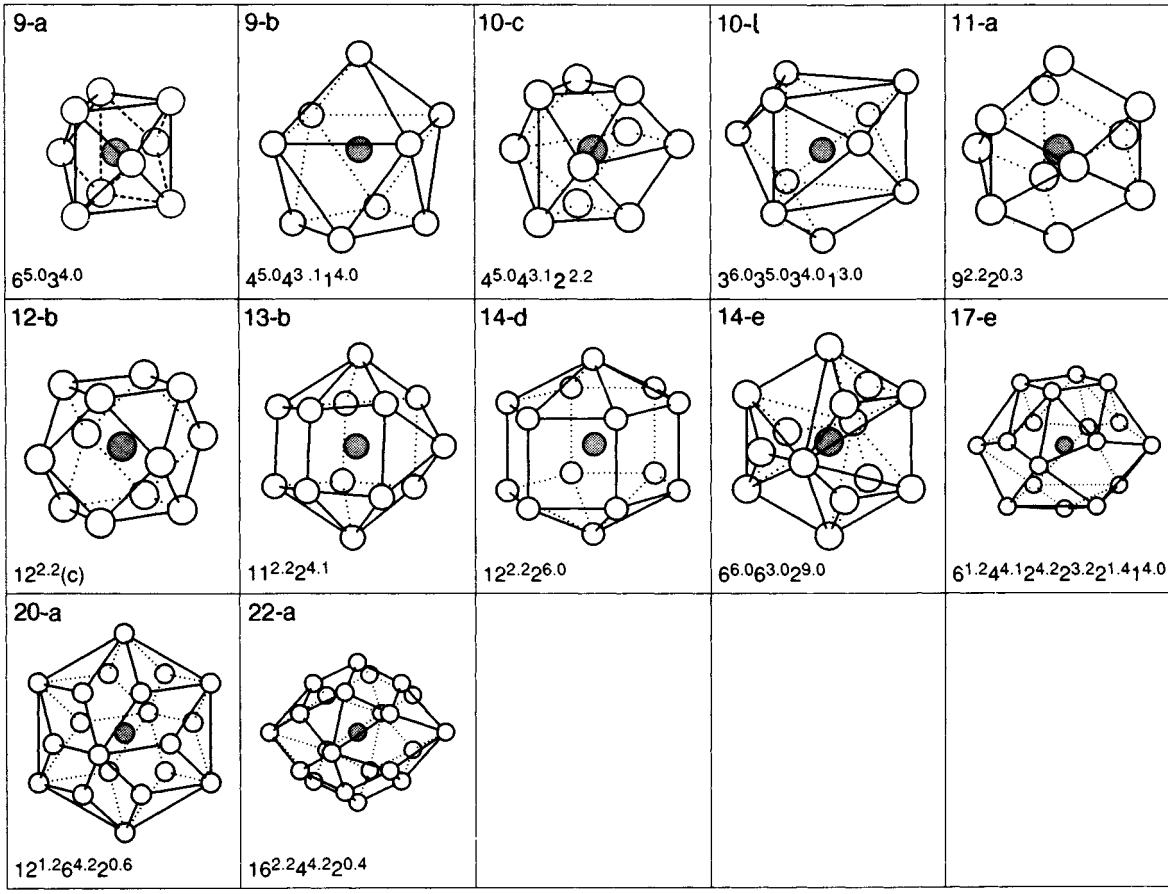

Figure 2. The 12 standard AETs as they are realized in the 10 analyzed structure types (idealized forms)

3. Observed Atomic Environments

3.1 General Remarks

Using the rules given above, we have analyzed all 10 structure types of Table 1. Our approach leads to conventional atomic-environment types for these structures. However, for those compounds crystallizing with an extreme range in the reported c/a ratio, e.g. hP3 AlB_2, we observed an irregular AE (IAE) for compounds with the highest c/a ratio. We consider normal AETs as environment types that can be visualized by coordination polyhedra with a convex volume, and IAETs as environment types that cannot be described as a convex volume. Our analysis showed that in the 10 structure types, with 24 point sets and about 2500 compounds, for a medium c/a ratio, 12 different AETs, as shown in Figure 2, are realized; wherever possible the standardized form of the AETs is depicted. In Table 3 we give the labels, explained in Daams and Villars (1993), the number of times that the AE is observed, and their suggested notation; see also Jensen (1989) and Parthé (1990). Most of these AETs have been observed in the already mentioned previous work and many of them belong, or are related to, the group of highly symmetric, frequently occurring AETs (basic AETs).

It has to be remarked that sometimes the differences between some of the 12 observed AETs are very small; for example, the AETs with the labels 9-a and 9-b (see Figure 2) can be regarded as a perfect trigonal prism with three atoms capping the side faces of the prism (9-a) and a distorted version thereof (9-b). In AET 9-b the three capping atoms are shifted outwards to a position in which two of them form a square with two prism atoms and consequently the AET (9-b) can be named a polar-capped square antiprism. A similar resemblance can be observed for the AETs with the labels 10-c and 10-l (see Figure 2). These minor changes in AE and the consequences for the crystal chemistry of the compound-families are still under investigation.

Table 3. List of observed AEs with their suggested description

Label	Number observed	Description
9-a	4	Equatorial-capped trigonal prism
9-b	3	Monopolar-capped square antiprism
10-c	1	Polar-capped square antiprism
10-l	1	Monopolar-equatorial-capped trigonal prism
11-a	2	Full-capped trigonal prism
12-b	2	Cubooctahedron
13-b	2	Polar, monoequatorial-capped, pentagonal prism
14-d	2	Polar-capped hexagonal prism
14-e	2	Polar-capped anti-cuboctahedron
17-e	2	Full-capped pentagonal prism
20-a	2	Full-capped hexagonal prism
22-a	1	Polar, eight-equatorial-capped, hexagonal prism

In the past 25 years the known compounds crystallizing in these 10 structure types have changed from mainly binary (Pearson, 1958, 1967) to almost completely ternary (Villars and Calvert, 1991). In our analysis this means that in the six structure types, where we have two occupied atom positions in the asymmetrical unit (see Table 2), we must have in ternary compounds two different atoms mixing on one position in the structures. From the geometrical (or chemical) point of view such mixing seems improbable in many cases, because, for example, the metallic radii of the mixing atoms differ sometimes by as much as 30%. In Section 3.5 this sometimes paradoxical behavior of metal atoms in crystal chemistry will be discussed in relation to the structure types.

In the following we will describe in detail, for two examples, hP3 AlB_2 and hP6 $CaIn_2$, the AEs as they are realized.

3.2 The AEs in hP3 AlB_2

In hP3 AlB_2 we observe different AEs for the two atoms in the asymmetrical unit as a function of the c/a ratio, which ranges in this structure type from 0.597 (for Bi_2Tl) to 1.083 (for AlB_2) to 1.474 (for Ag_2Nd). In this structure type both atoms are on specific positions with fixed coordinates, so there is no influence on the AEs of a changing atom coordinate.

For a medium c/a ratio, as in hP3 AlB_2, we observe for the atom on the 1a position (Al) the full-capped hexagonal prism as an AE and for the atom on the 2d position (B) the equatorial-capped trigonal prism.

If we analyze the AEs step-by-step through the NNH of the respective atoms in hP3 AlB_2, we see that the first 12 neighbors (B) of the Al atom form a hexagonal prism. The next six neighboring atoms (Al) are the capping atoms of the side faces of the prism, while the next two atoms (Al) are the polar caps, together leading to the full-capped hexagonal prism. The NNH of the Al atom is given in Figure 3, while the AE is depicted in Figure 2 with label 20-a. For the B atom we see that the first three neighbors (B) form an in-plane triangle around the central atom. The next six neighboring atoms form a triangular prism on which the first three neighbors are capping atoms on the side faces; taken together they form the equatorial-capped trigonal prism.

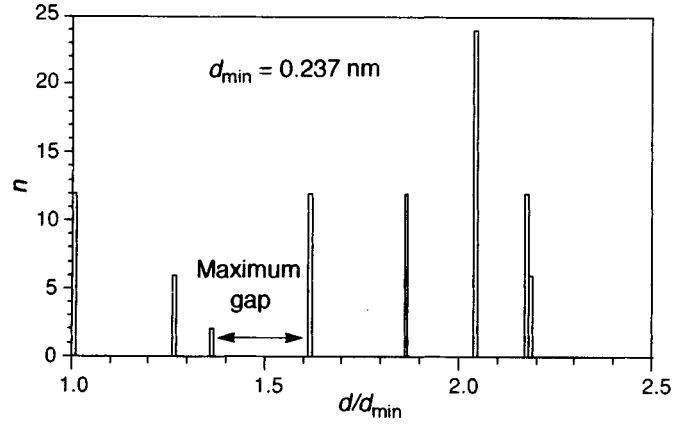

Figure 3. The NNH of the Al atom in hP3 AlB_2; the AET is shown in Figure 2 with label 20-a

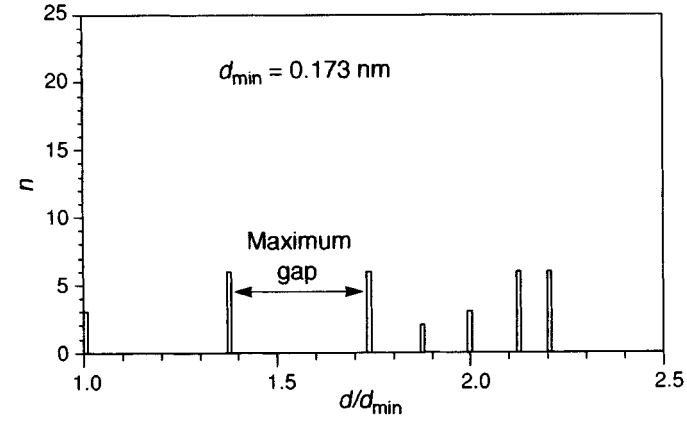

Figure 4. The NNH of the B atom in hP3 AlB_2; the AET is shown in Figure 2 with label 9-a

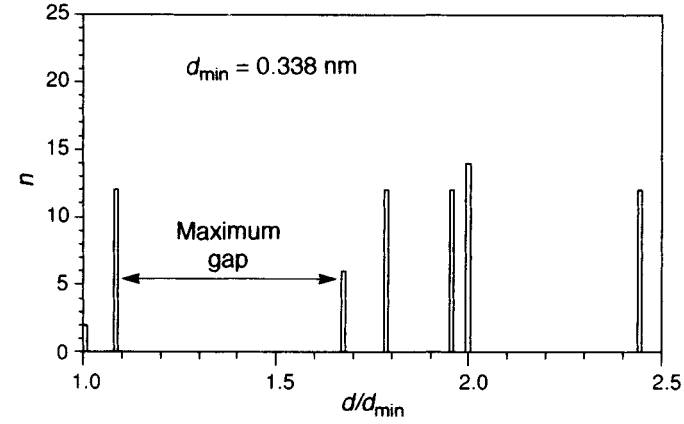

Figure 5. The NNH of the Tl atom in hP3 Bi_2Tl; the AET is shown in Figure 2 with label 14-d

The NNH of the B atom is given in Figure 4 and the AE is depicted in Figure 2 with label 9-a.

For the minimum c/a ratio, as in Bi_2Tl, we observe for the atom on the 1a position (Tl) as an AE the polar-capped hexagonal prism; see Figure 2 (with CN = 14, label 14-d). The NNH of the Tl atom is given in Figure 5 and we see that as a consequence of the different c/a ratio that the six in-plane Tl atoms are shifted to the right of the maximum gap and therefore no longer belong to the AE of the central (Tl) atom. For the atom on the 2d position (Bi) the full-capped trigonal prism is realized as the AE; see Figure 2 (with CN = 11, label 11-a). The NNH of the Bi atom is given in Figure 6, and here we observe that we have two Bi atoms forming caps on the triangular faces of the prism. These two Bi atoms are from the neighboring unit cells, above and below.

For the maximum c/a ratio, as in Ag_2Nd, we observe for the atom on the 1a position (Nd) the equatorial-capped hexagonal prism AE; see Figure 7 (with CN = 18, label 18-d); the two Nd atoms from the unit cells above and below belong no longer to the AE of the central (Nd) atom. For the atom on the 2d position (Ag) the central atom is in this arrangement surrounded by three Ag atoms forming a triangle; see Figure 8 (with CN = 3, label 3#b).

With this example we have shown that the AEs in a given structure type can change dramatically within that

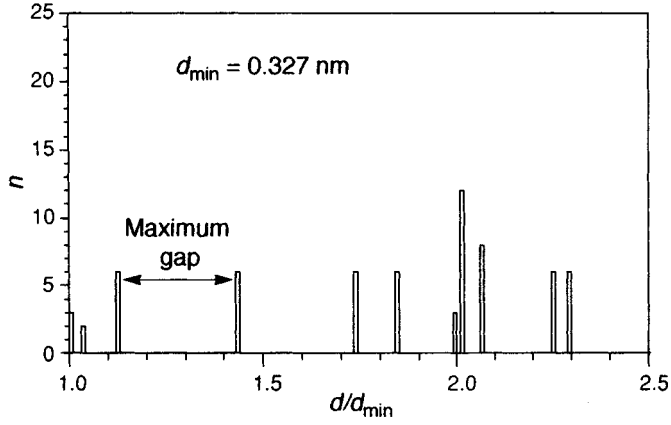

Figure 6. The NNH of the Bi atom in hP3 Bi_2Tl; the AET is shown in Figure 2 with label 11-a

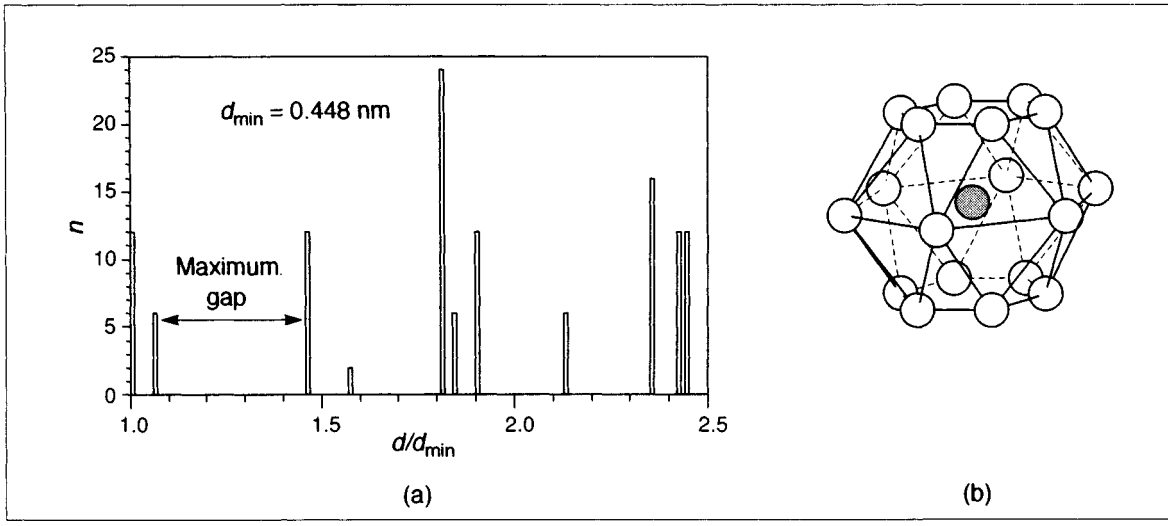

Figure 7. (a) The NNH of the Nd atom in hP3 Ag_2Nd and (b) the corresponding AET (CN = 18, label 18-d)

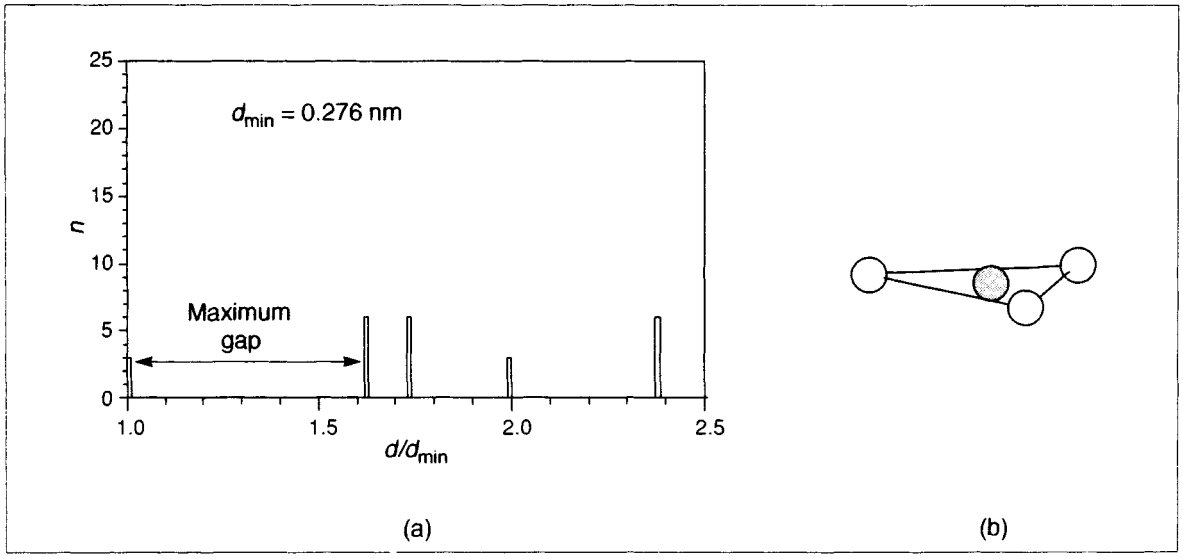

Figure 8. (a) The NNH of the Ag atom in hP3 Ag_2Nd and (b) the corresponding AET (CN = 3, label 3 # b)

structure type as a function of the *c/a* ratio. The CN for the atom on the 1a position varies from 14 (minimum *c/a*) to 20 (medium *c/a*) to 18 (maximum *c/a*), and the CNs for the atom on the 2d position are 11, 9 and 3 respectively.

It shows that, although the mathematical models describing these compounds are identical with all compounds assigned to this structure type having the same space group and same positions occupied, the compounds are not the same in terms of the short-range atomic arrangement for the respective atoms in the compounds.

Adding the AE information to the descriptive models means that hP3 AlB_2 can no longer be regarded as a 'single structure type', but that it should be recognized as consisting of different subtypes or, as we will explain later, of different coordination types. As a consequence, it also shows that it is incorrect to assign a given compound to a given structure type based only on the standard mathematical description.

This sometimes dramatic change in short-range atomic arrangement has been observed in many structure types in which the compounds show a wide range in *c/a* ratio, and this effect has therefore been described by many authors. For example Pearson (1972, 1979) already distinguished two groups of compounds crystallizing in hP3 AlB_2 based on the *c/a* ratio, whereby the compounds with the lowest *c/a* ratio ($c/a < 0.9$) mainly consisted of combinations with group I (alkaline) or group II (alkaline-earth) metals.

In the following example we show some changes in AEs, as a function of changing *c/a* ratio, which are less dramatic as compared with the example given above.

3.3 The AEs in hP6 $CaIn_2$

In hP6 $CaIn_2$ we also observe different AEs for the two atoms in the asymmetrical unit as a function of the *c/a* ratio. The *c/a* ratio ranges in this structure type from 1.382 (for CuGaTi) to 1.583 (for $CaIn_2$) to 1.812 (for LaPtSb).

For a medium *c/a* ratio, as in $CaIn_2$, we observe as an AE for the atom on the 2b position (Ca) a distorted polar-capped hexagonal prism and for the atom on the 4f position (In) the monopolar-equatorial-capped trigonal prism.

If we analyze the AEs step-by-step through the NNH (Figures 9(a) and 10(a)) of the respective atoms in hP6 $CaIn_2$, we see that the first six neighbors (In) of the Ca atom form a trigonal prism. Together with the next six neighboring atoms (In), these 12 atoms form a distorted hexagonal prism, on which the next two neighboring atoms (Ca) are polar caps; see Figure 9 (b). This AE is distorted because the In atoms do not form a planar six-membered ring owing to the slight displacement of the *z* coordinate from the ideal position ($0.455 \leftrightarrow 1/2$).

For the In atom we see that the first three neighbors (In) form a non-planar triangle with the central atom. Inclusion of the next atom (In) gives a tetrahedron, of which three side faces are capped by the next three atoms

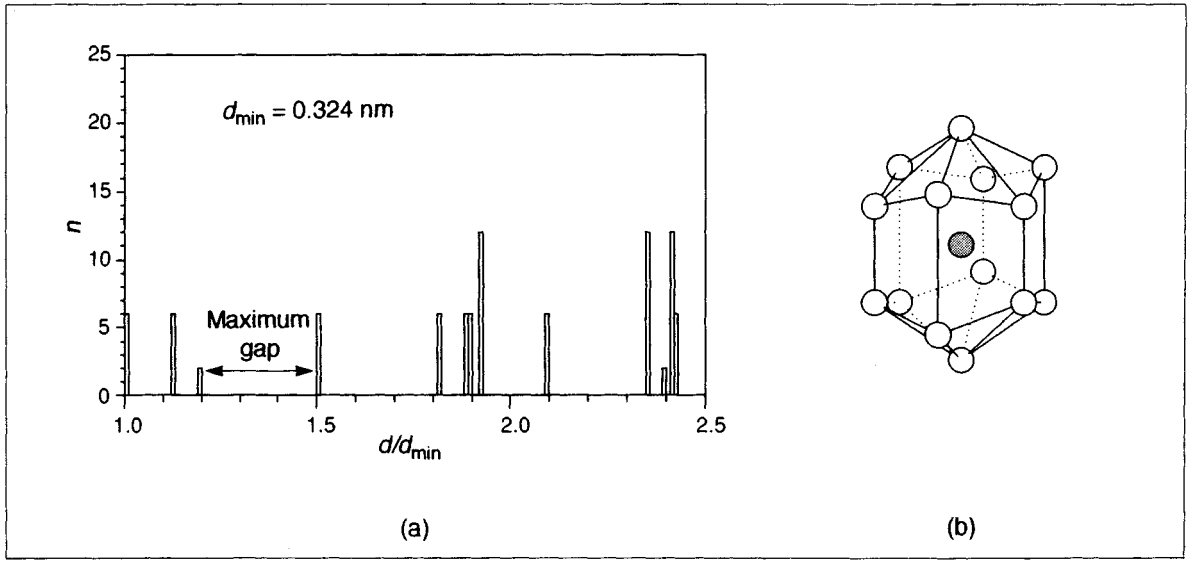

Figure 9. (a) The NNH of the Ca atom in hP6 $CaIn_2$ and (b) the corresponding AET; the idealized form of the AET is shown in Figure 2 with label 14-d

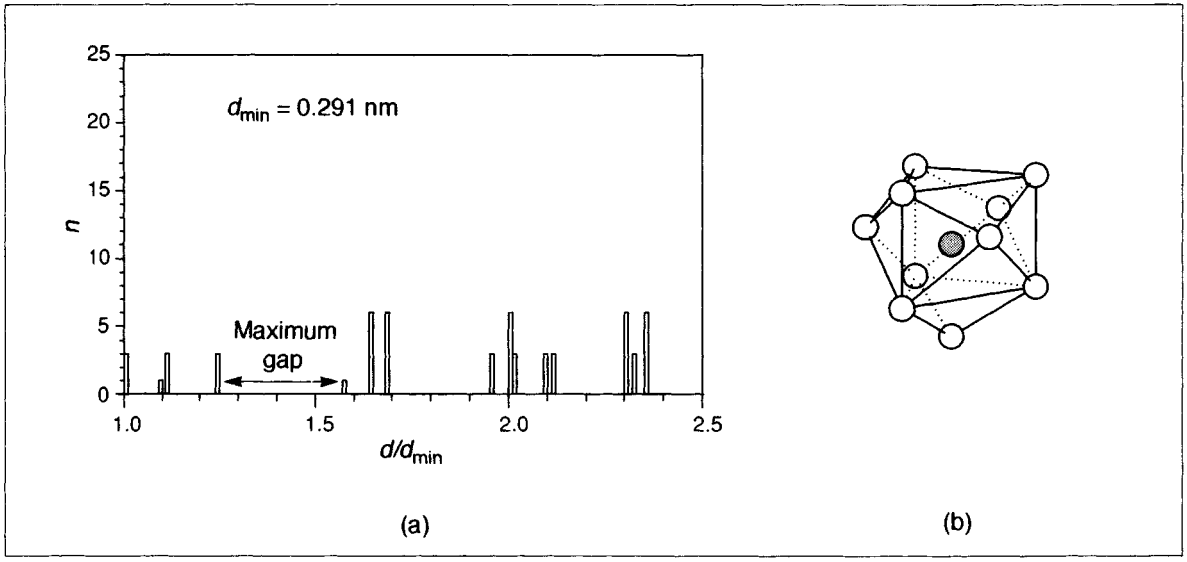

Figure 10. (a) The NNH of the In atom in hP6 $CaIn_2$ and (b) the corresponding AET, which is also shown in Figure 2 with label 10-l

(Ca). Including the next three atoms (Ca) gives the depicted AE, which shows a triangular prism of Ca atoms with three In atoms capping the equatorial faces and an In atom capping one of the triangular faces of the trigonal prism (Figure 10(b)).

For the minimum c/a ratio, as in CuGaTi, we observe as an AE for the atom on the 2b position (Ti) the same distorted polar-capped hexagonal prism as in $CaIn_2$ (see Figure 9), and for the atom on the 4f position (M = Ga, Cu) an elongated form of the full-capped trigonal prism (see Figure 11). It is clearly shown in the NNH that the extra M atom is practically in the middle of the maximum gap and it is an arbitrary decision to include it in the AE.

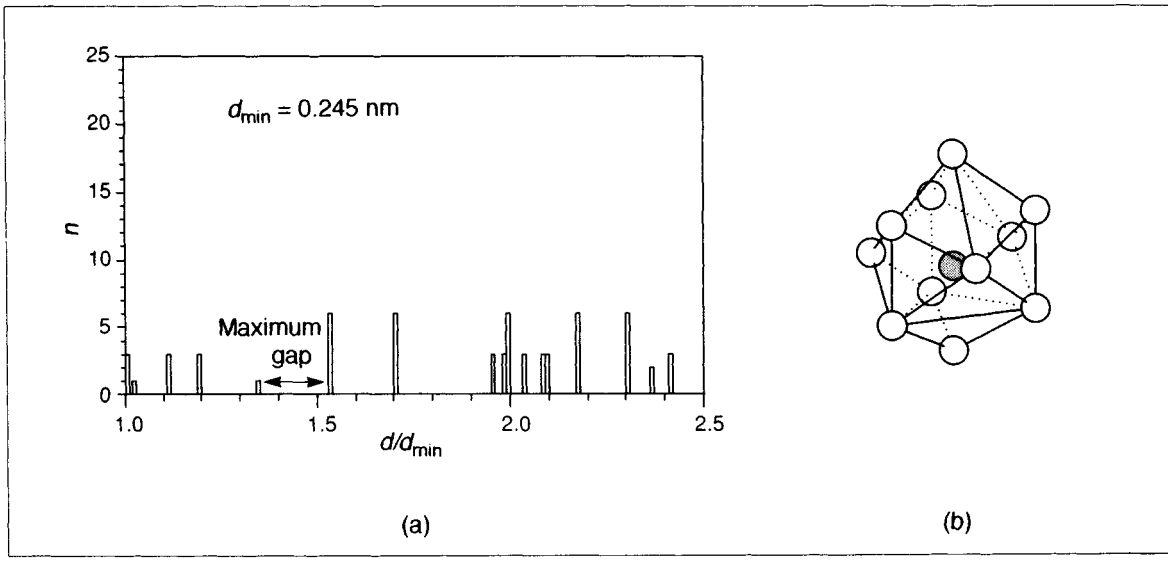

Figure 11. (a) The NNH of the M atom (M = Cu, Ga) in hP6 CuGaTi and (b) the corresponding AET; the idealized form of the AET is shown in Figure 2 with label 11-a

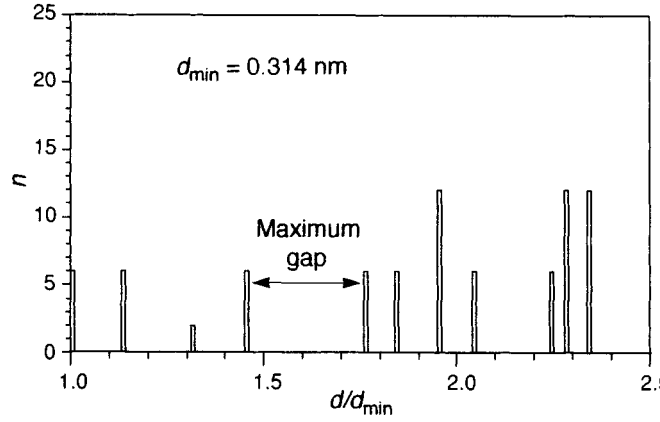

Figure 12. The NNH of the La atom in hP6 LaPtSb; the AET is shown in Figure 2 with label 20-a

For the maximum c/a ratio, as in LaPtSb, we observe for the atom on the 2b position (La) the full-capped hexagonal prism (see Figure 2, label 20-a) and for the atom on the 4f position (M = Pt, Sb) the monopolar-equatorial-capped trigonal prism (see Figure 2, label 10-l). The NNHs of both atoms are shown in Figure 12 (La) and Figure 13 (M = Pt,Sb).

3.4 Related Structure Types

The examples given in Section 3.3 demonstrate one of the advantages of our approach: it shows directly the resemblance in the short-range atomic arrangements between atoms in different structure types, and it gives us a tool to classify structure types with the same AEs. Therefore, we have defined a so-called *coordination type*. When in different structure types the same AEs and the same number of AEs are realized, we define these structure types as belonging to the same coordination type. In the group of 10 analyzed structure types we have two examples of structure types belonging to the same coordination type (see Table 4). In oC8 BCr and in oP8 BFe the same AEs are realized, as is also the case in hP3 AlB_2 and in tI12 Si_2Th.

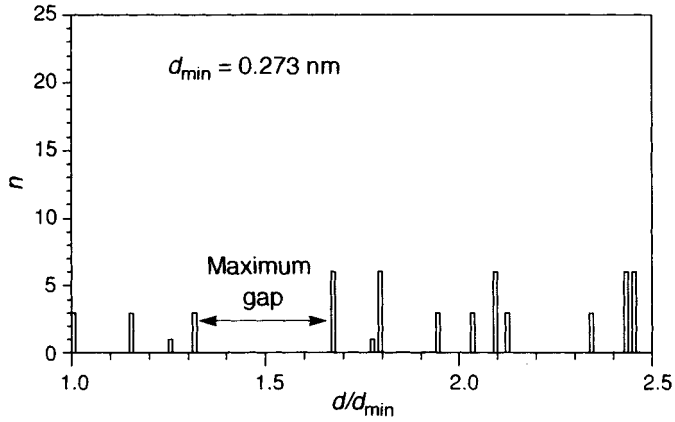

Figure 13. The NNH of the M atom (M = Pt, Sb) in hP6 LaPtSb; the AET is shown in Figure 2 with label 10-l

Table 4. Coordination types for a medium *c/a* ratio

Pearson symbol	Formula	Number of point-sets	Number of compounds	Coordination numbers	Observed Atomic Environment Types												Number of AETs
					9-a	9-b	10-c	10-l	11-a	12-b	13-b	14-d	14-e	17-e	20-a	22-a	
hP2	CW	2	35	14									■				1
tP6	Cu_2Sb	3	197	9/9/12		■				■							2
oC8	BCr	2	193	9/17	■									■			2
oP8	BFe	2	121	9/17	■									■			2
hP3	AlB_2	2	330	9/20	■										■		2
tI12	Si_2Th	2	82	9/20	■										■		2
oP12	Co_2Si	3	495	10/13/13			■				■						2
hP6	$CaIn_2$	2	149	10/14				■				■					2
hP6	$InNi_2$	3	154	11/11/14					■			■					2
tI10	Al_4Ba	3	723	9/12/22		■				■						■	3

If we include the AEs as they are realized in certain structure types as a function of *c/a* ratio, we have an increased number of partly overlapping structures and therefore of structures belonging to the same coordination type. The other realized AEs, in the 10 structure types, are depicted in Figure 14, and it is obvious that these AEs are distorted or derived forms of the normal AEs, with atoms sometimes included or excluded.

The relations between the 10 structure types, if we include the boundary compounds, can easily be seen in Table 5.

Relations between the 10 structure types and other structure types can be found in the same manner, when we compare the realized AETs with those of other structure types. As already mentioned, most of these structure types are depicted in Daams *et al.* (1991). A good example of a structure type with many related structure types is hP6 $InNi_2$. The realized AETs (11-a and 14-d) in this structure type are also realized in the structure types given in Table 6. Some of these relations are quite obvious, so hP6 Fe_2Si and Ni_2Si are refined (or assigned) to a space group with a lower symmetry, where the atomic coordinates of one of the atoms are

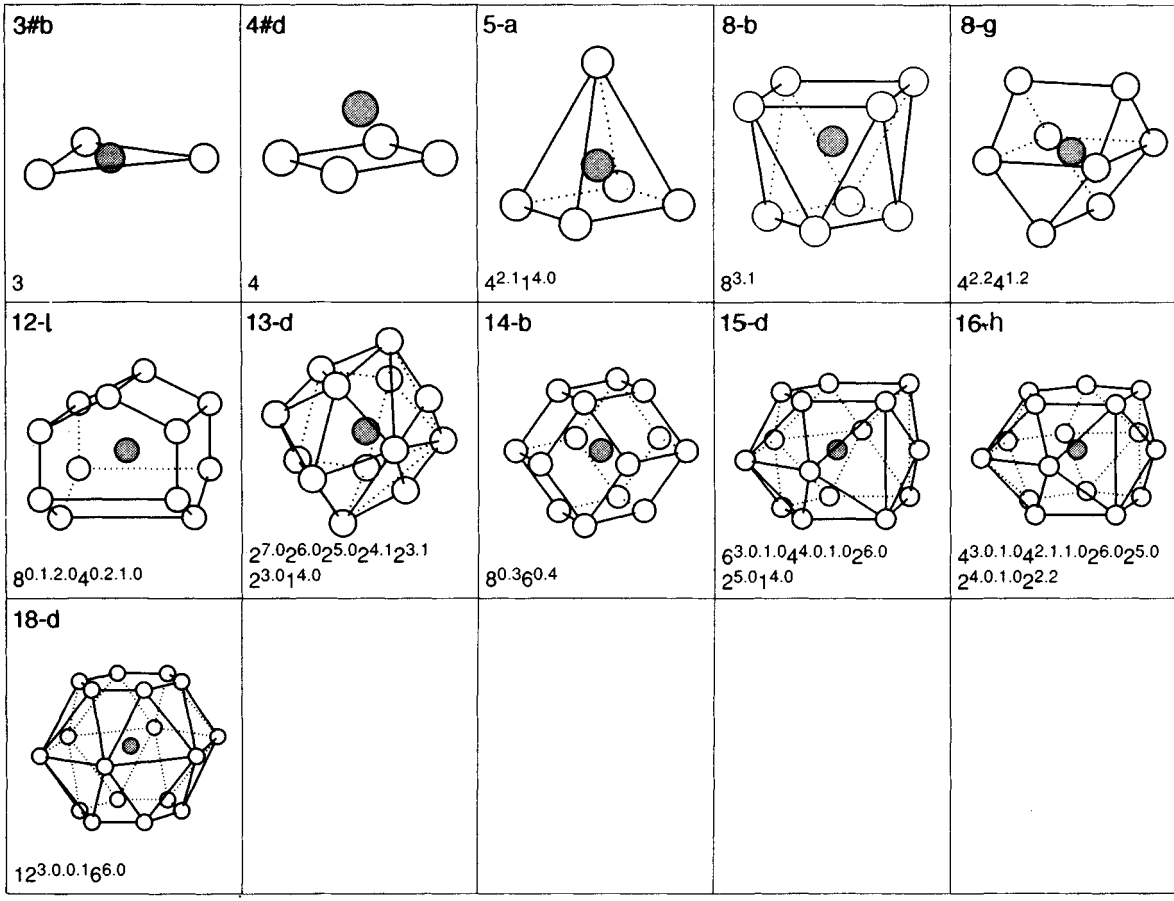

Figure 14. The remaining AEs as they are realized in the 10 structure types covering the whole range of *c/a* ratios

just fractions away from the ideal positions that occur in hP6 $InNi_2$.

For hP6 Ge_4Ni_7 we have to translate all atomic coordinates by 0, 0, 1/4 and then we obtain the same coordinates as in hP6 $InNi_2$. Related to hP3 AlB_2 is hP3 BaPtSb, and related to tI10 Al_4Ba are tI10 $BaNiSn_3$, tI10 H_2PdZr_2, and tI10 C_2IrU_2. The compounds crystallizing in hP3 AlB_2 with minimum *c/a* ratio, having AEs 11-a and 14-d, are related to the structure types of hP3 Cd_2Ce and hP3 $CuZn_3$, since in these structure types the same AEs are realized.

In this brief overview it is impossible to give a complete survey of all relations between the 10 analysed structure types and other structures. A complete analysis of all structure types, as they are listed in Villars and Calvert (1991), is at this moment only partly realized, and it will take us at least another two years to complete this analysis. We estimate that with our approach we can reduce the number of structure types from 2800 different mathematical descriptions to about 500 different coordination types.

Another approach for representing relations between especially complicated structures is the so-called intergrowth concept as proposed by Kripyakevich and Gladyshevskii (1972), among others. In this concept, relations between structure types are written as a linear homogeneous series of intergrowing identical segments, in which these segments are slabs of well-known structures. For a series of inhomogeneous linear structures the concept is described by Grin' *et al.* (1982), and in a lecture presented at the nineteenth International School of Crystallography, Grin' (1992) made an attempt to give a more systematic approach to the concept. An improvement to this concept could be

Table 5. Coordination types for the complete range of *c/a* ratios

Pearson symbol	Formula	Parent type	Coordination numbers	Observed Atomic Environment Types																				c/a ratio
				3#b	4#d	5-a	8-b	8-g	9-a	9-b	10-c	10-j	11-a	12-b	12-i	13-b	13-d	14-b	14-d	14-e	15-d	16-h	17-e	18-d	20-a	22-a	
hP3	Ag_2Nd	AlB_2	3/18	■																			■			maximal (max)
hP6	KPZn	$InNi_2$	3/3/18	■																			■			max
tI10	Cu_2Se_2Tl	Al_4Ba	4/8/20		■			■																■		max
tI10	Co_2LaP_2	Al_4Ba	4/8/22		■			■																	■	medium (med)
tI10	$GdGe_2Pt_2$	Al_4Ba	5/12/22			■								■											■	minimal (min)
tP6	HfSiTe	Cu_2Sb	8/8/17				■	■															■			max
tI12	$BaGe_2$	Si_2Th	9/12						■						■											min
tP6	Cu_2Sb	Cu_2Sb	9/9/12							■				■												min
tP6	MnSbZb	Cu_2Sb	9/9/12							■				■												min
oP12	AgTeTl	Co_2Si	9/12/16							■				■								■				min
tP6	Bi_2U	Cu_2Sb	9/12/17							■				■									■			med
tI10	Al_4Ba	Al_4Ba	9/12/22							■				■											■	min
oC8	BCr	BCr	9/17						■														■			med
oP8	SiTh	BFe	9/17						■														■			min
oP8	CeCu	BFe	9/17						■														■			med
oP8	BFe	BFe	9/17						■														■			med
oP8	DyNi	BFe	9/17						■														■			max
hP3	AlB_2	AlB_2	9/20						■															■		med
tI12	Si_2Th	Si_2Th	9/20						■															■		med
tI12	Si_2U	Si_2Th	9/20						■															■		max
hP6	AsAuCa	$InNi_2$	9/9/20						■															■		med
oP12	Co_2Si	Co_2Si	10/13/13								■					■										med
hP6	$CaIn_2$	$CaIn_2$	10/14									■							■							med
hP6	LaPtSb	$CaIn_2$	10/20									■												■		max
oC8	AlHf	BCr	11/13										■			■										max
hP3	Bi_2Tl	AlB_2	11/14										■						■							min
hP6	CuGaTi	$CaIn_2$	11/14										■						■							min
hP6	$BiIn_2$	$InNi_2$	11/11/14										■						■							min
hP6	$InNi_2$	$InNi_2$	11/11/14										■						■							min
oC8	BaSi	BCr	11/15										■								■					min
oP12	PRe_2	Co_2Si	13/13/15														■	■								max
hP2	CW	CW	14/14																	■						complete range

Table 6. List of related structure types for hP6 $InNi_2$

Pearson symbol	Formula	No. of compounds
hP3	$CuZn_3$	2
hP6	Fe_2Si	13
hP6	Ge_4Ni_7	1
hP6	Hg	1
hP6	Ni_2Si	1

the use of AEs in the descriptions of the slabs because it would show more directly the relations between the combining slabs and the structures in the series. In Chapter 12 by Hauck and Mika in this volume, the close-packed structures and the relations between them are extensively described, and they give a procedure for ordering them in structure maps.

3.5 Structure Types with Atoms Mixing on One Position

In some structure types, as for example hP3 AlB_2, when we look at the reported compounds, we can observe that a great variety of complicated intermetallics have been described in this rather simple structure. An element (Ti), binary, ternary, and even quaternary compounds have been described in terms of this binary structure type, with two atomic positions in the asymmetric unit. This means, for example in the ternary case, that structures have been described where we have two or more atoms randomly occupying the same position in the structure, and, given the published stoichiometries, also in a variety of ratios in that position. From the geometrical point of view, as in the hard-sphere model, this is only acceptable if the mixing atoms would have about the same metallic radii; otherwise we have a description of a structure in which an atom is not in close contact with its direct neighbors.

Solutions for this problem are often given by describing these structures by a lower-symmetry space group. For example, the hP3 BaPtSb structure type is described in space group 187 with the Pt and Sb atoms on the 1d and 1f positions with atomic coordinates 1/3, 2/3, 1/2 and 2/3, 1/3, 1/2, respectively. Although the atoms are now described on different positions, their actual position in the layer remains the same as would be the case if this compound were described in terms of hP3 AlB_2. This solution is in fact in many cases an even worse description than the random distribution description as in hP3 AlB_2, because in the former description the same atom is always on top of itself going from one unit cell to the other. As a result of large differences in metallic radii, this would introduce enormous strains in the crystal, and it is improbable that such a crystal can exist.

However, if we assume that these descriptions are correct, we must accept that atoms are not hard spheres but that they have a certain degree of compressibility, which, as already mentioned, is highly dependent on the alloying atom. Since almost all compounds described in these structure types have a transition-metal and a p element mixing on the same position, both atoms can show this compressibility. As observed and reported many times before, the metallic radii of the p elements especially show this behavior. It is therefore probably correct to state that their reported radii are only valid in the pure-element structures.

For compounds where we have two atoms mixing on the A position in an AB_2 structure, we observe the same behavior, e.g. in Mo_3YB_8 we have Mo and Y, with 1.40 and 1.81 Å as their reported metallic radii, respectively, occupying the same A position. The number of improbable combinations of this sort is, however, much smaller than the number of combinations for the other (B) position, wherein the biggest differences in radii appear only in combinations with

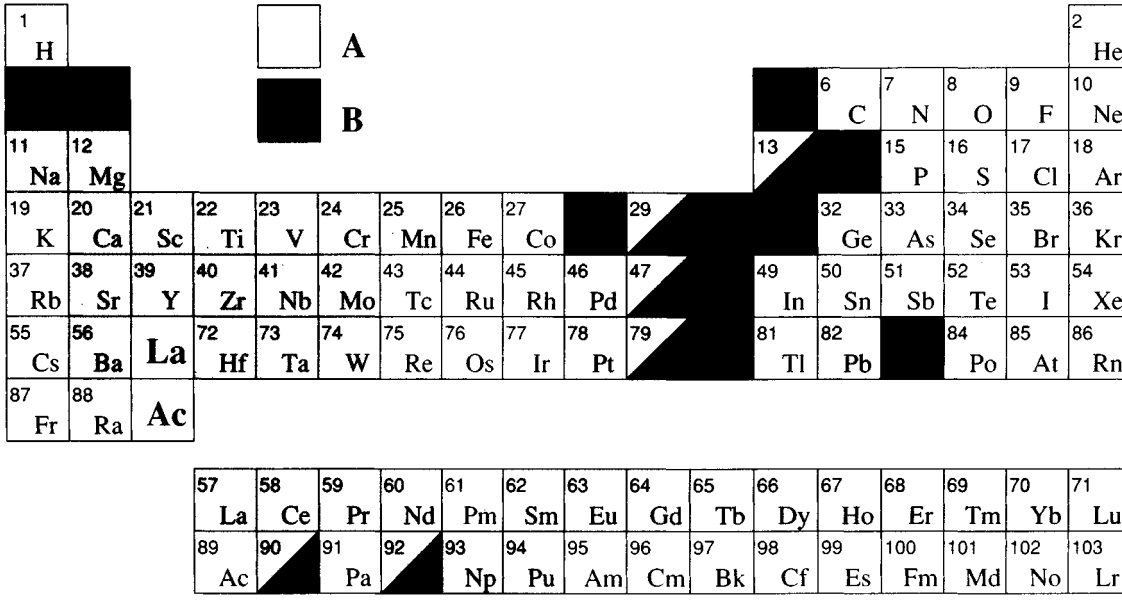

Figure 15. Periodic system representation of the binary 1:2 compounds crystallizing in hP3 AlB_2

the rare-earth metals. In most of the reported combinations there are two early d elements mixing, and they have in general much smaller differences in metallic radii.

In hP3 AlB_2 there are four quaternary compounds reported in which we have a rare-earth (RE) metal on the A position and three elements (Cu, Si, and Zn) mixing on the B position with the composition $RE_2CuZnSi_2$.

Before we consider some relations between the atomic radii and the (shortest) interatomic distance in the structure, we present some statistical information about the compounds crystallizing in hP3 AlB_2. This information can be very helpful for finding errors in structure descriptions.

For the reported binary compounds, crystallizing in this AB_2 type of structure with the ideal 1:2 stoichiometry, we have visualized the realized combinations in a so-called periodic system representation as shown in Figure 15. The elements observed on the A position are marked with a light gray shading and the elements observed on the B position with a darker gray shading, elements reported for the A as well as the B position have both shadings with a diagonal separator. Closer examination of Figure 15 shows us that we have six elements that can occupy the A as well as the B position, namely Al, Cu, Ag, Au, Th, and U. Three of these elements (Al, Ag, and Au) occupy the A position only in combination with boron. Th occupies the B position only in $CuTh_2$; and, because the other combination, Cu_2Th is also reported, it is likely that $CuTh_2$ is incorrect, especially since both compounds are reported with the same unit-cell dimensions. U occupies the B position only in combination with Ti in TiU_2, this compound being assigned to the hP3 AlB_2 structure type.

From the 153 ternary compounds crystallizing in hP3 AlB_2 with various $(A,A')B_2$ or $A(B,B')_2$ stoichiometry, we have about 30 compounds in which random mixing of atoms is reported on the A position, e.g. as in B_4CrMo where Cr and Mo occupy the A site. If we analyze the occurrence of the atoms in this structure in combination with the position of the elements in the periodic system (see Villars and Girgis, 1982), we observe that only a limited number of combinations are realized in this structure type.

In Table 7 we give the complete set of observed ternary combinations in hP3 AlB_2 for atoms mixing on the B position, their mixing ratios, and the elements reported on the A position. Not all of the elements reported on the A position form a compound with the given combination. For example, in the ternary compounds with Ag and Si, the 1:1 combination is only observed for Nd (NdAgSi), while the 2:4 combination is observed for Ce, Dy, Er, Eu, La, Nd, and Pr in the compounds $RE_3Ag_2Si_4$.

For some mixtures we observe that the combinations reported form an almost complete line compound series in the ternary phase diagram, e.g in the combinations of the rare-earth metals with Al and Ga. There is, however, so far no evidence from ternary phase diagrams that

Table 7. Binary combinations in hP3 AlB_2, for the atoms mixing on the B position (and their stoichiometric ratios) in the structure

B-position elements	B-position stoichiometric ratios	Elements reported on the A position
Ag-Si	1:1 2:4	La,Ce,Pr,Nd,Eu,Dy,Er
Al-Ga	3:1 7:3 5:3 1:1 4:6 1:3 1:15	Na,Sr,Ce,Nd,Sm,Gd, Tb,Dy,Ho,Er,Tm
Al-Ge	7:1 13:3 3:1	La,Ce,Nd
Al-Si	7:1 13:3 1:1	Sr,La,Ce,Nd
Al-Sn	7:1 13:3	La,Ce,Nd
As-Pt	29:11	Eu
Au-Si	1:3	Eu
B-Be	7:1 17:3 5:3 1:1	Ti,Zr,Hf,Ta
B-C	19:1	Ta
B-Co	3:1	Gd
Be-Ge	3:5	Ca,Sr
Be-Si	3:5	Ca,Sr,Ba
Co-Ga	1:3	Sm
Co-Ge	1:3	Ce
Co-Si	1:3 2:8	La,Ce,Pr,Nd,Sm,Eu,Gd,Th
Cu-Ga	1:3 1:5 1:9	Sm,Ho,Lu
Cu-Ge	1:1 2:4 1:3	Sr,Ba,Y,La,Ce,Pr,Nd,Sm, Gd,Tb,Dy,Ho,Er,Tm,Lu
Cu-In	1:3	La,Ce,Pr,Nd,Sm,Eu
Cu-Si	3:1 1:1 3:5 2:4 1:3	Sr,Ca,Y,La,Ce,Pr,Nd,Sm, Gd,Tb,Dy,Ho,Er,Tm
Cu-Sn	1:1	La
Fe-Ge	2:4	La,Nd
Fe-Si	1:3 2:8	La,Ce,Pr,Nd,Sm,Gd,U
Ga-Ni	39:1	Ho
Ga-Si	1:1	Ca
Ge-Ir	3:1	Na
Ge-Ni	3:1 1:1	La,Ce,Pr,Nd,Sm,Eu
Ge-Pd	8:2	Nd
Ge-Pt	8:2	Nd
Ge-Rh	3:1	Nd
Ge-Zn	1:1	Sr
In-Ni	3:1	La,Ce,Pr,Nd,Sm,Eu
Ni-Sb	1:1	Ce,Pr,Nd,Sm,Eu
Ni-Si	1:1 2:4 1:3 2:8	Sr,Ca,La,Ce,Pr,Nd,Sm, Gd,Dy,Er
P-Pt	5:2 27:13	Ca,Sr,Eu
Si-Ti	1:1	Gd
Si-Zn	1:1	Y,Ce,Nd,Sm,Eu,Gd,Tb, Dy,Ho
Ti-Zr	5:1	U

Table 8. Binary combinations in hP3 AlB_2, for the atoms mixing on the A position (and their stoichiometric ratios) in the structure

A-position elements	A-position stoichiometric ratios	Elements reported on the B position
Al-Mg	1:1	B_4
Cr-Mo	1:1	B_4
Cr-Ta	1:1	B_4
Cr-Ti	1:1	B_4
Cr-V	1:1	B_4
Hf-Nb	1:1	B_4
Hf-Ta	1:1	B_4
Hf-Ti	1:1	B_4
Hf-Zr	1:1	B_4
Mo-Ti	1:1	B_4
Mo-Zr	1:1	B_4
Nb-Ti	1:1	B_4
Nb-V	1:1	B_4
Nb-Zr	1:1	B_4
Np-Pu	1:1	B_4
Ta-Ti	1:1	B_4
Ta-V	1:1	B_4
Ta-Zr	1:1	B_4
Ti-V	1:1	B_4
Ti-Zr	1:1	B_4
Al-Nb	1:2	B_6
Al-Ta	1:3	B_8
Cr-Nb	2:2	B_8
Mn-Mo	2:2	B_8
Mo-Nb	2:2	B_8
Mo-Y	3:1	B_8
Gd-Nb	7:3	B_{20}
Ti-W	10:1	B_{22}
Gd-U	1:1	Ga_4
U-Y	2:3	Ga_{10}

this line compound series really exists. In the ternary phase diagram of Al-Ga-La, as collected in Bodak and Gladyshevskii (1985), we see that such a line compound series exists for $LaGa_{2-x}Al_x$ whereby x varies from 0 to 1.8 within the hP3 AlB_2 structure type. For $LaAl_2$ the reported structure type is cF24 $MgCu_2$ at low temperatures; at high temperatures (>1363 K) there is a compound reported (La_2Al_5) having the hP3 AlB_2 structure with the La and Al atoms mixed on both positions.

From the 330 compounds reported in the hP3 AlB_2 structure type, at least 10% of these compounds are reported with a stoichiometry differing from the ideal 1:2 composition. In compounds with stoichiometry ratios of 2:3, 2:5 or 3:5, as e.g. in Ho_2Ge_3 or Gd_3Si_5, we have, as mentioned before, atoms mixing on both positions or partly occupied positions.

In Table 8 we give the observed ternary combinations in hP3 AlB_2, where the atoms are mixed on the A position; in the compounds with the stoichiometry $AA'B_4$ the AA′ combinations are 1:1 mixed; for the other combinations the mixing ratios are given in the table.

In Section 3.6 we show for compounds crystallizing in some of the analyzed structure types the relation between the shortest interatomic distance in the structure and the mean radius of the atoms, at the shortest distance, in that structure.

3.6 Atomic Radii and Interatomic Distances

Pearson (1979) and Villars and Girgis (1982) reported a linear dependence between the interatomic distances and the (concentration-weighted) mean radii (d_{AB} vs. $\bar{R}$) for compounds crystallizing in various binary intermetallic structure types. With the help of some examples, we will show that this is correct for the main part of the compounds in a given structure type; but, for some subgroups of compounds within one structure type, different linear dependences can exist.

For demonstration purposes it is not necessary to make the rather complicated calculations given in the paper by Villars and Girgis; instead, we show this linear dependence by plotting the mean atomic radius of the atoms concerned versus half of the interatomic distance between these atoms.

In hP3 AlB_2 we have two atoms in the asymmetric unit and half of the interatomic distance between those

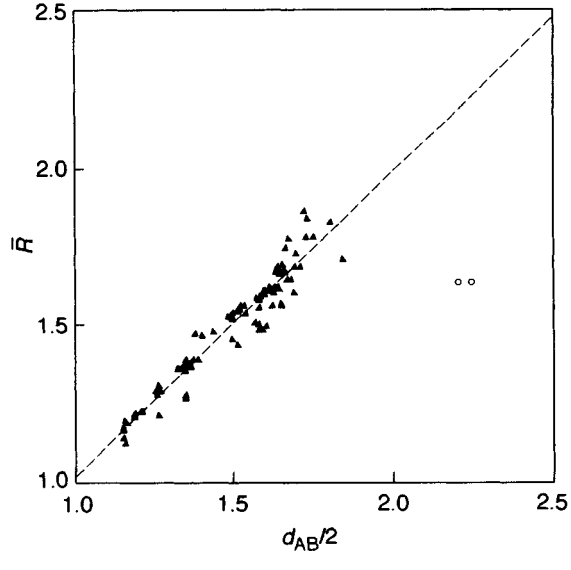

Figure 16. Plot of d_{AB} vs. $\bar{R}$ for the binary compounds crystallizing in hP3 AlB_2. Exceptional cases are noted in the text

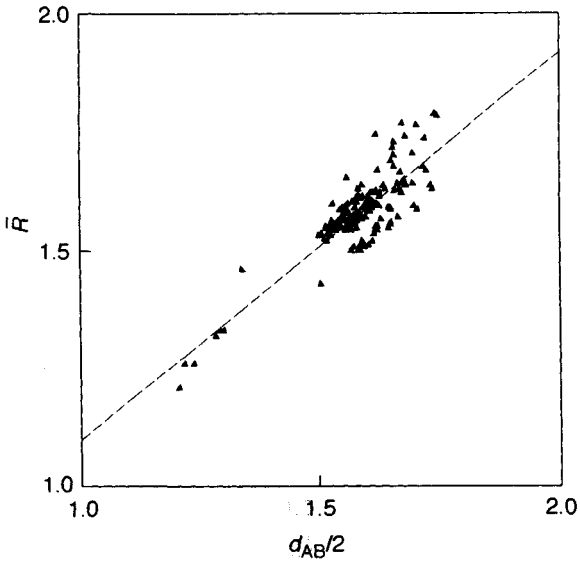

Figure 17. Plot of d_{AB} vs. $\bar{R}$ for the ternary compounds crysallizing in hP3 AlB_2

atoms is $1/2[1/3a^2+1/4c^2]^{1/2}$. For the binary compounds, the mean radius is the mean of the metallic radii of the atoms involved; for the ternary compounds, we first calculate the mean radius of the atoms mixing on the same position, weighted for the mixing concentration, and then calculate the mean radius of the atoms in the structure.

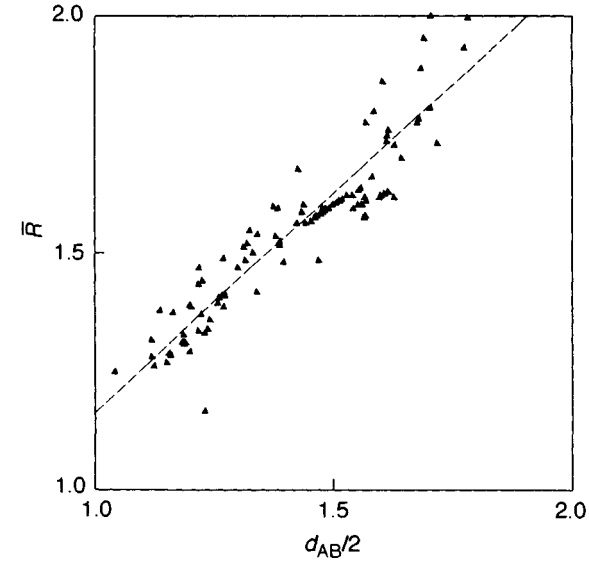

Figure 18. Plot of d_{AB} vs. $\bar{R}$ for the binary compounds crystallizing in oP12 Co_2Si

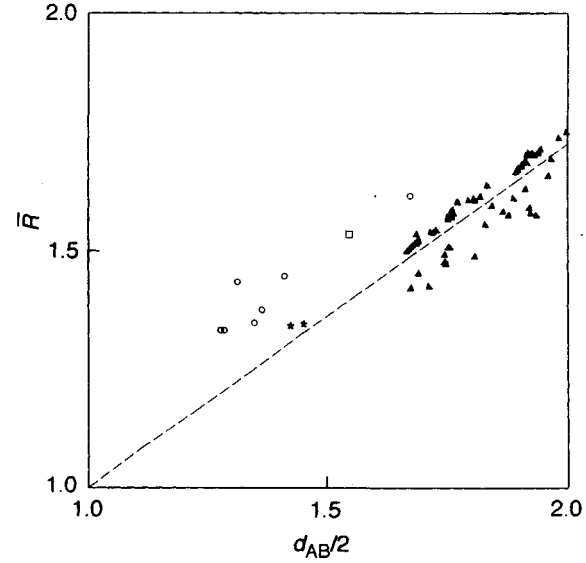

Figure 19. Plot of d_{AB} vs. $\bar{R}$ for the binary compounds crystallizing in tP6 Cu_2Sb. Exceptional cases are noted in the text

In Figures 16 and 17 this linear dependence is plotted for the binary and ternary compounds, respectively, crystallizing in hP3 AlB_2. We see that there is almost no difference between the two plots and that there is a 1:1 dependence, meaning that the mean radius of the atoms involved equals the available space in the structure. In Figure 16 we observe that two compounds, $NdAg_2$ and $PrAg_2$, shown by the open circles, are far away from the 1:1 dependence, the interatomic distance between the rare-earth atoms and the silver atom being too long (0.448 nm, see Figure 7(a)) compared with the mean of the metallic radii. This discrepancy is, of course, a direct consequence of the very long *c*-axis, and it is questionable whether these compounds are in fact realized in this structure type. It is more likely that these compounds are incorrectly classified under this structure type.

The next example shows that there is not always a 1:1 dependence, but that this dependence varies from structure type to structure type, with each of them combining their particular groups of atoms. In Figure 18 we have plotted this dependence for the binary (2:1) compounds crystallizing in oP12 Co_2Si. We see that in general the mean radii of the atoms are more than half the shortest interatomic distance, although a linear relationship still exists. The opposite is observed for the binary compounds crystallizing in tP6 Cu_2Sb, where in general the mean radii are smaller than half the shortest

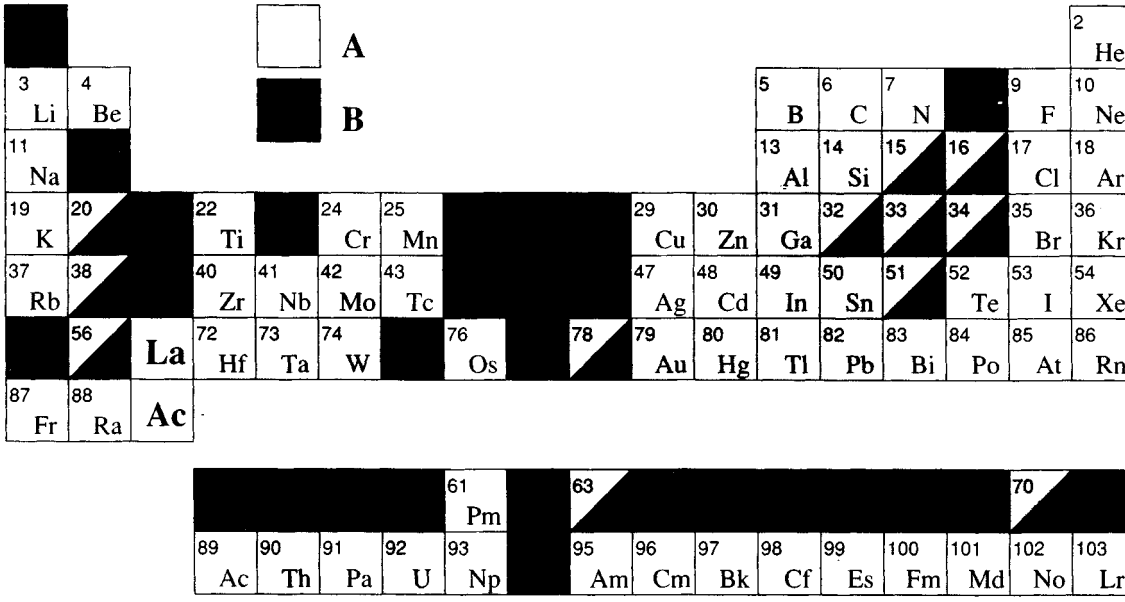

Figure 20. Periodic system representation of the binary 1:2 compounds crystallizing in oP12 Co_2Si

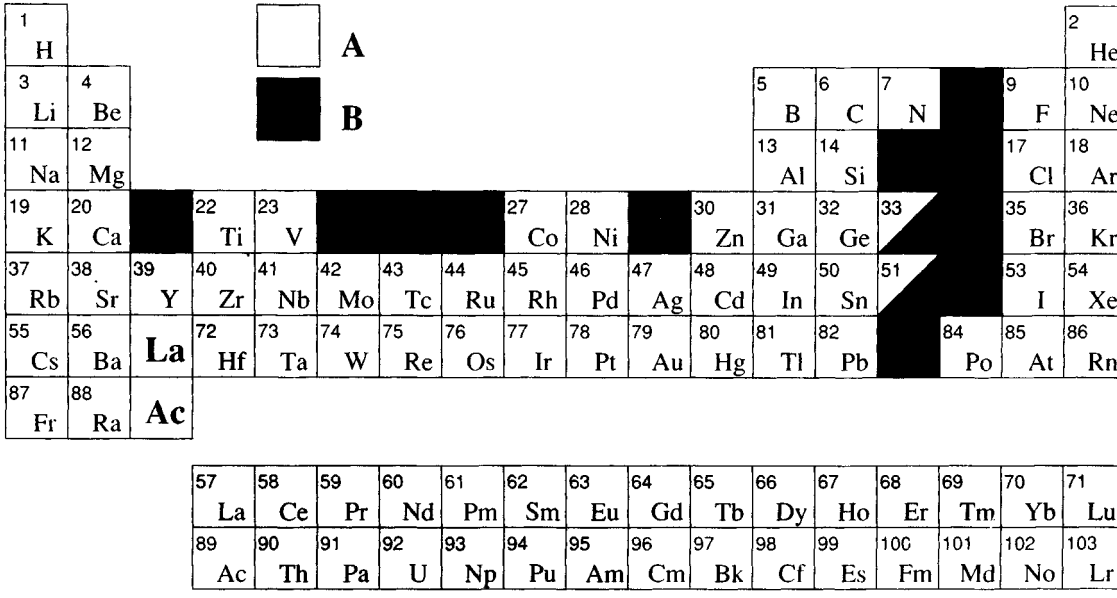

Figure 21. Periodic system representation of the binary 1:2 compounds crystallizing in tP6 Cu_2Sb

interatomic distance (see Figure 19). The broken lines in Figures 16 to 19 are the result of a least-squares analysis.

This contrasting behavior can be understood and explained if we compare, for two AB_2 structure types, the groups of atoms that are combined in the respective compounds. In Figure 20 we show in the periodic system representation oP12 Co_2Si compounds and in Figure 21 tP6 Cu_2Sb compounds. While in tP6 Cu_2Sb the rare-earth atoms are mainly on the A position, the

opposite is observed for oP12 Co_2Si, where they are on the B position.

Another remarkable difference is observed when we compare the combinations that are formed: tP6 Cu_2Sb is almost exclusively observed for combinations of rare earths with a p element, while in oP12 Co_2Si there is no such preference. This preference can explain the differences in the slopes of the lines drawn in Figures 18 and 19; in tP6 Cu_2Sb the bulk of the compounds have a covalent bonding character, which results in smaller radii, while in oP12 Co_2Si we have predominantly metallic bonding.

From the 72 reported binary tP6 Cu_2Sb compounds, with a 2:1 stoichiometry, in only seven combinations do we have a p element (As or Sb) on the A position and a d element (Sc, Cr, Mn, Fe or Cu) on the B position. Figure 19 shows that these seven compounds (marked by open circles) are also placed in this plot outside the main group of combinations, as are three other combinations, namely EuO_2 and GdO_2 (marked by an asterisk), and GdS_2 (marked by an open square). The two oxides probably have an ionic bonding character, while the third compound, GdS_2, is reported to be a high-temperature as well as a high-pressure phase.

To analyze the reported compounds in oP12 Co_2Si in the same manner is much more complex, because in this structure type there is a much wider variety of combinations formed. However, some of the combinations can give us valuable information about the possibilities in this structure type. Figure 20 shows that there are at least five combinations possible in which a rare-earth (Eu or Yb) or an alkaline-earth atom (Ca, Sr or Ba) is reported on the A position. If we look up all representatives in which this is realized, we see that this combination is only reported for compounds with hydrogen in the B position. Elements reported on the A as well as the B position are Pt, Ge, P, As, Sb, S, and Se. The latter two, S and Se, are on the A position only in combination with cesium, and As and Sb only in combination with rhodium. For P and Ge there are reported many combinations but e.g. Ge on the B position only occurs in combination with Mo or W, both compounds stable only at high temperatures.

With these brief examples, we have shown that the combination of a simple method, e.g. a mean radii vs. interatomic distance plot, and a periodic system array showing all possible combinations gives much information about the validity and the nature of the compounds crystallizing in a particular structure type. Such knowledge can be very helpful in explaining crystal structures, and to a certain extent the physical properties of old as well as new intermetallic compounds.

Thus this analysis illustrates the thesis set forth in Section 1 that examination of the AEs of the 10 seemingly diverse structure types of Table 1 leads to the following kinds of insights:

- Striking resemblance in the short-range atomic arrangements between the structure types and thus between compounds crystallizing therein.
- Simple recognition of relations between structures by introducing coordination types.
- Crystal chemical information available for addition to the standard mathetmatical description.
- Rather simple calculations for checking reported crystal-structure data.

4. Concluding Remarks

In this paper we have introduced our atomic-environment approach, and we have shown that these unambiguously defined AEs can be very useful in crystal chemistry, especially when we know that in intermetallic structures only a limited number of AEs are realized. From this and earlier work we have good reason to believe that within two years, after the completion of the analysis of all crystal symmetries, we will recognize about 25 standard atomic-environment types. These AETs can be used to explain crystal-structure data and to detect relations between structures. It is our firm belief that, by combining our AET with predictive models such as the Miedema model, the Villars structure stability diagrams and the structure maps of Pettifor, these models will gain in reliability as well as in predictability.

The observed atomic environments in the analyzed structures suggest a complementary classification method (classification in so-called coordination types), which will lead to a considerable decrease in structure types that are needed. This classification in coordination types gives, independent of the mathematical description of the structures, geometrical information about the short-range atomic arrangements in the structures.

In general, highly symmetrical AEs are formed in intermetallic compounds. Unusual AEs are only formed when there is a large difference in metallic radii of the atoms forming the compound. This deduction is confirmed by Aslanov in his paper concerning the crystal chemical model of atomic interactions of intermetallic phases (Aslanov, 1992). Although there are some differences between the definitions in the model of Aslanov (CCMAI) and in our approach, especially regarding the coordination sphere of an atom, the

resemblance of the AEs observed by both methods is in general so overlapping that a more thorough investigation is necessary to decide whether one method is preferable to the other.

We are convinced that the value of the intergrowth concept will be strengthened if in this model AEs are used in describing the intergrowing slabs. By introducing AEs for the atoms in the slabs, the relations between the respective structures and the slabs will be more visible, and it will also show whether there are improbable structure transformations.

We have shown that with simple calculations and plots we can visualize the bonding character of the compounds crystallizing in a structure type. Presenting all the compounds crystallizing in a particular structure type in a periodic system array gives us valuable information about the possible combinations (of groups of atoms) that are, or to some extent can be, realized in this structure type.

Combining the above methods shows systematically which of the published crystal-structure data are correct. Applying all these methods to new structure data can prevent us from publishing those data in a wrong description.

The importance of AEs, when combined with so-called structure stability diagrams (SSD) or quantum structure diagrams (QSD), is described in Chapter 11 by Villars in this volume. In that chapter and also in earlier work (Villars and Hulliger, 1987; Villars *et al.*, 1989), Villars shows that combining the AEs with the SSD improves the reliability of the SSD.

The metallic radii as they are published among others by Teatum *et al.* (1960) are not valid in most intermetallic compounds, probably due to the fact that the assumption that they are correct for CN = 12 is never met in most compounds. We have shown that (see Tables 4 and 5) the coordination numbers can vary from 3 to 22 in the structure types analyzed. In general we observed low coordination numbers, CN < 9, for the p elements, CN numbers between 9 and 14 for the d elements, and CN > 12 for the s and f elements.

5. Acknowledgements

The author is grateful to Dr P. Villars, H. W. Wondergem, and D. B. de Mooy for their interest in this work and their critical reading of the manuscript. Special thanks are due to Dr A. R. Miedema who, before his sudden death, enthusiastically supported our work on systematics in intermetallic structures, who was always available for advice, and who participated in numerous fruitful discussions.

6. References

Aslanov, L. A. (1989). *Structure of Substances* (in Russian). Moscow State University Press, Moscow.

Aslanov, L. A., and Markov, V. T. (1992). A Crystal Chemical Model of Atomic Interactions. 6. Intermetallic Phase Structures. *Acta Crystallogr.*, **A48**, 281–293.

Bodak, O. I., and Gladyshevskii, E. I. (1985). *Handbook of Ternary Systems Containing Rare-Earth Metals* (in Russian). L'vov State University Press, L'vov.

Brunner, G. O., and Schwarzenbach, D. (1971). Zur Abgrenzung der Koordinationssphare und Ermittlung der Koordinationszahl in Kristallstrukturen. *Z. Kristallogr.*, **133**, 127–133.

Bruzzone, G., Fornasini, M. L., and Merlo, F. (1970). Rare-Earth Intermediate Phases with Zinc. *J. Less-Common Met.*, **22**, 253–264.

Daams, J. L. C., and Villars, P. (1993). Atomic-Environment Classification of the Rhombohedral Intermetallic Structure Types. Proc. Workshop on Regularities, Classifications and Predictions of Advanced Materials. *J. Alloys and Compounds*, **197**, 243–269

Daams, J. L. C., Villars, P., and van Vucht, J. H. N. (1991). *Atlas of Crystal Structure Types for Intermetallic Phases*. ASM International, Materials Park, OH.

Daams, J. L. C., Villars, P., and van Vucht, J. H. N. (1992). Atomic-Environment Classification of the Cubic Intermetallic Structure Types. *J. Alloys and Compounds*, **182**, 1–33.

Grin', Yu. N. (1992). The Intergrowth Concept as a Useful Tool to Interpret and Understand Complicated Intermetallic Structures. In *Modern Perspectives in Inorganic Crystal Chemistry* (ed. E. Parthé). Kluwer, Dordrecht.

Grin', Yu. N., Yarmoluk, Ya. P., and Gladyshevskii, E. I. (1982). The Crystal Chemistry of Series of Inhomogeneous Linear Structures. *Sov. Phys. Crystallogr.*, **27**, 413–417.

Grin', Yu. N., and Gladyshevskii, R. E. (1989). *Gallides* (in Russian). Metallurgiya, Moscow.

Hahn, T. (ed.) (1983). *International Tables for Crystallography*, Vol. A., Reidel, Dordrecht.

Jensen, W. B. (1989). Crystal Coordination Formulas. In *The Structure of Binary Compounds* (eds F. R. de Boer and D. Pettifor). Elsevier, Amsterdam, pp. 105–146.

Kripyakevich, P. I., and Gladyshevskii, E. I. (1972). Homologous Series Including New Structure Types of Ternary Silicides. *Acta Crystallogr.*, **A28**, Supplement, s97.

Merlo, F. (1988). Volume Effects in the Intermetallic Compounds Formed by Ca, Sr, Ba, Eu and Yb with Other Elements. *J. Phys.*, **F18**, 1905–1911.

Miedema, A. R., and Niessen, A. K. (1982). Volume Effects upon Alloying of Two Transition Metals. *Physica*, **B114**, 367–374.

Parthé, E. (1990). *Elements of Inorganic Structural Chemistry*. Sutter Parthé, Petit-Lancy, Switzerland.

Pearson, W. B. (1958). *A Handbook of Lattice Spacings and Structures of Metals and Alloys*. Pergamon, London.

Pearson, W. B. (1967). *A Handbook of Lattice Spacings and Structures of Metals and Alloys*, Vol. 2. Pergamon, London.

Pearson, W. B. (1972). *The Crystal Chemistry and Physics of Metals and Alloys*. Wiley-Interscience, London.

Pearson, W. B. (1979). The Stability of Metallic Phases and Structures: Phases with the AlB_2 and Related Structures. *Proc. R. Soc.*, **A365**, 523–535.

Pearson, W. B. (1985a). The Cu_2Sb and Related Structures. *Z. Kristallogr.*, **171**, 23–39.

Pearson, W. B. (1985b). The Most Populous of all Crystal Structure Types, the Tetragonal $BaAl_4$ Structure. *J. Solid State Chem.*, **56**, 278–287

Pearson, W. B., and Villars, P. (1984). Analysis of the Unit-Cell Dimensions of Phases with the $BaAl_4$ ($ThCr_2Si_2$) structure I, II and III. *J. Less-Common Met.*, **97**, 119–143.

Teatum, E., Gschneidner, K., and Waber, J. (1960). Report LA-2345, US Department of Commerce, Washington, DC.

Villars, P., and Calvert, L. D. (1991). *Pearson's Handbook of Crystallographic Data for Intermetallic Phases*, 2nd edn. ASM International, Materials Park, OH.

Villars, P., and Daams, J. L. C. (1993). Atomic-Environment Classification of the Chemical Elements. Proc. Workshop on Regularities, Classifications and Predictions of Advanced Materials. *J. Alloys and Compounds*, **197**, 177–196

Villars, P., and Girgis, K. (1982). Regularities in Binary Intermetallic Compounds. *Z. Metallk.*, **73**, 455–462.

Villars, P., and Hulliger, F. (1987). Structural-Stability Domains for Single-Coordination Intermetallic Phases. *J. Less-Common Met.*, **132**, 289–315.

Villars, P., Mathis, K., and Hulliger, F. (1989). Environment Classification and Structural Stability Maps. In *The Structure of Binary Compounds* (eds F. R. de Boer and D. Pettifor). Elsevier, Amsterdam.

This chapter was originally published in 1995 as Chapter 15 in *Intermetallic Compounds*, Vol. 1: *Principles*, edited by J. H. Westbrook and R. L. Fleischer.

Chapter 6

Some Important Structures of Fixed Stoichiometry

Michael V. Nevitt

Department of Physics and Astronomy, Clemson University, Clemson, SC 29634, USA

Carl C. Koch

Department of Materials Science and Engineering, North Carolina State University, Raleigh, NC 27695, USA

1. Introduction

Well over 1000 intermetallic compounds have been reported for the nine varied structure types of fixed stoichiometry treated in this chapter, a number that is a substantial fraction of all the compounds whose structures have been recently described and tabulated (Villars and Hulliger, 1987; Villars and Calvert, 1991). While their structural features differ widely, the families of compounds discussed here exhibit several unifying threads as regards the atomic size and the positions of the components in the periodic table. These considerations will be explored throughout the chapter.

Since the first edition of this book (Westbrook, 1967) there has been a substantial increase in the number of compounds reported and compiled, so much so that it is no longer practicable to include complete lists of the phases. Villars and Calvert (1991) should be consulted for such compilations. A major factor in the growth has been the addition of large numbers of ternary compounds to earlier lists of primarily binary compounds.

An important benefit of the greatly enlarged database is the refinement of earlier rules and rationales for occurrence. Some of the earlier qualitative strictures regarding atomic size and valence have been weakened or invalidated as gaps in the data have been filled in. Newer, more quantitative, models are being developed for intermetallic phases (Nevitt, 1967; Villars, 1984; Pettifor, 1986a, b; Rajasekharan and Girgis, 1983; Miedema *et al.*, 1975); thus far, however, they have had only limited application to the compounds treated in this chapter, as will be noted.

The compound families treated in this chapter show, for the most part, close adherence to characteristic stoichiometries. The discussion will begin with three AB_2 compound families whose structure types are $MoSi_2$, $CuAl_2$, and $NiTi_2$. The closely related Fe_3W_3C type will be included with the last of the three. Two groups of compounds of more complex stoichiometry that are isostructural, or at least quasi-isostructural, will be treated next. These are the $Mn_{23}Th_6$ type and the $Cu_{16}Mg_6Si_7$ type. The discussion will then turn to three compound families possessing dissimilar structures, but having in common the dominant involvement by elements of the lanthanide and actinide periods. These compounds belong to the $NaZn_{13}$, CFe_3, and Th_3P_4 structure types. The last of these is unusually prolific in its occurrence: over 350 compounds have been reported.

Readers unfamiliar with the Wyckoff notation used in the tables of atomic positions that follow should consult the *International Tables for Crystallography* (Hahn, 1989) for clarification. Briefly, each Wyckoff notation, consisting of a number denoting the multiplicity and an arbitrary letter, refers to the position of a set of atoms in the unit cell that share the same point symmetry. The x, y, and z values, used in conjunction with the generalized atomic coordinates for the specific structure in the *International Tables*, provide the location of each atom in the unit cell.

Crystal Structures of Intermetallic Compounds. Edited by J. H. Westbrook and R. L. Fleischer

2. $MoSi_2$-Type Phases

This family of AB_2 compounds has been discussed and analyzed to a greater extent than the others covered in this chapter. Its treatment will be somewhat more detailed, therefore. The compounds have the Pearson symbol tI6 (*Strukturbericht* $C11_b$); the space group is I4/mmm and space group number 139. The atomic positions for the prototype $MoSi_2$ (Thomas *et al.*, 1985) are given in Table 1. The cell dimensions are $a = 0.3203$ nm, $c = 0.785$ nm and axial ratio $c/a = 2.45$.

Villars and Calvert (1991) list 84 binary or ternary compounds that crystallize in the $MoSi_2$-type structure. Many of these compounds involve a lanthanide as the A component and noble or group IVA (Ti group) metals as the B component, but sometimes as the A metal. It has long been recognized that these compounds can be classified into two main groups with respect to their axial ratios (Nevitt, 1967; Raynor, 1974); that is, a group of low axial ratio between 2.29 and 2.60, and a group of high axial ratio between 3.188 and 4.684. More recently Hellner and Pearson (1984) have divided these groupings into four as illustrated in the histogram of Figure 1. These include the large groupings of compounds around c/a ratios of either 2.45 or 3.45 as well as smaller groups with c/a at 3.0 and 4.24. They extended their study of the tetragonal distortion of I (body-centered) and F (face-centered) lattice complexes to phases with AB_2 stoichiometry with the $MoSi_2$-type structure. The geometry of these groupings is related to the relative sizes of the component atoms. From the geometry of the structure and the assumption that there are simultaneous contacts between spherical atoms in the A–A and A–B directions, it may be determined that the ideal radius ratio for $MoSi_2$-type phases is $R_A/R_B = 1$. However, the actual values of R_A/R_B vary from <0.8 to 1.25.

Table 1. Prototype $MoSi_2$

Atoms	Wyckoff notation	Symmetry	x	y	z	Occupancy
Mo	2(a)	4/mmm	0	0	0	1.0
Si	4(e)	4mm	0	0	0.333	1.0

The structure of $MoSi_2$-type phases has been described as a superstructure of the b.c.c. or CsCl structure with three subcells stacked along [001]. This is illustrated in Figure 2 for $CuTi_2$. The c/a ratio for the $MoSi_2$-type tetragonal cell varies from 2.207 to 4.684 corresponding to the distortion of the b.c.c. cells

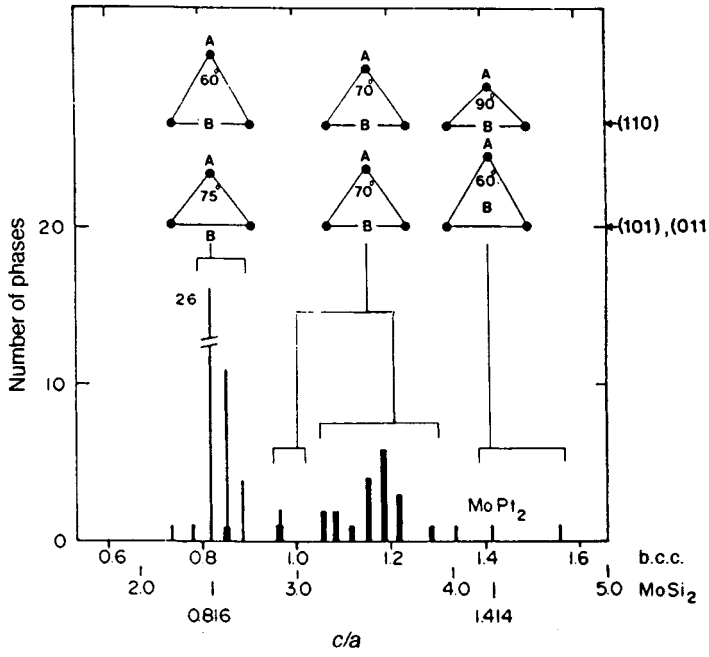

Figure 1. Histogram of the number of phases with the $MoSi_2$ structure having axial ratios lying about the indicated values. Thick lines indicate phases for which $R_B > R_A$. Above are indicated the three modes of stacking triangular layers of atoms. (Reproduced by permission of R. Oldenbourg Verlag from Hellner and Pearson, 1984)

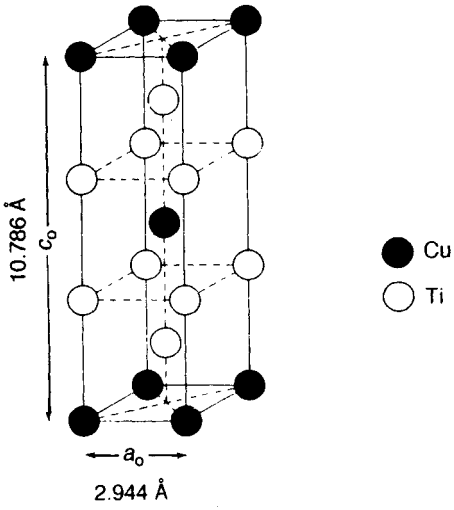

Figure 2. The unit cell of $CuTi_2$, an $MoSi_2$-type structure. (Reproduced by permission of John Wiley & Sons from Nevitt, 1967)

to c/a ratios of 0.736 to 1.561 respectively. Projections on (1 1 0) of the $MoSi_2$ structure for three 'ideal' axial ratios are given in Figure 3. For the AB_2 stoichiometry of $MoSi_2$-type phases, all but two phases grouped about $c/a = 2.45$ or $c/a = 3.0$ have A as the larger atom or $R_A \approx R_B$. In contrast to this, all known phases with c/a ratios grouped about 3.5 have B as the larger atom. From geometry, when A is the larger atom the axial ratio $c/a = 2.45$ provides a structure that gives a better separation of the A atom and its four A neighbors along [1 0 0] and [0 1 0] than an arrangement with a large c/a value where a_0 is smaller. This geometrical factor is consistent with the disposition of phases about an axial ratio of 2.45 when A is the larger component.

For phases with an axial ratio close to 3.0, the subcell corresponds to the nearly undistorted b.c.c. cell. It might be expected that phases with this axial ratio would have $R_A \approx R_B$. However, for $AlCr_2$ and MoU_2, Al (A) and U (B) are significantly larger than their partner species.

The phases occurring about the axial ratio $c/a = 3.5$ presumably form because it gives good sphere packing when the major component B is the larger atom. Raynor (1974) had previously suggested that the phases with high c/a values were attributable to the directional d-electron bonding of the B components Ti, Zr, or Hf. Subsequently, however, additional phases with c/a values near 3.5 have been discovered with other B components (e.g. Au, Ba, Pb, Bi), so geometry seems to be the controlling factor.

The two phases with axial ratios near 4.24, i.e. $TiAg_2$ with $c/a = 4.014$ and $CdTi_2$ with $c/a = 4.684$, are not well understood. From the atomic sizes one

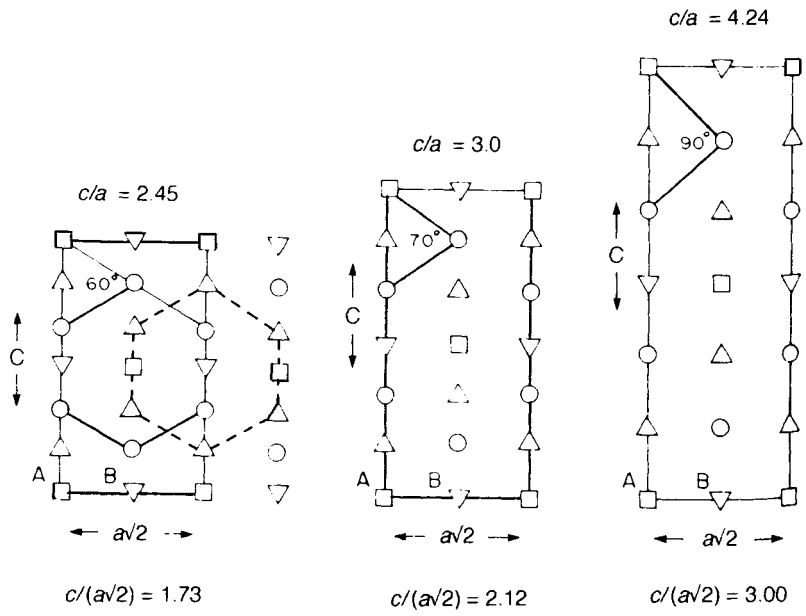

Figure 3. Projections of the $MoSi_2$ structure, AB_2, on (1 1 0) for the axial ratios indicated: (□) A atoms and (○) B atoms in the plane of the projection; (▽) A atoms and (△) B atoms in the layers above and below. (Reproduced by permission of R. Oldenbourg Verlag from Hellner and Pearson, 1984)

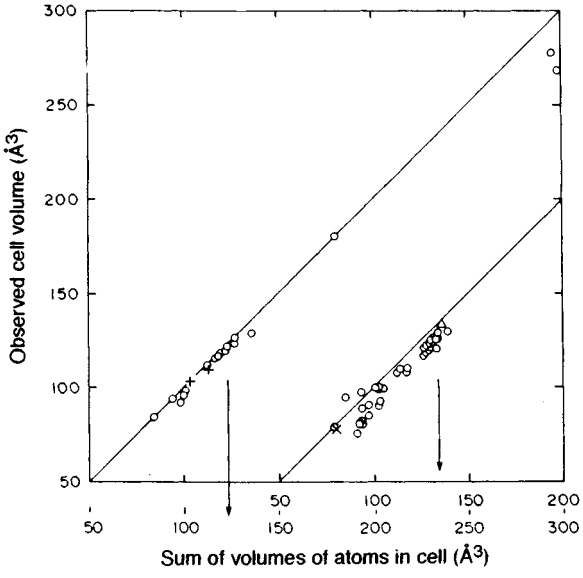

Figure 4. Observed unit-cell volume of phases with the $MoSi_2$ structure plotted against the sum of the elemental volumes of the atoms in the unit cell. Left: phases with $R_B > R_A$, together with $AgTi_2$ and $CrTi_2$ (+). Right: phases with $R_A > R_B$, including $AlCr_2$ (×) and $Hg_{35}Cd_{65}$ (▵). (Reproduced by permission of R. Oldenbourg Verlag from Hellner and Pearson, 1984)

might predict an axial ratio of ~2.45 (Hellner and Pearson, 1984).

Figure 4 illustrates that the volume of the unit cell of phases with the $MoSi_2$ structure follows closely the sum of the atomic volumes of the atoms in the unit cell. This is especially true for the phases where $R_B > R_A$.

Polymorphism has been observed for $MoSi_2$. The high-temperature phase, stable above 1850°C, has the $CrSi_2$-type structure (Svechnikov *et al.*, 1971). The $CrSi_2$ structure, hP9, space group $P6_222$, is made up of three close-packed 3^6 layers of atoms (3 specifies a triangle, and 6 gives the multiplicity) one above the other along [001] in the unit cell (Villars and Calvert, 1991). The close-packed layers are stacked in b.c.c. [110] stacking positions. Thus, $CrSi_2$ is part of the same family of structures based on b.c.c. [110] stacking of close-packed AB_2 layers as $MoSi_2$ (and $TiSi_2$) (Pearson, 1972).

While the atomic sizes and atomic packing of the components are important for the occurrence of the $MoSi_2$-type phases, and for the axial ratios observed, electronic factors also play a role in their occurrence. Figure 5 (Siegrist *et al.*, 1983) gives existence regions of transition-element MX_2 phases (M = transition element, X = p element (metalloid)) in a diagram of valence-electron number (= Σ group numbers) vs.

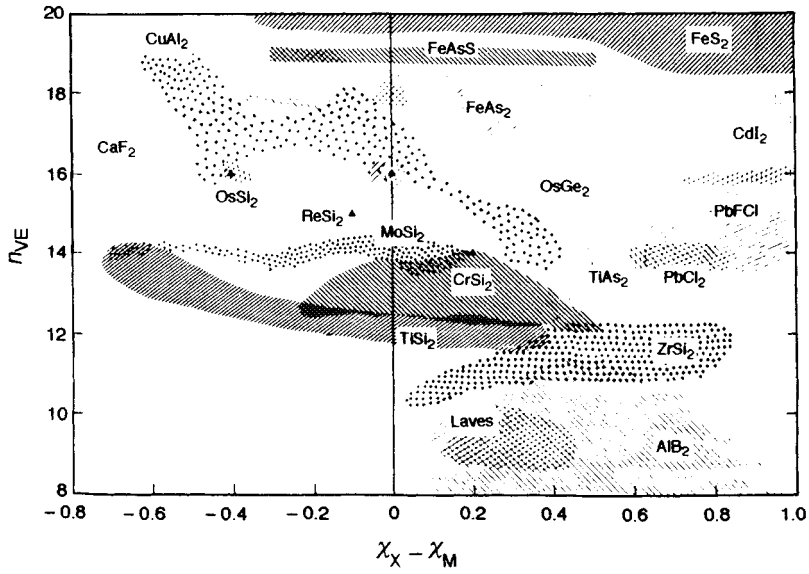

Figure 5. Existence regions of transition-element MX_2 phases (X ≡ p element) in a diagram of valence-electron number (n_{VE}) vs electronegativity difference ($\chi_X - \chi_M$; (▲) the non-metallic exceptions among the silicides ($ReSi_2$, $CrSi_2$, $FeSi_2$, and $OsSi_2$). The formulae refer to structure types. (Reproduced by permission of Elsevier Sequoia SA from Siegrist *et al.*, 1983)

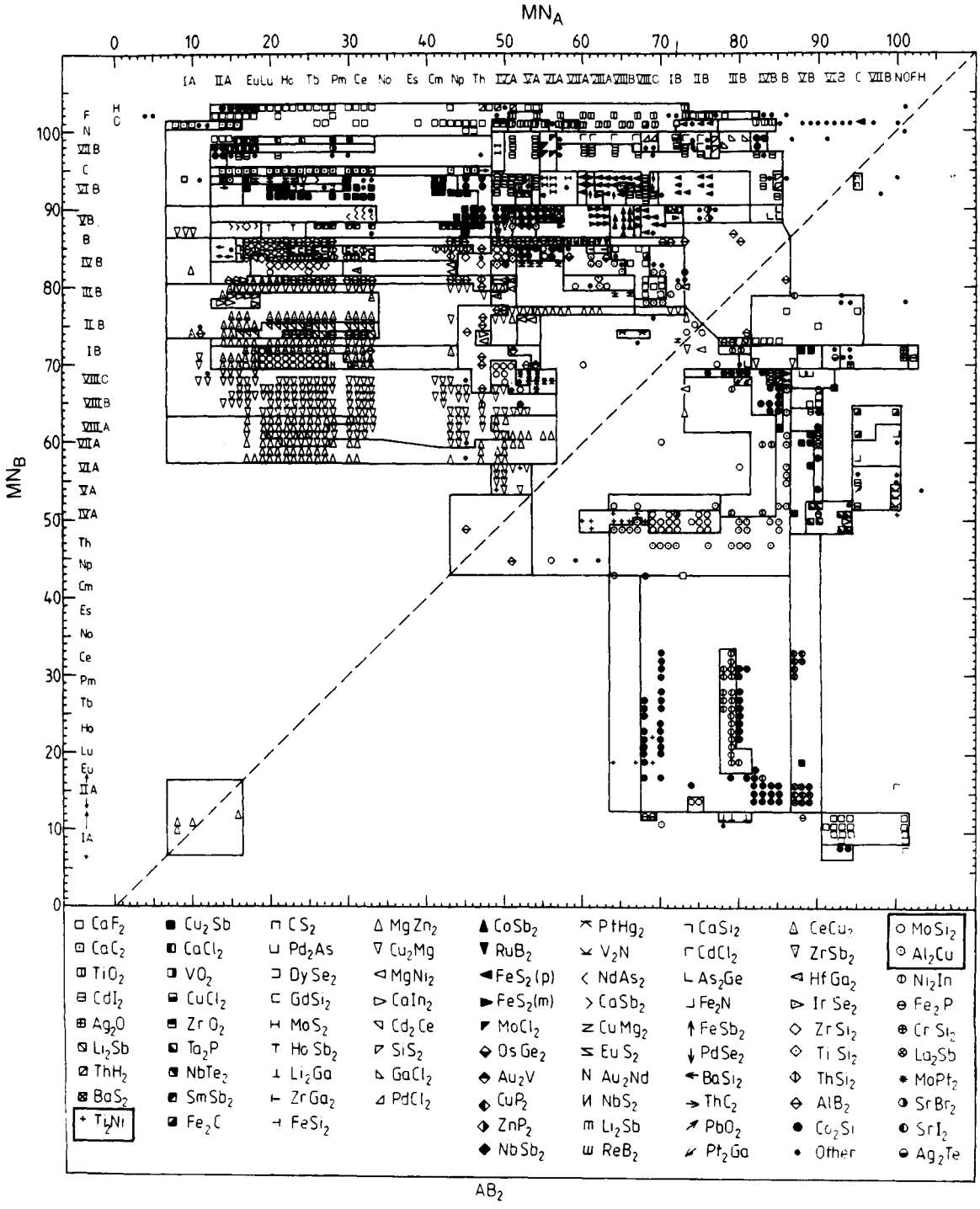

Figure 6. The AB_2 structural map developed by Pettifor. (From Pettifor, 1988)

electronegativity difference. The region for $MoSi_2$-type structure phases overlaps those for $CrSi_2$- and $TiSi_2$-type phases.

The most complete structural correlation using 'classical' concepts has been presented by Villars and co-workers (Villars and Hulliger, 1987; Villars, 1984). Three-dimensional maps ($\Delta\chi$, ΔR, ΣVE) are used to separate the structure types. Here $\Delta\chi$ is the magnitude of the Martynov–Batsanov electronegativities, ΔR the magnitude of the difference of Zunger's pseudopotential radii sums, and ΣVE the sum of the valence-electron numbers. Stability domains give good separation into $MoSi_2$ structure regions in this three-dimensional space. Of the 56 $MoSi_2$ structure compounds, only one was misplaced and only four non-$MoSi_2$ structure compounds were found in the $MoSi_2$ domains.

While the method does provide separation, the angular dependence of the valence orbitals, i.e. whether the electrons have s-, p-, or d-like quantum character, is not given by these classical coordinates. Pettifor (1986a, b, 1988) has proposed a phenomenological structure-map scheme based on assignment of numbers (Mendeleev numbers, MN) to the elements in the periodic table that does reflect the quantum character of the electronic structure and can form a two-dimensional map. This is accomplished by running a one-dimensional string through the periodic table. Excellent structural separation of binary compounds is achieved by plotting MN_A vs MN_B for a given stoichiometry such as AB_2. The Pettifor map for AB_2 stoichiometry is presented in Figure 6. There are several major groupings of $MoSi_2$ phases apparent in this map, and the two largest groupings represent the compounds with $c/a \approx 2.45$ and $c/a \approx 3.45$. However, there are many isolated $MoSi_2$ regions as well.

Another phenomenological alloying model has been applied to the $MoSi_2$ phases by Rajasekharan and Girgis (1983). These authors used Miedema's theory for the heat of formation of intermetallic phases (Miedema *et al.*, 1975). They plotted the Miedema parameter $\Delta\phi^*$, which measures the chemical potential (related to electronegativity), versus $(\Delta n_{WS})^{1/3}$, which represents the electron density at the surface of the Wigner–Seitz cell for each element. A $\Delta\phi^*$ vs $(\Delta n_{WS})^{1/3}$ map gave

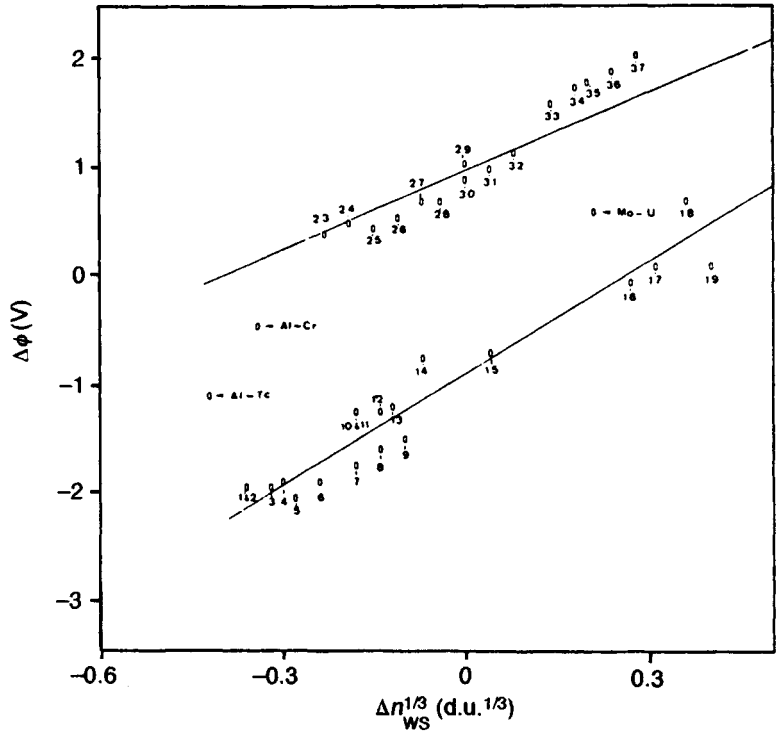

Figure 7. A plot of $\phi^*_A - \phi^*_B$ vs. $(n^A_{WS})^{1/3} - (n^B_{WS})^{1/3}$ for the binary systems in which $MoSi_2$-type phases occur. The upper curve represents compounds with $c/a \approx 3.5$, the lower curve those with $c/a \approx 2.5$, and labeled points in between these curves for $c/a \approx 3.0$. (Reproduced by permission of the American Physical Society from Rajasekharan and Girgis, 1983)

good resolution among the binary systems in which different structure types occur, indicating the importance of the enthalpy of formation of an intermetallic compound in deciding the crystal structure that it adopts. That is, the heat of formation is determined by the values of $\Delta\phi$ and Δn in Miedema's model (Miedema *et al.*, 1975). Such a plot is shown for $MoSi_2$ phases in Figure 7. Very good separation is observed for the $MoSi_2$-type compounds with $c/a \approx 2.45$ and $c/a \approx 3.45$, with the few compounds with $c/a \approx 3.0$ in between. Thus electronic structure as well as atomic packing plays a role in determining the structure of the $MoSi_2$-type structure phases.

The $MoSi_2$-type structure phases contain several compounds with interesting properties. $MoSi_2$, the prototype of these structures, has long been a practical material used for high-temperature furnace heating elements (see Chapter 10 by Kumar and Chapter 20 by Vedernikov in Volume 2). There is much interest presently in developing $MoSi_2$ as a high-temperature structural material because of its high melting temperature, low density, and excellent oxidation resistance (Fleischer, 1985; Petrovic and Vasudevan, 1992; Alman *et al.*, 1992).

3. $CuAl_2$-Type Phases

The $CuAl_2$-type structure, Pearson designation tI12 (*Strukturbericht* C16) is b.c.t. with the c/a ratio in the range 0.74 to 0.89 (Villars and Hulliger, 1987; Villars and Calvert, 1991). It exhibits the AB_2 stoichiometry with deviations from stoichiometry of either sign up to 7%. The space group is I4/mcm and space group number 140. The atomic positions in the unit cell of the prototype (Meetsma *et al.*, 1989) are given in Table 2.

There are 101 binary and ternary phases as tabulated by Villars and Calvert (1991). The unit cell for the $CuAl_2$ structure is illustrated in Figure 8. Figure 8(a) shows the unit cell and Figure 8(b) gives the atomic arrangement down [001].

Each Cu atom is surrounded by eight Al atoms situated at the corners of an Archimedean square antiprism, and it has two Cu atoms at a distance of $c/2$, forming linear chains. Each Al atom has four Cu atoms

Table 2. Prototype $CuAl_2$

Atoms	Wyckoff notation	Symmetry	x	y	z	Occupancy
Cu	4(a)	422	0	0	1/4	1.0
Al	8(h)	m.2m	0.1581	0.6581	0	1.0

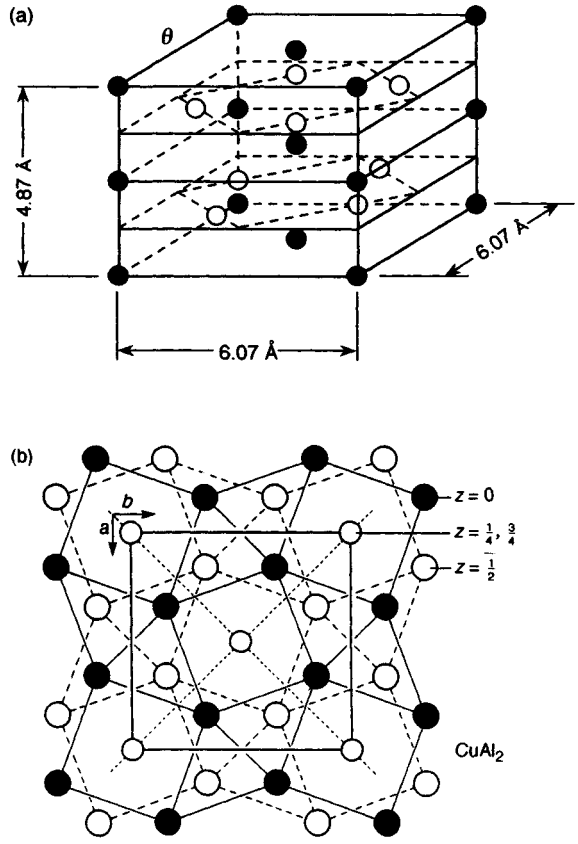

Figure 8. (a) Unit cell of $CuAl_2$. (Reproduced by permission of Chapman & Hall from Porter and Easterling, 1981, part of Figure 5.29). (b) Atomic arrangement in the $CuAl_2$ structure projected down [001]; large open and solid circles are Al atoms, at $z=0$ and $z=\frac{1}{2}$. Small open circles are Cu at $z=\frac{1}{4}, \frac{3}{4}$. (Reproduced by permission of John Wiley & Sons from Pearson, 1972)

as nearest neighbors and is also surrounded by a total of 11 (1+2+4+4) other Al atoms at distances d_1, d_2, d_3, and d_4, respectively, near to $2r_B$. The d_3 and d_4 distances are $>2r_B$ while d_1 is always, and d_2 almost always, smaller. These atoms form a convex CN 15 polyhedron about the Al atom. The main feature of this AB_2 structure type appears to be an interlocking honeycomb network of the Al atoms in hexagons in the (1 1 0) and (1 $\bar{1}$ 0) planes, while the Cu atoms lie in channels parallel to the c-axis.

Twenty-three quasibinary $CuAl_2$-type alloy systems are described by Havinga *et al.* (1972). In those systems where both end members have the $CuAl_2$ structure, 11 cases (all but three) exhibit continuous solid solubility. Of course, in systems where one end member is not isostructural, only a limited range of solubility will be

observed. For example, for $Ni_{1-x}Cu_xZr_2$ the $CuAl_2$-type structure is found up to $x=0.4$. For $x>0.6$ an $MoSi_2$-type structure phase is stable, and a two-phase field exists for $0.4<x<0.6$. Interstitial element contamination can influence the structure in certain systems. In $Fe_{1-x}Cu_xZr_2$ an $NiTi_2$-type phase is observed for $x<0.8$ if the samples are contaminated by C, N, or O. However, when sample preparation is carried out such as to make interstitial element contamination negligible, the $FeZr_2$ end member also crystallizes in the $CuAl_2$-type structure (as does $CoZr_2$, independent of contamination).

The atomic coordinate x and the axial ratio c/a exhibit maxima when plotted against the concentration of valence electrons per atom, e/a, at e/a values near 2 and 5 with a minimum in between, as illustrated in Figure 9 (Havinga *et al.*, 1972). This behavior suggests that e/a is the major parameter determining c/a. Illustrative of this suggestion is the behavior of the quasibinary system $AlTh_2$–$AgTh_2$. The end members have very similar atomic volumes and c/a ratios. While the atomic volumes remain essentially constant with alloying, i.e. changing e/a, the c/a ratio has a marked minimum, as shown in Figure 10. In addition, chemically very different compounds show similar c/a ratios for the same values of e/a. Havinga (1972) has presented a qualitative explanation for this oscillatory dependence of c/a ratio with e/a for the C16 (tI12) structure compounds based on pseudopotential calculations of band structure.

Havinga and Damsa (1972) analysed the $CuAl_2$-type (C16) structure with the aid of near-neighbor diagrams. They conclude that the C16 structure is stabilized by the presence of A–B as well as B–B contacts. The structure becomes unstable when the A–A or B–B pairs are very close to making contact. These geometric ideas predict that the C16 structure is limited to radius ratios of the components, R_A/R_B, in the range $0.655<R_A/R_B<0.905+1.35(0.8165-c/a)$. It was recognized earlier (Laves, 1956) that A–B contacts were important in stabilizing the structure. It was suggested (Nevitt, 1967) that its less restrictive atomic-size requirements favor its occurrence with respect to the similar $NiTi_2$- and $MoSi_2$-type structures. When R_A/R_B becomes unfavorably large for these structure types, the $CuAl_2$-type structure was thought to be favored. However, this generalization now seems less secure, as will be discussed in the next section.

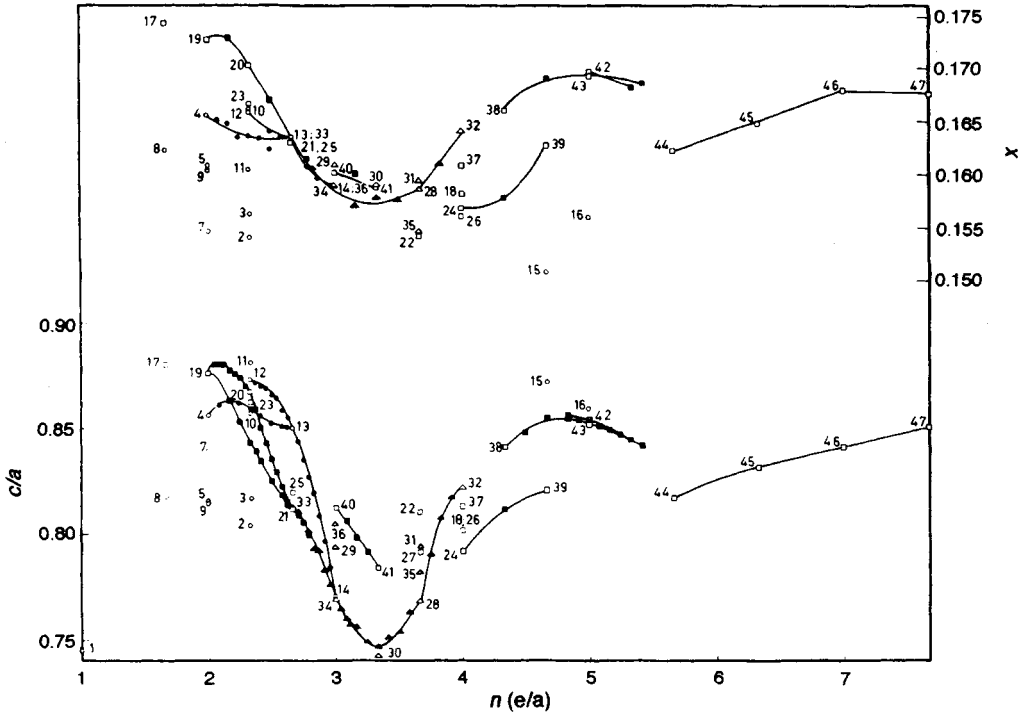

Figure 9. The atomic coordinate x and the axial ratio c/a as functions of valence-electron concentration per atom, n, for $CuAl_2$-type compounds and alloys. (Reproduced by permission of Elsevier Sequoia SA from Havinga *et al.*, 1972, Figure 7)

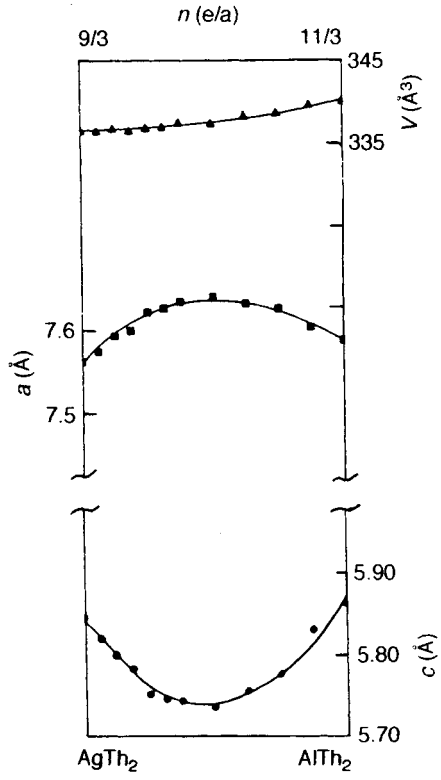

Figure 10. Lattice constants, a and c, and volume, V, of the unit cell for the system $Ag_{1-x}Al_xTh_2$. (Reproduced by permission of Elsvier Sequoia SA from Havinga *et al.*, 1972)

Villars' three-dimensional structural stability diagram (Villars, 1984) (see discussion of $MoSi_2$-type structure phases) for AB_2 binary compounds provides excellent separation for the 56 examples tested. Only two compounds, $AuPb_2$ and VSb_2, with the $CuAl_2$-type structure were misplaced in the structural stability diagram. Pettifor's structural map for AB_2 compounds (Pettifor, 1986a, b, 1988) also separates the phases into several domains, albeit with some admixture of other structure types in some cases.

4. $NiTi_2$-Type and Fe_3W_3C-Type Phases

In this section the AB_2 phases having the $NiTi_2$-type and the Fe_3W_3C-type structures will be discussed. The $NiTi_2$-type structure is cubic with 96 atoms per unit cell, Pearson symbol cF96. The space group is $Fd\bar{3}m$, carrying space group number 227. The prototype has the atomic positions filled as shown in Table 3 (Mueller and Knott, 1963).

Table 3. Prototype $NiTi_2$

Atoms	Wyckoff notation	Symmetry	x	y	z	Occupancy
Ti_1	16(d)	$.\bar{3}m$	5/8	5/8	5/8	1.0
Ni	32(e)	.3m	0.787	0.787	0.787	1.0
Ti_2	48(f)	2.mm	0.186	0	0	1.0

The structure is composed of interpenetrating arrays of Ti octahedra and Ni tetrahedra. The large f.c.c. cell can be visualized as eight cubic subcells. The two alternating patterns (a) and (b) shown in Figure 11 (Mueller and Knott, 1963) are stacked as shown in Figure 11(c). In pure $NiTi_2$, i.e. in the absence of interstitial H, O, N or C, the 'oxygen' positions (ii) in the subcell of Figure 11(b) are unoccupied. In the binary phases the B component is dominated by the group IV transition metals Ti, Zr, and Hf—40 out of the list of about 60 reported compounds (Villars and Calvert, 1991)—with minor representation by group III (Sc) and group V (Nb, Ta). Transition metals from the Fe, Co, and Ni groups are about equally represented as A elements. Pettifor's AB_2 structure map (Pettifor, 1986a, b, 1988) places $NiTi_2$-type phases in close proximity to $MoSi_2$- and $CuAl_2$-type phases, leading one to expect that more than one of them may coexist as polymorphic forms in some alloy systems. This point will be discussed further.

Ternary phases, which now outnumber the binary phases in the published compilation, fall into two categories. The first of these involves H as the third component (see also Chapter 21 by Schlapbach *et al.* in Volume 2). Reported compounds include H_3FeHf_2, H_3NiTi_2, H_3MnHf_2, and H_2RhHf_2 (Villars and Calvert, 1991). These H concentrations are probably nominal. It has been observed (Yvon and Fischer, 1988) that $NiTi_2$-type compounds, along with certain compounds having the $MoSi_2$- and $CuAl_2$-type structures, dissolve H interstitially. The specific interstitial sites occupied depend on the structure of the host lattice, but certain criteria apply in all cases: (1) octahedral and tetrahedral interstitial sites in the metallic lattice are preferred; (2) H atoms are mobile at ambient temperature; (3) the number of interstitial sites available is much larger than the number of H atoms absorbed. H is reported (Bonhomme *et al.*, 1992) to occur in the $NiTi_2$-type compound $H_{1.1}RhMg_2$, a hitherto unreported compound with this structure type that does not exist in the absence of interstitial H.

It is noteworthy that the two AB_2 families previously covered ($MoSi_2$ type and $CuAl_2$ type), as well as the $Mn_{23}Th_6$-type and CFe_3-type compounds yet to be

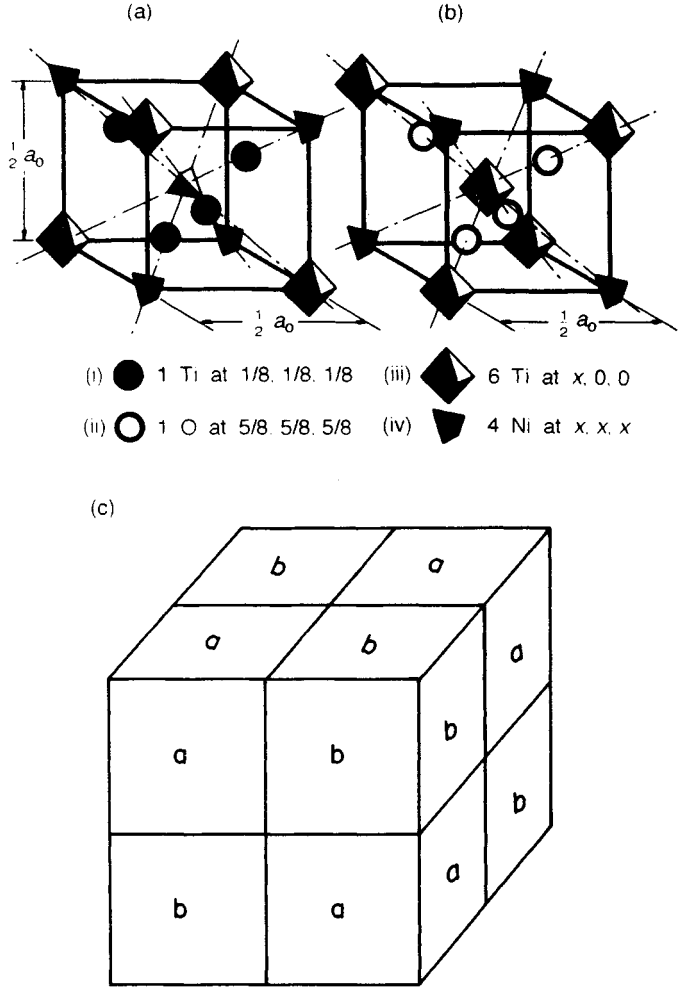

Figure 11. Schematic diagrams showing crystallographic subcells and their stacking in $NiTi_2$ and Ni_2Ti_4O (Reprinted with permission from Mueller and Knott, *Transactions of the Metallurgical Society*, Vol. 227 (1963) p. 674–8, a publication of The Minerals, Metals & Materials Society, Warrendale, Pennsylvania 15086)

discussed, are also reported to dissolve interstitial H (Yvon and Fischer, 1988). The same generalizations apply as regards the occupied sites.

The second group of ternary phases are solid solutions involving multiple A components. These are primarily from the transition-metal groups that form the binary phases. Compositions given in the compilation of Villars and Calvert (1991) are nominal. More detailed information of the location of the phase fields in the ternary systems is given in Nevitt *et al.* (1960).

Another group, smaller in number, appears to be uniquely ternary phases involving Si partially substituting for the A component (Gladyshevskii *et al.*, 1963; Kuz'ma *et al.*, 1964; Bardos and Beck, 1966). The atomic positions of Si are not certain in the absence of detailed crystallographic studies.

The Fe_3W_3C-type structure, Pearson symbol cF112 (*Strukturbericht* $E9_3$), is cubic with 112 atoms per unit cell. The space group and number are the same as those of the $NiTi_2$-type, i.e. $Fd\bar{3}m$ and 227. In the prototype the atomic positions indicated in Table 4 are occupied (Bojarski and Leciejewicz, 1967).

W atoms form an array of octahedra with C atoms in interspersed positions similar to those occupied by O atoms in subcell (b) of Figure 11. Fe atoms form tetrahedra arrayed between the W octahedra. Twelve

Table 4. Prototype Fe_3W_3C

Atoms	Wyckoff notation	Symmetry	x	y	z	Occupancy
C	16(c)	$.\bar{3}m$	1/8	1/8	1/8	1.0
Fe_1	16(d)	.3m	5/8	5/8	5/8	1.0
Fe_2	32(e)	.3m	0.8297	0.8297	0.8297	1.0
W	48(f)	2.mm	0.1828	0	0	1.0

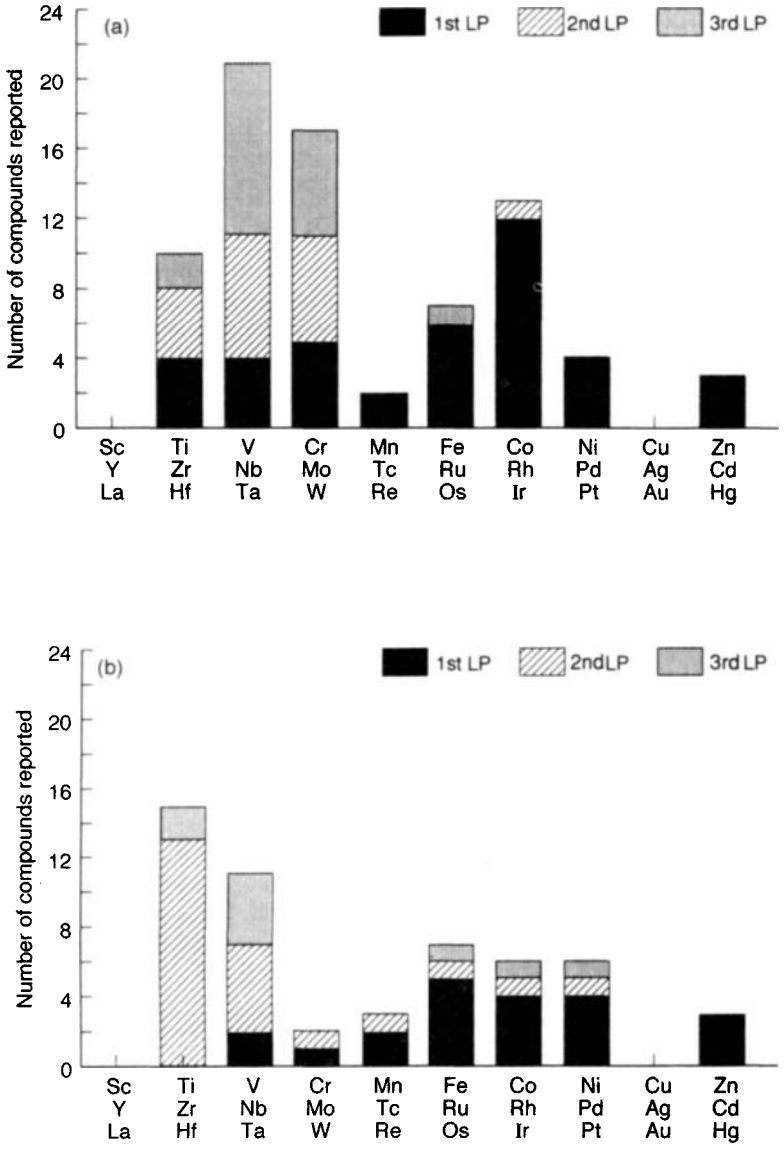

Figure 12. Composition profiles for (a) carbon-containing M_6C, and (b) nitrogen-containing M_6N Fe_3W_3C-type phases

atoms, two C, four W and six Fe, form a distorted icosahedron around a W atom. Fe2 atoms are also surrounded by a distorted icosahedron of six Fe and six W. Subcells (a) and (b) are stacked to form the array shown in Figure 11(c).

There are now approximately 70 phases reported to have this structure (Villars and Calvert, 1991). This family of compounds is frequently called η-carbide or M_6C. However, Yakel (1985) takes into account its wider compositional range and assigns the general formula $(T_xM_{12-x})X_y$, where $6<x<8$ and $0<y<3$. T is a transition element from the Ti, V or Cr group; M is an element from the Fe, Co or Ni group or a non-transition element; and X is a non-metal, C, N or O. The previously discussed $NiTi_2$ type corresponds to $y=0$, and the widely occurring M_6C carbides correspond to $y=2$. There is no conclusive evidence that compounds with different values of x coexist in the same system, e.g. T_2M_4C and T_3M_3C, or that intermediate compositions generally occur (Yakel, 1985). This discussion will focus therefore on the nominal compositions A_2B_4X and A_3B_3X, where A and B correspond, respectively, to Yakel's T and M, and X is C or N.

Known carbon-containing phases outnumber nitrogen-containing phases in a roughly 8/5 ratio (Villars and Calvert, 1991). The carbon and nitrogen phases differ in their composition profiles in two respects. First, A_3B_3X compounds exceed A_2B_4X compounds in the carbon-containing phases, while the reverse is true in the nitrogen-containing phases. Second, the metal-atom populations differ, as shown in Figure 12. For both families there is a minimum in the vicinity of the Mn group, indicating a natural division between the A elements to the left and B elements to the right. The M_6C (carbon-phase) population has a more peaked distribution with rather sharp maxima at the V and Co groups. There is a blunter distribution in the M_6N (nitrogen-phase) population. Figure 12 does not suggest a tight atomic-size constraint. For example, the CN 12 metal-atom radius ratio varies widely ($1.06<R_A/R_B<1.29$) for the M_6C and M_6N phases treated as a single population. A more quantitative correlation such as that of Villars and Hulliger (1987) may be more definitive, but it has not yet been generated for this multi-coordination structure.

As was mentioned earlier, the three structure types, $MoSi_2$, $CuAl_2$, and $NiTi_2$, appear in overlapping or contiguous domains in the AB_2 Pettifor map (Pettifor, 1986a, b, 1988) shown in Figure 6. We might expect, therefore, that the three structure types are competing for stability in some two-component and higher-order

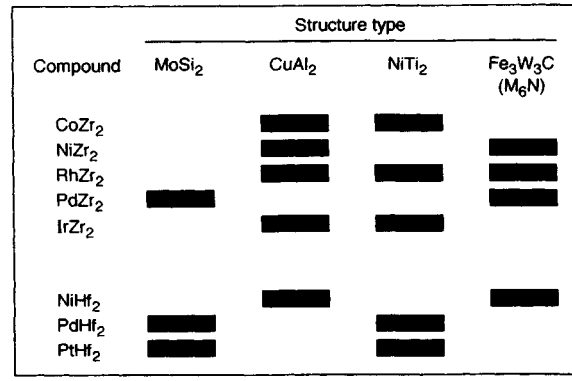

Figure 13. Reported coexistence of $MoSi_2$-, $CuAl_2$-, $NiTi_2$-, and nitrogen-containing Fe_3W_3C-type phases in compounds involving Zr or Hf

systems, and this competition might reveal itself in coexisting polymorphic forms, whose stability depends on composition, temperature, pressure, or on other factors including interstitial ('stabilizing') components. At present, only an incomplete viewpoint can be presented. Figure 13, based on the compilation of Villars and Calvert (1991), puts this point in perspective. It shows that in a group of compounds that pairs Zr or Hf with Co- and Ni-group elements sub-groups are reported to form more than one of the three AB_2 structure types. Most noteworthy is the apparent coexistence of $CuAl_2$-type structures and structures of the $NiTi_2$ type and/or M_6N/Fe_3W_3C type. It is not unreasonable to suspect that some of the entries in the $NiTi_2$ column may be N-stabilized Fe_3W_3C-type phases, but there is presently insufficient information to clarify this point.

5. $Mn_{23}Th_6$-Type Phases

Carrying the Pearson symbol cF116 (*Strukturbericht* $D8_a$), the $Mn_{23}Th_6$ structure type is reported to occur in 200 compounds. The space group is $Fm\bar{3}m$ and number 225. In the prototype phase (Florio *et al.*, 1952), Mn and Th atoms are located as indicated in Table 5.

Table 5. Prototype $Mn_{23}Th_6$

Atoms	Wyckoff notation	Symmetry	x	y	z	Occupancy
Mn_1	4(b)	$m\bar{3}m$	1/2	1/2	1/2	1.0
Mn_2	24(d)	m.mm	0	1/4	1/4	1.0
Th	24(e)	4m.m	0.203	0	0	1.0
Mn_3	32(f)	.3m	0.378	0.378	0.378	1.0
Mn_4	32(f)	.3m	0.178	0.178	0.178	1.0

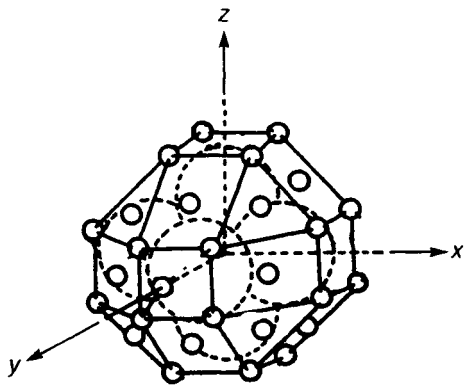

Figure 14. Polyhedron of 44 Mn atoms (small circles) surrounding octahedral cluster of six Th atoms (large dotted circles). (Reproduced by permission of John Wiley & Sons from Pearson, 1972, p. 546)

The structure is cubic with 116 atoms per unit cell. The prominent structural feature is a large polyhedron of 44 Mn_2, Mn_3 and Mn_4 atoms that encases an octahedron of Th atoms, as shown in Figure 14. The polyhedra are packed together in a face-sharing pattern and Mn_1 atoms occupy the interstitial holes between the polyhedra.

About one-quarter of the reported compounds are binary $A_{23}B_6$ phases in which Mn or another first-long-period element, Fe, Co, Ni, Cu or Zn, is the A element. A lanthanide including Y, an actinide, Zr, or Hf serves as the B element. Most of the compounds are ternary phases, and they fall into two groups. One group represents miscibility between two of the binary phases. Examples are $Mn_{23}Th_3Y_3$ and $Fe_{25}Mn_{21}Sm_{12}$. Available information does not indicate the extent to which complete or partial miscibility occurs. The second, and larger, group consists of free-standing ternary phases, which from their composition can tentatively be assumed to have the slightly different $Cu_{16}Si_7Mg_6$-type structure. In the prototype, Si atoms replace Mn_1 and Mn_2 atoms, Mg atoms occupy the Th positions, and Cu atoms replace Mn_3 and Mn_4 atoms. The two structures differ in a minor way in several atomic parameters (Pearson, 1972).

Although there are some stoichiometric variants, most of the reported compounds in the latter group have the formula $(A,C)_{23}B_6$, and most frequently $A_{16}C_7B_6$, where A and C have a very wide periodic-table range, from Be through the transition metals of the Fe, Co and Ni groups, and on through the Cu, Al and Si groups. This wide range, along with a corresponding wide variation in atomic radii, makes it difficult to discern controlling valence and atomic-size effects, especially so in the absence of the detailed crystallographic studies needed to fix the locations and coordinations of the component atoms. The B-atom component for this group of ternary compounds excludes for the most part the lanthanides and actinides, but enlarges the range of the transition-metal partners to include Sc, Y, Ti, Nb, and Ta, as well as Zr and Hf. A more complete understanding of this widely occurring compound type must await more detailed compositional and crystallographic studies.

6. $NaZn_{13}$-Type Phases

The structure of $NaZn_{13}$ is f.c.c., carrying Pearson symbol cF112 (*Strukturbericht* $D2_3$). The space group is $Fm\bar{3}c$, number 226. One-hundred and twelve atoms are arranged in the prototype unit cell (Shoemaker *et al.*, 1952) as shown in Table 6.

In the prototype, the large alkali-metal atom, Na, is surrounded by 24 Zn atoms forming a structure resembling a cube flattened at its corners. This large atom–small atom 'fit' is the primary feature of the structure. Pearson (1972) has used a near-neighbor diagram to show that this structure type has a particularly favorable chance of occurring when the atomic diameter ratio D_A/D_B lies between 1.6 and 1.7, providing thereby a high coordination factor in the structure. Figure 15, also from Pearson (1972), shows that in $NaZn_{13}$-type phases, and in several other structure types containing one large component atom, the reported compounds occur for a wide range of atomic-diameter ratios, but nevertheless the ability of this structure type to accommodate a large A–B atomic-size disparity is clear. The small Be atom ($R_{Be} = 1.128$ Å) is paired with a wide range of larger A partners in over a third of the 90 reported compounds (Villars and Calvert, 1991). More obvious yet is the involvement of the large lanthanide A partners (including Sc and Y) and the actinides; more than two-thirds of the reported compounds have atoms from these periods as the A component. Ternary phases account for a substantial fraction of the compounds;

Table 6. Prototype $NaZn_{13}$

Atoms	Wyckoff notation	Symmetry	x	y	z	Occupancy
Na	8(a)	432	1/4	1/4	1/4	1.0
Zn_1	8(b)	$m\bar{3}.$	0	0	0	1.0
Zn_2	96(i)	m..	0	0.1806	0.1192	1.0

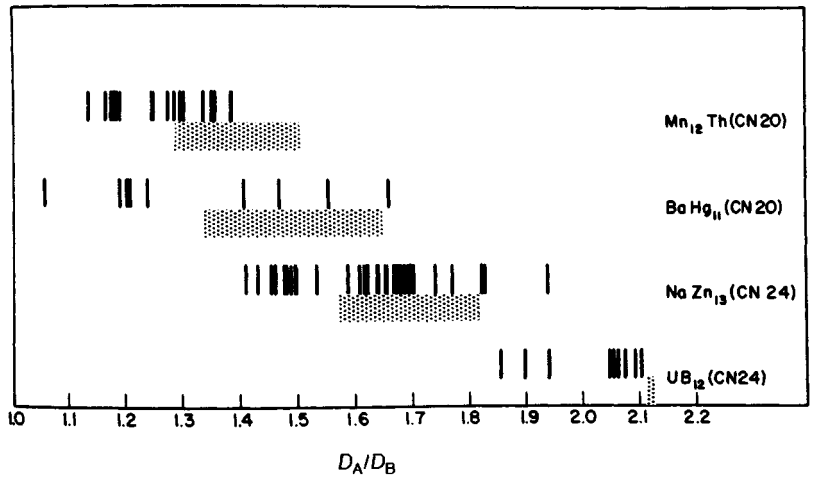

Figure 15. Distribution of $NaZn_{13}$-type phases and other high-coordination phases with atomic diameter ratio. The shaded band indicates the radius ratio range satisfying a high coordination factor. (Reproduced by permission of John Wiley & Sons from Pearson, 1972, p. 75)

multiple components representing A and B occur extensively.

7. Fe_3C-Type Phases

The Fe_3C-type structure phases have AB_3 stoichiometry and the orthorhombic structure with Pearson symbol oP16 (*Strukturbericht* $D0_{11}$). This structure has the space group Pnma with space group number 62. The atomic positions for the prototype Fe_3C (Meinhardt and Krisement, 1962) are given in Table 7, with cell dimensions $a = 0.5089$ nm, $b = 0.6743$ nm, and $c = 0.4524$ nm.

Villars and Calvert (1991) list 137 binary or ternary compounds that crystallize in the Fe_3C-type structure. The structure of the prototype can be described as distorted close-packed layers of iron atoms 'rumpled' into a series of troughs and crests running parallel to the a_0-axis. The atomic arrangement in Fe_3C viewed down [001] is illustrated in Figure 16 (Pearson, 1972). The structure has been described as *near*-close-packing of iron atoms, with carbon in the interstices. Therefore, the Fe_3C-type structure has often been classified as an

Table 7. Prototype Fe_3C

Atoms	Wyckoff notation	Symmetry	x	y	z	Occupancy
C	4(c)	.m.	0.881	0.25	0.432	1.0
Fe_1	4(c)	.m.	0.044	0.25	0.837	1.0
Fe_2	8(d)	1	0.181	0.063	0.337	1.0

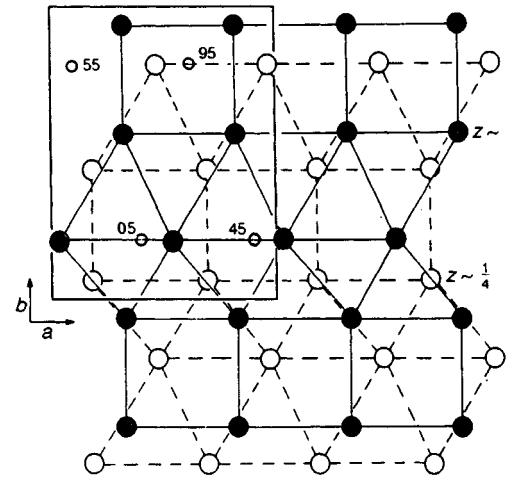

Figure 16. Atomic arrangement in Fe_3C (oP16) viewed down [001]: large open and solid circles are Fe at $z \sim \frac{1}{4}$ and $z \sim \frac{3}{4}$. Small open circles are C at the indicated fractional elevations along z direction. (Reproduced by permission of John Wiley & Sons from Pearson, 1972)

'interstitial phase', which is mainly controlled by atomic-size factors (Hume-Rothery *et al.*, 1969). While many of the Fe_3C-type phases do contain a metalloid 'interstitial' atom such as carbon or boron, more than one-half of the compounds reported are metal–metal systems. Many of these metallic AB_3 structures have a lanthanide element as the B atom and a transition or noble metal as the A atom. The radius ratios of the phases lie between 0.61 and 0.87.

Several ternary silicide or germanide compounds with an ordered version of the Fe_3C-type structure have been synthesized. Moreau *et al.* (1982) reported on isotypic compounds RPd_2Si with R = Ce, Pr, Nd, Sm, Gd, Tb, Dy, Ho, Er, Tm, Lu, and Y, and RPt_2Si with R = Gd, Tb, Dy, Ho, Er, Tm, Lu, and Y. The R and Pd or Pt atoms occupy the Fe sites in this ordered version of Fe_3C. Similarly, Jorda *et al.* (1983) found RPd_2Ge and RPd_2Ga to be of the ordered Fe_3C-type derivative structure. Here R stands for all the lanthanide elements except Pm and Yb, and also includes Y.

The prototype for this structure class, Fe_3C, cementite, is of course well known as an important constituent of ferrous alloys.

8. Th_3P_4-Type Phases

This highly populous family of compounds, whose prototype is Th_3P_4, has a cubic crystal structure with 28 atoms per unit cell. The Pearson symbol is cI28 (*Strukturbericht* $D7_3$) and the space group is $I\bar{4}3d$, number 220. In the prototype phase (Meisel, 1939), atoms lie as shown in Table 8.

Table 8. Prototype Th_3P_4

Atoms	Wyckoff notation	Symmetry	*x*	*y*	*z*	Occupancy
Th	12(a)	$\bar{4}$..	3/8	0	1/4	1.0
P	16(c)	.3.	0.083	0.083	0.083	1.0

Compared to the structures previously discussed, this structure is characterized by polyhedra with lower coordination numbers. P atoms have six Th neighbors in a greatly distorted octahedron, while Th has eight P neighbors in a non-cubic configuration (Pearson, 1972) as shown in Figure 17. There are short planar strips of atoms lying normal to {001} planes and zigzagging alternately + and − about ⟨100⟩ directions. An array of interpenetrating 'staircases' results from this configuration (Pearson, 1972).

The reported binary phases, numbering over 100, show high selectivity as regards the component atoms. A is a member of the P or S group, while B is a lanthanide (including Y) or an actinide. A still larger family of isostructural compounds—over 200—are ternary phases, and these fall into two categories. One category involves multiple A or multiple B components, where A or B have the identities cited above. In the

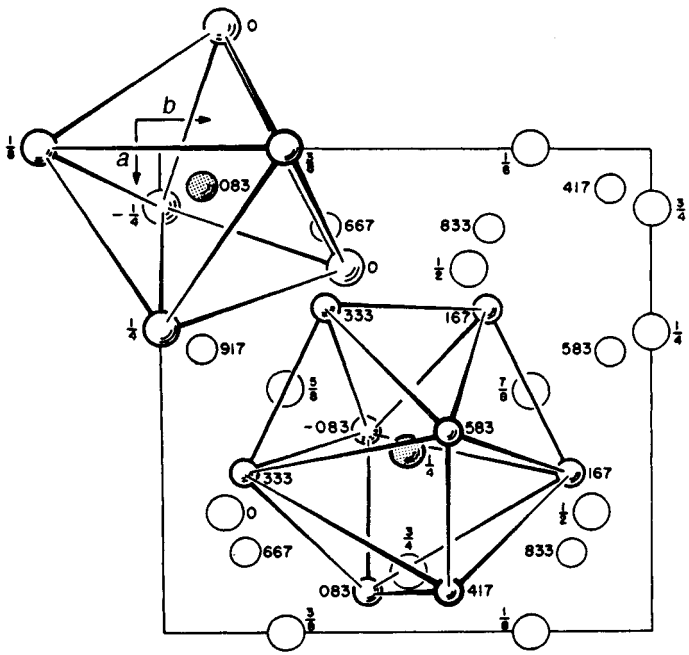

Figure 17. The Th_3P_4 structure viewed down [001]. The coordinations of the P and Th atoms are shown. (Reproduced by permission of John Wiley & Sons from Pearson, 1972, p. 773)

second category a divalent atom (Be, Mg, Ca, Sr, Ba or Cd), or monovalent Ag, substitutes in part for the lanthanide B atom when A is S or Se. Pettifor (1986a, b, 1988) is able to sequester a limited number of these compounds on his A_3B_4 structure map, noting an observation by Wells (1975) that the 8:6 coordination of Th_3P_4 arises from the fact that the stoichiometric basis is built around eight PTh_6 vertex-sharing octahedra.

9. Summary

Over 1000 intermetallic compounds are represented by the nine structure types treated in this chapter. Given the expanded number of reported compounds and the recent availability of comprehensive compilations, it is now possible to clarify relationships between the structure types and to observe periodic-table and atomic-size regularities that were not previously obvious.

With few exceptions, these families of compounds occur at fixed, characteristic A_mB_n stoichiometries; A or B is frequently a composite of several isovalent elements. The roles of the non-metals H, O, C, and N are clarified, particularly for the η-carbide compounds. Phenomenologically based structural stability models show promise as a means of correlating the occurrence of these structure types. These tools have been applied to the $MoSi_2$-, $CuAl_2$- and $NiTi_2$-type compounds, but not to the more complex, multi-coordination structures that are also discussed in this chapter. Further progress in the development of such models should lead to significant advances in the understanding of these intermetallic compounds.

10. References

Alman, D. E., Shaw, K. G., Stoloff, N. S., and Rajan, K. (1992). *Mater. Sci. Eng.*, **A155**, 95.

Bardos, D. M., and Beck, P. A. (1966). *Trans. AIME*, **236**, 40–48.

Bojarski, Z., and Leciejewicz, J. (1967). *Arch. Hutn.*, **12**, 255–263.

Bonhomme, F., Selvam, P., Yoshida, M., Yvon, K., and Fischer, P. (1992). *J. Alloys Compounds*, **178**, 167–172.

Fleischer, R. L. (1985). *J. Met.*, **37**, 16.

Florio, J. V., Rundle, R. E., and Snow, A. I. (1952). *Acta Crystallogr.*, **5**, 449–457.

Gladyshevskii, E. I., Kuz'ma, Yu. B., and Kripyakevich, P. I. (1963). *J. Struct. Chem.*, **4**, 343–349.

Hahn, T. (ed.) (1989). *International Tables for Crystallography*. International Union of Crystallography; Kluwer Academic, Boston.

Havinga, E. E. (1972). *J. Less-Common Met.*, **27**, 187.

Havinga, E. E., and Damsa, H. (1972). *J. Less-Common Met.*, **27**, 269.

Havinga, E. E., Damsa, H., and Hokkeling, P. (1972). *J. Less-Common Met.*, **27**, 169.

Hellner, E., and Pearson, W. B. (1984). *Z. Kristall.*, **168**, 273–291.

Hume-Rothery, W., Smallman, R. E., and Haworth, C. W. (1969). *The Structure of Metals and Alloys*. Institute of Metals, London, pp. 273–275.

Jorda, J. L., Ishikawa, M., and Hovestreydt, E. (1983). *J. Less-Common Met.*, **92**, 155–161.

Kuz'ma, Yu. B., Gladyshevskii, E. I., and Byk, D. S. (1964). *J. Struct. Chem.*, **5**, 518–522.

Laves, F. (1956). *Theory of Alloy Phases*. American Society for Metals, Cleveland, OH.

Meetsma, A., de Boer, J. L., and van Smaalen, S. (1989). *J. Solid State Chem.*, **83**, 370–372.

Meinhardt, D., and Krisement, O. (1962). *Arch Eisenhuettenwes.*, **33**, 493–499.

Meisel, K. (1939). *Z. Anorg. Allg. Chem.*, **240**, 300–312.

Miedema, A. R., Boom, R., and de Boer, F. R. (1975). *J. Less-Common Met.*, **41**, 283.

Moreau, J. M., Le Roy, J., and Paccard, D. (1982). *Acta Crystallogr.*, **B38**, 2446–2448.

Mueller, M. H., and Knott, H. W. (1963). *Trans. AIME*, **227**, 674–678.

Nevitt, M. V. (1967). In *Intermetallic Compounds* (ed. J. H. Westbrook). Wiley, New York, pp. 224–227.

Nevitt, M. V., Downey, J. W., and Morris, R. A. (1960). *Trans. AIME*, **218**, 1019–1023.

Pearson, W. B. (1972). *The Crystal Chemistry and Physics of Metals and Alloys*. Wiley-Interscience, New York, pp. 75, 546, 592, and 773.

Petrovic, J. J., and Vasudevan, A. K. (1992). *Intermetallic Matrix Composites II* (eds D. B. Miracle, D. L. Anton, and J. A. Graves). *Mater. Res. Soc. Symp. Proc.*, **273**, 229.

Pettifor, D. G. (1986a). *New Scientist*, **110**, 1510.

Pettifor, D. G. (1986b). *J. Phys.*, **C19**, 285.

Pettifor, D. G. (1988). *Mater. Sci. Technol.*, **4**, 675–691.

Porter, D. A., and Easterling, K. E. (1981). *Phase Transformations in Metals and Alloys*. Van Nostrand Reinhold, Wokingham, UK, p. 297.

Rajasekharan, T., and Girgis, K. (1983). *Phys. Rev.*, **B27**, 910–920.

Raynor, G. V. (1974). *J. Less-Common Met.*, **37**, 247–255.

Shoemaker, D. P., Marsh, R. E., Ewing, F. J., and Pauling, L. (1952). *Acta Crystallogr.*, **5**, 637–644.

Siegrist, T., Hulliger, F., and Travaglini, G. (1983). *J. Less-Common Met.*, **92**, 119–129.

Svechnikov, V. N., Kocherzhinskii, Yu. A., and Yupko, L. M. (1971). *Diagrammy Sostoyaniya Metal Sistemi*. Nauka, Moscow, pp. 116–119.

Thomas, O., Senateur, J. P., Madar, R., Laborde, O., and Rosencher, E. (1985). *Solid State Commun.*, **55**, 629–632.

Villars, P. (1984). *J. Less-Common Met.*, **99**, 33–43.

Villars, P. and Calvert, L. D. (1991). *Pearson's Handbook of Crystallographic Data for Intermetallic Phases*, Vols 1–3. ASM International, Metals Park, OH, Vol. 1, pp. 135, 176–7, 257, 260, 264, 270, and Vol. 3, p. 2742.

Villars, P. and Hulliger, F. (1987). *J. Less-Common Met.*, **132**, 289–315.

Wells, A. F. (1975). *Structural Inorganic Chemistry*, 4th edn. Clarendon, Oxford.

Westbrook, J. H. (ed.) (1967). *Intermetallic Compounds*. Wiley, New York.

Yakel, H. L. (1985). *Int. Met. Rev.*, **30**, 17–40.

Yvon, K. and Fischer, P. (1988). In *Hydrogen in Intermetallic Compounds* (ed. L. Schlapbach). Springer-Verlag, Berlin, pp. 87–138, and references therein.

This chapter was originally published in 1995 as Chapter 16 in *Intermetallic Compounds*, Vol. 1: *Principles*, edited by J. H. Westbrook and R. L. Fleischer.

Chapter 7

Topologically Close-Packed Structures

Evgen I. Gladyshevskii and Oksana Bodak

Department of Inorganic Chemistry, L'viv State University, Lomonosova str. 6, 290005, Lviv 5, Ukraine

1. Introduction

One of the most important problems in the crystal chemistry of intermetallic compounds is the determination of the relations between structure types. It is known that there are more than 2700 intermetallic-compound structure types,* that is to say varieties of atomic arrangements in crystals that are described by a unit cell of a certain symmetry, lattice parameters, Wyckoff sites of a certain space group, and atomic arrangement on those sites with certain positional coordinates. The lattice parameters, angles, and positional coordinates of a structure type can have a range of values within which the variation of the values does not lead to essential changes in the arrangement of the atoms and the coordination features (coordination numbers (CN) and coordination polyhedra (CP)).

Classifications of the structure types may be constructed on the basis of the following different themes: relation to the structure types of the elements (simple substances); quantitative ratios of component species (stoichiometric type); symmetry (type of Bravais lattice); presence of closely connected atoms (island, chain, net, and frame structures); or atomic coordination. For example, Pearson (1972) used as the basis of his classification the type of Bravais lattice, but he further classified intermetallics by employing other indicators (the presence of similar nets, atomic coordinations, and type of chemical bonds). Another classification of all the structure types, based on the various relations between the different types of crystal structures, was suggested by Smirnova (1975).

Considering Belov's (1947) classification of the structure types as more preferable, since it is based primarily on the coordination features, we shall classify structure types of intermetallic compounds (IMCs) by the coordination number (CN) and coordination polyhedron (CP) of the atoms according to Kripyakevich's (1977) systematic scheme.

In the structures of IMCs there are CN from 24 to 2. The atoms that form the structure can have equal or different radius values. Atoms of smaller size have a smaller assortment of CN (from 12 to 2). Therefore, the structure-type systematization is based on CN and CP of the atoms with smaller size. Then all of the structure types can be divided among this small number of classes (Figure 1).

Usually, for equal atomic sizes, the structures found are those for which CN = 12 and which have as CP a cubooctahedron or its hexagonal analog (class 1 of the systematization). Only in a few structures with atoms of equal sizes is their CN = 14 and their CP a rhombododecahedron, as in the structures related to α-Fe (class 2), or a 14-vertices polyhedron, as in the disilicides of Mo, Cr, and Ti (class 3). Both atoms in the FeSi structure have CN = 13 and a 13-vertices polyhedron (class 4).

If atoms of smaller size are placed in the center of a cubooctahedron and then the cubooctahedron is

*All known structure types of intermetallic compounds and all representatives of these types are systematized and collected by Villars and Calvert (1991). An essential and very important supplement to this indispensable reference book is the monograph of Parthé *et al.* (1994). Questions of the chemical bonds of intermetallic compounds are considered in a number of K. Schubert's works (see e.g. Schubert, 1964).

Crystal Structures of Intermetallic Compounds. Edited by J. H. Westbrook and R. L. Fleischer

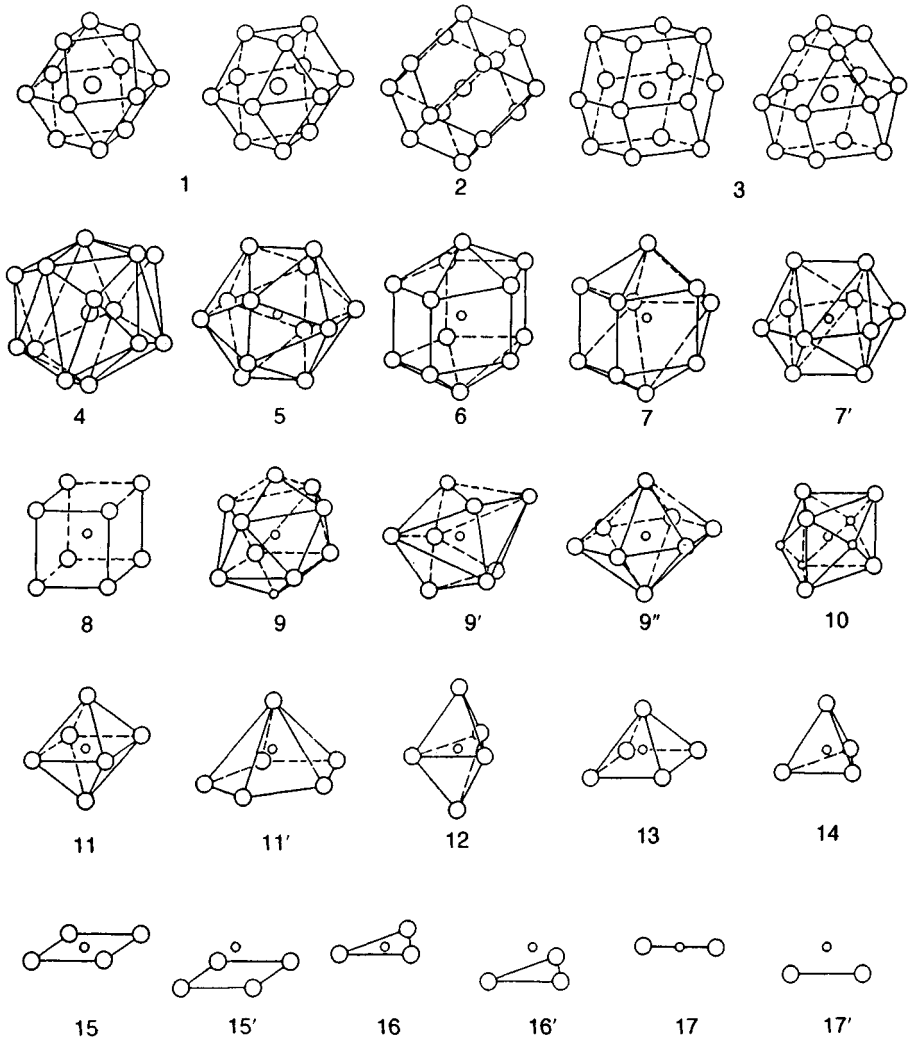

Figure 1 Coordination figures in the structure of IMCs. The classes are as follows: 1, cubooctahedron and its hexagonal analogs, CN = 12 (examples of the structure types—Cu, TiCd, $CdMg_3$); 2, rhombododecahedron, cube plus octahedron, CN = 8 + 6 (α-Fe, Cr_2Al, Fe_3Si); 3, 14-vertices polyhedra of two kinds, CN = 14 ($MoSi_2$, $CrSi_2$, $TiSi_2$); 4, 13-vertices polyhedron for both atoms, CN = 13 (FeSi); 5, icosahedron, CN = 12 (Cr_3Si, $MgZn_2$, $CaCu_5$, $ThMn_{12}$); 6, 12-vertices polyhedron, pentagonal prism plus pentagonal dipyramid, CN = 12 (Hg_5Mn_2); 7, defect icosahedron, CN = 10 ($MnAl_6$, $Al_{13}Os_4$); 7′, normal 10-vertices polyhedron, CN = 10 (In_4Ti_3); 8, defect rhombododecahedron, cube plus defect octahedron, CN = (8 − *m*) + 6, or defect cube plus octahedron, CN = 8 + (6 − *m*), or cube, CN = 8(γ-brass, Cu_2Sb, CaF_2); 9, tetragonal antiprism with one or two additional vertices, CN = 8 to 10 (Al_2Cu, Mg_2Cu, Ni_3P, $BaAl_4$); 9′, normal eight-vertices polyhedron, CN = 8 ($Mn_{11}Si_{19}$, Zr_2Al_3); 9″, hexagonal dipyramid, CN = 8 ($Hg_{0.17}Sn_{0.83}$); 10, trigonal prism and its derivatives, CN = 6 to 11 (AlB_2, α-$ThSi_2$, $PbCl_2$, FeB, U_3Si_2, Fe_3C); 11, octahedron, CN = 6 (Fe_2N, AsNi, NaCl); 12, trigonal dipyramid, CN = 5 ($InNi_2$, UPt_3); 13, tetragonal pyramid, CN = 5 (CaC_2 − I, $BaSi_2$, Si_2Ni_3); 14, tetrahedron, CN = 4 (SZn, Fe_4C, $SiFe_3$, La_2O_3); 15, square or rectangle, CN = 4 ($ZrGa_2$, CaB_6); 16, triangle, CN = 3 (C graphite, $TiCu_2$, B_4C); 17, linear or angle, CN = 2 (Ni_5P_4, UB_{12})

twisted, a 12-vertices polyhedron with only triangular faces, the icosahedron, is more favorable. The large number of structure types with icosahedral coordination of the smaller atoms belong to class 5. With further decrease in CN of the smaller atom, the number of structure-type classes is increased.

The structure types with CN = 8 and CP as a trigonal prism belong to class 10. Structure types with CN = 4

and CP as a tetrahedron belong to class 14; structure types with linear or angular coordination (CN = 2) belong to class 17.

For the other classes of structure types, CN are intermediate between those named above. Some of the classes are divided into two or three subclasses, in which the small atoms have equal CNs but related or different CPs (classes 7 and 7′, 9, 9′ and 9″ or 11 and 11′).

Kripyakevich's systematic scheme is applicable to the structures of elements, and binary, ternary, and multicomponent compounds. All structure types of intermetallic compounds are divided into 17 classes. Each class is the sum of all the structure types that have, for the smallest atoms, the same coordination polyhedron, including its deformed derivatives.

We use a classification of relations between the structure types of intermetallic compounds in accordance with Kripyakevich's (1977) scheme. It is based on the common features of the types compared and on the ways of effecting the conversion by which one structure type may be transformed into another (Table 1).

The closest relation is observed between structure types with equal or nearly equal positions for all atoms. The structures are more distantly related if one can distinguish only the same common motifs from the separate atoms that form the structure type in different ways.

Table 1 Relationships between structure types of intermetallic compounds showing common features and ways of transformation

Common features of structure types	Ways of transformation		Examples of structure types[a] (Parent) Transformed structure
Equal positions for all atoms	Ia	Ordered substitution (superstructure formation)	(Cu) $AuCu_3$, ($ThMn_{12}$) $CeMn_4Al_8$
	Ib	Redistribution of the different component atoms	($MgCu_2$) $AuBe_5$ = (AuBe) Be_4, ($MgCu_2$) $MgSnCu_4$
Approximately equal positions for all atoms	II	External deformation[b] Internal deformation	(Cu) α-Mn ($MgCu_2$) $TbFe_2$
Equal positions for only part of the atoms	IIIa	Multiple substitution	($CaCu_5$) $ThMn_{12}$, ($CaCu_5$) Zr_4Al_3
	IIIb	Redistribution of the atoms or substitution of an atomic group	(Th_2Ni_{17}) Th_2Zn_{17}
	IIIc	Inclusion or elimination and redistribution of included atoms	(Cu) γ′-Fe_4N[a], (Mg) CdI_2[a], (CdI_2[a]) FeS_2[a]
All structure details (fragments) are equal	IVa	Homeotectics[c] (stackings of closely packed networks)	($CdMg_3$) $BaPb_3$, ($MgZn_2$) $MgCu_2$
	IVb	Certain modes of stacking of slabs (polyhedra), homogeneous homologous[d] series	(AlB_2[a]) α-$ThSi_2$[a], (Zr_5Si_4[a]) Sm_5Ge_4[a]
Details (fragments) are only partially equal	V	Inhomogeneous homologous series, interchanges different in two or more details:	
	Va	One-dimensional	($AuCu_3$, CaF_2) $HoCoGa_5$, Ho_2CoGa_8
	Vb	Two-dimensional	(Cr_3Si, Zr_4Al_3) σ phase, (Cr_3Si, Zr_4Al_3, $MgZn_2$) P phase, (Zr_4Al_3, $MgZn_2$) μ phase
	Vc	Three dimensional	(AlB_2[a], α-Fe[e]) $Ce_{24}Co_{11}$[a]

[a]Structure types γ′-Fe_4N (L′1, cP5), CdI_2 (C6, hP3), FeS_2 (C2, cP12), AlB_2 (C32, hP3), α$ThSi_2$ (C_c, tI12), Zr_5Si_4 (tP36), Sm_5Ge_4 (oP36), α-Fe (A_2, cI2), and $Ce_{24}Co_{11}$ (hP70) do not belong to the family of close packing. They are shown for illustration of the transitions IIIc, IVb, and Vc.

[b]External deformation is connected with changing of the *c/a* ratio. Internal deformation is a result of a change of the atomic parameters.

[c]'Homeotectic'—this term, which was suggested by Laves and Witte (1935), is related to structures that have similar composition and equal CN but different ways of mutual placement of the fragments (for example, flat layers in the close-packed structures).

[d]'Homology' suggests the possibility of the construction of structures with similar sets of fragments (details) but with different quantitative ratios. The term was adopted from organic chemistry (Magnéli, 1953).

2. Close Packing of Atoms with Equal and Nearly Equal Sizes

2.1 Close Packings in the Structures of Simple Substances and Solid Solutions Based on Them

The structures that have CN = 12 for all the atoms and form the cubooctahedron or its hexagonal analog as a CP are close packings of atoms with equal or nearly equal sizes and are grouped in class 1 of Kripyakevich's classification. Superstructures of the close-packed structures and their deformed derivatives belong to the same class. The structures of real metals and intermetallic compounds are frequently based on stackings of close packings with $n = 2, 3, 4, 6, 8, 9, 10, 12$, where n is the number of layers in the repeat period.

There are four known undeformed close-packed structures that are characteristic of the elements: hexagonal two-layered, h_2[†] (Mg type, A3, hP2); cubic three-layered, c_3 (Cu type, A1, cF4); hexagonal four-layered, $(ch)_2$ (α-Nd type, A3′, hP4); and rhombohedral nine-layered, $(chh)_3$ (α-Sm type, C19, hR3). Another five structures of the elements are considered as derivatives of ideally close-packed structures produced by deformation: e.g. for the Zn type there is an external deformation from that of the Mg type; the α-U type (A20, oC4) is formed from the Cu type and is connected with both an internal and an external deformation. The In (A6, tI2), γ-Mn (tI2), and α-Hg (A10, hR1) types are also formed from the Cu type by external deformation (see Chapter 12 by Hauck and Mika in this volume).

The crystallization of binary and ternary compounds in the above types of close-packed structures supposes a statistical substitution of atoms in the positions of the starting structures, which imposes certain limits connected with the atomic sizes. An example that illustrates this point is the interaction between the rare-earth metals (lanthanides, Ln). All the studied binary systems Ln–Ln′ may be divided into three main groups by the type of interaction with one another at temperatures lower than 600–800°C (Gladyshevskii and Bodak, 1982).

Systems with isostructural components (La–Ce, Pr–Nd, Gd–(Tb,Dy,Ho,Er,Lu), and Yb–(Ho,Er,Lu)) forming continuous solid solutions with each other belong to the first group. The second group includes the systems La–Nd,Ce–Nd, Nd–Sm, and Sm–Gd with non-isostructural components forming limited solid solutions. The third group comprises systems in which changing the concentration leads to the formation of various sequences of binary phases with the close-packed structure types Mg, α-Sm, α-Nd, and Cu (Figure 2). The studies of Gschneidner and Valetta (1968) show that the interchange of these four structure types occurs as a function of the ratio of the metal radii and the radii of their 4f shells (r_{Ln}/r_{4f}). The hexagonality (h, %) of the close-packed structures is increased with increase of this ratio, both in the lanthanides (Ln) (excluding Eu and Yb) and in their alloys.

2.2 Superstructures of the Close-Packed Structures

The structure types now compared can have equivalent positions of all the atoms (are isopunctal) but are distinguished by the type and number of atoms of the components that occupy these positions. Then the symmetry and the shape (unit-cell characteristics, which include form and size) of the unit cell can also be changed. Ordered substitution of at least a part of the Wyckoff sites by different atoms leads to the appearance of a superstructure or ordered structure (in German, *Ueberstrukture*) (Table 2). The superstructure can be formed for a particular stoichiometric ratio of the components as a consequence of the ordered redistribution of atoms on the Wyckoff sites with a concomitant change in symmetry, for example, AuCu-I and $AuCu_3$ (both superstructures I). Superstructures with the same symmetry and shape as the starting structure type are named superstructures of the second kind (superstructures II). Some researchers do not consider them as a separate structure type.

The superstructures of the close packings can be systematized based on the stoichiometry and on the type of (arrangement of) the close-packed layer, that is to say on the way the different types of atom are distributed on it. For binary compounds in which the L and M atoms have similar effective radii, 13 stoichiometric types of superstructures are known: LM, L_4M_5, L_2M_3, L_3M_5, LM_2, L_2M_5, L_3M_8, LM_3, L_3M_{10}, LM_4, L_3M_{13},LM_5, and LM_7. The main stoichiometric compositions are LM and LM_3; the other superstructures may be constructed by combinations of layers that contain fragments of these compositions. Composition LM may be obtained in two ways: stacking of equal numbers of close-packed layers, one composed of L atoms and the other of M atoms (LiRh (hP2) and

[†]In this notation, h indicates a stacking in which atoms in layers immediately above and below the reference layer have the same positions, and c indicates that these positions are different. The subscript indicates the number of such stackings before the sequence repeats.

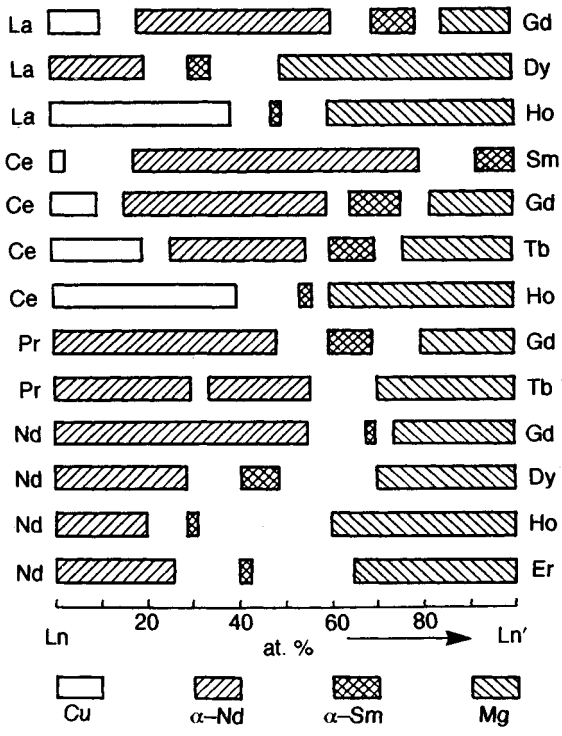

Figure 2 Mutual solubility and occurrence of phases with the Cu, α-Nd, α-Sm, and Mg structure types in the systems Ln–Ln′ at the temperatures 600–800°C (the system La–Dy is shown at 200°C)

PtCu $L1_1$ (hR32) types); or stacking of layers each containing equal numbers of L and M atoms. Structures with close-packed layers of the same composition LM are numerous (types α-AuCd (B19, oP4), TiAl (tP2), AuCu-I ($L1_0$, tP2), α-TaRh (oP12), UPb (tP8), AuCu-II (oI40), TiCd (tP4), etc.). LM_3 structures are distinguished both by the type of layers and by the type

Table 2 Appearance of superstructures by ordering on one or both sublattices

Symmetry	Shape of the unit cell	
	Same	Different
Same	Superstructure II α-Mn→Ti_5Re_{24} $MgZn_2$→Mg_2Cu_3Si $CaCu_5$→$CeCo_3B_2$	Superstructure I Mg→$CdMg_3$
Different	Superstructure I Cu→$AuCu_3$ $MgCu_2$→$MgSnCu_4$ $MgCu_2$→$AuBe_5$	Superstructure I $AuCu_3$→$TiAl_3$ Cu→AuCu-I Cu→$TiAl_3$

of close packings (Beattie, 1967). The most essential factor that influences the crystallization of real binary and ternary compounds in superstructures of close-packed structures is the size factor. This may be illustrated by using the binary $LnAl_3$ and ternary $(Ln,Ln')Al_3$ compounds. The binary compounds $LnAl_3$ crystallize in five related structure types: $AuCu_3$ ($L1_2$, cP4), $HoAl_3$ (hR20), $TiNi_3$ ($D0_{24}$, hP16). $BaPb_3$ (hR12), and $CdMg_3$ ($D0_{19}$, hP8). The determination of the $LnAl_3$ structure type is connected with the difference $r_{Ln} - r_{4f}$ (where r_{Ln} is the radius of the Ln atoms calculated from the unit-cell volume of the compound structure, considering the number of Ln and Al atoms), just as in the structures of the elements and binary phases in the systems Ln–Ln′ (Figure 3). With increasing difference $r_{Ln} - r_{4f}$, as in the Ln elements and also in the $LnAl_3$ compounds, the hexagonality of the structures increases. In the structure of the Ln elements, the hexagonality of stacking increases from light Ln to heavy Ln, and in the $LnAl_3$ compounds in the opposite direction (Pearson, 1967).

There are also size-factor influences on the composition of ternary compounds $Ln_{1-x}Gd_xAl_3$. The binary compound $TbAl_3$ has a structure of the $BaPb_3$ type; to form compounds with the same structure type with Dy, Ho, Er, Tm, or Lu, it is necessary to replace part of

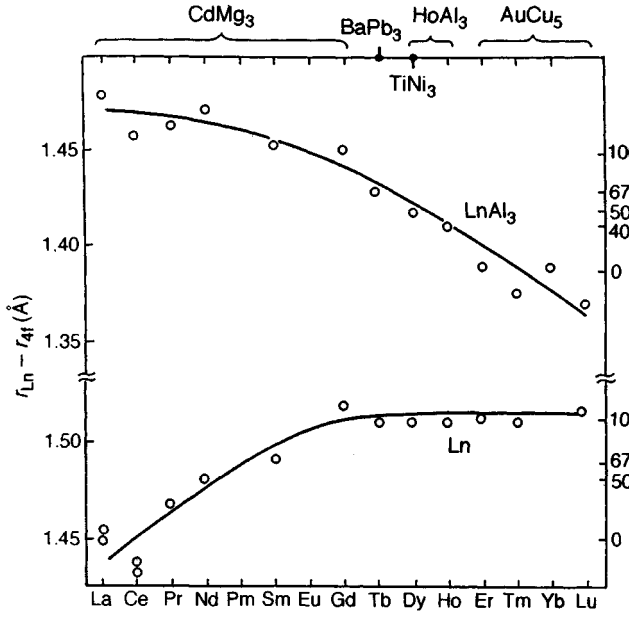

Figure 3 Hexagonality of stacking variants (h, %) in the structures of Ln and $LnAl_3$ compounds depending on $r_{Ln} - r_{4f}$

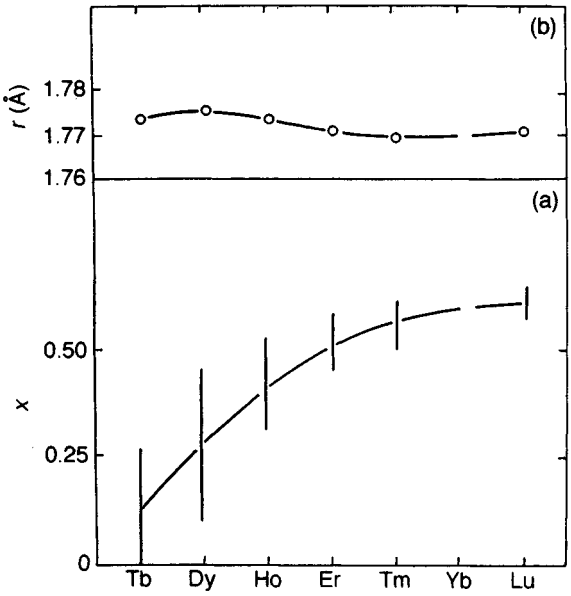

Figure 4 (a) The content of Gd in the compounds $Ln_{1-x}Gd_xAl_3$ with the $BaPb_3$ structure type and (b) the average radius of the atoms (Ln + Gd) as functions of Ln atomic number

the Ln atoms by the bigger Gd atom (Figure 4). The Gd quantity required increases with the progression from Dy to Lu in the compounds; the average radius ($\bar{r}$) of the statistical Ln = Ln′ mixture is constant, approximately equal to 1.77, corresponding to the Tb atom radius.

Superstructures of the close-packed structures may be the basis of the description of new structure types using different ways of transformation. For example (Figure 5) (Gladyshevskii *et al.*, 1985), the structure of Pt_2NiGe (oF32) is formed as the result of an internal deformation of the $AuCu_3$ structure with the simultaneous formation of a superstructure. The volume of the unit cell is increased eight times and the symmetry is lowered from cubic to orthorhombic. Another structure related to the $AuCu_3$ type is the structure $U_4Re_7Si_6$ (cI34); it is formed not only as the result of an internal deformation, but also as the result of the inclusion of two Re atoms in positions with coordinates 0, 0, 0 and $\frac{1}{2}$, $\frac{1}{2}$, $\frac{1}{2}$. The volume of the unit cell is increased by eight times in comparison with $AuCu_3$, and the face-centered cubic cell is replaced by a body-centered cubic one.

Fragments of the superstructures of the close-packed structures may be used as 'building blocks' to form more complex structures. The structure types $HoCoGa_5$ (tP7) and Ho_2CoGa_8 (tP11) form a one-dimensional homologous series that is based on fragments of the $AuCu_3$ and $PtHg_2$ (tP3) types (Figure 6). One can obtain a series of hypothetical structures, which are described by the formula $R_mR'_{3m+2n}X_n$ (m and n are the numbers of fragments of $AuCu_3$ and $PtHg_2$ in the unit cell, respectively), by interchanging the packing sequence and choosing certain quantitative ratios of the fragments $AuCu_3$ and $PtHg_2$. Examples of such structures known to exist are the type $HoCoGa_5$ ($m = 1$, $n = 1$) and the type Ho_2CoGa_8 ($m = 2$, $n = 1$) (Grin *et al.*, 1979).

3. Close Packing of Atoms with Unequal Sizes

In close packings of atoms with equal or nearly equal sizes, every atom is surrounded by 12 atoms with the

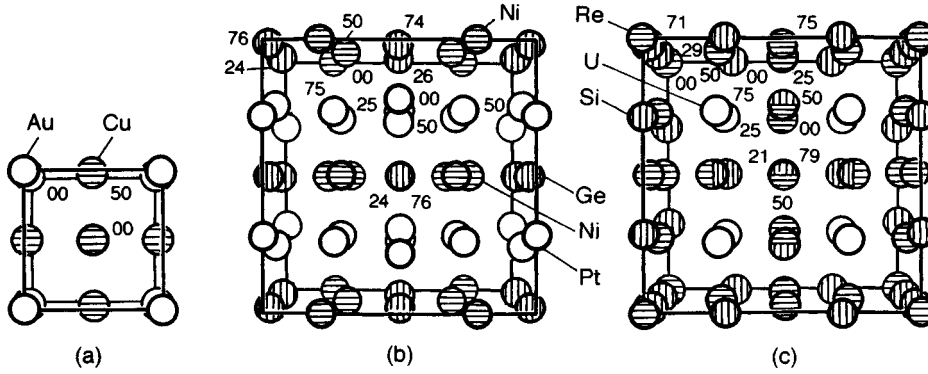

Figure 5 Structure types related to (a) $AuCu_3$, (b) Pt_2NiGe, and (c) $U_4Re_7Si_6$. Coordinate z is shown in multiples of 0.01

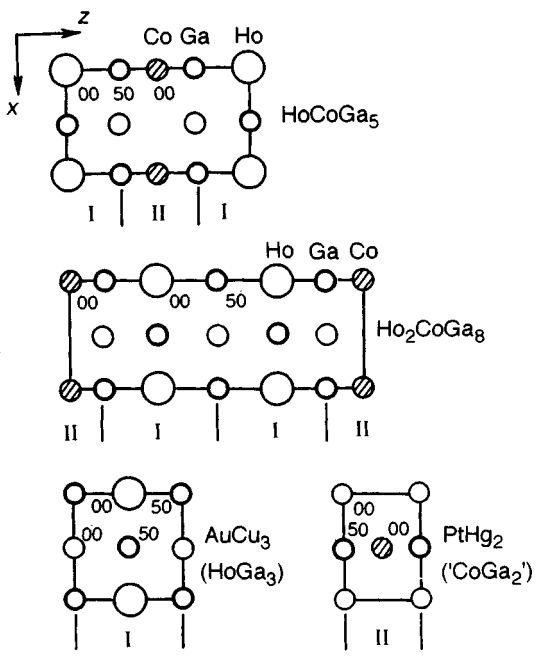

Figure 6 Structures $HoCoGa_5$ and Ho_2CoGa_8—members of the linear homologous series based on fragments of the structure types $AuCu_3$ and $PtHg_2$. Coordinate y is shown in multiples of 0.01

same radius, forming a cubooctahedron or its hexagonal analog. These polyhedra have square and triangular faces (Figure 7). If in the centre of this cubooctahedron one places an X atom with a smaller radius than the R atoms, a more compact placement of the outlying atoms is necessary to preserve the close packing; a 12-coordinated polyhedron with exclusively triangular faces (icosahedron) then appears. The ratio r_R/r_X for it is equal to 1.111. Not only R atoms but also X atoms may be at the vertices of the icosahedron. Simultaneously the CN of the R atoms is increased. Such structures are said to be topologically close packed.

There is a large group of intermetallic-compound structure types with close packing of atoms of unequal sizes and with icosahedral coordination of the smaller atoms. They belong to class 5 of the structure types of Kripyakevich's system and will be discussed below. The coordination numbers of the R atoms in these structures are between 13 and 24. Crystal structures of this sort with CN = 12, 14, 15, and 16 were described for the first time by Frank and Kasper (1958); the generally accepted name for them is 'Frank–Kasper structures'. The progenitors of this group of structures are the three binary structure types Cr_3Si, $MgZn_2$, and $CaCu_5$, in which the CN of R atoms is equal to 14 (for Cr), 16 (for Mg), and 20 (for Ca).

3.1 Structure Types Cr_3Si and Zr_4Al_3 and their Derivatives

The connection of the structure type Cr_3Si (A15, cP8) (Boren, 1933) with the close packings can be illustrated by the following scheme (Figure 8). Cr and Si atoms at $z = 0$ and 1/2 substitute at the positions of the M atoms in the LM_3 layer (symmetry pmm); the positions of the L atoms are vacant. The other Cr atoms are at the origin with $z = 1/4$ and 3/4. So, the structure Cr_3Si may be represented as that formed from two types of nets—a compactly occupied one that is a derivative of the close-packed layer, and an intermediate sparsely occupied one, which alternate with each other.

The structure type Zr_4Al_3 (hP7) (Wilson *et al.*, 1960) may be considered in the same way as Cr_3Si. It may be represented as being formed from a compactly occupied net of Al atoms ($z = 0$), which is a derivative of a close-packed layer LM_3 (symmetry p6m) with vacancies in position 0, 0, and a second compactly occupied net of Zr atoms ($z = 1/2$), which has vacancies in positions 0, 0. These nets alternate with the sparsely occupied ones of Zr atoms ($z = 1/4$ and 3/4).

Every unit cell for the structures Cr_3Si and Zr_4Al_3 has two general and two intermediate nets. Since the distances between nets in both structures are equal or nearly equal, complex structures with unit cells formed by linking of the side faces of the unit cells of the starting structures can occur. In this way are formed the tetragonal unit cell of the structure Nb_2Al (tP30) (Figures 9 and 10) and numerous binary and ternary derivatives of this type (σ phases), in which Wyckoff sites are occupied by atoms of different components or their statistical mixtures, for example $CrMn_3$, Cr_2Fe_3, $Cr_{53}Co_{47}$, $Cr_{13}Ni_5Si_2$, $Mo_{37}Mn_{63}$, $Mo_{60}Co_{40}$, and others (see transformation type Vb of Table 1).

3.2 Structure Type $MgZn_2$ and its Derivatives

Proceeding from the values of the interatomic distances, one can see (Friauf, 1927; Laves and Witte, 1935) that the ratio of the effective radii r_R/r_X in the $MgZn_2$ (C14, hP12) structure equals $\sqrt{3/2} = 1.225$. A value close to this can be found by analyzing the connection between the $MgZn_2$ structure and the close-packed one. For its formation, it is necessary to substitute half of the X atoms by half as many atoms with the larger size ($X_4 \rightarrow RX_2$); then $r_R/r_X = \sqrt[3]{2}/1 = 1.260$.

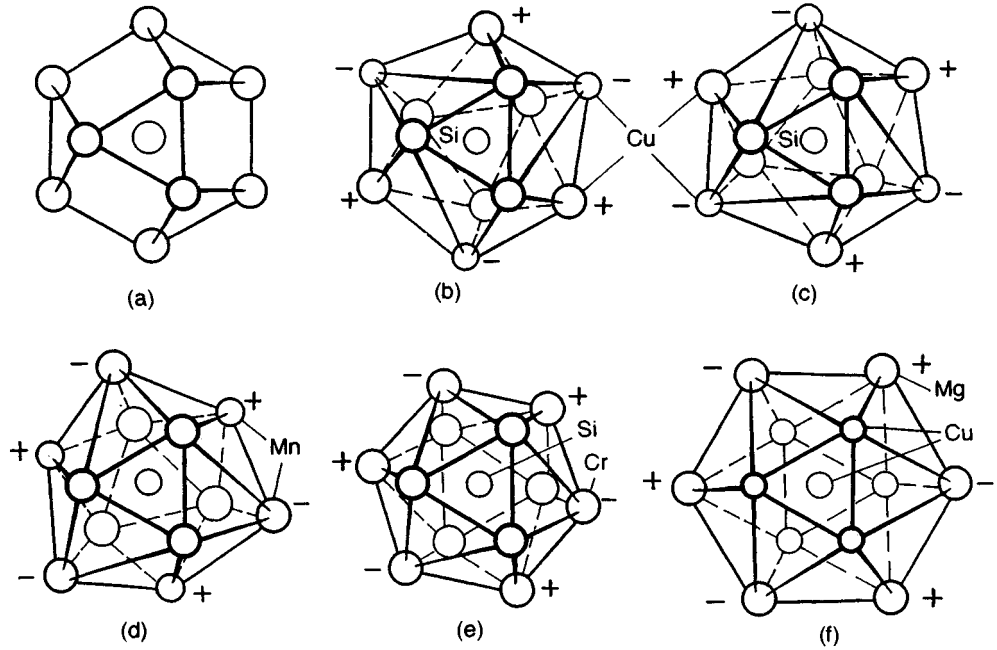

Figure 7 Projections of the 12-coordination polyhedra in some intermetallic compounds: (a) hexagonal cubooctahedron ($MgMg_{12}$) in the structure Mg; (b) left- and (c) right-twisted icosahedra ($SiCu_{12}$) in the structure $Cu_{15}Si_4$ ($D8_6$, cI176); (d) icosahedron ($MnMn_{12}$) in the structure α-Mn (A12, cI58); (e) 'crystallographical' icosahedron ($SiCr_{12}$) in the structure Cr_3Si; and (f) icosahedron ($CuMg_6Cu_6$) in the structure Cu_2Mg

The structure type $MgZn_2$ may be represented in the way described above as the sum of nets situated along the directions [0 0 1] or [1 1 0]. Nets of two kinds—flat (A,B,C) and crimped (a',b',c')—alternate along a direction perpendicular to the *Z* axis (Figure 11). In the flat net LM_3 (p6m), the L positions are vacant (kagomé nets), and the M positions are occupied by Zn atoms. The crimped net contains Zn atoms between triangles of two flat nets and double the number of Mg atoms between a hexagon and a triangle. Along the direction [1 1 0] one can distinguish general nets consisting of pentagons and triangles with Mg and Zn atoms at vertices and the intermediate ones sparsely occupied by Zn atoms (Figure 12). The relative distances between nets and the mutual displacement are the same as in the Cr_3Si structure.

Structures that are derivatives of the $MgZn_2$ type (Laves phases) arise most often as a result of changing the stacking of the close-packed layer (homeotectic) types (Teslyuk, 1969): $MgZn_2$ structure type (indicated in phase diagrams as λ_1, two-layer packing with $n=2$, stacking symbol h_2, type symbol L_2; $MgCu_2$ structure type, C15, cF24 (λ_2, $n=3$, c_3, L_3); and $MgNi_2$ structure type, C36, hP24 (λ_3, $n=4$, (ch_2), L_4). It was found that a series of multilayer Laves phases (L_5, L_6, L_8, L_9, L_{10}, L_{14}, and L_{16}) occurs among the ternary intermetallic compounds. Multilayer structures, derived from $MgZn_2$, are formed in the Mg–Li–Zn system (Melnyk, 1974). Their formation is connected with a change in the valence-electron concentration (VEC) and the values of the ratio $r_R/\bar{r}_X$, where $\bar{r}_X$ is the average radius of the atoms X and X' (Li and Zn) in the mixture. The hexagonality of the packing increases with the increase of these values (Table 3). A number of multilayer Laves phases (L_2, L_4, L_6, L_9, L_{10}, and L_{16}) have been found in the system Mg–Cu–Al by means of electron microscopy (Kitano *et al.*, 1977). Derivatives of the types $MgZn_2$ and $MgCu_2$ may also arise as a result of ordered substitutions ($R_2X_4 \rightarrow R_2X_3X'$, $R_2X_4 \rightarrow RR'X_4$, and possibly $R_2X_4 \rightarrow RR'X_3X'$) and/or of deformation. For example, Mg_2Cu_3Si (L_2') and $MnInCu_4$ (L_2'') are superstructures of the $MgZn_2$ type; and Mg_2Cu_3Al (L_3') and $MgSnCu_4$ (L_3'') are superstructures of the $MgCu_2$ type. The structure type $AuBe_5$ ($C15_b$, cF24) is formed by the redistribution of X and R atoms ($R_2X_4 \rightarrow RXX_4$) in the $MgCu_2$ structure type (Misch, 1935). There are also deformed derivatives of $MgZn_2$—orthorhombic URe_2 (oC24) (Hatt, 1961)—and

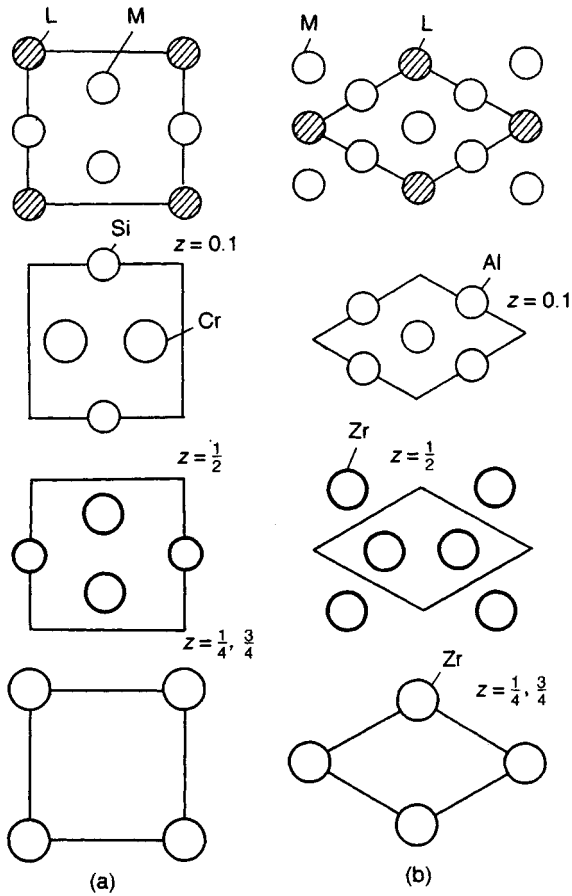

Figure 8 The formation of the structures of the compounds (a) Cr_3Si and (b) Zr_3Al_4 through occupancy of a planar network LM_3 with the symmetries pmm and p6m, respectively

of $MgCu_2$—rhombohedral $TbFe_2$ (hR6) (Dwight and Kimball, 1974).

There is a series of derivative structure types (class V of Table 1) in which Laves phases, Cr_3Si and Zr_4Al_3 types are the 'building blocks' (for example, the P phase, shown in Figure 10, has been investigated by Shoemaker and Shoemaker (1967)). From the survey of the structure types in Table 4, in which fragments of Cr_3Si, Zr_4Al_3, and $MgZn_2$ structures are combined, one can see that the weighted-average coordination number ($\bar{\nu}$) depends linearly (Figure 13) on the content of atoms with icosahedral coordination (C_{12}) (Jarmoljuk and Kripyakevich, 1974):

$$\bar{\nu} = 13.6 - 0.4C_{12}$$

The increase in the ratio of the effective radii of components (r_R/r_X) in the series $Cr_3Si \rightarrow Zr_4Al_3 \rightarrow MgZn_2$ leads to an increase in CN of the R atoms; but, at the same time, the content of the larger R atoms is decreased, and as a result $\bar{\nu}$ remains within the limits 12.9 and 13.5. This regularity was named the 'Jarmoljuk–Kripyakevich phenomenon' and may aid in the proper choice of CN and CP (E. I. Gladyshevskii *et al.*, 1992).

The structures with giant cells investigated by Samson (1967, 1968) also belong to class 5 (Figure 1) of the structure types.

3.3 Structure Type $CaCu_5$ and its Derivatives

The structure type $CaCu_5$ ($D2_d$, hP6) (Haucke, 1940) may be considered to be the result of the substitution by an R atom of three of the eight X atoms with the larger size ($X_8 \rightarrow RX_5$) in the hexagonal close packing

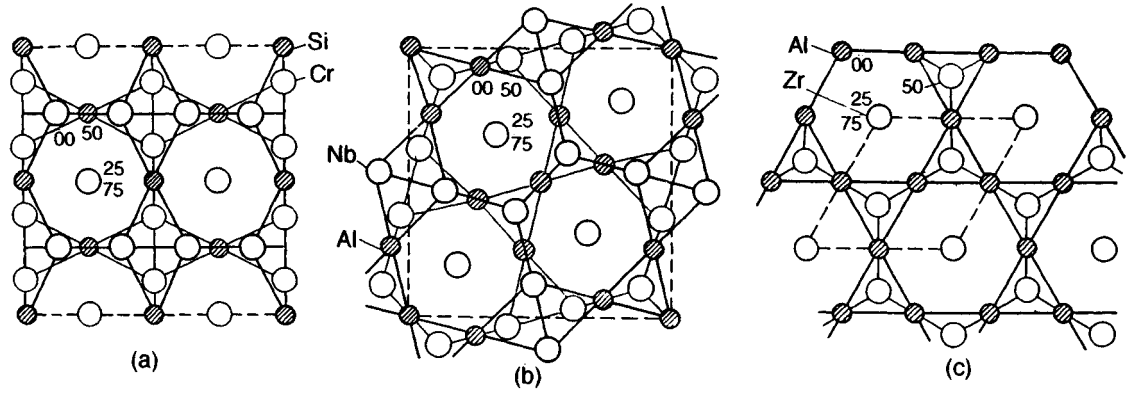

Figure 9 Projections of the structures (a) Cr_3Si, (b) Nb_2Al, and (c) Zr_3Al_4 on planes parallel to the close-packed layers. Coordinate z is shown in multiples of 0.01

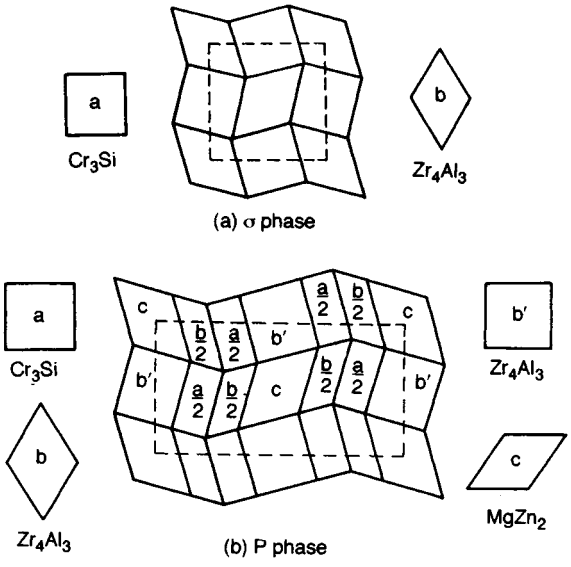

Figure 10 Formation of (a) σ phase (Nb_2Al) unit cell by the combination of the Cr_3Si and Zr_4Al_3 unit cells and (b) P phase by combination of Cr_3Si, Zr_4Al_3, and $MgZn_2$ unit cells

(Figure 11). At that degree of substitution, the ratio of atom radii is $r_R/r_X = \sqrt[3]{3}/1 = 1.44$, which is greater than the ratio in the $MgZn_2$ structure. The structure has a defect layer of symmetry p6m as in the $MgZn_2$ and Zr_4Al_3 structures. Along the [1 1 0] direction, $CaCu_5$ may be represented as consisting of two types of nets: general (pentagons and triangles) and intermediate (rectangles) (Figure 12). In the type $CaCu_5 = CaCu_2Cu_3'$, atoms of Cu occupy two crystallographic positions: R atoms form a simple hexagonal stacking, and X atoms form a frame from the empty tetrahedron (X_4).

Recently some ternary structure types $R_xM_yX_z$ derived from $CaCu_5$ have been described by Bodak *et al.* (1990). One of these is the undeformed superstructure $CeCo_3B_2$ (hP6) (Kuzma *et al.*, 1969) (Table 5, Figure 14). When the conditions for simple substitution (superstructure formation) are not suitable, deformed and/or defect derivatives arise. The structure type $HoNi_{2.6}Ga_{2.4}$ (hP6) (Grin and Gladyshevskii, 1989) is partly a statistically substituted variant of $CaCu_5$ with the elimination and inclusion of R atoms. The deformed derivatives retain approximately the same positions of all the atoms in the starting type, but differ in their unit cells (symmetry, unit-cell parameters). They are realized just as in the preceding group of structure types at the expense of an increase in the number of components in the compound.

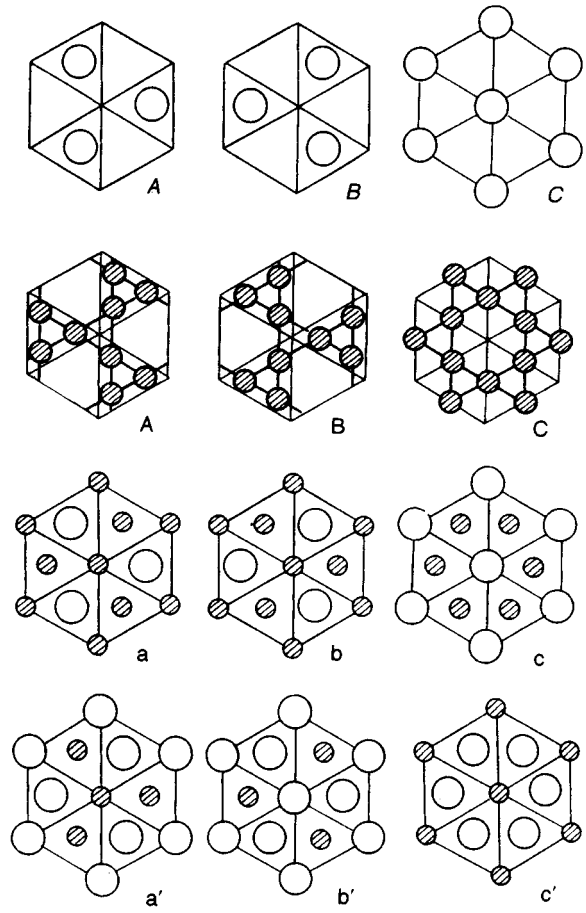

Figure 11 Atom nets perpendicular to the six and threefold axes in close-packed structures (nets *ABC*—the upper row), in the structure $MgZn_2$ and other Laves phases (ABC, a'b'c'—the second and fourth rows), and in $CaCu_5$ structure (ABC, abc—second and third rows). $MgZn_2$ structure: Ca'Ba' (= Ac'Bc'), in the crimped a' net $z_{Mg} = 2/16 \pm 1/16$. $MgCu_2$: Ca'Bc'Ab', in the a'(c'b') nets $z_{Mg} = 4/24 \pm 1/24$ ($= 12/24 \pm 1/24$, $= 20/24 \pm 1/24$). $MgNi_2$: Ca'Ba'Cb'Ab', in the a' net $z_{Mg} = 4/32$ (and $12/32) \pm 1/32$, in the b' net $z_{Mg} = 20/32$ (and $28/32) \pm 1/32$. $CaCu_5$: both nets Cc are planar, in C nets—Cu, in c—Ca and Cu atoms

The next group of new structure types may be considered as defect derivatives of the $CaCu_5$ type. Only a part of the atom positions are the same as for the starting structure. The inclusion–elimination of R atoms in the majority of cases occurs with the stoichiometry preserved, corresponding to that of the type $CaCu_5$, and leads to a mutual shift of R atoms along a single direction. The elimination of the M component leads to a change of stoichiometry from the starting type.

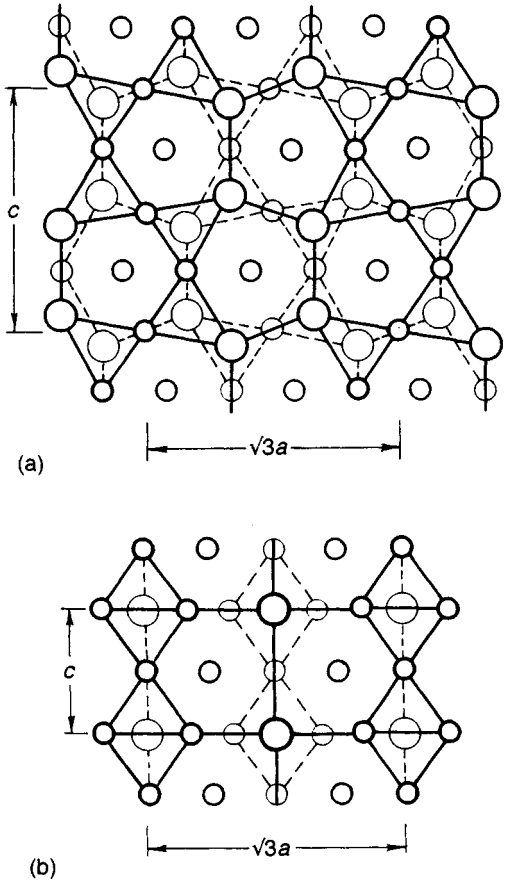

Figure 12 Atomic arrangement in the (a) $MgZn_2$ and (b) $CaCu_5$ structures projected onto the (1 1 0) plane. In the general nets consisting of pentagons and triangles are Mg and Zn or Ca and Cu atoms. The other Zn or Cu atoms are in the intermediate sparsely occupied nets

The structure types that are formed by various R atom substitutions by X_2 pairs preserve the same part of the atomic positions as in the $CaCu_5$ type (Table 6). The different ways of substitution and the number of R atoms that are substituted lead to the occurrence of new structure types. Other structure types derived from $CaCu_5$ are also known. Type $CeAl_8Mn_4$ is a superstructure to the $ThMn_{12}$ type ($D2_b$, tI26) (Zarechnyuk and Kripyakevich, 1962). There are two more types of undeformed superstructures R_2X_{17}—Th_2Zn_{17} (hR19) and U_2Zn_{17} (hP114) (Makarov and Vinogradov, 1956), which are homeotectic. The structures $BaZn_5$ (oC24) and $SrZn_5$ (oP24) (Baenziger and Corant, 1956) are also derived from the $CaCu_5$ type and are formed as the result of a shift of a part of the layers; and structure $CeCu_6$ (oP28) (Cromer *et al.*, 1960) is formed as a result of the inclusion of additional X atoms in the $BaZn_5$ structure type. The structure $LaNi_2Al_3$ is an undeformed superstructure of the type $BaZn_5$ (R. Gladyshevskii *et al.*, 1992).

Analyzing the composition of the ternary representatives of the $CaCu_5$ type and the new structure types that are derivatives of $CaCu_5$, one notices that to preserve the necessary correlation of the atomic sizes the majority of them occur in the ternary systems R-X-X′ or R-R′-X, where R and R′ are alkali, alkaline-earth, and rare-earth metals, and X and X′ are d metals and the elements B, Al, Ga, Si, and Ge. In the systems R-M-B, ternary borides have been found that crystallize in the structure types $CeCo_4B$ (hP12), $Ce_3Co_{11}B_4$ (hP18), $Nd_3Ni_{13}B_2$ (hP18), $Ce_2Co_7B_3$ (hP24), and $CeCo_3B_2$ (hP6) (Figure 15); they form with the structures of the binary compounds, which belong to the $CaCu_5$ type, a homologous series. Type $CaCu_5$ and a superstructure of it, $CeCo_3B_2$, are the progenitors of this series. The unit-cell compositions of the structures

Table 3 Multilayered Laves phases in the ternary system Mg–Li–Zn (L_3' and L_4' are superstructures to the types L_3 and L_4, respectively)

Compound	Pearson code	VEC	r_R/r_X	Type code	Stacking formula	Hexagonal stacking (%)
$MgZn_2$	hP12	2.000	1.149	L_2	h_2	100.0
$MgLi_{0.07}Zn_{1.93}$	hP48	1.977	1.144	L_8	$(hhhc)_2$	75.0
$MgLi_{0.11}Zn_{1.89}$	hP84	1.963	1.141	L_{14}	$(hhchhhc)_2$	71.4
$MgLi_{0.20}Zn_{1.80}$	hR18	1.933	1.136	L_9	$(hhc)_3$	66.7
$MgLi_{0.23}Zn_{1.77}$	hP60	1.923	1.134	L_{10}	$(hchhc)_2$	60.0
$MgLi_{0.25}Zn_{1.75}$	hP24	1.917	1.132	L_4	$(hc)_2$	50.0
$MgLi_{0.50}Zn_{1.50}$	hP96	1.833	1.116	L_4'	$(hc)_2$	50.0
$MgLi_{0.56}Zn_{1.44}$	hR6	1.813	1.112	L_3'	c_3	0
$MgLi_{0.77}Zn_{1.23}$	cF24	1.743	1.098	L_3	c_3	0

Table 4. Structure types—hybrids of the types Cr_3Si, Zr_4Al_3, and $MgZn_2$

Number on Figure 10	Structure types[a]	Pearson code	Content of atoms (at.%) with different coordination				Average CN, $\bar{\nu}$	Number of fragments in formula units		
			CN = 16	15	14	12		R_3X	R_4X_3	RX_2
1	Cr_3Si	cP8	0	0	75.0	25.0	13.500	1	—	—
2	Nb_2Al (σ)	tP30	0	13.4	53.3	33.3	13.466	2	1	—
3	Zr_4Al_3	hP7	0	28.6	28.6	42.8	13.428	—	1	—
3	P phase	oP56	7.2	14.3	35.7	42.8	13.428	1	1	1
3	δ phase	oP56	7.2	14.3	35.7	42.8	13.428	1	1	1
4	R phase	hR53	15.1	11.3	22.6	51.0	13.396	2	3	8
5	W_6Fe_7 (μ)	hR13	15.4	15.4	15.4	53.8	13.385	—	1	2
6	T phase	cI162	24.7	7.4	7.4	60.5	13.358	—	3	20
7	$MgZn_2$ (λ_1)	hP12	33.3	0	0	66.7	13.333	—	—	1

[a] P, $Mo_3(Mo,Cr)_5(Cr,Ni)_6$.
δ, $Mo_3(Mo,Ni)_5Ni_6$.
R, $Mo_{14}(Mo,Mn,Fe)_{12}(Mn,Fe)_{27}$.
T, $Mg_{32}(Zn,Al)_{49}$.

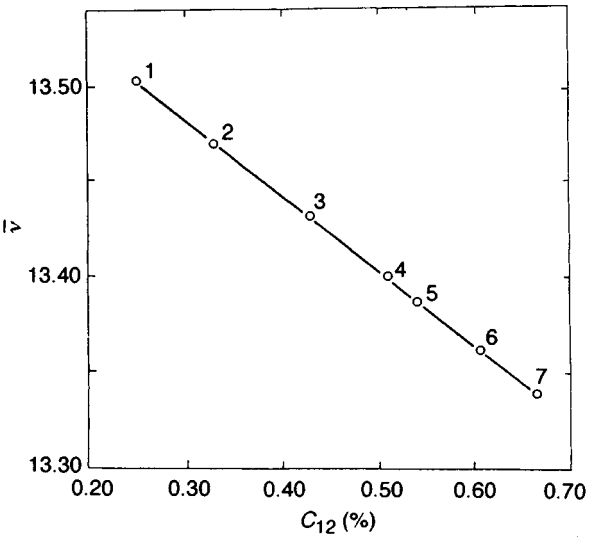

Figure 13 The weighted-average coordination number $\bar{\nu}$ for structures derived from Cr_3Si, Zr_4Al_3, and $MgZn_2$ types ((1) Cr_3Si, (2) σ phase, (3) Zr_4Al_3, P and σ phases, (4) R phase, (5) μ phase, (6) T phase, (7) λ_1 phase) as a function of content of the atoms with icosahedral coordination

that belong to this series are described by the formula $R_{m+n}M_{5m+3n}X_{2n}$, where m is the number of $CaCu_5$ fragments and n is the number of $CeCo_3B_2$ fragments. Representatives are known of another homologous series of structures based on the types $CeCo_3B_2$ and $MgZn_2$ (Figure 16). The members of this series—$Dy_3Ni_7B_2$ (hP24) and $Ce_2Co_5B_2$ (hP36)—are described by the formula $R_{2m+n}M_{4m+3n}X_{2n}$, where m and n are the numbers of $MgZn_2$ and $CeCo_3B_2$ fragments, respectively.

The structure type $CaCu_5$ is the progenitor of still other homologous series of structures, both one-dimensional and two-dimensional. Type $CaCu_5$ with type $MgZn_2$ form a one-dimensional homologous series that is described by the formula $R_{m+2n}X_{5m+4n}$ (m is the number of $CaCu_5$ layers, n is the number of $MgZn_2$ layers). Known representatives of this series are the $CeNi_3$ (hP24) type ($m=1$, $n=1$), the Ce_2Ni_7 (hP36) type ($m=2$, $n=1$), and the Sm_5Co_{19} (hR24) type ($m=3$, $n=1$). The structures $PuNi_3$ (hR12), Gd_2Co_7 (hR18), and Ce_5Co_{19} (hR24) comprise a homologous series that is described by the same formula. It is constructed from the types $CaCu_5$ and $MgCu_2$. The structures of this homologous series have no representatives among the ternary compounds. The structure types $CeNi_5Sn$ (hP28) and $CeCu_6$ (oP28) belong to a two-dimensional series of structures; the progenitors of this series are $CaCu_5$ and the hypothetical RX_7, which has no real representatives.

4. Summary

From the known 2700 structure types of all intermetallic compounds* we have considered approximately 220 structure types that are characterized by close packings of atoms with the same, nearly the same or different sizes and with CN = 12 for all or part of the atoms (atoms that have smaller size) and CN > 12 (from 13 to 24) for atoms of bigger size, R atoms. For the latter,

*Or 1600 structure types without considering compounds containing elements of group VI, which in most cases differ from the structures of compounds of the metals with each other and with the elements of groups III–V.

Table 5. Examples of $CaCu_5$ superstructures, their distorted and defect derivatives

Way of transformation	Structure type $R_xM_yX_z$	Pearson code	Space-group symbol	Unit-cell parameters (a,b,c) expressed via $CaCu_5$ parameters (A,C)		
				a	b	c
Substitution	$CeCo_3B_2$	hP6	P6/mmm	A	—	C
Deformation	$ErRh_3Si_2$	oI24	Immm	$2C$	$\sqrt{3}A$	A
	$LaRu_3Si_2$	hP12	$P6_3/m$	A	—	$2C$
Elimination or inclusion of R atoms	$HoNi_{2.6}Ga_{2.4}$	hP18	P6/mmm	$\sqrt{3}A$	—	$2C$
	$Ba_2Ni_9B_6$	hR34	R3c	$\sqrt{3}A$	—	$4C$
	$Er_{1.03}Co_3Ge_2$	hP16	$P6_3/mcm$	A	—	$2C$
Elimination of M atoms	$CaRh_2B_2$	oF40	Fddd	A	$\sqrt{3}A$	$2C$
	$Sr_5Rh_{14}B_{10}$	oF116	Fmmm	$2A$	$\sqrt{3}A$	$6C$

the following name has been suggested: structure types with high coordination numbers (Kripyakevich, 1960).

Investigations of the conditions for the formation of isostructural compounds, the changes in their structures with changing temperature (or pressure), and the law-governed transitions of one structure into others on changing the identity of the components or their relative proportion are problems of separate aspects of crystal chemistry: isomorphism (isostructure), polymorphism (allotropy), and morphotropy, which have been of interest to many researchers. We have considered the morphotropic series that are formed with increasing atomic number of Ln atoms in phases of the systems Ln–Ln′ and in $LnAl_3$ compounds. Here the

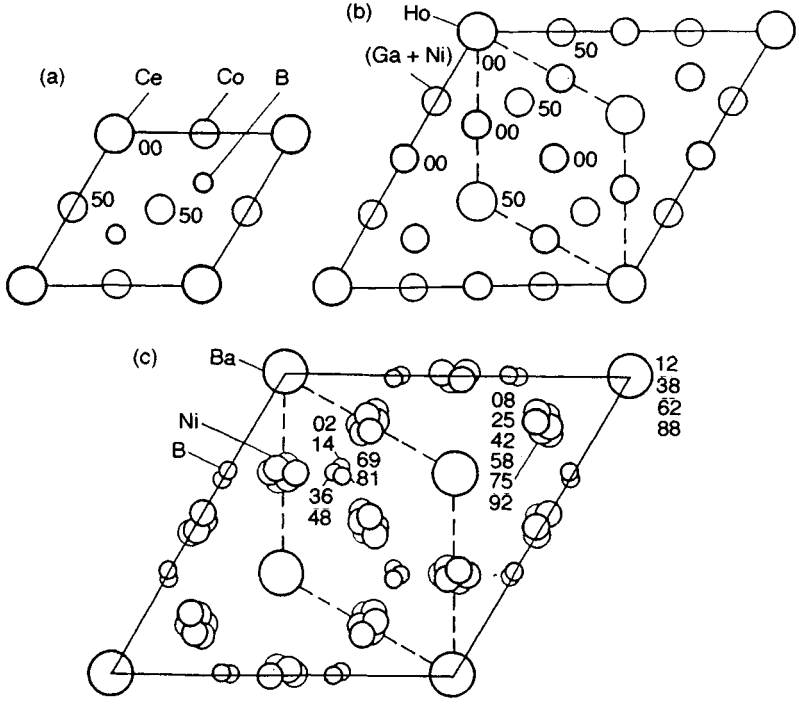

Figure 14 Projection of the structure types (a) $CeCo_3B_2$ (b) $HoNi_{2.6}Ga_{2.4}$, and (c) $BaNi_2B_2$ along the [0 0 1] direction. Coordinate z is shown in multiples of 0.01

Table 6. Structure types formed by the partial substitution of R atoms by X_2 pairs in the structure type $CaCu_5$

Way of substitution	Substitution scheme $R \rightarrow X_2$	Structure type	Pearson code	Space-group symbol	Unit-cell parameters (a,c) expressed via $CaCu_5$ parameters (A,C)	
					a	*b*
Statistical	$RX_5 \rightarrow R_{0.78}X_{5.44}$	$TbCu_7$	hP8	P6/mmm	*A*	*C*
	$RX_5 \rightarrow R_{0.5}X_6$	YCo_6Ge_6	hP8	P6/mmm	*A*	*C*
Ordered	$R_4X_{20} \rightarrow R_3X_{22}$	Ce_3Zn_{22}	tI100	$I4_1/amd$	$\sqrt{3}A$	$4C$
	$R_3X_{15} \rightarrow R_2X_{17}$	Th_2Ni_{17}	hP38	$P6_3/mmc$	$\sqrt{3}A$	$2C$
	$R_2X_{10} \rightarrow RX_{12}$	$ThMn_{12}$	tI26	I4/mmm	$\sqrt{3}A$	$2C$
		$LiCo_6Ge_6$	hP13	P6/mmm	*A*	$2C$

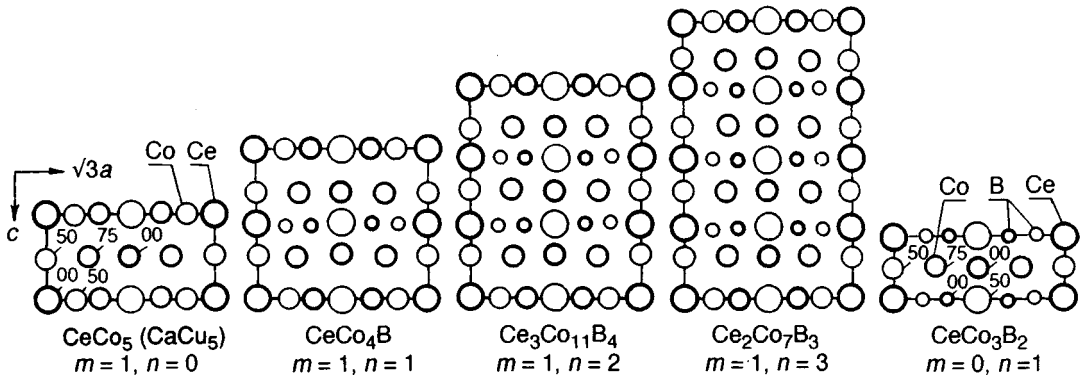

Figure 15 The linear quasihomogeneous homologous series with fragments of the structures $CeCo_5$ ($CaCu_5$ type) and $CeCo_3B_2$

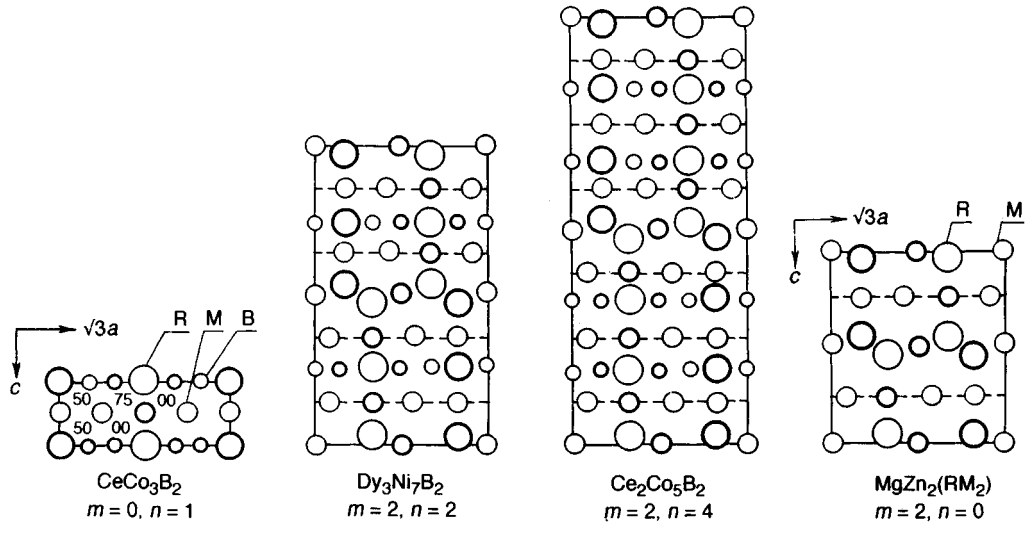

Figure 16 The linear heterogeneous homologous series of structures containing fragments of the $CeCo_3B_2$ and $MgZn_2$ structure types

Plate I

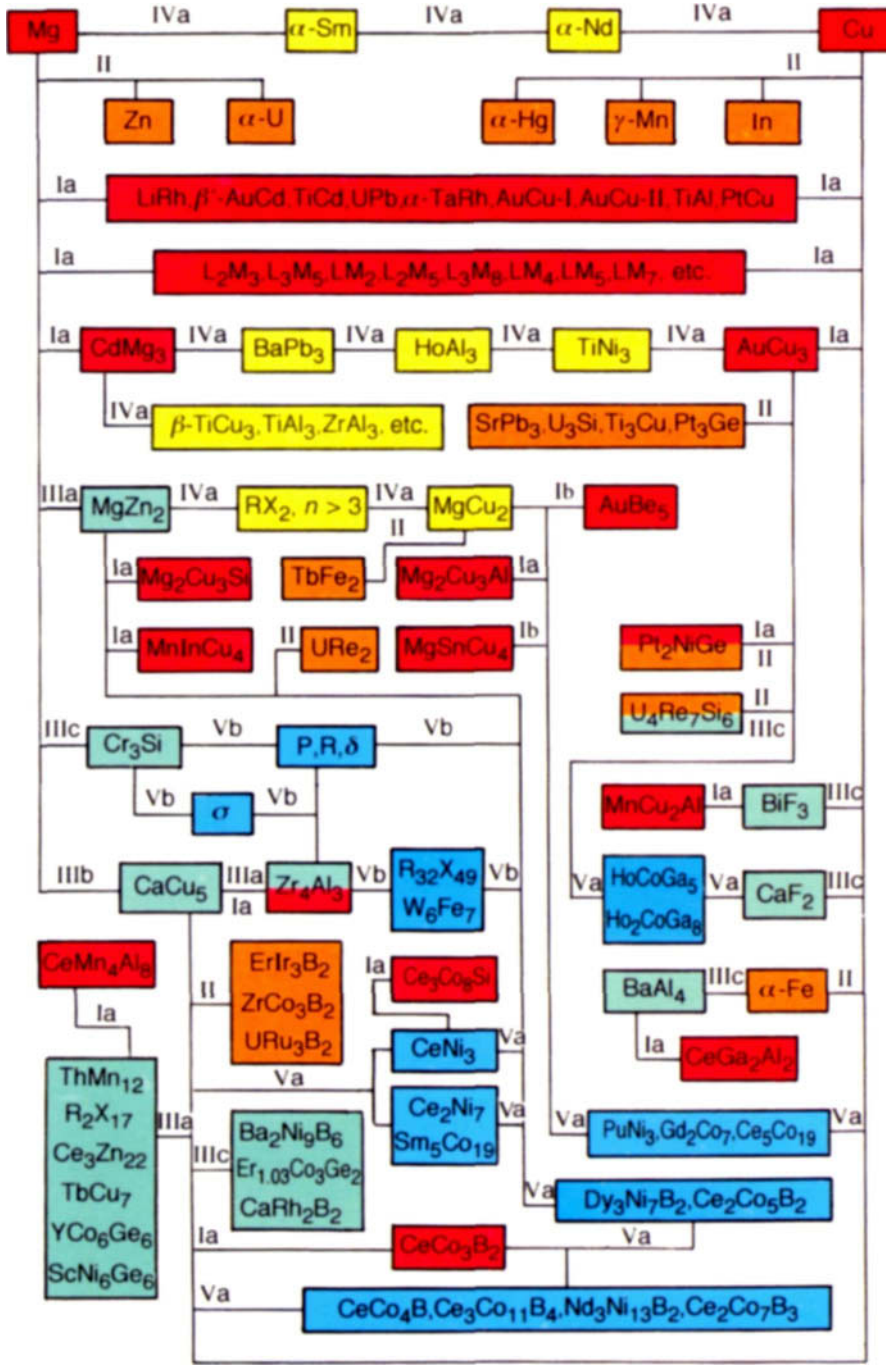

Figure 17 Structural relationships diagram of the structure types related to Mg and Cu ($AuCu_3$, $MgZn_2$, $MgCu_2$, Cr_3Si, $CaCu_5$, Zr_4Al_3, and others); Roman numerals I-V are related to the ways of transformation used in Table 1

general cause of the occurrence of a new structure is the size factor. One more example of the influence of the size factor on structures formed with high CN is the series of R_mX_n compounds. For these, the content of the X component and the maximum CN of the R atoms depend typically on the relative atomic size $k = r_R/r_X$ (Kripyakevich, 1952) as follows: type W_6Fe_7, $D8_5$, hR13 ($k = 1.11$, X content 53.9 at.%, CN = 15 for R atoms); Laves phases RX_2 (1.23, 66.7, 16); $CaCu_5$ (1.45, 83.5, 20); and $NaZn_{13}$, $D2_3$, cF112 (1.56, 92.9, 24).

The influence of electron factors (e.g. VEC) on the formation of the close-packed structures is undoubted. For example, a VEC-governed shift of the homogeneity range of the σ-phases in the binary systems R–X (R = V, Cr, Mo, and X = Mn, Fe, Co) and in the ternary systems V–Mn–X and Cr–Mn–X with the substitution of Fe by Co and Ni has been observed (Wernick, 1967). Isostructural and simultaneously isoelectronic (with the same VEC) series are known in which ternary compounds with certain structure types are formed only with the substitution for Zn in the binary compounds by statistical mixtures (Cu + Al) or (Ni + Si) in the ternary ones (Gladyshevskii, 1971). For example, the following series exist: Ce_2Zn_{17} (structure with the type Th_2Ni_{17})→$Ce_2Cu_{6.5}Al_{10.5}$→$Ce_2Ni_{15}Si_2$; $GdZn_{12}$ ($ThMn_{12}$ type)→$GdCu_4Al_8$→$GdNi_{10}Si_2$; and $LaZn_{13}$ ($NaZn_{13}$ type)→$LaCu_{10.0-5.5}Al_{3.0-7.5}$→$LaNi_{10.5}Si_{2.5}$. So, for the formation of compounds with Cu and Ni that are isostructural with Zn compounds, it is necessary in order to preserve a limiting electron concentration to substitute part of the Cu or Ni atoms by Al and Si respectively.

Consideration of the interrelationships of a large number of hybrid structures that belong to different homologous series has turned out to be very fruitful in the search for new intermetallic compounds and in the prediction of their possible crystal structures. The composition of the unit cell of a series of structural representatives can be described by a single formula, and their crystal structures are formed by the association of planar fragments (nets) or volume fragments (polyhedra), cut out from simpler starting structures. Some examples of such homologous series constructed from simpler close-packed structures have been described above in Sections 2.2, 3.2, and 3.3. The homologous series of intermetallic compounds may be homogeneous, quasihomogeneous, or heterogeneous. The first type includes fragments of a single structure type, but joined in different ways (for example, AlB_2→α-$ThSi_2$); the second includes two related fragments of the same structure type (for example, fragments of the structure and its superstructure or defect derivative, $CeCo_5$→$CeCo_3B_2$); and the third includes fragments of two or more different structures ($MgZn_2$→$CeCo_3B_2$). Combinations of the fragments may be one-dimensional (linear), two-dimensional (planar), or three-dimensional (spatial). Knowing the symmetry of the fragments and the possible ways in which they are joined, one can predict the symmetry of the structure as a whole, and also the quantitative composition of the compound. Systematic investigations of such homologous series were started at Lviv University at the beginning of the 1970s (Kripyakevich, 1970; Gladyshevskii and Kripyakevich, 1972) and have been reported in more than 50 works. Similar investigations have been carried out in other crystal-chemistry laboratories (Parthé and Chabot, 1984; Fornasini *et al.*, 1989; Parthé, 1991; Rogl, 1991) and were the main subject of extensive discussions at the recent International School of Crystallography (Parthé, 1992).

The genetic connections of the close-packed structures, related types, and the ways of transforming from one to another may be illustrated by a generalized diagram (Figure 17, Plate 1). Some derivatives from the face-centered cubic Cu type, which do not belong to the close-packed structures, but whose fragments together with fragments of close-packed structures form new hybrid structure types belonging to different homologous series, are also included in the diagram.

5. References

Baenziger, N. C., and Corant, J. W. (1956). *Acta Crystallogr.*, **9**, 361.

Beattie, H. J., Jr (1967). Close-packed Structures. In *Intermetallic Compounds* (ed. J. H. Westbrook). Wiley, New York, ch. 9, p. 144.

Belov, N. W. (1947) *Structure of Ionic Crystals and Metallic Phases* (in Russian). Izd. AN SSSR, Moscow, p. 3.

Bodak, O. I., Oleksin, O. J., Pecharskiy, V. K., Belskiy, V. K., and Zhukov, S. G. (1990). *Dop. AN URSR*, **B** (2), 30.

Boren, B. (1933). *Ark. Kemi, Miner., Geol.*, **A11**, 1.

Cromer, D. T., Larson, A. C., and Roof, R. B. (1960). *Acta Crystallogr.*, **13**, 913.

Dwight, A. E., and Kimball, C. W. (1974) *Acta Crystallogr.*, **B30**, 2791.

Fornasini, M. L., Mugnoli, A., and Palenzona, A. (1989). *J. Less-Common Met.*, **154**, 149.

Frank, F. C., and Kasper, J. S. (1958). *Acta Crystallogr.*, **11**, 184.

Friauf, J. B. (1927). *Phys. Rev.*, **29**, 34.

Gladyshevskii, E. I. (1971) *Crystal Chemistry of Silicides and Germanides* (in Russian). Metallurgiya, Moscow, p. 271.

Gladyshevskii, E. I., and Bodak, O. I. (1982). *Crystal Chemistry of the Intermetallic Compounds of the Rare-*

Earth Metals (in Russian). Vyshcha Shkola, Lviv, pp. 184–203.
Gladyshevskii, E. I., and Kripyakevich, P. I. (1972). *Ninth General Assembly and Intl. Congr. of IUCr*, Kyoto. Coll. Abstr., p. 97.
Gladyshevskii, E. I., Bodak, O. I., and Pecharskij, V. K. (1985). *Zh. Vses. Chim. Obshch. Mendeleeva*, **30**, 515.
Gladyshevskii, E. I., Gorelenko, Yu. K., Grin, J. M., and Yarovetz, V. I. (1992). *Kristallografiya*, **37**, 141.
Gladyshevskii, R. E., Cenzual, K., and Parthé, E. (1992). *Acta Crystallogr.*, **B48**, 389.
Grin, J. N., and Gladyshevskii, R. E. (1989). *Gallides* (in Russian). Metallurgizdat, Moscow, p. 129.
Grin, J. M., Jarmoljuk, J. P., and Gladyshevskii, E. I. (1979). *Kristallografiya*, **24**, 242.
Gschneidner, K. A., and Valetta, R. M. (1968). *Acta Metall.*, **16**, 477.
Hatt, B. A. (1961) *Acta Crystallogr.*, **14**, 119.
Haucke, W. (1940). *Z. Anorg. Allg. Chem.*, **244**, 17.
Jarmoljuk, J. P., and Kripyakevich, P. I. (1974). *Kristallografiya*, **19**, 539.
Kitano, Y., Komura, Y., and Kajiwara, H. (1977). *Trans. Japan Inst. Met.*, **18**, 39.
Kripyakevich, P. I. (1952). *Dop. AN USSR*, **85**, 321.
Kripyakevich, P. I. (1960). *Kristallografiya*, **5**, 79.
Kripyakevich, P. I. (1970). *Kristallografiya*, **15**, 690.
Kripyakevich, P. I. (1977). *Structure Types of Intermetallic Compounds* (in Russian). Nauka, Moscow, pp. 3–91.
Kuzma, J. B., Kripyakevich, P. I., and Bilonizhko, N. S. (1969). *Dop. AN URSR*, **A**, 939.
Laves, F., and Witte, H. (1935). *Metallwirtschaft*, **14**, 645.
Magnéli, A. (1953). *Acta Chem. Scand.*, **6**, 495.
Makarov, E. S., and Vinogradov, S. I. (1956). *Kristallografiya*, **1**, 634.
Melnyk, E. W. (1974). *Dop. AN URSR*, **A**, 949.
Misch, L. (1935). *Metallwirtschaft*, **14**, 897.
Parthé, E. (1991). *Elements of Inorganic Structural Chemistry (A Course on Selected Topics)* K. Sutter Parthé, Switzerland, p. 67.
Parthé, E. (1992). *19th Course on Modern Perspectives in Inorganic Crystal Chemistry*, Lecture notes and poster abstracts. International School of Crystallography, Erice, Trapani, Sicily.
Parthé, E., and Chabot, B. (1984). In *Handbook on the Physics and Chemistry of Rare Earths* (eds K. A. Gschneidner, Jr and L. R. Eyring). North-Holland, Amsterdam, ch. 48, p. 113.
Parthé, E., Gelato, L., Chabot, B., Penzo, C., Cenzual, K., and Gladyshevskii, R. (1994). *Typix. Standardized Data and Crystal Chemical Characterization of Inorganic Structure Types*. In Press.
Pearson, W. B. (1967). *J. Less-Common Met.*, **13**, 626.
Pearson, W. B. (1972). *The Crystal Chemistry and Physics of Metals and Alloys*. Wiley, New York, p. 303.
Rogl, P. (1991). *Existence and Crystal Chemistry of Borides in Inorganic Reaction and Methods* (ed. A. Hagen). VCH Publishers, New York, pp. 85–167.
Samson, S. (1967). *Acta Crystallogr.*, **23**, 586.
Samson, S. (1968). In *Structural Chemistry and Molecular Biology*. W. H. Freeman, San Francisco, p. 687.
Schubert, K. (1964). *Kristallstrukturen zweikomponentiger Phasen*. Springer-Verlag, Berlin.
Shoemaker, C. B., and Shoemaker, D. P. (1967). *Acta Crystallogr.*, **23**, 231.
Smirnova, N. L. (1975). *Krystallografia*, **20**, 524.
Teslyuk, M. J. (1969). *Metal Compounds with the Structure of Laves Phases* (in Russian). Nauka, Moscow, p. 65.
Villars, P., and Calvert, L. D. (1991). *Pearson's Handbook of Crystallographic Data for Intermetallic Phases*, 2nd Edn. American Society for Metals, Metals Park, OH.
Wernick, J. H. (1967). In *Intermetallic Compounds* (ed. J. H. Westbrook). Wiley, New York, ch. 12, p. 197.
Wilson, C. G., Thomas, D. K., and Spooner, F. J. (1960). *Acta Crystallogr.*, **13**, 56.
Zarechnyuk, O. S., and Kripyakevich, P. I. (1962). *Kristallografiya*, **7**, 543.

This chapter was originally published in 1995 as Chapter 17 in *Intermetallic Compounds*, Vol. 1: *Principles*, edited by J. H. Westbrook and R. L. Fleischer.

Chapter 8
Structure Mapping

David G. Pettifor
Department of Materials, University of Oxford, Parks Road, Oxford OX1 3PH, UK

1. Introduction

Crystal-structure and materials' properties are intimately linked. Currently, alloy developers are searching for new *cubic* alloys with good mechanical properties (see, for example, Dimiduk and Miracle, 1989), new *tetragonal* alloys with good permanent magnetic properties (see, for example, de Mooij and Buschow, 1987), new *perovskite*-type ceramics with good superconducting or ferroelectric properties (see, for example, Rabe *et al.*, 1992), and new *icosahedrally* based alloys as stable quasicrystals (see, for example, Rabe *et al.*, 1991). At the outset, the alloy developer is faced with the problem of deciding which particular alloy constituents will stabilize a required structure type. A useful initial guide may be provided by structure mapping, which attempts to order the known experimental database on the structures of binary, ternary, and quaternary compounds within a limited number of two- or three-dimensional structure maps.

Historically, the majority of these structure maps have been constructed by taking coordinates that reflect the most important *physical* factors determining the structural stability of the particular class of compounds under consideration. For example, Mooser and Pearson (1959) in their pioneering study of valence compound structures chose the electronegativity difference ΔX as one coordinate and the average value of the principal quantum number $\bar{n}$ as the other. They argued that directionally bonded phases would be expected to lie in the region where ΔX and $\bar{n}$ were both small, whereas ionic phases would lie in the region of large ΔX. Phillips and Van Vechten (1969), on the other hand, in their highly successful separation of the structure types within sp-valent AB octet semiconductors and insulators, used the physically motivated coordinates E_h and C, the covalent and ionic contribution to the average spectroscopic energy gap, respectively.

The Mooser–Pearson and Phillips–Van Vechten maps were restricted to valence compounds. In an attempt to handle the broad spectrum of intermetallic compounds, Zunger (1980) followed the earlier ideas of St John and Bloch (1974) and chose R_σ and R_π as his two coordinates, the latter being defined in terms of quantum-mechanically derived s and p core radii, as we will see later in Section 2.2. He found that he was able to obtain a reasonable structural separation of all the known AB compounds within three separate *two*-dimensional maps (R_σ, R_π). In order to obtain a structural separation of all isostoichiometric binary compounds within a single framework, Villars (1983, 1984a,b) introduced his *three*-dimensional maps (ΔX, ΔR, $\bar{N}$), where the three coordinates reflect the importance of the electronegativity difference ΔX, the atomic-size difference ΔR, and the average number of valence electrons per atom $\bar{N}$ in the determination of the structural stability (see, for example, Pearson, 1972; Chapter 2 by Turchi in this volume). Recently these three coordinates have been generalized in order to treat ternaries and quaternaries (Villars and Hulliger, 1987; Rabe *et al.*, 1992; see also Chapter 11 by Villars in this volume).

An alternate approach to the construction of structure maps has been proposed by the author (Pettifor, 1988a).

Crystal Structures of Intermetallic Compounds. Edited by J. H. Westbrook and R. L. Fleischer

At the microscopic level it is well-known that structural stability is determined by *at least* four factors, namely the electronegativity difference, the atomic-size difference, the electron-per-atom ratio, and the angular character of the s, p, and d valence orbitals (see, for example, Pettifor and Podloucky, 1986; Cressoni and Pettifor, 1991). Thus, in principle, it is not possible to order perfectly the structures of *all* isostoichiometric binary compounds within a single two- or three-dimensional map with the use of *physical* coordinates. Logic demands that, if binary systems are to be represented within two-dimensional plots, then each element in the periodic table should have a unique single coordinate. Since the only single physical coordinate that allows structural prediction from first principles is the atomic number Z, and this clearly fails to order binary A_mB_n compounds within the two-dimensional map (Z_A, Z_B), a *phenomenological* coordinate was proposed instead. The coordinate was determined by running a one-dimensional string through the two-dimensional periodic table, the path of the string being chosen to give the best structural separation for the binary AB compounds. Pulling the ends of the string apart orders all the elements along a one-dimensional axis, their sequential order being given by the relative ordering number $\mathcal{M}$. Structure maps based on $\mathcal{M}$ have been given that include most binary and ternary intermetallic compounds (Pettifor, 1986, 1988a,b).

This chapter discusses the art of structure mapping and its relevance to the search for new intermetallics with a required structure type. In Section 2 illustrative examples of Mooser–Pearson, Zunger, Villars, and Pettifor maps will be presented for *binary* compounds. In Section 3 the latter two approaches will be generalized to *ternary* systems. In Section 4 we conclude.

2. Binary Structure Maps

2.1 Mooser–Pearson Maps

The first successful structure maps were constructed by Mooser and Pearson (1959) for valence compounds. As we have seen above, they took as their two coordinates the difference in the electronegativity ΔX and the average value of the principal quantum number $\bar{n}$. They believed that directionally bonded phases would fall in the region where ΔX and $\bar{n}$ were both small, whereas ionic phases would fall in the region of large ΔX. These expectations were borne out among the restricted class of valence compounds that they considered. For example, Figure 1 shows the Mooser–Pearson map for *octet* sp-valent AB compounds, which

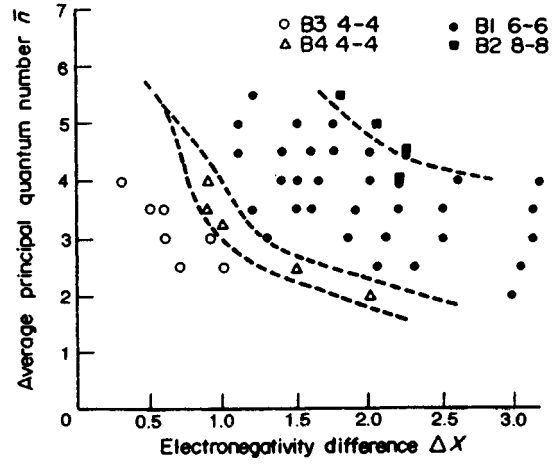

Figure 1. The Mooser–Pearson map for sp-valent *octet* compounds formed from group A cations only (From Mooser and Pearson, 1959. Reproduced with permission)

are formed from group A cations *only* and have eight valence electrons per AB unit. Excellent separation has been achieved between the B1 (NaCl) with Pearson symbol cF8, B2 (CsCl) cP2, B3 (cubic ZnS, zincblende) cF8, and B4 (hexagonal ZnS, wurtzite) hP4 structure types. Moreover, small values of ΔX and $\bar{n}$ correspond to the directionally bonded, fourfold-coordinated ZnS lattices, whereas large values of ΔX and $\bar{n}$ correspond to the ionically bonded eightfold-coordinated CsCl lattice.

However, intermetallic compounds that do not satisfy normal valence rules were not well-separated into different structural domains by the two coordinates ΔX and $\bar{n}$. Zunger (1980), for example, has shown that the Mooser–Pearson map for 360 non-octet AB compounds gives extremely poor structural separation between the 14 different structure types considered.

2.2 Zunger Maps

The maps of Zunger (1980) were the first to order the structures of a broad range of intermetallic compounds with a single consistent choice of coordinates. Watson and Bennett (1978a,b) in two important earlier papers had obtained structure maps for AB, AB_2 and AB_3 compounds but had found it necessary to use a different choice of coordinates for transition element–transition element bonding compared to sp–sp or sp–transition element bonding. Following St John and Bloch (1974), Zunger (1980) constructed two-dimensional AB maps based on the dual coordinates

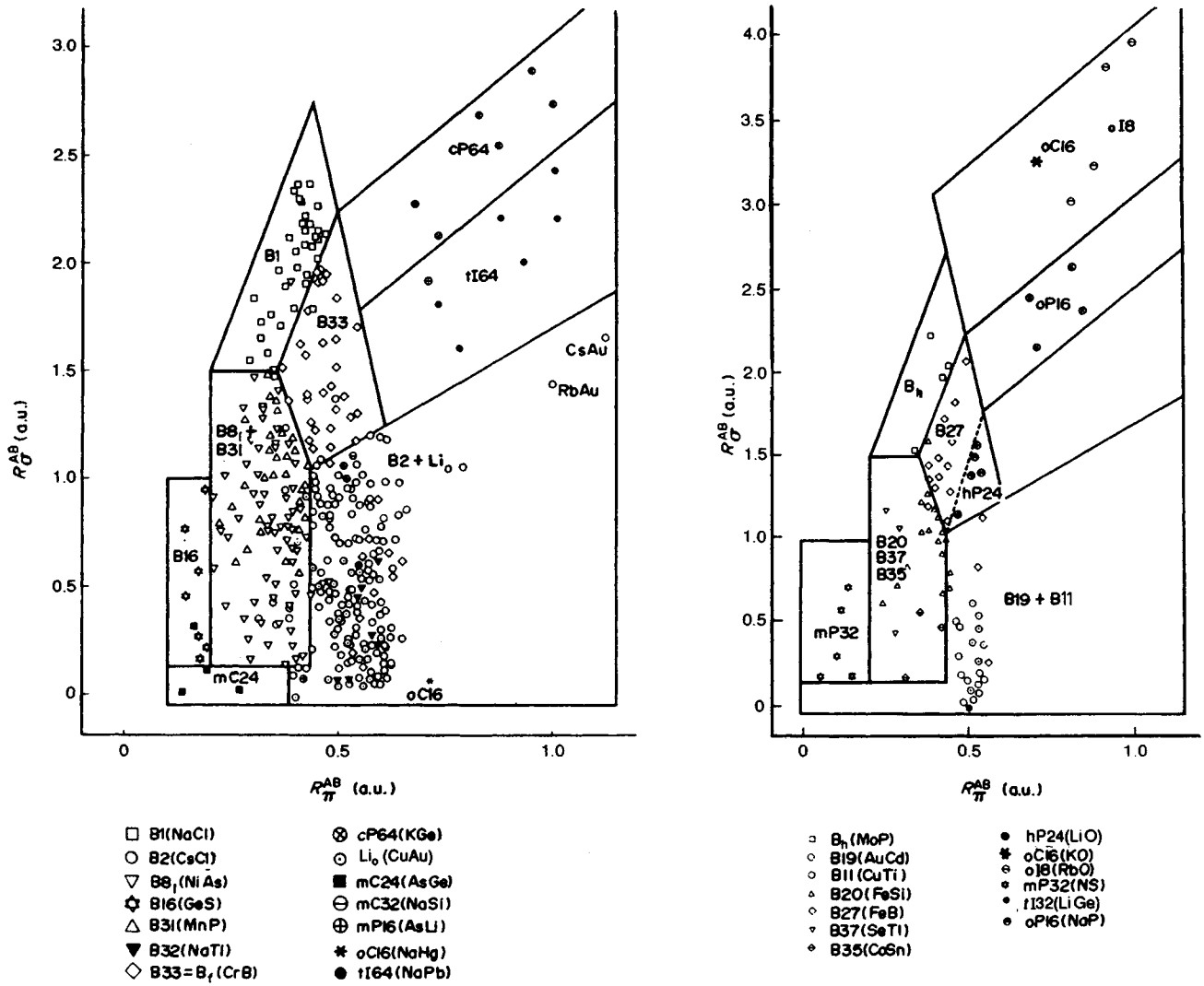

Figure 2. The Zunger maps for *non-octet* AB compounds (from Zunger, 1980. Reproduced with permission)

$$R_\sigma^{AB} = |(r_p^A + r_s^A) - (r_p^B + r_s^B)| \quad (1)$$

and

$$R_\pi^{AB} = |(r_p^A - r_s^A) + (r_p^B - r_s^B)| \quad (2)$$

where r_s and r_p are s and p core radii, respectively. These core radii were calculated and tabulated for the first five rows of the periodic table using pseudopotential theory (Zunger and Cohen, 1978; Zunger, 1980). The sum $(r_s + r_p)/2$ is a direct measure of the average radius of the core, whereas $(r_p - r_s)/2$ is an indirect measure of the s-to-p promotion energy (compare, for example, the plots of the s and p atomic energy levels across the periodic table with that of the inverse s and p core radii in figures 4 and 7 of Pettifor (1983)). Thus, from equations (1) and (2), R_σ^{AB} is a measure of the size mismatch between the A and B atoms, whereas R_π^{AB} is a measure of the average propensity of the two atoms to form sp hybrids.

Figure 2 shows the structural separation achieved by the Zunger maps for 437 *non-octet* AB compounds displaying 27 different structure types. Two maps have been drawn for clarity, since several different structure types occur in the same domain. We see that a good structural separation has been achieved, although structures with similar local coordinations have not been resolved. For example, the following structure types have common domains: $B8_1$ (NiAs) with Pearson symbol hP4, B20 (FeSi) cP8, and B31 (MnP) oP8; B27 (FeB) oP8 and B33 (CrB) oC8; B2 (CsCl) cP2, B11 (CuTi) tP4, B19 (AuCd) tP4, and $L1_0$ (CuAu) tP4, respectively. MnP is a distorted NiAs structure type; FeB and CrB have identical nearest-neighbour coordination polyhedra; CsCl and CuTi are b.c.c.-derivative structures; and hexagonal AuCd and tetragonal CuAu are 12-fold-coordinated close-packed polytypes (see, for example, Pearson, 1972; Wells, 1975).

The left-hand panel of Figure 3 from Yeh *et al.* (1992) shows the structural separation achieved with the (R_σ, R_π) map for *octet* AB compounds (with eight valence electrons per AB unit) using the orbital radii r_s and r_p predicted by pseudopotential theory. Figure 3 excludes compounds containing transition elements (except Mn). We see that reasonable structural separation has been achieved between the cubic zinc blende, the hexagonal wurtzite, NaCl, NiAs, graphite, and cinnabar structure types. The last two structure types are the ground-state structures of BN and HgO, and of HgS, respectively. Figure 3(a) has incorrectly placed BeO in the zinc-blende rather than the wurtzite domain, and MnS, MnSe, MgS, and MgSe in the zinc-blende rather than the NaCl domain. Interestingly a near-perfect separation is found

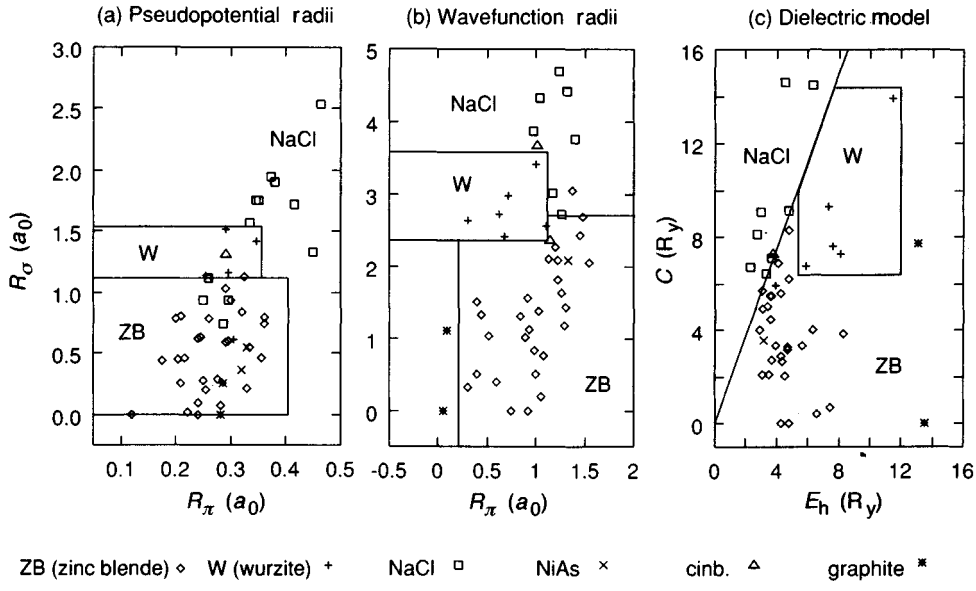

Figure 3. Structure maps for *octet* non-transition-element AB compounds using (a) pseudopotential orbital radii, (b) maximum radial probability density radii, and (c) Phillips–Van Vechten dielectric coordinates E_h and C (see text for details). The left-hand panel (a) also includes MnX (X = O, S, Se, and Te) compounds. The right-hand panel (c) does not include HgO (From Yeh *et al.*, 1992. Reproduced with permission)

H 1 2.10[a] 1.25[b]																
Li 1 0.90 1.61	Be 2 1.45 1.06											B 3 1.90 0.795	C 4 2.37 0.64	N 5 2.85 0.54	O 6 3.32 0.465	F 7 3.78 0.405
Na 1 0.89 2.65	Mg 2 1.31 2.03											Al 3 1.64 1.675	Si 4 1.98 1.42	P 5 2.32 1.24	S 6 2.65 1.10	Cl 7 2.98 1.01
K 1 0.80 3.69	Ca 2 1.17 3.00	Sc 3 1.50 2.75	Ti 4 1.86 2.58	V 5 2.22 2.43	Cr 6 2.00 2.44	Mn 7 2.04 2.22	Fe 8 1.67 2.11	Co 9 1.72 2.02	Ni 10 1.76 2.18	Cu 11 1.08 2.04	Zn 12 1.44 1.88	Ga 3 1.70 1.695	Ge 4 1.99 1.56	As 5 2.27 1.415	Se 6 2.54 1.285	Br 7 2.83 1.20
Rb 1 0.80 4.10	Sr 2 1.13 3.21	Y 3 1.41 2.94	Zr 4 1.70 2.825	Nb 5 2.03 2.76	Mo 6 1.94 2.72	Tc 7 2.18 2.65	Ru 8 1.97 2.605	Rh 9 1.99 2.52	Pd 10 2.08 2.45	Ag 11 1.07 2.375	Cd 12 1.40 2.215	In 3 1.63 2.05	Sn 4 1.88 1.88	Sb 5 2.14 1.765	Te 6 2.38 1.67	I 7 2.76 1.585
Cs 1 0.77 4.31	Ba 2 1.08 3.402	La 3 1.35 3.08	Hf 4 1.73 2.91	Ta 5 1.94 2.79	W 6 1.79 2.735	Re 7 2.06 2.68	Os 8 1.85 2.65	Ir 9 1.87 2.628	Pt 10 1.91 2.70	Au 11 1.19 2.66	Hg 12 1.49 2.41	Tl 3 1.69 2.235	Pb 4 1.92 2.09	Bi 5 2.14 1.997	Po 6 2.40 1.90	At 7 2.64 1.83
Fr 1 0.70[a] 4.37[b]	Ra 2 0.90[a] 3.53[b]	Ac 3 1.10[a] 3.12[b]														

Ce 3 1.1[a] 4.50[b]	Pr 3 1.1[a] 4.48[b]	Nd 3 1.2[a] 3.99[b]	Pm 3 1.15[a] 3.99[b]	Sm 3 1.2[a] 4.14[b]	Eu 3 1.15[a] 3.94[b]	Gd 3 1.1[a] 3.91[b]	Tb 3 1.2[a] 3.89[b]	Dy 3 1.15[a] 3.67[b]	Ho 3 1.2[a] 3.65[b]	Er 3 1.2[a] 3.63[b]	Tm 3 1.2[a] 3.60[b]	Yb 3 1.1[a] 3.59[b]	Lu 3 1.2[a] 3.37[b]
Th 3 1.3[a] 4.98[b]	Pa 3 1.5[a] 4.96[b]	U 3 1.7[a] 4.72[b]	Np 3 1.3[a] 4.93[b]	Pu 3 1.3[a] 4.91[b]	Am 3 1.3[a] 4.89[b]									

Figure 4. Values of the valence-electron number, the Martynov–Batsanov electronegativity X, and the Zunger s and p pseudopotential radii sum R that are used to construct Villars maps. Electronegativities with the superscript a are Pauling values (Pauling, 1960). Pseudopotential radii sums with the superscript b are estimated from a comparison of Zunger's radii with the radii of maximum radial electron density determined by Herman–Skillmann calculations (Girifalco, 1976) (From Villars *et al.*, 1989. Reproduced with permission)

in Figure 3(b) when r_s and r_p are defined by the outer maxima in the radial probability density of the appropriate atomic orbitals (Yeh *et al.*, 1992; Chapter 14 by Parthé). The resultant structural separation in the middle panel is as good as that achieved by the Phillips–Van Vechten map (E_h, C) in the right-hand panel, where E_h and C are the covalent and ionic contributions to the average spectroscopic energy gap, respectively. This systemization of the cubic versus hexagonal fourfold-coordinated octet structure types is directly relevant to the development of wide-gap III–V and II–VI semiconductors, since the minimum band gap is very structure-sensitive, changing by nearly 40% in going from cubic to hexagonal SiC, for example (Yeh *et al.*, 1992).

2.3 *Villars Maps*

Villars (1983, 1984a,b) has constructed *three-dimensional* maps (ΔX, ΔR, $\bar{N}$) in order to display all the isostoichiometric binary data within a single framework. He found that the best structural separation was achieved by using the orbital electronegativities of Martynov and Batsanov (1980) and the orbital radii ($r_s + r_p$) of Zunger (1980). These, together with the choice of the number of valence electrons associated with each element, are given in Figure 4.

Figure 5 shows two cross-sections through the three-dimensional Villars map for AB compounds, corresponding to the octet compounds with $\bar{N} = 4$ and the non-octet compounds with $\bar{N} = 6.5$, respectively. Sixteen such figures with different values of $\bar{N}$ are required to display all the structural information for this particular stoichiometry. We see that reasonable structural separation is achieved, although again, like the non-octet Zunger maps in Figure 2, the domains often contain more than one structure type. However, a major drawback is that the fifth most common structure type, $B8_1$ (NiAs) hP4, was unable to be separated and was omitted from the AB map (Villars, 1983). This probably reflects the importance of the angular character of the valence orbitals, since this has not been included explicitly in the choice of coordinates (ΔX, ΔR, $\bar{N}$). It is clear that the structures of the elements would not be separated within this map because they lie along the $\bar{N}$ axis corresponding to ($\Delta X = 0$, $\Delta R = 0$), so that tetrahedrally coordinated silicon and close-packed titanium, for example, would both be characterized by the same point $\bar{N} = 4$.

2.4 *Pettifor Maps*

Rather than using *physical* coordinates, the author has suggested using a *phenomenological* coordinate, which

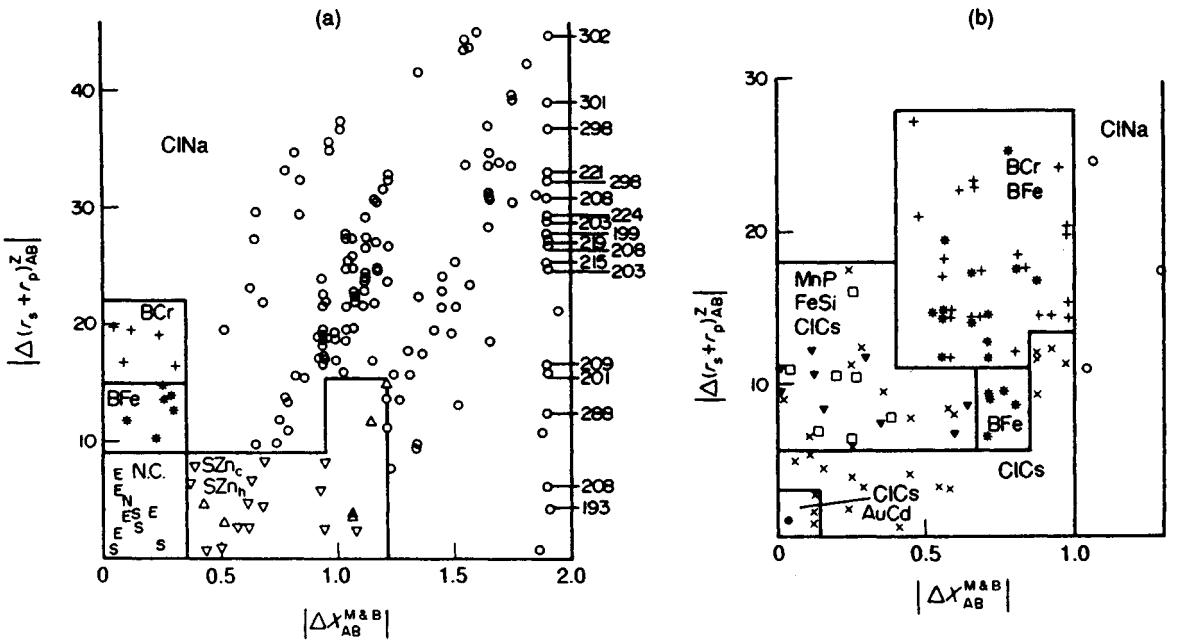

Figure 5. The Villars maps for AB compounds corresponding to the average electron-per-atom ratio of $\bar{N} = 4$ and 6.5 respectively (From Villars, 1983. Reproduced with permission). (a) $\bar{N} = 4$; (b) $\bar{N} = 6.5$

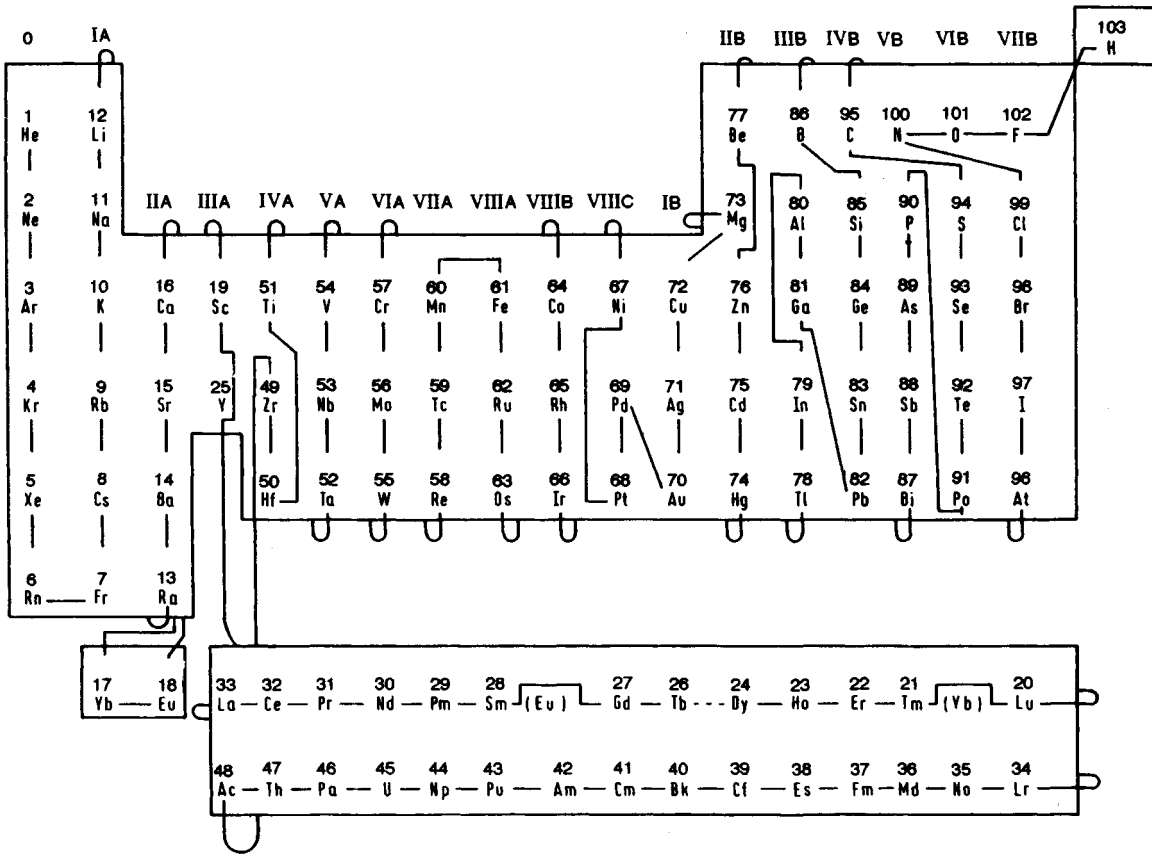

Figure 6. The string through this modified periodic table puts all the elements in sequential order, thereby defining the relative ordering number $\mathscr{M}$. Note that the group IIA elements Be and Mg have been grouped with group IIB, the divalent rare earths have been separated from the trivalent, and Y has been slotted between Tb and Dy (From Pettifor, 1988a)

is obtained by running a string through the periodic table as shown in Figure 6. Pulling the ends of the string apart orders all the elements along a one-dimensional axis, their sequential order defining the relative order number $\mathscr{M}$. This simple procedure, which defines a purely phenomenological coordinate, is found to provide excellent structural separation of all binary compounds with a given stoichiometry A_mB_n within a single *two-dimensional* map ($\mathscr{M}_A$, $\mathscr{M}_B$) (Pettifor, 1984, 1986, 1988a,b).

Figure 7 shows the AB ground-state structure map using the experimental database of Villars and Calvert (1985). The bare patches correspond to regions where compounds do not form owing to either positive heats of formation or the competing stability of neighboring phases with different stoichiometry. The boundaries do not have any significance other than that they were drawn to separate compounds of different structure type. In regions where there is a paucity of data, the boundary is usually chosen as the line separating adjoining groups in the periodic table. We see that excellent structural separation has been achieved between the 52 different AB structure types that have more than one representative compound each. The two most common structure types, namely B1 (NaCl) cF8 and B2 (CsCl) cP2, are well-separated, the NaCl lattice being found only outside the region defined by $\mathscr{M}_A$, $\mathscr{M}_B \leqslant 81$, which encloses the main *metallic* CsCl domain. We see that at normal temperature and pressure the ionic B2 (CsCl) lattice is restricted to the very small region of Cs-containing salts. The AB structure map successfully demarcates even closely related structure types such as B27 (FeB) oP8 and B33 (CrB) oC8; $B8_1$ (NiAs) hP4 and B31 (MnP) oP8; and B3 (cubic ZnS, zinc blende) cF8 and B4 (hexagonal ZnS, wurtzite) hP4. Moreover, coherent phases with respect to the b.c.c

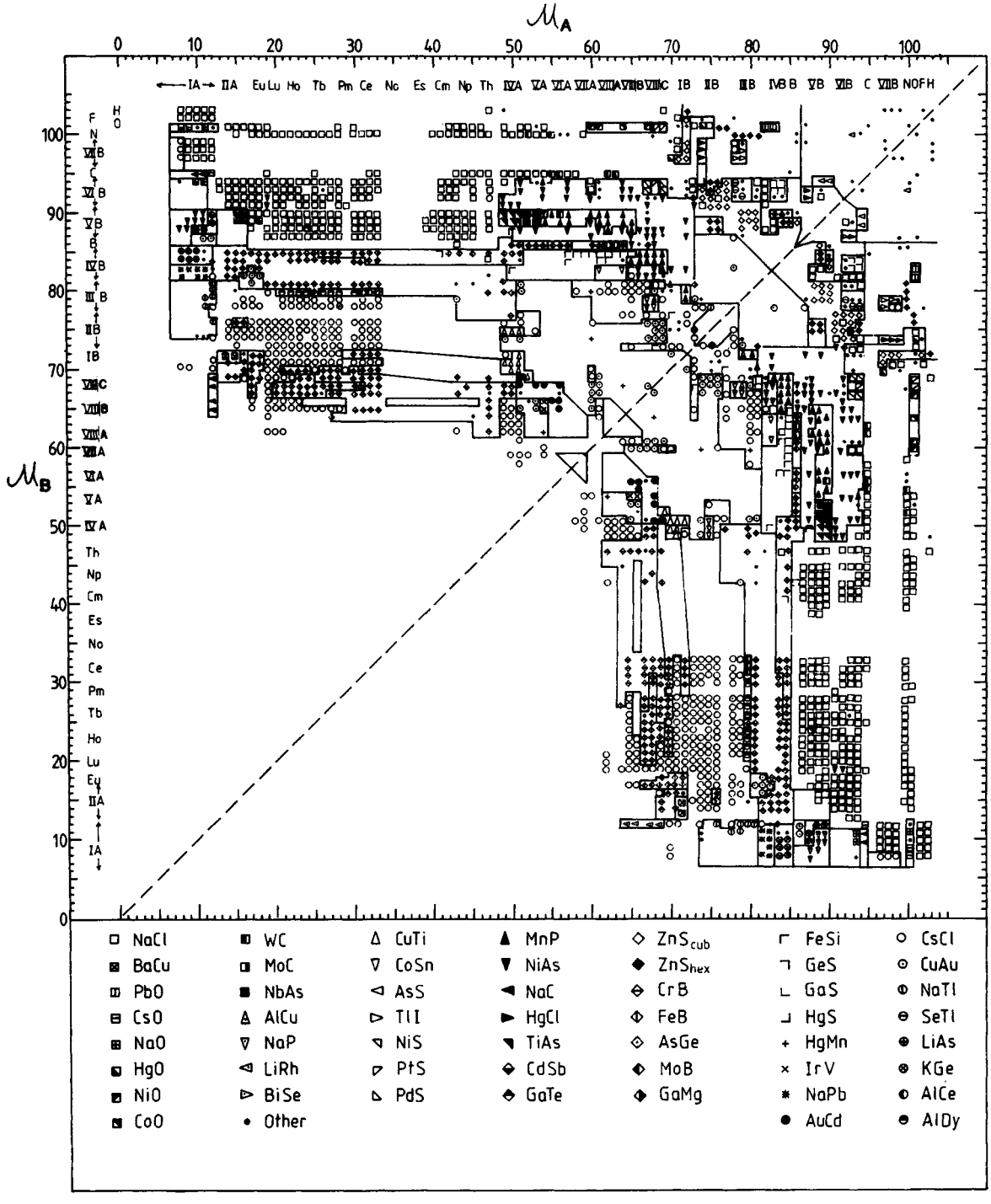

Figure 7. The Pettifor map for AB compounds (from Pettifor, 1988a)

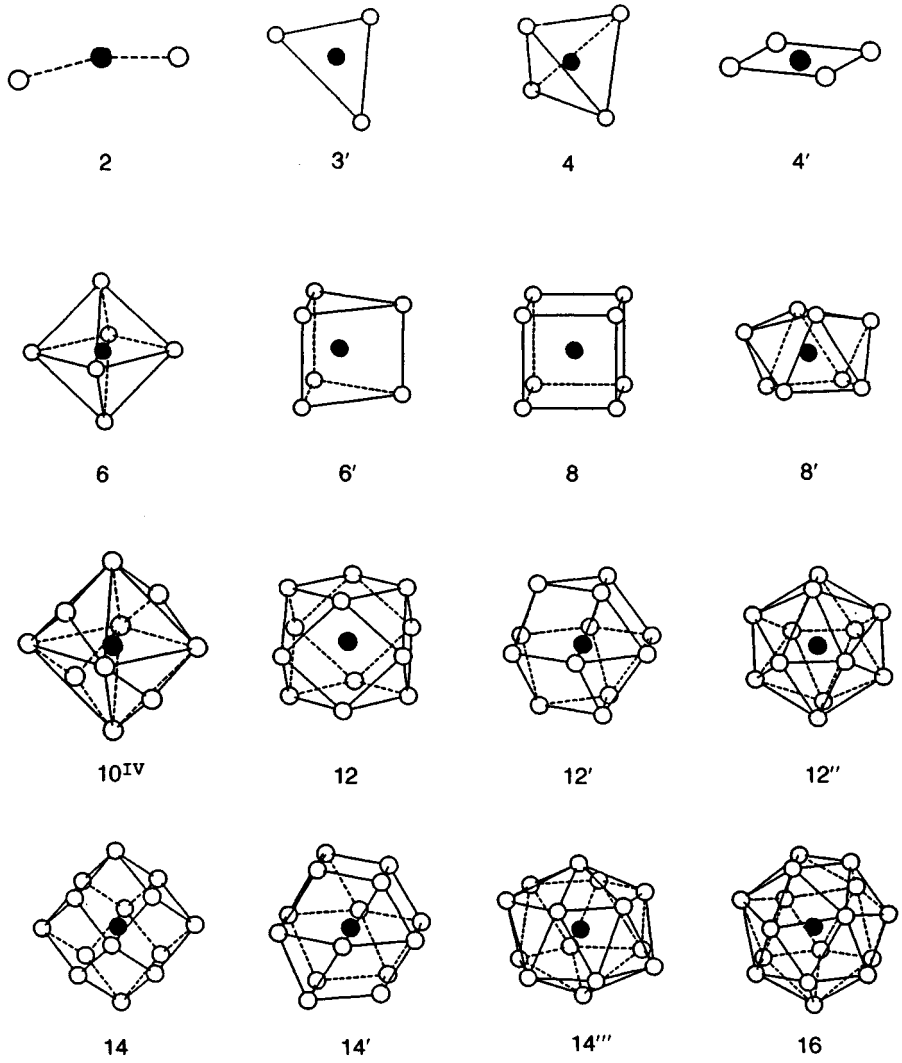

Figure 8. Some commonly occurring local coordination polyhedra with generalized Jensen notation

lattice, namely B2 (CsCl) cP2, B11 (CuTi) tP4, and B32 (NaTl) cF16, are also well-separated, as too are the close-packed polytypes cubic $L1_0$ (CuAu) tP4 and hexagonal B19 (AuCd) oP4.

As might be expected, neighboring domains often have similar local coordination (see figure 2 of Pettifor, 1986). Recently, Villars *et al.* (1989) have assigned local coordination polyhedra to all binary structure types with more than five representative compounds each. Figure 8 illustrates some of the more commonly occurring coordination polyhedra, labeled according to a generalized Jensen notation (see table 5 of Jensen, 1989, and figures 3 and 4 of Villars *et al.*, 1989). Structure types can then be characterized not simply by their *stoichiometric* formulas, such as NaCl and NiAs, but by their *crystal coordination* formulas, such as $^3_\infty$ [$NaCl_{6/6}$] and $^3_\infty$ [$NiAs_{6/6'}$] (Jensen, 1989). This immediately informs us that NaCl and NiAs are infinite three-dimensional framework structures. Moreover, the symmetry of the coordination polyhedron about the Na, Cl, or Ni sites is that of an octahedron (denoted by 6), whereas that about the As site is that of a trigonal prism (denoted by 6′), as can be seen from Figure 8. It is, therefore, not surprising that the NaCl and NiAs

domains adjoin each other in Figure 7 and that there is a small domain of $\frac{3}{\infty}$ [$NbAs_{6/6'}$] stability in their midst.

Figure 9 shows that excellent structural separation has been achieved between the 84 different AB_2 structure types that have more than one representative compound each. The 8:4 coordinated fluorite structure C1 (CaF_2) cF12 with crystal coordination formula $\frac{3}{\infty}$ [$CaF_{8/4}$] is observed in the *ionic* regions at the top left and bottom right of Figure 9, although it also occurs elsewhere, as for example in the small domains centered on Mg_2Si, Rh_2P, and Al_2Pt respectively. The latter domains are *metallic*. In these cases it is more sensible to define the local coordination polyhedron about the fluorine site by including the six next-nearest-neighbor fluorine atoms in addition to the four tetrahedrally configured calcium first-nearest neighbors. This leads to the 10-atom configuration polyhedron 10^{IV} that is shown in Figure 8 (Villars *et al.*, 1989). A similar type of assignment must be made for the B2 (CsCl) cP2 lattice: in the *ionic* region only first-nearest-neighbor unlike atoms are retained so that the crystal coordination formula is $\frac{3}{\infty}$ [$CsCl_{8/8}$], whereas in a very large *metallic* domain of Figure 7 the six second-nearest-neighbor like atoms (which are only 14% more distant) are also included to define the 14-atom configuration polyhedron 14 that is drawn in Figure 8 (see section 2.8 of Jensen, 1989).

The 6:3 coordinated rutile structure C4 (TiO_2) tP6 with its crystal coordination formula $\frac{3}{\infty}$ [$TiO_{6/3'}$] is stable only with the very electronegative constituents hydrogen, oxygen, and fluorine. The corresponding compounds with the less electronegative halogens form the two-dimensional layer structures C19 ($CdCl_2$) hR3 and C6 (CdI_2) hP3 in which the metal atom is sixfold *octahedrally* coordinated. They thus have the crystal coordination formula $\frac{2}{\infty}$ [$CdCl_{6/3}$] and $\frac{2}{\infty}$ [$CdI_{6/3}$] respectively. These two structures are very similar in energy because they differ only in the stacking of the composite layers, which are held together by weak van der Waals interactions. $CdCl_2$ has the halogen atoms arranged on an f.c.c. lattice, whereas CdI_2 has them on an h.c.p. lattice. The metal atoms can also be sandwiched so that they have sixfold *trigonal* symmetry; α- and β-MoS_2 with crystal coordination formula $\frac{2}{\infty}$ [$MoS_{6'/3}$] correspond to the different stacking sequences 3R and $2H_1$ respectively (see Figure 4.11 of Wells, 1975). They are found among the early transition-metal sulfides, selenides, and halides.

The two forms of FeS_2, namely C2 (pyrites) cP12 and C18 (marcasite) oP6, are well-separated in Figure 9. They have the same sixfold octahedral coordination about the Fe site and are characterized by the S atoms occurring in pairs. The pyrites structure is derived from the NaCl structure by replacing Na with Fe and Cl with S_2 dimers pointing along ⟨1 1 1⟩ directions.

$C11_b$ ($MoSi_2$) tI6, C40 ($CrSi_2$) hP9, and C54 ($TiSi_2$) oF24 are polytypes that result from stacking close-packed planes of AB_2 stoichiometry in a b.c.c. (1 1 0) stacking sequence, so that it is not surprising that $MoSi_2$ is characterized by the distorted b.c.c. local coordination polyhedron 14, and $CrSi_2$ and $TiSi_2$ by the variant 14′ (see Figure 8). The C16 ($CuAl_2$) tI12 structure type neighbors both these polytypes and CaF_2, which is not unexpected since it can be derived from the b.c.c. lattice (Burdett, 1982; see also Chapter 13 by Hellner in this volume). Finally, the well-known space-filling AB_2 Laves phases are found almost in their entirety above the diagonal in Figure 9 and are seen to be well-separated among the C14 ($MgZn_2$) hP12, C15 ($MgCu_2$) cF24, and C36 ($MgNi_2$) hP24 structure types. The maps show only the ground-state structures; polytypism is often exhibited by those compounds falling near domain boundaries. The larger A atom is surrounded by 16 atoms within the Frank–Kasper coordination polyhedron 16, whereas the smaller B atom is surrounded icosahedrally by 12 atoms as illustrated by 12″ in Figure 8. See also Chapter 17 by Gladyshevskii and Bodak.

Figure 10 shows that excellent structural separation has also been achieved between the 52 different AB_3 structure types that have more than one representative compound each. The simplest three-dimensional framework structure with AB_3 stoichiometry that can be built from the octahedral AB_6 complex is cubic ReO_3 in which every octahedron is joined to six others through their vertices. This structure with crystal coordination formula $\frac{3}{\infty}$ [$ReO_{6/2'}$] is adopted by the trifluorides ZrF_3, TaF_3, and NbF_3. Like their AB_2 counterparts, the less-electronegative halogens form two-dimensional layer structures but with the A atoms occupying only two-thirds of the *octahedral* holes within the close-packed sandwich of B atoms. $\frac{2}{\infty}$ [$AlCl_{6/2}$] has the halogen atoms arranged on an f.c.c. lattice, whereas $\frac{2}{\infty}$ [$FeCl_{6/2}$] has them on an h.c.p. lattice. The halogens with group IVA form the one-dimensional chain structures $TiCl_3$ and TiI_3 in which the AB_6 octahedra share opposite faces. Distorted tricapped *trigonal* prismatic coordination is shown by the halogens within the actinides and some rare-earth and group IIIA elements; YF_3, LaF_3, and UCl_3 structure types have ninefold coordination about metal sites (see Chapter 12 by Hauck and Mika in this volume).

It is clear from Figure 10 that many 1:3 stoichiometric compounds take close-packed structure types with either

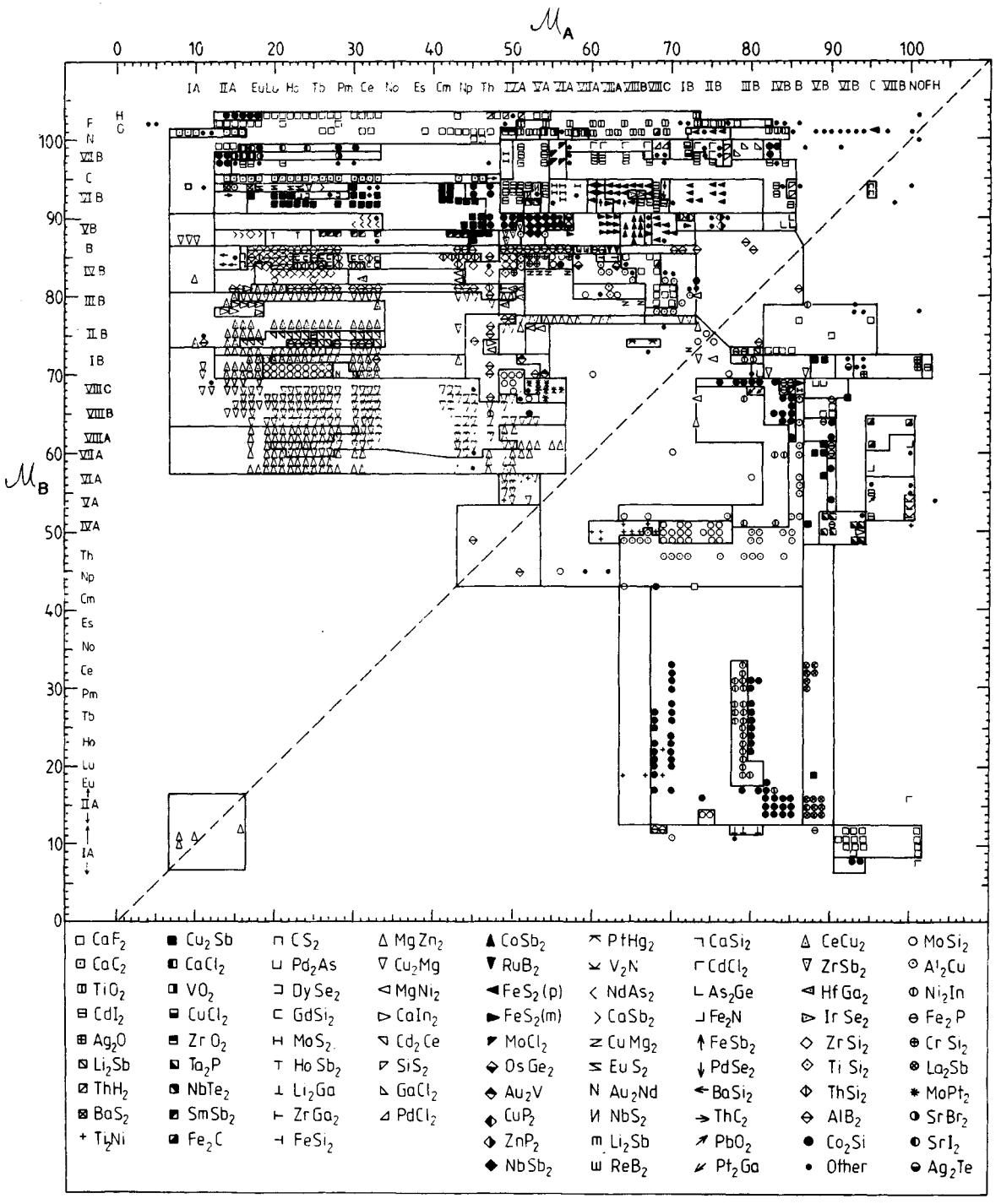

Figure 9. The Pettifor map for AB_2 compounds (from Pettifor, 1988a)

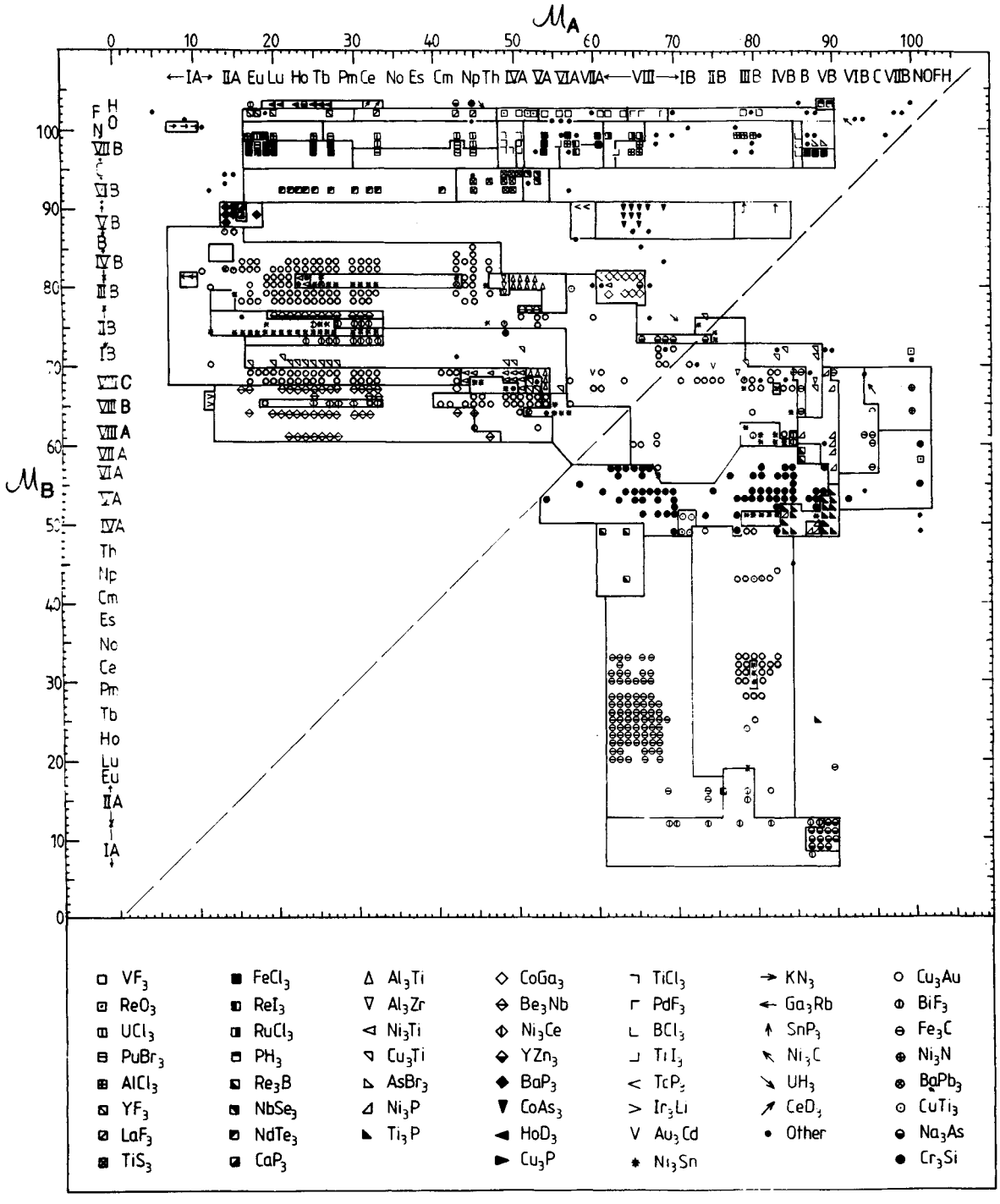

Figure 10. The Pettifor map for AB_3 compounds (from Pettifor, 1988a)

the (distorted) cubic 12 or hexagonal 12′ local coordination polyhedron (see Figure 8). Consider first the close-packed layer of MN_3 stoichiometry with a *triangular* arrangement of the M atoms (see Figure 7.15 of Pearson, 1972). These close-packed layers may be stacked one above the other in the usual close-packed positions A, B or C, so that the M atoms have only N atoms as nearest neighbors. The following polytypes have been marked explicitly on the structure map: $L1_2$ (Cu_3Au) cP4 with cubic ABC stacking sequence; $D0_{19}$ (Ni_3Sn) hP8 with hexagonal close-packed AB stacking sequence; $D0_{24}$ (Ni_3Ti) hP16 with double hexagonal close-packed (DHCP) sequence ABAC; and $BaPb_3$ with the hexagonal cell containing nine close-packed layers in the sequence ACACBCBAB. The $CuTi_3$ structure type is a tetragonal distortion of Cu_3Au. Finally, the structure types $D0_{22}$ (Al_3Ti) tI8 and Cu_3Ti are polytypes that are based on the stacking of close-packed MN_3 layers with *rectangular* arrangement of the M atoms (see Figure 7.21 of Pearson, 1972). They are well-separated from each other and from another close-packed superstructure $D0_{23}$ (Al_3Zr) tI16.

Finally, most AB_3 compounds with B from groups IVA, VA or VIA take the A15 (Cr_3Si) cP8 structure type. The A atoms form a b.c.c. lattice through which lines of B atoms run parallel to the edges of the cubic cell. The A15 structure is compact with the A atoms surrounded icosahedrally by 12 B atoms with coordination polyhedron 12″. The B atoms sit at the center of a 14-atom polyhedron 14‴, which is formed from four A and 10 B nearest neighbors. The $D0_3$ (BiF_3) cF16 structure type is an ordered structure based on the b.c.c. lattice with the local coordination polyhedron 14.

The pure elements would lie along the diagonal line $\mathscr{M}_A = \mathscr{M}_B$ in these binary structure maps. It is, therefore, not surprising that the diagonal in Figure 7 for the AB stoichiometry cuts through the CsCl, CuAu, and cubic ZnS domains where the elemental b.c.c., f.c.c., and diamond lattices are stable, whereas in Figure 10 for the AB_3 stoichiometry it passes through the Cu_3Au, Ni_3Sn, and Cr_3Si domains where the elemental f.c.c., h.c.p., and β-W lattices are found. Thus the phenomenological relative ordering number $\mathscr{M}$ should also order the elements according to their structure type. This is broadly the case as can be seen from table 1 of Pettifor (1988a), where the string runs from the close-packed noble-gas and metallic elements through the more open metalloid elements to the halogens and hydrogen, which solidify as dimers held together on the lattice by very weak van der Waals interactions. Running the string from right to left through the lanthanides and actinides preserves the continuity of elemental structure and is in accordance with quantum-mechanical theory, which predicts the structural trend from h.c.p. to d.h.c.p. as the core size and corresponding number of valence d electrons increases through these trivalent systems (Duthie and Pettifor, 1977).

These structure maps for the ground-state structures of the *binary* compounds suggest that it might be possible to move from one structural domain to another by the suitable addition of a third or more alloying element. If it is assumed that the ternary and quaternary additions C and D go preferentially to the A and B sites, then the alloy $(A_xC_{1-x})_m(B_yD_{1-y})_n$ may be regarded as the *pseudobinary* $\bar{A}_m\bar{B}_n$ characterized by the average relative ordering numbers

$$\bar{\mathscr{M}}_A = x\mathscr{M}_A + (1-x)\mathscr{M}_C \tag{3}$$

and

$$\bar{\mathscr{M}}_B = y\mathscr{M}_B + (1-y)\mathscr{M}_D \tag{4}$$

Figures 6 and 7 of Pettifor (1988a) show that this simple scheme orders the 1:1 and 1:3 pseudobinaries in the database of Villars and Calvert (1985) within the same structural domains as for the pure AB and AB_3 binaries in Figures 7 and 10 respectively.

It should be noted, however, that there are important exceptions, which may occur when a particular alloy system with a given structure type straddles a *narrow domain* with a related, but different, structure type (Pettifor, 1988a). For example, the NiAs structure-type ternary alloy system $(Bi_xPb_{1-x})Pt$ straddles a narrow MnP domain in Figure 7, whereas the Cu_3Au structure-type ternary alloy system $(Pb_xTl_{1-x})_3La$ straddles a narrow Ni_3Sn domain in Figure 10. Both these cases involve linking the binary alloys of heavy atoms Hg, Tl, Pb or Bi where relativistic effects lead to the formation of lone-pair s electrons. This dependence of the bonding on the principal quantum number is sufficient to determine the delicate balance between these very similar structure types, NiAs and MnP or Cu_3Au and Ni_3Sn, respectively, as Mooser and Pearson (1959) proposed.

These maps have been used as a guide in the search for new pseudobinaries with a required structure type, in particular *cubic* transition-metal aluminides with good mechanical properties and *tetragonal* rare-earth–iron intermetallics with good permanent magnetic properties. The relative ordering number allows all the known data on the ground-state structures of binary compounds $A_{1-x}B_x$ to be presented within the single

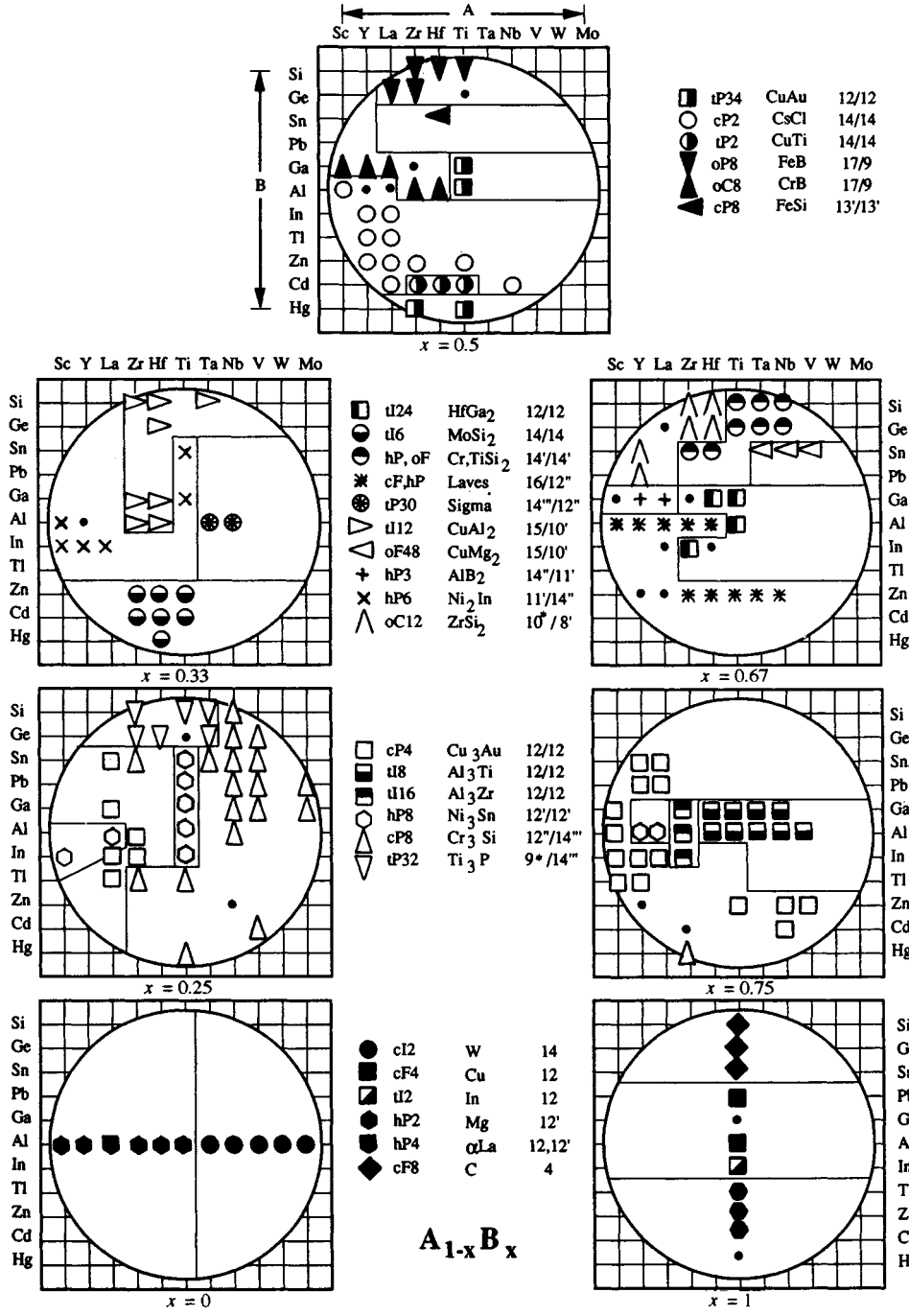

Figure 11. The titanium–aluminum neighborhood maps (from Pettifor, 1992)

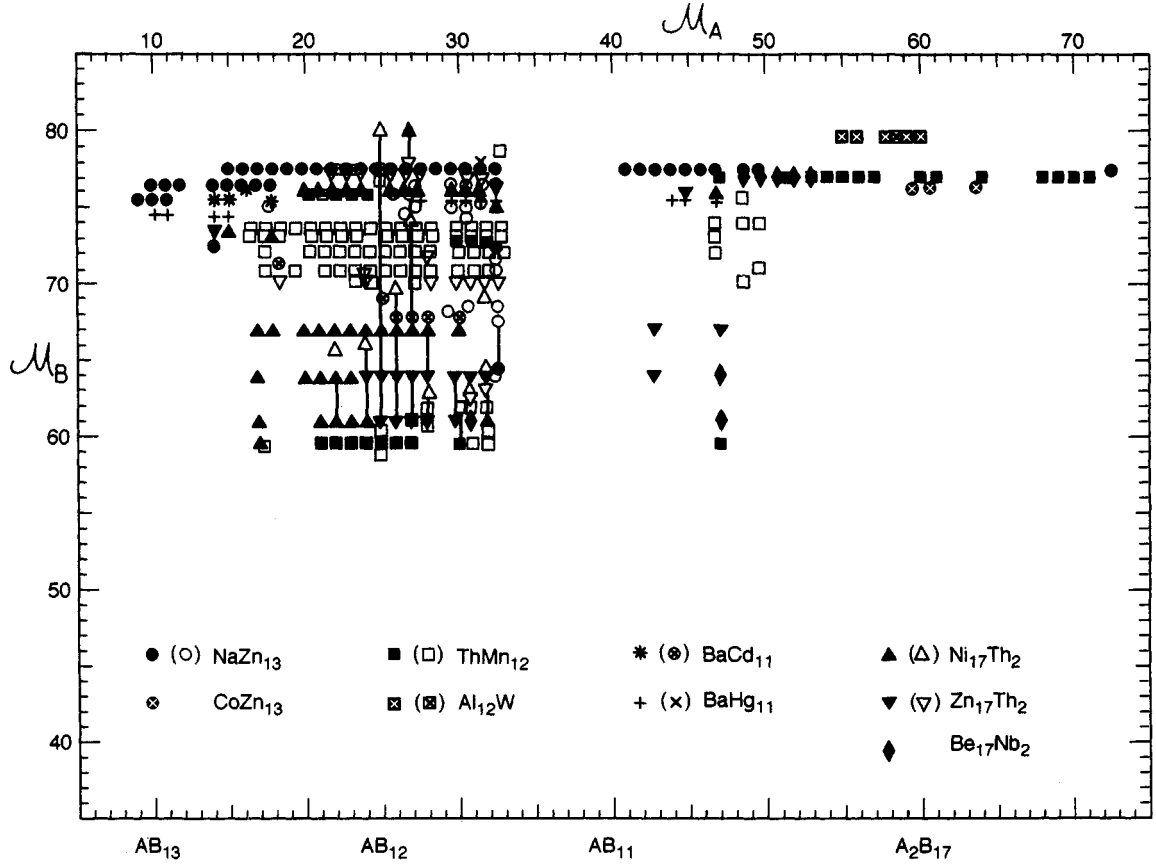

Figure 12. The Pettifor map for AB_{13}, AB_{12}, AB_{11}, and A_2B_{17} stoichiometries. The full and open symbols denote binaries and pseudobinaries respectively (from Pettifor, 1988b)

three-dimensional map ($\mathcal{M}_A$, $\mathcal{M}_B$, x). Figure 11 shows the resultant titanium–aluminum neighborhood maps, which are two-dimensional cross-sections for fixed x through the three-dimensional cylinder whose axis is centered on ($\mathcal{M}_A = 51$, $\mathcal{M}_B = 80$) corresponding to the coordinates of titanium and aluminum (Pettifor, 1992). The sp-bonded elements Be, B, C, N, and O have been excluded from such neighborhood maps because their small size and high electronegativity give them unique properties. The key in Figure 11 gives not only the Pearson symbol but also the recently proposed generalized Jensen notation for the local coordination polyhedra about the A and B sites; see table 5 of Jensen (1989), Figures 3 and 4 of Villars *et al.* (1989), and Figure 8.

We see that the brittle intermetallic Ti_3Al and transition-metal trialuminides $HfAl_3$, $TiAl_3$, $TaAl_3$, $NbAl_3$, and VAl_3 sit in *hexagonal* $D0_{19}$(hP8) and *tetragonal* $D0_{22}$(tI8) domains, respectively. However, the latter domains are adjacent to *cubic* $L1_2$(cP4) domains, which suggested that it might be possible to stabilize the cubic structure (with possibly better mechanical properties) by alloying so that the resultant average coordinates ($\bar{\mathcal{M}}_A$, $\bar{\mathcal{M}}_B$) fall in the cubic domain. This was known to be the case for tetragonal Al_3Ti, which could be transformed into the cubic $L1_2$ phase by replacing some of the aluminum with Cu, Ni or Fe (see, for example, Villars and Calvert, 1985, and Chapters 7 and 8 in Volume 2 by Yamaguchi, Inui and by Das).

This hope of stabilizing cubic phases has only been partially realized, however. Schneibel and Porter (1989) have indeed succeeded in stabilizing cubic $ZrAl_3$ by alloying to take the average relative ordering number $\bar{\mathcal{M}}_B$ down into the cubic domain. But attempts to stabilize cubic Ti_3Al from hexagonal $D0_{19}$ or cubic $NbAl_3$ from tetragonal $D0_{22}$ have failed (Liu *et al.*, 1989; Subramanian *et al.*, 1989). The failure to stabilize cubic Ti_3Al is probably due to the adjacent cubic domain being taken only by 4d and 5d transition elements, not 3d ones. This is another example of the

importance of the Mooser–Pearson (1959) principal-quantum-number factor when dealing with very narrow domains of structural stability. The failure to stabilize cubic $NbAl_3$ is due to the rapid oscillatory behavior of cubic versus tetragonal stability in going from group IV to group V, which is wave-mechanical in origin (Pettifor and Aoki, 1991). Although $TiAl_3$ and $NbAl_3$ both lie in the same $D0_{22}$ domain adjacent to a cubic $L1_2$ domain in Figure 11, the energy required to transform $NbAl_3$ to the cubic phase is predicted to be nearly an order of magnitude greater than that for $TiAl_3$, as discussed in Chapter 3 by Carlsson and Meschter in this volume. It is, therefore, extremely unlikely that cubic $NbAl_3$ will ever be stabilized by alloying additions, supporting recent experimental evidence that a 1964 report of the $L1_2$ phase $Nb_2(Al_5Ni)$ is incorrect (Subramanian *et al.*, 1989).

Another example of the application of structure maps is provided by the search for new rare-earth–iron-based pseudobinaries with the *tetragonal* structure types $BaCd_{11}$, $ThMn_{12}$, and $NaZn_{13}$ for use as permanent magnets (Mitchell *et al.*, 1989). Figure 12 shows the structure map for binary and pseudobinary phases with the A_2B_{17}, AB_{11}, AB_{12}, and AB_{13} stoichiometries using Villars and Calvert's (1985) database (Pettifor, 1988b). These four stoichiometries correspond to alloys A_xB_{1-x} with $x=0.105$, 0.083, 0.077, and 0.071, respectively. Figure 12 is, therefore, a projection on the two-dimensional ($\mathcal{M}_A$, $\mathcal{M}_B$) plane of the data points lying in the three-dimensional space ($\mathcal{M}_A$, $\mathcal{M}_B$, x) with $0.071 \leqslant x \leqslant 0.105$. We see that the different structure types are located in well-defined domains, although there is some overlap between them. *Binary* rare-earth–iron phases take the 2:17 stoichiometry, as can be seen in Figure 12, where $\mathcal{M}_B = 61$ for iron. Unfortunately, they have too low a Curie temperature for use as permanent magnets.

Figure 12 suggests that, if we are looking for cheap iron-based *pseudobinaries* in which the majority of the atoms are iron, then it would be best to search in the lower $ThMn_{12}$ domain by replacing iron by transition elements to its left in the periodic table (Pettifor, 1988b). Independently, de Mooij and Buschow (1987) have done extensive experimental work in just this area. They have stabilized $R(Fe,X)_{12}$ pseudobinaries with the tetragonal $ThMn_{12}$ structure for the cases where X = Ti, V, Cr, Mo or W, which would all fall within the lower $ThMn_{12}$ domain in Figure 12. (They also stabilized the $ThMn_{12}$ structure with X = Si, which would fall in the 2:17 domain of Figure 12. Nevertheless, silicon appears to be exceptional since the $ThMn_{12}$ structure was not found for the other sp-valent elements Al, Ga, Ge or Sn.) De Mooij and Buschow (1987) have found these tetragonal pseudobinaries to be good permanent magnets. In particular, $Sm(Fe_{11}Ti)$ has a Curie temperature and magnetic anisotropy that are very similar to the market leader, the novel ternary compound $Nd_2Fe_{14}B$. However, at room temperature it has an average iron moment of only $1.6\,\mu_B$ compared to the $2.0\,\mu_B$ for $Nd_2Fe_{14}B$, so that a pseudobinary has not yet displaced the ternary boride from its perch as the most powerful known permanent magnet.

3. Ternary Structure Maps

3.1 *Villars Maps*

The three-dimensional Villars maps have been generalized to ternary systems by defining the coordinates

$$\Delta X = 2x(X_A - X_B) + 2x(X_A - X_C) + 2y(X_B - X_C) \quad (5)$$

$$\Delta R = 2x(R_A - R_B) + 2x(R_A - R_C) + 2y(R_B - R_C) \quad (6)$$

$$\bar{N} = xN_A + yN_B + zN_C \quad (7)$$

for $A_xB_yC_z$ with $x \leqslant y \leqslant z$ and $x + y + z = 1$ (Villars and Hulliger, 1987). Quaternaries can be included by averaging the atomic coordinates of the two most electronically similar elements and using the above coordinate definitions for the ternaries.

Since, to date, there are more than two *thousand* different intermetallic ternary structure types compared to the several *hundred* binary structure types, Villars and Hulliger (1987) and Villars *et al.* (1989) ordered the structural database with respect to the local coordination polyhedra or atomic environment types taken by the lattice (see, for example, Figure 8). They found, for example, that of the 147 binary structure types with more than five representative compounds each, 25 structure types with 1347 representatives displayed only a *single* atomic environment, whereas 51 structure types with 1952 representatives displayed *two* different atomic environments, 34 structure types with 879 representatives displayed *three* different atomic environments, and 28 structure types with 543 representatives displayed *four* different atomic environments. Only nine structure types with 114 representatives required more than four different atomic environment types for a complete description of the local coordination.

Villars and Hulliger (1987) have found that 98% of the 2532 binary, ternary, and quaternary compounds

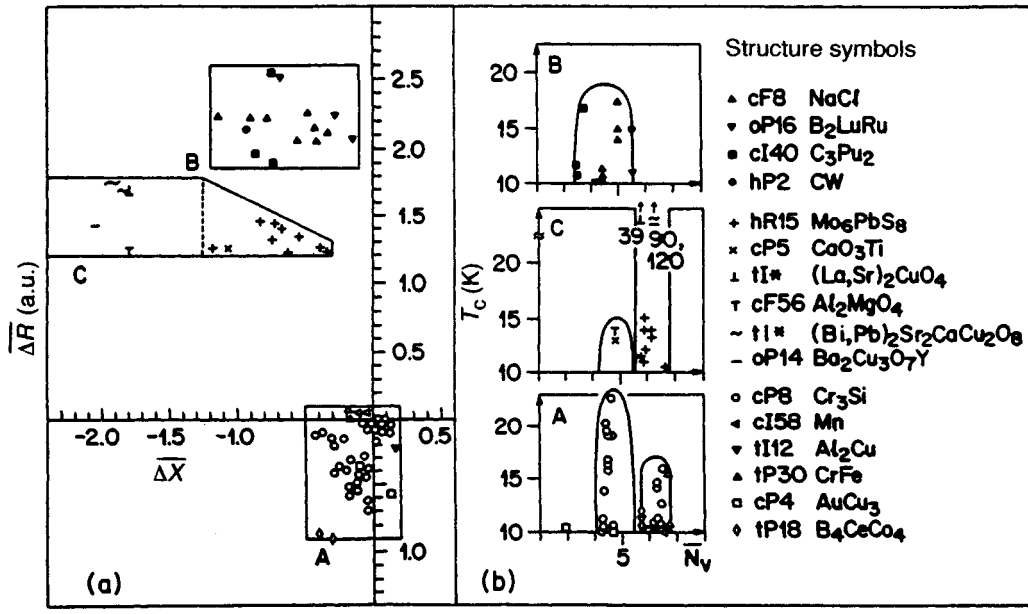

Figure 13. The Villars map for high-T_c superconductors. The left-hand panel (a) shows the compounds projected on the ($\Delta\overline{X}$, $\Delta\overline{R}$) plane, whereas the right-hand panel (b) plots their transition temperatures as a function of $\overline{N}$ for the three domains A, B, and C (from Rabe *et al.*, 1992. Reproduced with permission)

with *single-environment* structure types are characterized by one of the following five local coordination polyhedra: the tetrahedron, the octahedron, the cubooctahedron, the truncated hexagonal eclipsed bipyramid, and the rhombic dodecahedron, respectively. They are labeled by 4, 6, 12, 12′, and 14 respectively in Figure 8. Within the three-dimensional map ($\Delta\overline{X}$, $\Delta\overline{R}$, $\overline{N}$) these single-environment compounds tended to separate into many different domains dominated by one or other of the five local coordination polyhedra.

These generalized Villars maps are being used in the search for new stable quasicrystals and high-temperature ferroelectrics and superconductors (see Rabe *et al.*, 1992, and references therein). To date, there are nine known *stable* quasicrystals: $CuLi_3Al_6$, $Ca_{20}Mg_7Zn_{43}$, $A_{15}Cu_{20}Al_{65}$ (A = Fe, Ru, Os), $Cu_{15}Co_{20}Al_{65}$, $Co_{15}Ni_{15}Al_{70}$, and (Mn,Re)Pd_2Al_7. These all fall on the Villars map within the restricted range $-0.6 \leqslant \Delta\overline{X} \leqslant 0.3$ and $-0.2 \leqslant \Delta\overline{R} \leqslant 0.7$. Unfortunately, many thousands of potential ternaries also fall within this domain, so that a sensible screening procedure needs to be adopted; several such strategies are considered by Rabe *et al.* (1992). For high-temperature superconductors with $T_c > 10$ K, the Villars map separates the database into three domains A, B, and C as shown in Figure 13 from Rabe *et al.* (1992). (Note that copper and zinc are assumed to have one and two valence electrons respectively in insulating compounds.) Domains A and B are dominated by the A15 (Cr_3Si) cP8 and B1 (NaCl) cF8 *binary* structure-type superconductors respectively. Domain C contains the Chevrel (hR15) and perovskite (cP5) *ternary* structure-type superconductors. Interestingly, high-temperature ferroelectrics occupy the space in domain C between the Chevrel phases and the cuprate superconductors, indicating the close connection between ferroelectricity and superconductivity stressed much earlier by Matthias (1970). Rabe *et al.* (1992) have discussed various screening strategies for sorting between the thousands of potential ternary compounds that fall within these regions of high-temperature superconductivity.

3.2 Pettifor Maps

Most of the non-hydrogen-, -carbon-, -nitrogen- or -oxygen-containing phases of ternary structure type can be separated and displayed within only seven two-dimensional structure maps (Pettifor, 1988a). This is because the structural information for many *different* ternary stoichiometries $A_lB_mC_n$ can be presented on the *same* figure. This is illustrated by the two structure maps for the ternary chalcogenides, namely $AB(S,Se,Te)_n$ and $A_lB_{m>l}(S,Se,Te)_n$, which include

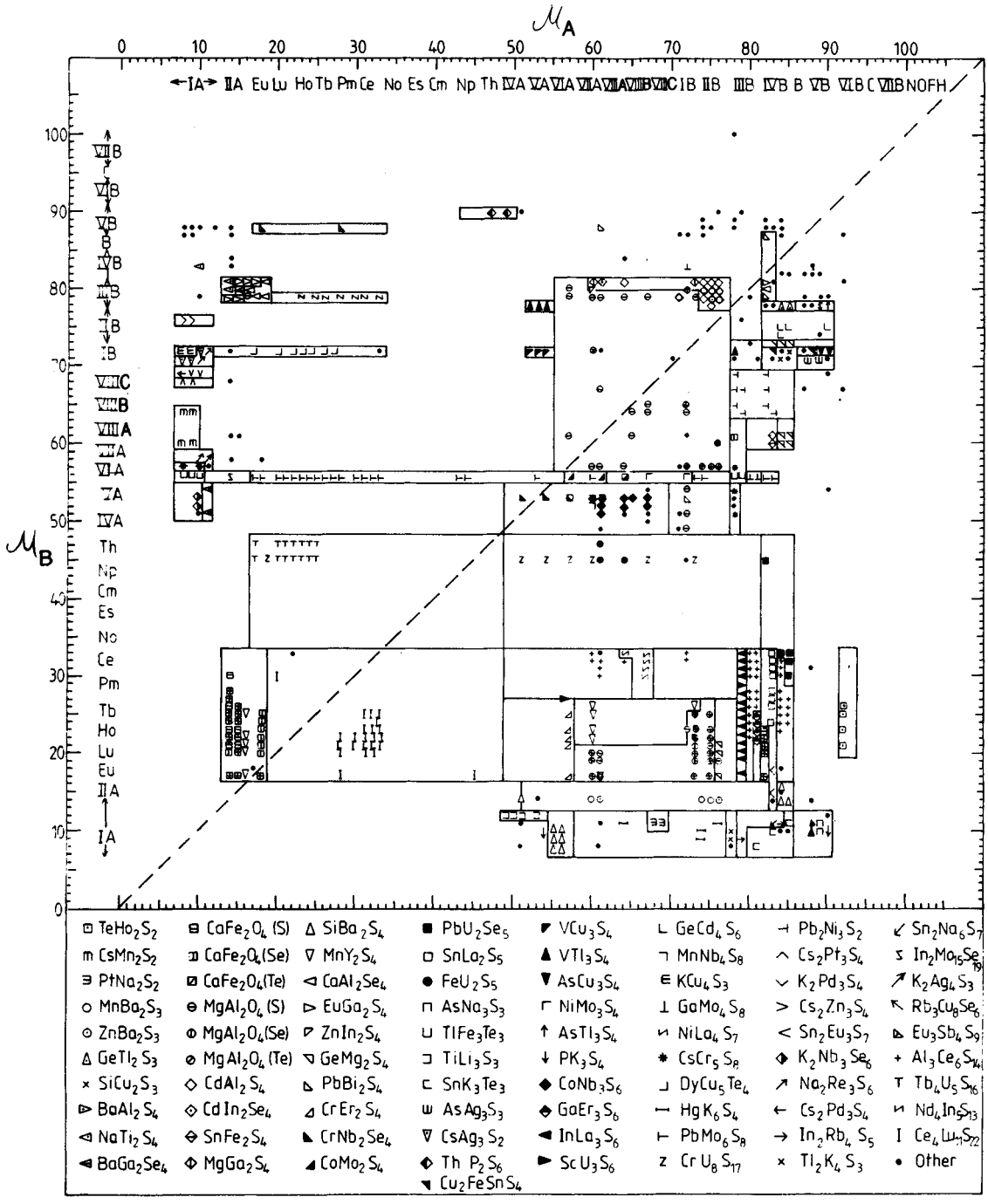

Figure 14. The Pettifor map for the ternary chalcogenides with $A_lB_{m>l}$ (S, Se, Te)$_n$ stoichiometry. The chalcogen in brackets after a given structure type indicates that only it is present in the ternary compound represented by the particular symbol. More than one symbol may be superimposed at a given point on the map (From Pettifor, 1988a)

more than one-third of all the different ternary structure types listed by Villars and Calvert (1985) with more than one representative compound each. The latter map $A_lB_{m>l}(S,Se,Te)_n$ is shown in Figure 14. We see, for example, that the Chevrel phases $PbMo_6S_8$ occupy the very narrow domain corresponding to $\mathscr{M}_B = 56$ for molybdenum. The relationship between neighboring structural domains within the ternary intermetallic structure maps has not yet been explored in detail. The ongoing work of Daams, Villars, and colleagues (Daams *et al.*, 1992; Daams and Villars, 1993) in finding the local coordination polyhedra or atomic environment types of *all* binary, ternary, and quaternary structure types will be crucial in revealing the underlying structural patterns beneath the surface of ternary structure maps such as Figure 14.

4. Conclusion

Structure maps, by ordering the very large database into domains of different structure type, have proven important both as a pedagogical aid in structural chemistry and as an initial guide in the search for new intermetallics with a required structure type. However, we have seen that they must be used with caution in their predictive mode. The difference in energy between competing structure types such as cubic and hexagonal close-packed phases will be of the order of one-thousandth of the cohesive energy. The maps can suggest which alloys *might* take a given structure type, but they cannot, of course, provide any firm guarantee owing to the subtle competition between many different phases and stoichiometries. Electron theory provides an essential complementary input through its new-found ability to predict the relative energies of different (simple) competing phases. This is discussed in Pettifor and Cottrell (1992) and in Chapter 2 by Turchi and Chapter 3 by Carlsson and Meschter in this volume.

5. References

Burdett, J. K. (1982). *J. Solid State Chem.*, **45**, 399.

Cressoni, J. C., and Pettifor, D. G. (1991). *J. Phys.: Condens. Matter*, **3**, 495.

Daams, J. L. C., and Villars, P. (1993). *J. Alloys Compounds*, **197**, 243.

Daams, J. L. C., Van Vucht, J. H. N., and Villars, P. (1992). *J. Alloys Compounds*, **182**, 1.

de Mooij, B., and Buschow, K. H. J. (1987). *Philips J. Res.*, **42**, 246.

Dimiduk, D. M., and Miracle, D. B. (1989). *Mater. Res. Soc. Symp. Proc.*, **133**, 349.

Duthie, J. C., and Pettifor, D. G. (1977). *Phys. Rev. Lett.*, **38**, 564.

Girifalco, L. A. (1976). *Acta Metall.*, **24**, 759.

Jensen, W. B. (1989). In *The Structures of Binary Compounds* (eds F. R. de Boer and D. G. Pettifor). North-Holland, Amsterdam, p. 105.

Liu, C. T., Horton, J. A., and Pettifor, D. G. (1989). *Mater. Res. Soc. Symp. Proc.*, **133**, 37.

Martynov, A. J., and Batsanov, J. S. (1980). *Russ. J. Inorg. Chem.*, **25**, 1737.

Matthias, B. T. (1970). *Mater. Res. Bull.*, **5**, 665.

Mitchell, I. V., Coey, J. M. D., Givord, D., Harris, I. R., and Hanitsch, R. (eds) (1989). *Concerted European Action on Magnets*. Elsevier Applied Science, London.

Mooser, E., and Pearson, W. B. (1959). *Acta Crystallogr.*, **12**, 1015.

Pauling, L. (1960). *The Nature of the Chemical Bond*, 3rd Edn. Cornell University Press, Ithaca, NY.

Pearson, W. B. (1972). *The Crystal Chemistry and Physics of Metals and Alloys*. Wiley-Interscience, New York.

Pettifor, D. G. (1983). In *Physical Metallurgy* (eds R. W. Cahn and P. Haasen). North-Holland, Amsterdam, p. 73.

Pettifor, D. G. (1984). *Solid State Commun.*, **51**, 31.

Pettifor, D. G. (1986). *J. Phys.*, **19**, 285.

Pettifor, D. G. (1988a). *Mater. Sci. Technol.*, **4**, 2480.

Pettifor, D. G. (1988b). *Physica*, **B149**, 3.

Pettifor, D. G. (1992). *Mater. Sci. Technol.*, **8**, 345.

Pettifor, D. G., and Aoki, M. (1991). *Phil. Trans. R. Soc.*, **A334**, 439.

Pettifor, D. G., and Cottrell, A. H. (eds) (1992). *Electron Theory in Alloy Design*. Institute of Materials, London.

Pettifor, D. G., and Podloucky, R. (1986). *J. Phys.*, **C19**, 315.

Phillips, J. C., and Van Vechten, J. A. (1969). *Phys. Rev. Lett.*, **22**, 705.

Rabe, K. M., Kortan, A. R., Phillips, J. C., and Villars, P. (1991). *Phys. Rev.*, **B43**, 6279.

Rabe, K. M., Phillips, J. C., Villars, P., and Brown, I. D. (1992). *Phys. Rev.*, **B45**, 7650.

Schneibel, J. H., and Porter, W. D. (1989). *Mater. Res. Soc. Symp. Proc.*, **133**, 335.

St John, J., and Bloch, A. N. (1974). *Phys. Rev. Lett.*, **33**, 1095.

Subramanian, P. R., Simmons, J. P., Mendiratta, M. G., and Dimiduk, D. M. (1989). *Mater. Res. Soc. Symp. Proc.*, **133**, 51.

Villars, P. (1983). *J. Less-Common Met.*, **92**, 215.

Villars, P. (1984a). *J. Less-Common Met.*, **99**, 33.

Villars, P. (1984b). *J. Less-Common Met.*, **102**, 199.

Villars, P., and Calvert, L. D. (1985). *Pearson's Handbook of Crystallographic Data for Intermetallic Phases*, Vols 1, 2, 3. American Society for Metals, Metals Park, OH.

Villars, P., and Hulliger, F. (1987). *J. Less-Common Met.*, **132**, 289.

Villars, P., Mathis, K., and Hulliger, F. (1989). In *The Structures of Binary Compounds* (eds F. R. de Boer and D. G. Pettifor). North-Holland, Amsterdam, p. 1.

Watson, R. E., and Bennett, L. H. (1978a). *J. Phys. Chem. Solids*, **39**, 1235.

Watson, R. E., and Bennett, L. H. (1978b). *Phys. Rev.*, **B18**, 6439.

Wells, A. F. (1975). *Structural Inorganic Chemistry*. Clarendon, Oxford.

Yeh, C.-Y., Lu, Z. W., Froyen, S., and Zunger, A. (1992). *Phys. Rev.*, **B15**, **46**, 10 086.

Zunger, A. (1980). *Phys. Rev.*, **B22**, 5839.

Zunger, A., and Cohen, M. L. (1978). *Phys. Rev. Lett.*, **41**, 53.

This chapter was originally published in 1995 as Chapter 18 in *Intermetallic Compounds*, Vol. 1: *Principles*, edited by J. H. Westbrook and R. L. Fleischer.

Chapter 9

Magnetic Structures

Walter L. Roth

Department of Physics, State University of New York at Albany, Albany, New York 12222, USA

1. Introduction

To understand the magnetic properties of a material, it is necessary to consider its magnetic structure. This chapter gives an overview of the magnetic structures in transition metals, rare-earth metals, alloys, and intermetallic compounds, with emphasis on the latter. The intention is not to give a comprehensive review of magnetic structures in intermetallic compounds, but rather to discuss examples that illustrate why the atomic moments on a particular group of atoms are arranged in one way rather than another. The interrelation of magnetic properties and magnetic structure are treated in Chapter 40 by Kouvel in this volume. Technological applications (see Chapter 14 by Stadelmaier and Reinsch and Chapter 19 by McGahan in Volume 2) and the extrinsic structural parameters that affect the design of practical materials—shape and size of the specimen, particle size, impurities—are not considered here. Following a brief description of types of magnetic order, models of magnetic exchange interactions, and methods of determining magnetic structure, examples of magnetic structures are considered in five groups of materials: (1) transition metals, (2) transition-metal intermetallic compounds, (3) rare-earth metals, (4) rare-earth intermetallic compounds, and (5) metallic systems with small-scale order.

2. Exchange Interactions and Magnetic Structure

The concept of a magnetic structure as a spatially ordered arrangement of atomic moments on a lattice preceded its experimental validation by neutron diffraction. Weiss (1907) and Néel (1948) explained measurements of magnetization and magnetic susceptibility by a 'molecular field' that aligned the moments of a paramagnetic substance. Magnetic exchange interactions were supposed to result in three types of collinear arrangement of the atomic moments: (1) antiferromagnetic, an antiparallel alignment of equal moments; (2) ferrimagnetic, an antiparallel alignment of moments unequal in magnitude or number; and (3) ferromagnetic, a parallel alignment of the moments.

Ferromagnetism and ferrimagnetism are characterized by a spontaneous magnetic moment below the Curie temperature, T_C. The transition from paramagnetism to antiferromagnetism is recognized by a well-defined kink in the susceptibility vs. temperature curve at the Néel temperature, T_N. It is now known from neutron diffraction that magnetic structures are more complex than originally envisioned; the atomic spins are usually non-collinear, and they may be organized in spiral, helical, and cone-like arrays that are incommensurate with the crystal lattice. The terms 'ferromagnetic' and 'antiferromagnetic' are now taken to refer to interactions that orient the moments on two atoms in a direction that has either the same or the opposite sense.

When some materials are cooled from the paramagnetic state, the spin directions become fixed or 'frozen in' without long-range order. The names used in the literature for such solids include amorphous ferromagnets, spin glasses, cluster glasses, and mictomagnets. Amorphous ferromagnet (Luborsky, 1980) usually implies a magnetically concentrated substance with a non-crystalline or amorphous atomic arrangement. There is less general agreement about spin

Crystal Structures of Intermetallic Compounds. Edited by J. H. Westbrook and R. L. Fleischer

glass, a term that was originally applied to dilute crystalline alloys containing about 1% of magnetic impurities. A proposed definition (Mydosh and Nieuwenhuys, 1980) is a random, metallic, magnetic system characterized by a random freezing of the moments without long-range order at a rather well-defined freezing temperature, T_f. The spin configuration in a spin glass is random but static below T_f, and the macroscopic moment in zero external field is zero. As the concentration of magnetic impurity in a spin glass is increased, concentration fluctuations and chemical attractive forces result in the formation of magnetic clusters with very large effective moments, ~ 20 to $20\,000\,\mu_B$. Materials in which the magnetic behavior is dominated by the presence of large magnetic clusters have been called mictomagnets (Tustison and Beck, 1977) and cluster glasses (Murani *et al.*, 1976).

Ferromagnetic interactions are essentially unaltered by the absence of a periodic lattice. The intrinsic magnetic properties of amorphous ferromagnets are qualitatively the same as for crystalline alloys with appropriate modification to take into account that the local environment around each atom differs from site to site. In contrast to ferromagnetic interactions, antiferromagnetic interactions can be 'frustrated' by disorder. This is a situation in which it is impossible to satisfy simultaneously the interactions between atoms on different sites, resulting in a random, non-collinear configuration of the atomic moments.

The main experimental technique for determining magnetic structure is neutron diffraction (James, 1989). By coupling high-resolution instrumentation with the Rietfeld method of analysis, structural detail rivaling that previously obtained only on single crystals can now be obtained from powders (Rietfeld, 1969). The magnetic structure of an ordered magnetic material is specified by the position, magnitude, and orientation of the atomic moments in a magnetic unit cell. The interpretation of magnetic Bragg scattering gives two kinds of information about the magnetic moments in solids: (1) the magnetic structure, and (2) the spatial extension of the magnetic electrons. In an ordered alloy, specific kinds of atoms occupy crystallographically distinguishable lattice sites, and individual magnetic moments are obtained from the magnetic Bragg scattering. In a disordered alloy, different kinds of atoms are distributed randomly on a lattice, and the individual moments are obtained from measurements of neutron diffuse scattering.

The procedure for determining the arrangement of moments in magnetic materials in similar to crystal-structure analysis, differing mainly in the need to determine the orientation of the atomic spins. The magnetic structure factor, F_{hkl}, for a reflection with Miller indices hkl is given by

$$F_{hkl}(\text{magnetic}) = \sum(\boldsymbol{\lambda}\cdot\mathbf{q}_i)p_i \exp\left[2\pi_i(hx_i + ky_i + lz_i)\right]$$

The summation is over i atoms in the magnetic unit cell; $\boldsymbol{\lambda}$ is a unit vector in the direction of polarization of the neutrons; $\mathbf{q}_i$ is the magnetic interaction vector; and p_i is the magnetic scattering amplitude of the atom. The magnetic scattering amplitude of the atom depends on the spin quantum number S and the quantum number L if there is an orbital contribution to the magnetic moment. The values of x_i, y_i, z_i, $\mathbf{q}_i$ and p_i are obtained from the diffraction intensity data by least-squares and Fourier techniques.

Other methods that are available for investigating magnetic structure are nuclear magnetic resonance and Mössbauer spectroscopy (Chien, 1981). These techniques measure the effective magnetic field at the nucleus; they are particularly useful as local probes for investigating variations in the local environment about nuclei in amorphous and chemically disordered solids.

The magnetic structure of a substance is the result of exchange interactions. It is not possible to obtain exact solutions for exchange interactions in three-dimensional crystals, and approximate models—direct exchange, spin-density waves, the Ruderman–Kittel–Kasuya–Yoshida interaction, superexchange, double exchange—are used to explain the magnetic arrangements found by neutron diffraction.

Direct exchange is due to overlap of the wavefunctions of nearest neighbor atoms; it is the main interaction that orders the moments in 3d transition metals. Direct exchange is short-range, and its dependence on interatomic distance often is represented by a Slater–Néel-type diagram, which predicts a negative exchange integral (antiferromagnetic interaction) at short interatomic distance and a positive exchange integral (ferromagnetic interaction) at large interatomic distance (Somerfeld and Bethe, 1933). The treatment of exchange interactions between 3d transition elements is complicated by uncertainty about whether the magnetic electrons are localized or itinerant. A mechanism proposed for propagating magnetic interactions over long distances by itinerant electrons is spin-density waves (SDW) (Overhauser and Arrott, 1960). In the rare earths and dilute alloys of the transition elements, the primary exchange mechanism is the Ruderman–Kittel–Kasuya–Yoshida (RKKY) interaction (Ruderman and Kittel, 1954). The RKKY mechanism depends on conduction electrons that carry

information on the orientation of the localized spin from one atom to another; it is long-range and gives rise to an oscillatory spatial polarization as a function of interatomic distance. The main interaction mechanisms in ionic compounds are superexchange and double exchange. Both depend on overlap of the d orbitals of the magnetic atoms with the p orbitals of an intermediate anion. Superexchange usually is antiferromagnetic and a maximum when the cation–anion–cation angle is 180°; double exchange is ferromagnetic and arises from charge transfer between multivalent ions in solid solution. Superexchange and double exchange are not important exchange mechanisms in metallic systems but may have a role in composite materials.

3. Magnetic Structures

The magnetic structures of most intermetallic compounds are non-collinear arrangements of unequal moments on two or more chemically different atoms. They are difficult to display in two-dimensional drawings and usually are presented in the form of tables of parameters of the position, magnitude, and orientation of the magnetic moments in the unit cell (see Cox, 1973). Magnetic structures of current interest are difficult to describe in words for, as Eddington (1948) remarked when discussing an elementary particle, words are a kind of Jabberwocky applied to 'something unknown' that is 'doing we don't know what.' Heeding Alice's query in Wonderland when she asked 'what is the use of a book without pictures or conversation,' schematic, simplified drawings are given of several unusual types of magnetic structure that are important issues of current research. Readers are referred to reviews by Bacon (1962a), Willis (1970), Nathans and Pickart (1963), Goodenough (1963), and Kouvel (1967) for descriptions of magnetic structures of intermetallic compounds that were solved in the initial period following the discovery that neutron diffraction could be used to investigate magnetism in solids. Examples of more recent reviews are: Nakamura and Franse (1987), Moon and Nicklow (1991), Gignoux and Schmitt (1991), and Jensen and Mackintosh (1991).

3.1 Transition Metals

Many of the principles that determine the magnetic arrangements of intermetallic compounds and alloys have been obtained from studies of the magnetic structures in the transition-element metals. The magnetism of the transition elements is a central issue in the theory of magnetism. Iron, cobalt, and nickel are ferromagnets with collinear spin arrangements; manganese and chromium are antiferromagnets with complicated spin arrangements; vanadium, niobium, molybdenum, and tungsten do not order at all, at least at temperatures as low as 4 K. The different magnetic behavior has its origin in the electronic structure of the 3d transition metals, which is intermediate between the cases where the electrons can be regarded as localized or itinerant.

Iron (body-centered cubic, structure type A2 (cI2)), cobalt (both hexagonal, structure type A3 (hP2), and face-centered cubic, structure type A1 (cF4)), and nickel (face-centered cubic, structure type A1 (cF4)) are ferromagnets with collinear arrangements of the atomic moments. The magnetic moment of iron is less than the free-ion value, and an objective of early neutron diffraction studies was to determine if iron was a ferrimagnet, i.e. that the reduced moment resulted from antiferromagnetic coupling between iron atoms with different moments. The ferrimagnet hypothesis was rejected after it was established that the moment measured by neutron diffraction was the same as determined by magnetic measurements, and that there was no evidence for either an ordered or a disordered arrangement of atoms with different magnetic moments.

Subsequent studies to understand the reduced magnetic moment of iron focused on the distribution and symmetry of the magnetic electrons (Shull and Yamada, 1962). Measurements of the magnetic form factor show that the total magnetic moment of iron, $2.177\,\mu_B$, is the result of a positive contribution of $2.39\,\mu_B$ from the 3d electrons and a negative contribution of $0.21\,\mu_B$ from the 4s electrons. Figure 1 displays a portion of the (1 1 0) plane intersecting the two iron atoms in the unit cell. The magnetic electron density is not spherically symmetric around the nucleus. The electron density contours are not circular, as they should be for a spherical atom, but compressed in the [1 1 1] space diagonal, or nearest-neighbor, direction, with very small density between nearest-neighbor iron atoms. The asymmetry of the magnetic spin density is explained by attributing 53% of the 3d quenched electron magnetization to electrons with E_g symmetry (the concentration along the [1 0 0] cube edges) and 47% to electrons with T_{2g} symmetry (the concentration along the [1 1 1] cube diagonals).

Magnetic form-factor studies on nickel give for the individual contributions to the magnetization: 3d spin, $+0.656\,\mu_B$; 3d orbit, $+0.005\,\mu_B$; conduction electrons, $-0.105\,\mu_B$.

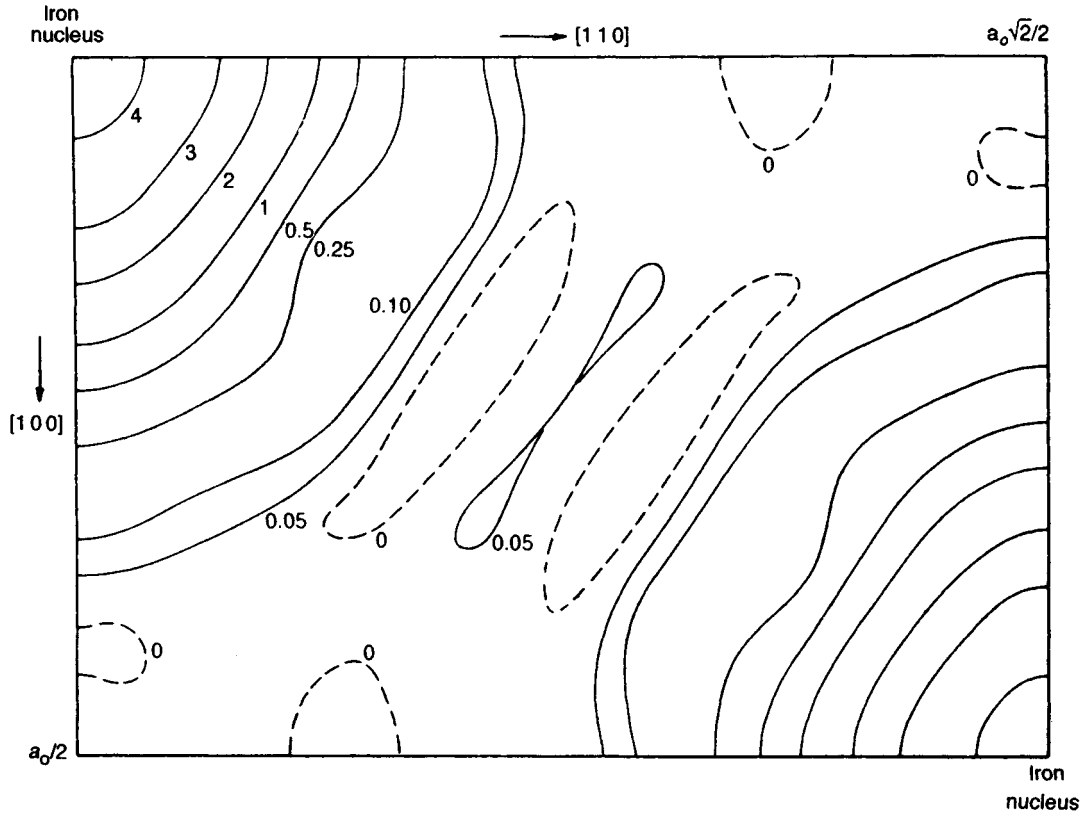

Figure 1. Magnetic spin-density distribution in the (1 1 0) diagonal plane of the iron unit cell. Contours are shown in units of μ_B Å^{-3}. Two nearest-neighbor iron atoms are shown in this section. Very small density is to be noted in the mid-region between these atoms (After Shull and Yamada, 1962)

In contrast to α-iron, which has the same body-centered crystal structure (structure type A2 (cI2)) and is ferromagnetic, chromium is antiferromagnetic. The magnetic structure of chromium has been the subject of many investigations, originally to understand why it shows no macroscopic magnetic properties even though it possesses strong atomic moments. The problem was resolved when it was shown by neutron diffraction that chromium is an antiferromagnet. Subsequent studies have been concerned with the resolution of its complex spin arrangement. In addition to the fundamental Bragg scattering peaks that are expected for antiferromagnetic coupling of two magnetic atoms in the cubic unit cell, the neutron diffraction pattern displays peaks of a magnetic superlattice and a magnetic structure change at 121 K. The model that was originally advanced to explain the magnetic superstructure was antiphase domains in which there is a 180° spin reversal every 14 unit cells. Alternatives to the antiphase domain model that have been proposed are a spiral arrangement of the spins with the same periodicity, a sinusoidal modulation of the magnetic scattering amplitude, and spin-density waves. An investigation (Shirane and Takei, 1962) of the structure on single crystals concluded that the sinusoidal model was preferred and obtained for the atomic moment $\mu_{Cr} = 0.59\,\mu_B$ at 78 K and $\mu_{Cr} 0.41\,\mu_B$ at 125 K (Figure 2). The chromium moments are parallel to the propagation vector below the 121 K transition and perpendicular to the propagation vector above the transition. The temperature dependence of the intensities of the satellites is consistent with spin-density waves; however, the field-cooling effect predicted by the spin-density-wave model did not give conclusive results.

Manganese is also antiferromagnetic, but in contrast to chromium the magnetic electrons appear to be localized. The crystal structure of α-Mn (body-centered cubic, structure type A12 (cI58) is a powerful tool for

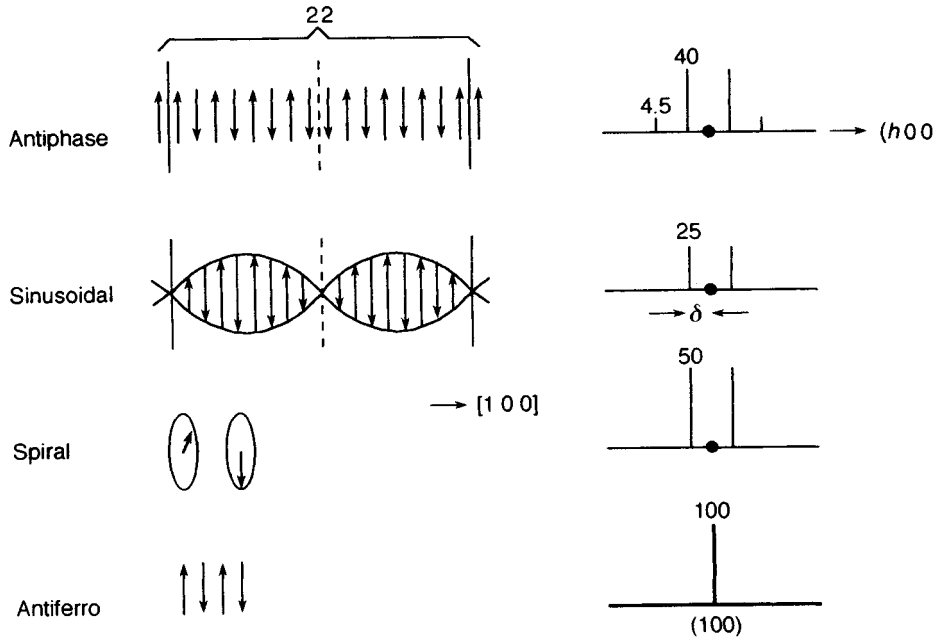

Figure 2. Models for Cr spin arrangement with their magnetic intensities, calculated with a periodicity of 22 unit cells. This spin direction corresponds to the high-temperature phase (After Shirane and Takei, 1962)

investigating the effect of the chemical environment on the atomic moment of manganese. The unit cell contains 58 Mn atoms in four non-equivalent sites, and the four crystallographically independent manganese atoms have different numbers of neighbors at different distances. The atomic spins are arranged in a single non-collinear configuration through the temperature range below the Néel temperature (Yamada *et al.*, 1970) (Figure 3). Single-crystal structure refinements indicate that a localized-moment model is preferable to a spin-density-

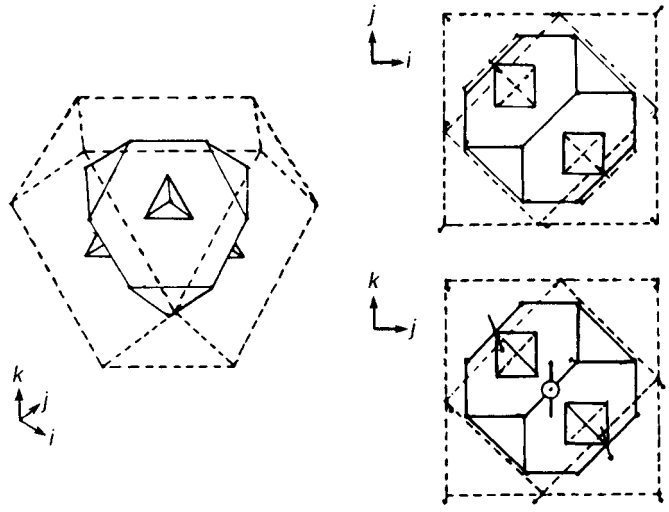

Figure 3. Magnetic structure of α-Mn. A view of the atomic configuration in a cell (left) and projections of the magnetic configuration onto the *i*–*j* and *j*–*k* planes (After Yamada *et al.*, 1970)

wave model, and that the moments of manganese at 4.4 K in the four different sites are $\mu_{Mn_I} = 1.9\,\mu_B$, $\mu_{Mn_{II}} = 1.7\,\mu_B$, $\mu_{Mn_{III}} = 0.6\,\mu_B$, $\mu_{Mn_{IV}} = 0.2\,\mu_B$.

3.2 Transition-Metal Intermetallic Compounds

The magnetic structures in transition-metal alloys in general are similar to metals after taking into account that the magnetic moments and exchange interactions depend on the chemical environment of the constituents. In only a few instances, such as Fe_3Al, have the structures of alloys been analyzed in sufficient detail to determine the effect of alloying on the atomic moment and the electronic configuration of the constituent atoms.

Fe_3Al (cubic, $BiF_3(D0_3)$ structure type (cF16)) is a ferromagnet with $T_C \sim 750$ K. There are two chemically different Fe atoms in the unit cell: Fe_I with eight Fe nearest neighbors and six Al next-nearest neighbors; and Fe_{II} with four Al and four Fe nearest neighbors. The magnetic moment and the electronic structure of the iron atoms have been investigated by neutron diffraction with the polarized beam technique by Pickart and Nathans (1961). Their results in Figure 4 show that the local chemical environment has a large influence on both the moment and the electronic configuration of iron. The iron moment in the two sites is $\mu_{Fe_I} = 2.18\,\mu_B$ (the same as in pure iron) and $\mu_{Fe_{II}} = 1.50\,\mu_B$. The magnetic symmetry of the two iron atoms is: Fe_I, 60% E_g, 40% T_{2g}; and Fe_{II}, 48% E_g, 52% T_{2g}.

FeRh is an example of an alloy in which a change in electronic structure with temperature changes its magnetic properties. At about 350 K, FeRh (cubic, CsCl (B2) structure type (cP2)) undergoes a first-order transformation from antiferromagnetism to ferromagnetism. There is an isotropic change in volume at the transition, and no change is observed in crystal structure or symmetry. In the antiferromagnetic state, the atomic spins on nearest-neighbor atoms are collinear and antiparallel: $\mu_{Fe} = 3.17\,\mu_B$, $\mu_{Rh} = 0.9\,\mu_B$. Approximately the same moments were found by Bertaut *et al.* (1962) in the ferromagnetic state: $\mu_{Fe} = 3.2\,\mu_B$ and $\mu_{Rh} = 0.9\,\mu_B$. The implication of subsequent neutron diffraction and Mössbauer experiments by Shirane *et al.* (1963) is that the magnetic polarization of the conduction electrons is opposite to that of the d electrons and sensitive to the nearest-neighbor environment of the iron atoms.

The magnetic properties of manganese alloys are difficult to predict, in large part because the moments may be either localized or delocalized. Their magnetic structures typically are complicated and not completely resolved. An example is Ni_3Mn, which is non-magnetic in the disordered state and magnetic in the (Cu_3Au, $L1_2$ (cP4)) ordered state (Goldman, 1953). A manganese alloy in the which the moments are localized

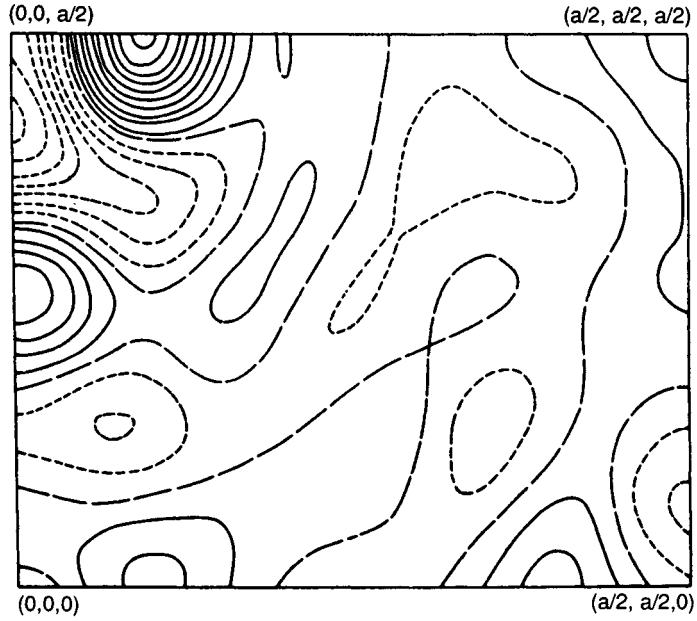

Figure 4. Projection of excess scattering density above calculated spherical density in the (1 1 0) plane of Fe_3Al. This illustrates the different magnetic electron symmetry of the two species of iron atoms. A pronounced deficiency is noted along the nearest-neighbor connecting line and an excess along the cube edge (After Pickart and Nathans, 1961)

is MnNi (tetragonal, CuAu ($L1_0$) structure type (tP4)), which is antiferromagnetic with Néel temperature above 600 K. The spins on nearest-neighbor manganese atoms are antiparallel and perpendicular to the tetragonal axes. The Mn moments at 77 K are $\mu_{Mn} = 4.0 \pm 0.1\,\mu_B$ and $\mu_{Ni} < 0.6\,\mu_B$ (Kasper and Kouvel, 1959).

In contrast to MnNi, the magnetic structures in Mn–Au and Mn–Si alloys indicate that the moments are partially delocalized. In the composition range near 50 at.% Mn, Mn–Au alloys have a tetragonally distorted variant of the cubic, CsCl (B2 (cP2)) crystal structure. Bacon (1962b) found that the magnetic structure is built up of ferromagnetic planes of Mn separated by planes of non-magnetic Au atoms. The manganese moments lie within the ferromagnetic sheets, $\mu_{Mn} = 4.2\,\mu_B$, whose orientation varies with composition but remains perpendicular to the shorter crystal axis. Increasing the gold content to $MnAu_2$ (complex $MoSi_2$, $C11_b$ (tI6) crystal structure) results in an atomic arrangement in which the sheets of Mn atoms are separated by two sheets of Au atoms. The Mn moments lie within ferromagnetic sheets, and the moment direction in adjacent sheets is rotated by an angle ϕ, which varies with temperature ($\phi = 51°$ at room temperature). The magnetic structure is a spiral or helical arrangement of spins with propagation vector parallel to the tetragonal axis (Herpin and Meriel, 1960).

Mn_3Si is a Heusler-type alloy with a body-centered cubic Fe_3Al ($D0_3$) type (cF16) crystal structure at low temperature. The Mn moments in Mn_3Si are delocalized, as evidenced by the magnetic structure. The spins on the two Mn atoms in the unit cell were found by Tomiyoshi and Watanabe (1975) to be arranged in a sinusoidal or a screw structure with moments $\mu_{Mn_I} = 1.72\,\mu_B$ and $\mu_{Mn_{II}} = 0.19\,\mu_B$ (Figure 5). The temperature dependence of the propagation vector is similar to that in antiferromagnetic chromium, and the modulated structure may be due to spin-density waves.

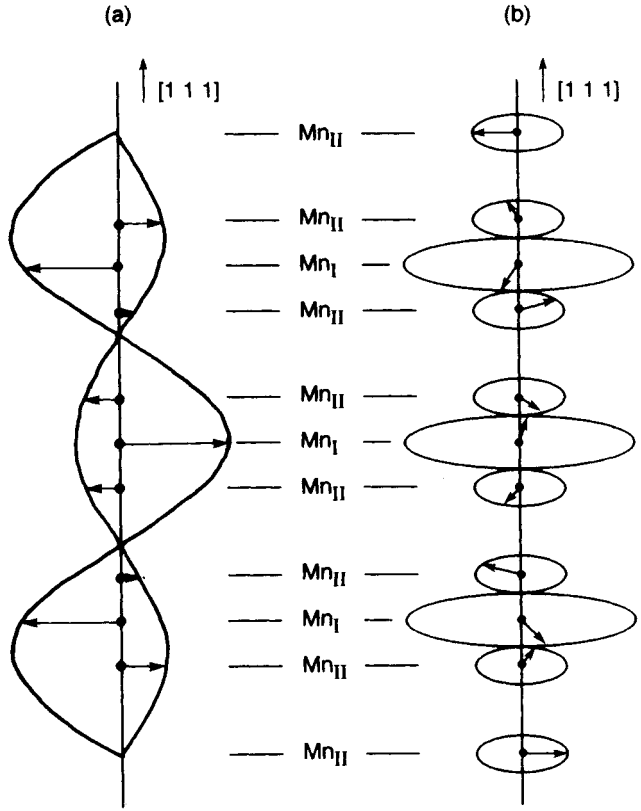

Figure 5. Magnetic structure of Mn_3Si along the ⟨1 1 1⟩ direction: (a) transverse sinusoidal structure; (b) proper screw structure (After Tomiyoshi and Watanabe, 1975)

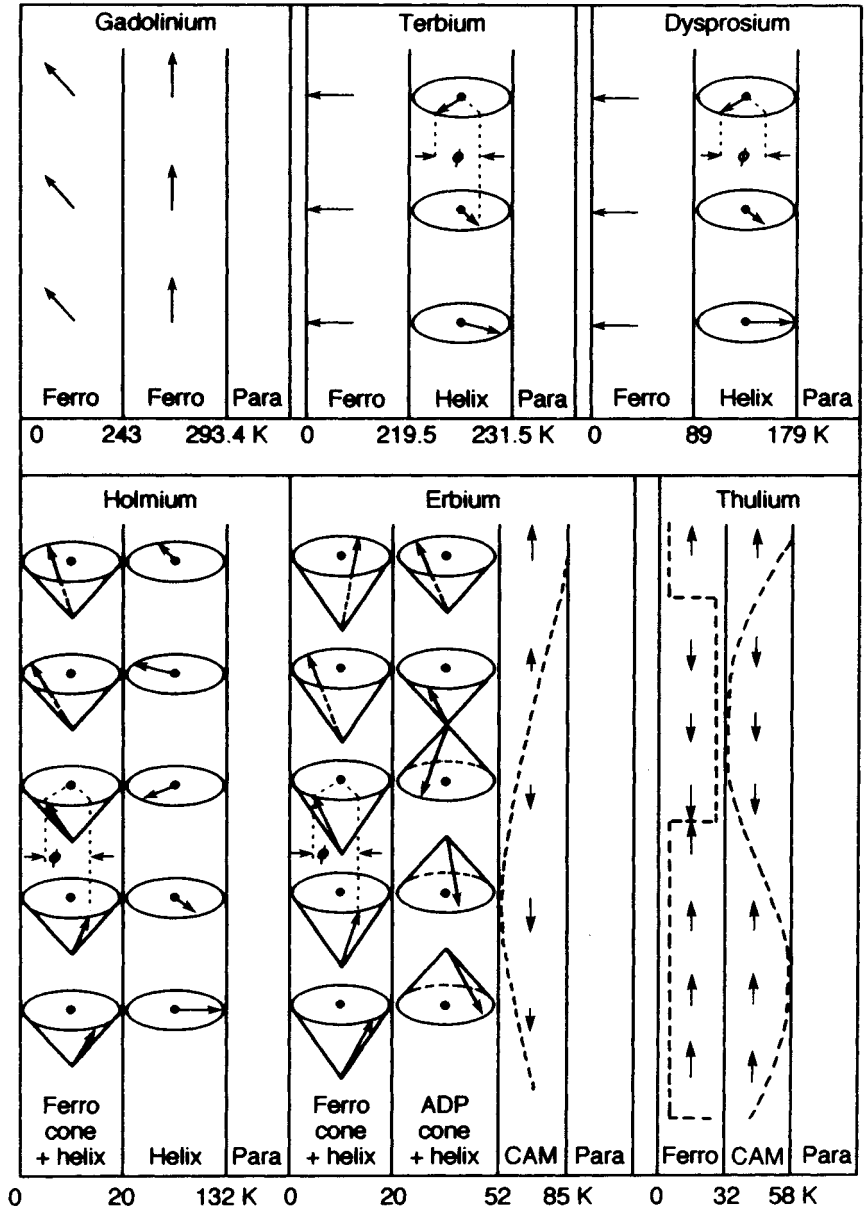

Figure 6. Magnetic ordering in the heavy rare-earth metals (After Legvold, 1980)

3.3 Rare-Earth Metals and Alloys

Magnetic structure in the rare earths is a compromise between crystal-electric-field interactions and magnetic exchange interactions of the RKKY type. With the exception of gadolinium, the atomic moments are ordered in modulated arrangements with long repetition periods. The magnitude of the propagation vectors and the spin orientations are sensitive to magnetostrictive strain, and the structures transform into a multiplicity of spin arrangements at different temperatures.

Gadolinium (h.c.p. A3 structure type (hP2)) is ferromagnetic ($T_C = 293.4$ K), and the easy direction of magnetization is parallel to the crystallographic *c*-axis at room temperature. Gd exhibits a change in magnetization at 140 K, and neutron diffraction was

used to determine if the magnetization anomaly was the result of a change in the magnetic structure. The structure is ferromagnetic at all temperatures, and the change in magnetization is the result of a change in orientation of the atomic spins (Cable and Wollan, 1968). As the temperature is lowered, the spin direction rotates from the *c*-axis, reaches a maximum deviation of 75° at 195 K, and rotates back toward the *c*-axis until the deviation has fallen to 30° at 4.2 K.

Legvold (1980) has summarized the magnetic ordering in the heavy rare earths as found by neutron diffraction (Figure 6). The magnetic structures range from the ferromagnetic arrangement found in gadolinium to complicated sinusoidal and helical structures in the elements beyond gadolinium. The magnetic periodicity is not necessarily commensurate with the crystal reciprocal lattice, and magnetic ordering may involve several sublattices.

The moments in terbium (h.c.p. A3 structure type (hP2)) form a helical arrangement in the temperature interval from 219 to 231.5 K, the Néel point, with an interlayer turn angle ~18–20°, corresponding to a periodicity of about 20 atomic layers. Terbium is ferromagnetic below 219.5 K, and the moments lie in the basal plane. Dysprosium has a helical spin structure from 179 to 89 K; it then becomes ferromagnetic with the easy axis of magnetization parallel to the crystallographic *a*-axis. The magnetic moments in holmium are parallel to the basal plane below $T_N = 132$ K and ordered in a spiral arrangement. At lower temperature the moments tilt out of the basal plane and form a conical structure. The magnetic structure of erbium is still more complicated. In addition to helical spin arrangements above 85 K, lowering the temperature results in incommensurate *c*-axis-modulated (CAM) sinusoidal arrangements, which transform to conical ferromagnetism below 20 K. The magnetic structure of thulium below 32 K is built up of antiphase domains in which four moments point up along the *c*-axis followed by three moments that point down.

The magnetic structure of neodymium is extremely complex, and, although investigated extensively, many details of the arrangement are not resolved (Moon and Nicklow, 1991). The crystal structure of neodymium is a double-hexagonal close-packed atomic arrangement (hP4), built up of alternating cubic close-packed (C) and hexagonal close-packed (H) layers. On cooling below $T_N = 19.1$ K, the spins order in an antiferromagnetic structure, which on further cooling undergoes second-order transitions to different magnetic structures at 8.2, 7.5, 6.2, and 5.7 K. The complex magnetic phase diagram is explained by competing antiferromagnetic interactions in the H and C layers. The 19 K transition is to an antiferromagnetic structure in which the spins in the H sites are ordered in longitudinally polarized incommensurate domains. The 8.2 K transition is explained by ordering of the moments on the C sites. At still lower temperature, multiple propagation vectors, multiple moment components, and multiple domains are required to represent the spin arrangements.

The magnetic structures of alloys of rare earths with other rare earths and with non-magnetic elements in general are similar to the rare-earth metals. They are explained by competition between RKKY exchange and crystal-field interactions, and the spin arrangements span a broad range of helical, cone, in-plane, and out-of-plane ferromagnetic and *c*-axis-modulated structures. The stability ranges of the magnetic structures are conveniently displayed in magnetic phase diagrams (Moon and Nicklow, 1991).

3.4 Rare-Earth Intermetallic Compounds

The magnetic structures of intermetallic compounds of rare earths (R) with transition elements (M) are the result of three types of magnetic interaction: R–R, M–M, and R–M interactions. Of these, the M–M interaction is the strongest, owing to the large radial distribution of the 3d wavefunctions and the strong overlap of the wavefunctions between neighboring atoms. The rare earths interact by spin polarization of the 4s electrons (the RKKY interaction), which is long-range and oscillatory. There is little overlap of the rare-earth 4f wavefunctions, and the R–R interactions are the weakest.

Intermetallic compounds with the Th_6Mn_{23} structure (cF116) have been studied extensively because the lattice is a good framework in which to substitute rare-earth and transition elements in order to determine the relative importance of direct exchange and RKKY exchange (Crowder and James, 1983). The crystal structure of R_6M_{23} (D8a (cF116) structure type) is built up of six octahedrally coordinated clusters of rare-earth atoms surrounded by 50 transition-metal atoms on the faces and corners of the octahedron. The transition elements, either Mn or Fe, occupy four crystallographically independent sites: b, d, f1, and f2 (Wyckoff notation). Figure 7 displays the magnetic structure of Y_6Mn_{23}. Yttrium does not carry a moment, and in Y_6Mn_{23} each of the crystallographically independent manganese atoms has a unique moment: b, 2.25 (2.81) μ_B; d, 1.72 (2.07) μ_B; f1, −1.52 (−1.79) μ_B; f2, −1.27 (−1.77) μ_B. The first moment shown is at room temperature and the second (in parentheses) at 4.2 K.

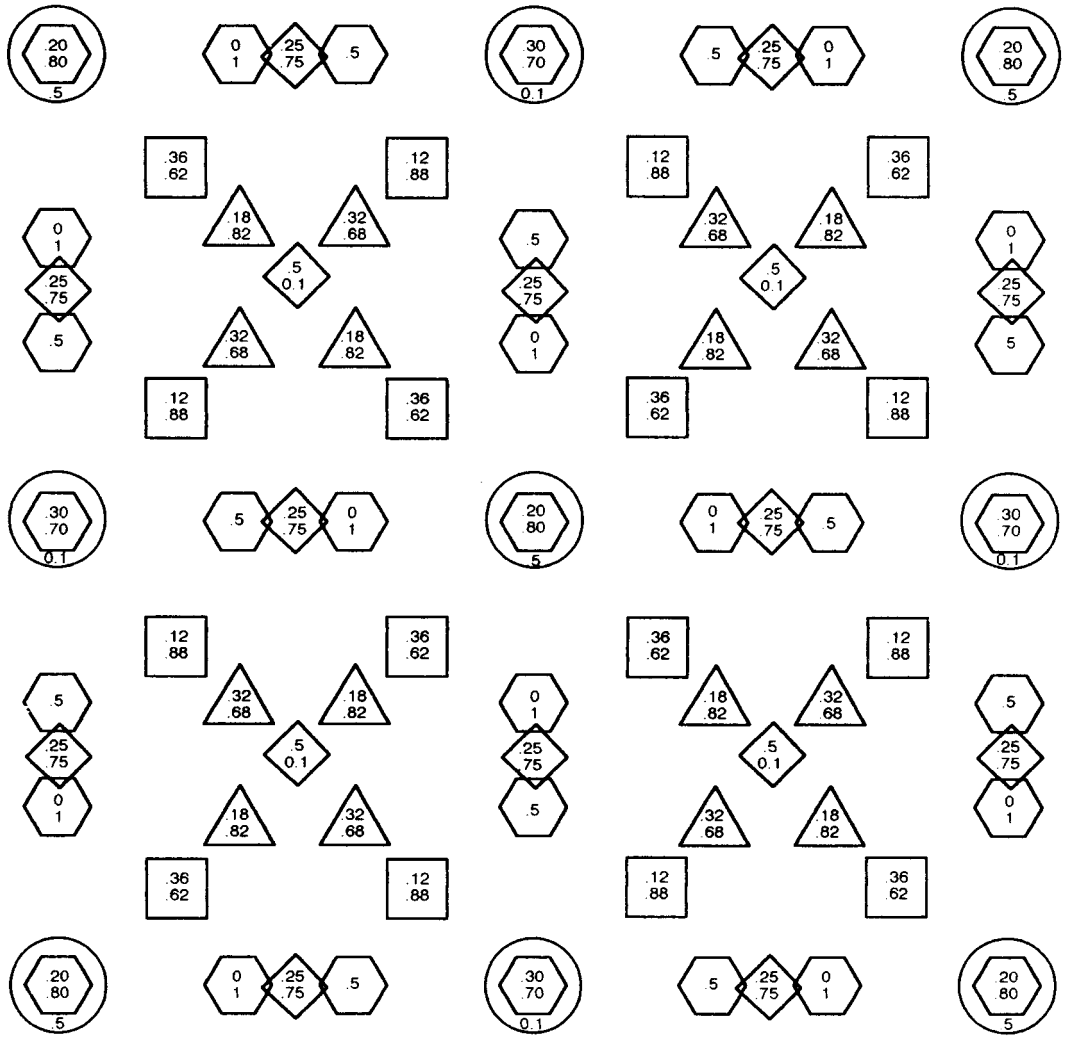

Figure 7. The Th_6Mn_{23} structure: large circle, Mn 4b site; diamond, Mn 24d site; triangle, Mn 36f_1 site; square, Mn 36f_2 site; hexagon, Y 24e site (After Crowder and James, 1983)

The moments on the b and d sites couple antiferromagnetically with those on the f1 and f2 sites. If R is a heavy rare-earth element and M = Fe, the R–M interactions are antiparallel. If M = Mn, the manganese lattice is ferrimagnetic and the rare-earth moments couple parallel to the net manganese moment.

The magnetic properties of mixed compounds, $Y_6(Fe_{1-x}Mn_x)_{23}$, are strongly dependent on composition. For example, there is a marked decrease in magnetization and Curie temperature as Mn is substituted for Fe and Fe is substituted for Mn. No magnetic order is observed, even at 4 K, for x between 0.48 and 0.69, and the structure of compounds in the intermediate concentration range has not been resolved.

Spectacular changes occur in the magnetic properties of $Y_6(Fe_{1-x}Mn_x)_{23}$ compounds that have absorbed hydrogen: Y_6Mn_{23} is ferrimagnetic with $T_C = 486$ K, but after hydrogen absorption shows no net magnetization, even at 4.2 K. The changes have been attributed to disorder and changes in the electronic structure due to the introduction of hydrogen.

Magnetic ordering in RMn_{12} compounds ($D2_b$ structure type (tI26)) is antiferromagnetic and occurs well below room temperature (magnetic properties of this family are discussed in Chapter 14 by Stadelmaier

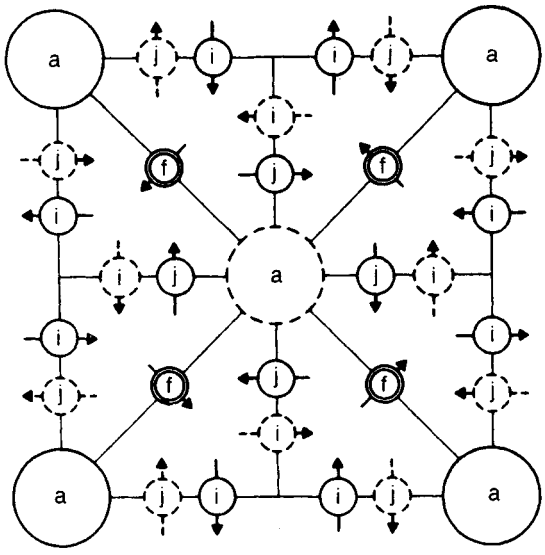

Figure 8. Magnetic structure of YMn_{12}. Y atoms on the sites 2(a) and Mn atoms on the sites 8(i) and 8(j) lie in the planes $z=0$ (full lines) or $z=1/2$ (broken lines). Mn atoms on the sites 8(f) lie in $z=1/4$ and $z=3/4$ (After Deportes *et al.*, 1977)

and Reinsch in Volume 2). The manganese moments in YMn_{12} were found by Deportes *et al.* (1977) to order in a complicated non-collinear antiferromagnetic arrangement below $T_N = 120$ K. A schematic representation of the non-collinear spin arrangement is shown in Figure 8. The mean magnetic moment of manganese is $0.4\,\mu_B$, and the magnetic interactions between the Mn moments vary strongly with the interatomic separation. The yttrium and manganese sublattices appear to order more or less independently at temperatures $T_R \ll T_N$.

3.5 Small-Scale Magnetic Order

Materials in which the atomic moments are not ordered on a long-range scale are of scientific and technological interest for investigating magnetic materials with compositions and structures that are not accessible in their crystalline counterparts. Examples of these materials are amorphous ferromagnets, spin glasses, and magnetic rare-earth 'superlattices.'

Amorphous ferromagnets are mainly alloys of transition metals with metalloids and rare earths made by very rapid quenching from the molten state (Luborsky, 1980). The atomic arrangements of amorphous ferromagnets, inferred from radial distribution functions computed from X-ray and neutron scattering intensity data, are approximated by models based on dense random packing of hard spheres. Magnetic interactions are short-range, and the local magnetic structure in systems characterized by small-scale magnetic order is expected to be about the same as in substances with long-range order. The intrinsic magnetic properties of amorphous ferromagnets are

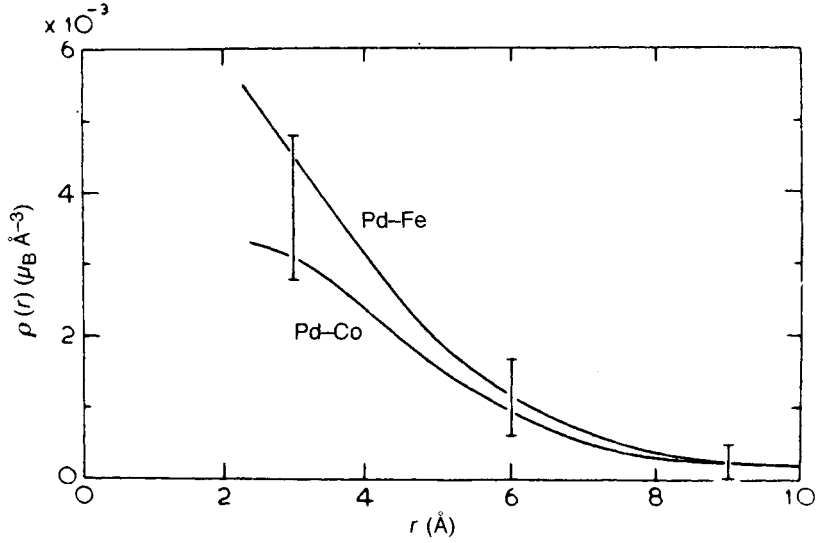

Figure 9. Magnetic moment density as a function of the distance from the solute site in dilute **Pd**Fe and **Pd**Co alloys (After Low and Holden, 1966)

consistent with assuming that the local magnetic structure is not significantly affected by the absence of a crystal lattice.

Spin-glass alloys are examples of magnetic materials in which the small concentration of the magnetic component does not allow the moments to order on a significant scale. Nuclear magnetic resonance and Mössbauer studies of the effective magnetic field in the vicinity of the magnetic atoms show that the magnetic clusters in spin-glass alloys are predominantly ferromagnetic and have very large effective moments, ~ 20 to $20\,000\,\mu_B$. The giant moments are attributed to the bare moment of the magnetic atom and a surrounding cloud of partly polarized host atoms. The existence of magnetic clusters has been confirmed by Low and Holden (1966) using diffuse magnetic neutron scattering. Figure 9 shows the magnetic moment density as a function of the distance from the solute site in disordered **Pd**Fe and **Pd**Co solid-solution alloys: the magnetic moment density peaks at the solute site, and the rest of the giant moment is spatially distributed over the matrix for a distance greater than 6 Å.

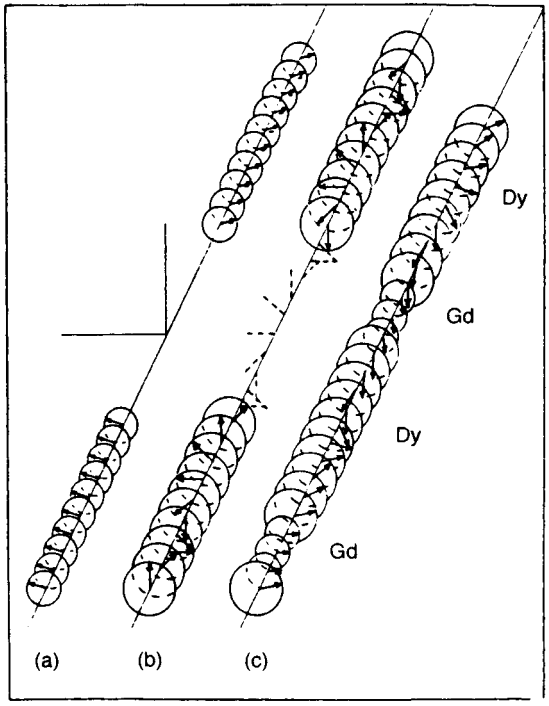

Figure 10. Schematic representation of the basal-plane component directions in three rare-earth 'superlattice' systems: (a) Gd–Y canted antiphase domain structure; (b) Dy–Y coherent, incommensurate spiral; and (c) Gd–Dy 'asymmetric' state (After Majkrzak *et al.*, 1988)

Rare-earth 'superlattices' are unusual magnetic materials in which magnetic order is long-range in two dimensions and short-range in the third dimension. Advances in molecular-beam epitaxy techniques have made it possible to grow stratified magnetic layers consisting of a discrete number of atomic planes deposited alternately with non-magnetic or other magnetic layers (Majkrzak *et al.*, 1988). These materials are of theoretical interest for investigating the consequences of reduced dimensionality and of technological interest for fabricating devices with novel magnetic properties. The magnetic structure in Dy–Y multilayers is a helical spin arrangement with the propagation vector along the *c*-axis, the same as pure dysprosium (Figure 10). Different behavior is found in Gd–Y multilayers. The Gd moments within a single layer are coupled ferromagnetically and oriented in the basal plane. In going from one Gd layer to the next, there is a phase change of either 0 or π, depending on the thickness of the intervening yttrium layer. The structure is attributed to coherent propagation by the RKKY interaction of magnetic correlations across the non-magnetic yttrium layer.

4. Remarks

Although it is not possible to formulate a general theory for predicting magnetic structure from composition and crystal structure, approximate exchange interaction models can be used to explain why the magnetic moments on a particular group of atoms interact in one way rather than another. One of the main issues that limits understanding of the magnetic structures and properties of transition-metal intermetallic compounds and alloys is determining whether in a particular collection of atoms the magnetic electrons are to be treated as localized or delocalized. A possible appoach to better understanding of the behavior of magnetic electrons is to determine the distribution of magnetic moments and spin density in model systems with polarized neutron scattering and resonance techniques with the expectation that the knowledge would provide a basis for theoretical models relating electron delocalization to composition. The magnetic structures of materials in which competing interactions lead to frustration of long-range order could be investigated with similar techniques.

5. References

Bacon, G. E. (1962a). *Neutron Diffraction*, 2nd Edn. Oxford University Press, London.

Bacon, G. E. (1962b). *Proc. Phys. Soc.*, **79**, 938.

Bertaut, E. F., Delapalme, A., Forrat, F., Roult, G., de Bergevin, F., and Pauthenet, R. (1962). *J. Appl. Phys. Suppl.*, **33**, 1123.

Cable, J. W., and Wollan, E. O. (1968). *Phys. Rev.*, **168**, 733.

Chien, C. L. (1981). In *Nuclear and Electron Resonance Spectroscopies Applied to Materials Science* (eds E. N. Kaufmann and G. K. Shenoy). North-Holland, Amsterdam.

Cox, D. E. (1973). *Magnetic Structures Data Sheets*. Prepared under the Auspices of the Neutron Diffraction Commission of the International Union of Crystallography.

Crowder, C. E., and James, W. J. (1983). A Review of the Magnetic Structures and Properties of the R_6M_{23} Compounds and their Hydrides. *J. Less-Common Met.*, **95**, 1.

Deportes, J., Givord, D., Lemaire, R., and Nagai, H. (1977). *Physica*, **86–88B**, 69.

Eddington, A. S. (1948). *The Nature of the Physical World*. Cambridge University Press, London.

Gignoux, D., and Schmitt, D. (1991). *J. Mag. Mag. Mat.*, **100**, 139.

Goldman, J. E. (1953). *Rev. Mod. Phys.*, **25**, 108.

Goodenough, J. B. (1963). *Magnetism and the Chemical Bond*. Wiley-Interscience, New York.

Herpin, A., and Meriel, P. (1960). *C. R. Acad. Sci. Paris*, **250**, 1450.

James, W. J. (1989). Neutron Scattering Characterization of Magnetic Materials. *Mater. Sci. Eng.*, **B3**, 387.

Jensen, J., and Mackintosh, A. R. (1991). *Rare Earth Magnetism: Structures and Excitations*, International Monographs on Physics, No. 81. Oxford University Press, London.

Kasper, J. S., and Kouvel, J. S. (1959). *J. Phys. Chem. Solids*, **11**, 231.

Kouvel, J. S. (1967). In *Intermetallic Compounds* (ed. J. H. Westbrook). Wiley, New York.

Legvold, S. (1980). In *Ferromagnetic Materials*, Vol. 1 (ed. E. P. Wohlfarth). North-Holland, Amsterdam, p. 183.

Low, G. G., and Holden, T. M. (1966). *Proc. Phys. Soc.*, **89**, 119.

Luborsky, F. E. (1980). In *Ferromagnetic Materials*, Vol. 1 (ed. E. P. Wohlfarth). North-Holland, Amsterdam, p. 451.

Majkrzak, C. F., Gibbs, D., Boni, B., Goldman, A. I., Kwo, J., Hong, M., Hsieh, T. C., Fleming, R. M., McWhan, D. B., Yafet, Y., Cable, J. W., Bohr, J., Grimm, H., and Chien, C. L. (1988). *J. Appl. Phys.*, **63**, 3447.

Moon, R. M., and Nicklow, R. M. (1991). *J. Magn. Magn. Mater.*, **100**, 139.

Murani, A. P., Roth, S., Radhakrishna, P., Rainford, B. D., Coles, B. R., Ibel, K., Goeltz, G., and Mezei, F. (1976). *J. Phys.*, **F6**, 425.

Mydosh, J. A., and Nieuwenhuys, G. J. (1980). In *Ferromagnetic Materials*, Vol. I (ed. E. P. Wohlfarth). North-Holland, Amsterdam, p. 71.

Nakamura, Y. and Franse, J. J. M. (eds) (1987). Magnetism of Intermetallic Compounds. *J. Magn. Magn. Mater.*, **70**, 462.

Nathans, R., and Pickart, S. J. (1963). Spin Arrangements in Metals. In *Magnetism*, Vol. III (eds G. T. Rado and H. Suhl). Academic Press, New York.

Néel, L. (1948). *Ann. Phys.*, **3**, 137.

Overhauser, A. W., and Arrott, A. (1960). *Phys. Rev. Lett.*, **4**, 226.

Pickart, S. J., and Nathans, R. (1961). *Phys. Rev.*, **123**, 1163.

Rietfeld, H. M. (1969). *J. Appl. Crystallogr.*, **2**, 65.

Ruderman, M. A., and Kittel, C. (1954). *Phys. Rev.*, **96**, 99.

Shirane, G., and Takei, W. J. (1962). *J. Phys. Soc. Japan*, **17**, 35.

Shirane, G., Chen, C. W., Flinn, P. A., and Nathans, R. (1963). *J. Appl. Phys.*, **34**, 1044.

Shull, C. G., and Yamada, Y. (1962). *J. Phys. Soc. Japan*, **17**, *Suppl.* B-III, 1.

Somerfeld, A., and Bethe, H. A. (1933). Ferromagnetism. In *Handbuch der Physik*, Vol. 24, Part II (ed. S. Flügge). Springer, Berlin.

Tomiyoshi, S., and Watanabe, H. (1975). *J. Phys. Soc. Japan*, **93**, 295.

Tustison, R. W., and Beck, P. A. (1977). *Solid State Commun.*, **21**, 517.

Weiss, P. (1907). *J. Physique*, **6**, 661.

Willis, B. T. M. (ed.) (1970). *Thermal Neutron Diffraction*. Oxford University Press, London.

Yamada, T., Kunitomi, N., Nakai, Y., Cox, D. E., and Shirane, G. (1970). *J. Phys. Soc. Japan*, **28**, 615.

This chapter was originally published in 1995 as Chapter 19 in *Intermetallic Compounds*, Vol. 1: *Principles*, edited by J. H. Westbrook and R. L. Fleischer.

Chapter 10

Quasicrystals and Related Structures

Kenneth F. Kelton

Department of Physics, Washington University, St. Louis, MO 63130, USA

1. Introduction

The icosahedron, a Platonic solid consisting of 20 slightly distorted tetrahedra packed around a common vertex, is a compact, stable, configuration (Frank, 1952), possibly explaining why this structure dominates the local symmetry of many complex crystalline intermetallic phases, and is presumed to occur frequently in undercooled liquids and glasses. It is well known, however, that the rotational symmetries of the icosahedron are incompatible with translational periodicity. It came as a tremendous surprise, then, when Shechtman *et al.* (1984) announced the unprecedented discovery of a new non-crystallographic phase in a rapidly quenched alloy of aluminum and manganese that produced diffraction patterns containing a distribution of sharp peaks showing an icosahedral rotational symmetry. These new phases, now called quasicrystals, are the subject of this chapter.

Sharp criticism of this radical interpretation of the observed diffraction patterns was quickly raised by Pauling (1985, 1987, 1988) and others (Field and Fraser, 1985; Carr, 1986; Anantharaman, 1988). Various, more conventional, explanations, ranging from twinning of ordinary crystals, to previously unknown, large-unit-cell crystals containing a significant amount of local icosahedral order, were offered. Dark-field images (Shechtman and Blech, 1985), high-resolution electron microscopy (Shechtman *et al.*, 1985; Hiraga *et al.*, 1985; Bursill and Lin, 1985; Knowles *et al.*, 1985), convergent-beam studies (Kelton and Wu, 1985; Bendersky, 1985), X-ray diffraction (Bancel *et al.*, 1985), and field ion microscopy (Melmed and Klein, 1986; Elswij *et al.*, 1988) have ruled out the possibilities of twins. Large-unit-cell crystals are more of a problem, though diffraction line widths of largely defect-free Al–Cu–Fe, an equilibrium quasicrystal, are resolution-limited; the best data would imply a crystal unit-cell size greater than 185 Å for their explanation (Bancel *et al.*, 1989).

The evidence appears to be overwhelming: quasicrystals constitute a new phase of condensed matter that is characterized by a non-crystallographic orientational symmetry and quasiperiodicity (cf. Section 2). Their non-crystallographic orientational symmetry is the key, setting quasicrystals apart from other physical systems that also exhibit quasiperiodicity, such as incommensurate crystals, which also give sharp diffraction patterns that are different from normal crystalline patterns, requiring more than three indices to index them (de Wolff, 1974; Janner and Janssen, 1977; Janssen, 1992).

Quasicrystals are now common. Besides the icosahedral quasicrystal, phases displaying other forbidden rotational symmetries have also been discovered. These include the octagonal phase (eightfold symmetry), the decagonal phase (a two-dimensional quasicrystal showing 10-fold symmetry in two dimensions but is periodic in the third), and several one-dimensional quasicrystals. Although the earliest quasicrystals were metastable, transforming upon heating to more stable crystalline phases, equilibrium quasicrystal phases have now been discovered. Some of these are largely defect-free, demonstrating the existence of long-range quasiperiodic translational order.

Most attention has centered on determining the quasilattice (the equivalent of the Bravais lattice for crystalline systems) and the atomic decorations of that lattice. We now know that quasicrystals can be related

Crystal Structures of Intermetallic Compounds. Edited by J. H. Westbrook and R. L. Fleischer

to complex crystalline phases with large cell sizes that were previously undreamed-of for metallic alloys. Why some alloys have a strong tendency to form quasicrystals and complex crystals is unknown, although some phenomenological approaches have led to the discovery of new quasicrystals. Little is known about the materials properties of these new phases, but the recent availability of better samples is leading quickly to an improved understanding; some applications are even being discussed.

In this chapter the prominent structural features of quasicrystals are discussed, placing this new class of intermetallic solids firmly within the framework of more traditional, crystalline intermetallic compounds. General characteristics, emphasizing diffraction features, of the icosahedral and decagonal quasicrystals are discussed in Section 2 and 3, related crystalline structures are discussed in Section 4, while the similarities between quasicrystals and liquids and glasses are briefly reviewed in Section 5. Real-space models are discussed in Section 6, listing the competing models for the quasilattice and the methods for decorating that framework with atoms. A very brief description of their properties appears near the end of this chapter (Section 7).

For further information, the reader is referred to the review articles and books enumerated under the heading 'Further Reading', following the list of references. A series of books entitled *Aperiodicity and Order* contains several articles on the structures of quasicrystals, their relation to other incommensurate phases, their stability and metallurgical properties, and related topics. *Quasicrystals* is a compilation of many of the early papers in the field and provides a source for many of the ideas that now guide the field. *Quasicrystals: The State of the Art* is a recent collection of review articles.

2. The Icosahedral Phase

2.1 General Metallurgy

Quasicrystals are now common; a recent compilation lists over one hundred alloys in which they have been reported (Kelton, 1993). Most familiar are the quasicrystals with icosahedral symmetry (icosahedral or i-phases), forming readily in Al–3d transition-metal (TM), i(Al–TM), and Ti–3d transition-metal, i(Ti–TM), alloys, though there have been a few reports in other systems such as i(PdUSi) (Poon *et al.*, 1985), i(CdCu) (Bendersky and Biancaniello, 1987), i(PdBi) (Lilienfeld, 1988), and i(GaMgZn) (Ohashi and Spaepen, 1987). Icosahedral phase formation has even been reported in stainless steel (Hu *et al.*, 1990).

Although first discovered by rapid quenching, quasicrystals have now been obtained by devitrification of glasses (Lilienfeld *et al.*, 1985; Holzer and Kelton, 1991), vapor condensation (Csanady *et al.*, 1987; Saito *et al.*, 1987), solidification under high pressure (Sekhar and Rajasekharan, 1986), electrodeposition (Grushko and Stafford, 1989a,b), solid-state precipitation (Nishitani *et al.*, 1986; Cassada *et al.*, 1986), interdiffusion of multilayers (Follstaedt and Knapp, 1986), mechanical alloying (Eckert *et al.*, 1989), and ion implantation (Budai and Aziz, 1986). In a few cases, the quasicrystal appears to be the equilibrium phase in a limited temperature range; these include i(AlLiCu), i(GaMgZn), i(AlCuFe), and the decagonal phases (cf. Section 3) in (Al,Si)–Co–Cu, Al–Pd–Mn, and Al–Pd–Fe alloys. There, quasicrystals can form even in slowly cooled ingots.

Most structural, metallurgical, and phase-stability studies have concentrated on the Al–TM alloys (for reviews see Schaefer and Bendersky, 1988; Kelton, 1989); the properties of the Ti–TM quasicrystals are less well known. There are many similarities between the Al–TM and the Ti–TM icosahedral phases: (a) in most cases, the i-phase occurs as a metastable phase in a multiphase mixture; (b) the grains are typically mottled with a coral-like, weakly dendritic, shape, and are usually 1 to 2 μm in diameter (Shechtman *et al.*, 1984, 1985; Kelton and Wu, 1985; Kelton *et al.*, 1988); (c) the i-phase often grows with a strong orientational relation to complex crystalline phases, suggesting a similarity in their short-range atomic order (Guyot and Audier, 1985; Koskenmaki *et al.*, 1986; Zhang and Kelton, 1991a); and (d) Si often plays an important, but little understood, role in i-phase formation (Schaefer *et al.*, 1986; Chen and Chen, 1986; Bendersky and Kaufman, 1986; Dunlap and Dini, 1986a; Sabes *et al.*, 1989; Zhang and Kelton, 1991b). There are also important differences: (a) the binary phase diagrams of the Al–TM alloys frequently contain a series of intermetallic compounds formed by peritectic reactions on the Al-rich side (Schaefer *et al.*, 1986), while Ti–TM phase diagrams are generally much simpler, with metastable quasicrystals often forming with a solid solution and simple crystalline phase; (b) the concentration of the 3d transition metal in Al–TM alloys is generally near 20 at.% (Inoue *et al.*, 1986; Schaefer *et al.*, 1986; Kimura *et al.*, 1985; Krishnan *et al.*, 1986), while it is closer to 37 at.% in the Ti–TM alloys (Sabes *et al.*, 1989); and (c) although Al–TM i-phases frequently show localized diffuse scattering in the diffraction patterns, this diffuse scattering is much stronger and occurs in all of the Ti–TM i-phases (cf. Section 2.5).

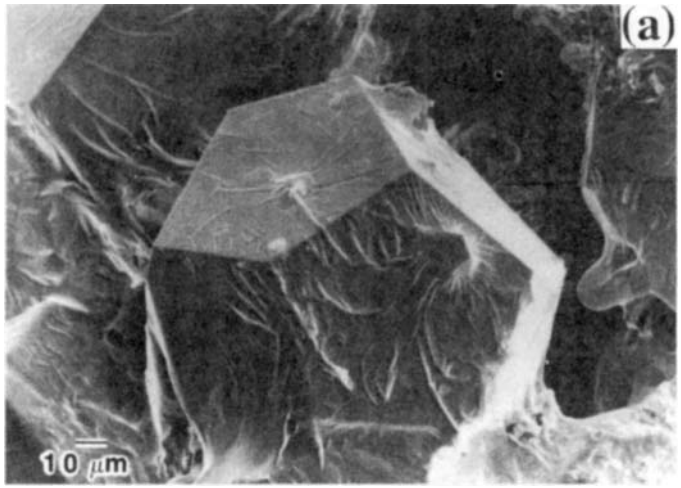

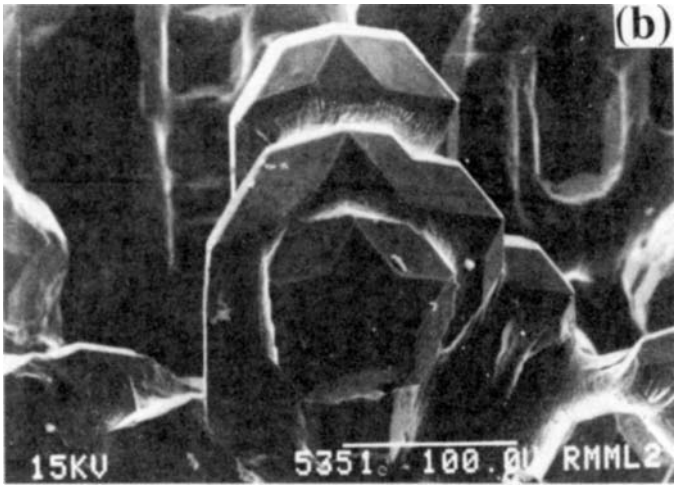

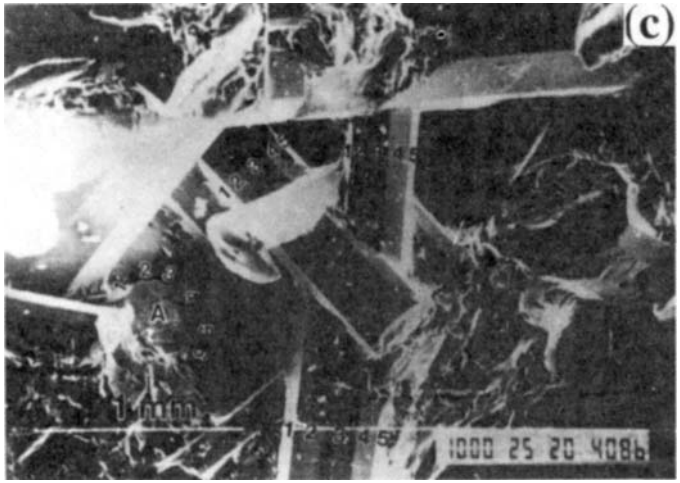

Figure 1. (a) Single grains of i(AlCuFe) with a pentagonal dodecahedral shape. (b) Grains of i(AlLiCu) with the shape of a rhombic triacontahedron (courtesy of F. W. Gayle). (c) Decaprismatic grains of decagonal (Al,Si)-Co-Cu (by permission of L. X. He)

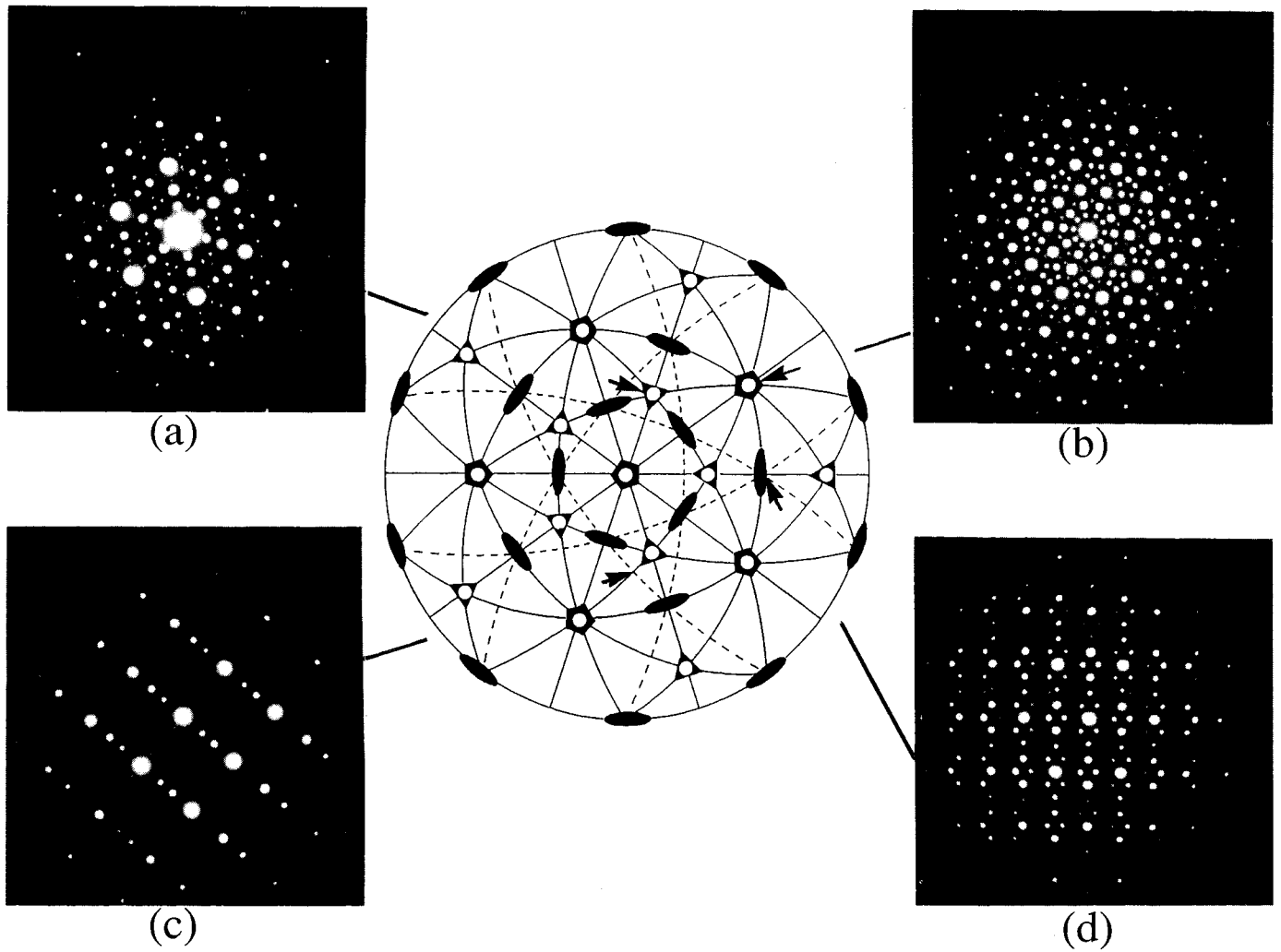

Figure 2. TEM selected-area diffraction (SAD) patterns of i(AlMn): (a) threefold; (b) fivefold; (c) $[\bar{\tau}10]$, in the notation of Chattopadhyay *et al.* (1985b); (d) twofold. Arrows are drawn from the patterns to the zone axes on the stereographic projection for which they are approximately aligned

In spite of their lack of translational periodicity, quasicrystals have a tendency to facet; several theoretical explanations for this have been offered (Jaszczak *et al.*, 1989; Ingersent and Steinhardt, 1989; Ho *et al.*, 1989; Stephens, 1989). While metastable Al–Mn i-phases develop pentagonal dodecahedral growth morphologies (Robertson *et al.*, 1986; Nishitani *et al.*, 1986; Nissen *et al.*, 1988; Yu-Zhang *et al.*, 1988a), the most striking examples of faceting are found in the stable i-phases, forming pentagonal dodecahedral grains in i(GaMgZn) (Ohashi and Spaepen, 1987) and i(AlCuFe) (Tsai *et al.*, 1987) (Figure 1(a)) and rhombic triacontahedral grains in i(AlLiCu) (Gayle, 1987) (Figure 1(b)). Stable decagonal phases frequently contain decagonal prismatic grains (Kortan *et al.*, 1989; He *et al.*, 1990) (Figure 1(c)). For most i-phases, growth from the liquid is most rapid along the threefold direction (Fan *et al.*, 1987; Nissen *et al.*, 1988; Macko *et al.*, 1988). In i(AlLiCu) (Gayle, 1987) and i(TiFeMnSi) (Zhang and Kelton, 1992), however, the fivefold direction is the direction of most rapid growth.

2.2 Diffraction

Figure 2 shows the locations and symmetries of the diffraction patterns obtained by transmission electron microscopy (TEM) rotation studies on the i-phase. The zone axes are indexed following Chattopadhyay *et al.* (1985b). This phase has the rotational symmetry of the icosahedral point group ($m\bar{3}\bar{5}$), having zones that display the expected two-, three-, and fivefold symmetric diffraction patterns, which are separated by the correct angular distances. While the fivefold diffraction pattern in Figure 2 appears to have a 10-fold symmetry, rotation studies about axes that are 36° apart produce a different sequence of diffraction patterns, demonstrating that the apparent 10-fold symmetry is actually the fivefold inversion symmetry of the icosahedron. Several high-symmetry mirror patterns are also observed; one of these, the $(\bar{\tau}10)$, is included in Figure 2.

In addition to their non-crystallographic rotational symmetry, quasicrystals are quasiperiodic. An examination along any of the axes of the fivefold pattern shown in Figure 2 shows that the ratio of distances to consecutive bright diffraction spots is an irrational number, not an integer as expected for crystals. The spots cannot, therefore, be indexed using a single length scale; instead, two incommensurate length scales, l and τl, are required, where τ is the golden mean $(\tau = (1+\sqrt{5})/2 = 2\cos(\pi/5))$, an irrational number associated with the geometries of the pentagon and icosahedron. The distances between prominent diffraction spots in the fivefold directions of the twofold patterns from most quasicrystals scale as τ^3 (Figure 3(a)). The spots at τ and τ^2 are forbidden by parity constraints (Elser, 1985a,b). Those spots are present in the diffraction patterns of a few icosahedral phases, such as i(AlCuFe), i(AlCuRu), and i(AlPdMn) (Figure 3(b)), and are explained by chemical ordering leading to centering (Ebalard and Spaepen, 1989).

The most common example of quasiperiodicity is the Fibonacci series (Struik, 1967), a one-dimensional quasiperiodic series, such as $0, 1, 1, 2, 3, 5, 8, 13, 21, \ldots$, where each successive element of the series is the sum of the previous two elements. As will be discussed in Section 2.3, the relation between this series and quasicrystals is best understood by noting that the Fibonacci series can also be represented by a particular sequence of short (S) and long (L) segments: . . .SLSLLSLSL. . ., where the ratio of the number of long to short segments equals τ. Other phases such as incommensurate crystals have the property of quasi-periodicity. Quasicrystals are set apart by their additional non-crystallographic rotational symmetry.

2.3 Projection From a Higher-Dimensional Space

The icosahedral quasiperiodic lattice is conveniently viewed as a projection from a six-dimensional (6D) hypercubic lattice onto a space that has an irrational orientation with respect to the original lattice (de Bruijn, 1981; Duneau and Katz, 1985; Elser, 1986; Kalugin *et al.*, 1985; Kramer and Neri, 1984). This technique, called the strip-projection method, allows quasicrystals and related crystalline structures to be studied, enables the systematic introduction of disorder into the quasilattice, and provides the most direct method for determining the atomic decoration. It is useful for calculating the Fourier transform of the quasiperiodic lattice, related to the diffraction peaks, thus providing a method for indexing the quasicrystal diffraction patterns.

The strip-projection method is best illustrated by considering a projection from a two-dimensional (2D) square lattice, E^2, to obtain a one-dimensional (1D) incommensurate crystal (Figure 4(a)). This also provides a useful method for describing the experimentally observed one-dimensional quasicrystals reported in (Al,Si)–Cu–Co, Al–Ni–Si, and Al–Cu–Mn (He *et al.*, 1988a; Daulton and Kelton, 1991). Here, the projection space, $x_\parallel$, is an axis that is inclined with an irrational slope to the periodic square lattice; $x_\perp$ is perpendicular to $x_\parallel$. Two additional lines are constructed parallel to $x_\parallel$, forming a window or strip denoted by $W(x_\perp)$. All

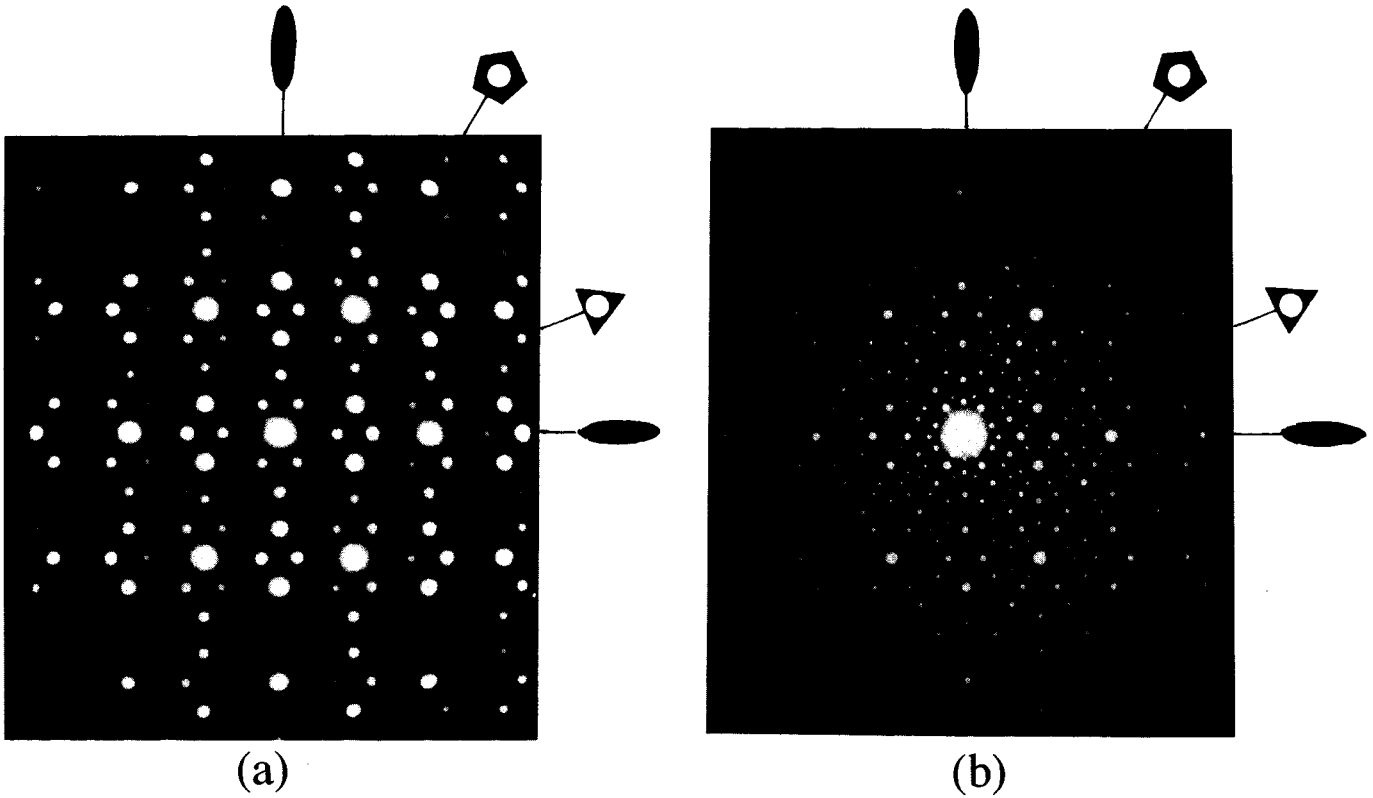

Figure 3. SAD patterns taken along the twofold direction of (a) i(AlMn), a simple i-phase, and (b) i(AlCuFe), a body-centered i-phase

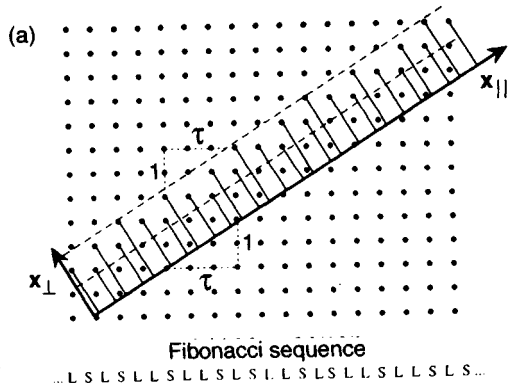

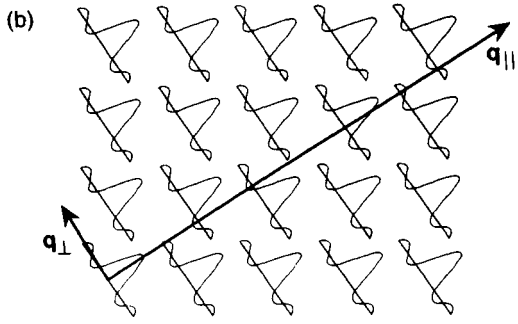

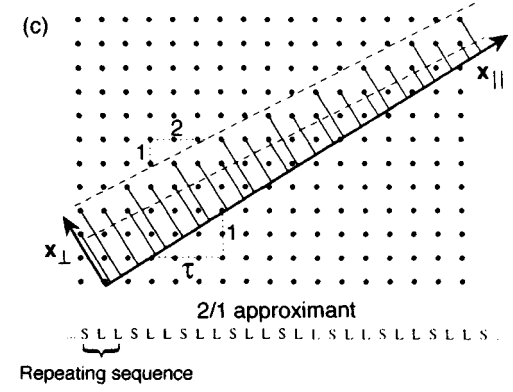

Figure 4. Projection from two dimensions to one dimension. (a) Projection in real space from 2D periodic lattice from a window onto a line, both inclined with slope τ^{-1}. (b) Projection in reciprocal space showing the intensity about each reciprocal lattice point from the Fourier transform of the window function. (c) Projection in real space with the window inclined with a slope that is a rational approximant to τ^{-1}, here 1/2; the resulting 1D structure approximates a segment of a Fibonacci sequence in each repeat distance

points of E^2 that lie within this window are projected onto $\chi_{\parallel}$ as illustrated. The width of the strip is chosen to obtain structures with physically reasonable densities, generally containing exactly one unit cell of the original lattice. The resulting structure depends critically on the angle of inclination of both the window and $x_{\parallel}$. (Note that the window and $x_{\parallel}$ are *not* constrained to have the same slope.) To preserve the fundamental length between relative projections, only the slope of the window will be changed in this chapter. The slope of $x_{\parallel}$ will be fixed at τ^{-1}.) If the slope of the window is irrational with respect to the original lattice, the projected sequence never repeats; if the slope is chosen equal to τ^{-1}, the Fibonacci sequence is obtained. If the slope of the window is taken as an integer approximant to τ^{-1}, the projected sequence of points repeats with a long period; locally the spots will follow the Fibonacci sequence (Figure 4(c)). This is called a rational approximant (cf. Section 4).

Since the subspace chosen, Z^2, is the region of E^2 truncated by $W(x_{\perp})$,

$$Z^2 = E^2(x,y) \times W(x_{\perp}) \tag{1}$$

the reciprocal lattice is given by

$$Q^2 = F[Z^2] = F[E^2(x,y)] \otimes F[W(x_{\perp})] \tag{2}$$

As illustrated in Figure 4(b), along $q_{\parallel}$, true Bragg diffraction peaks are predicted since the Fourier transform of each lattice point is a delta function. The intensity of the diffraction spot is determined by the amplitude of the Fourier transform along $q_{\perp}$, which is $f(g_{\perp}) = \sin(g_{\perp}L)/g_{\perp}L$, within normalizations and phase factors for this simple case. Spots near the projection window, therefore (with low values of $g_{\perp}$), are more intense than those farther away (high values of $g_{\perp}$). Even though the projection space is densely filled, those spots with $g_{\perp}$ greater than some value will not be observed.

The strip-projection method has limitations. It can only produce a limited subset of the possible quasilattices and, except for special cases, it cannot be used to calculate the diffraction pattern from a decorated quasilattice. A more general approach, the cut-projection method proposed by Bak (1986), obtains the projection by the intersection of the lower-dimensional space with a basis embedded in the higher-dimensional space. More complicated structures are then possible and chemical decorations are readily obtained by changing the basis in the hypercubic lattice. The strip projection is a special case of this method.

2.4 Projections and Diffraction-Pattern Indexing

For a crystalline diffraction pattern, the position of any diffraction peak can be indexed by the integer multiples h, k, l (the Miller indices) of three basis vectors (**a**, **b**, **c**), which are inversely related to the physical vectors defining the unit cell. Owing to the incommensurability of the length scales, six vectors are required to index the diffraction patterns from the icosahedral phase. Two indexing schemes for the icosahedral phase are used most frequently. One, due to Elser (1985a,b), emphasizes the structural relations to the icosahedron; the other, due to Cahn *et al.* (1986), emphasizes the relations to cubic symmetry.

Let $\mathbf{a}^1$ to $\mathbf{a}^6$ be the unit basis vectors of a six-dimensional cubic lattice (E^6). The construction of a quasicrystal, with a fivefold rotational axis, requires that E^6 be projected onto the three-dimensional parallel space, $E^3_\parallel$, so that the projected basis vectors, $\mathbf{e}^1_\parallel$ to $\mathbf{e}^6_\parallel$, point to six vertices of an icosahedron as defined in Figure 5. This is accomplished using a projection matrix **P**

$$\mathbf{P} = \frac{1}{2\sqrt{5}} \begin{bmatrix} \sqrt{5} & 1 & 1 & 1 & 1 & 1 \\ 1 & \sqrt{5} & 1 & -1 & -1 & 1 \\ 1 & 1 & \sqrt{5} & 1 & -1 & -1 \\ 1 & -1 & 1 & \sqrt{5} & 1 & -1 \\ 1 & -1 & -1 & 1 & \sqrt{5} & 1 \\ 1 & 1 & -1 & -1 & 1 & \sqrt{5} \end{bmatrix} \tag{3}$$

giving

$$(\mathbf{e}^1_\parallel, \ldots, \mathbf{e}^6_\parallel) = \sqrt{2}(\mathbf{a}^1, \ldots, \mathbf{a}^6)\mathbf{P} \tag{4}$$

The basis vectors in the perpendicular space, $E^3_\perp$, are found using the projector $\mathbf{P}' = \mathbf{I} - \mathbf{P}$:

$$(\mathbf{e}^1_\perp, \ldots, \mathbf{e}^6_\perp) = \sqrt{2}(\mathbf{a}^1, \ldots, \mathbf{a}^6)\mathbf{P}' \tag{5}$$

Since a vector in the 6D space has components in the parallel and perpendicular spaces, the factor of $\sqrt{2}$ in both equations is required if the basis vectors in the 3D and 6D spaces have unit magnitude.

The Bragg vector for each diffraction peak can be expressed as a linear combination of the basis vectors, multiplied by integer indices and scaled by some prefactor,

$$\mathbf{g}_\parallel = g_0 \sum_{i=1}^{6} n_i \mathbf{e}^i_\parallel \tag{6}$$

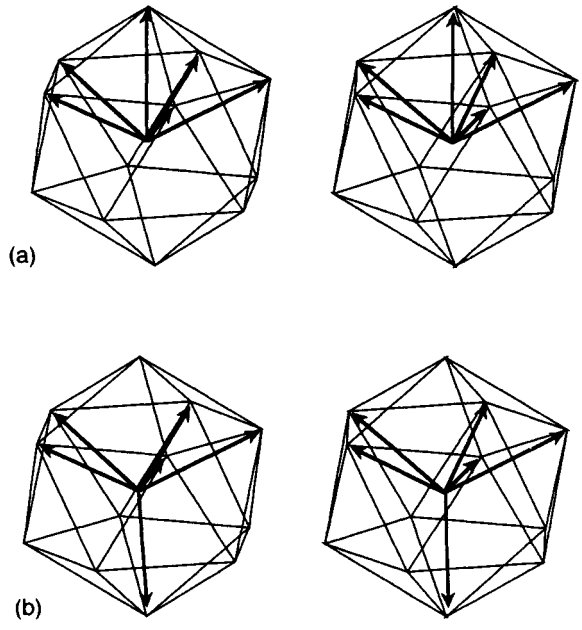

Figure 5. A stereopair showing the icosahedral basis vectors used in the Elser indexing scheme: (a) for the parallel space and (b) for the perpendicular space. To see the 3D image, stare at a point between the left and right figures and cross your eyes. This stereopair may also be viewed with stereoglasses if the figure is photocopied and the members of the pair are exchanged (by permission of T. L. Daulton)

Owing to their incommensurability, the choice of the prefactor g_0, is not unique in quasicrystals; it can only be determined to within a factor of τ^3 (Elser, 1986). One popular choice for i(Al–Mn) (Elser, 1986) takes the weak peak at $q = 0.68$ Å along the fivefold axis as the fundamental (100000), giving $g_0 = \pi/a_R$, where a_R is the edge length of the rhombohedral bricks in the Penrose tiling model of a quasicrystal (cf. Section 6). Bancel *et al.* (1985) assigned the fundamental to the bright spot at $q = 2.894$ Å, producing an indexing scheme that differs from Elser's by a scale factor of τ^3.

The basis vectors may be expressed using different coordinate systems. Elser arbitrarily chose the z-axis to lie along $\mathbf{e}^1_\parallel$, giving

$$\mathbf{e}^1_\parallel = (0, 0, 1) \tag{7}$$

$$\mathbf{e}^n_\parallel = \left(\sin\beta \cos\left[\frac{2}{5}\pi(n-2)\right], \sin\beta \sin\left[\frac{2}{5}\pi(n-2)\right], \cos\beta\right)$$

where $\cos\beta = 1/\sqrt{5}$ and $n = 2, \ldots, 6$. These vectors point to the upper vertices of an icosahedron (Figure 5(a));

the vectors in the perpendicular space, $\mathbf{e}_\perp$, are oriented as shown in Figure 5(b).

It is often convenient to express the basis vectors in the parallel and perpendicular spaces using a coordinate system aligned with three perpendicular twofold axes of the icosahedron (Cahn *et al.*, 1986). This is particularly convenient for indexing cubic crystalline approximants (cf. Section 4). The unit vectors in $E^3_\parallel$ and $E^3_\perp$ are related to the basis vectors in the 6D lattice by a rotation matrix, **R**,

$$(\mathbf{a}^x_\parallel, \mathbf{a}^y_\parallel, \mathbf{a}^z_\parallel, \mathbf{a}^x_\perp, \mathbf{a}^y_\perp, \mathbf{a}^z_\perp) = (\mathbf{a}^1, \ldots, \mathbf{a}^6)\mathbf{R} \tag{8}$$

where

$$\mathbf{R} = \frac{1}{\sqrt{2(2+\tau)}} \begin{bmatrix} 1 & \tau & 0 & -1 & \tau & 0 \\ \tau & 0 & 1 & \tau & 0 & -1 \\ 0 & 1 & \tau & 0 & -1 & \tau \\ -\tau & 1 & 0 & \tau & 1 & 0 \\ 1 & 0 & -\tau & 1 & 0 & \tau \\ 0 & -\tau & 1 & 0 & \tau & 1 \end{bmatrix} \tag{9}$$

The six columns of the top three rows of **R** give the 3D coordinates of the 6D basis vectors, projected into the physical space, $\mathbf{e}_\parallel$. The columns of the bottom three rows give the 3D coordinates of $\mathbf{e}_\perp$. Noticing the form of the vertex vectors expressed within this coordinate system, Cahn *et al.* (1986) introduced an indexing system that employs three pairs of integer indices $(h/h', k/k', l/l')$, where $h/h' = h + h'\tau$, $k/k' = k + k'\tau$, and $l/l' = l + l'\tau$.

2.5 Structural Defects

The X-ray diffraction peaks from the i-phase are generally broad, indicating a considerable amount of structural disorder. Frequently they are shifted from their expected positions, with the least intense spots (largest value of $\mathbf{g}_\perp$) deviating most. This is due to a novel type of disorder, not found in crystalline phases, called a phason strain (Levine *et al.*, 1985; Lubensky *et al.*, 1985, 1986; Socolar *et al.*, 1986), originating from the three additional degrees of freedom in the quasicrystal arising from its incommensurability. Phason strain arises from non-uniform displacements in the perpendicular space; within the quasilattice model (cf. Section 6.1), this is equivalent to modifications in the local tiling arrangements (Socolar *et al.*, 1986).

Phason strain is also evident in the real-space structures. For example, viewing the high-resolution electron microscopy (HREM) image shown in Figure 6(a) at a grazing incidence shows rows of contrast spaced in a Fibonacci sequence and aligned along the five twofold directions. Locations where the rows of contrast shift discontinuously (jog) arise from phason strain. The high density of jogs in this rapidly quenched quasicrystal indicate a high density of phason strain, a conclusion supported by the broad peaks and peak shifts observed in its diffraction patterns.

The essential features of phasons can be obtained using a density-functional approach (Levine *et al.*, 1985; Lubensky *et al.*, 1985). The mass density of atoms is given by

$$\rho(\mathbf{r}) = \sum_q \rho_q \exp(\mathrm{i}\mathbf{q}\cdot\mathbf{r}) = \sum_q |\rho_q| \exp(\mathrm{i}\phi_q) \exp(\mathrm{i}\mathbf{q}\cdot\mathbf{r}) \tag{10}$$

Since $\rho(\mathbf{r})$ is real, $\rho^*_q = \rho_{-q}$, and $\phi_q = -\phi_{-q}$. Minimizing the free energy with respect to the phases of the density waves fixes all but six of the phases, generally expressed in terms of the six possible degrees of freedom:

$$\phi_q = \sum_{i=1}^{3} q^i_\parallel u_i + \sum_{i=1}^{3} q^i_\perp w_i \tag{11}$$

where $q^i_\parallel$ and $q^i_\perp$ are the components of the real-space and perpendicular-space reciprocal lattice vectors, respectively. The u_i are displacements in real space, phonons in normal crystalline materials, and the w_i are the displacements in the perpendicular space, the phasons. The peak displacements and the large peak widths are explained by linear variations in the phason field. Assuming that $\mathbf{w} = \mathbf{M}\cdot\mathbf{r}$, where **M** is a second-rank tensor (the phason strain tensor), peak positions at **g** are shifted by $\Delta\mathbf{g} = \mathbf{g}_\perp \cdot \mathbf{M}$, proportional to $\mathbf{g}_\perp$ rather than $\mathbf{g}_\parallel$, as would be the case for an elastic strain in the phonon field (Warren, 1990). Diffraction peaks also frequently show a strong shape anisotropy (Kelton *et al.*, 1988; Zhang and Kelton, 1990, 1991a; Heiney *et al.*, 1987; Bancel and Heiney, 1986; Urban *et al.* 1986). These can arise from a superposition of shifted peaks from different domains of the sample with different phason strain fields (Socolar and Wright, 1987), or from an extremely fine-grained, multiply twinned rhombohedral structure (Audier and Guyot, 1988). Supporting the former view, diffraction patterns taken from small domains show no spot anisotropy and have peak shifts consistent with a uniform phason strain. High-$\mathbf{g}_\perp$ diffraction peaks in patterns taken from large regions, presumably containing several domains, are not shifted, but have a triangular shape, owing to the superposition of diffraction peaks from the regions of different phason strain.

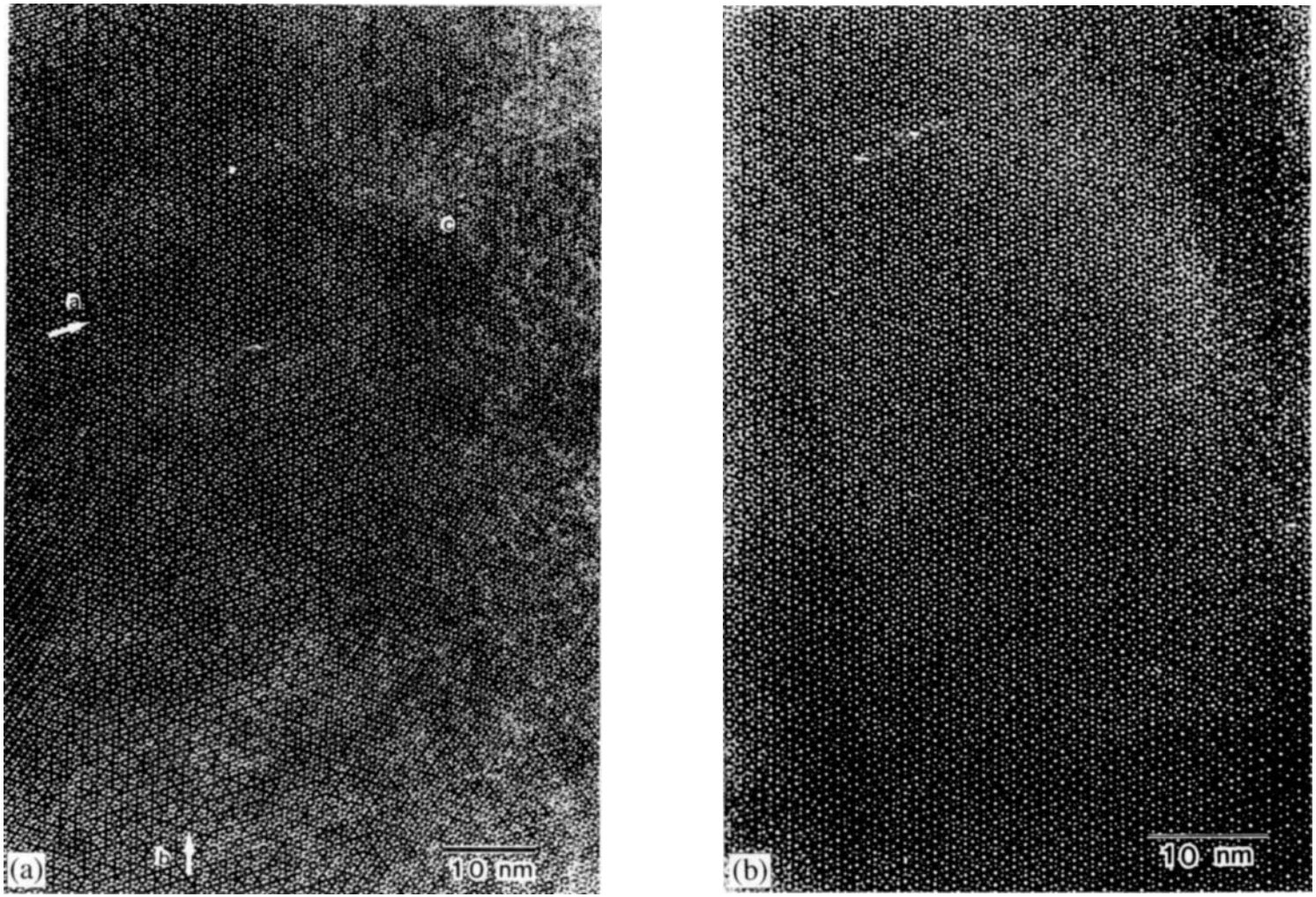

Figure 6. High-resolution electron microscopy images of (a) i(AlMn), showing many jogs and defects, and (b) i(AlCuFe), showing few defects (Courtesy of K. Hiraga)

Non-uniform spatial displacements set up elastic deformations that carry an energy penalty. Similarly, phasons change the local atomic configuration (leading to tiling flips within a tiling model; cf. Section 6) and are also energetically costly. While the elastic strain can relax quickly by phonon modes, phason strain relaxation requires atomic diffusion, giving a very slow relaxation rate. Phason strain fields resulting from sample preparation, therefore, should remain relatively unchanged, leading some to suggest in the early days of the field that defect-free quasicrystals could not be obtained experimentally. With the discovery of the stable i-phases, however, this view changed. It is now possible to obtain essentially phason-strain-free samples by annealing slowly cooled i(AlCuFe) and i(AlCuRu). Their narrow resolution-limited diffraction peaks, implying a coherence length for quasiperiodic order that exceeds 8000 Å (Bancel *et al.*, 1989), demonstrate that disorder is not an inherent property of quasicrystals. As shown in Figure 6(b), this order is also evident in HREM images; this image is virtually free from the jogs shown in Figure 6(a).

Structural defects, including slightly misoriented domains, twins, stacking faults, and dislocations, are also found in quasicrystals. Like crystal dislocations, dislocations in quasicrystals (Devaud-Rzepski *et al.*, 1989; Ebalard and Spaepen, 1990; Zhang *et al.*, 1990; Wollgarten *et al.*, 1992; Zhang and Zhaung, 1992; Yu *et al.*, 1992) exhibit diffraction contrast that vanishes for particular diffraction vectors, enabling a determination of the direction of their Burgers' vector, **b**, representing the displacement field in the quasilattice. The column approximation is used to determine the conditions for extinction in crystals (Hirsch *et al.*, 1977), by determining the scattering amplitude at some point P on the bottom of the sample by the scattering within a column that is 10 to 20 Å in diameter. Extinction is determined by the phase factor, Γ,

$$\Gamma = \exp[2\pi i(\mathbf{g}\cdot\mathbf{u} + sz)] \tag{12}$$

where s is a parameter characterizing the deviation of the defect-free lattice from the Bragg orientation, z is a coordinate along the column, **g** is the diffraction vector, and **u** is the displacement-field vector in the column. In crystals, the condition for extinction is that this phase factor be minimized, given by $\mathbf{g}\cdot\mathbf{b} = 0$, where **b** is the Burgers' vector of the dislocation. Urban *et al.* (1993) extended this analysis to quasicrystals, properly assigning perpendicular and parallel components for both **g** and **b**, and deriving the analogous condition for extinction:

$$\mathbf{g}_{\parallel}\cdot\mathbf{b}_{\parallel} + \mathbf{g}_{\perp}\cdot\mathbf{b}_{\perp} = 0 \tag{13}$$

Two cases must be distinguished: (a) the weak extinction in which the phonon and phason phaseshifts inside the column are nonzero, but mutually cancel, i.e. $\mathbf{g}_{\parallel}\cdot\mathbf{b}_{\parallel} = -\mathbf{g}_{\perp}\cdot\mathbf{b}_{\perp}$; and (b) the strong extinction in which the phase terms are individually zero, i.e. $\mathbf{g}_{\parallel}\cdot\mathbf{b}_{\parallel} = \mathbf{g}_{\perp}\cdot\mathbf{b}_{\perp} = 0$. Both extinction conditions have been observed (Urban *et al.*, 1993; Wollgarten *et al.*, 1992; Yu *et al.*, 1992). Interestingly, while the strain field of dislocations in i-phases is preferentially localized in planes in both parallel and reciprocal space, the amplitude in the perpendicular space is almost an order of magnitude larger.

Strong localized diffuse scattering has been observed in diffraction patterns taken along twofold zones (Figure 7(a)); it is absent in the three- and fivefold patterns. Weak diffuse scattering was first observed following low-temperature annealing in Al–Mn (Mukhopadhyay *et al.*, 1987); it is particularly strong and present in all titanium-based quasicrystals (Kelton *et al.*, 1988; Zhang and Kelton, 1990, 1991a; Kelton and Gibbons, 1993). In all cases, the arcs of diffuse scattering are centered on odd-parity spots normally missing in the simple icosahedral reciprocal lattice. Detailed studies of the arcs in $Ti_{61}Mn_{37}Si_2$ (Gibbons *et al.*, 1989) have shown that the arcs are formed by intersections of the Ewald sphere with approximately spherical surfaces of diffuse scattering in reciprocal space that are invariant under the rotational symmetry of the icosahedral point group. The origin of the scattering is unknown. Chemical ordering (Chattopadhyay and Mukhopadhyay, 1987; Henley, 1988; Mukhopadhyay *et al.* 1989a), topological disorder (Goldman *et al.*, 1988; Gibbons and Kelton, 1992; Robertson and Moss, 1993), phason strain (Levitov, 1988), and the presence of extremely small grains of another phase (Kelton *et al.*, 1989) have been suggested. If the diffuse scattering arises from chemical ordering, the intensity should be less in the Ti-based quasicrystals owing to the similarities of the atomic structure factors. That the opposite is found indicates that chemical ordering models are suspect. This conclusion is supported by recent studies showing no effect of alloying on the arc intensity or location in titanium quasicrystals (Gibbons and Kelton, 1992). The icosahedral glass model (cf. Section 6) provides the best agreement with the observed diffuse scattering (Figure 7(b)), suggesting that topological disorder is the cause (Gibbons *et al.*, 1989). Annealing of the Al–Mn i-phase, however, leads to the appearance of the odd-parity spots inside the rings of diffuse scattering, supporting a chemical ordering

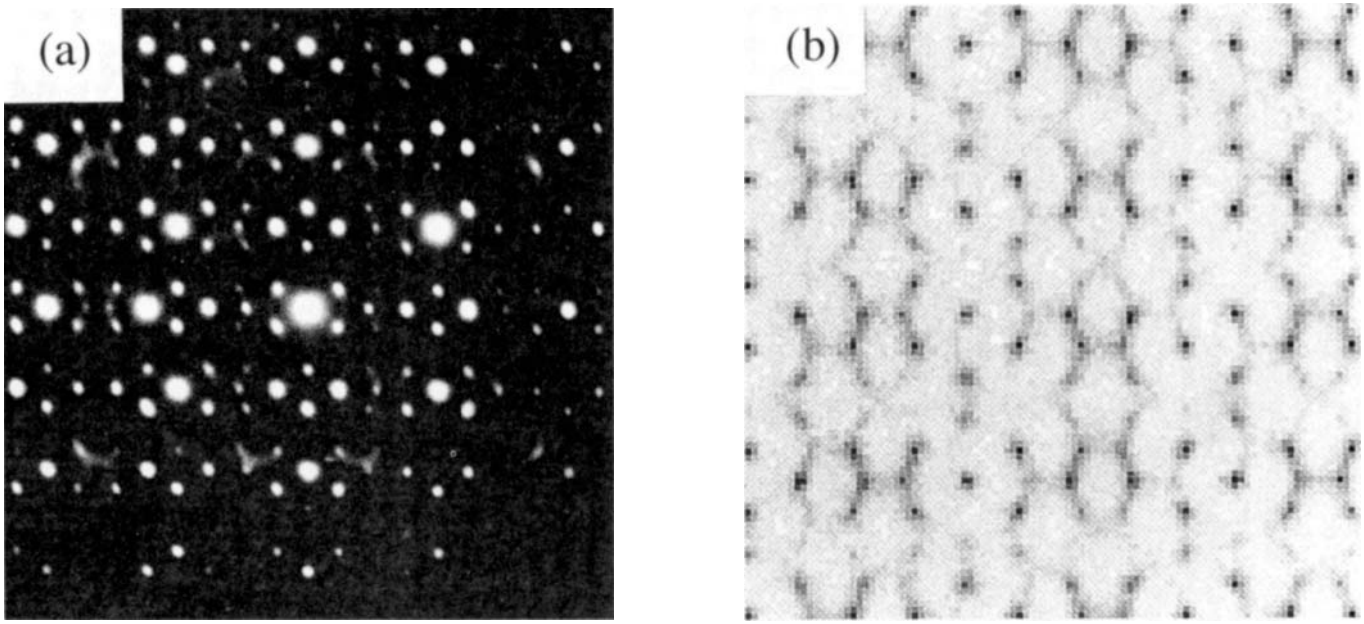

Figure 7. (a) SAD pattern taken along the twofold direction of i(TiMnSi) showing strong localized diffuse scattering. (b) Calculation of twofold pattern, from icosahedral glass model, demonstrating agreement with (a)

argument (Mukhopadhyay *et al.*, 1989a), although annealing might also decrease the topological disorder.

2.6 Phase Transformations

Most quasicrystals are metastable; upon thermal annealing at sufficiently high temperatures, they transform to other phases with lower free energies. This phase transition is typically first-order, proceeding by nucleation and growth, though apparently continuous transformations have been reported in some cases (Chattopadhyay and Mukhopadhyay, 1987). It is also generally irreversible. Detailed crystallization studies have been made on only a few systems, primarily Al–Mn and Ti–Mn alloys. The transformation mode, the kinetics, and the products depend strongly on the alloy composition (Bagley and Chen, 1985; Kimura *et al.*, 1986; McAlister *et al.*, 1987; Yu-Zhang *et al.*, 1988b), as does the stability of the i-phase (Chen and Chen, 1986; Schaefer *et al.*, 1986; Dunlap and Dini, 1985, 1986b; Kelton and Holzer, 1988a). The transformation products for Al–Mn alloys are typically Al_6Mn, Al_4Mn, and α-Al, an f.c.c. solid solution. Based on a detailed study of the transformation kinetics, Kelton and Holzer (1988a,b) placed a lower bound for the interfacial energy between the i-phase and Al_6Mn of $0.03\ J\ m^{-2}$, much smaller than a typical orientationally averaged interfacial energy between unlike crystalline phases, but similar to the interfacial energies between a crystal and its melt (Turnbull, 1950; Kelton, 1991). The icosahedral phase in $Ti_{61}Mn_{37}Si_2$ crystallizes to a series of previously unknown, complicated crystalline phases, that appear to be constructed from different packings of the fundamental icosahedral clusters found in the i-phase (Holzer *et al.*, 1989; Levine *et al.*, 1992).

Chattopadhyay and Mukhopadhyay (1987) first suggested that quasicrystals might transform by passing through a series of rational approximants, complex crystalline phases that approximate the local structure of the quasicrystal (cf. Section 4). Since long-wavelength phasons locally modify the atomic structure, they might 'lock' into special values to produce these approximants (Ishii, 1989). There is some evidence for such phason-based transformations. Annealing studies in rapidly quenched (Al,Si)–Cu–Co suggest a continuous evolution from the decagonal phase (cf. Section 3) to different crystal approximant phases (Daulton and Kelton, 1991). Further, reversible transformations have been observed in quasicrystals that are stable at high temperature, to crystalline phases that are stable at lower temperatures. X-ray and TEM investigations of i(AlCuFe) suggest the onset of a structural transformation at $\approx 670°C$ to a lower-symmetry phase, possibly an extremely fine-grained (≈ 100 Å) rhombohedral phase (Audier and Guyot, 1988, 1989a; Zhang *et al.*, 1991a). The intensities of the high-$g_\perp$ peaks increase dramatically during the transformation, possibly indicating a soft phason mechanism analogous to the more familiar phonon softening mode for some phase transformations in crystals (Bancel, 1989). The order of this transformation is not known, but there are theoretical reasons to suspect that it is first-order (Ishii, 1990). There is no evidence for nucleation, though several reports of the development of a modulated quasicrystal during the transformation (Audier *et al.*, 1991) suggest that the phase transition may be spinodal (Liu and Köster, 1993).

3. Decagonal Phase

3.1 General Metallurgy

Other than the i-phase, the best-studied quasicrystal is the decagonal phase (also often called the t-phase), which has a 10-fold rotational symmetry in the quasiperiodic plane, while being periodic in the third dimension. The point-group symmetry for most decagonal phases is 10/m or 10/mmm (Bendersky, 1985), belonging to the cylindrical family of groups G_1. The decagonal phase is closely related to the icosahedral phase, often growing in competition with, and sometimes epitaxially on, that phase. In many ways it can be considered as an approximant structure to the i-phase. Intense activity has focused recently on the study of the decagonal phase, partially because it is felt that the reduction in the dimensionality of the quasiperiodicity might make structural determinations possible.

Chattopadhyay *et al.* (1985a) and Bendersky (1985) first identified the decagonal phase in rapidly quenched Al–Mn alloys. Subsequently, decagonal phase formation has been reported in many alloys, mostly aluminum-based (see Kelton, 1993). Though icosahedral phase formation has been reported in many titanium–transition-metal alloys, there are no substantiated reports of decagonal phase formation there.

Like the i-phase, the decagonal phase typically is metastable, generally formed by rapid quenching, where it frequently occurs with the i-phase, solid solution phases, and complicated monoclinic and orthorhombic

crystalline phases. Ledges or steps are often found in TEM images, suggesting a lateral growth mechanism (Portier *et al.*, 1985; Gronsky *et al.*, 1985). The grain size varies from 0.1 μm to a few micrometers depending on the sample composition and the quench conditions (Chattopadhyay *et al.*, 1985a; FitzGerald *et al.*, 1988; Daulton *et al.*, 1991). TEM images typically show striations that vanish when viewed along the 10-fold

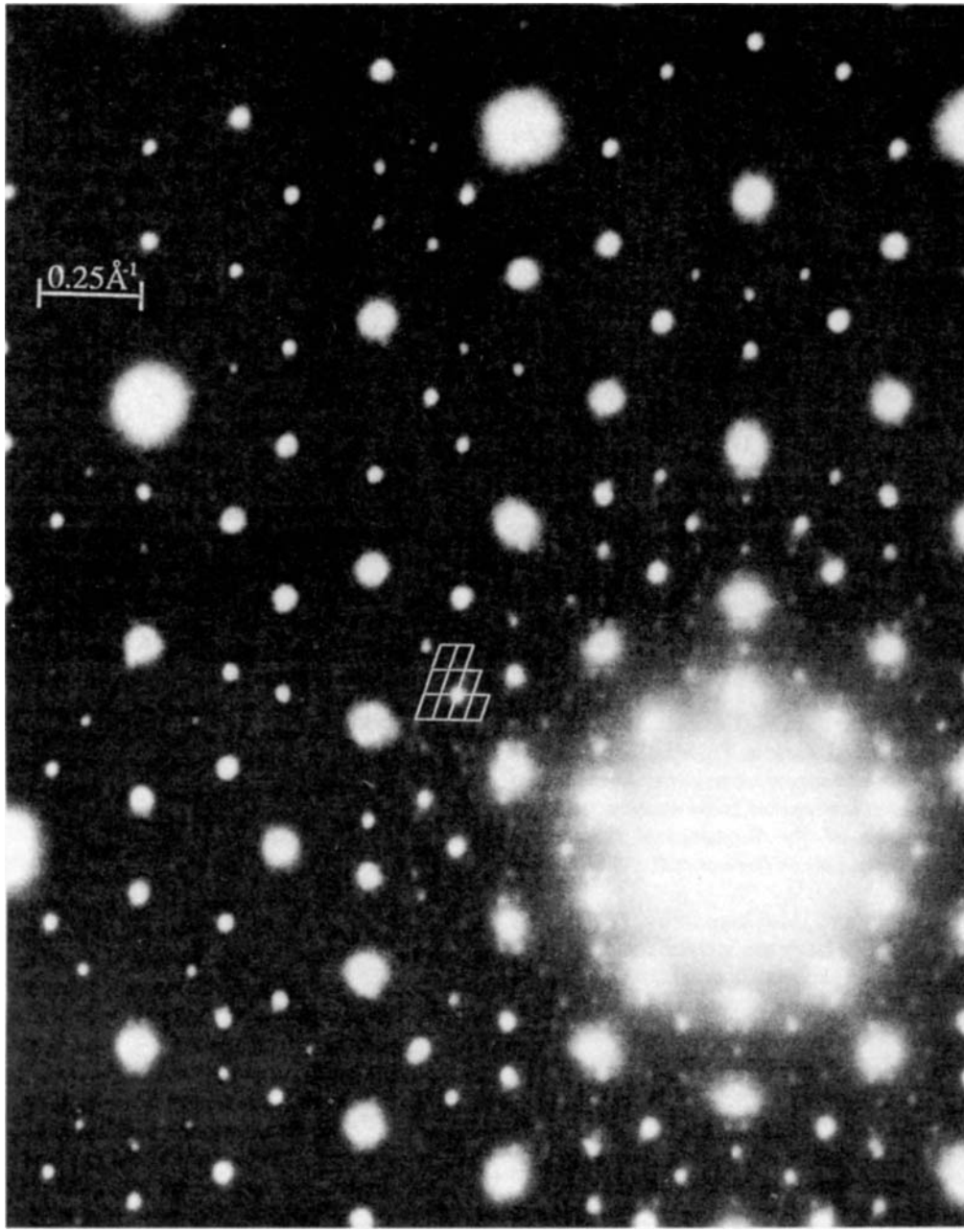

Figure 8. SAD pattern taken along the pseudo-10-fold direction of a decagonal approximant phase in (Al,Si)–Co–Cu. Part of the rhombic lattice of periodic diffraction spots has been emphasized. They correspond to an edge length of the crystal unit cell of order 100 Å (Taken from Daulton *et al.*, 1992a)

zone axis, suggesting planar defects (Perez-Campos *et al.*, 1986; Daulton *et al.*, 1991). Like the i-phase, other defects, including twins, dislocations, dislocation loops, and planar faulting, have also been observed (Suryanarayana and Menon, 1987; Menon and Suryanarayana, 1988). A variety of microstructures have been reported, including rosette, nodular, cellular-dendritic, and plate-like grain morphologies (Suryanarayana and Menon, 1987; Inoue *et al.*, 1987; Dong *et al.*, 1987a; Li and Kuo, 1988). There are two alloys in which the decagonal phase is believed to be stable: (Al,Si)–Co–Cu and Al–Pd–Mn. In these, the phase forms with a beautiful grain morphology, decagonal prismatic needles several millimeters in length (Menon and Suryanarayana, 1988; Hiraga *et al.*, 1992) (see Figure 1(c)).

As in many icosahedral-phase-forming alloys, Si sometimes plays a necessary, but poorly understood, role in phase selection. In Al–Mn, for example, the addition of only a few atomic percent of Si can completely suppress decagonal phase formation (Ranganathan and Chattopadhyay, 1987). In contrast, it improves decagonal phase formation in Al–Co–Cu alloys, where complex crystalline phases with diffraction patterns virtually identical to those from the decagonal phase often form without its addition (Launois *et al.*, 1991; Dong *et al.*, 1991; Hiraga *et al.*, 1991b; Daulton and Kelton, 1991, 1992; Daulton *et al.*, 1992a) Figure 8, for example, shows a pseudo-10-fold diffraction pattern taken from one of these crystals. The rhombic array of weak periodic spots highlighted on the figure indicates a phase with a periodicity in one dimension of almost 100 Å; a complete structural determination is lacking. Increasing the amount of Si further, beyond 4.5 at.% in this alloy, leads to a one-dimensional quasicrystal (Daulton and Kelton, 1991).

If proper account is taken of the sample thickness and TEM defocus condition, HREM images taken along the 10-fold zone can provide an accurate representation of the quasiperiodic structure. Figure 9(a), for example, shows an HREM image of the decagonal phase in (Al,Si)–Co–Cu. The light and dark regions represent the average of the electron density projected along the direction parallel to the incident electron beam. A characteristic feature is the pentagonal arrangement of small cluster-like features, forming wheels. Similar cluster-like objects are observed in scanning tunneling microscopy (STM) images of the quasiperiodic plane (Figure 9(b)), though the wheels are not as evident, indicating that they likely arise from a projection of the atoms from several layers. The STM image clearly shows steps (the jagged lines), supporting the notion of a ledge-growth mechanism.

3.2 Diffraction

The diffraction patterns from the decagonal phase strongly resemble patterns obtained from the icosahedral phase, indicating a structural similarity between these two phases. Figure 10 shows the prominent zone axes from an irreducible section of the stereographic project for the Al–Mn decagonal phase. A 10-fold rotational symmetry with quasiperiodic diffraction spots is obtained along direction A. A rotation to a location for an equivalent pattern in the i-phase reveals a pseudo-fivefold pattern (J). Pseudo-threefold patterns are also located at the approximate locations for true icosahedral threefold patterns (M and I). Two different twofold patterns separated by 18° (G and H) are both located 90° from A; G is similar to the icosahedral twofold pattern, while H is an approximation to the $(\bar{7}10)$ of the i-phase (see Figure 2). In G and H, the diffraction spots along the line pointing to A are periodic. In the perpendicular direction, the peak locations follow a Fibonacci series, establishing that this structure is quasiperiodic in two dimensions and periodic in the third.

The twofold patterns of many decagonal phases show pronounced streaking perpendicular to the periodic axis (Bendersky, 1985), indicating planar defects in the quasiperiodic plane, in agreement with the TEM image studies mentioned previously. In Al–Fe, the streaking is parallel to the 10-fold zone, suggesting stacking faults along the periodic direction (Fung *et al.*, 1986).

Decagonal phases can be classified on the basis of their periodicity: 0.4 nm in Al–Ni (Li and Kuo, 1988), 0.8 nm in Al–Cu–TM (TM = Mn, Fe, Co or Ni) (He *et al.*, 1988b, 1989), 1.24 nm in Al–Mn and Al–Mn–Pd (Bendersky, 1985; Beeli *et al.*, 1991), and 1.6 nm in Al–Fe (Fung *et al.*, 1986). All of these periodicities have been reported as a function of composition in Al–Co (Menon and Suryanarayana, 1988) and $Al_{65}Cu_{20}TM_{15}$ (TM = Mn, Fe, Co or Ni) (He *et al.*, 1988b, 1989) and in the same alloy of $Al_{65}Cu_{20}Co_{15}$ (He *et al.*, 1988c). That all periodicities are multiples of 0.4 nm suggests that decagonal phases are layered structures, built from stackings of nearly identical atomic planes. Detailed studies of the complete stereographic projections (Daulton and Kelton, 1992, 1993a; Daulton *et al.*, 1992b) imply two classes of decagonal phases: (1) those with 0.8 nm, 1.6 nm, and presumably 0.4 nm periodicities; and (2) the 1.24 nm periodic phases.

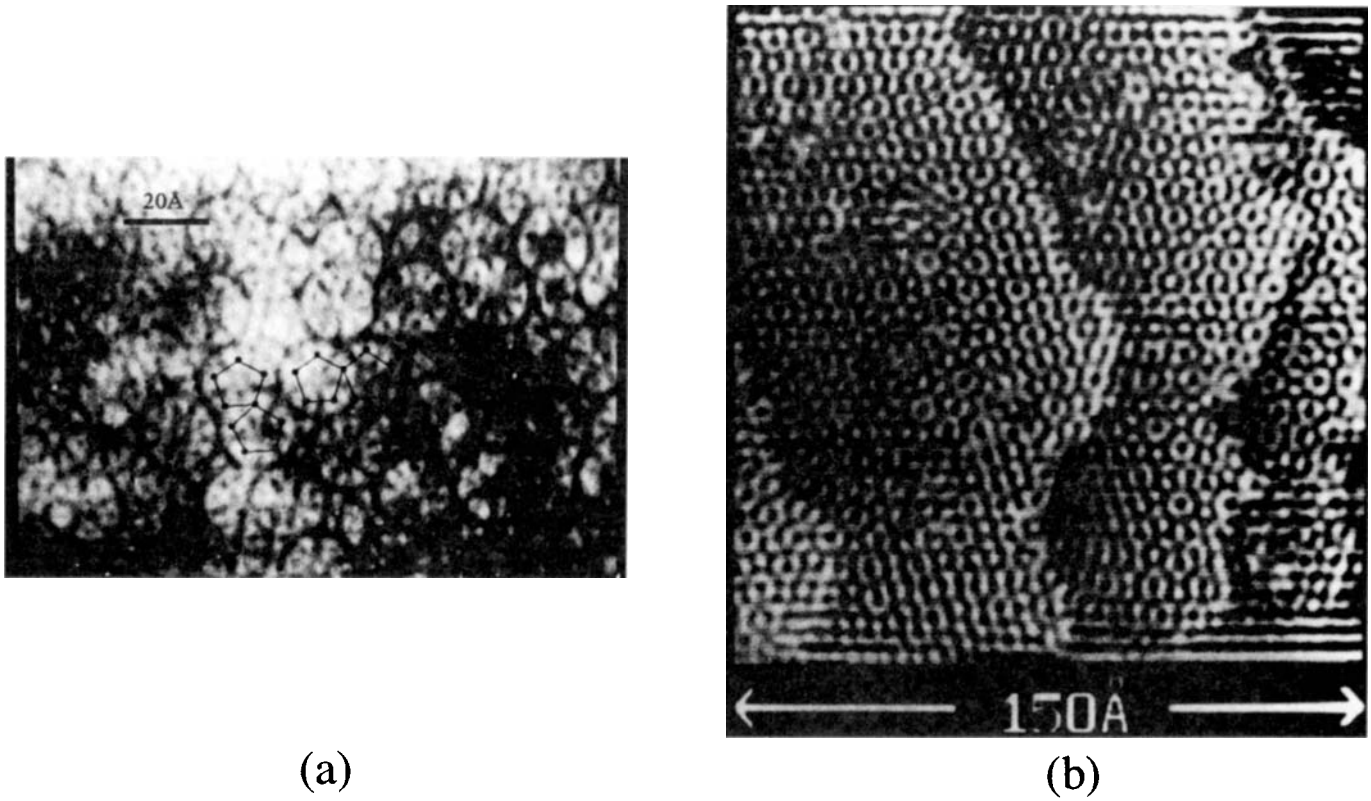

Figure 9. (a) High-resolution electron microscopy (HREM) lattice image of decagonal (Al,Si)–Co–Cu. The pentagonal arrangement of clusters is emphasized. (b) Scanning tunneling microscopy (STM) image of layer of the same decagonal phase, showing evidence for clusters and ledges (Reproduced with permission from Kortan *et al.*, 1990)

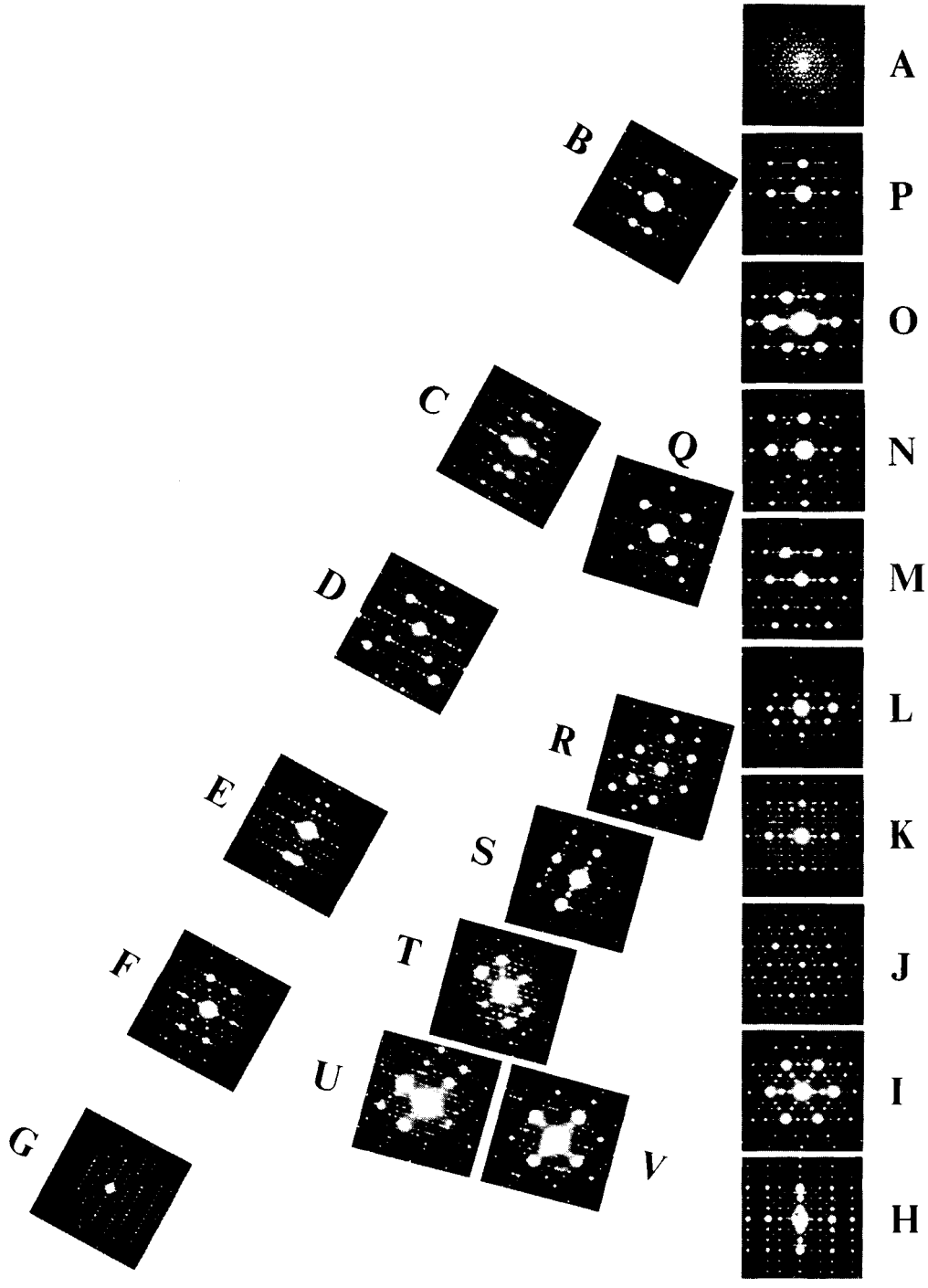

Figure 10. Irreducible 18° section of the stereographic projection of the decagonal phase in Al–Mn, showing the diffraction patterns from all pseudozones (Taken from Daulton *et al.*, 1991)

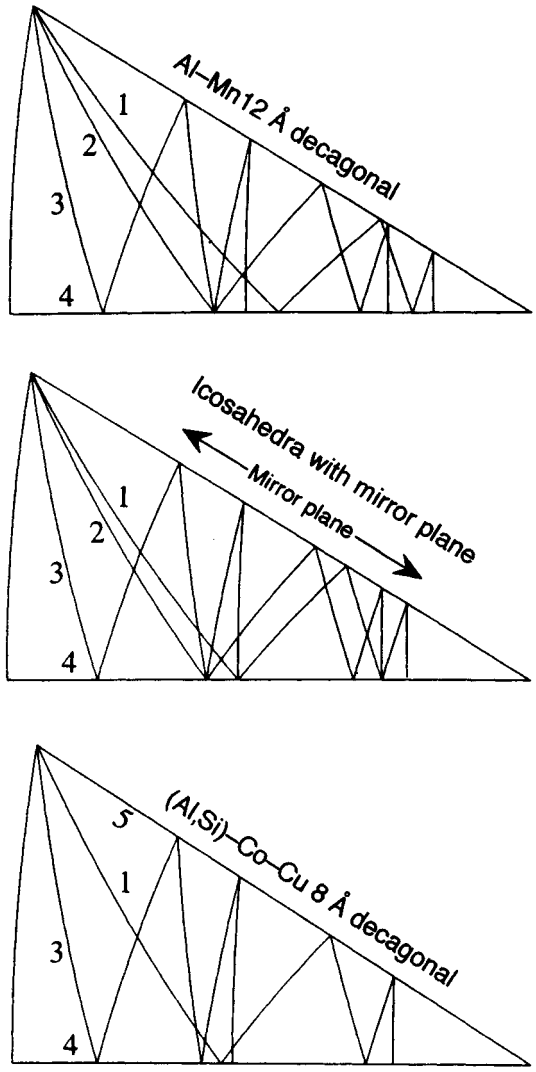

Figure 11. Schematic of the irreducible 18° section of the stereographic projections, showing the locations of the Kikuchi bands for (a) the 12 Å Al–Mn decagonal phase, (b) a perfect icosahedron with the insertion of a mirror plane, and (c) the 8 Å (Al,Si)–Co–Cu decagonal phase. The numbers in the figure label the great circles of the stereograph. Great circle number 5 is missing in the Al–Mn phase and in the icosahedral mirror-plane construction. Great circle 2 merges with great circle 1 in the (Al,Si)–Co–Cu phase

Figure 11(a) shows a diagram of the irreducible 18° stereographic section for decagonal Al–Mn or Al–Mn–Pd, indicating the intersections of the great circles constructed from the Kikuchi bands. While the stereographic projection of the decagonal phase resembles that predicted by the addition of a mirror plane to the icosahedral rotational point-group symmetry (Figure 11(b)), there are systematic shifts in the positions of the great circles between the two projections. These inconsistencies are removed if the icosahedron is distorted along the line connecting two of the opposite vertices taken to point in the periodic direction (Daulton and Kelton, 1992; Daulton *et al.*, 1992b). Figure 11(c) shows a schematic diagram of the stereographic section for the 8 Å (Al,Si)–Co–Cu phase. One of the great circles has vanished and the positions of the others are shifted from their positions in Al–Mn, consistent with a different magnitude of distortion. The decagonal phase, then, appears itself to be an approximant to the icosahedral phase. The Al–Mn or Al–Mn–Pd decagonal phases appear to be better approximants to the i-phase than is the (Al,Si)–Co–Cu decagonal phase, since the required distortion in (Al,Si)–Co–Cu removes the intersection at J, eliminating the pseudo-fivefold symmetry.

The availability of large single crystals of the decagonal phase in (Al,Si)–Co–Cu and Al–Pd–Mn has allowed precision X-ray studies of the structure to be made (Steurer and Kuo, 1990; Steurer, 1991). The pentagonal arrangements of clusters in this layered structure, indicated in the STM and HREM images (Figure 9), are evident in the projected electron densities, reconstructed using a Patterson function analysis.

3.3 Diffraction-Pattern Indexing

The restriction that one direction of the decagonal phase be periodic reduces the required number of basis vectors from six to five (one along the periodic direction and four in the quasiperiodic plane). While one might imagine that this would simplify the task of indexing the diffraction patterns, no scheme currently exists that can unambiguously index both the reciprocal lattice diffraction patterns and the real-space zone axes.

One method, similar to the four-vectors approach used to index hexagonal crystalline phases, employs six basis vectors (Takeuchi and Kimura, 1987; Choy *et al.*, 1988). A set of five reciprocal lattice vectors are arranged in the basal, quasiperiodic plane, separated by 72°; the sixth vector is perpendicular to the other five, pointing along the decagonal periodic direction:

$$\begin{aligned} \mathbf{a}_j^* &= a^* R_j(\theta)\mathbf{x} \\ \mathbf{a}_6^* &= c^*\mathbf{z} \end{aligned} \tag{14}$$

where $\mathbf{R}_j(\theta)$ represents a rotation about the z-axis through the positive (counter-clockwise) angle $(j-1)\theta$. This procedure has been used to index the diffraction

patterns of the 8, 12 and 16 Å decagonal phases, though an inherent ambiguity exists, giving rise to several proposed methods for correctly choosing the indices (Mukhopadhyay *et al.*, 1989b; Ranganathan *et al.*, 1989; Daulton *et al.*, 1991).

The zone axes for all decagonal phases can be indexed unambiguously using 11 vectors pointing to the vertices of a properly distorted icosahedron (Daulton and Kelton, 1992; Daulton *et al.*, 1992b). This representation can be reduced to a five-vector set using simple symmetry arguments. The five-vector method discussed previously is a special case, corresponding to a particular distortion of the icosahedral cluster that has not been observed. At this time, however, this method has not been used to index the zone axes and the diffraction patterns consistently.

Muller (1987), considering projection methods for obtaining the decagonal phase, showed that a projection from a five-dimensional space produces a point-group symmetry C5, lacking the required mirror symmetry. Two schemes have been proposed for a six-dimensional projection. Ho (1986) originally suggested that the projection be made from an oblique 6D lattice, and Mandal and Lele (1991) proposed a 6D tetragonal lattice. Neither method was able to describe satisfactorily all diffraction features of the decagonal phase.

4. Crystalline Approximants

Many complex crystalline phases contain large clusters of atoms in a nearly perfect tetrahedral coordination. Similar clusters have been inferred in the structures of liquids, glasses, and quasicrystals. These crystal phases, called crystal approximants, are closely related to quasicrystals, forming under similar conditions and

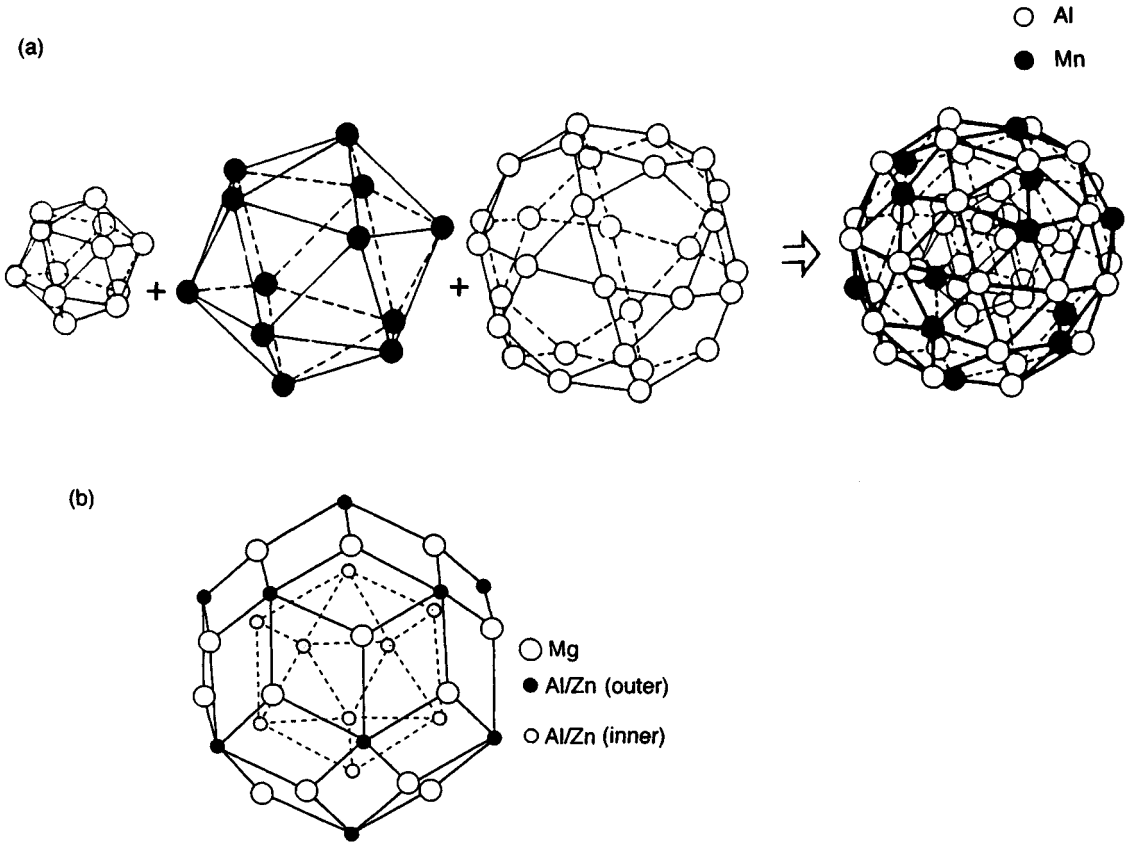

Figure 12. Fundamental clusters in 1/1 crystal approximants to the i-phase. (a) The construction of the 54-atom Mackay icosahedron for i(AlMn). The center is vacant in α(AlMnSi); it is filled in α(TiCrSi). (Taken from Audier and Guyot, 1989b). (b) The Pauling triacontahedron, the fundamental cluster for i(AlMgZn); the atom types are indicated (Taken from Mukhopadhyay *et al.*, 1989c)

Index

Note: compounds are listed in this index in strict alphabetic sequence, e.g. AlNi **not** NiAl.

Note: Figures and Tables are indicated [in this index] by *italic page numbers*